# ALS associated mutations in ANXA11 cause distal axonopathy, disrupt calcium signalling, and influence RNA dynamics in patient derived motor neurons

Hedges, Erin

*Awarding institution:*
King's College London

# ALS associated mutations in *ANXA11* cause distal axonopathy, disrupt calcium signalling, and influence RNA dynamics in patient derived motor neurons

**Erin C. Hedges**

Thesis submitted in fulfilment of the degree of Doctor of Philosophy

Department of Basic & Clinical Neuroscience

Institute of Psychiatry, Psychology, and Neuroscience

King's College London

2022

***Abstract***

The neurodegenerative disease amyotrophic lateral sclerosis (ALS) is characteristically heterogeneous in both genetic causality and cellular pathology. In ALS, the upper and lower motor neurons that mediate voluntary movement degenerate and die. The associated clinical phenotype presents as loss of control of movement, resulting in gradual paralysis, with a predicted survival time of only three to five years. Multiple genetic mutations have been associated with disease onset, and mutations in the gene *ANXA11* were recently shown to cause a subset of ALS cases. Neuronal functions of the corresponding protein, Annexin A11, are not well defined, and the cellular phenotypes associated with *ANXA11* ALS mutations are poorly understood.

Utilisation of induced pluripotent derived stem cells (iPSCs) to generate disease relevant cell types enables the comparison of dysregulated cellular pathways in patient and heathy cells, however iPSC models of many ALS associated genes do not exist, including for *ANXA11*. To address this, iPSCs were generated from five ALS patients with previously identified non-synonymous single nucleotide polymorphisms in *ANXA11*, and five sex-matched control individuals. Novel iPSC lines were subject to quality control analysis to ensure that they were pluripotent in nature and had maintained genomic stability in the reprogramming process. Efficient differentiation of iPSCs into motor neurons was established, alongside optimisation of motor neuron-astrocyte co-culture to generate a disease relevant platform for subsequent analyses.

Initial characterisation of *ANXA11* patient and control neuronal cultures included high-throughput protein localisation analysis of Annexin A11, as well as disease hallmark TDP-43 and phosphorylated TDP-43. This was completed in motor neuron monocultures and motor neuron-astrocyte co-cultures at two time points. Protein characteristics varied across culture conditions, however did not indicate any striking disease associated protein phenotype in *ANXA11* patient motor neurons. Spontaneous calcium activity in motor neuron-astrocyte co-cultures was shown at two time points and indicated an increased calcium fluctuation propensity in some *ANXA11* patient-derived lines, which was not mirrored by any change in electrophysiological readout. Neurite outgrowth analysis revealed

comparable neurite characteristics in young motor neurons, however utilisation of microfluidic devices indicated reduced integrity of distal axons in *ANXA11* ALS motor neurons.

Annexin A11 localises to stress granules and has a role in tethering RNA binding proteins (RBPs) to lysosomes to enable RBP transport along axons. To interrogate RNA dynamics in *ANXA11* patient motor neurons, stress granule analysis was completed. Annexin A11 localised to G3BP1 positive stress granules in motor neurons, and reduced stress granule formation propensity was seen in *ANXA11* R235Q motor neurons compared to control. Global axonal RNA transport velocity was assessed, revealing an increase in RNA transport velocity in patient motor neurons. A role of Annexin A11 in local translation was hypothesised due to its function in tethering RBPs to membrane bound vesicles, and the distal axon phenotype identified in microfluidic devices. Annexin A11 was shown to localise to focal points of translation in ribopuromycylation analysis, and Annexin A11 and the ALS associated protein FUS localised to overlapping sites of local translation in motor neurons. Using microfluidics to compartmentalise distal axons, Annexin A11 and FUS protein were assessed at sites of local translation in control and *ANXA11* patient motor neurons. This highlighted increased Annexin A11 signal and decreased FUS signal at sites of local translation in patient lines, and a potential reduction in co-localisation.

Collectively these data implicate *ANXA11* ALS mutations in a multilevel pathology, whereby dysregulation of overlapping cellular pathways collectively lead to motor neuron vulnerability. Many of the implicated pathways are associated with other genetic forms of ALS, highlighting overlapping cellular perturbations across the ALS spectrum.

## *Author's declaration*

I hereby declare as the author of this thesis, submitted for the degree of Doctor of Philosophy, this work is my own composition and that the data presented here is original work completed by me. Exceptions to this are as follows:

**Chapter 3**

G-band karyotyping was completed by TDL Genetics (The Doctors Laboratory, U.K.) or The Genome Editing and Embryology Core Facility (King's College London, U.K.). STR analysis was completed by Source Bioscience (U.K.) and Sanger sequencing was completed by GATC (Eurofins, Germany).

**Chapter 4**

Electrophysiological analysis of motor neurons was completed by Dr Seung Chan Kim.

This work has not been submitted for fulfilment of any other degree.

**Erin Hedges**, September 2022

***Acknowledgment***

This work was made possible by funding from the **Motor Neurone Disease Association** and I am so grateful that I was given the opportunity to embark on this project alongside my first job as a Scientist. I am thankful to the **patients** who have made donations so that others might benefit from their generosity.

I remember enrolling to this PhD project as a part-time student and immediately feeling totally overwhelmed at how long it might take me to finish, and I was right to be. The last six years have at times been incredibly fun, and at others incredibly exhausting, at often-times both. I have lots of people to thank – many that have come and gone over the last six years, and many that I know will be around for years to come.

I first need to thank my supervisors, **Chris Shaw** for giving me the opportunity to become a member of his lab, for financial support, for allowing me to think and act independently. I have learnt so much through being a member of your group. **Agnes Nishimura**, who I am eternally grateful to, for choosing me as her student what now feels so long ago, for supporting my ideas and boosting my confidence, for always putting my well-being before anything else. A huge thank you for reading this thesis and helping me to improve it, and for teaching me so much over the last six years. I would also like to thank **Brad Smith**, whose enthusiasm for science is infectious and whose expertise and guidance helped me learn how to balance the good and the bad, for having me as a guest lab member so that we could get excited about Annexin A11, and **Graham Cocks** for being a beacon of stem cell knowledge and solidifying my obsessive attention to detail, for the better or worse.

To all of the lab members and colleagues who I overlapped with – I have been fortunate to work with and learn from so many wonderful people. There are many who were around when I started, and others who have been a great support in recent times, some made a small difference and others big, and I appreciate it all – **Sarah Mueller**, **Martina de Majo**, **Amina McDiarmid**, **Gaby Clarke**, **Niamh O'Brien**, **Tilly Baldacchino**, **Conor McLoughin**, **Keith Mayl**, **Jenny Greig**, **George Wardley**, **Shiden**

**Solomon**, **Sarah Freckleton**, **Darija Šoltić**, **Chun Hao Wong**, **Alinda Fernandez**, **Zoe Walker**, **Sara Tacconelli**, **Afra Abdien, Nada Alahmady**, **Marc-David Ruepp**, **Sarah Mizielinska**, **Jackie Mitchell**, **Bex Gresham**, **Jean-Marc Gallo, Simon Topp**, **Caroline Vance**, **Han-Jou Chen**, **Younbok Lee**, **George Chennel**, and everyone else who makes the Wohl tick over. I'm sure I will have missed someone - six years is a long time (sorry!).

I am so lucky that I am surrounded by incredible friends, so many of whom have played a part in encouraging and listening to me, always making me feel like I am capable, for forgiving me when I was too busy, particularly this year, and for making sure that I took time to have fun. I count myself so phenomenally lucky that there are too many people for me to list, but every word of encouragement is remembered and without your eternal support this process would have been so much more difficult.

**Mum**, **Dad**, and **Adam** – my wonderful family. For always listening when I was overwhelmed and keeping my head in shape, for always feigning interest when I talk too much about work, for being my constant stream of encouragement. Words don't do justice to how much I appreciate you.

And last but by no means least, thank you to **Alish**. For being my sounding board in all aspects of life, for singing my praises more highly than I could hope anyone would, for being so patient when I have been so preoccupied. I'm so grateful you were by my side this whole time.

## *Table of Contents*

## *List of figures*

***List of tables***

***List of Appendix figures***

***Abbreviations***

| | |
|---|---|
| °C | Celsius |
| AA | Amino acid |
| AA2P | L-Ascorbic acid 2-phosphate (magnesium salt hydrate) |
| ADAR2 | Adenosine Deaminase RNA Specific B1 |
| AFP | $\alpha$-fetoprotein |
| AHA | L-azidohomoalanine |
| ALDH1L1 | Aldehyde Dehydrogenase 1 Family Member L1 |
| ALG-2 | Apoptosis-Linked Gene 2 Protein Homolog (Programmed cell death 6) |
| ALS | Amyotrophic lateral sclerosis |
| ALS2 | Alsin Rho Guanine Nucleotide Exchange Factor ALS2 |
| AM | Astrocyte media |
| AMPA | α-Amino-3-Hydroxy-5-Methyl-4-Isoxazolepropionic Acid |
| ANO1 | Anoctamin 1 |
| ANOVA | Analysis of variance |
| ANXA11 | Annexin A11 |
| ANXA11mut | ALS associated mutant ANXA11 |
| APEX | Ascorbate peroxidase |
| ASO | Antisense oligonucleotide |
| ATP | Adenosine triphosphate |
| ATXN2 | Ataxin 2 |
| B3TUJ/B3Tuj | $\beta$3-Tubulin |
| BAPTA | 1,2-Bis(2-aminophenoxy)ethane-N,N,N',N'-tetraacetic acid |
| Bcl-2 | BCL2 Apoptosis Regulator |
| BDNF | Brain-Derived Neurotrophic Factor |
| BET1L | Bet1 Golgi Vesicular Membrane Trafficking Protein Like |
| BMAA | β-Methylamino-L-alanine |
| BSA | Bovine serum albumin |
| BZLF1 | BamHI Z Fragment Leftward Open Reading Frame 1 |
| C-MYC | MYC Proto-Oncogene, BHLH Transcription Factor |
| C. elegans | Caenorhabditis elegans |
| C9ORF72 | Chromosome 9 Open Reading Frame 72 |
| CaCl | Calcium chloride |
| CALB1 | Calbindin 1 |
| CAPRIN1 | Cell Cycle Associated Protein 1 |
| CCNF | Cyclin F |
| CCR2 | C-C Motif Chemokine Receptor 2 |
| cDNA | Complementary DNA |
| CGH | Comparative genomic hybridization |
| ChAT | Choline Acetyl Transferase |
| CHCHD10 | Coiled-Coil-Helix-Coiled-Coil-Helix Domain Containing 10 |
| CHMP2B | Charged Multivesicular Body Protein 2B |
| CHMP7 | Charged Multivesicular Body Protein 7 |
| CK2 | Casein Kinase 2 Alpha 1 |

| | |
|---|---|
| CNS | Central nervous system |
| $CO_2$ | Carbon dioxide |
| CRISPR | Clustered regularly interspaced short palindromic repeats |
| CSF | Cerebrospinal fluid |
| DAO | D-Amino Acid Oxidase |
| DAPI | 4’,6-diamidino-2-phenylindole |
| DAPT | N-[N-(3,5-Difluorophenacetyl)-L-alanyl]-S-phenylglycine t-butyl ester |
| DCTN1 | Dynactin Subunit 1 |
| DCX | Doublecortin |
| DDH20 | Double distiled H2O |
| DDX17 | DEAD-Box Helicase 17 |
| DMEM | Dulbecco's Modified Eagle Medium |
| DMEM/F12 | Dulbecco's Modified Eagle Medium/Nutrient Mixture F-12 |
| DMSO | Dimethyl sulfoxide |
| DNA | Deoxyribonucleic acid |
| DPBS | Dulbecco's phosphate-buffered saline |
| DPR | Dipeptide repeat protein |
| DTT | Dithiothreitol |
| E8 Flex | Essential 8™ Flex Medium |
| EAAT2 | Excitatory Amino Acid Transporter 2 |
| EB | Embryoid body |
| EBM | Embryoid body media |
| EBNA1 | Epstein–Barr Nuclear Antigen 1 |
| EBV | Epstein Barr virus |
| ELAVL3 | ELAV Like RNA Binding Protein 3 |
| ELP3 | Elongator Acetyltransferase Complex Subunit 3 |
| ER | Endoplasmic reticulum |
| ERBB4 | Erb-B2 Receptor Tyrosine Kinase 4 |
| ERES | Endoplasmic reticulum exit site |
| ESC | Embryonic stem cell |
| EWSR1 | EWS RNA Binding Protein 1 |
| FACS | Fluorescence-activated cell sorting |
| fALS | Familial ALS |
| FBS | Fetal bovine serum |
| FDA | The Food and Drug Administration |
| FGF23 | Fibroblast Growth Factor 23 |
| FIG4 | FIG4 Phosphoinositide 5-Phosphatase |
| FMR1 | Fragile X Messenger Ribonucleoprotein 1 |
| FMRP | Fragile X Mental Retardation Protein |
| FTD | Frontotemporal dementia |
| FUS | Fused in Sarcoma |
| G3BP1 | G3BP Stress Granule Assembly Factor 1 |
| GABRE | Gamma-Aminobutyric Acid Type A Receptor Subunit Epsilon |
| GAD2 | Glutamate Decarboxylase 2 |
| GAPDH | Glyceraldehyde-3-Phosphate Dehydrogenase |

| | |
|---|---|
| GDNF | Glial-Derived Neurotrophic Factor |
| GFAP | Glial Fibrillary Acidic Protein |
| GFP | Green Fluorescent Protein |
| GluR2 | Glutamate Ionotropic Receptor AMPA Type Subunit 2 |
| GPC3 | Glypican 3 |
| GSK3 | Glycogen Synthase Kinase 3 |
| GWAS | Genome-wide association study |
| HB9 | Motor Neuron And Pancreas Homeobox 1 |
| HDAC6 | Histone Deacetylase 6 |
| HEPES | 4-(2-hydroxyethyl)-1-piperazineethanesulfonic acid |
| HERV | Human endogenous retrovirus |
| hESC | Human embryonic stem cell |
| hFGF-BASIC | Human Fibroblast Growth Factor basic |
| hLIF | Human Leukemia Inhibitory Factor |
| hnRNPA1 | Heterogeneous Nuclear Ribonucleoprotein A1 |
| hnRNPA2B1 | Heterogeneous Nuclear Ribonucleoprotein A2/B1 |
| hnRNPK | Heterogeneous Nuclear Ribonucleoprotein K |
| HTR2B | 5-Hydroxytryptamine Receptor 2B |
| IGF | Insulin-Like Growth Factor |
| IGG | Immunoglobulin G |
| IGY | Immunoglobulin Y |
| IL18RAP | Interleukin 18 Receptor Accessory Protein |
| iPSC | Induced pluripotent stem cell |
| iSIM | Instant Structured Illumination Microscope |
| Islet 1 | ISL LIM Homeobox 1 |
| kb | Kilobase |
| KCl | Potassium chloride |
| KCL1 | Kinesin Light Chain 1 |
| kDa | Kilodalton |
| KIF5A | Kinesin Family Member 5A |
| KLF4 | KLF Transcription Factor 4 |
| LCL | Lymphoblastoid cell line |
| LMP1 | Latent Membrane Protein 1 |
| LRP10 | LDL Receptor Related Protein 10 |
| MACS | Magnetic-activated cell sorting |
| MAM | Mitochondria-Associated ER membrane |
| MAP1B | Microtubule-Associated Protein 1B |
| MAP2 | Microtubule-Associated Protein 2 |
| MAPK | Mitogen-Activated Protein Kinase |
| MAPT | Microtubule-Associated Protein Tau |
| MATR3 | Matrin 3 |
| MEF | Mouse embryonic fibroblast |
| MgCl | Magnesium chloride |
| mGluR 1 | Metabotropic Glutamate Receptor 1 |
| mGluR5 | Metabotropic Glutamate Receptor 5 |

| | |
|---|---|
| MICU1 | Mitochondrial Calcium Uptake 1 |
| MICU2 | Mitochondrial Calcium Uptake 2 |
| Mitf/TFEB | Melanocyte-Inducing Transcription Factor/Transcription Factor EB |
| MM | Motor neuron maturation media |
| MOPS | 3-(N-morpholino)propanesulfonic acid |
| mRNA | Messenger RNA |
| MSC-NTF | Autologous Cultured Mesenchymal Bone Marrow Stromal Cells Secreting Neurotrophic Factors |
| 0mV | Millivolt |
| NaCl | Sodium chloride |
| NAD+ | Nicotinamide Adenine Dinucleotide |
| NEAA | Non-essential amino acid |
| NEFH | Neurofilament Heavy Chain |
| NEK1 | NIMA Related Kinase 1 |
| NEM | Neural expansion media |
| NES | Nuclear export signal |
| Neurod | Neuronal Differentiation |
| NF-H | Neurofilament Heavy |
| NF-L | Neurofilament Light |
| NF-M | Neurofilament Medium |
| NIM | Neural induction media |
| NIS | Nuclear import signal |
| NLS | Nuclear localisation sequence |
| NMDA | N-methyl-D-aspartic acid |
| NMJ | Neuromusular junction |
| NPC | Neural progenitor cell |
| $O_2$ | Oxygen |
| Oct-3/4 | POU Class 5 Homeobox 1 |
| OPTN | Optineurin |
| Orip | Origin of Plasmid Replication |
| PABP | Poly(A) Binding Protein |
| PARP | Poly(ADP-ribose) polymerase |
| PBS | Phosphate-buffered saline |
| PCR | Polymerase chain reaction |
| Pea3 | Polyomavirus Enhancer Activator 3 Homolog |
| PET | Positron emission tomography |
| PFA | Paraformaldehyde |
| PFN1 | Profilin 1 |
| PGRN | Progranulin |
| PI(3,5)P2 | Phosphatidylinositol 3,5-bisphosphate |
| PLO | Poly-L-ornithine |
| pNF-H | Phosphorylated Neurofilament Heavy |
| PolyHEMA | Poly(2-hydroxyethyl methacrylate) |
| PON1-3 | Paraoxonase 1-3 |
| PRPH | Peripherin |
| pTDP-43 | Phosphorylated TDP-43 |

| | |
|---|---|
| PTPIP51 | Protein Tyrosine Phosphatase Interacting Protein 51 |
| PVDF | Polyvinylidene fluoride |
| Rab7 | Ras-Related Protein Rab7a |
| Rab9 | Ras-Related Protein Rab9 |
| RAN | Repeat-associated non-ATG translation |
| RBP | RNA binding protein |
| RCF | Relative centrifugal force |
| RIPA | Radioimmunoprecipitation |
| RM | Reprogramming media |
| RNA | Ribonucleic acid |
| RNP | Ribonucleoprotein |
| ROCK inhibitor | Rho-associated protein kinase inhibitor |
| ROS | Reactive oxygen species |
| RPM | Revolutions per minute |
| RRM | RNA recognition motif |
| RT-PCR | Reverse-transcription PCR |
| S100A6 | S100 Calcium Binding Protein A6 |
| S6 | Ribosomal Protein S6 |
| sALS | Sporadic ALS |
| SARM1 | Sterile Alpha And TIR Motif Containing 1 |
| SD | Standard deviation |
| SDS | Sodium dodecyl sulfate |
| SEM | Standard error of the mean |
| SETX | Senataxin |
| SeV | Sendai Virus |
| SFPQ | Splicing Factor Proline And Glutamine Rich |
| SIGMAR1 | Sigma Non-Opioid Intracellular Receptor 1 |
| SMA | Spinal muscular atrophy |
| SNP | Single nucleotide polymorphism |
| snRNA | Small nuclear RNA |
| snRNP | Small nuclear RNP |
| SOD1 | Cu/Zn Supra Oxide Dismutase |
| SOX2 | SRY-Box Transcription Factor 2 |
| SPAST | Spastin |
| SPG11 | SPG11 Vesicle Trafficking Associated, Spatacsin |
| SQSTM1 | Sequestosome 1 (p62) |
| SREBF2 | Sterol Regulatory Element Binding Transcription Factor 2 |
| SS18L1 | SS18L1 Subunit Of BAF Chromatin Remodeling Complex |
| SSRI | Selective serotonin reuptake inhibitor |
| STAT3 | Signal Transducer And Activator Of Transcription 3 |
| sTDP-43 | Short TDP-43 |
| STR | Short tandem repeat |
| SUMO | Small Ubiquitin-Like Modifier |
| SUnSET | Surface sensing of translation |
| TAF15 | TATA-Box Binding Protein Associated Factor 15 |

| | |
|---|---|
| TARDBP | TAR DNA Binding Protein |
| TBK1 | TANK Binding Kinase 1 |
| TBST | Tris-buffered saline, Tween® 20 |
| TDP-43 | TAR DNA Binding Protein 43 |
| TGF-$\beta$(1) | Transforming Growth Factor Beta(1) |
| TIA1 | TIA1 Cytotoxic Granule Associated RNA Binding Protein |
| TIAR-2 | TIA-1/TIAL RNA binding protein homolog |
| TMEM106B | Transmembrane Protein 106B |
| TNF | Tumor Necrosis Factor |
| TORC1 | Target of Rapamycin Complex 1 |
| TRIS-HCL | Tris(hydroxymethyl)aminomethane hydrochloride |
| TUBA1A | Tubulin Alpha 1a |
| TUBA4A | Tubulin Alpha 4a |
| U.K. | United Kingdom |
| U.S. | United States of America |
| UBQLN2 | Ubiquilin 2 |
| UNC13A | Unc-13 Homolog A |
| USD | United States Dollar |
| UTR | Untranslated region |
| UV | Ultraviolet |
| VAChT | Vesicular Acetylcholine Transporter |
| VAPB | VAMP Associated Protein B And C |
| VCP | Valosin Containing Protein |
| VEGF | Vascular Endothelial Growth Factor A |
| vGLUT2 | Vesicular-Glutamate Transporter 2 |
| WT | Wild type |
| YBX1 | Y-Box Binding Protein 1 |

***Amino Acid Code***

| | | |
|---|---|---|
| Alanine | Ala | A |
| Arginine | Arg | R |
| Asparagine | Asn | N |
| Aspartic acid | Asp | D |
| Cysteine | Cys | C |
| Glutamic acid | Glu | E |
| Glutamine | Gln | Q |
| Glycine | Gly | G |
| Histidine | His | H |
| Isoleucine | Ile | I |
| Leucine | Leu | L |
| Lysine | Lys | K |
| Methionine | Met | M |
| Phenylalanine | Phe | F |
| Proline | Pro | P |
| Serine | Ser | S |
| Threonine | Thr | T |
| Tryptophan | Trp | W |
| Tyrosine | Tyr | Y |
| Valine | Val | V |

# Chapter 1 Introduction

## *1.1 Amyotrophic lateral sclerosis*

In the late 1860s, the condition known today as amyotrophic lateral sclerosis (ALS) was described in lectures by Jean-Martin Charcot, who is often credited with formally recognising ALS as a distinct disease (Katz et al., 2015). Charcot was not the first clinician to describe diseases of muscle wasting and paralysis but is responsible for unifying prior research into progressive muscular weakness to form a foundation for classification of ALS as a unique pathology. Since then, our understanding of the disease has progressed enormously, however successful therapeutics remain elusive. ALS causes gradual paralysis, with an average prognosis of 3-5 years from diagnosis (Traxinger et al., 2013), and is currently untreatable and incurable. ALS is characteristically heterogeneous in clinical presentation, cellular phenotype, and genetic causation. Such complex aetiology has contributed to an overriding failure to treat disease, as incomplete understanding of pathology renders accurate drug-targeting impossible. With the global incidence set to increase over the coming years (Feigin et al., 2017; Logroscino & Piccininni, 2019) the need for further understanding of the disease pathology and subsequent development of viable therapeutics is of great importance.

## *1.2 Epidemiology*

ALS onset is most common between ages 50-65 years (Logroscino et al., 2008), however young (onset before age 45) and juvenile (onset before age 25) cases are also reported (Turner et al., 2012). It affects more males than females, and the ratio of sex difference is affected by the age and location of the patient cohort. A U.K. based study found the male to female ratio to drop from 2.5 in young patients to 1.4 in the older patient population (Manjaly et al., 2010). Mean disease duration from symptom onset to death is 20-48 months (Chio et al., 2009), and only 20% of patients survive between 5-10 years after the onset of symptoms (Talbot, 2009). Meta-analysis suggests that the

global incidence is 1.68 cases per 100,000 people, with higher incidence in North Europe (1.89/100,000) and lower incidence in East Asia (0.83/100,000) (Marin et al., 2017). When considering age-specific incidence, the incidence peaks at 6.98-8.17/100,000 in North American and European populations, representing an age group of 71.6-77.4 years. The peak incidence in Asia is lower at 2.20/100,000, which represents an age group of approximately 75 years (Marin et al., 2018). Global cases have been predicted to increase to over 370,000 by 2040, which represents an increase of 69% in the number of cases over 25 years (Arthur et al., 2016). Indeed, the global number of incidences increased by 72.4% from 1990 to 2015, with the number of motor neuron disease deaths due to ALS increasing by 97.3% in the same period (Feigin et al., 2017). The aging population is a global phenomenon, where advances in medicine and quality of life are resulting in a higher average age of death. This results in a larger population and increased numbers of neurological disorder cases. It has been noted that ALS and other neurodegenerative diseases that are currently of higher incidence in developed countries will become more prevalent in developing countries, where average life span is also increasing (Logroscino & Piccininni, 2019).

In addition to the huge suffering caused by the ALS, the economic impact of the disease is large; estimated at 279-472 million USD in 2015 in the U.S. alone (Gladman & Zinman, 2015). The cost for each patients' care is high and increases as disability progresses (Meng et al., 2018), and many considerations must be made for the costs for affected individuals, such as costs of caregiving and early retirement (López-Bastida et al., 2009). It should be recognised that these effects will vary depending on each patients' country of residence, influenced by the standard of healthcare and other socioeconomic factors. The additional burden of healthcare costs to individuals suffering with the disease is an unsettling and important consideration for patients and carers. The tragedy of ALS is highlighted by evidence that in The Netherlands one in five patients with ALS ultimately die by euthanasia or physician assisted suicide, which is not as a result of unmet palliative care needs (Maessen et al., 2014; Veldink et al., 2002).

### *1.3 Clinical presentation*

Both the upper motor neuron and lower motor neuron tracts are affected in ALS (Cleveland & Rothstein, 2001). The associated phenotype is characterised by gradual paralysis as motor neurons governing voluntary movement degenerate, which leads to muscle wasting as tissues are rendered inactivated. Limb onset occurs in ~70% of patients and often presents as foot drop or loss of hand coordination. Bulbar onset displays as difficulty with swallowing or speech and accounts for ~25% of patients. The remaining 5% of patients have onset in the trunk or respiratory system (Kiernan et al., 2011). Symptoms become progressively worse with time, and eventually respiratory innervation is depleted which results in reliance on ventilator support. The most common cause of death in ALS patients is respiratory failure, or diseases affecting the respiratory system such as pneumonia (Corcia et al., 2008). Symptoms can include muscle twitching, which arise from abnormal electrical activity as surviving motor axons attempt to re-innervate orphan muscle fibres whose motor neuron input has degenerated. This leads to large and sustained axon potentials, which present as uncontrollable muscle twitching (Bashford et al., 2020). Patients can also experience symptoms including, but not limited to; dyspnoea (shortness of breath), disturbed sleep, anorexia, cramps, spasticity, and fatigue (Zarei et al., 2015). Notably, ocular motor neurons are spared until the end stage of disease and have been shown to harbour different gene expression profiles to spinal motor neurons (Patel & Mathew, 2020).

Although motor neurons are predominantly affected in disease, other brain regions have been implicated: Cerebellar pathology is present in ALS associated with specific genetic profiles (Bede et al., 2021), brain stem pathology has been linked with pseudobulbar affect (Tu et al., 2021), and loss of taste has been associated with central white matter loss (Ashary et al., 2020). Some non-central nervous system (CNS) systems have also been implicated, including the peripheral immune (McCombe et al., 2020).

## *1.4 The ALS-FTD spectrum*

There is significant co-morbidity across ALS and frontotemporal dementia (FTD), such that the two are considered to constitute a disease spectrum. FTD is characterised by degeneration of the frontal and temporal lobes and commonly manifests as changes in behaviour, difficulty with language, and loss of executive function. Behavioural changes can be particularly challenging for family members, friends, and carers, as patients may exhibit antisocial and irresponsible behaviours that lead to financial and reputable damage. Diagnosis often takes years, and establishing the level of patient autonomy over their actions and behaviours can be difficult (Seelaar et al., 2011).

The ALS-FTD spectrum is both symptomatic and genetic. Disease can manifest as "pure" ALS or FTD, however an overlap of clinical phenotypes is common. Cognitive impairment is seen in approximately 50% of ALS patients, with 15% meeting the criteria for FTD diagnosis (Portet et al., 2001; Ringholz et al., 2005), and 50% of patients with FTD show symptoms of probable or definite ALS (Lomen-Hoerth et al., 2002). It has been noted that even if cognitive symptoms are not present at the time of ALS diagnosis, they can manifest as the disease progresses, and evidence of cognitive decline can be predictive of shorter survival time (Bersano et al., 2020). Multiple genes have been associated with both ALS and FTD, including *C9ORF72* (DeJesus-Hernandez et al., 2011), *VCP* (Bersano et al., 2009; Johnson et al., 2010), *UBQLN2* (Deng et al., 2011; Synofzik et al., 2012), and *CHMP2B* (Parkinson et al., 2006; Skibinski et al., 2005).

## *1.5 Diagnosis and neuropathology*

No imaging or laboratory test can confirm ALS diagnosis, which is currently based on clinical diagnostic criteria. The El Escorial criteria are often used in clinical trials (Brooks et al., 2000), and questionnaire-based diagnostic tools are being updated and improved (Fournier et al., 2020). The time from symptom onset to formal diagnosis takes an average of 13-18 months, and includes a range of imaging, electrophysiological, and lab tests to rule out other diseases with similar clinical

presentation (Zarei et al., 2015). Screening for known genetic mutations can also aid diagnosis, particularly in cases where multiple family members are affected.

Post-mortem analysis of spinal cord and brain tissue can reveal presence of typical ALS cellular pathologies to confirm diagnosis after death. TDP-43 aggregates are often associated with loss of nuclear TDP-43, can be hyper-phosphorylated, ubiquitinated, include cleaved forms of the full-length protein, and are present in ~97% of ALS cases (Neumann et al., 2006). Additional p62-positive ubiquitinated inclusions are often present in neurons and glia (Mizuno et al., 2006), and loss of myelin sheath in white matter tracts, loss of spinal motor neurons in the anterior horn of the spinal cord and motor cortex, shrinkage of surviving neurons, vacuolization of motor cortex, and microglial activation are commonly observed (Saberi et al., 2015). In cases with known genetic causes, additional neuropathology might be observed, for example aggregation or mislocalisation of FUS (Kwiatkowski et al., 2009; Vance et al., 2009) or Annexin A11 (Smith et al., 2017; Teyssou et al., 2020), and presence of RNA foci and dipeptide repeat proteins (DPRs) in *C9ORF72* ALS (DeJesus-Hernandez et al., 2011; Mizielinska et al., 2013).

Efforts to develop biomarkers for ALS are ongoing and will be essential for reliable diagnosis at early or prodromal time-points as well as for monitoring disease progression, including in clinical trials. The neurofilament proteins NF-L and pNF-H are increased in ALS patient cerebrospinal fluid (CSF) and plasma compared to control and other motor neuron disease samples (Behzadi et al., 2021). MicroRNAs are being explored as potential biomarkers (Joilin et al., 2019; Laneve et al., 2021), including in extracts from blood vesicles (Sproviero et al., 2021). FGF23 has been identified as a muscle biomarker and is upregulated in ALS patient skeletal muscle and mouse models of ALS (Si et al., 2021). Despite the identification of these biomarkers, a single test for confirmation of ALS is yet to be discovered, and it may be necessary to employ multiple analyses to achieve concrete diagnosis. Development of imaging biomarkers such as PET ligands will enable non-invasive monitoring of ALS progression (Chew & Atassi, 2019), and analysis of fasiculations, which often occur prior to the onset

of other symptoms, is being developed as a means to aid diagnosis and monitor disease progression (Bashford et al., 2019).

## *1.6 Genetics*

### *1.6.1 Genetic heterogeneity in ALS*

Approximately 90% of the ALS patient population are categorised as sporadic ALS (sALS), with the remaining 10% accounting for familial ALS (fALS). In cases of fALS, genetic mutations can show autosomal dominant, autosomal recessive, or X-linked inheritance (Chen et al., 2013). Genes associated with fALS are often also implicated in sALS, and so identification of candidate genes in affected families frequently leads to the detection of additional mutations in sALS cases. Genetic association in ALS has spanned the last 30 years of research, with multiple methods of genetic association leading to the identification of ALS-associated variants. To date, more than 50 genes have been published in association with ALS, and additional genes are associated with FTD. In the absence of functional studies, the true causality of multiple published genes is subject to debate, highlighting the necessity of functional characterisation in addition to robust genetic analysis of newly implicated genes. Identification of ALS-associated genes has improved our understanding of the disease and enables opportunities for genetic counselling which in some instances can benefit patient understanding and autonomy (Turner et al., 2017). Development of therapeutics which act against specific mutations, such as gene therapies, is further reason to screen patient cohorts for identification of novel and known mutations. Similarly, the large disease heterogeneity seen in ALS might warrant patient stratification for the development of new therapeutics. A “one-drug-fits-all” approach may be reductive, and one way of stratifying patients, for example in clinical trials, is through the identification and grouping of genetic mutations.

The gene that accounts for the highest proportion of known genetic cases of ALS is *C9ORF72*, which accounts for 4-20% and 20-40% of sALS and fALS cases, respectively (DeJesus-Hernandez et al., 2011;

Majounie et al., 2012; Renton et al., 2011). This is followed by *SOD1* (2% sALS, 20% fALS), *TARDBP* (1% sALS, 5% fALS), and *FUS* (1% sALS, 5% fALS) (Sreedharan et al., 2008; Taylor et al., 2016). In addition to these, there are many ALS associated genes that each account for a small percentage of ALS cases.

### *1.6.2 C9ORF72 (chromosome 9 open reading frame 72)*

A $(G_4C_2)_n$ hexanucleotide repeat region in the first intron of the *C9ORF72* gene usually comprises 2-19 repeats, however this is expanded to 250-2100 repeats in patients with *C9ORF72* mutations (DeJesus-Hernandez et al., 2011; Renton et al., 2011). There is significant variability with repeat length, with some ALS patients having between only 24-30 repeats (Iacoangeli et al., 2019). Some repeat carriers show no symptoms of disease, however this observed incomplete penetrance might be due to variable age of onset. At 58 years of age 50% of expansion carriers show disease characteristics, however this increases to almost 100% by 80 years (Majounie et al., 2012). *C9ORF72* repeat expansions account for 11.7% of familial FTD (DeJesus-Hernandez et al., 2011), with as few as 20-22 repeats being associated with FTD onset (Gómez-Tortosa et al., 2013). The relationship between repeat length, disease severity, and age of onset is complicated, and conflicting data mean that no clear predictions for disease status can be made based on repeat length (Van Mossevelde et al., 2017).

The cellular pathology of *C9ORF72* is unique. Aberrant transcription of the repeat expansion results in mRNA species in the sense and antisense directions, and foci comprised of this RNA are detectable in the nuclei and cytoplasm of patient neurons (DeJesus-Hernandez et al., 2011; Zu et al., 2013). Expansion specific repeat associated non-ATG (RAN) translation also occurs: In the absence of typical start codons, RAN translation of the repeat RNA gives rise to five poly-peptide species as the sense and antisense mRNA is translated from different starting points (Ash et al., 2013; Mori, Weng, et al., 2013). The resulting DPRs; GA, GP, GR, PR, and PA, are detailed in Figure 1.1.


***Figure 1.1 C9ORF72 expansion associated dipeptide species***

Multiple reading frames in (A) sense and (B) antisense mRNA from transcription of the *C9ORF72* repeat expansion undergo RAN translation, giving rise to five dipeptide species; glycine-alanine (GA), glycine-proline (GP), glycine-arginine (GR), proline-arginine (PR), and proline-alanine (PA).

RNA-foci comprised of *C9ORF72* repeat sense and antisense RNA bind to and sequester RNA binding proteins (RBPs) (Donnelly et al., 2013; Lee et al., 2013; Mori, Lammich, et al., 2013). The sequestration of RBPs by repeat expansion foci results in upregulated transcription of genes encoding these RBPs, including an enriched population of RNA splicing proteins, which then leads to splicing inconsistencies in patients (Cooper-Knock et al., 2015). RNA foci co-localise with p62-positive protein inclusions, indicating that they have a role in seeding or upholding disease-associated protein aggregates (Mori et al., 2013). Sense and antisense foci display different tissue specific staining patterns within the CNS, however bind to an overlapping group of interacting proteins. The presence of antisense foci in motor neurons correlates with TDP-43 mislocalisation, indicating that the antisense RNA might be more toxic (Cooper-Knock et al., 2015).

The functional consequences of DPR species include compromised nucleocytoplasmic transport (Freibaum et al., 2015; Zhang et al., 2015), inhibition of DNA repair mechanisms (Andrade et al., 2020), nucleolar stress and interference with stress granule dynamics (Tao et al., 2015), altered calcium influx and synaptic vesicle release (Jensen et al., 2020), and perturbed transport dynamics

and neuronal branching defects (Burguete et al., 2015; Fumagalli et al., 2021). Additional features of *C9ORF72* disease include altered neuronal excitability (Burley et al., 2022), altered mitochondria-endoplasmic reticulum (ER) tethering (Gomez-Suaga et al., 2022), and endosomal-lysosomal dysfunction (Lorenzini et al., 2020). There is some evidence that haploinsufficiency of the C9ORF72 protein contributes to pathology, although little is known about the protein function. The protein has a role in vesicle trafficking and lysosomal biogenesis in induced pluripotent stem cell (iPSC)-derived motor neurons, and reduced expression of C9ORF72 protein results in excitotoxicity and impaired protein clearance (Shi et al., 2018). *C9ORF72* loss of function animal models mainly indicate immune dysfunction (Burberry et al., 2016; O'Rourke et al., 2016) with some evidence of motor abnormality (Ciura et al., 2013).

### *1.6.3 SOD1 (Cu/Zn superoxide dismutase 1)*

The first genetic loci to be associated with ALS was identified in 1991 through linkage analysis (Siddique et al., 1991). The specific gene was subsequently identified as *SOD1* in 1993 (Rosen et al., 1993). SOD1 is an antioxidant which converts highly reactive superoxide into hydrogen peroxide and molecular oxygen through the reduction and reoxidation of the copper ion in its active site (Fridovich, 1981; McCord & Fridovich, 1969). For many years *SOD1* was the only known genetic contributor to ALS, and so extensive characterisation of *SOD1* mutations was achieved in the absence of other ALS disease models. *SOD1* pathology is typically associated with SOD1 protein misfolding and aggregation (Bosco et al., 2010; Khare et al., 2006; Münch et al., 2011; Rakhit et al., 2002). Pathology is also associated with neurofilament imbalance (Chen et al., 2014), aberrant RNA binding (Li et al., 2009), and altered TGF-$\beta$ signalling (Namboori et al., 2021), to name a few. Hallmark TDP-43 pathology is not consistently observed in *SOD1* ALS, suggesting the pathology is somewhat disparate from other instances of ALS, however a handful of reports suggest there may be some TDP-43 pathology in *SOD1* ALS (Feneberg et al., 2020; Jeon et al., 2019; Okamoto et al., 2011; Sumi et al., 2009).

### *1.6.4 TARDBP (transactive response DNA binding protein)*

The search for mutations in *TARDBP* began when the corresponding protein, TDP-43, was identified in aggregated and ubiquitinated protein inclusions in post-mortem spinal cord tissue in over 97% of ALS patients (Arai et al., 2006; Neumann et al., 2006). Mutations in *TARDBP* were identified two years later, solidifying the importance of TDP-43 in ALS pathogenesis (Kabashi et al., 2008; Sreedharan et al., 2008). TDP-43 is a DNA/RNA binding protein with multiple functions in RNA metabolism. The majority of *TARDBP* mutations reside in the glycine rich C-terminal domain which is the site of many protein-protein interactions, and can affect liquid-liquid phase-separation (Conicella et al., 2016; Prasad et al., 2019). Instances of mutations near or within the RNA recognition motifs have been reported, resulting in perturbed RNA recognition and splicing (Chen et al., 2019) and altered RNA stability (Chiang et al., 2016). Evidence of TDP-43 pathology in both *TARDBP* mutation carriers and other ALS cases are discussed in detail in 1.9.

### *1.6.5 FUS (fused in sarcoma)*

Much like TDP-43, FUS is a DNA/RNA binding protein which functions in DNA repair, transcription regulation, splicing, and translation (Ishigaki et al., 2012; Rogelj et al., 2012; Sévigny et al., 2020; Yasuda et al., 2013). Mutations in the *FUS* gene were identified in ALS patients by two independent studies in 2009 (Kwiatkowski et al., 2009; Vance et al., 2009), and FUS aggregates define a subset of FTD cases (Neumann et al., 2009). FUS is predominantly nuclear, although it shuttles in and out of the cytoplasm, and typical pathology includes cytoplasmic accumulation and aggregation of FUS. FUS inclusions or mislocalisation are being recognised in non-mutant *FUS* cases (Tyzack et al., 2019), and are associated with downregulation of the retrograde transport protein dynactin 1 in sALS spinal motor neurons (Ikenaka et al., 2020). However, FUS mislocalisation is not consistently observed as an early phenotype in non-*FUS* mutant ALS iPSC-derived spinal motor neurons (Szewczyk et al., 2021).

FUS belongs to a family collectively termed the FET proteins, which also includes EWSR1 and TAF15. These proteins possess similar structures, harbouring low-complexity domains, RNA binding regions, and a zinc-finger motif, and all three FET proteins and genes are implicated in ALS pathology (Iko et al., 2004; Lee et al., 2019; Svetoni et al., 2016). A novel coding sequence within the *FUS* gene, which encodes an alternative protein in addition to the annotated sequence, was recently shown to contribute to autophagy mediated toxicity, and may explain how some ALS associated synonymous single nucleotide polymorphisms (SNPs) that are present in the annotated sequence influence pathology by exerting a missense effect on the alternative FUS protein (Brunet et al., 2020). Mutations in the nuclear localisation signal of FUS affect its interaction with Transportin, which results in cytoplasmic accumulation in disease (Dormann et al., 2010), and notably, many ALS-associated FUS mutations are located near this domain. FUS binds mRNA to regulate splicing and translation, and mutant FUS strongly binds to and sequesters mRNA involved in membrane trafficking and cytoskeletal dynamics, as well as targets that are associated with ALS, such as *VCP* (Garone et al., 2020).

*FUS* pathology includes aberrant neuronal branching and axon growth (Akiyama et al., 2019; Garone et al., 2021), dysregulated stress granule response (An et al., 2021), altered splicing (Jutzi et al., 2020; Reber et al., 2016), disrupted autophagy and lysosome function (Baskoylu et al., 2022; Ling et al., 2019; Trnka et al., 2021), impaired DNA damage repair (Fortuna et al., 2021), aberrant transcription and translation (Birsa et al., 2021; Gadgil et al., 2021; Kamelgarn et al., 2018; Kerk et al., 2022), defective nucleocytoplasmic transport (Lin et al., 2021), altered neuromuscular junction (NMJ) and synaptic integrity (Markert et al., 2020; Sahadevan et al., 2021; Salam et al., 2021; Sephton et al., 2014), altered excitability and transport (Guo et al., 2017), altered microtubule stability (Yasuda et al., 2017), and dysfunctional nonsense mediated decay, mitochondrial dysfunction, altered proteostasis, and brain connectivity (Ho et al., 2021). Some of the functional consequences of mutant FUS protein are associated with altered interaction with binding partners such as SFPQ (Ishigaki et al., 2020). Inhibition of HDAC6, which has a role in histone modification and therefore gene

expression, alleviates pathology in mutant *FUS* iPSC derived neurons (Guo et al., 2017). Increased methylation of an upstream *FUS* promoter, and an associated increase in DNA methyltransferase levels, were identified specifically in mutant *FUS* motor neurons (Hartung et al., 2021), collectively suggesting that DNA modification might be a therapeutic target in *FUS* ALS. FUS has a further role in DNA replication, which may be of reduced relevance for post-mitotic motor neurons, however could impact supportive cells that undergo mitosis to maintain proper neuronal support (Jia et al., 2021).

### *1.6.6 Functional grouping of ALS genes*

The vast heterogeneity of ALS is often simplified by grouping risk genes into functional categories, although classification of these groups varies amongst the literature to some degree. Broadly, ALS genes can be segregated into those involved in DNA/RNA metabolism; genes involved in protein homeostasis (proteostasis) including protein folding, trafficking, and degradation; genes associated with oxidative stress and mitochondria; and genes implicated in cytoskeletal dynamics. Genes that do not fit neatly into these categories have been associated with ALS, and varying degrees of functional evidence for associated genes exist, rendering the complete genetic landscape of ALS undetermined. In addition to the genes mentioned here, publications implicating additional genes exist, and directories such as ALSoD (https://alsod.ac.uk/) aim to consolidate these. It should be noted that many of the genes typically assigned to one functional group have influence over other cellular mechanisms, and it would be reductive to suggest that the functions of different groups of genes are mutually exclusive.

Multiple stages of DNA and RNA metabolism are affected by genetic mutations associated with ALS (Zaepfel & Rothstein, 2021). As alluded to above, the four most characterised ALS-associated genes, *C9ORF72, SOD1, TARDBP,* and *FUS,* are all implicated in DNA or RNA metabolism in some capacity. In addition, several genes with functions in transcription regulation, pre-mRNA splicing, mRNA transport, stress granule dynamics, and mRNA translation have been associated with ALS. Implicated genes with functions in DNA/RNA metabolism include *ATXN2* (Daoud et al., 2011; Elden et al., 2010),

*hnRNPA1* (Kim et al., 2013; Liu et al., 2016), *hnRNPA2B1* (Kim et al., 2013), *MATR3* (Johnson et al., 2014), *SETX* (Ma et al., 2018), *TBK1* (Cirulli et al., 2015; Lu et al., 2022), *SS18L1* (Chesi et al., 2013), *TIA1* (Mackenzie et al., 2017), *TAF15* (Ticozzi et al., 2011), *SETX* (Ma et al., 2018; McCann et al., 2021), and *ELP3* (Simpson et al., 2009). Many of the corresponding proteins interact directly with RNA, and the functional consequences of altered RNA dynamics in ALS are discussed in 1.10.

Protein homeostasis, or proteostasis, describes the many converging cellular pathways that mediate the biogenesis, folding, trafficking, and degradation of proteins. Genes involved in proteostatic pathways that are implicated in ALS include *VAPB* (Nishimura et al., 2004), *CHMP2B* (Parkinson et al., 2006), *UBQLN2* (Daoud et al., 2012; Deng et al., 2011; Synofzik et al., 2012; Williams et al., 2012), *FIG4* (Chow et al., 2009), *SQSTM1* (Fecto et al., 2011), *SIGMAR1* (Al-Saif et al., 2011), *OPTN* (Maruyama et al., 2010), *VCP* (Al Khleifat et al., 2022; Johnson et al., 2010; Koppers et al., 2012), *LRP10* (Ni et al., 2021), and *CCNF* (Williams et al., 2016). The functional implications of such mutations include protein aggregation, perturbed endosomal signalling, dysfunctional synapses, and inefficient protein degradation.

Cytoskeletal and transport dynamics are dysregulated in ALS, and mutations have been identified in multiple associated genes including *DCTN1* (Puls et al., 2003), *PFN1* (Wu et al., 2012), *SPG11* (Daoud et al., 2012), *TUBA4A* (Pensato et al., 2015; Smith et al., 2014), *NEFH* (Al-Chalabi et al., 1999; Figlewicz et al., 1994; Tomkins et al., 1998), *ALS2* (Hadano et al., 2001; Yang et al., 2001), *PRPH* (Corrado et al., 2011), *NEK1* (Kenna et al., 2016), *SPAST* (Brugman et al., 2005; Münch et al., 2008), and *KIF5A* (Faruq et al., 2019; Nicolas et al., 2018). The impact of cytoskeletal dysfunction in ALS is discussed in 1.15.

Mitochondrial dysfunction is highly implicated in ALS, including inefficient response to oxidative stress and altered tethering to the ER. Mutations in genes associated with mitochondrial function include *CHCHD10* (Bannwarth et al., 2014; Johnson et al., 2014), *DAO* (Mitchell et al., 2010), and *PON1-3* (Ticozzi et al., 2010), and mitochondrial and metabolomic disturbances in ALS are discussed in 1.14.

Mutations in *ANXA11* were recently identified as causative of ALS (Smith et al., 2017), and are the subject of this thesis. Multiple non-synonymous point mutations in *ANXA11* have been identified in the ALS population, and the functions of the corresponding protein Annexin A11 are discussed in detail in 1.18-1.22. Annexin A11 binds to ribonucleoproteins (RNPs) and interacts with membrane-bound vesicles (Liao et al., 2019), indicating a role in both RNA biology and proteostasis via vesicle processing or function. It is noteworthy that the functions of Annexin A11 span multiple groups when considering ALS genetics as mechanistic categories.

Many of the genetic mutations discussed here are associated with protein coding changes, namely missense SNPs that alter the protein sequence and are sometimes associated with the introduction of an early stop codon. In addition to these genetic changes, diverse genetic perturbations are recognised in ALS. *ERBB4* encodes a receptor tyrosine kinase with enzymatic activity, and an insertion in this gene was recently associated with ALS; >70% of patients with respiratory onset were found to harbour this genotype (Al Khleifat et al., 2022), and the same study identified an ALS-associated inversion in *VCP*. Genome wide association studies (GWAS) highlight risk genes that influence disease progression; *UNC13A,* which encodes a synaptic protein, is often identified in ALS GWAS (van Es et al., 2009; van Rheenen et al., 2016). Additionally, SNPs have been identified as disease modifiers, including a homozygous SNP in *TMEM106B,* which encodes an endosome/lysosome membrane protein, and exacerbates TDP-43 pathology (Mao et al., 2021), and a homozygous SNP in the serotonin receptor gene *HTR2B* is associated with longer survival (El Oussini et al., 2016).

### *1.6.7 Limitations of genetic studies*

Despite extensive efforts to determine the genetic causes of ALS, most cases remain without an identified genetic component. It remains to be determined whether cases exist where disease onset is entirely caused by environmental factors, however the vast array of genetic evidence and associated functional analyses suggest that this is not the case. An explanation for why such a large proportion of the patient population remain without a known genetic cause therefore depends on

limitations of current genetic analysis techniques. There are multiple methods that have contributed to identification of ALS mutations including exome sequencing, linkage analysis, and GWAS. Linkage analysis is based on the tendency of groups of genes to be inherited together due to their proximity within chromosomes. Utilising such analysis as a means for identification of disease-causing mutations is dependent on large pedigrees with multiple generations, including family members that are affected and unaffected, which describes only a small subset of the ALS population. Linkage analysis can also be complicated by late disease onset and unavailability of DNA from some family members for laboratory analysis. Many ALS mutations display reduced penetrance, which is often confounded by the age of mutation carriers, with incidence of mutation-specific disease increasing with age (Volk et al., 2018). It may be the case that the statistical filtration necessary for identification of candidate genes excludes genes with incomplete penetrance by necessity of excluding common variants.

Exome sequencing is efficient for the identification of mutations in coding region of genes, and many ALS-associated mutations have been discovered this way. Intronic mutations can have consequences for transcription or splicing and may confer genetic vulnerability in addition to protein coding mutations. As an example, multiple ALS-associated intronic mutations in *TBK1* result in inefficient mRNA splicing factor binding, as well as introduction of premature stop codons, resulting in haploinsufficiency (Lu et al., 2022). Identification of intronic mutations may be possible with whole genome sequencing, which is much costlier and more time consuming compared to exome sequencing. A common limitation with whole genome sequencing is the absence of large control cohorts, which are necessary for elimination of non-disease associated variants. Further, the filtration analysis is computationally huge, and has not been viable in historic studies. Recent studies have utilised whole genome sequencing for discovery of novel ALS mutations, resulting in identification an inversion in *VCP* and an expansion in *ERBB4* as associated with increased risk of ALS (Al Khleifat et al., 2022), and recognition of 3'UTR variants in *IL18RAP* mRNA as protective in ALS (Eitan et al., 2022). Next generation long-read sequencing platforms will also be useful in future

studies for identification of *de novo* mutations that might be missed with current protocols, and as data for the reference human genome increases, identification of disease associated changes will become more efficient (Noyes et al., 2022). Polygenic risk is largely unexplored in ALS but may be important. Compounding low risk SNPs may be individually harmless, but collectively result in increased disease susceptibility. Some evidence of polygenic risk in ALS has been reported (McCann et al., 2021) and this may be an important avenue for understanding the complex nature of ALS genetics.

### *1.7 Environmental factors*

Twin studies indicate that ALS heritability is ~60%, suggesting that although there is an overriding genetic component, environmental factors also contribute to the disease aetiology (Al-Chalabi et al., 2010; Goutman et al., 2022). A role of infectious and endogenous viruses in ALS has been posited, and previous exposure to viral infection is implicated in development of other motor neuron diseases, such as multiple sclerosis (Bjornevik et al., 2022). Human endogenous retroviruses (HERVs) are ancient viral DNA fragments that have retrovirally inserted into the human genome throughout evolution, and up to 8% of the human genome is comprised of these viral genes (Douville & Nath, 2017). They usually lie dormant and silenced in the genome, however specific HERV mRNA (*HML6_3p21.31c*) is increased in post-mortem motor cortex tissue from ALS patients (Jones et al., 2021). Forced expression of HERV-K leads to motor neuron degeneration in mice, alongside dendrite abnormalities, DNA damage, and loss of motor cortex volume (Li et al., 2015). Retrotransposons are transposable elements that replicate themselves throughout the genome and they include, but are not limited to, HERVs. Retrotransposon expression was implicated in an unbiased machine learning algorithm which stratified the molecular signatures of a large sample (148) of ALS post-mortem cortex tissue: 20% of the cohort showed high expression of retrotransposon transcripts, alongside signatures of TDP-43 dysfunction. Importantly, TDP-43 was shown to silence retrotransposon transcripts *in vivo*, and aggregation of TDP-43 correlated with viral transcript “de-silencing” (Tam et

al., 2019). Additionally, motor neurons derived from patients with *FUS* mutations show exacerbated ALS phenotype in culture when exposed to insult by various single stranded RNA viruses (Bellmann et al., 2019). Collectively these data indicate a role of viral gene expression and/or viral protein translation in exacerbating or contributing to disease progression.

The impact of environmental toxins on ALS pathogenesis could explain some of the gene-environment interaction that is indicated by low penetrance genetics. Incorporation of the non-protein coding amino acid BMAA into proteins results in protein misfolding and aggregation, is associated with several neurodegenerative diseases, and has been associated with causing ALS-parkinsonian type neurodegeneration (Bradley & Mash, 2009, 2009; Fiore et al., 2020; Murch et al., 2004). Despite epidemiological data linking the presence of BMAA with ALS, BMAA was not detected in CSF from patients with ALS, suggesting more research is needed to solidify this relationship (Bereman et al., 2020). A meta-analysis identified an association between onset of ALS and exposure to some heavy metals, agricultural chemicals, organic solvents, and formaldehyde, with varying degrees of impact. The same study found no association between ALS and recreational sports, however some association was seen between ALS incidence and professional athleticism, high school or college/University level sports, and a history of having had an electric shock showed a strong association with ALS onset (Wang et al., 2017).

The role of the gut microbiome is well established in neurodegeneration, particularly in Parkinson's disease (Sampson et al., 2016), however the contribution of gut microbiome health to ALS is less well understood. *C9ORF72* mice were shown to have a more severe phenotype when housed in environments with abundant immunologically challenging bacteria, which was reversed by the addition of microflora from mice housed in a protective environment (Burberry et al., 2020).

### *1.8 Multi-level cellular dysfunction in ALS*

Multiple overlapping cellular pathways have been implicated in ALS, contributing to a "multi-hit" pathology, and are summarised in Figure 1.2. It is important to emphasise that cellular pathways are

not mutually exclusive, that multiple pathologies occur and influence one another in the same cell, and that evidence for one disease mechanism does not negate the involvement of another. The initial driving force for such a range of pathologies is undetermined, if indeed one universal disease-inducing event exists. It might be more likely that separate pathological events are causing the same clinical phenotype, perhaps due to a specific vulnerability of motor neurons to stress, yet are mechanistically separate. Understanding the range of cellular pathologies linked to motor neuron degeneration is important for understanding how misregulated pathways link together, or alternatively how individual cases of ALS are segregated, and is vital for development of viable therapeutics. Some key findings are discussed in the following sections, however are not exhaustive, and literature describing cellular pathologies in ALS encompasses a huge amount of data. As more evidence is produced, untangling the predominant pathways affected in ALS is paramount, and consideration of how separate data link together will be essential for understanding disease aetiology.

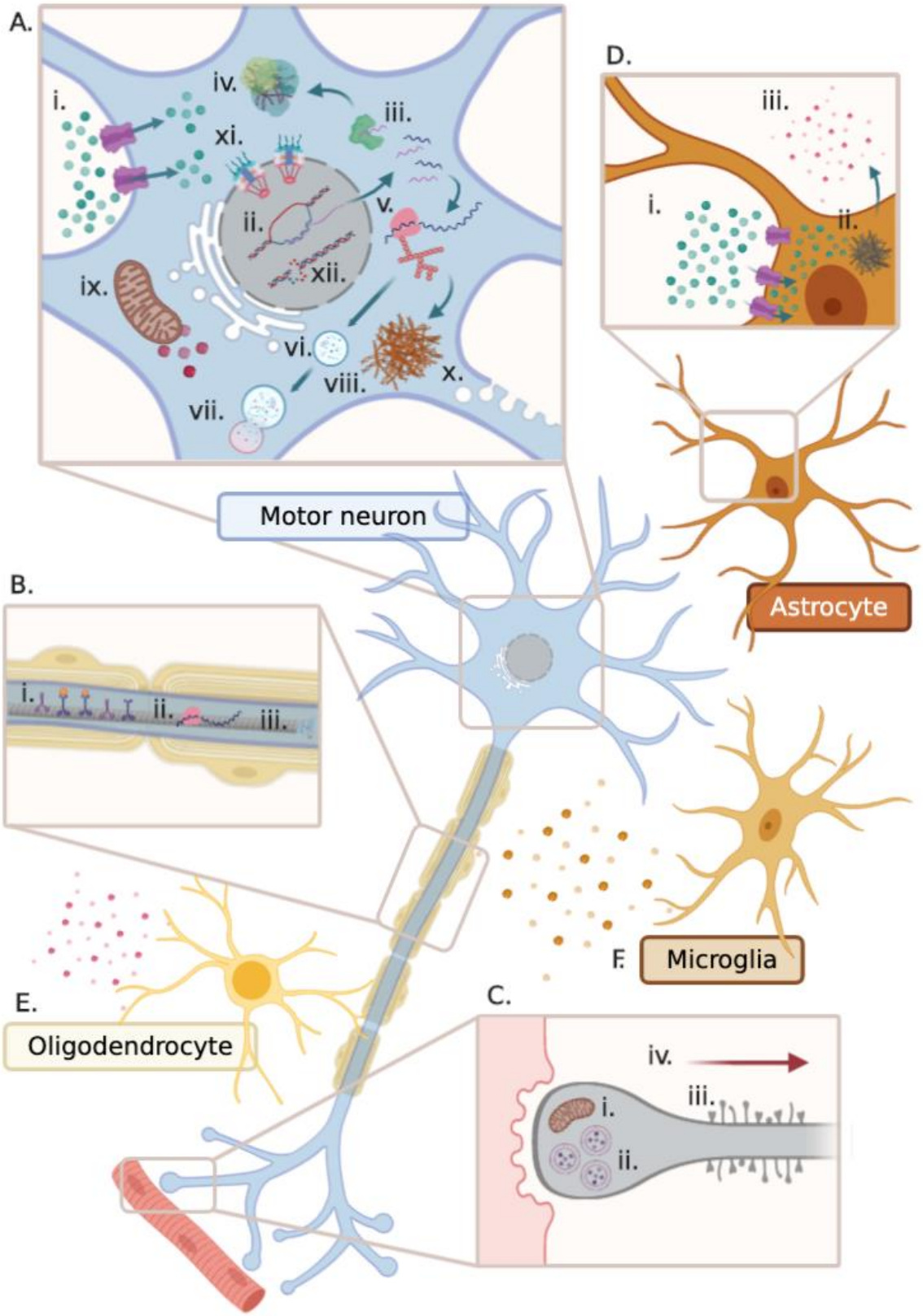


***Figure 1.2 Cellular pathologies in ALS***

Multiple cellular pathways are implicated in ALS. (A) Pathways and/or cellular components implicated in motor neuron pathology include; (i) excitotoxicity, (ii) transcription and splicing, (iii) RNA binding proteins, (iv) stress granule response, (v) protein translation, (vi) autophagy, (vii) lysosome function, (viii) protein aggregation, (ix) mitochondria including production of reactive

oxygen species, (x) vesicle biogenesis and processing, (xi) nucleocytoplasmic transport, and (xii) DNA damage and repair. (B) Axonal processes implicated in ALS include; (i) axonal transport, (ii) local protein translation, (iii) and microtubule dynamics. (C) Dysregulated NMJ components include; (i) mitochondrial defects, (ii) synaptic vesicle maintenance and release, and (iii) dendritic spine abnormalities (throughout the axon; not exclusive to the NMJ), (iv) NMJ degeneration is implicated in the "dying back" hypothesis. (D) Astrocyte pathology in ALS includes (i) contribution to excitotoxicity, (ii) protein aggregation, (iii) and secretion of toxic species. (E) Oligodendrocytes might release toxic factors in some ALS cases. (F) Microglia are implicated in excessive neuroinflammation in ALS. Figure created in BioRender.com.

### *1.9 TDP-43*

TDP-43 pathology is present in >97% of ALS cases and is the hallmark of a subset of non-tau mediated FTD cases (Arai et al., 2006; Ling et al., 2013; Mackenzie et al., 2007; Neumann et al., 2006). Faster disease progression and decreased survival is associated with TDP-43 burden in the spinal cord (Cathcart et al., 2021), and mutant TDP-43 affects an array of cellular pathways. Ubiquitinated protein aggregates were identified in motor neurons of ALS patients in 1991 (Leigh et al., 1991), however it wasn't until 2006 that this aggregated protein was identified as TDP-43. Full-length TDP-43 is predominantly nuclear in histological analysis however it frequently shuttles between the nucleus and cytoplasm. Characteristic TDP-43 pathology includes accumulation of TDP-43 in the cytoplasm, which co-insides with loss of nuclear TDP-43 (Neumann et al., 2006). Interestingly, the RBP ELAVL3 is downregulated across many types of ALS including sALS, and the corresponding protein mislocalises in models of ALS prior to TDP-43 mislocalisation (Diaz-Garcia et al., 2021). This suggests that TDP-43 pathology is downstream of other cellular disturbances.

TDP-43 contains a nuclear import signal (NIS), and until recently was assumed to harbour a nuclear export signal (NES). The true functional relevance of this domain is uncertain, with data suggesting that the predicted NES is non-functional, and that nuclear export occurs independently of Exportin-1 (Ederle et al., 2018). TDP-43 proteinopathies are multifactorial, and a plethora of reviews highlight the complexity and abundance of TDP-43 dysregulation in neurodegeneration (Aikio et al., 2021;

Berning & Walker, 2019; Bright et al., 2021; Buratti, 2018; Chen & Mitchell, 2021; Chhangani et al., 2021; Eck et al., 2021; Jo et al., 2020; Keating et al., 2022; Prasad et al., 2019; Suk & Rousseaux, 2020; Tziortzouda et al., 2021; Wood et al., 2021). These emphasise the influence of post-translational modifications in TDP-43 pathology, including phosphorylation, truncation, ubiquitination, acetylation, methylation, SUMOylation, and nitrosylaiton.

TDP-43 aggregates often co-localise with p62, a ubiquitin binding protein which functions in autophagy and often associates with pathological protein inclusions (Neumann et al., 2006). Two distinct mechanisms for TDP-43 aggregation have been identified; one relying on microtubule proteins, HDAC6, and aggresomes, and another mediated by liquid phase-separation-dependent interaction with RBPs (Watanabe et al., 2020). The same study identified that half of the skein-like inclusions in sALS spinal cord tissue associate with HDAC6, whereas round granular aggregates do not, highlighting diversity in TDP-43 aggregates and implicating multiple pathways for inclusion formation. Misfolded cytoplasmic TDP-43 can self-propagate and induce further misfolding in a prion-like manner, leading to progressive spreading of pathology (Jo et al., 2020; March et al., 2016; McAlary et al., 2019). TDP-43 spread can occur via direct cell-to-cell transmission mediated by the protein N-terminal (Sackmann et al., 2020), and TDP-43 and other ALS-associated proteins are found in extracellular vesicles in sALS patient plasma, indicating that disease may also spread through vesicle-mediated transmission (Sproviero et al., 2018). Further, treating iPSC derived cerebral organoids with ALS spinal cord extracts can induce TDP-43 pathology, indicating that intercellular toxic species can induce and spread disease (Tamaki et al., 2022).

RNA processing functions of TDP-43 include pre-mRNA splicing (Polymenidou et al., 2011), axonal mRNA transport (Alami et al., 2014), mRNA translation (Neelagandan et al., 2019), maintaining RNA transcript stability (Izumikawa et al., 2017), and regulation of non-coding RNA (Lourenco et al., 2015). The RNA recognition motifs (RMM) in TDP-43 – RRM1 and RRM2 – facilitate interactions between TDP-43 and RNA. Many interacting partners of TDP-43 are themselves involved in RNA metabolism, including roles in splicing and translation. Some of these TDP-43 protein interactions do not require

RNA, however other interactions are mediated by the presence of RNA (Freibaum et al., 2010). Depletion of mRNA by inhibition of transcription leads to loss of nuclear TDP-43, suggesting that RNA binding has a role in retaining normal nucleocytoplasmic ratios of TDP-43 (Ederle et al., 2018). The presence of a K181E mutation adjacent to RRM1 inhibits TDP-43 binding to RNA and reduces TDP-43 solubility and phosphorylation, suggesting that RNA binding has a role in preventing TDP-43 aggregation (Chen et al., 2019). TDP-43 interacts with G-quadruplex mRNA via its glycine-rich region (Ishiguro et al., 2020), recognises RNA through both $(TG)_n$ and $(TG)_nTA(TG)_m$ binding sites (Bhardwaj et al., 2013; Sephton et al., 2011; Tollervey et al., 2011), and homodimerized TDP-43 can bind TG- and UG-rich sequences (Kuo et al., 2014), highlighting the complex nature of TDP-43 RNA recognition. Unpublished data indicate that RNA methylation also influences TDP-43 binding, which may be dysregulated in ALS (McMillan et al., 2022). Many of the TDP-43 RNA binding targets encode proteins that are implicated in ALS and FTD pathology, including FUS, progranulin, Tau, Ataxin 1, and Ataxin 2 (Sephton et al., 2011).

Multiple TDP-43 RNA isoforms and protein species exist; the namesake major western blot band of 43kDa is the predominant isoform, however various fragments are now acknowledged. The presence of a C-terminally truncated short TDP-43 (sTDP-43) isoform was recently described (Weskamp et al., 2020). The truncation introduces a new NES, and hyperexcitability results in upregulation and aggregation of sTDP-43 in the cytoplasm. Importantly, sTDP-43 accumulation is seen in neurons and glia in ALS patient tissue (Weskamp et al., 2020). Additional C-terminally truncated TDP-43 splice isoforms have been identified, sharing a unique 18AA region in the N-terminal of the truncated proteins, which includes the novel NES as demonstrated in sTDP-43, and TDP-43 species containing this 18AA sequence are upregulated in ALS patient spinal motor neurons (Shenouda et al., 2022). C-terminal fragments have been shown to mediate toxicity (Kitamura et al., 2016; Wang et al., 2013), however it has been noted that not all TDP-43 fragments detected in murine models of ALS faithfully recapitulate human disease (D'Alton et al., 2014).

TDP-43 autoregulation is disrupted in ALS: In healthy cells, when nuclear levels of TDP-43 are increased, TDP-43 protein binds to a 3'UTR region within its own pre-mRNA, resulting in splicing changes that result in nonsense mediated mRNA decay (Ayala et al., 2011; Polymenidou et al., 2011). This is disrupted in ALS, leading to a breakdown of the negative feedback loop and a gradual increase in total TDP-43. The phase-separation and oligomerisation properties of TDP-43 are necessary for autoregulation (Koehler et al., 2022), and inhibition of the cryptic exon splicing that causes *TARDBP* mRNA degradation causes an increase in fragmented and insoluble TDP-43, leading to motor neuron degeneration (Sugai et al., 2019). DNA demethylation in the 3'UTR region that is associated with autoregulation reduces alternative splicing, leading to an increase in expression of *TARDBP* mRNA, and demethylation of this region increases with age in the motor cortex (Koike et al., 2021). The importance of tight TDP-43 regulation is emphasised by evidence from mouse models that either lack or overexpress TDP-43. Homozygous TDP-43 null mice are non-viable (Kraemer et al., 2010; Sephton et al., 2010; Wu et al., 2010), and inducible post-natal knockout of TDP-43 causes motor neuron degeneration adult mice (Iguchi et al., 2013). Conversely, overexpression of wildtype (WT) TDP-43 causes neurodegenerative phenotypes in mice (Xu et al., 2010; Yang et al., 2022). Misbalance of TDP-43, whether it is up- or down- regulated, is pathogenic.

## *1.10 DNA, RNA, and ALS*

### *1.10.1 DNA damage*

Many genes encoding DNA/RNA binding proteins have been linked to ALS, as discussed in 1.6.6. DNA damage describes several genomic aberrations that occur in response to stressful events, and an inability to properly repair damaged DNA can lead to genomic instability, alterations to transcription and replication, and ultimately cell death (Chatterjee & Walker, 2017). Both TDP-43 and FUS have a role in sensing DNA damage and promoting repair, and multiple lines of evidence for ALS associated proteins in DNA damage response exist, including in in *C9ORF72*, *SOD1*, *VCP*, *p62*, *NEK1*, and *CCNF*

associated ALS (Konopka & Atkin, 2022). FUS mediated DNA repair is dependent on phase-separation (Levone et al., 2021), and PARP mediated DNA damage response is impaired in mutant *FUS* models of ALS, leading to downstream cytoplasmic aggregation (Naumann et al., 2018). Further, *C9ORF72* associated DPRs can inhibit homology directed repair (Andrade et al., 2020).

### *1.10.2 Liquid-liquid phase-separation in RNA and RBP function*

In addition to direct interaction with DNA, many ALS proteins bind to and regulate RNA. The transcriptomic signature of axons and dendrites varies from that of the soma, which is vital for cellular compartmentalisation. mRNA repression and expression are spatially and temporally regulated and change in response to various intracellular and extracellular cues. One of the main governing forces over such highly controlled and dynamic gene expression is RBPs. Many ALS associated RBPs have been shown to phase-separate, including TDP-43, FUS, TIA1 (Levone et al., 2021; Mackenzie et al., 2017; Murakami et al., 2015; Reber et al., 2016), Matrin 3 (Iradi et al., 2018), and Annexin A11 (Nahm et al., 2020), and phase-separating protein condensates can seed pathological inclusions (Fernandopulle et al., 2019). Phase-separation is associated with low-complexity domains, sometimes referred to as prion-like domains. In specific instances, for example in FUS, amino acid motifs outside of the low-complexity domain have been shown to regulate low-complexity mediated phase-separation (Bogaert et al., 2018), highlighting how protein folding and 3D structure impact phase-separation. Phase-separation of ALS associated proteins including FUS, TDP-43, and Annexin A11 is dependent on hydrophobic and non-ionic interactions (Krainer et al., 2021), and phase-transition of proteins is mediated by RNA (Mann & Donnelly, 2021).

### *1.10.3 RNA transcription and splicing*

Broad changes to splicing regulation can result in huge changes in protein expression and may have major implications for cell organisation and function. Many genes implicated in ALS encode splicing factors, including *TARDBP*, *FUS*, and *hnRNPA1*. Depletion of TDP-43 in the adult mouse brain led to

965 detectable splicing changes, with the most striking dysregulation occurring in mRNA whose corresponding genes contain long introns and are involved in synaptic function (Polymenidou et al., 2011). TDP-43 represses splicing of non-conserved cryptic exons, thus maintaining intron integrity. In the absence of normal TDP-43 function, cryptic exons are retained leading to nonsense mediated decay of mRNA transcripts, and such cryptic exon repression is impaired in ALS/FTD (Ling et al., 2015). An important example of ALS-associated splicing disturbance is that TDP-43 nuclear depletion is associated with inclusion of a cryptic exon in *UNC13A*, leading to mRNA nonsense mediated decay and loss of the corresponding synaptic protein UNC13A (Brown et al., 2022; Ma et al., 2022). *UNC13A* is often highlighted in ALS GWAS (Nicolas et al., 2018; Shatunov et al., 2010; van Es et al., 2009; van Rheenen et al., 2016), and prior to the discovery of TDP-43 mediated cryptic exon splicing, the functional relevance of these genetic associations was undetermined.

FUS also regulates splicing events that are involved in neuron survival and maintenance (Fortuna et al., 2021; Orozco et al., 2012), however FUS knockdown results in splicing changes predominantly different to those seen when TDP-43 is knocked-down (Lagier-Tourenne et al., 2012). Notably, a subset of RNA whose corresponding genes have long introns and are essential for neuronal integrity are altered in response to either FUS or TDP-43 knockdown (Lagier-Tourenne et al., 2012). Similarly, RNA binding sites and target exons for regulation by FUS do not consistently overlap with TDP-43 targets, however both proteins regulate transcripts involved in neuronal development (Rogelj et al., 2012). Small nuclear riboproteins (snRNPs) form the minor spliceosome and are enriched in FUS-interacting protein fractions detected by mass-spectrometry, and knockdown of- or mutations in-FUS results in dysregulation of many minor-intron containing mRNAs (Gadgil et al., 2021; Reber et al., 2016).

*C9ORF72* repeat expansions result in dynamic splicing inconsistencies in patient-derived lymphoblastoid cell lines (LCLs) and iPSC-neurons due to sequestration of RNA processing proteins by RNA foci (Cooper-Knock et al., 2015). *SOD1* is occasionally implicated in RNA or DNA metabolism, and ALS mutant SOD1 protein was shown to bind with increased affinity to mRNAs, including *VEGF*,

which is essential for motor neuron maintenance, leading to dysregulation of the mRNA in disease models (Li et al., 2009). Additionally, RNA sequencing of isogenic iPSC-derived neurons harbouring a heterozygous *SOD1* point mutation revealed altered levels of transcripts of genes involved in signal transduction, extracellular matrix organisation, calcium homeostasis, and neurogenesis. Notably this included downregulation of *ANXA11*, which is the subject of this thesis (Wang et al., 2017).

General splicing defects have been identified in multiple instances of ALS, and abnormal intron retention is observed in multiple ALS subtypes including sALS, *VCP*, *SOD1*, and *FUS* (Luisier et al., 2018; Tyzack et al., 2021). One of the most marked cases of intron retention is in the *SFPQ* transcript, which is splicing factor itself, and whose protein binds strongly to the retained intron within its own mRNA (Luisier et al., 2018). Loss of SFPQ protein due to intron retention leads to activation of multiple cryptic exons which leads to premature loss of multiple transcripts, and multiple SFPQ cryptic exon targets are found aberrantly expressed in ALS iPSC-derived neurons (Gordon et al., 2021). Patients can be stratified based on the dysregulation of specific splicing factors, suggesting splicing abnormalities might be important for patient segregation in development of new therapeutics (La Cognata et al., 2020).

### *1.10.4 Translation*

In addition to transcription and splicing abnormalities in ALS, the subsequent translation of proteins is also affected. Alterations to global protein translation have been demonstrated in multiple forms of ALS including *TARDBP* (Charif et al., 2020; Russo et al., 2017), *ANXA11* (Nahm et al., 2020), and *FUS* (Kamelgarn et al., 2018). Local translation is an essential process for the longevity of neurons, and the unique structure of neurons necessitates local translation of mRNAs that have been transported away from the soma along axons and dendrites, allowing plasticity and compartmentalisation of neuronal regions. Multiple isoforms of many mRNA species exist, sometimes differentiated by 3’ UTR length. Interestingly, longer 3’UTR isoforms are enriched in subcellular regions of neurons and have increased half-life compared with their short 3’UTR

counterparts, and long 3'UTR isoforms enriched in neurons are associated with axons, dendrites, and synapses (Tushev et al., 2018). In retinal ganglion cells, Rab7-positive late endosomes act as platforms for local protein synthesis, and disruption of Rab7a results in impaired local protein synthesis and axon integrity (Cioni et al., 2019). Local translation is dysregulated in ALS associated with FUS (Birsa et al., 2021; Kamelgarn et al., 2018; López-Erauskin et al., 2018; Murakami et al., 2015; Yasuda et al., 2013), and TDP-43 (Altman et al., 2021; Briese et al., 2020; Gao et al., 2021; Majumder et al., 2016). Non-canonical translation of *C9ORF72* repeat expansion RNA to form disease associated DPRs further hints towards abnormal translation events in ALS (Ash et al., 2013). Axonal protein synthesis is regulated by TORC1 (Campbell & Holt, 2001), linking autophagy with altered local protein synthesis. Additionally, the role of local translation in non-neuronal cells is largely underexplored and has been proffered as an important avenue for further investigation (Barton et al., 2019).

### *1.10.5 Stress granules*

Stress granules are transient membraneless organelles comprised of mRNAs and RBPs that form in response to cellular stress. Sequestration of mRNA into stress granules via interaction with stress granule proteins proposedly halts translation of non-essential mRNA, which is then reversed as cellular homeostasis rebalances once the stressor is removed (Wheeler et al., 2016). Post-translational modifications can affect stress granule dissolution; TIA1 is a stress granule protein whose corresponding gene harbours mutations associated with ALS (Mackenzie et al., 2017), and the *C. elegans* homologue TIAR-2 retains axonal mRNA in response to axon injury, which is dependent on TIAR-2 phosphorylation (Andrusiak et al., 2019). Similarly, the well-characterised stress granule protein G3BP1 forms axonal stress granules in response to axonal damage, which disassemble as G3BP1 is phosphorylated (Sahoo et al., 2018). G3BP1 stress granules can be degraded by the ubiquitin pathway or in the ER, depending on the stress inducing event (Gwon et al., 2021; Takahashi et al., 2022). Small ubiquitin-like modifier (SUMO) modification to stress granules regulates their

disassembly (Keiten-Schmitz et al., 2020; Marmor-Kollet et al., 2020): SUMOylation of the stress granule protein senataxin is required for proper stress granule disassembly (Bennett & La Spada, 2021), and SUMOylation control of stress granule dynamics is dysregulated in *C9ORF72* ALS (Marmor-Kollet et al., 2020). Stress granules can also be targeted by autophagy, and ALS associated mutations in *VCP* can affect disassembly of stress granules (Gwon et al., 2021).

Genetic mutations affecting the phase-separation of the stress granule protein TIA1 results in abnormal stress granule kinetics (Ding et al., 2021; Mackenzie et al., 2017), and ALS associated proteins with low-complexity domains often localise to stress granules. TDP-43 localises to inclusions positive for stress granule proteins in ALS and FTD brain tissue (Liu-Yesucevitz et al., 2010) and cellular models (Ratti et al., 2020), and TDP-43 is required for efficient stress granule dynamics (Khalfallah et al., 2018; McDonald et al., 2011). Additionally, some evidence suggests that increased abundance of TDP-43 in the cytoplasm leads to impaired formation of stress granules (Besnard-Guérin, 2020; Orrù et al., 2016). Small molecule mediated reduction of TDP-43, FUS, and hnRNPA2B1 localisation to stress granules reduces cytoplasmic TDP-43 accumulation induced by transient stress granule formation (Fang et al., 2019). Mutant FUS incorporates into stress granules (Bosco et al., 2010; Gal et al., 2011), and stress granule alterations have been demonstrated in the context of mutations In *ANXA11* (Liao et al., 2019; Nahm et al., 2020), *hnRNPA2B1* (Martinez et al., 2016), *C9ORF72* (McGurk et al., 2014), and *SOD1* (Lee et al., 2020), to name a few, but by no means all, examples.

In addition to the extensive evidence that processing of protein encoding mRNA is disrupted in ALS, recent evidence implicates non-coding RNA in disease. These include long non-coding RNA (Chen & Chen, 2020) and microRNAs (Rizzuti et al., 2018, 2022), and specific microRNA signatures have been identified in ALS skeletal muscle (Aksu-Menges et al., 2021).

## *1.11 Excitotoxicity*

Exitotoxicity is mediated by altered calcium and glutamate metabolism, and has been linked with mitochondrial impairment, induction of autophagy, reactive oxygen species (ROS) production, and dysfunctional calcium homeostasis, to name a few (Armada-Moreira et al., 2020). L-glutamate is the most abundant free amino acid in the brain, it functions as an excitatory neurotransmitter and is involved in many metabolic pathways. In glutamatergic neurons, L-glutamate is highly concentrated at synaptic terminals in order that it can be rapidly released into the synaptic cleft, where it stimulates the post-synaptic neuron (Zhou & Danbolt, 2014). Free glutamate in the extracellular space is tightly regulated by glial cells to avoid over stimulation of neurons, which can lead to cell death, a process known as excitotoxicity. Defective glutamate transport in ALS has been acknowledged for 30 years (Rothstein et al., 1992), and evidence for excitotoxicity in ALS includes a high abundance of L-glutamate receptors on motor neurons, and the current reliance on Riluzole, an anti-excitatory drug, in the treatment of ALS.

### *1.11.1 Excitatory transmission and calcium homeostasis*

Many aspects of excitotoxicity are associated with calcium dysregulation, and loss of calcium homeostasis links receptor and channel mediated neuronal activity with altered intracellular organelle function, including ER and mitochondrial dysfunction (Tedeschi et al., 2021). Neuronal excitability can be detected in the cortex and peripheral axons of ALS patients (Higashihara et al., 2021; Park et al., 2017; Vucic & Kiernan, 2006; Wainger et al., 2021), and multiple disease models implicate excitability as an important factor in pathology. However, whether excitability is causal or consequential in disease remains elusive.

Glutamate AMPA receptors are comprised of subunits including GluR2, which is dysregulated in sALS. GluR2 deficient AMPA receptors are more permeable to calcium, motor neurons derived from GluR2 deficient mice are more susceptible to AMPA mediated excitotoxicity, and crossbreeding GluR2

deficient mice with *SOD1* mice accelerates disease progression (Van Damme et al., 2005). GluR2 Q/R RNA editing is a common feature in the adult CNS, however this editing is incomplete or absent in most sALS patients in specific CNS regions (Kawahara et al., 2004; Kwak & Kawahara, 2005; Takuma et al., 2001). Altered GluR2 Q/R RNA editing is associated with downregulation of the RNA editing enzyme ADAR2 in ALS affected motor neurons (Hideyama et al., 2012), and AMPA receptor antagonism reduces ALS progression and cellular pathology in a motor neuron-specific *ADAR2* knockout ALS mouse model (Akamatsu et al., 2016, 2022). Astrocytes partially mediate neuronal expression of GluR2, indicating that non-cell autonomous mechanisms affect neuronal excitability (Van Damme et al., 2007).

In addition, metabotropic glutamate receptors mGluR1 and mGluR5 are increased in spinal cord axon terminals in *SOD1* mice (Bonifacino et al., 2019), and activation of presynaptic mGluR1 and mGluR5 is associated with increased glutamate release upon mild stimulation in *SOD1* mice (Giribaldi et al., 2013). Interestingly, astrocytes are also vulnerable to metabotropic receptor mediated excitotoxicity: Degeneration of motor neuron-adjacent astrocytes was associated with mGluR5 activation in *SOD1* mice, and mGluR5 blockage slowed degeneration of astrocytes and delayed disease onset (Rossi et al., 2008). Further, D-serine is a microglia-derived co-antagonist of the NMDA receptor which enhances glutamate toxicity in ALS motor neurons, and D-serine levels are increased in the spinal cord of fALS and sALS patients (Sasabe et al., 2007).

*CALB1, GAD2, and GABRE* are downregulated in ALS patient spinal tissue (Patel & Mathew, 2020). *CALB1* encodes calbindin 1, which has a role in calcium buffering upon stimulation of glutamate receptors. *GAD2* and *GABRE* are both involved in GABAergic signalling and so downregulation might lead to reduced inhibitory regulation. In these instances, expression of these genes was unperturbed in oculomotor neurons, which are largely spared from degeneration in ALS, suggesting disrupted control over excitatory signalling in ALS sensitive neurons (Patel & Mathew, 2020). Altered levels of calcium permeable receptor subunits have been identified in *C9ORF72* and *TARDBP* motor neurons (Dafinca et al., 2020; Selvaraj et al., 2018), and altered calcium influx, glutamate receptor changes,

and evidence of excitotoxicity have been detected in models of *C9ORF72* ALS (Jensen et al., 2020; Shi et al., 2018). Comparison of multiple ALS associated mutations in iPSC-derived neurons revealed gene specific perturbations to glutamate receptor and calcium dynamics: *TARDBP* mutants harboured increased basal calcium and increased amplitude of AMPA mediated signal; *C9ORF72* expansion neurons displayed increased spontaneous calcium transients and increased expression of kainate receptors and voltage-gated calcium channels; mutant *FUS* was associated with increased expression of AMPA and kainate receptors; and *SOD1* mutations were associated with increased expression of metabotropic glutamate receptors (Bursch et al., 2019). These data are important in highlighting mutation specific cellular alterations that converge on an overlapping dysfunctional pathway, perhaps providing an explanation for how heterogeneous ALS genetics can cause similar pathology.

### *1.11.2 Glutamate homeostasis*

EAAT2, one of the main glial glutamate transporters, maintains physiological levels of L-glutamate in the extra cellular space, and has been implicated in ALS. EAAT2 levels are reduced in ALS patient motor cortex and spinal cord (Jiang et al., 2019; Rothstein et al., 1995), and reduced expression of EAAT2 correlates with severity of motor neuron loss in ALS spinal cord (Sasaki et al., 2000). Knockout of the glial ER protein membralin resulted in TNF receptor-mediated reduced expression of EAAT2, resulting in accumulation of extracellular glutamate and motor dysfunction in mice (Jiang et al., 2019). Additionally, astrocyte-specific expression of mutant TDP-43 in rats resulted in motor neuron degeneration which was associated with gradual loss of EAAT2 (Tong et al., 2013). Increased expression of EAAT2 in astrocytes in a mouse model of ALS delayed symptom onset and progression, however did not ameliorate disease, indicating that inhibition of excitotoxicity might delay disease, but may not be the root cause of degeneration (Guo et al., 2003). Gene delivery of *EAAT2* to astrocytes in symptomatic *SOD1* mice did not rescue the ALS phenotype, despite inducing robust

expression of EAAT2 in GFAP positive astrocytes, further indicating that targeting glutamate homeostasis after disease onset may not be a viable solution in ALS (Li et al., 2015).

### *1.11.3 Neuronal vulnerability to excitotoxicity*

Hyperexcitability in immature *C9ORF72* iPSC-derived neurons is associated with increased release of calcium from internal stores, with no alteration to membrane potential, with the phenotype reducing with culture maturity, indicating a developmental perturbation or a vulnerability that is temporarily mediated (Burley et al., 2022). Similarly, unpublished data indicate that *TARDBP* mutant neurons initially display hyperexcitability, becoming hypoexcitable with further aging (Harley et al., 2022). Analysis of intrinsic excitability of motor neurons innervating fast- and slow-twitch muscle fibres found that disease-vulnerable fast-twitch innervating motor neurons were not hyper-excitable in neonatal *SOD1* mice, yet disease-spared slow-twitch innervating motor neurons were (Leroy et al., 2014). This emphasises that delineation of motor neuron subtypes will be important for elucidating the developmental and temporal effects of excitotoxicity. Additionally, some evidence from *SOD1* mouse models indicates that early-postnatal increases in excitability are associated with neuronal protection (Saxena et al., 2013), suggesting that hyperexcitability might initially be employed to preserve neurons. Selective depletion of TDP-43 in pyramidal neurons in adult mice showed that loss of TDP-43 function initially causes calcium hyperactivity, followed by activity decline alongside loss of neurons (Liang et al., 2022). Longitudinal analysis of intrinsic excitability and transcriptomic changes in *C9ORF72* iPSC-derived motor neurons revealed an early upregulation of synaptic proteins alongside increased activity, and both culture activity and synapse expression diminished with culture aging (Sommer et al., 2022). The consequences of increased excitability include cytoplasmic increase of a sTDP-43, which subsequently aggregates and sequesters full length TDP-43 (Weskamp et al., 2020). Spontaneous neuronal hyperexcitability has been associated with ER stress and apoptosis, although in this instance was not investigated in the context of ALS (Chanaday et al., 2021).

### *1.11.4 The role of interneurons in excitotoxicity*

Interneurons might influence excitotoxicity by exerting negative control over upregulated neuronal firing, and loss of inhibitory input onto motor neurons could elevate post-synaptic activity. Post-mortem analysis of sALS ventral and lumbar spinal cord revealed loss of motor neurons and interneurons, and loss of both cell types increased with disease duration, however it was not clear whether interneurons were lost before, concurrently with, or after motor neurons (Stephens et al., 2006). The wobbler ALS mouse model displays cortical hyperexcitability, including increased hippocampal synaptic excitation prior to symptom onset, and symptomatic mice show a reduced number of parvalbumin interneurons compared to control and non-symptomatic mice (Thielsen et al., 2013). Degeneration of interneurons before motor neuron death has been demonstrated in *SOD1* ALS models (Allodi et al., 2021; Martin et al., 2007), and *SOD1* zebrafish harbour interneuron stress and reduced inhibitory input onto motor neurons prior to alterations at the NMJ (McGown et al., 2013). Additionally, *SOD1* mice show altered interneuron characteristics selectively in cortical regions influencing motor control (Minciacchi et al., 2009) as well as in spinal regions (Salamatina et al., 2020). Notably, investigation into interneuron loss has predominantly focused on models of *SOD1* pathology, and it will be important to characterise interneurons in other ALS models. Some evidence of reduced interneuron number in *TARDBP* ALS mice exists, however the authors imply this is due to neurodevelopmental influence as opposed to degenerative loss of neurons (Lin et al., 2021). Age-related poly-ubiquitinated protein aggregates were detected in the hippocampus in *TARDBP* mutant mice, with some aggregates co-localising with the interneuron proteins parvalbumin and calretinin (Tsuiji et al., 2017), indicating potential degeneration of interneurons across multiple ALS genes.

## *1.12 Protein aggregation and disrupted proteostasis*

Protein aggregation is a common feature across ALS and FTD. In addition to TDP-43 inclusions, as discussed in 1.9, many proteins are found aggregated in surviving motor neurons in ALS post-mortem

tissue. Proteins whose corresponding genes are mutated in ALS often aggregate in disease including Ubiquilin-2 (Deng et al., 2011), FUS (Vance et al., 2009), Annexin A11 (Smith et al., 2017; Teyssou et al., 2020), PFN1 (Wu et al., 2012), and SOD1 (Bruijn et al., 1998). Proteinopathy varies between cases, and alterations in aggregate burden and identification of aggregates in different brain/spinal cord regions is genotype-specific (Nolan et al., 2020). Multiple mechanisms by which pathological protein aggregates form have been recognised. Phase-separation of proteins might seed aggregates, and phase-separating proteins can form fibrils which go on to form stable structures, mediated in part by the cellular environment (Babinchak & Surewicz, 2020). Alternative protein aggregation pathways are dependent on microtubule dynamics (Farrawell et al., 2015; Watanabe et al., 2020), suggesting that multiple dysregulated pathways converge on pathological aggregation.

Protein quality control in the ER ensures that proteins are properly folded before they are released into the cytoplasm. The ALS-associated protein VAPB is essential for proper protein quality control, and ALS-associated mutations in *VAPB* can result in ER-stress and protein accumulation (Larroquette et al., 2015; Moustaqim-Barrette et al., 2014; Nishimura et al., 2004). Protein regulation is also mediated by heat-shock proteins, which are implicated in TDP-43 processing (Chen et al., 2016; François-Moutal et al., 2022).

Protein aggregates, including TDP-43 positive inclusions, are often ubiquitinated (Blokhuis et al., 2013), and sequestration of ubiquitin by misfolded ALS-associated proteins, leading to disruption of ubiquitin homeostasis, is a common feature across ALS (Farrawell et al., 2020). Ubiquitin is a major factor in proteasome-mediated protein degradation, and ubiquitin binds to target proteins to the end that poly-ubiquitinated proteins are recognised for degradation by the proteasome. ALS-associated mutations in *UBQLN2* (Williams et al., 2012) and *CCNF* (Williams et al., 2016), which encode proteins involved in ubiquitin-proteasome degradation, reiterate the importance of this system in motor neuron degeneration. Proteasome subunits or cofactors are often sequestered by pathological protein species, including *C9ORF72* associated DPRs (Guo et al., 2018; May et al., 2014).

An alternative protein degradation pathway that is also disrupted in ALS is autophagy, which describes the degradation of proteins sequestered into autophagosomes by fusion with lysosomes. Ubiquilin-2 also has a role in autophagy, and mutations in *UBQLN2* have been shown to impede normal autophagy function, highlighting that the two protein degradation pathways are not mutually exclusive (Wu et al., 2020). Interestingly, it has been suggested that separate TDP-43 species are degraded by specific mechanisms; soluble TDP-43 is cleared by the proteasome system, and autophagy is required to clear larger TDP-43 aggregates (Scotter et al., 2014). Autophagy has been implicated in *C9ORF72* (Nassif et al., 2017), and ALS associated genes often function in autophagy, including *OPTN* (Maruyama et al., 2010), *SQSTM1/p62* (Deng et al., 2020), *TBK1* (Freischmidt et al., 2015), and *VCP* (Ju et al., 2009). Induction of autophagy alleviates pathology in multiple models: In mutant *TARDBP* mice, induction of autophagy with the novel small molecule IMS-088 ameliorates TDP-43 mediated transcriptional changes, including restoration of neurofilament mRNA translation (Kumar et al., 2021). Multiple studies utilizing iPSC-derived cultures with a variety of ALS-causing mutations have shown phenotype rescue with autophagy enhancement (Barmada et al., 2014; Imamura et al., 2017; Marrone et al., 2018), or have shown decreased cell viability with autophagy inhibition (Almeida et al., 2013).

### *1.13 Nucleocytoplasmic transport*

Nucleocytoplasmic transport is the mechanism by which cargos, including proteins and RNA species, shuttle between the nucleus and cytoplasm. This includes both passive transport, where small molecules diffuse through nuclear pores based on diffusion gradients, and active transport which is ATP-dependent. Nucleocytoplasmic transport is dysregulated in *C9ORF72* ALS (Freibaum et al., 2015; Zhang et al., 2015), and DPRs have been shown to disrupt the nuclear membrane (Chien et al., 2021). The frequent observation that the nucleocytoplasmic ratio of ALS associated proteins is unbalanced in ALS, for example in cases with TDP-43 and FUS proteinopathy, suggest that nucleocytoplasmic transport might be dysfunctional in ALS (Ederle & Dormann, 2017). An increase in the nuclear

abundance of CHMP7 initiates injury to the nuclear pore, which is upstream of TDP-43 mislocalisation in iPSC-neurons derived from sALS and *C9ORF72* patients (Coyne et al., 2021). Impaired interaction of mutant FUS with the nucleocytoplasmic transport protein Karyopherin$\beta$2 has been demonstrated (Basu et al., 2022), and mutant FUS interacts with nucleoporins resulting in reduced nucleocytoplasmic transport and nucleoporin density on the nuclear membrane (Lin et al., 2021). This highlights how nucleocytoplasmic transport can be affected by both breakdown of transport channels and impaired transport protein function. Indeed, insoluble TDP-43 aggregates sequester both nuclear pore proteins and transport factors, and nuclear pore pathology is present in brain tissue from sALS, *TARDBP*, and *C9ORF72* patients (Chou et al., 2018).

Nuclear pore dysfunction is linked to autophagy, and *C9ORF72* pathology may be associated with reduced nuclear import of the autophagy factors Mitf/TFEB, leading to improper control of autophagy flux (Cunningham et al., 2020). Nuclear pore integrity can be impaired by ALS and FTD associated microtubule abnormalities (Giampetruzzi et al., 2019; Paonessa et al., 2019), hinting that divergent cellular dysfunctions might overlap in causing damage to the nuclear pore and transport systems. Many proteins that make up the nuclear pore have a particularly long half-life, indicating they might be sensitive to aging in post-mitotic neurons. Replenishment and protein turnover is comparatively slow, leading to nuclear pore leakage in aged cells, which may be relevant for typically late-onset ALS (D'Angelo et al., 2009).

### *1.14 Mitochondria, endoplasmic reticulum, and metabolism*

Mitochondria have multiple functions including synthesis of ATP for bioenergetic transfer, mediation of calcium homeostasis, signal transduction, lipid homeostasis, and activation of apoptosis. Neurons are particularly energy-dependent and metabolically demanding, and, importantly, abnormal mitochondria are detected in ALS post-mortem tissue (Sasaki & Iwata, 2007; Wang et al., 2019). Increased mitochondrial demand leads to upregulation of ATP synthesis by oxidative phosphorylation, which subsequently results in increased levels of ROS; noxious free radicals that

are generated as an intrinsic by-product in ATP synthesis. ROS cause oxidative stress to multiple organelles and molecules, including mitochondria, ER, lipids, DNA, and proteins; thus, under normal conditions ROS are processed by multiple antioxidant enzymes, such as SOD1, to prevent ROS-induced damage. Hence, ROS-mediated cellular stress may be indicative of a decrease in antioxidative processing. A large-scale transcriptomic screen of post-mortem ALS cortex samples revealed that 61% display evidence of oxidative- and ER-stress (Tam et al., 2019), highlighting the prevalence of oxidative stress in ALS. Molecular profiling of subsets of vulnerable and resilient neurons in the motor cortex of a *SOD1* mouse model revealed improper handling of ROS in vulnerable cells, which was likely associated with subsequent degeneration (Moya et al., 2022). Accumulation of mutant SOD1 is associated with activation of apoptosis though sequestration of Bcl-2, an anti-apoptotic protein, and by activating caspase-dependent cell death (Pasinelli et al., 2004; Takeuchi et al., 2002, 2016).

Mitochondrial instability has been demonstrated at early time points in ALS models, and mitochondrial destruction occurs as early as postnatal day 15 in upper motor neurons of mouse models of *TARDBP*, *PFN1*, and *SOD1* ALS (Gautam et al., 2022; Gautam, Jara, et al., 2019; Gautam, Xie, et al., 2019), and as early as postnatal day 6 at the muscle pre-synapse in mutant *FUS* mice (So et al., 2018). iPSC-derived motor neurons from sALS and fALS patients have increased ROS, impaired oxidative phosphorylation, depolarized mitochondria, defective mitochondrial protein import, and loss of ATP compared to control, and these features were absent in undifferentiated neural precursors (Singh et al., 2021). ALS-associated mutations in *CHCHD10* are associated with disorganised mitochondria cristae, respiratory chain deficiency, fragmentation of the mitochondrial network, and impaired mitochondrial genome maintenance (Bannwarth et al., 2014; Genin et al., 2016). The importance of mitochondrial DNA in ALS pathology is becoming recognised, and analysis of post-mortem pre-frontal cortex revealed a reduction in mitochondrial DNA copy number in *C9ORF72* patients compared to control, which was most evident in ALS patients with abundant TDP-43 aggregates (Alvarez-Mora et al., 2022).

TDP-43 pathology is heavily implicated in mitochondrial dysfunction, including; impaired ER-calcium uptake (Peggion et al., 2021); TDP-43 sequestration of mitochondrial genes and increased sensitivity to oxidative stress (Zuo et al., 2021); decreased mitochondrial membrane potential, increased ROS production, and mitochondrial unfolded protein response activation (Wang et al., 2019); and loss of transcripts involved in mitochondrial energy metabolism alongside perturbed axonal mitochondrial function (Briese et al., 2020). Full length TDP-43 localises to the mitochondrial matrix in cell models (Salvatori et al., 2018), directly interacts with mitochondrial proteins (Davis et al., 2018), and causes release of mitochondrial DNA into the cytoplasm (Yu et al., 2020). Suppression of TDP-43 mitochondrial localisation prevents mitochondrial damage and neuronal loss, and improves symptoms in *TARDBP* transgenic mice (Wang et al., 2016).

Mitochondria-ER tethering occurs at distinct sites, and the ER membrane regions involved in these connections are typically referred to as mitochondrial-associated ER membrane (MAM). VABP localises to the ER and binds to the mitochondrial protein PTPIP51, allowing calcium exchange between mitochondria and ER. VABP-PTPIP51 tethers are disrupted in *C9ORF72* patient derived motor neurons and transgenic mice, and disease associated DPRs disrupt VAPB-PTPIP51 interaction resulting in perturbed transfer of calcium from the ER to mitochondria (Gomez-Suaga et al., 2022). Impaired mitochondrial bioenergetic function and mitochondrial transport are also dysregulated in *C9ORF72* iPSC-neurons, and transcriptomic profiling revealed reduced expression of genes involved in the electron transport chain encoded by mitochondrial DNA (Mehta et al., 2021). In addition to the influence of MAM integrity on disease progression, ER-stress has been demonstrated in ALS, including in sALS (Sasaki, 2010), and models of *TARDBP*, *SOD1*, *FUS*, *ATXN2,* and *VAPB* associated ALS (Larroquette et al., 2015; Matus et al., 2013; Moustaqim-Barrette et al., 2014). The presence of ER throughout the entire neuron, including in axons, has been linked to the control of neurotransmission and synaptic function (Kuijpers et al., 2020; Öztürk et al., 2020), indicating a potential link between mitochondria/ER function and altered neuronal activity. Altered neuronal excitability might also be associated with dysfunctional calcium homeostasis, which is affected by

mitochondrial function: The mitochondrial calcium protein uniporter is an inner mitochondrial membrane channel that prevents mitochondrial calcium overload, and an imbalance of the uniporter regulators MICU1 and MICU2 is present in *C9ORF72* and *TARDBP* mutations (Dafinca et al., 2020). These models also displayed upregulation of calcium permeable AMPA and NMDA receptors, highlighting how calcium regulation is disrupted by inefficient inter- and intra- cellular calcium regulation.

Mitochondrial dysfunction is the focus of a large branch of ALS research, and in addition to the examples included here, the influence of mitochondria and ER function on pathology have been well reported, encompassing a wealth of evidence for the role of metabolism in ALS (Chen et al., 2021; Cheng et al., 2022; Jaiswal, 2014; Jankovic et al., 2021; Jurcau, 2021; Loncke et al., 2021; Madruga et al., 2021; Matus et al., 2013; Zhao et al., 2022). Metabolic disturbance in ALS is also associated with the co-enzyme NAD+, and extensive evidence indicates that manipulation of NAD+ pathways may be beneficial in therapeutic targeting in ALS (Harlan et al., 2016, 2020; Obrador et al., 2021).

### *1.15 Cytoskeleton and axonal transport*

The cytoskeleton physically and physiologically supports neurons, comprising a system of microtubules and filaments that offer structural support and provide a network for transport and subcellular organisation. The prevalence of ALS-associated mutations in multiple cytoskeletal genes hints toward the importance of the cytoskeleton in motor neuron degeneration (1.6.6), and transcriptomic profiling of sALS spinal motor neurons highlights downregulation of genes mediating transport and microtubule-associated proteins (Jiang et al., 2005, 2007). Some cytoskeletal or transport proteins aggregate in models of ALS (Levy et al., 2006; Smith et al., 2014), and axonal swellings in post-mortem ALS patient corticospinal tracts contain neurofilaments (Okamoto et al., 1990; Sasaki & Maruyama, 1992). The motor neuron cytoskeleton is comprised of microtubules, which are made up of $\alpha$- and $\beta$-actin subunits, and intermediate neurofilaments including NF-L, NF-

M, NF-H, $\alpha$-internexin, and peripherin, which undergo various post-translational modifications (Castellanos-Montiel et al., 2020).

Reduced axon integrity in ALS may be linked to TDP-43 accumulation, and TDP-43 mediates the translation of cytoskeletal components, including MAP1B (Majumder et al., 2016). TDP-43 stabilises NF-L mRNA by directly binding to its 3' UTR (Strong et al., 2007), and data from zebrafish models implicates TDP-43 in NF-L splicing (Demy et al., 2020). FUS also regulates the splicing of genes involved in axonal growth and cytoskeletal dynamics, including *MAPT* which encodes the microtubule-associated protein Tau (Ishigaki et al., 2012; Orozco et al., 2012; Rogelj et al., 2012). TDP-43 phosphorylation and insolubility are exacerbated by co-expression with mutant forms of *PFN1*, highlighting bidirectional feedback whereby TDP-43 affects cytoskeletal function and cytoskeletal proteins influence TDP-43 dynamics (Tanaka et al., 2016). ALS-associated mutations in *PFN1*, whose corresponding protein polymerises actin from its globular to filamentous form to enable filament elongation, result in reduced axon outgrowth and stability (Wu et al., 2012). *C9ORF72* protein directly interacts with cofilin, which acts in opposition to PFN1 by severing actin filaments, and *C9ORF72* knockdown or repeat expansion perturb motor neuron axon branching (Sivadasan et al., 2016). *TUBA1A* encodes an $\alpha$-tubulin subunit, and ALS-associated mutations in *TUBA1A* destabilise the microtubule network including impaired microtubule assembly resulting in increased pausing of trafficked organelles and decreased tubulin acetylation (Buscaglia et al., 2020; Smith et al., 2014). The enzyme HDAC6 has a role in actin deacetylation, and decreasing HDAC6 levels by pharmacological intervention or by genetic knockdown in *FUS* patient-derived motor neurons alleviates axonal transport deficits and increases $\alpha$-tubulin acetylation (Guo et al., 2017). Additionally, cellular models of *UBQLN2* ALS display increased levels of total and acetylated tubulin, in addition to decreased phosphorylation of FUS and upregulation of MAP1B (Strohm et al., 2022).

The polarised nature and sometimes extraordinary length of neurons means that many molecules and organelles need to be efficiently transported, and axonal transport proteins are essential for synaptic function and stability, including at the NMJ (Allen et al., 1999; Bercier et al., 2019; Eaton et

al., 2002; Yu et al., 2018). Axonal transport of cellular cargos occurs in anterograde and retrograde directions and relies on the motor protein complexes kinesin (anterograde) and dynactin (retrograde). ALS-causative mutations in *KIF5A,* which encodes a kinesin associated motor protein, lead to truncation of the protein, altered transport dynamics, and altered gene expression and splicing, highlighting the importance of axonal transport in regulating the transcriptome (Baron et al., 2022). Mutations-in or knockdown-of the retrograde transport factor *DCTN1* are associated with impaired transport of autophagosomes (Ikenaka et al., 2013) and vesicles that have budded from the ER and Golgi (Laird et al., 2008). Additionally, Dynactin subunit 1 depletion leads to neuromuscular synapse instability and functional abnormalities independent of its role in axonal transport, highlighting how ALS associated genes often influence multiple cellular functions (Bercier et al., 2019).

Transport of RNPs is essential for neuronal function and multiple mechanisms for RNP transport exist, including direct interaction of RNPs with transport machinery and interaction with intermediate proteins. RNPs containing SFPQ interact directly with KIF5a and KCL1 containing kinesin complexes in sensory neurons, and this interaction is essential for axon survival (Fukuda et al., 2021). Although not ALS specific, the same study found that compensating for lost SFPQ RNA cargos at the distal axon reverted disease phenotype in Charcot-Marie Tooth disease models, which mirror many ALS cellular pathologies. Annexin A11 acts as a tether between RNPs and lysosomes that are being transported along axons by motor proteins, such that RNPs “hitchhike” along axons (Liao et al., 2019), and mutations in the corresponding gene *ANXA11* are associated with ALS (Smith et al., 2017). In addition to these examples, multiple RNP transport mechanisms exist, and it may be beneficial for therapeutic targeting to identify specific transport pathways that are affected in disease.

Abnormal transport dynamics of various organelle and RNA cargos have been demonstrated in multiple genetic forms of ALS including *MATR3* (Zhao et al., 2020), *SOD1* (Gibbs et al., 2018), *C9ORF72* (Mehta et al., 2021), and *TARDBP* (Alami et al., 2014; Sleigh et al., 2020), highlighting dynamic misregulation of axonal transport across ALS. Additionally, cytoskeletal abnormalities are

associated with other cellular pathways that are implicated in ALS: Improper actin polymerization can affect nuclear pore integrity and cause alterations to nuclear import and mRNA post-transcriptional regulation, and nuclear pore defects induced by *C9ORF72* expansion or mutant *PFN1* can be rescued by stabilizing actin homeostasis (Giampetruzzi et al., 2019). Additionally, FTD associated *MAPT* mutations cause deformation of the nucleus which affects nucleocytoplasmic transport (Paonessa et al., 2019).

### *1.16 Non-cell-autonomous mechanisms and neuroinflammation*

Multiple lines of evidence exist for non-cell-autonomous toxicity in ALS, and motor neuron death has been linked to impaired trophic support and damage to neurons caused by release of toxic species by neighbouring cells. Molecular stratification of ALS subtypes revealed that 19% of a large cohort of ALS post-mortem tissue samples (148) displayed predominant glial activation signatures, which included upregulation of astrocytic, oligodendritic, and microglial genes, alongside upregulation of microglia-associated innate immune pathways including interferon and antigen processing pathways (Tam et al., 2019).

#### *1.16.1 Astrocytes*

Astrocytes collected from sALS and fALS patient post-mortem tissue are toxic to co-cultured motor neurons (Haidet-Phillips et al., 2011), and healthy astrocytes can delay degeneration and extend motor neuron survival *in vivo* (Clement et al., 2003). A meta-analysis including data from multiple human iPSC- and mouse-derived astrocyte studies identified upregulation of genes involved in the extracellular matrix, immune response, and ER-stress, and downregulation of genes involved with neuronal support including synaptic integrity and uptake of glutamate (Ziff et al., 2021). Astrocytes mirror some pathology seen in neurons in ALS, including altered intron retention (Ziff et al., 2021), TDP-43 aggregation, and increased levels of insoluble proteins (Barton et al., 2020). In co-culture models, ALS astrocytes cause toxicity to motor neurons, including in models of *C9ORF72* (Birger et

al., 2019), *FUS* (Kia et al., 2018), and sALS (Smethurst et al., 2020). *miR-146a* is reduced in *SOD1* mutant astrocytes, and pharmacological replenishment in astrocytes prevents microglial activation and neuronal damage when subsequently maintained in co-culture (Barbosa et al., 2021; Gomes et al., 2020, 2022).

Astrocyte-mediated spread of disease has been shown to occur via Connexin 43 hemichannels between astrocytes: Increased levels of Connexin 43 in ALS tissues correlate with accelerated ALS progression, patient-derived astrocytes show enrichment of Connexin 43 at the membrane, and blockage of these astrocytic hemichannels is neuroprotective of motor neurons (Almad et al., 2016, 2020). Transformation of astrocytes from a homeostatic/functional state to a reactive state has been associated with a failure to support neurons and may explain why initially protective astrocytes can exacerbate disease at later stages. Both control and *SOD1* mutant reactive astrocytes reduce motor neuron health when in co-culture, which is associated with increased release of TGF-$\beta$1 from reactive astrocytes (Tripathi et al., 2017). A recent study identified increased levels of inorganic polyphosphate as a robust feature of astrocytes from multiple ALS models and of ALS patient CSF and post-mortem tissue, and in the context of various genetic mutations (Arredondo et al., 2022). Additionally, reactive astrocytes were shown to cause neuronal toxicity via generation of saturated lipids (Guttenplan et al., 2021), indicating that toxic astrocytic species include a range of metabolic entities. In addition, the influence of astrocytes on neuronal excitotoxicity, namely through function of the glutamate transporter EAAT2, is discussed in 1.11.

### *1.16.2 Microglia and neuroinflammation*

*C9ORF72* haploinsufficient mouse models display neuroinflammation and immunity dysregulation including in microglia (Burberry et al., 2016; O'Rourke et al., 2016), and *C9ORF72* deficiency leads to an inflammatory microglial state that results in increased synaptic pruning and loss (Lall et al., 2021). Molecular characterisation of microglia from a *SOD1* mouse model revealed upregulation of both neuroprotective and toxic factors, and *SOD1* microglia displayed a different molecular signature to

WT microglia activated by lipopolysaccharide, indicating disease specific microglial changes (Chiu et al., 2013). Patient-derived microglia-like-cells display defective phagocytosis and elevated inflammatory response associated with abnormal actin polymerisation, implicating cytoskeletal perturbations across multiple cell-types in ALS (Noh et al., 2020). Moreover, conditioned media from iPSC-derived astrocytes and microglia altered neurofilament deposition in motor neurons, highlighting the influence of glial function on neuronal cytoskeletal dynamics (Allison et al., 2022). Mutant *FUS* iPSC-derived microglia displayed altered expression of chemoreceptor genes leading to altered calcium signalling, in this instance release of cytokines and phagocytosis were not affected, suggesting microglial abnormalities may be gene specific in ALS (Kerk et al., 2022). sALS patient monocyte-derived microglia-like-cells harbour TDP-43 and pTDP-43 inclusions, and show impaired phagocytosis, altered cytokine signatures, and neuroinflammatory morphology (Quek et al., 2022). In addition to altered microglia function, some evidence suggests that CCR2-expressing monocytes can infiltrate the CNS, increasing inflammation and accelerating ALS progression (Komiya et al., 2020), and natural killer cells have been shown to infiltrate and accumulate in the motor cortex and spinal cord in ALS tissue (Garofalo et al., 2020).

### *1.16.3 Other non-cell-autonomous mechanisms*

In addition to the influence of astrocytes and microglia on motor neuron degeneration, patient derived oligodendrocytes can induce motor neuron death via direct interaction with neurons or application of conditioned media (Ferraiuolo et al., 2016). TDP-43 directly binds to *SREBF2* RNA, which is a master regulator of cholesterol, and thus myelin, and depletion of TDP-43 results in reduced expression of SREBF2 and cholesterol (Ho et al., 2021). Derivation of skeletal myocytes from ALS patient iPSCs revealed downregulation of *BET1L*, *DCX*, *GPC3*, and *HNRNPK* transcripts, and Bet1L protein localises to the basal lamina of the NMJ and decreases in abundance with disease progression (Lynch et al., 2021), indicating muscle cell dysfunction may influence loss of NMJ integrity. Moreover, multiple lines of evidence for myoblast dysfunction in ALS have been reported

(Manzano et al., 2013; Scaramozza et al., 2014; Tokutake et al., 2015). Muscle biopsy of sALS patients revealed distinct microRNA signatures in subsets of the patient cohort, and dysregulated microRNAs were enriched for ALS relevant pathways in gene ontology analysis, such as regulation of transcription and dendrite morphogenesis (Aksu-Menges et al., 2021). Data yet to be peer reviewed indicate that muscle cells secrete neurotoxic vesicles in sALS patients (Gall et al., 2021), and intriguingly TDP-43 is implicated in several myopathies (Versluys et al., 2022).

### *1.17 Treatment strategies in ALS*

Despite great research efforts being made, there are currently no curative treatment strategies for ALS. The only drug that is licensed in the U.K., Riluzole, does not improve symptoms but prolongs survival for 2-3 months (Lacomblez et al., 1996). A retrospective study found that Riluzole mediated survival occurs in the last clinical stage of ALS, indicating that increased lifespan occurs during the disease stage where symptoms are most severe (Fang et al., 2018). Edaravone was approved by the U.S. FDA (United States Food and Drug Administration) after clinical trials indicated slower loss of motor function over placebo, however, as with Riluzole, Edaravone does not halt disease entirely nor improve symptoms, and only a small subset of ALS patients appears to be responsive to the drug (Bhandari et al., 2018; Writing Group & Edaravone (MCI-186) ALS 19 Study Group, 2017). Interestingly these drugs are understood to work via different mechanisms: Riluzole is widely regarded as an anti-excitatory agent, although its precise mechanism is not fully understood. It has been suggested to work by indirect antagonism of glutamate receptors, or by inactivation of neuronal voltage-gated sodium channels (Cheah et al., 2010). There is some evidence that Riluzole can affect the function of acetylcholine receptors on muscle fibres, however the consequences of this interaction are unknown (Deflorio et al., 2012). Edaravone is a potent antioxidant, reducing motor neuron toxicity by scavenging free radicals (Ohta et al., 2020). These contrasting mechanisms of action emphasise how multiple cellular pathways are disrupted in ALS, and consequently how challenging it has been to understand and cure the disease.

Huge efforts are being made to establish more efficacious therapies. Gene therapy is an exciting prospect and multiple targets have been posited. Gene therapy describes therapeutics that utilise genetic material by delivering DNA or RNA into cells to correct misregulated pathways. In cases where patients harbour genetic mutations known to cause loss of function of associated proteins, it may be possible to supply correct copies of genes, thus enabling host cells to produce the corresponding functional protein. An example is *PGRN*, where FTD-associated mutations result in reduced progranulin protein (Arrant et al., 2018). In cases of toxic gain of function, development of gene therapies may be more complicated, as functional protein might need to be introduced, as well as the toxic species inhibited. In cases of functional redundancy knockdown of the mutant mRNA may be sufficient. This might be achieved with microRNA or antisense oligonucleotides (ASO) that are delivered in a viral vector. This is relevant to *C9ORF72* ALS, where aberrant repeat expansion RNA species can be targeted (Sareen et al., 2013), and recent data indicates that targeting mutant *FUS* with an ASO delays motor neuron degeneration (Korobeynikov et al., 2022). These targets are applicable to small patient groups as single genetic mutations often account for <1% of the ALS population, pointing towards the necessity for personalised medicine in ALS/FTD. Genes that either positively or negatively mediate a broad spectrum of ALS cases are an attractive target as they could be beneficial to a wider patient population. Examples might include *ATXN2*, which has been shown to mediate TDP-43 toxicity which is present in the vast majority of ALS cases (Elden et al., 2010). An ASO targeting the microRNA *miR-129-5p* was shown to improve survival and neuromuscular phenotype in *SOD1* mice, and the same microRNA is upregulated in peripheral blood in sALS patients, suggesting that this could be a useful target in cases with no known genetic cause (Loffreda et al., 2020). Additionally, regulation of genes involved in commonly affected pathways such as the stress granule response or protein degradation pathways might be suitable targets. The main consideration here is whether genetic interference with cellular pathways with broad influence throughout the body can be appropriately targeted in the CNS, and with continued uncertainty about the driving force of disease, selection of suitable targets is ongoing. The challenges faced with developing gene therapy are broad: Avoiding toxicity, establishing viral load, and optimising delivery of therapies to

target regions are all important. Delivery of therapeutics across the blood brain barrier is a limiting step in the treatment of many neurological disorders, both degenerative and otherwise, and the same is relevant for gene therapy. Development of vectors that deliver gene therapies in an optimal spatiotemporal manner will be essential.

Cell replacement therapies are being explored as a means to replenish cells that are lost in disease. A Phase 3 Clinical Trial transplanting NurOwn® MSC-NTF cells was recently completed: Autologous bone marrow derived mesenchymal stem cells were collected from ALS patients and induced to secrete neurotrophic factors, then re-implanted back into patients. The results are yet to be disclosed (Brainstorm-Cell Therapeutics, 2021), however data from Phase 2 clinical trials indicate that transplantation is safe, and indicated early signs of efficacy (Berry et al., 2019; Petrou et al., 2016). In addition to transplantation of supportive cell types, stem cell therapies which aim to replace dying motor neurons are being developed. iPSC derived neural progenitor cells (NPCs) were injected into mutant *SOD1* rats and caused increased survival and preservation of motor neurons, but transplanted cells did not differentiate into motor neurons, indicating that any beneficial effect was via alteration to the cellular environment as opposed to generation of new neurons (Forostyak et al., 2020). Multiple studies have investigated the possibility of mesenchymal stem cell transplants in ALS, broadly indicating that such therapies are non-toxic (Boucherie et al., 2009; Kim et al., 2010; Mazzini et al., 2010, 2012; Vercelli et al., 2008; Zhao et al., 2007). Development of autologous transplants, i.e. mesenchymal or iPSC-derived cells, aims to mitigate transplant rejection, and it will be important to ensure that development of tumours and other toxicities are avoided. Further, development of functional and appropriate connections between host and transplanted cells is challenging, and further understanding of cellular integration into pre-existing systems will be necessary. Generation of biomaterials to enhance stem cell differentiation and integration in the host offer a promising development in cell replacement therapy, and may be essential for the future success of cellular transplants (Kharbikar et al., 2022).

In the absence of reliable therapeutics, much of the current management strategy for ALS is with technology, such as access to eye-tracking devices, which do not slow the disease, but enable patients to continue to communicate once they have lost the ability to speak. Research into brain-computer interface technology is working towards improving patient communication and autonomy. For example, companies such as Synchron© are making efforts to develop means for patients to control robotic arms when they have lost all voluntary muscle control. In addition to development of supportive technologies, research into caregiving practice and burden aims to improve the lives of those living with ALS, and those that care for them. In some cases, caregiving falls to relatives and even youth caregivers such as children (<19 years of age) of those affected, and support and development in this area are an important aspect of current disease management (Kavanaugh et al., 2018, 2020; Klavžar et al., 2020) .

As is the case for ALS, no curative treatments are currently available for FTD. Selective serotonin reuptake inhibitors (SSRIs) are occasionally prescribed, and in rare cases anti-psychotics. This aims to alleviate FTD symptoms but does not treat the underlying cause of disease (Kaye et al., 2010; Tsai & Boxer, 2014). The lack of viable treatment strategies alludes to the complexity of ALS and FTD, and the broad range of implicated cellular pathologies renders drug targeting ineffective: To better develop therapies, we need to better understand the disease.

### *1.18 Annexins*

Mutations in the protein coding gene *ANXA11* cause ALS (Smith et al., 2017). The corresponding protein, Annexin A11, belongs to a family of calcium dependent phospholipid binding proteins collectively termed the Annexins. Some of these proteins were independently studied prior to their association with one another and invention of the Annexin nomenclature in 1987 (Geisow et al., 1987). The vertebrate Annexins (A1-A11, A13) conduct a range of cellular functions and are identified by a conserved tertiary structure of the C-terminal phospholipid binding domain. Each domain usually includes four core domain repeats, with the exception of Annexin A6 which has eight repeats

(Gerke & Moss, 2002). Each Annexin repeat is approximately 70AA in size and comprises five $\alpha$-helices, each containing a motif for calcium binding. These $\alpha$-helices are wound into a super helix, forming a flattened disk structure (Moss & Morgan, 2004). The N-terminals differ between each Annexin and give rise to specific protein functions. Although these proteins are closely related and display structural homology, the specific functions of Annexins are diverse. This is evidenced by strikingly different phenotypes in Annexin knockout mice. These are summarised by Moss & Morgan, who also note the disparity between cellular knockouts of Annexins compared with murine models, perhaps an indication of the functional redundancy of some Annexins (Moss & Morgan, 2004).

### *1.19 Annexin A11 structure*

The N-terminal of Annexin A11 is long (270AA), rich in proline, tyrosine, and glycine (Bances et al., 2000), and disordered: It has been shown to enable liquid-liquid phase-separation of the protein (Nahm et al., 2020), and prior to this discovery was identified as a prion-like domain with the propensity to phase-separate (March et al., 2016). Annexin A11 interacts with RNPs via its low-complexity domain (Liao et al., 2019), however RNA binding sites for *ANXA11* have not been determined, and it would be insightful to elucidate whether a direct interaction between Annexin A11 and RNA occurs. The disordered N-terminal has not been crystallised due do its low complexity, and Annexin A11 protein structure modelled in AlphaFold indicates very low model confidence of the N-terminal (Jumper et al., 2021; The UniProt Consortium, 2019; Varadi et al., 2022), highlighting the region disorder (Figure 1.3). Structural modelling of the Annexin A11 N-terminal using multiple alignment of 30 mammalian orthologue sequences predicted two $\alpha$-helices at residues 40-44 and 51-59 (Smith et al., 2017).

The structure of recombinant mouse Annexin A11 was the first Annexin A11 to be characterised and was shown to contain $\alpha$-helices in the C-terminal and random coils in the N-terminal, which respectively increase and decrease when Annexin A11 is bound to calcium, and calcium induced structural changes increased Annexin A11 thermal stability (Lecona et al., 2003). One of largest

segments to be structurally resolved is rat Δ188AnnexinA11, which has sequence homology with human Annexin A11 of 93.3% for the full-length protein and 96.5% for the core structure. Crystallisation of rat Δ188AnnexinA11 indicates classic Annexin C-terminal structure with four subdomains each containing $\alpha$-helices, and a trimeric assembly of monomeric proteins, with all calcium binding sites on the same face to support membrane binding (Figure 1.3). Calcium binding causes a localised conformational change that allows membrane binding but does not alter the gross tertiary structure of the core Annexin domain (Lillebostad et al., 2020). Some evidence for post-translational modification of Annexin A11 exists, including phosphorylation in multiple cellular models (Furge et al., 1999; Mizutani et al., 1993)

*ANXA11* contains 15 exons and 14 introns (Morgan et al., 1998). Three isoforms of *ANXA11* mRNA have been reported in humans, however it has been noted that there is only one known protein product (Bances et al., 2000). Two isoforms are included in the protein database UniProt, which indicates that alternative splicing at the N-terminal leads to the presence of two isoforms, with one missing the first 33 amino acids (The UniProt Consortium, 2019). No characterisation of neuronal *ANXA11* isoforms have been reported, perhaps due to its relatively recent implication in neurodegeneration and neuronal function as a whole. Although certain *ANXA11* genetic regions, including mutation hotspots which are discussed in the following section, are highly conserved (Smith et al., 2017), there is some evidence that splicing patterns differ across species (Bances et al., 2000). Elucidation of *ANXA11* splicing patterns in motor neurons may be of significance, particularly in light of evidence that splicing abnormalities are a common feature of ALS (1.10).

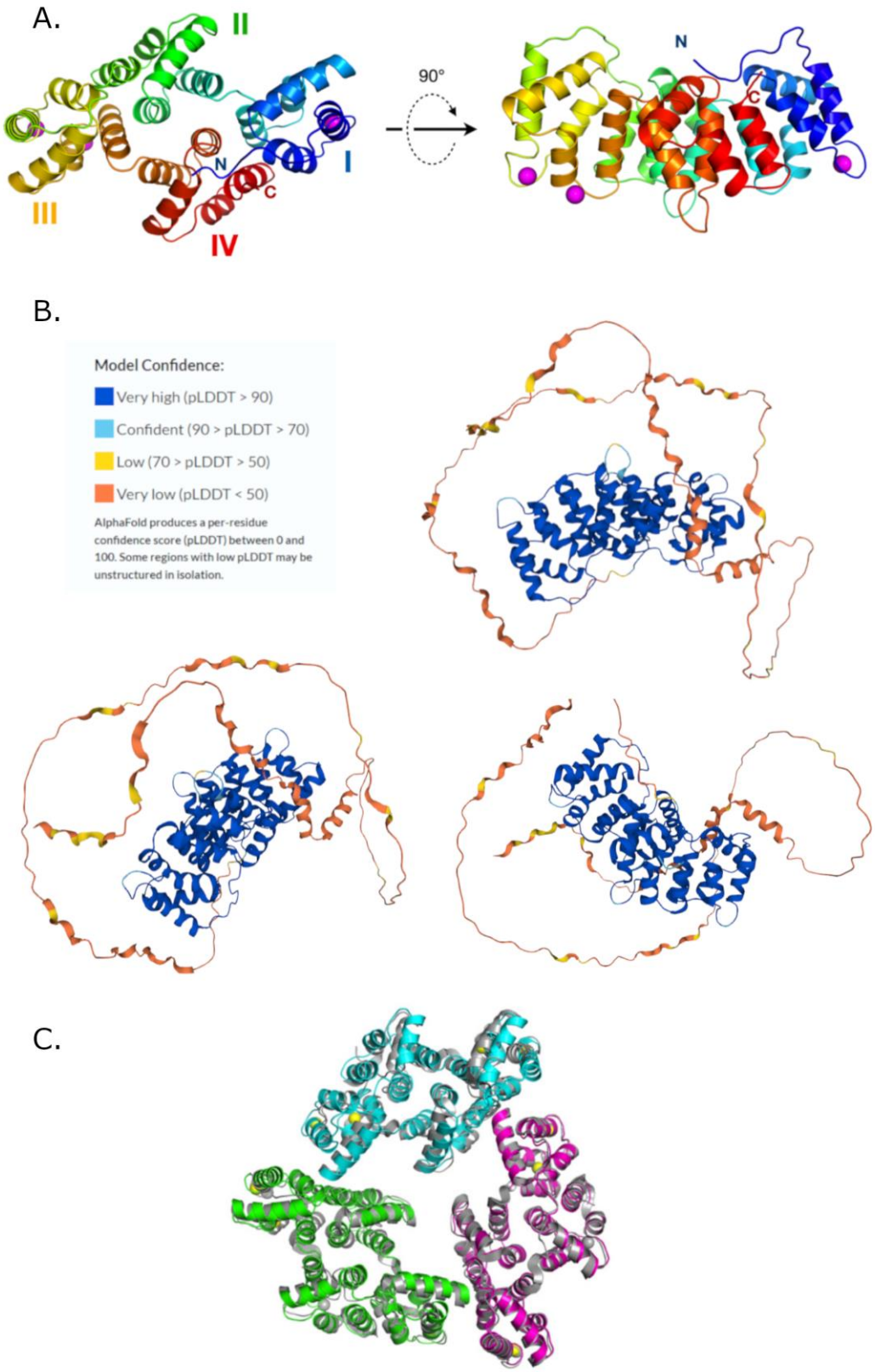


***Figure 1.3 Structure of Annexin A11***

(A) The most well-defined crystal structure of Annexin A11 is the C-terminal of rat Δ188AnnexinA11, which has four Annexin A11 core repeats that contain $\alpha$-helices, calcium molecules are represented

as pink spheres to indicate calcium binding sites. (B) Protein structure prediction in AlphaFold indicates an $\alpha$-helices rich C-terminal with very high model confidence and a long, disordered N-terminal with very low model confidence (the same model is shown from different angles). (C) C-terminal domains of rat Δ188AnnexinA11 (in colour) likely create a tetrad with calcium binding regions on the same face, which is similar to that of Annexin A5 (superimposed in grey). (A) and (C) are from (Lillebostad et al., 2020), and (B) is taken from UniProt (The UniProt Consortium, 2019).

### *1.20 Mutations in ANXA11 cause ALS*

Mutations in *ANXA11* were associated with ALS through exome sequencing of 751 familial ALS cases in a European population, leading to the recognition of *ANXA11* missense mutations in 12 individuals. The D40G mutation was initially identified in two separate British kindreds, where multiple family members were affected by disease, and the same mutation was subsequently identified in additional unrelated fALS and sALS patients, alongside other non-synonymous point mutations (Smith et al., 2017). Disease onset in the initial patient cohort occurred in the limb or bulbar region between the ages of 50-83, with a mean age of onset of 67 years and disease duration of 12-181 months, indicating a broad clinical presentation. None of these patients showed signs of FTD, however *ANXA11* mutations in patients presenting with ALS-FTD have since been recognised (Teyssou et al., 2020; Wang et al., 2022; Zhang et al., 2018). Further evidence of *ANXA11* mutations in ALS has been reported in multiple populations, including in additional European, African, South American, and Asian genetic cohorts, highlighting the global impact of *ANXA11* mutations (Liu et al., 2019; Müller et al., 2018; Nagy et al., 2022; Nahm et al., 2020; Nel et al., 2022; Nunes Gonçalves et al., 2021; Sainouchi et al., 2021; Teyssou et al., 2020; Wang et al., 2022; Zhang et al., 2018). A summary of published ALS associated genetic mutations in *ANXA11* is included in Figure 1.4 and it should be noted that functional confirmation of pathology has not been completed in every instance.

ALS associated *ANXA11* mutations (from now collectively referred to as *ANXA11mut*) predominantly reside in the disordered N-terminal, perhaps suggesting an interference with protein-protein interactions, or affectation to the phase-separation properties of Annexin A11. Mutations also occur

in the core Annexin phospholipid binding domain of *ANXA11,* and elucidation of whether the same cellular phenotype exists when mutations reside in different functional domains of the gene will be necessary.

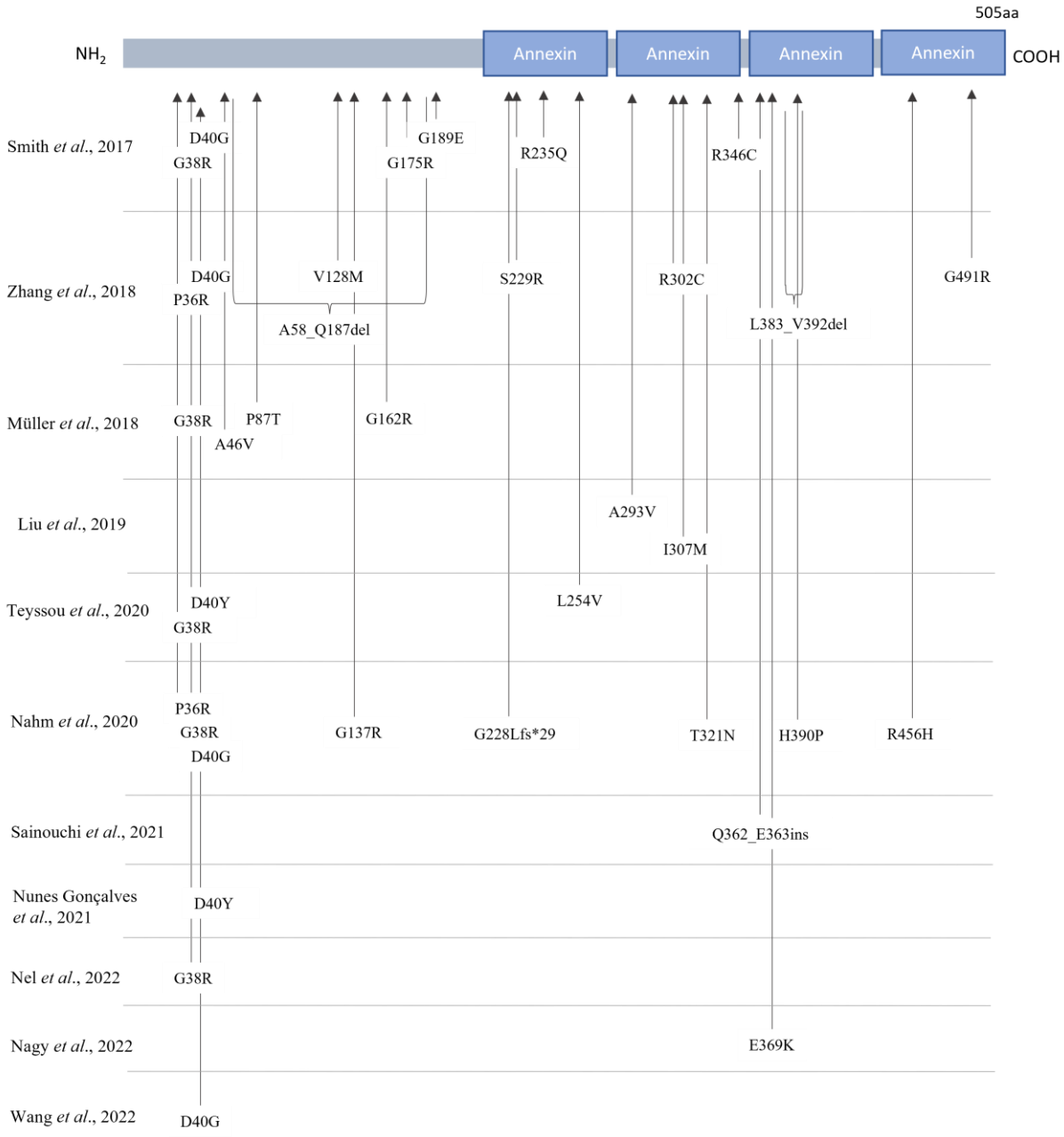


***Figure 1.4 ALS-associated genetic mutations in ANXA11***

Multiple ALS-associated mutations in *ANXA11* have been identified since 2017 and reside in both the disordered N-terminal and the C-terminal core Annexin domain.

### *1.21 Histopathology in ANXA11 ALS*

Perhaps the most striking evidence for *ANXA11* association with ALS pathology was the identification of large inclusions positive for Annexin A11 in patient post-mortem tissue: Spinal motor neurons from one sALS patient harbouring the *ANXA11* D40G mutation showed basket-like and filamentous Annexin A11 inclusions, which were absent in control and non-*ANXA11* ALS tissue (Smith et al., 2017). Annexin A11 positive aggregates were seen alongside typical TDP-43 pathology, with additional evidence of ubiquitin and pTDP-43 inclusions, and Annexin A11 aggregates were also detected in the motor cortex (Smith et al., 2017). Annexin A11 aggregates were later detected in post-mortem spinal cord, frontal cortex, motor cortex, dentate gyrus, caudate nucleus, and dentate nucleus tissues from a sALS patient with an *ANXA11* G38R mutation (Teyssou et al., 2020). Tissue from a patient with an *ANXA11* splice variant showed Annexin A11 positive aggregates in multiple spinal cord and brain regions, and Annexin A11 and pTDP-43 were shown to partially co-localise in some skien-like neuronal cytoplasmic inclusions (Sainouchi et al., 2021). Some of the histopathology identified in these cases are included in Figure 1.5. In addition to these examples from *ANXA11mut* ALS patients, Annexin A11 aggregation has been reported in brain tissue harbouring a mutation in *FUS* (Nahm et al., 2020), and in a non-*ANXA11* sALS case in rare neurons (Sainouchi et al., 2021).

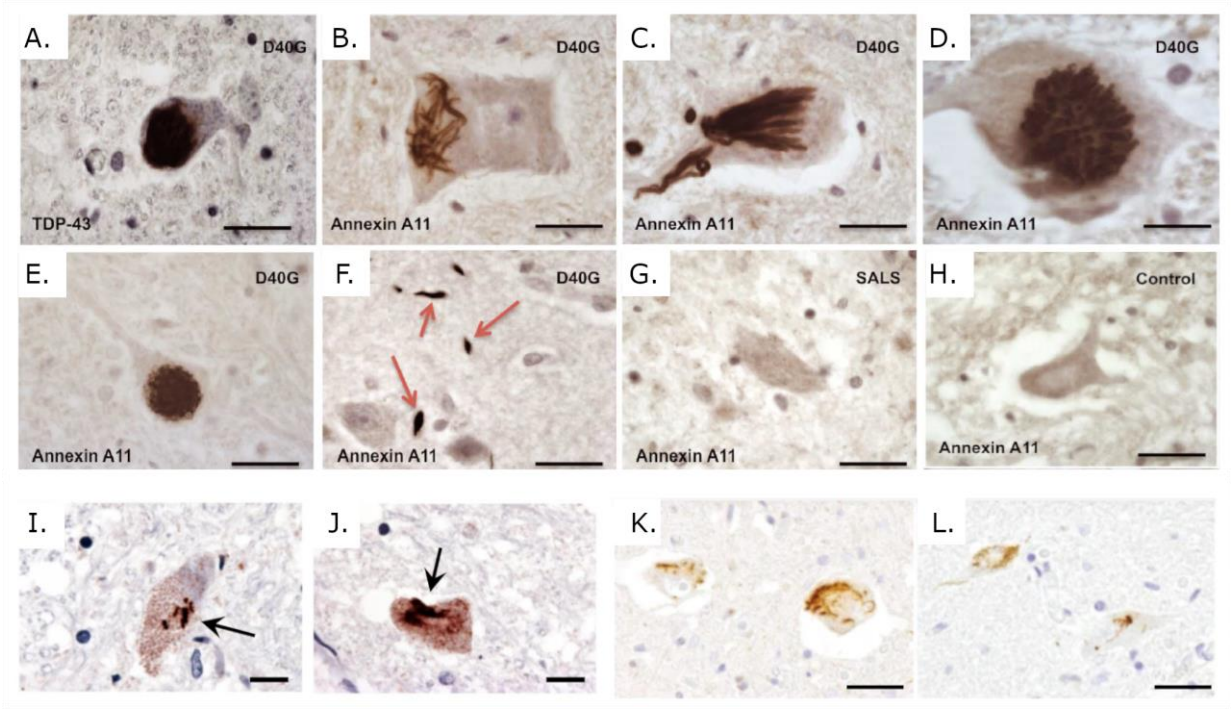


***Figure 1.5 Post-mortem tissue analysis in ANXA11 ALS***

Reported evidence of protein aggregation in post-mortem analysis includes spinal cord tissue from a sALS patient with an *ANXA11* D40G mutation, revealing (A) ALS typical pTDP-43 cytoplasmic accumulation and (B-E) Annexin A11 positive inclusions in the spinal cord, as well as (F) Annexin A11 positive inclusions in the motor cortex. Annexin A11 inclusions were not detected in (G) sALS or (H) control spinal cord. (I, J) Spinal cord tissue from a patient with an *ANXA11* G38R mutation included Annexin A11 positive aggregates. A patient with an *ANXA11* splice mutation had Annexin A11 positive aggregates in (K) the anterior horn and (L) hypoglossal nucleus. (A-H are taken from (Smith et al., 2017); I-J are taken from (Teyssou et al., 2020); K-L are taken from (Sainouchi et al., 2021)). Scale bars represent: 30µm (A, E, G); 20µm (B, C); 15µm (D); 50µm (F); 25µm (H); 10µm (I, J); 60µm (K, L).

## *1.22 Annexin A11 function in health and disease*

Annexin A11 is expressed throughout the body, with multiple cellular functions and varying patterns of localisation dependent on cell-type and cell-cycle, as demonstrated by The Human Protein Atlas (https://www.proteinatlas.org/ENSG00000122359-ANXA11/subcellular). Due to its ubiquitous nature, the known functions of Annexin A11 have often been demonstrated in specific cell types, and whether these functions translate to neuronal processes is not clear. Annexin A11 redistributes

from the cytoplasm to the mitotic spindle during the cell cycle in HEp-2 cells (a cancerous cell line), can fluctuate between nuclear and cytoplasmic localisation in response to calcium levels in COS-7 cells (monkey kidney-derived fibroblast-like cells), and localises to granules in neutrophils and eosinophils (Farnaes & Ditzel, 2003). In cholangiocytes (liver cells), Annexin A11 localises to membranes and mediates expression of the membrane chloride channel ANO1 (Herta et al., 2021), and there is some evidence that Annexin A11 is involved in release of insulin from pancreatic $\beta$-cells (Iino et al., 2000). These examples demonstrate the broad functions of Annexin A11, and it will be necessary to focus on CNS and ALS specific characteristics to understand why specific mutations result in motor neuron degeneration.

Annexin A11 is present in both the nucleus and cytoplasm of multiple cell types, however the mechanisms mediating its localisation are unknown. It has been demonstrated that the N-terminal is necessary for nuclear localisation in COS-7 cells (Mizutani et al., 1995), and a potential Karyopherin$\beta$2 nuclear localisation signal recognition site has been identified in the N-terminal, but functional evidence has not been reported (Lee et al., 2006). Overexpression of WT Annexin A11 in mouse primary neurons reveals a punctate staining pattern throughout neurites, alluding to a neuronal role in vesicle trafficking, and this punctate pattern was altered in the presence of *ANXA11* G38R and R235Q, but not D40G, mutations (Smith et al., 2017). Annexin A11 binds to multiple phospholipids (Lecona et al., 2003; Liao et al., 2019), strengthening the notion that it may be involved in vesicle trafficking or metabolism. One of the primary interactors of Annexin A11 is S100A6, also known as calcyclin. This interaction was first characterised alongside evidence that Annexin A11 locates to the nucleus in response to changes in intracellular calcium. The same study found that Annexin A11 is present at the midbody during cytokinesis, and at the regenerating nuclear membrane after cellular fission (Tomas & Moss, 2003). Although this may be of reduced relevance for post-mitotic neurons, it alludes to a role of Annexin A11 in nuclear membrane repair which may be of relevance to nucleocytoplasmic transport dynamics in ALS (1.13). Additionally, RNA sequencing data indicate that *ANXA11* mRNA transcripts are more abundant in astrocytes and microglia than

neurons (Zhang et al., 2014, 2016), indicating that mitotic functions of Annexin A11 could influence neuronal health in a non-cell-autonomous manner. S100A6 is an EF-hand calcium-binding protein expressed in multiple cell-types including some neurons and astrocytes, and it has functions in proliferation, apoptosis, stress response, and cytoskeleton dynamics (Donato et al., 2017). Expression of S100A6 is upregulated by species that evoke oxidative stress (Leśniak et al., 2005), and S100A6 is overexpressed in a *SOD1* mouse model of ALS (Hoyaux et al., 2000), in astrocytes associated with impaired motor axons in both mouse and human ALS models (Hoyaux et al., 2002), and in D40G *ANXA11* ALS and sALS spinal cord (Smith et al., 2017). *ANXA11* G38R and D40G reside near the S100A6 binding domain (Sudo & Hidaka, 1998), and were anticipated to disrupt a predicted $\alpha$-helix structure (Smith et al., 2017). Functional characterisation showed that while *ANXA11* mutations D40G, G189E, and R235Q resulted in reduced S100A6 binding compared to WT, binding was markedly increased in the context of the G38R mutation (Smith et al., 2017). Knockdown of TDP-43 can result in increased expression of S100A6 transcripts (Polymenidou et al., 2011), and TDP-43 aggregates are found in *ANXA11* ALS post-mortem tissue (Figure 1.5), suggesting a link between TDP-43 pathology, Annexin A11, and S100A6.

Annexin A11 directly interacts with FUS, EWSR1, and hnRNPA1 in a calcium dependent manner, and endogenous FUS becomes more cytoplasmic when mutant, but not WT, *ANXA11-GFP* is overexpressed in NSC-34 cells (Nahm et al., 2020). Downregulation of *ANXA11* mRNA was detected in iPSC-derived motor neurons harbouring a mutation in *VAPB*, highlighting the potential relevance of Annexin A11 across multiple ALS types, however this wasn't consistent across all cell lines included in this study (Oliveira et al., 2020). The binding of Annexin A11 to partners ALG-2 and sorcin was not altered in functional studies investigating ALS-specific mutations (Smith et al., 2017), indicating motor neuron pathology may be independent of these interactions. A reduction in Annexin A11 protein stability has been suggested to result from G38R and D40G mutations *in vitro*, without affecting protein solubility, indicating a potential loss of function (Liao et al., 2018). Expression of *ANXA11* constructs in HEK293 cells showed comparable solubility of *ANXA11* G38R, D40G, and G189E

compared to WT, but highlighted an increase in insolubility when *ANXA11* R235Q was expressed (Smith et al., 2017). Co-expression of *ANXA11* R235Q and *S100A6* constructs reduced insolubility of the mutant Annexin A11 protein, which was restored on inhibition of proteasomal degradation, indicating that S100A6 has a role in maintaining Annexin A11 solubility and that mutant Annexin A11 aggregates are processed by the ubiquitin proteasome pathway (Smith et al., 2017). Analysis of Annexin A11 degradation in rat lung tissue suggests that it occurs independently of calpain activity (Barnes & Gomes, 2002), however the proteolytic pathways that mediate Annexin A11 turnover are poorly defined.

In transfected HeLa cells, WT, G38R, and D40G Annexin A11 localise to the nuclear membrane in response to ionomycin induced calcium increase, however mutations in the phospholipid membrane binding domain result in ionomycin induced aggregation of Annexin A11 (Nahm et al., 2020). The same study showed that *ANXA11* ALS patient fibroblasts harbour increased basal calcium levels compared to control, alongside reduced calcium release in response to thapsigargin treatment, indicating disrupted calcium homeostasis in *ANXA11* ALS. Annexin A11 interacts with phospholipids in a calcium dependent manner, including $PI(3,5)P_2$ (Liao et al., 2019). Notably, mutations in *FIG4* have been associated with ALS, and the corresponding FIG4 protein regulates this phospholipid (Chow et al., 2009). $PI(3,5)P_2$ is expressed in Lamp1 positive lysosomes, and the interaction between Annexin A11 and $PI(3,5)P_2$ was shown to enable RNP hitchhiking on lysosomes that are being transported along axons, using Annexin A11 as a tether, and this interaction is impaired in the context of ALS *ANXA11* mutations (Liao et al., 2019). The Annexin A11 low-complexity N-terminal interacts with RNPs including G3BP1, and the core Annexin domain interacts with phospholipid membrane bound vesicles. The importance of RBPs in ALS pathology is discussed in 1.10, and evidence of RNP regulation by Annexin A11 is intriguing. The function of Annexin A11 as a molecular tether may extend beyond interactions between lysosomes and RNPs: Local protein translation in retinal ganglion axons localises to membrane-bound late endosomes (Cioni et al., 2019), and it is plausible that Annexin A11 also stabilises this process through its unique two-part structure. In

HT1080 (a fibrosarcoma cell line) and HEK293 cells, Annexin A11 stabilises the ER exit site (ERES), the initial point at which vesicular cargos are released after processing within the ER, via the Golgi, for transport within or from the cell (Shibata et al., 2015). Collectively these data suggest a possible role of Annexin A11 in stabilising local translation at multiple points; by constituting connections between vesicles and mRNA-bound RBPs, and by stabilising the site at which newly synthesised proteins are released into the cell. Further, Annexin A11 has been shown to interact with the stress granule protein G3BP1 (Liao et al., 2019; Markmiller et al., 2018), which has been shown to negatively regulate translation in response to axonal injury (Sahoo et al., 2018). The importance of axonal local protein synthesis in ALS is discussed in 1.10 and is an interesting point of investigation: It might explain why specific mutations in *ANXA11* can lead to motor neuron degeneration despite the expression of Annexin A11 throughout the body.

Annexin A11 has been shown to localise to stress granules in multiple overexpression models. In HeLa cells, comparable Annexin A11-GFP inclusion to mCherry-TIA1 stress granules was seen across WT, G38R, D40G, H390P, and R456H Annexin A11-GFP in response to sodium arsenite treatment, however reduced stress granule disassembly was seen in the presence of *ANXA11* ALS mutations (Nahm et al., 2020). U20S cells expressing *ANXA11* constructs showed Annexin A11 localisation to stress granules when WT or D40G Annexin A11 was expressed, but Annexin A11 R235Q and R346C localisation to stress granules was reduced (Liao et al., 2019). WT and mutant *ANXA11-GFP* encoded proteins were shown to aggregate in the cytoplasm in NSC-34 cells in response to sorbitol treatment, and D40G and H390P Annexin A11-GFP co-aggregated with FUS in the cytoplasm 30 minutes after stress recovery, whereas WT Annexin A11 stress granules dissolved (Nahm et al., 2020). In patient fibroblasts, Annexin A11 inclusion into sodium arsenite induced stress granules was comparable across control and patient-derived cells, however pre-treatment with the calcium chelator BAPTA inhibited only WT Annexin A11 inclusion to TIA1 positive stress granules, and did not affect the inclusion of mutant Annexin A11, indicating that mutant Annexin A11 is not properly mediated by calcium (Nahm et al., 2020).

In addition to its role in ALS, genetic alterations in *ANXA11* are associated with sarcoidosis, autoimmune disease, neurofibromatosis type 1, and multiple cancers (He et al., 2022; Hua et al., 2018; Hubers et al., 2018; Karakaya et al., 2022; Liu et al., 2015, 2016; Mirsaeidi et al., 2016; Song et al., 2009; Wang et al., 2014). A D40Y *ANXA11* mutation was detected in a kindred with multi-system pathology including ALS/FTD and inclusion body myopathy, with evidence of cerebral white matter damage in the corticospinal tracts, and TDP-43 and Annexin A11 pathology in muscle (Leoni et al., 2021). The same D40Y mutation was recently identified in a Greek family affected by adult-onset muscular dystrophy without ALS diagnosis (Johari et al., 2022). The ubiquitous expression of Annexin A11 throughout the body, as well as association of *ANXA11* mutations with multiple diseases, alludes to a neuron-specific function that is selectively affected by ALS associated mutations. The recent identification of mutations in *ANXA11* as causative of ALS means that consequent cellular pathologies are not well understood, and to develop viable targets for therapeutic intervention a clearer characterisation of Annexin A11 motor neuron function is necessary. As with many genetic mutations that cause disease in a small percentage of the total patient population, elucidation of dysregulated pathways may shed light on pathogenesis that is applicable across many cases. Investigation into the consequences of *ANXA11* mutations in motor neurons is therefore of great interest in the pursuit of treatment strategies for ALS.

### *1.23 Induced pluripotent stem cells – an important model for ALS research*

Despite huge efforts in searching for viable treatments for ALS, the thousands of clinical trials that have been conducted over the last 20 years have been largely unsuccessful (Petrov et al., 2017). There are many variables contributing to the failure of clinical trials, and it has been posited that one reason is the reliance on testing therapies in animal models that do not fully recapitulate human disease. The use of human stem cells has circumvented some of these issues as differentiation of stem cells into various cell types enables the assessment of live human-derived cells. There are

limitations with cellular models when compared to the complexities of an entire organism, but they fill an important role as human-derived research models.

Early studies utilising human stem cells relied on embryonic stem cells (hESCs) which are burdened with ethical implications, and so the search for an alternative human stem cell model was prioritised. This goal was realised in 2006 with the discovery of iPSC technology (Takahashi & Yamanaka, 2006). iPSCs are stem cells that have been derived through forced expression of pluripotency genes in a somatic cell, causing reversal of differentiation, which returns the cell to a naïve stem cell fate. Prior to this discovery, the success of cloning studies had demonstrated that the nucleus of an adult cell has the potential to orchestrate the development of an entire animal, and therefore that epigenetic silencing of stem cell and developmental genes is reversible (Campbell et al., 1996). It was 10 years later that the successful reprogramming of mouse fibroblasts into cells that mimicked the characteristics of ESCs was reported by Takahashi and Yamanaka. Through screening pluripotency genes for the potential to induce a stem cell state, four key reprogramming genes were identified: *OCT-3/4*, *SOX2*, *C-MYC*, and *KLF4* (Takahashi & Yamanaka, 2006). One year later the same factors were shown to successfully induce reprogramming of human fibroblasts into iPSCs – a milestone in modern research (Takahashi et al., 2007). These cells were shown to behave as hESCs, mimicking their morphology and differentiating into cells from the three germ layers of the blastocyst. Since then, production of iPSCs from multiple somatic tissue-types has been reported, including keratinocytes (Aasen et al., 2008), peripheral blood mononuclear cells (Quintana-Bustamante & Segovia, 2014), immortalised LCLs (Barrett et al., 2014), and even renal tubular cells found in urine (Zhou et al., 2011).

The brilliance of iPSCs is that they can be derived from members of the healthy population, and from those with disease. There is now a wealth of research that shows that iPSC models derived from diseased patients recapitulate the human pathology in the laboratory. Optimisation of differentiation protocols by multiple research groups has made it possible to produce cultures of highly specified cell types from iPSCs, with relevance to tissue specific disease. In the case of ALS and

FTD, protocols are readily available that produce cultures of spinal motor neurons, cortical neurons, glial cells such as astrocytes, and skeletal muscle.

In addition to differentiation of iPSCs into desired cell types, some studies have utilised direct conversion of patient fibroblasts into neurons and glia through forced expression of cell-fate specific genes and transcription factors, bypassing the iPSC reprogramming process (Caiazzo et al., 2015; Quist et al., 2022; Vierbuchen et al., 2010). The patient fibroblast source is more finite, and multiple studies have recognised the necessity of low-passage fibroblasts for efficient conversion. However, they have the benefit of epigenetic profile retention, and have been shown to display some added age-associated gene expression effects when compared to iPSC-derived cells (Mertens et al., 2015, 2021). Notably, published conversion protocols utilise fibroblasts and no other somatic cell types, and this could be due to the derivation of both neurons and fibroblasts from the neuroectoderm, hinting toward some limitations of direct conversion. As an example of direct fibroblast conversion in ALS research, astrocytes generated from sALS, *SOD1*, and *C9ORF72* ALS patients exert non-cell autonomous toxicity on motor neurons when in co-culture (Meyer et al., 2014).

### *1.23.1 CRISPR-Cas9*

In addition to patient derived lines, it is possible to genome edit iPSCs with CRISPR-Cas9 technology. CRISPR-Cas9 can be used to insert disease-causing mutations into WT iPSC lines, correct known mutations to transform patient derived lines into their WT counterparts, and produce homogenous and heterogeneous knockout lines. One utilisation of CRISPR-Cas9 edited lines is to confirm causality of genes identified in genetic association studies. As many SNPs are inherited together in haplotypes, confirmation that specific genes or variants within that loci are responsible for the associated phenotype can be challenging. It is possible to target risk genes with CRISPR, for example by "inserting" suspect SNP changes, and observing the consequences. This replaces the need for overexpression constructs, which can result in phenotypic changes due to increased expression of genes, and do not represent endogenous expression levels. The benefit of creating isogenic iPSC

lines, where CRISPR-Cas9 is utilised to create a pair of cell lines that differ only in the target mutation, is that the influence of genetic background on cellular phenotypes is removed.

Once iPSCs have been genome edited, it is vital to undertake thorough characterisation of cell lines. It should be confirmed that no on- or off-target effects have occurred, and the only resulting change is in the target gene, ideally with whole genome sequencing. PCR and Sanger sequencing can give misleading results if large on-site insertions have been introduced, and a screen of 27 isogenic iPSC lines revealed that 33% had large genomic onsite abnormalities that had been missed by PCR/Sanger sequencing (Simkin et al., 2022). It is well recognised that many ALS genes display reduced penetrance, suggesting that additional genomic and environmental factors are necessary for identified mutations to cause disease. Therefore when utilising CRISPR/Cas9 generated models of ALS it might be necessary to insert mutations into multiple control lines to truly elucidate the consequences of disease-causing mutations. Evidence of isogenic line variability is poorly published, but examples include altered cryptic exon inclusion in mutant *TARDBP* isogenic iPSC lines derived in different laboratories and from different control lines (Smith et al., 2021). Although the authors simultaneously report multiple correlating phenotypes across different isogenic lines (including protein mislocalisation and mitochondrial abnormalities), it is important to note that variability is present, hence multiple cell lines should be included in robust study design, regardless of whether cell models are isogenic or patient-derived.

### *1.23.2 Lessons from iPSCs in ALS research*

iPSCs are particularly useful for modelling sALS, where genetic factors are unidentified and therefore using patient tissue is the only way to represent these genetic landscapes in an experimental setting. As an example, multiple iPSC lines were generated from sALS patients and screened for novel treatment compounds, identifying ropinirole as a potential therapeutic candidate (Fujimori et al., 2018). Neuronal excitability in iPSC-derived motor neurons was established with high-throughput live imaging, and a screen identified 67 small molecules that reduced hyperexcitability in mutant

*SOD1* motor neurons. Bioinformatics analysis was then implemented to delineate common targets of efficacious small molecules, identifying AMPA receptors, Kv7.2/3 ion channels, and D2 dopamine receptors as modulators of motor neuron excitability (Huang et al., 2021). Additionally, high-throughput analysis of the neurotoxic effects of small molecules on iPSC-derived neurons representing multiple large haplotype populations has been demonstrated as a means to exclude new therapeutics from further development (Huang et al., 2022). The vast majority of publications utilising iPSCs in ALS research focus on the four most prevalent and well-characterised genetic models: *C9ORF72*, *SOD1*, *TARDBP*, and *FUS,* and the generation of iPSCs that represent smaller patient populations both increases the representation of ALS heterogeneity and enlightens new disease mechanisms. Many disease phenotypes are recapitulated in CNS cells derived from ALS patient and CRISPR-Cas9 edited iPSCs, including protein aggregation, altered electrophysiological state, changes in neurite outgrowth, mitochondrial deficits, and transcriptomic alterations, to name a few, and examples have been referenced throughout this thesis.

### *1.24 Thesis aims and hypotheses*

iPSCs that have been derived from patients with known ALS causing genetic mutations are now utilised in many instances of ALS research, with increasing availability of lines leading to better understanding of disease. iPSC lines harbouring mutations in *ANAX11* are yet to be published, excluding some of those that were generated-for and included-in this thesis (Hedges et al., 2021). The present doctoral thesis includes a summary of the production and characterisation of novel iPSC lines from control and ALS patients with *ANXA11* mutations, and the utilisation of iPSC-derived motor neurons and astrocytes for investigation of ALS pathogenesis. These lines include *ANXA11* G38R, D40G, and R234Q mutations, representing point mutations in both the disordered N-terminal and the core annexin domain (Smith et al., 2017).

As mutations in *ANXA11* were recently associated with ALS, little is known about the role of Annexin A11 protein in neurons, or how *ANXA11* mutations lead to motor neuron degeneration. Gross

localisation of Annexin A11 and TDP-43 protein, calcium dynamics, stress granule response, and other potentially disrupted pathways remain undefined in patient-derived cultures. Further, Annexin A11 has a potential and unexplored role in stabilising local protein translation in motor neurons, which may explain the specific motor neuron vulnerability seen in *ANXA11* ALS. In addition to initial cellular phenotyping of novel *ANXA11* iPSC lines, a hypothesis was established: ALS associated mutations in *ANXA11* lead to motor neuron pathology, including altered neuronal architecture and activity, and perturbed RNA biology encompassing stress granule dynamics, RNA transport, and local translation.

Utilising patient lines collected from individuals harbouring *ANXA11* mutations, the following aims were established:

- Generation of iPSC models from *ANXA11mut* patients, and age- and sex-matched controls (Chapter 3)
- Optimisation of motor neuron-astrocyte co-culture to enable assessment of disease-relevant cells (Chapter 3)
- Assessment of Annexin A11 protein distribution in patient-derived models (Chapter 4)
- Assessment of ALS-hallmark TDP-43 in *ANXA11* ALS patient-derived models (Chapter 4)
- Investigation of neuron-specific cell compartment vulnerability with neurite outgrowth analysis (Chapter 5)
- Interrogation of spontaneous calcium activity in *ANXA11* ALS motor neurons (Chapter 5)
- Investigation of axonal RNA transport in the context of *ANXA11* mutations (Chapter 6)
- Analysis of Annexin A11 inclusion to stress granules (Chapter 6)
- Assessment of the role of Annexin A11 in local protein synthesis (Chapter 6)

# Chapter **2** **Materials & Methods**

Unless otherwise specified, cell culture reagents were acquired from Thermo Fisher Scientific and chemicals were purchased from Merck KGaA. Experiments were performed at ambient room temperature in all instances where the specific temperature is not stated.

## *2.1 Cell culture*

Cell culture was performed in a Class II laminar flow hood under sterile conditions, and cells were maintained in humidified incubators set to 37°C with 5% $CO_2$. Hypoxic incubators were set to 5% $O_2$. Media was pre-warmed before use.

### *2.1.1 Preparation of cell culture plates*

Unless otherwise stated, cells were cultured on Nunc Cell Culture Plastics coated with extracellular matrices. Aliquoted Geltrex™ was defrosted on ice for approximately 1 hour, resuspended in cold plain DMEM in a 1:100 dilution, added to cultureware, and maintained in an incubator for 1 hour before use. Residual solution was removed before the addition of cell suspension. Matrigel® (Corning) extracellular matrix was prepared in the same way with the exception that preparation of aliquots was based on the data sheet for each Matrigel® lot. Aliquots prepared from the 'dilution factor' detailed on each data sheet were diluted in 25mL for NPC culture, and in 40mL for astrocyte culture. Preparation of cultureware for motor neurons or motor neuron-astrocyte co-culture is detailed in 2.1.8. Geltaine coating was prepared by dissolving 100mg porcine gelatine in 100mL PBS and autoclaving, then adding to cultureware or glass coverslips for 1 hour before addition of cells.

### *2.1.2 Induced pluripotent stem cell culture*

iPSCs were cultured in hypoxic incubators with Essential 8 flex™ growth media (E8 flex) on Geltrex™ coated 6-well plates. Media was changed every 2-3 days following the manufacture guidelines. When

at ~80-90% confluency, iPSCs were passaged with Versene® (Lonza) in a 1:6 ratio. Briefly, spent media was removed and 1mL Versene was added to each well on a 6-well plate. Once gaps emerged between cells at the edges of colonies, Versene was removed and fresh E8 flex was added, causing cells to lift from the plate. Care was taken to avoid titration to the point of single cell suspension, and small colonies were transferred to new Geltrex™ coated plates. To freeze iPSCs, the same protocol was followed, however after removal of Versene, cells were resuspended in freezing media consisting of E8 flex with 10% DMSO and 10μM ROCK inhibitor to increase cell survival. Approximately 1mL freezing media was used to resuspend each well of a 6-well plate, and one well was transferred to one cryovial. Cryovials were transferred to Nalgene® Mr. Frosty (Merck KGaA) or CoolCell® (Corning) containers. These were immediately transferred to a -80°C freezer, and vials were transferred to liquid nitrogen stores within the following week.

### *2.1.3 Lymphoblastoid cell line culture*

LCLs were grown in 5% $CO_2$ normoxic incubators in RPMI 1640 with 10% fetal bovine serum (FBS) and 1x GlutaMAX™, in non-adherent T25 flasks. Spent media was replaced every 2-3 days by carefully removing media with low power aspiration, and fresh media was added. To passage LCLs, cells were titrated with fresh media and ~25% of the cell suspension was transferred to a new flask. For cryopreservation cells were resuspended in FBS with 10% DMSO, transferred to cryovials, placed in Nalgene® Mr. Frosty or CoolCell® containers, and transferred to a -80°C freezer. Frozen vials were transferred to liquid nitrogen vessels within one week for long term storage.

### *2.1.4 Reprogramming LCLs into iPSCs with episomal plasmids*

Reprogramming with episomal plasmids was adapted from (Barrett et al., 2014). Two days before electroporation (day -1), LCL aggregates were gently titrated to form a single cell suspension to encourage cell division. The next day, ~350,000 mitomycin C inactivated mouse embryonic fibroblasts (MEF) were plated per well of a 6-well plate coated with 0.1% gelatine in MEF media

(DMEM, 1x GlutaMax™, 10% FBS). On Day 1, electroporation was performed following exactly the Amaxa™ Human B Cell Nucleofector™ kit using programme E-010 in a Nucleofector™ 2b Device (Lonza). One million LCLs were transfected with 1.5µg of each plasmid (addgene codes: #*20927*, #*27077*, #*27080*, #*27078*), placed directly onto inactivated MEF in 2mL LCL media after removal of spent MEF media, and maintained under normoxic conditions. The next day, 3mL of LCL media was added. On days 5, 6, and 7, 1mL reprograming media (RM) (Table 2.1) was added to each well. On day 8, total spent media was removed and replaced with fresh RM. Spent RM was replaced every 1-2 days depending on cell confluency and evidence of media depletion. By approximately day 15 small colonies were identified and media was transitioned to E8 flex until colonies were large enough to manually collect using an in-hood microscope with a P200 pipette. Once collected, new iPSC colonies were transferred to Geltrex® coated plates in E8 flex supplemented with 10µM ROCK inhibitor and transferred to a hypoxic incubator. iPSCs were maintained in E8 flex until large enough to passage using Versene as detailed in 2.1.2. A schematic of iPSC derivation including emergence of a new iPSC colony is detailed in Figure 2.1. iPSCs were frozen as original stocks soon after derivation, as fully characterised seeding stocks, and as working stocks which had been expanded from seeding stocks for use in experiments (Figure 2.2). No stocks were frozen from "left-over" working stocks so that genomic stability and low passage number for experimental procedures were maintained.

***Table 2.1 Reprogramming media (RM)***

| Reagent | Final concentration |
|---|---|
| **DMEM/F12, Glutamax™** | 1x |
| **Non-essential amino acids (NEAA)** | 1x |
| **N-2 Supplement** | 1x |
| **B-27™ Supplement** | 1x |
| **$\beta$-mercaptoethanol** | 0.1µM |
| **hFGF-basic (PeproTech)** | 100ng/mL |
| **hLIF (Merck KGaA)** | 1000units/mL |
| **PD-0325901 (BioVision)** | 0.5µM |
| **CHIR99021 (Cayman Chemical)** | 3µM |
| **HA-100 (Santa-Cruz Biotechnology)** | 10µM |
| **A83-01 (BioVision)** | 0.5µM |

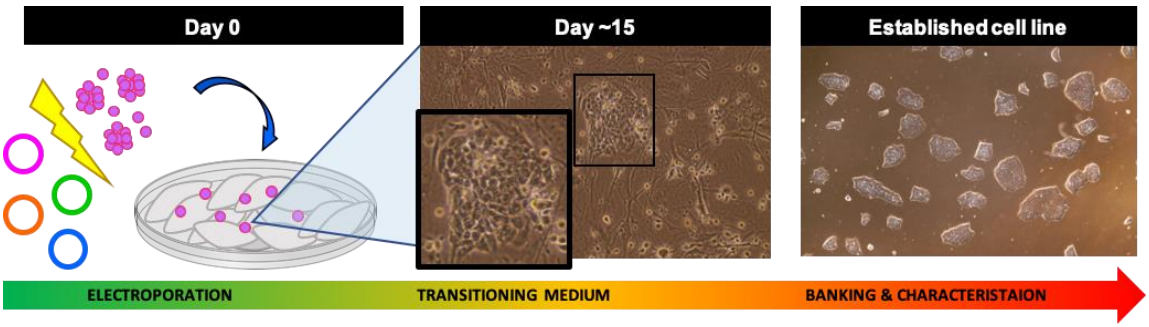


***Figure 2.1 Reprogramming LCLs into iPSCs with episomal plasmids***

LCLs were nucleofected with plasmids harbouring reprogramming factors and maintained on inactivated MEF. Media was transitioned to allow reprogramming to occur, and new iPSC clones were identified. These were selected and expanded in cell culture to produce established cell lines that were banked and characterised before use in experiments.

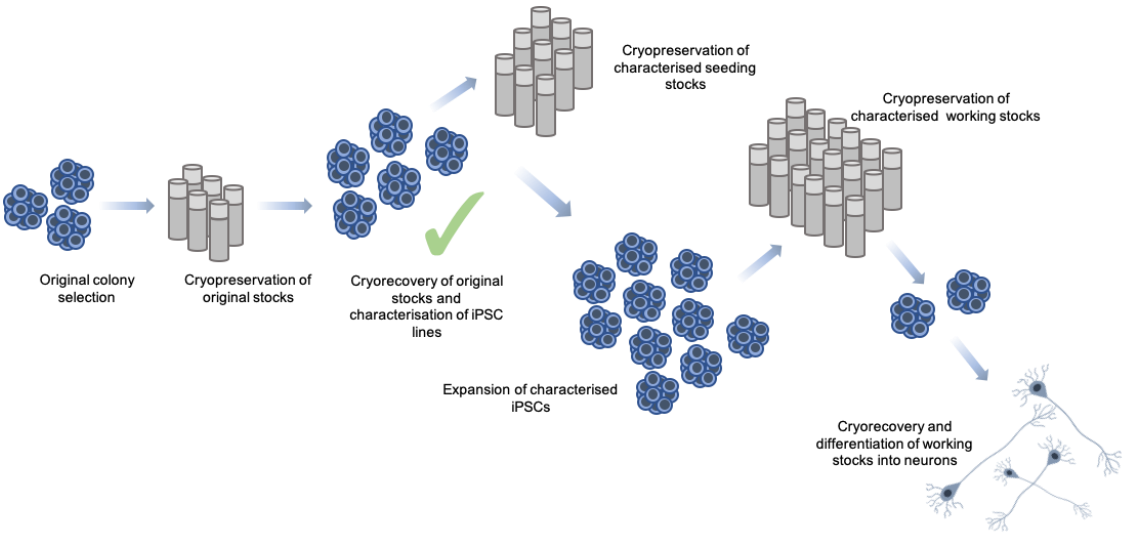


***Figure 2.2 Production of original, seeding, and working iPSCs stocks***

Newly reprogrammed iPSCs were cryopreserved as original stocks. Clones were then subject to characterisation experiments. Once these were successfully completed, seeding stocks of fully characterised clones were cryopreserved. One vial of seeding stock was passaged 2-3 times to produce working stocks. Due to low number of passages from seeding stock to working stock (2-3), the characterisation results from seeding stocks are applicable to working stocks. Working stocks were used for experiments, and iPSCs left over from experiments were discarded and never re-frozen.

### *2.1.5 Reprogramming LCLs into iPSCs with Sendai Virus*

In some instances, LCLs were reprogrammed into iPSCs using Sendai virus (SeV) harbouring pluripotency genes using the CytoTune™-iPS 2.0 Sendai Reprogramming Kit (Thermo Fisher Scientific). On day one, 150,000 cells were transduced as per manufacturer instructions, with an additional "spinfection" centrifugation step of 2250 RPM for 90 minutes in a large benchtop centrifuge, immediately after the virus was added to LCLs. LCLs were maintained in LCL media for 48 hours, with a media change at 24 hours. LCLs were transferred onto inactivated MEF and maintained in LCL media until day 5. Transition to RM (Table 2.1) and selection of colonies was then completed as described in 2.1.4.

### *2.1.6 Mouse embryonic fibroblast inactivation*

MEF were used as a feeder layer in reprogramming experiments to enable LCL attachment and successful reprogramming (2.1.4; 2.1.5). To prevent MEF from overpopulating the cell culture, they were pre-treated with mitomycin C to cross-link double stranded DNA, thus inhibiting cell division. Commercially acquired MEF (Merck KGaA) were grown in T175 flasks on 0.1% gelatine in MEF media (DMEM, GlutaMAX™, 10% FBS) under normoxic conditions until confluent. Mitomycin C was diluted to 10µg/mL in MEF media, filtered, and added to cells for 3 hours. Spent media was removed and cells were washed three times with pre-warmed PBS to remove any residual mitomycin C. Cells were dissociated with Trypsin, collected in DMEM, and centrifuged at 1000 RPM for 4 minutes in a large benchtop centrifuge. The supernatant was removed and the cell pellet was resuspended in MEF media for counting. One million cells were frozen per cryovial, in freezing media consisting of FBS with 10% DMSO, using Nalgene® Mr. Frosty or CoolCell® containers at -80°C. Frozen vials were transferred to liquid nitrogen vessels within 1 week for long term storage.

### *2.1.7 Motor neuron differentiation*

Motor neuron differentiation was driven by small molecule induction (Maury et al., 2015), following a protocol optimised in the Shaw group by Dr Jenny Greig.

To form embryoid bodies (EBs), iPSCs were incubated with fresh E8 flex with 10µM ROCK inhibitor (Day 0). After 3-4 hours, media was collected in a 15mL tube and cells were incubated with Versene to dissociate cells. Versene was removed and the kept media was used to collect and resuspend cells to form single cell suspension. Cells were centrifuged at 1000 RPM for 4 minutes in a large benchtop centrifuge, the supernatant removed, and the pellet was resuspended in Media 1 (Table 2.2) to form a single cell solution with gentle titration. $1x10^5$ cells were transferred to each well of a U-bottom 96-well plate in 200µL of Media 1. Immediately prior to centrifugation, cells were gently titrated with a multi-channel pipette to resuspend any sunken cells, and plates were centrifuged at 1500 RPM in a large benchtop centrifuge for 4 minutes with a slow break. Plates were transferred to a hypoxic incubator and left overnight. The next day (Day 1), EBs were transferred to a 6-well plate using a sterile Pasteur pipette in Media 2 (Table 2.2), with a maximum of ten EBs per well. Media changes were performed by tilting plates, allowing EBs to settle to the bottom edge of the well, and removing spent media with a pipette. Fresh media was added with small molecule and growth factor changes on specific days, as detailed in Figure 2.3 and Table 2.2. On day 11, EBs were transferred to 15mL tubes with a Pasteur pipette and all residual media was removed, 2mL of room temperature Accutase was added and EBs were incubated at 37°C for ~10 minutes. 1-2mL of motor neuron maturation media (MM) (Table 2.2) with 5µM ROCK inhibitor was added, and EBs were gently but thoroughly titrated with a P1000 pipette to yield single cell suspension. Cells were centrifuged at 1000 RPM for 4 minutes in a large bench top centrifuge, supernatant was removed, and pellets were resuspended in MM with 5µM ROCK inhibitor. Cells were counted and plated onto astrocytes (2.1.10) or directly onto pre-prepared cultureware (2.1.8). The number of motor neurons plated in different conditions are detailed in Table 2.3. Differentiated neurons were maintained in 5% $CO_2$ normoxic incubators, with partial MM changes every 2-3 days, until ready for use in experiments.

DAPT was included in MM for 1 week after EB dissociation and was then excluded from MM for long term culture.

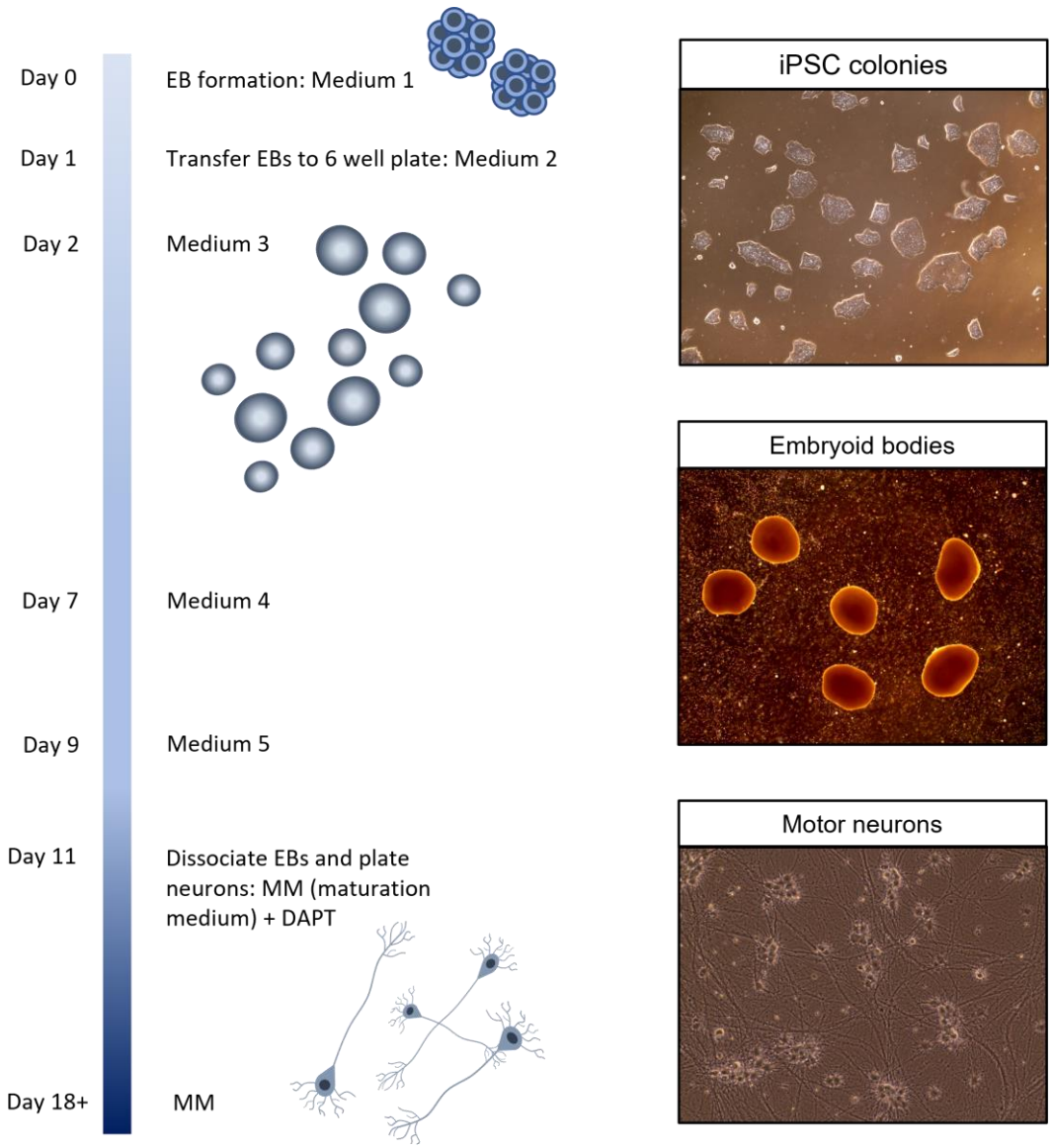


***Figure 2.3 Differentiation pipeline for generation of motor neurons***

iPSCs were differentiated into motor neurons by formation of embryoid bodies and gradual transition of media containing various small molecules and growth factors. Media included in differentiation are detailed in Table 2.2.

***Table 2.2 Motor neuron differentiation media changes***

| **Day of protocol – media changes** | **Media name** | **Media components** |
|---|---|---|
| **All days** | Basal media (included in every motor neuron differentiation media) | 50% Neurobasal™ Medium<br>50% DMEM/F-12, GlutaMAX™<br>1x N-2 Supplement<br>1x B-27™ Supplement<br>200µM AA2P (stabilised ascorbic acid)<br>0.01% $\beta$-mercaptoethanol |
| **0**<br>**(EB formation)** | Medium 1 | 40µM SB431542<br>2µM dorsomorphin<br>3µM CHIR-99021<br>5µM ROCK inhibitor |
| **1** | Medium 2 | 40µM SB431542<br>2µM dorsomorphin<br>3µM CHIR-99021 |
| **2** | Medium 3 | 40µM SB431542<br>2µM dorsomorphin<br>3µM CHIR-99021<br>1µM EC23 (retinoic acid equivalent)<br>500nM smoothened agonist |
| **4** | Medium 3 | 40µM SB431542<br>2µM dorsomorphin<br>3µM CHIR-99021<br>1µM EC23 (retinoic acid equivalent)<br>500nM smoothened agonist |
| **7** | Medium 4 | 1µM EC23 (retinoic acid equivalent)<br>500nM smoothened agonist |
| **9** | Medium 5 | 10µM DAPT |
| **11**<br>**(EB dissociation)** | Motor neuron maturation media (MM) | 10µM DAPT<br>20ng/mL BDNF<br>20ng/mL GDNF<br>20ng/mL IGF |

***Table 2.3 Cell counts for culture paradigms***

| **Culture plate** | **Number of motor neurons** | **Number of astrocytes** |
|---|---|---|
| Corning Falcon 96-well plate or Perkin Elmer CellCarrier™ Ultra 96-well plate | 6000 per well | 2000 per well |
| 13mm 1.5H coverslips maintained in 24-well plates | 70,000 per well | 30,000 per well |
| 6-well plate | $5x10^5$ per well | $5x10^5$ per well |
| Microfluidic device | 70,000 per device | 12,000 per device |

### *2.1.8 Motor neuron culture plate preparation*

Prior to plating neurons, plastic plates or 1.5H 13mm glass coverslips were coated with Poly-L-ornithine (PLO) solution (Scientific Laboratory Supplies) in 1:1 dilution with PBS for 24 hours at 37°C. The next day, laminin (Sigma) was thawed on ice and diluted to 25ng/µL in cold DMEM. Residual PLO was removed, rinsed once with PBS, and laminin solution was added for 24 hours at 37°C. When plating cells, laminin solution was removed, plates were rinsed with DMEM, and a small volume of pre-warmed media was added to wells so that when motor neurons were dissociated and counted they could be immediately added to the cultureware to preserve viability.

### *2.1.9 Astrocyte differentiation*

Differentiation of astrocytes was based on a published protocol describing efficient derivation of astrocytes by maintenance of neural progenitor cells in commercially available astrocyte medium (AM) (ScienCell) (Tcw et al., 2017). iPSCs were differentiated into NPCs using Thermo Fisher PSC Neural Induction Medium (NIM) following the manufacture guidelines. Briefly, high quality iPSCs were dissociated to single cell suspension with Accutase and 250,000 single cells were transferred to one well of a Geltrex™ coated 6-well plate in E8 flex with 10µM ROCK inhibitor. The next day (Day 1), 2.5mL NIM was added. On Day 2, uniform cell morphology was confirmed and fresh NIM was added. By Day 4, cells were reaching confluency and were fed with a larger volume of 5mL NIM, and cells with non-neuronal morphology were manually removed by scraping away with a P200 pipette. On Day 7, cells were gently washed with DPBS (-CaCl, -MgCl), and 1-2mL Accutase was added per well. When most cells had lifted they were transferred to a 15mL tube, and DPBS (-CaCl, -MgCl) was used to rinse and collect any residual cells from the plate. Cells were gently titrated to dissociate clumps and then passed through a 100µm cell strainer. The cell suspension was centrifuged for 4 minutes at 300 RCF, supernatant removed, and the pellet was resuspended in Neural Expansion Medium (NEM) (50% Neurobasal™ Medium, 50% Advanced™ DMEM⁄F-12, 1x Neural Induction Supplement) with 5µM ROCK inhibitor, and 50,000 cells were added to each well of a Geltrex™

coated 6-well plate. The next day, spent media was replaced with fresh NEM, which was then replaced every 2-3 days. When confluent, NPCs were passaged with Accutase in a 1:6 ratio, and 5µM ROCK inhibitor was included for passages 1-4. By passage 5, NEM was switched to an expansion media consisting of DMEM/F12, GlutaMax™, 1x N-2 Supplement, 1x B-27™ Supplement, and 20ng/mL hFGF-basic (PeproTech). NPCs were expanded and cryopreserved by dissociation with Accutase and resuspension of cell pellets in freezing media consisting of expansion media with 10% DMSO, using Nalgene® Mr. Frosty or CoolCell® containers at -80°C. Frozen vials were transferred to liquid nitrogen vessels within 1 week for long term storage.

To differentiate NPCs into astrocytes, NPCs were dissociated with Accutase to achieve a single cell suspension and plated on Matrigel® at a density of 15,000 cells/cm in expansion media. The next day (Day 0), total media was replaced with AM, excluding antibiotics. AM was replaced every 2-3 days for 30 days which was the endpoint of astrocyte induction, and cells were routinely passaged approximately once a week when they became confluent. During differentiation and after 30 days, astrocytes were passaged using Accutase and plated at a density of 15,000 cells/cm as single cells on Matrigel®, or in a 1:3 ratio after 30 days.

To avoid astrocyte overcrowding in subsequent motor neuron-astrocyte co-cultures, stocks of astrocytes pre-treated with mitomycin C were prepared. T75 flasks of astrocytes were incubated with 10µg/mL mitomycin C in AM for 3 hours. Flasks were washed with PBS three times and fresh AM was added. The next day, treated astrocytes were incubated with Accutase for 5-10 minutes at 37°C to dissociate cells, titrated with AM, centrifuged at 1000 RPM for 4 minutes in a large benchtop centrifuge, and $1x10^6$ astrocytes were frozen per cryovial in FBS + 10% DMSO using Nalgene® Mr. Frosty or CoolCell® containers, and were transferred to liquid nitrogen for long term storage.

### *2.1.10 Motor neuron-astrocyte co-culture*

For co-culture experiments, astrocytes were plated the day before EB dissociation (2.1.7). Mitomycin C pre-treated astrocytes were recovered from liquid nitrogen stores and grown on Matrigel® coated

T25 flasks in AM 1-2 days before plating. The day before motor neuron EB dissociation, astrocytes were incubated with Accutase for 5-10 minutes at 37°C, dissociated to single cell suspension in AM, centrifuged at 1000 RPM for 4 minutes in a large benchtop centrifuge, and resuspended in fresh AM. Cells were counted and plated as detailed in Table 2.3, onto plates prepared as described in 2.1.8. These were maintained in a normoxic incubator for 24 hours. Motor neuron EBs were dissociated the next day and motor neurons were added directly to the astrocytes.

Time points for experiments were selected based on the criteria detailed in Table 2.4, and throughout this thesis cultures are referred to as "day-*x* neurons" in line with day of motor neuron differentiation, starting with formation of EBs from iPSCs on day 0.

### *2.1.11 Microfluidics*

XonaChip® 450µm barrier microfluidic devices were acquired from Xona Microfluidics® (U.S.). Coating was completed following manufacturer instructions which included periodical coating of the four microfluidic wells, allowing coating liquid to move from one well to the next through the microgrooves, avoiding the introduction of bubbles. Solution was applied to the top left well and left for 1.5 minutes, solution was then applied to the bottom left well and left for 5 minutes so that solution moved through the central microgrooves. Solution was added to the top right well and left for 1.5 minutes, and finally solution was added to the bottom right chamber for 3 minutes. When removing one solution in preparation for addition of the next, a small amount of residual solution was left to prevent the introduction of bubbles into the microgrooves. XC Pre-Coat™ solution (Xona Microfluidics) was first applied, followed by two washes with PBS. PLO and laminin were then applied in the manner described here, with the dilutions and incubation times described in 2.1.8. When plating cells, astrocytes and neurons were plated as described (2.1.10) and were added to wells on one side of the microfluidic microgrooves only.

***Table 2.4 Experimental time points***

| Time point | Reasoning | References |
|---|---|---|
| **Day 17** | The original motor neuron differentiation protocol detailed that neurons are positive for the motor neuron marker Islet 1 by day 17, as confirmed in 3.3.4. | (Maury et al., 2015) |
| **Day 21** | Feasibility of completing many experiments on the same day of differentiation meant some delay was necessary from day 17. | n/a |
| **Day 25** | Neurites grew through microfluidics microgrooves by this time point, enabling assessment of distal neurites for ribopuromycylation, and ensuring microgrooves were suitable for RNA imaging. | n/a |
| **Day 40/42** | The original astrocyte differentiation protocol indicated that astrocytes are viable for 30 days without FBS. | (Tcw et al., 2017) |
| **Day 60** | The effects of extended culture maturation were compared to day-40/42 cultures. | n/a |

### *2.1.12 Cell counting*

The same cell counting protocol was used for all cell-types. Cells suspended in appropriate media were gently titrated to achieve a uniform single cell suspension. Cells were added to Solution 13 (100µg/mL DAPI, 30µg/mL acridine orange) in a 19:1 ratio (19µL cell suspension and 1µL Solution 13), 10µL of the mixture was transferred to a well in a NC-Slide A8™ (Chemometec), and cells were immediately counted using a NucleoCounter® NC-3000™ image cytometer (Chemometec) with the Cell Count & Viability Assay. The live cell count was used for calculations.

## *2.2 Induced pluripotent stem cell characterisation*

### *2.2.1 iPSC pluripotency immunocytochemistry*

A detailed description of immunocytochemistry is included in 2.4.1. Immunolabelled iPSC colonies were imaged with a Zeiss Axioscope Upright Epi-Fluorescence Microscope. Pluripotency was confirmed by expression of Oct-3/4 in all cells with DAPI counterstain.

### *2.2.2 Embryoid body assay*

Spontaneous differentiation of iPSCs into EBs harbouring cells from the three germ layers was completed to confirm pluripotency of stem cells. PolyHEMA plates were prepared by dissolving 1.2g polyHEMA in 50mL ethanol with gentle heating to 37°C to prepare a stock solution, which was diluted 1:10 to prepare a working solution, and 1mL was added per well of a 6-well plate. Plates were left open in sterile laminar flow hoods to allow ethanol to evaporate, and in-hood UV light was subsequently applied to ensure sterilisation of plates. iPSCs were dissociated into small clumps with Versene and transferred to polyHEMA coated plates in E8 flex with 10uM ROCK inhibitor. The next day (Day 1), media was replaced with EB media (EBM) (KnockOut™ DMEM, 10% KnockOut™ Serum Replacement, 5% FBS, 1x GlutaMAX™, 1x NEAA, 12ng/mL hLIF (Merck KGaA), 0.055mM $\beta$-mercaptoethanol). EBM was replaced every 2-3 days for 7 days. On day 8, individual EBs were transferred to 0.1% gelatine coated glass coverslips using a sterile Pasteur pipette and allowed to attach. Media was changed every 2-3 days for 2-3 weeks, and cultures were fixed with 4% PFA for 15 minutes and subject to immunocytochemistry.

Immunocytochemistry was completed as described in 2.4.1, and the antibodies used for embryoid body analysis are included in Table 2.8. Cells were imaged with Zeiss Axioscope Upright Epi-Fluorescence Microscope. The presence of cells originating from the neuroectoderm was confirmed by detection of ectodermal $\beta$3-Tubulin cells with typical neuronal morphology, cells from the mesodermal lineage were confirmed by probing for $\alpha$-smooth muscle actin, and $\alpha$-fetoprotein was used to label endodermal cells.

### *2.2.3 G-band karyotyping*

G-band karyotyping was outsourced to TDL Genetics (The Doctors Laboratory, U.K.) or to the Genome Editing and Embryology Core (King's College London, U.K.). Analysis of 20 metaphases was initially attempted, however in some instances this was not achieved (3.3.3).

### *2.2.4 Short tandem repeat profiling*

DNA was extracted from cell pellets harvested from LCL and iPSC cultures using a DNeasy Blood & Tissue Kit (Qiagen) following the manufacture's protocol. Short tandem repeat (STR) profiling was outsourced to Source BioScience (U.K.) which included analysis of 16 microsatellite regions, and STR profiles were compared across LCL and iPSC DNA samples to ensure that iPSCs were correctly attributed to parent LCL samples.

### *2.2.5 Sanger sequencing*

DNA was extracted from cell pellets harvested from iPSC cultures using a DNeasy Blood & Tissue Kit (Qiagen) following the manufacture's protocol. PCR was conducted using Q5® Hot Start High-Fidelity 2X Master Mix (New England BioLabs) following the manufacturer's guidelines with cycle conditions; 98°C for 30 seconds, 35 cycles of 98°C for 10 seconds, 61-66°C for 20 seconds, and 72°C for 20 seconds, followed by 72°C for 2 minutes, with hold at 4°C. Primer and DNA solutions were sent to GATC (Eurofins Genomics, Germany) for Sanger sequencing. Electropherograms were assessed for the inclusion of ALS associated SNPs. Primers included for sequencing mutant regions are included in Table 2.5.

***Table 2.5 Primers for Sanger sequencing***

| Gene target | Primer sequence |
|---|---|
| ***ANXA11* G38R**<br>***ANXA11* D40G** | Forward: CCTGGGAGCTCTCATCTCTG |
| | Reverse: GGAAAAGTGAGACCCAGAGAG |
| ***ANXA11* R235Q** | Forward: TGTGGACTCCTTTAGATACTCCAAC |
| | Reverse: CTCCTGCTCCTTACTGTCCATC |

### *2.2.6 Screening for loss of Epstein Barr Virus DNA*

iPSCs were serially passaged and screened for loss of Epstein Barr virus (EBV) genes in genomic DNA extracts. DNA was extracted and PCR completed as described in 2.2.5, with primers targeting EBV genes to detect any residual episomal EBV genomic material. The house keeping gene SDHA was

included to ensure presence of DNA in samples. Primers included in EBV screening are included in Table 2.6. PCR products were mixed with Gel Loading Dye, Purple (6X), no SDS (New England BioLabs), separated by gel electrophoresis in a 0.2µg/mL ethidium bromide 2% agarose gel with Quick-Load® Purple 1kb DNA Ladder (New England Biolabs), and imaged with a UV transilluminator.

***Table 2.6 Primers for EBV screening***

| Gene target | Primer sequence |
|---|---|
| ***EBNA2*** | Forward: CATAGAAGAAGAAGAGGATGAAGA |
| | Reverse: GTAGGGATTCGAGGGAATTACTGA |
| ***Orip*** | Forward: TCGGGGGTGTTAGAGACAAC |
| | Reverse: TTCCACGAGGGTAGTGAACC |
| ***BZLF1*** | Forward: CACCTCAACCTGGAGACAAT |
| | Reverse: TGAAGCAGGCGTGGTTTCAA |
| ***LMP1*** | Forward: ATGGAACACGACCTTGAGA |
| | Reverse: TGAGCAGGATGAGGTCTAGG |
| ***SDHA*** | Forward: TGGGAACAAGAGGGCATCTG |
| | Reverse: CCACCACTGCATCAAATTCATG |

### *2.2.7 Mycoplasma screening*

iPSCs were routinely screened for mycoplasma infection using a MycoAlert® Mycoplasma Detection Kit (Lonza) and the MycoAlert™ Assay Control Set (Lonza) following the manufacturer instructions. Spent media that had been in contact with cells for at least 24 hours was collected and 2mL was centrifuged at 200 RCF for 5 minutes. 100µL of the supernatant and positive and negative controls were added to one well of an opaque white 96-well plate with 100µL MycoAlert™ Reagent in duplicate and left for 5 minutes. Luminescence was measured with a FLUOstar Omega multi-mode microplate reader (BMG Technologies) (Reading A). 100µL MycoAlert™ Substrate was added to each sample, incubated for 10 minutes, and the luminescence read a second time. The ratio of Reading B/Reading A was calculated for each sample and the controls, with ratios <0.9 indicating the absence of mycoplasma infection. LCLs and iPSCs were routinely screened for mycoplasma during the reprogramming process, and before stocks were frozen.

## *2.3 Drug treatment conditions*

### *2.3.1 Stress granules*

Motor neurons were treated with sodium arsenite, puromycin, and sorbitol to induce stress granule formation. Drug concentrations and treatment times are included in Table 2.6. All stress granule inducing drugs were solubilised in $H_2O$ and so control treatment conditions were included by adding new media to cells. Cells were fixed immediately after the end of the drug treatment period. Fixation and subsequent immunocytochemistry and imaging are included in 2.4.

***Table 2.7 Stress granule drug treatment conditions***

| Drug | Concentration | Incubation time |
|---|---|---|
| **Puromycin** | 10µg/ml | 24 hours |
| **Sodium arsenite** | 500µM | 1 hour |
| **Sorbitol** | 600mM | 3 hours |

### *2.3.2 Ribopuromycylation*

Motor neurons were co-treated with emetine and puromycin to label sites of nascent protein synthesis. Puromycin incorporates into the C-terminal of elongating nascent peptide chains which inhibits protein synthesis, and antibodies that bind to puromycin can be used to visualise puromycin-labelled newly synthesised proteins. Emetine is an irreversible translation elongation inhibitor which binds to the 40S ribosomal subunit and enhances localisation of nascent peptides to ribosomes in puromycylation-treated cells (Bastide et al., 2018; David et al., 2013; Graber et al., 2013). Cells were incubated with 200µM emetine and 100µM puromycin for 5 minutes at 37°C, washed once with 0.0003% digitonin in 25mM HEPES on ice, washed with plain DMEM, and fixed with 4% PFA and 4% sucrose for 15 minutes. Cultures were subject to immunocytochemistry (2.4) and imaged with super resolution microscopy (2.4.3). Details of image analysis for ribopuromycylation experiments are included in 6.3.3.

### *2.3.3 Global protein translation*

Motor neuron-astrocyte co-cultures were incubated with 100µM puromycin in fresh media for 5 minutes, washed once with 0.0003% digitonin, and fixed with 4% PFA and 4% sucrose for 15 minutes. Subsequent immunocytochemistry and imaging are detailed in 2.4.

## *2.4 Immunocytochemistry and microscopy*

### *2.4.1 Immunocytochemistry*

For immunocytochemistry experiments, cells were fixed in 4% PFA for 15 minutes. Motor neuron monocultures and astrocyte-motor neuron co-cultures were fixed with 4% PFA and 4% sucrose for 15 minutes. After fixation cells were rinsed three times with PBS, permeabilised with 0.25% Triton X-100 in PBS for 15 minutes, rinsed with PBS, and blocked for 1 hour in 10% donkey serum in PBS. Primary antibodies were diluted in 5% donkey serum and added to cells overnight at 4°C. The next day, primary antibody dilution was removed, cells were washed three times with PBS, and secondary antibodies diluted 1:500 in 5% donkey serum were added for 1 hour. After incubation, cells were washed three times with PBS, incubated with 1.25µg/mL DAPI for 5 minutes, washed three times with PBS, and cells on coverslips were mounted with ProLong™ Diamond Antifade Mountant and left to set overnight. When conjugated antibodies were utilised, they were added to cells after secondary antibodies, ensuring that multiple PBS washes had removed any residual antibodies from previous steps. Conjugated antibodies were diluted in 5% donkey serum and added to cells for overnight incubation at 4°C. The next day cells were washed three times with PBS and mounted as described. Primary and conjugated antibodies are included in Table 2.8, and secondary antibodies are included in Table 2.9.

*Table 2.8 Primary and conjugated antibodies used in immunocytochemistry*

| Antibody target | Specification | Utilisation | Dilution | Product code |
|---|---|---|---|---|
| **Oct-3/4** | Goat polyclonal | Confirmation of pluripotency | 1:200 | sc-8628 (Santa Cruz Biotechnology) |
| **$\beta$3-Tubulin** | Mouse monoclonal | Embryoid body assay | 1:400 | T8660 (Sigma-Aldrich) |
| **$\alpha$-fetoprotein (AFP)** | Goat polyclonal | Embryoid body assay | 1:200 | sc-8108 (Santa Cruz Biotechnology) |
| **$\alpha$-smooth muscle actin** | Rabbit polyclonal | Embryoid body assay | 1:200 | ab5694 (Abcam) |
| **Islet 1** | Rabbit monoclonal | Motor neuron characterisation | 1:200 | ab109517 (Abcam) |
| **Islet 1** | Mouse monoclonal | Motor neuron characterisation | 1:200 | 562547 (BD Pharmingen) |
| **Annexin A11** | Rabbit monoclonal | Neuronal characterisation | 1:300 | HPA027545 (Atlas Antibodies) |
| **Annexin A11** | Mouse monoclonal | Ribopuromycylation (with FMRP only) | 1:300 | SAB1405463-50UG (Sigma-Aldrich) |
| **TDP-43** | Rabbit monoclonal | Neuronal characterisation, ribopuromycylation | 1:400 | 10782-2-AP (Proteintech) |
| **TDP-43** | Mouse monoclonal | Co-stain with Annexin A11 (rabbit) and G3BP1 | 1:400 | ab57105 (Abcam) |
| **pTDP-43** | Mouse Monoclonal | Neuronal characterisation | 1:500 | TIP-PTD-M01 (CosmoBio) |
| **G3BP1** | Mouse monoclonal | Stress granule analysis, ribopuromycylation | 1:300 | 05-1938 (Sigma-Aldrich) |
| **MAP2** | Chicken polyclonal | Microfluidics and sorbitol stress granules | 1:500 | ab92434 (Abcam) |
| **ALDH1L1** | Rabbit polyclonal | Astrocyte characterisation | 1:500 | RPCA-ALDH1L1 (Universal Biologicals) |
| **S100A6** | Mouse monoclonal | Astrocyte characterisation | 1:500 | S5049 (Sigma-Aldrich) |
| **GFAP** | Goat polyclonal | Co-culture example | 1:200 | ab53554 (Abcam) |
| **Puromycin** | Mouse monoclonal-647 | Protein translation assay, ribopuromycylation | 1:300 | MABE343-AF647 (Sigma-Aldrich) |
| **$\beta$3-Tubulin** | Mouse monoclonal-488 | Neuronal characterisation | 1:300 | 5060338 (BD Pharmingen) |
| **Rab7** | Mouse monoclonal | Ribopuromycylation | 1:300 | ab50533 (Abcam) |

| | | | | |
|---|---|---|---|---|
| **Lamp1** | Mouse monoclonal | Ribopuromycylation | 1:300 | sc-20011 (Santa Cruz Biotechnology) |
| **FUS** | Mouse monoclonal | Ribopuromycylation | 1:300 | 60160-1-1g (Proteintech) |
| **S6** | Mouse monoclonal | Ribopuromycylation | 1:200 | 2317 (Cell Signalling) |
| **FMRP** | Rabbit polyclonal | Ribopuromycylation | 1:300 | 4317 (Cell Signalling) |
| **U1 snRNP 70** | Mouse monoclonal | Ribopuromycylation | 1:300 | sc-390899 (Santa Cruz Biotechnology) |
| **vGLUT2** | Goat polyclonal | Neuronal characterisation | 1:300 | ab101760 (Abcam) |
| **Bassoon** | Mouse monoclonal | Neuronal characterisation | 1:240 | ab82958 (Abcam) |
| **Synapsin 1** | Rabbit monoclonal | Neuronal characterisation | 1:120 | 5297 (Cell Signalling) |
| **ChAT** | Goat polyclonal | Neuronal characterisation, ribopuromycylation | 1:300 | AB144P (Sigma-Aldrich) |

*Table 2.9 Secondary antibodies used in immunocytochemistry*

| Antibody | Product code |
|---|---|
| **Goat anti-Rabbit IgG (H+L) Highly Cross-Adsorbed Secondary Antibody, Alexa Fluor™ Plus 647** | A32733 (Thermo Fisher Scientific) |
| **Donkey Anti-Goat IgG H&L (Alexa Fluor® 568) preadsorbed** | ab175704 (Abcam) |
| **Donkey Anti-Mouse IgG H&L (Alexa Fluor® 568)** | ab175472 (Abcam) |
| **Donkey Anti-Mouse IgG H&L (Alexa Fluor® 488)** | ab150105 (Abcam) |
| **Goat anti-Chicken IgY (H+L) Cross-Adsorbed Secondary Antibody, Alexa Fluor™ Plus 647** | A32933 (Thermo Fisher Scientific) |
| **Donkey anti-Mouse IgG (H+L) Cross-Adsorbed Secondary Antibody, DyLight™ 550** | SA5-10167 (Thermo Fisher Scientific) |
| **Donkey anti-Mouse IgG (H+L) Cross-Adsorbed Secondary Antibody, DyLight™ 488** | SA5-10166 (Thermo Fisher Scientific) |
| **Donkey anti-Rabbit IgG (H+L) Cross-Adsorbed Secondary Antibody, DyLight™ 488** | SA5-10038 (Thermo Fisher Scientific) |
| **Donkey anti-Rabbit IgG (H+L) Cross-Adsorbed Secondary Antibody, DyLight™ 550** | SA5-10039 (Thermo Fisher Scientific) |
| **Cy™3 AffiniPure Donkey Anti-Goat IgG (H+L)** | 05-165-003 (Jackson ImmunoResearch) |

### *2.4.2 Opera Phenix® High-Content Screening System*

High-throughput image collection and analysis was completed with an Opera Phenix® High-Content Screening System and Harmony® software. In all instances, biological repeats (separate motor neuron inductions) each included three technical replicates (three wells in a 96-well plate per condition) and multiple fields of view (15-30) were imaged per technical replicate. The total number of images collected varied across experiments but was always consistent across cell lines within the same experiment. Confocal *z*-stacks were collected and subsequent analysis was completed for each *z*-plane, with results for each cell line taken as an average of all images for that biological replicate.

Image analysis in Harmony® was optimised separately for monocultures and co-cultures: This involved addition of 'analysis blocks' to detect and measure cellular regions, named 'objects'. This included 'find nuclei', 'find cytoplasm', 'find neurites', and 'find spots', to name a few examples. An example of object identification including nuclei, cytoplasm, neurites, and spots in day-17 motor neuron monocultures is included in Figure 2.4. Optimisation of analysis pipelines included exclusion of incorrectly identified 'objects' highlighted by 'analysis blocks', which resulted in stratification of

cellular populations for inclusion in quantification. A persistent challenge that occurred in Harmony® analysis was the incorrect identification of 'objects' in image regions with few or no cells. This was overcome by inclusion of additional 'analysis blocks' that subsequently filtered out incorrectly identified 'objects', and an example of this is included in Figure 2.5 to highlight how incorrectly identified 'objects' were excluded from final analyses. In all instances where motor neurons were co-cultured with astrocytes, linear classification (machine learning) was used to stratify neuronal and astrocytic nuclei, such that neurons could be specifically quantified. An example of the delineation of neuronal cells for quantification in co-cultures is included in Figure 2.6.

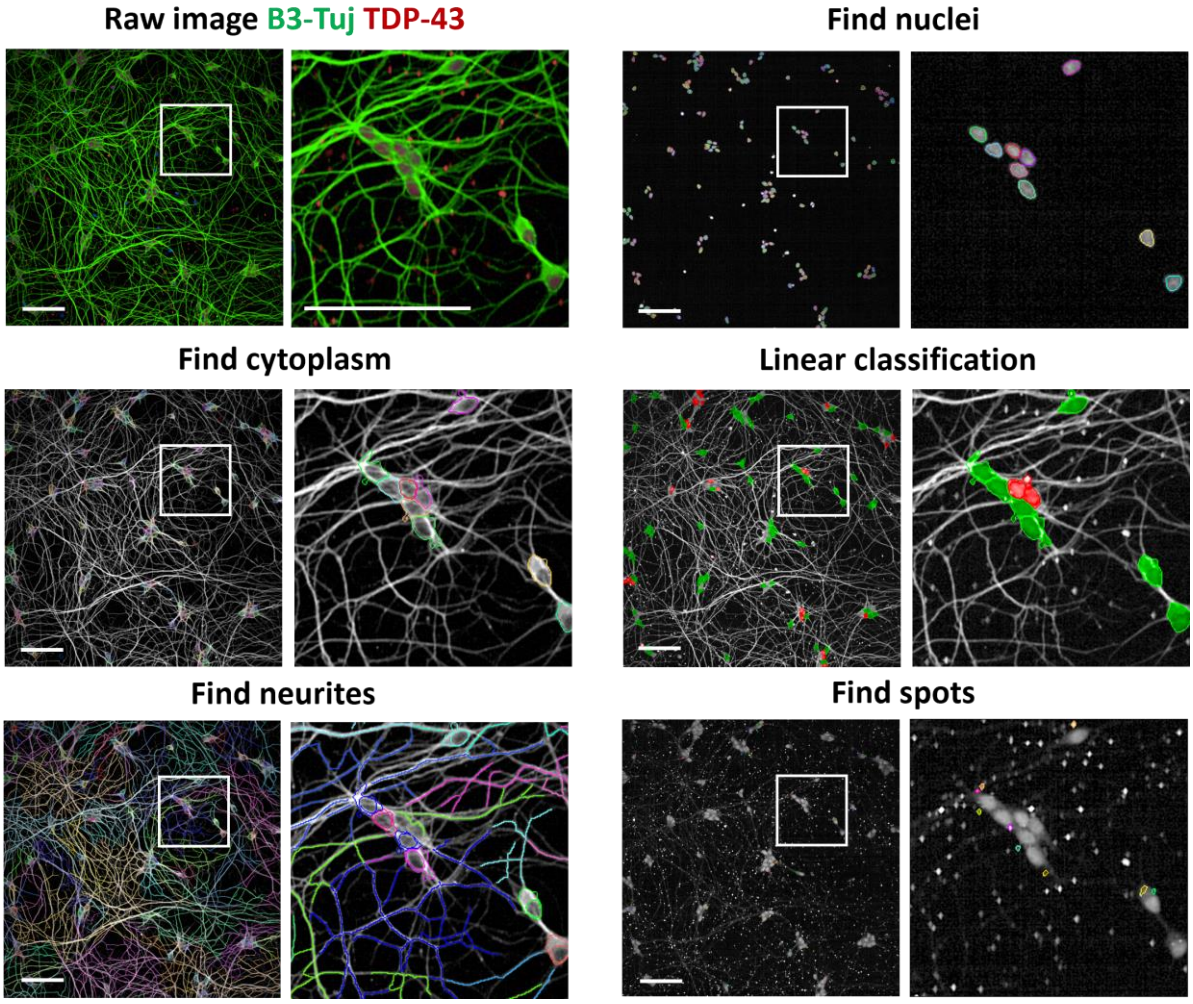


***Figure 2.4 Neuronal classification and cell compartment selection in Harmony®***

Motor neurons were imaged with the Opera Phenix® High Content Screening System and analysed using Harmony® software. 'Find nuclei', 'find cytoplasm', 'find neurites', and 'find spots' were used to detect cellular regions. 'Linear classification' was implemented to exclude debris or dead cells that

had been incorrectly identified. This led to some exclusion of neurons from analysis (see red cells in linear classification panel), which was preferable compared to the inclusion of debris in quantification data.

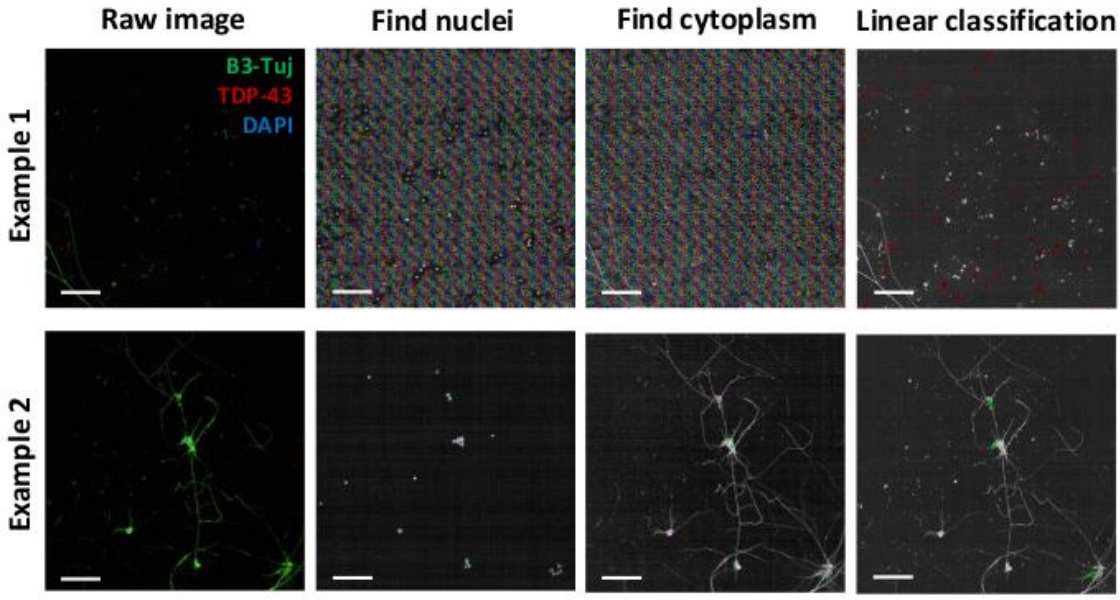


***Figure 2.5 Exclusion of null 'objects' in Harmony®***

Incorrect identification of 'objects' including nuclei and cytoplasm was common in images where few or no cells were present, and the software would incorrectly classify empty background as many small objects. In Example 1 the 'find nuclei' and 'find cytoplasm' panels show incorrect identification of 'objects' (highlighted by multi-coloured traces), additional 'analysis blocks' were included to exclude these from quantification, and the linear classification panel highlights the exclusion of any remaining null object (red 'objects' are excluded and green objects, which represent neuronal nuclei, are absent). In Example 2, application of filtration steps to exclude null 'objects' results in the exclusion of some neuronal cells from analysis (included objects are highlighted in green in the linear classification panel), which was a consequence of excluding debris from analysis.

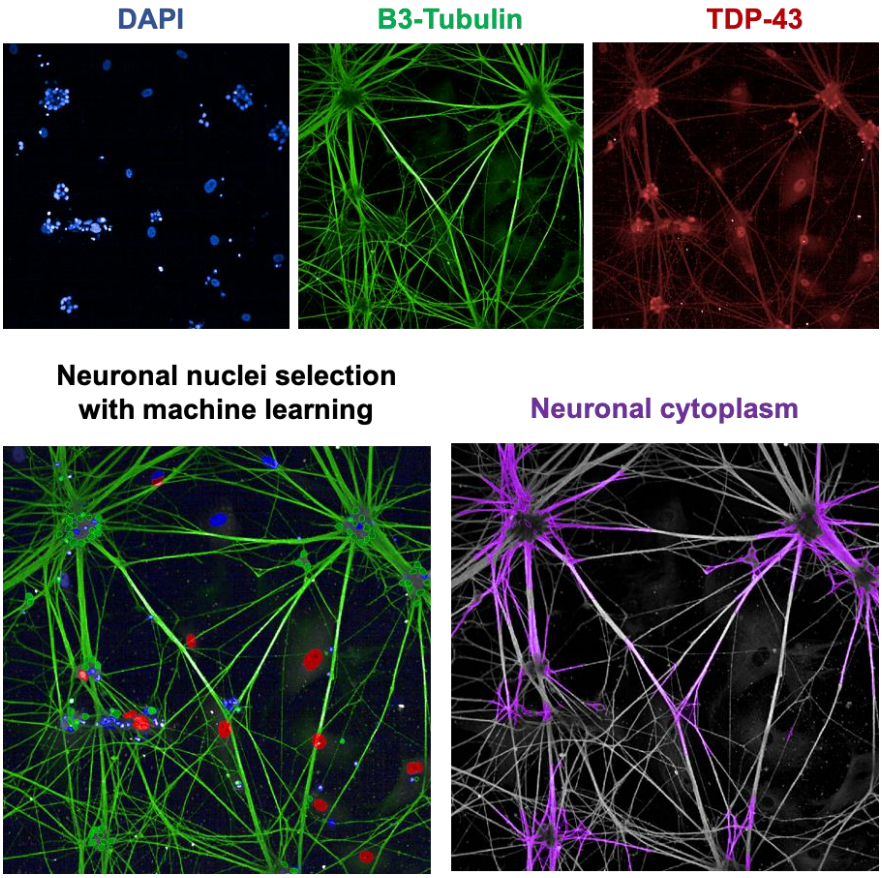


***Figure 2.6 Stratification of neurons with machine learning in Harmony®***

Co-cultures imaged with the Opera Phenix® High-Content Screening System were analysed in Harmony®. 'Linear classification' (machine learning) was implemented to classify nuclei as neuronal (green) or astrocytic (red), and an additional debris category (blue) was included to exclude incorrectly detected nuclei (bottom left image). Subsequent identification of the cytoplasm (purple, bottom right image) utilised neuronal nuclei to identify appropriate cytoplasmic regions.

### *2.4.3 Fixed cell microscopy*

Super high-resolution imaging was completed using a structured illumination microscope (iSIM) with a Hamamatsu Flash4.0 sCMOS camera. For cells on glass coverslips a 100x 1.4NA oil immersion lens (Nikon) was used, and cells maintained in optically clear plastic microfluidic devices were imaged with a 100x 1.35NA silicone immersion lens (Nikon). Images acquired by iSIM were processed by Richard-Lucy deconvolution with 20 iterations in Nikon NIS-Elements.

Additional imaging was completed with a Nikon Eclipse Ti Inverted Spinning Disk Confocal System with a Yokogawa CSU-X1 spinning disk unit and Andor EMMCD camera utilising a 40x 1.1NA water

immersion lens (Nikon) or a 20x 0.75NA air interface lens (Nikon). Images were processed with the Nikon NIS-Elements Denoise.ai module.

### *2.4.4 Live imaging of spontaneous calcium fluctuations*

Spontaneous calcium fluctuations were measured using the cell permeant dye Fluo-4 AM, which increases in fluorescent intensity >100 fold in the presence of calcium. Motor neuron-astrocyte co-cultures were maintained in a 96-well plate for 40 and 60 days from motor neuron induction. Fluo-4 AM was reconstituted in DMSO and diluted to 2µM in imaging media (Table 2.10) plus 0.02% Pluronic-F27 and added to cells for 30 minutes in an incubator. Media was removed and cells were rinsed with PBS, and fresh imaging media was added. After 5 minutes, an area of culture where neuronal cell bodies were visible in the field of view was imaged with a Nikon Eclipse Ti Inverted Spinning Disk Confocal System with a Yokogawa CSU-X1 spinning disk unit and Andor EMMCD camera, utilising a 20x 0.75NA air interface lens (Nikon) in an enclosed Okolab incubator at 37°C with 5% $CO_2$. Each imaging period lasted for 1 minute with continuous image collection, and this was repeated eight times for each cell line in each biological replicate, with neuronal regions randomly selected across the entire well. Images were processed by Nikon NIS-Elements Denoise.ai to increase image quality, and fluctuations in fluorescent intensity were calculated using ΔF/F0, which is described in detail in 5.3.2.

***Table 2.10 Imaging media***

| Media component | Final concentration |
|---|---|
| **FluoroBrite™ DMEM** | 1x |
| **N-2 Supplement** | 1x |
| **B-27™ Supplement** | 1x |
| **$\beta$-mercaptoethanol** | 0.01% |
| **GlutaMAX™** | 1x |
| **BDNF (Peprotech)** | 20ng/mL |
| **GDNF (Peprotech)** | 20ng/mL |
| **IGF (Peprotech)** | 20ng/mL |

### *2.4.5 RNA transport live imaging*

Live imaging of RNA was performed using SYTO® RNASelect™ Green Fluorescent Cell Stain. This cell-permeant dye emits a bright fluorescent signal when bound to RNA, and a weak background fluorescence when bound to DNA. Motor neuron-astrocyte co-cultures were grown in microfluidic devices until day 25 of motor neuron differentiation, and cells were stained following the manufacturer's protocol. Briefly, 5µM intermediate stock was prepared by diluting 1µL 5mM stock in 1mL media, then 100µL of intermediate stock was diluted in 900µL pre-warmed media and immediately added to cells in place of spent media. Cells were incubated at 37°C for 20 minutes, washed twice with PBS, and imaging media (Table 2.10) was added. Cells were rested for 5 minutes at 37°C, and neurons were imaged with a Nikon Eclipse Ti Inverted Spinning Disk Confocal System with a Yokogawa CSU-X1 spinning disk unit and Andor EMMCD camera, utilising a 40x 1.1NA Water Immersion Lens (Nikon) in an enclosed Okolab incubator at 37°C with 5% $CO_2$. Details of RNA molecule transport velocity quantification are included in 6.3.2.

### *2.4.6 Image quantification*

Quantification of confocal images was performed in Nikon NIS-Elements, FIJI, and KymographDirect, and specific details of quantification parameters are included in the relevant results chapters in this thesis. Where representative images are shown throughout this thesis, images were saved with the same brightness and contrast for each cell line and condition in each experiment. Numerical data were processed in Microsoft Excel and GraphPad Prism 8.4.1, and all statistical analysis was completed in GraphPad Prism 8.4.1 and is described in 2.7.

## *2.5 Protein quantification with western blotting*

### *2.5.1 Western blotting and protein assay*

Cultured cells were directly lysed from culture plates: Spent media was removed and cells were washed with PBS to remove residual media, plates were put on ice and pre-cooled RIPA buffer (Table 2.11) was added directly to cells, cells were scraped into buffer, sonicated for 20 seconds on ice, and centrifuged at 13,000 RPM for 30 minutes at 4°C in a bench top microcentrifuge. Supernatant was collected and quantified using DC™ Protein Assay Kit (Bio-Rad) using bovine serum albumin (BSA) protein standards prepared in RIPA buffer. Briefly, 2µL of each standard and sample was loaded to optically clear 96-well plate in duplicate. 25µL of a solution made from Reagent A and Reagent S in a 1:50 ratio was added to each sample, followed by 200µL Reagent B. Optical density was measured with a FLUOstar Omega multi-mode microplate reader (BMG Technologies), and sample protein concentration was calculated using the linear equation from plotted BSA standards. 8µg of each sample was diluted with 6µL 4x sample buffer (Table 2.12) and RIPA buffer to achieve a total volume of 24µL. Samples were boiled at 95°C for 10 minutes then loaded into pre-cast 26-well NuPAGE® Novex® 4-12% Bis-Tris Midi Protein Gels with Precision Plus Protein™ Standards (Bio-Rad) in a XCell4 SureLock Midi Cell (Thermo Fisher Scientific) electrophoresis tank filled with 1x NuPAGE® MOPS SDS running buffer. Blots were transferred to PVDF membranes with an iBlot 2 Dry Blotting System and stained with Revert™ Total Protein Stain (LI-COR Biosciences) following the manufacturer's protocol: After transfer, membranes were rinsed with ultrapure water and incubated with Revert 700 Total Protein Stain for 5 minutes. The stain was removed and Revert Wash Solution was added for 30 seconds twice, membranes were rinsed with ultrapure water and imaged with an Odyssey® Imaging System (LI-COR Biosciences). Once complete, the protein stain was removed by rinsing with ultrapure water and incubation with Revert Destaining Solution until the stain was no longer visible, for no more than 10 minutes. De-stained membranes were rinsed with ultrapure water and blocked for 1 hour with 5% skimmed milk in TBST (Table 2.13) and incubated with primary antibodies in 1%

skimmed milk in TBST at 4°C overnight. The next day membranes were washed three times with TBST for 5 minutes, secondary antibodies diluted 1:5000 in 1% skimmed milk in TBST were added for 1 hour, and membranes were washed three times with TBST for 5 minutes. Membranes were scanned with an Odyssey® Imaging System (LI-COR Biosciences). All wash and incubation steps were carried out on a benchtop roller with membranes kept in cylinders. Antibodies included in western blot analyses are included in Table 2.14 and Table 2.15.

***Table 2.11 RIPA buffer***

| Component | Final concentration |
|---|---|
| **Sodium chloride (NaCl)** | 150mM |
| **Sodium deoxycholate** | 0.5% |
| **Sodium dodecyl sulfate (SDS)** | 0.1% |
| **Tris-HCl (pH 7.4)** | 50mM |
| **Triton X-100** | 1x |
| **PhosSTOP™ (Roche)** | 1x |
| **cOmplete™ (Roche)** | 1x |
| **dd$H_2O$** | To required volume |

***Table 2.12 4x Sample buffer***

| Component | Final concentration |
|---|---|
| **Tris-HCl pH 6.8** | 200mM |
| **Glycerol** | 40% |
| **Sodium deodecyl sulfate (SDS)** | 8% |
| **Bromophenol blue** | ~0.2% |
| **DTT** | 400mM |

***Table 2.13 TBST (tris-buffered saline, Tween® 20)***

| Component | Final concentration |
|---|---|
| **Tris-HCl, pH 7.4** | 25mM |
| **Sodium chloride (NaCl)** | 150mM |
| **Potassium chloride (KCl)** | 2mM |
| **Tween® 20 (Sigma-Aldrich)** | 0.1% |

***Table 2.14 Primary antibodies used in western blotting***

| Antibody target | Specification | Dilution | Product code |
|---|---|---|---|
| **Annexin A11** | Rabbit polyclonal | 1:1000 | HPA027545 (Atlas Antibodies) |
| **TDP-43** | Mouse monoclonal | 1:5000 | ab57105 (Abcam) |
| **FUS** | Mouse monoclonal | 1:1000 | 60160-1-1g (Proteintech) |
| **FMRP** | Rabbit polyclonal | 1:1000 | 4317 (Cell Signalling) |

***Table 2.15 Secondary antibodies used in western blotting***

| Antibody | Product code |
|---|---|
| **Goat anti-Mouse IgG (H+L) Secondary Antibody, DyLight™ 680** | 35518 |
| **Goat anti-Mouse IgG (H+L) Secondary Antibody, DyLight™ 800 4X PEG** | SA5-35521 |
| **Goat anti-Rabbit IgG (H+L) Secondary Antibody, DyLight™ 680** | 35568 |
| **Goat anti-Rabbit IgG (H+L) Secondary Antibody, DyLight™ 800 4X PEG** | SA5-35571 |

### *2.5.2 Western blot quantification*

Total protein stain was selected to normalise western blot signal from target proteins as many traditionally used housekeeping proteins such as GAPDH are implicated in cellular pathways that are misregulated in neurodegeneration (Tisdale et al., 2009; Tristan et al., 2011). Additionally, the comparison of protein abundance across different cell-types is more robust when using total protein for normalisation. Further, using total protein stain frees both imaging channels for use with target antibodies. Western blots were quantified using Image Studio™ Light (LI-COR Biosciences). For each blot, total protein bands were traced and the signal measured, and the largest value identified. Each total protein signal was divided by the value for the largest band to give the lane normalisation factor; a measure of the relative total protein abundance of each sample. Target protein bands were traced and measured, and each signal was divided by the normalisation factor for that sample, yielding normalised values for target protein abundance. Statistical analyses were completed as described in 2.7.

## *2.6 Reverse transcription polymerase chain reaction (RT-PCR)*

RNA was extracted with a RNeasy Kit (Qiagen) following exactly the manufacturer's protocol, and measured with a Nanodrop™ Spectrophotometer (Thermo Fisher Scientific), followed by the iScript™ cDNA Synthesis Kit (Bio-Rad Laboratories) following the manufacturer's instructions. PCR was conducted as described in 2.2.5 and PCR products were mixed with Gel Loading Dye, Purple (6X), no

SDS (New England BioLabs), separated by gel electrophoresis in a 0.2µg/mL ethidium bromide 2% agarose gel with a Quick-Load® Purple 1kb DNA Ladder (New England Biolabs), and imaged with a UV transilluminator. Primers used for RT-PCR are included in Table 2.16.

***Table 2.16 RT-PCR primers***

| Gene target | Primer sequence |
|---|---|
| **HB9** | Forward: GCACCAGTTCAAGCTCAAC |
| | Reverse: GCTGCGTTTCCATTTCATCC |
| **ChAT** | Forward: TGAGTACTGGCTGAATGACATG |
| | Reverse: AGTACACCAGAGATGAGGCT |

## *2.7 Statistical analysis*

Details of specific statistical tests are included in figure legends. Here, different motor neuron inductions (2.1.7) are referred to as biological replicates, and in every instance direct comparison of 'biological replicates' indicates that the cultures were generated on different days. 'Technical replicates' refers to cultures that have been included in the same experiment that have been generated from the same motor neuron induction but maintained separately (different cultureware or different plate wells). Where figure legends include '*n*' this refers to the biological replicate and thus the number of separate motor neuron inductions, unless otherwise stated.

When assessing a single variable, a one-way ANOVA was applied with post-hoc comparisons. When *ANXA11mut* groups were compared to the control group, Dunnett's multiple comparisons test was used. When all groups/cell lines were compared to one other, Tukey's multiple comparisons test was used. In some instances in high-throughput analyses, data did not fit a Gaussian distribution due to differences occurring between motor neuron differentiation replicates, rather than the presence of separate cell populations within groups (Appendix Figure 9.1). If non-normal distribution of data within groups had been caused by subpopulations of cells lines within one group, for example, it would be necessary to include non-parametric statistical analysis. However, interrogation of raw data highlighted that variability was caused by specific replicates of motor neuron differentiation, which lead to a non-normal distribution of data arising from one specific experimental repeat, which

was relevant for all cell lines. Additionally, the low number of data points meant that the true nature of how data were distributed was difficult to assess. Therefore, it was deemed appropriate to include parametric analyses. In a few cases when data were not normally distributed, Kruskal-Wallis one-way analysis of variance with Dunn's multiple comparisons test was used. Specifically, this was applied to RNA velocity data and Annexin A11 and FUS intensity at ribopuromycylation hotspots. These datasets did not pass normality tests (not shown), and unlike in instances of high-throughput analyses it was deemed appropriate to use non-parametric testing to analyse these data.

When two variables were compared in high-throughput analyses (WT vs. *ANXA11mut* and cell culture paradigm) and stress granule analysis (WT vs. *ANXA11mut* and untreated vs. treated) a two-way ANOVA was applied. Although it is difficult to assess Gaussian distribution in small data sets, normality tests were included in two-way ANOVA, and in every instance at least one test indicated normal distribution of data (details not shown). When categorised data were statistically compared, chi-squared test was used, and details of this analysis are included in the relevant results chapter.

In some analyses and graphical representations, control cell lines are grouped and *ANXA11mut* lines are grouped by mutation, and standard error of the mean (SEM) is included to show the spread of data within each population/group. When data is presented for individual cell lines or biological replicates, standard deviation (SD) is included to highlight experimental variability. In some cases where one-way ANOVA was used as the statistical test the SD was not equal across groups as measured by normality of residuals tests (not shown), and so Brown-Forsythe ANOVA was applied, which does not assume equal SDs.

When appropriate, data were log-transformed using Microsoft Excel (function; =log10(value)) to meaningfully compare data measured in arbitrary units. This was relevant for western blot data and quantification of fluorescent intensity with immunocytochemistry and ensured that SEM or SD across biological repeats were not inappropriately inflated by the nature of quantification of arbitrary units, and made data more normally distributed for parametric testing. An alternative would be to normalise data from each cell line to one control line, representing the data for each

cell line as a fold change compared to one cell line. In this case the measure of data spread (SEM or SD) is lost for the normalisation cell line or group, and so log transformation was preferentially included to ensure spread of all data can be considered. It was not appropriate to normalise data in this way when assessing certain readouts, for example percentage. Additionally, in examples where the natural scale was particularly informative, for example nucleocytoplasmic ratio or spot count, data was not log transformed as it was more useful to interoperate the true value than to log transform data to increase the robustness of the statistical analyses.

# Chapter 3 Induced pluripotent stem cell models of *ANXA11* ALS

## *3.1 Overview*

The development of iPSC models for ALS research has enabled the exploration of pathology in human cells and has broadened the scope of *in vitro* mechanistic studies. ALS is vastly heterogeneous in clinical presentation and genetic aetiology, and iPSC models are lacking for the large majority of ALS-associated mutations. To address this, my colleagues and I created a biobank of LCL-derived iPSCs from ALS patients and controls. These 35 newly generated iPSCs constitute part of The UK MND Collections and will be available to the ALS research community. This biobank includes five lines derived from patients with non-synonymous SNPs in *ANXA11*. The N-terminal of *ANXA11* represents a mutation hotspot (Figure 1.4), and four iPSC lines were generated from patients with mutations in this region. iPSCs were derived from two patients carrying the G38R mutation, from the same family, and two patients from a separate family carried the D40G mutation. The fifth line was generated from a patient with the R235Q mutation, which resides in the Annexin core domain. Five age- and sex-matched control lines were selected, and together these novel *ANXA11* and control iPSC lines are the basis of this thesis.

*ANXA11* mutations are predominantly associated with an ALS phenotype, with a less well-characterised association with FTD (Müller et al., 2018; Nahm et al., 2020; Smith et al., 2017; Teyssou et al., 2020; Zhang et al., 2018). Therefore, exploration of *ANXA11* ALS pathology was conducted in iPSC-derived motor neurons. *ANXA11mut* and control motor neurons were assessed for motor neuron-specific markers, and optimisation of motor neuron-astrocyte co-culture was completed to improve culture longevity and to better recapitulate CNS organisation. This presents a novel system for investigation of *ANXA11*-associated ALS that will enable functional characterisation of *ANXA11* pathology and provide a platform for future therapeutic development.

## *3.2 Methods*

### *3.2.1 Derivation of iPSCs from lymphoblastoid cell lines and cell culture*

iPSCs were derived from LCLs (2.1.4; 2.1.5), maintained, and cryopreserved (2.1.1). Characterised iPSCs were differentiated into motor neurons by exposure to small molecules and growth factors (2.1.7). In some instances, iPSC-derived motor neurons were maintained in co-culture with iPSC-derived astrocytes (2.1.9; 2.1.10). Astrocytes that were used in motor neuron-astrocyte co-culture were pre-treated with mitomycin C to prevent cell division and overpopulation when in culture with neurons (2.1.9).

### *3.2.2 Cellular characterisation*

iPSCs, motor neurons, and astrocytes were subject to characterisation to ensure that the cellular models utilised in experiments were faithfully representing target cell types. Immunocytochemistry with cell lineage-specific antibodies was used in the characterisation of all cell types (2.4), and cells were imaged with the Opera Phenix® High-Content Imaging System and quantified with Harmony® (2.4.2), or with epifluorescence microscopy (2.4.3). An example of expression of motor neuron-specific genes in iPSC-derived motor neurons was demonstrated by RT-PCR (2.6). iPSCs were subject to more vigorous characterisation which included evidence of pluripotency in the context of the embryoid body assay (2.2.2) and assessment of genomic characteristics including sequencing *ANXA11* mutation regions (2.2.5), G-band karyotyping (2.2.3), and STR profiling to ensure newly derived iPSCs were matched to parent cell lines (2.2.4). iPSCs were serially passaged to induce the loss of EBV genes used in the derivation of parent LCL lines, which was measured by PCR (2.2.6). Additionally, iPSCs were subject to mycoplasma screening as culture quality control (2.2.7).

## *3.3 Results*

### *3.3.1 Summary of iPSC lines*

iPSC lines produced for this project are included in Table 3.1, alongside information about the age and sex of patients, the reprogramming method used for iPSC derivation, and the passage at which they became EBV negative. Control lines were selected based on age and sex proximity to *ANXA11* ALS patient lines.

***Table 3.1 Summary of iPSC lines***

| Cell line | ALS Status | Sex | Age at collection | Reprogramming method | Passage EBV negative |
|---|---|---|---|---|---|
| **Control 1** | - | Female | 71 | Episomal plasmids | P13 |
| **Control 2** | - | Female | 84 | Sendai virus | P22 |
| **Control 3** | - | Male | 71 | Episomal plasmids | P31 |
| **Control 4** | - | Male | 61 | Episomal plasmids | P30 |
| **Control 5** | - | Female | 69 | Episomal plasmids | P27 |
| ***ANXA11* G38R 1** | fALS | Male | 63 | Episomal plasmids | P15 |
| ***ANXA11* G38R 2** | fALS | Male | 51 | Sendai virus | P22 |
| ***ANXA11* D40G 1** | fALS | Female | 75 | Episomal plasmids | P17 |
| ***ANXA11* D40G 2** | fALS | Female | 76 | Episomal plasmids | P23 |
| ***ANXA11* R235Q** | sALS | Female | 66 | Episomal plasmids | P26 |

### *3.3.2 Newly derived iPSCs show typical stem cell morphology and evidence of pluripotency*

Newly derived iPSC lines showed typical stem cell morphology with small round cells with clear nuclei, grouped together in colonies (Appendix Figure 9.2), and iPSCs were positive for the pluripotency marker Oct-3/4 (Figure 3.1; Figure 3.2). Cells positive for $\beta$3-tubulin (ectoderm), $\alpha$-smooth muscle actin (mesoderm), and $\alpha$-fetoprotein (endoderm) were detected in embryoid bodies from all cell lines (Figure 3.3; Figure 3.4). Collectively these data show that the newly derived control and *ANXA11* patient iPSCs are pluripotent and as such can appropriately be used for further investigation.

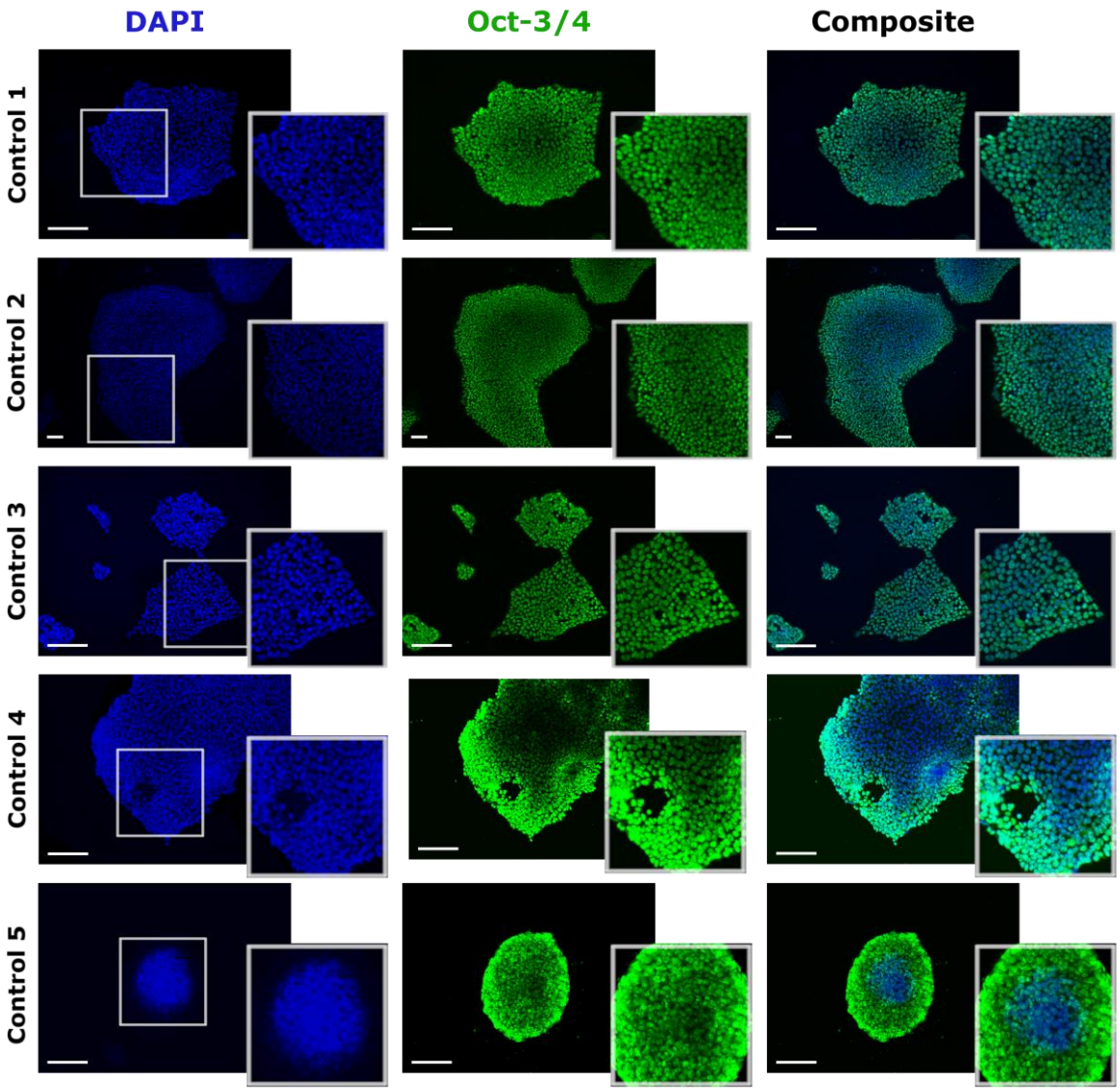


***Figure 3.1 iPSCs derived from controls are positive for Oct-3/4***

iPSCs were subject to immunocytochemistry with an antibody detecting pluripotency marker Oct-3/4 (green), and nuclei are stained with DAPI (blue). Scale bars represent 100µm.

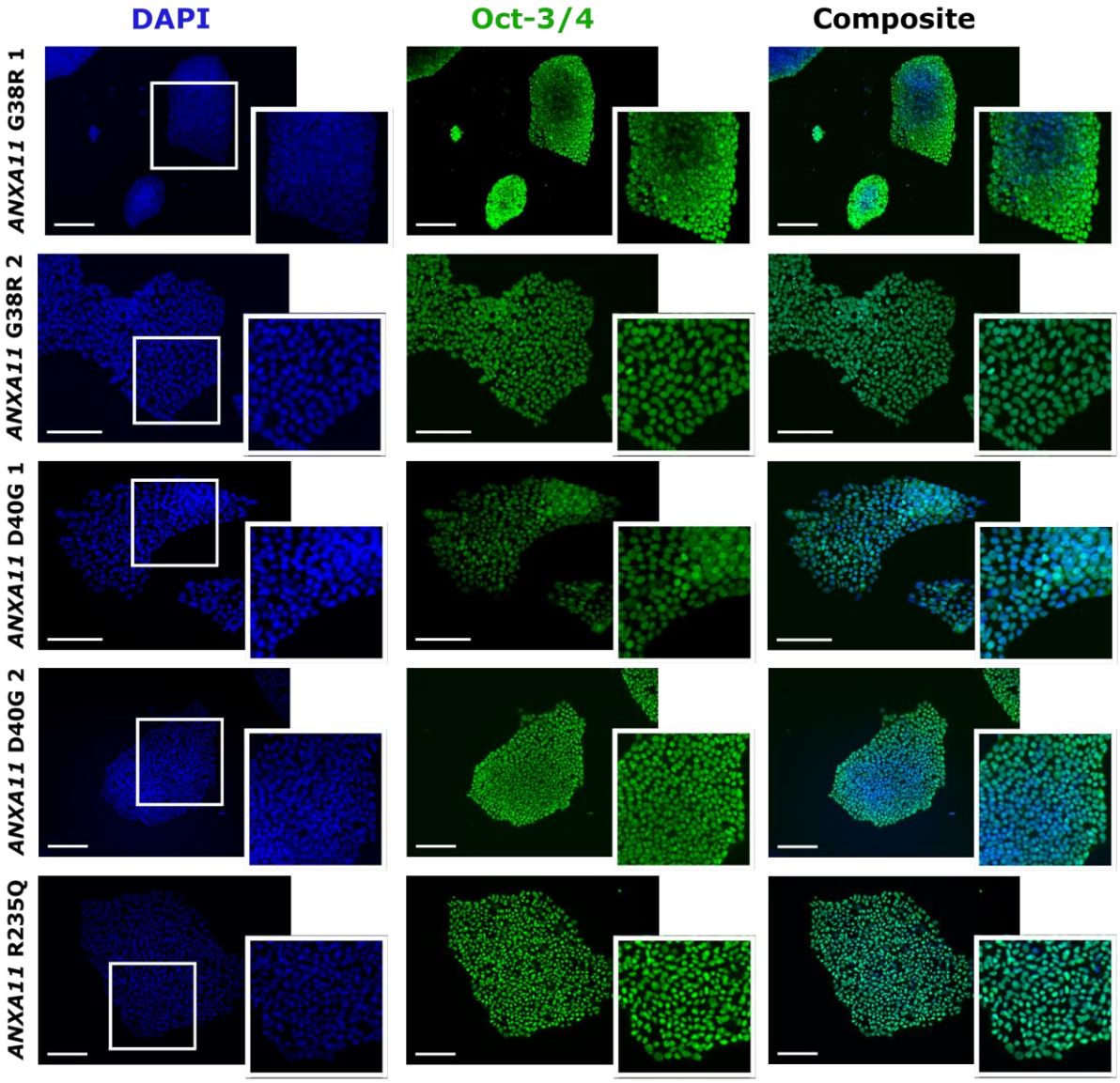


***Figure 3.2 iPSCs derived from ANXA11 ALS patients are positive for Oct3/4***

iPSCs were subject to immunocytochemistry with an antibody detecting pluripotency marker Oct-3/4 (green) and nuclei are stained with DAPI (blue). Scale bars represent 100µm.

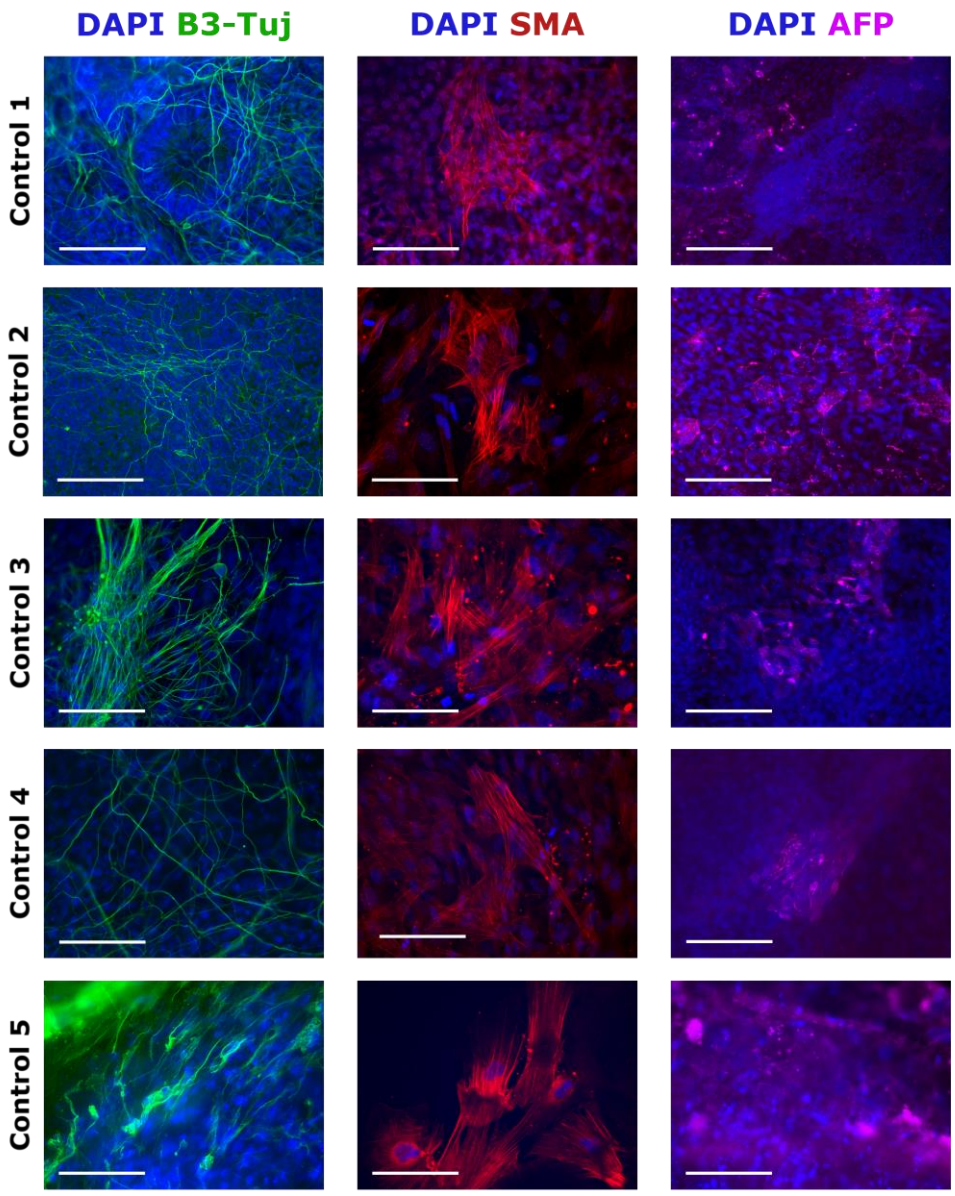


***Figure 3.3 Control iPSCs differentiate into cells from the three germ layer lineages***

EBs were generated from control iPSCs, seeded onto coverslips, and allowed to spontaneously differentiate into various cell-types. EBs were then fixed and probed for markers of cells originating from the three germ layers of the blastocyst. $\beta$3-tubulin was used to identify neuronal cells originating from the ectoderm (B3-Tuj, green), $\alpha$-smooth muscle actin was used to identify mesodermal cells (SMA, red), and $\alpha$-fetoprotein was used as a marker of endodermal cells (AFP, magenta). Scale bars represent 100µm.

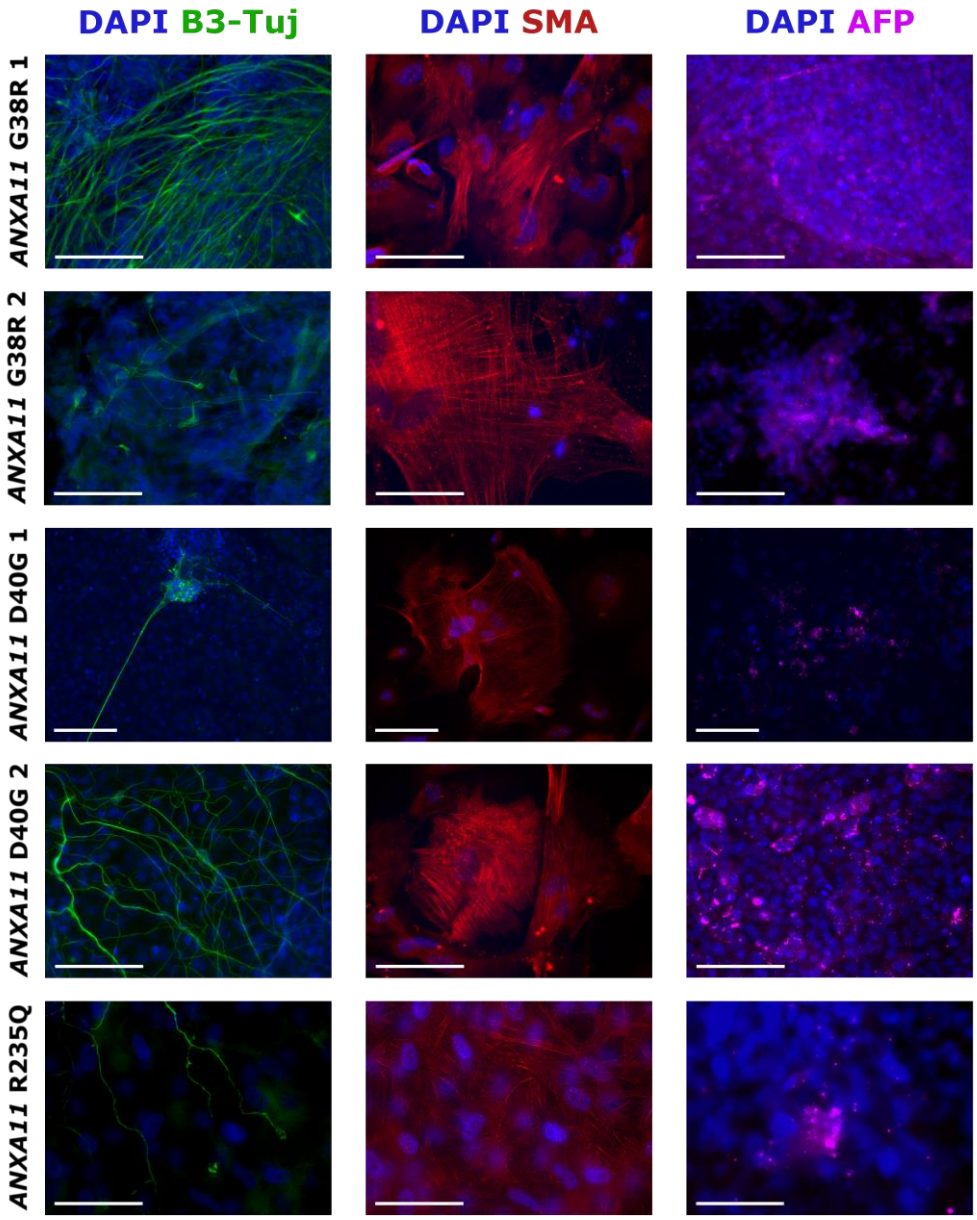


***Figure 3.4 ANXA11mut iPSCs differentiate into cells from the three germ layer lineages***

EBs were generated from *ANXA11* ALS iPSCs, seeded onto coverslips, and allowed to spontaneously differentiate into various cell-types. EBs were then fixed and probed for markers of cells originating from the three germ layers of the blastocyst. $\beta$3-tubulin was used to identify neuronal cells originating from the ectoderm (B3-Tuj, green), $\alpha$-smooth muscle actin was used to identify mesodermal cells (SMA, red), and $\alpha$-fetoprotein was used as a marker of endodermal cells (AFP, magenta). Scale bars represent 100µm.

### *3.3.3 Genomic characterisation of iPSC lines*

iPSCs were subject to G-band karyotyping to confirm that no gross chromosomal abnormalities had occurred in the reprogramming process. In all instances the goal was to analyse the metaphases of 20 cells, which is generally considered sufficient to rule out mosaicism and/or the presence of an abnormal karyotype. In many instances fewer than 20 metaphases were characterised due to technical difficulties encountered by the laboratory completing the karyotype analysis. The number of normal metaphases analysed for each cell line is listed underneath each representative karyotype image, alongside the total number of analysed metaphases (number of normal metaphases/total number of analysed metaphases) (Figure 3.5). Occasionally, the number of normal metaphases reported is fewer than the total number of metaphases analysed due to some metaphases having lost one or more chromosomes. It was reported by the testing laboratory that this was most likely due to preparation artefact as in these instances chromosomal changes were inconsistent, and each was only found in one cell. Most cell lines showed a normal karyotype, however, the patient line *ANXA11* D40G 2 showed an abnormal female karyotype with an apparently balanced translocation between the long arm of chromosome 4q23 and the long arm of a chromosome 22q11.2. This was seen in 15 cells and no other consistent metaphases were seen in the culture, indicating that although the cell line displayed an abnormal karyotype this was not mosaic in nature.

Genomic DNA from iPSC lines derived from *ANXA11* ALS patients was sequenced at the relevant mutant region, confirming that non-synonymous SNPs were present (Figure 3.6). STR profiling of parent LCLs and daughter iPSCs confirmed cell lineage, as each LCL and iPSC pair shared the same number of repeats at each STR loci, of which there were 16 (STR results not shown in line with patient data protection).

LCLs are immortalised with EBV to cause continuous cell division, enabling maintenance of cell stocks by reducing senescence, however the presence of viral DNA in iPSC lines is undesirable. iPSCs were serially passaged and routinely subject to PCR with genomic DNA extracts and primers targeting EBV

genes until the target genes were no longer detectable (3.7). In some instances, EBV genes were not lost from iPSC clones by passage 35, in these cases a new iPSC clone from the same cell line was selected for serial passaging. iPSC clones that did not lose EBV genes accounted for approximately 25% of newly derived clones. Once loss of EBV genes was confirmed, iPSCs were banked and subject to remaining characterisation experiments.

**Control 1**


***ANXA11* G38R 1**

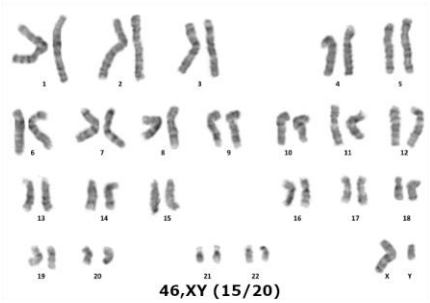


**Control 2**

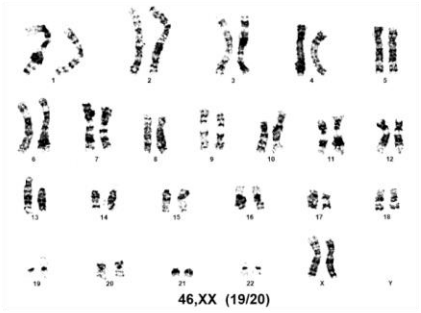


***ANXA11* G38R 2**

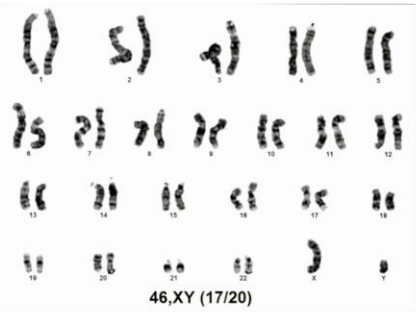


**Control 3**

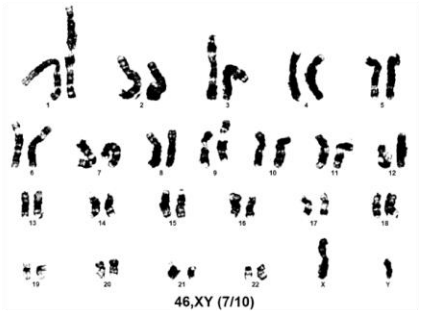


***ANXA11 D40G* 1**

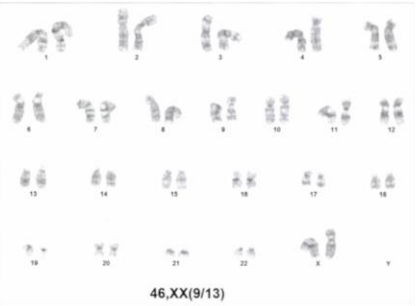


**Control 4**

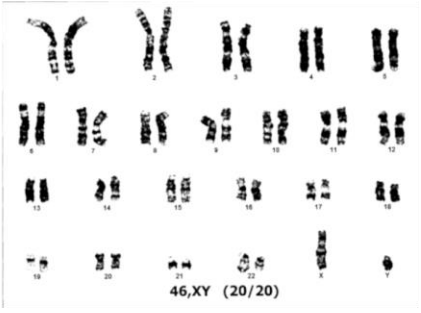


***ANXA11 D40G 2***


**Control 5**

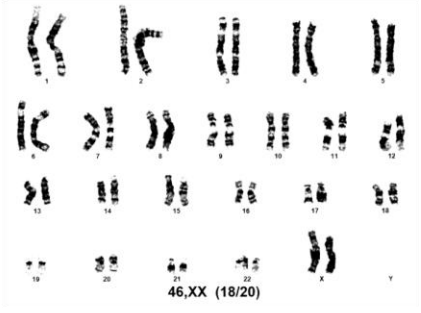


***ANXA11* R235Q**

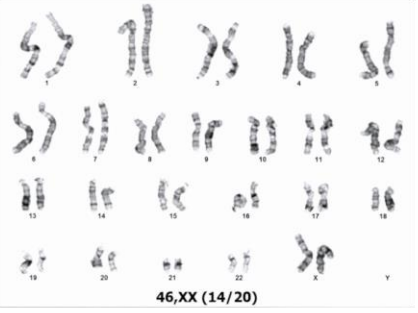

***Figure 3.5 G-band karyotyping of newly derived iPSCs***

iPSCs were subject to G-band karyotyping as a measure of genomic stability. All iPSC lines showed a normal karyotype, with the exception of *ANXA11* D40G 2 which showed a balanced translocation involving chromosome 4q23 and chromosome 22q11.2.

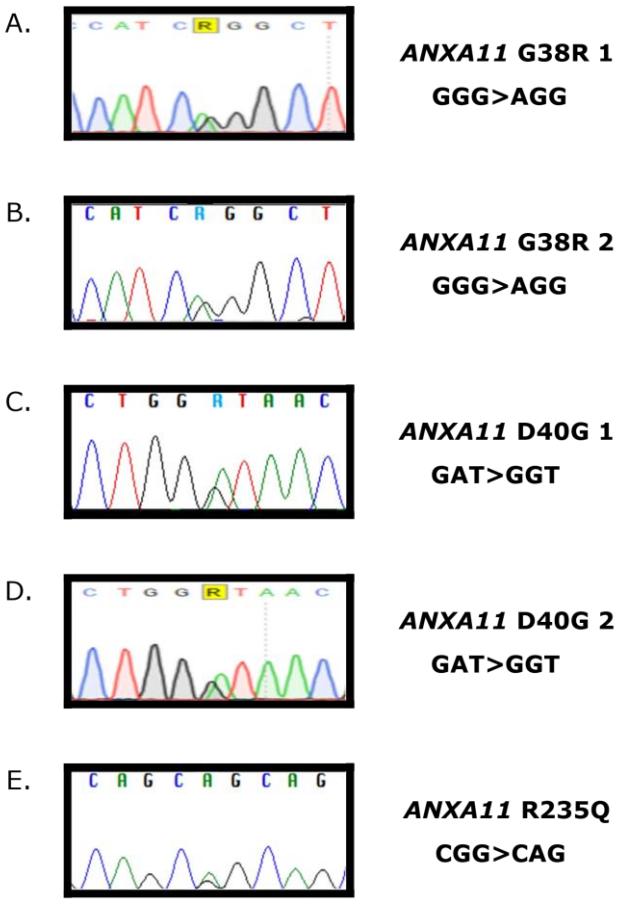


***Figure 3.6 Confirmation of ANXA11 point mutations with Sanger sequencing***

Electropherograms from *ANXA11* ALS patient-derived iPSCs depicting (A) *ANXA11* G38R 1, (B) *ANXA11* G38R 2, (C) *ANXA11* D40G 1, (D) *ANXA11* D40G 2, and (E) *ANXA11* R235Q. Point mutations are shown at the midpoint of each chromatogram.

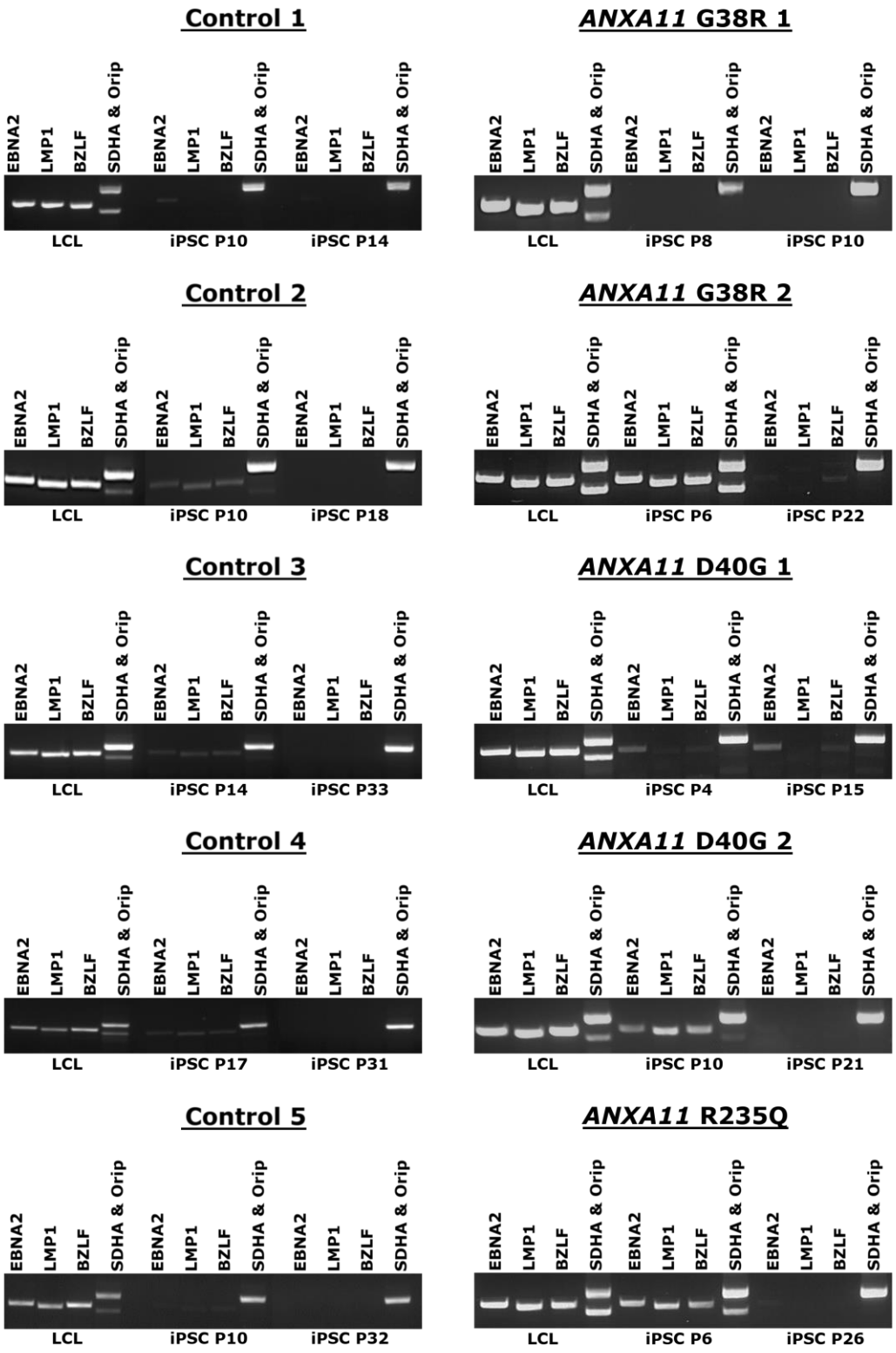


***Figure 3.7 Epstein Barr virus genes are lost from iPSCs after multiple passages***

LCLs are immortalised for extended culture by transduction with EBV genes including *EBNA2*, *LMP1*, *BZLF*, and *Orip*, which are observed in genomic PCR products from LCLs. The house keeping gene *SDHA* was probed for in multiplex PCR with *Orip*, confirming the presence of DNA in each sample. iPSCs were serially passaged until EBV genes were absent from genomic DNA extractions. Some

residual EBV gene PCR products are observed in iPSC DNA, and the passage number that each iPSC clone was banked at, after losing EBV genes, is included in Table 3.1.

### *3.3.4 Control and ANXA11mut iPSC lines differentiate into motor neurons*

Differentiation of iPSCs into motor neurons yielded pure populations of $\beta$3-Tubulin positive neurons with typical neuronal morphology as indicated by a small soma and long elongated neurites (Figure 3.8; Figure 3.9). On day 17 of motor neuron differentiation, 70-80 % of nuclei were positive for the motor neuron-specific transcription factor Islet 1 (Figure 3.10). The number of Islet 1 positive nuclei was not stastistcally different between *ANXA11mut* lines and the control group, however *ANXA11mut* lines showed a slight trend towards reduced Islet 1 postive nuclei (control, 79%; *ANXA11* G38R, 72%; *ANXA11* D40G, 70%; *ANXA11* R235Q, 74%) (Figure 3.10). iPSC-derived motor neurons maintained in co-culture with astrocytes until day 42 of differentiation were positive for the cholinergic marker ChAT (Figure 3.11).

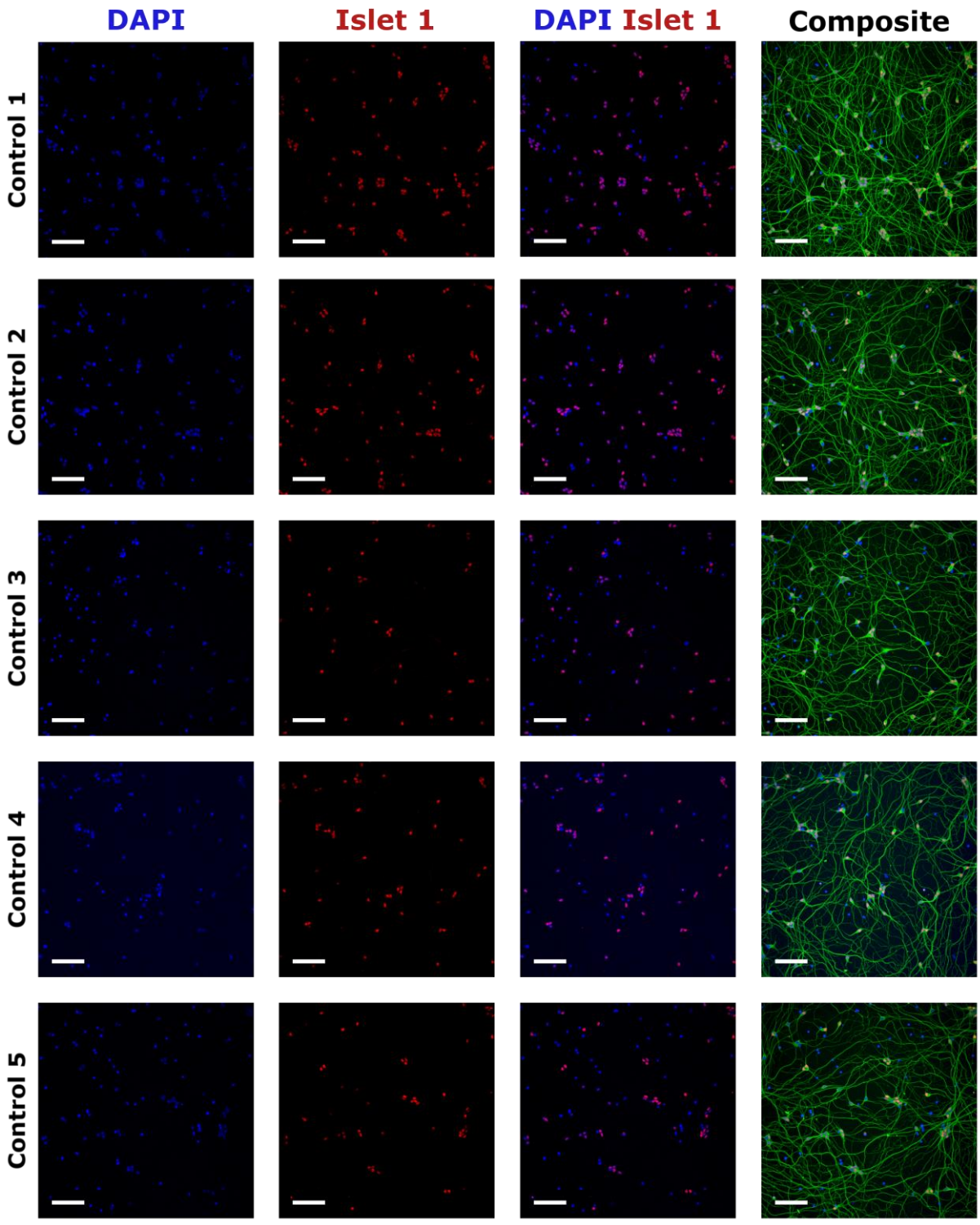


***Figure 3.8 Islet 1 positive motor neurons differentiate from control iPSCs***

Control iPSCs were differentiated into motor neurons, fixed on day 17 of differentiation, and imaged with the Opera Phenix® High-Content Screening System. Cells were immunolabelled for $\beta$3-Tubulin (green) to visualise all neurons, and the motor neuron marker Islet 1 (red). Cells were co-stained with DAPI to highlight nuclei, small bright DAPI spots with no visible cytoplasm are cell debris. Scale bars represent 100µm.

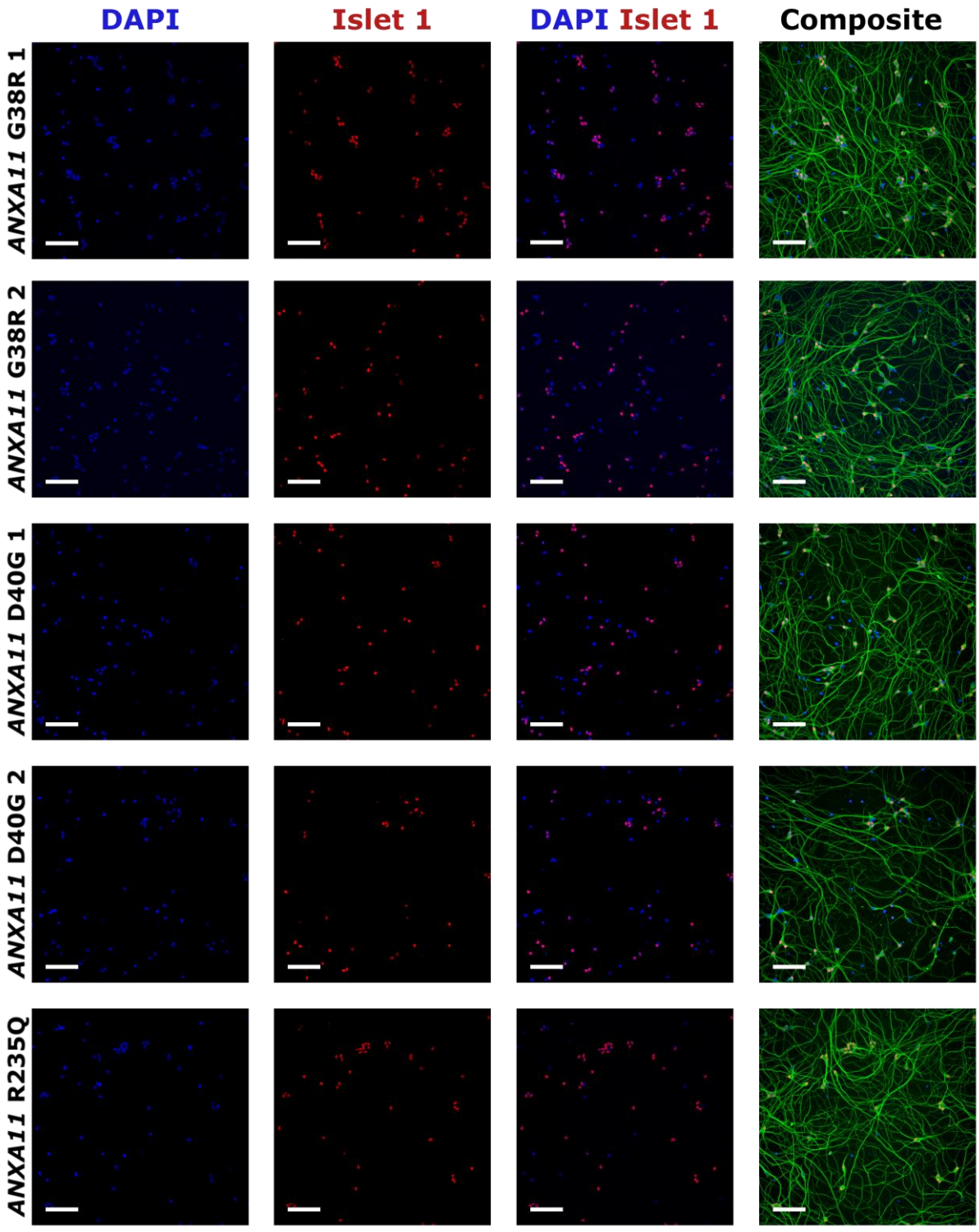


***Figure 3.9 Islet 1 positive motor neurons differentiate from ANXA11 ALS iPSCs***

*ANXA11* ALS patient-derived iPSCs were differentiated into motor neurons, fixed on day 17 of differentiation, and imaged with the Opera Phenix® High-Content Screening System. Cells were immunolabelled for $\beta$3-Tubulin (green) to visualise all neurons, and the motor neuron marker Islet 1 (red). Cells were co-stained with DAPI to highlight nuclei, small bright DAPI spots with no visible cytoplasm are cell debris. Scale bars represent 100µm.

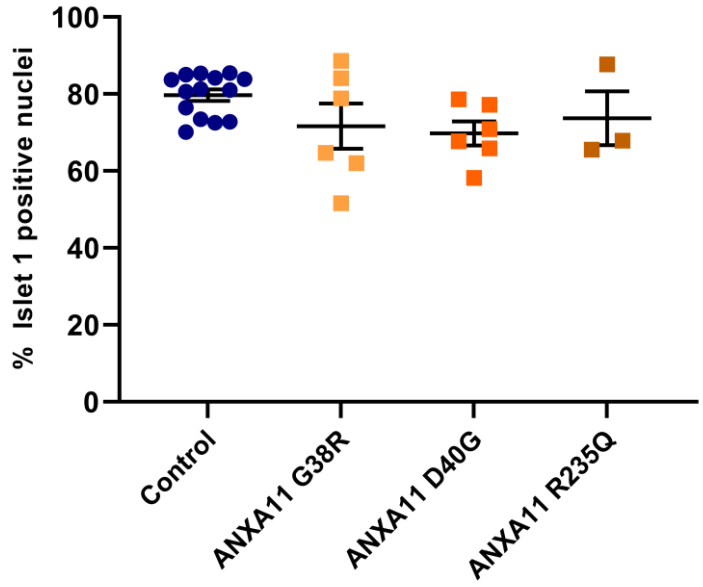


***Figure 3.10 Percentage of Islet 1 positive nuclei in iPSC derived motor neurons***

Quantification of motor neurons as shown in Figures 3.8 and 3.9. The average percentage of motor neurons as defined by Islet 1 positive nuclei was 79% for control lines, 72% for *ANXA11* G38R, 70% for *ANXA11* D40G, and 74% for *ANXA11* R235Q. Data are represented as mean ± SEM, number of motor neuron inductions = 3. Each data point represents the percentage of Islet 1 positive nuclei in one cell line in one motor neuron induction, with each induction comprised of three technical replicates. Control lines are pooled into one control group and *ANXA11* ALS patient lines are grouped by mutation. Statistical analysis: Brown-Forsythe one-way ANOVA with Dunnett's multiple comparisons test ($p > 0.05$).

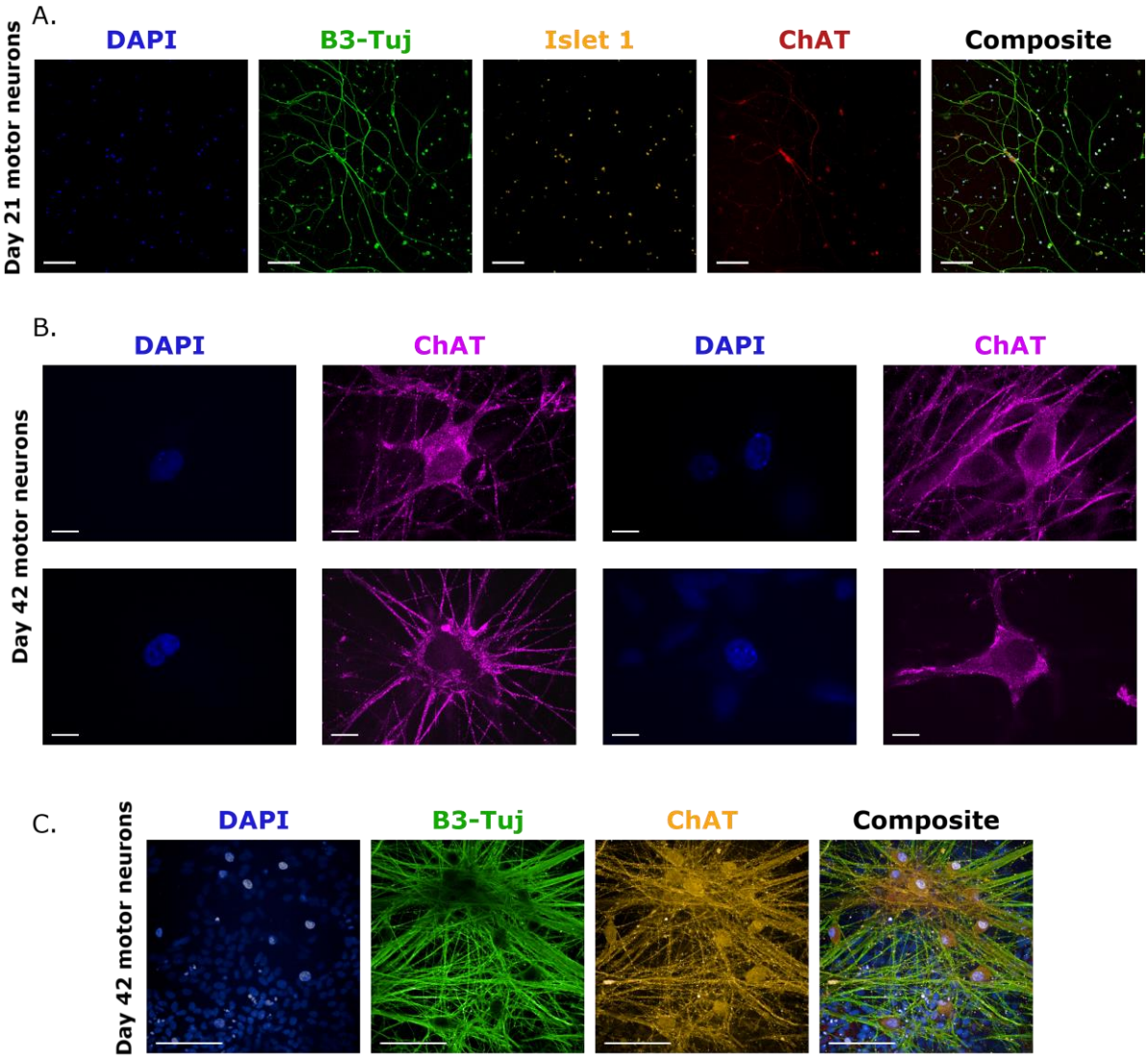


***Figure 3.11 iPSC derived motor neurons express Islet 1 and ChAT***

(A) Representative images of motor neurons fixed on day 21 of differentiation, positive for the neuronal marker $\beta$3-Tubulin (B3-Tuj, green), and the motor neuron specific protein Islet 1 (orange) and ChAT (red) imaged with the Opera Phenix™ High Content Imaging System. (B) Motor neurons maintained in co-culture with astrocytes were fixed on day 42 of differentiation and are positive for ChAT (magenta) when imaged with super resolution microscopy, and (C) in high content imaging (orange), co-labelled with $\beta$3-Tubulin (B3-Tuj, green). Scale bars represent 100µm (A, C) and 10 µm (B).

### *3.3.5 Control and ANXA11mut iPSCs differentiate into astrocytes*

iPSCs derived from control and *ANXA11* ALS patients were differentiated into astrocytes and fixed at two time-points: Astrocytes on day 35 of differentiation were interrogated, representing the time

point at which neurons were added into co-culture with astrocytes. Astrocytes at day ~50 of differentiation were analysed to measure any age-associated features of astrocytes maintained in culture. Astrocyte lineage was confirmed by typical astrocyte morphology, and immunocytochemistry detecting ALDH1L1 confirmed the expression of astrocyte-specific protein (Beyer et al., 2021; Yoon et al., 2017). Immunocytochemistry detecting S100A6 was also included as it is a binding partner of Annexin A11 and has been shown to be upregulated in astrocytes from sporadic and *SOD1* ALS patients and rodents (Hoyaux et al., 2000, 2002). Both young (Figure 3.12; Figure 3.13) and aged (Figure 3.14; Figure 3.15) astrocytes displayed typical astrocyte morphology, with large nuclei surrounded by a large flat cytoplasm, often with long-reaching protrusions. The mean ALDH1L1 fluorescent intensity was consistent across mutation groups at both levels of culture maturity (Figure 3.16.A; Figure 3.16.B), as was the amount of S100A6 (Figure 3.16.E; Figure 3.16.F).

As a measure of cellular localisation of astrocytic proteins, the nucleocytoplasmic ratio of ALDH1L1 and S100A6 was calculated, and remained consistent across cell lines, with a slight trend towards nuclear localisation of ALDH1L1 and S100A6 in young *ANXA11* R235Q astrocytes, which was not statistically significant. The localisation of ALDH1L1 and S100A6 became slightly more nuclear in day ~50 astrocytes compared to day 35 astrocytes, across all *ANXA11* mutation status groups (Figure 3.16). As no pan-cellular marker was included in immunocytochemistry due to antibody availability and time restraints, the percentage of astrocytes was not directly measured. Additional examples of ALDH1L1 positive astrocytes are included in Appendix Figure 9.3 to demonstrate ALDH1L1 cellular localisation at an increased magnification. These data indicate that successful derivation of astrocytes was achieved, suggesting suitability for co-culture with neurons. Representative images indicate an increase in the number of astrocytes in cultures on day ~50 compared to day 35 (Figure 3.12; Figure 3.13; Figure 3.14; Figure 3.15). Although astrocytes were pre-treated with mitomycin C to inhibit cell division, the potential increase in cell number may indicate that some cell division still occurs, albeit at a rate that does not prohibit analysis of neurons, as indicated in Figure 3.11.B and Figure 3.11.C.

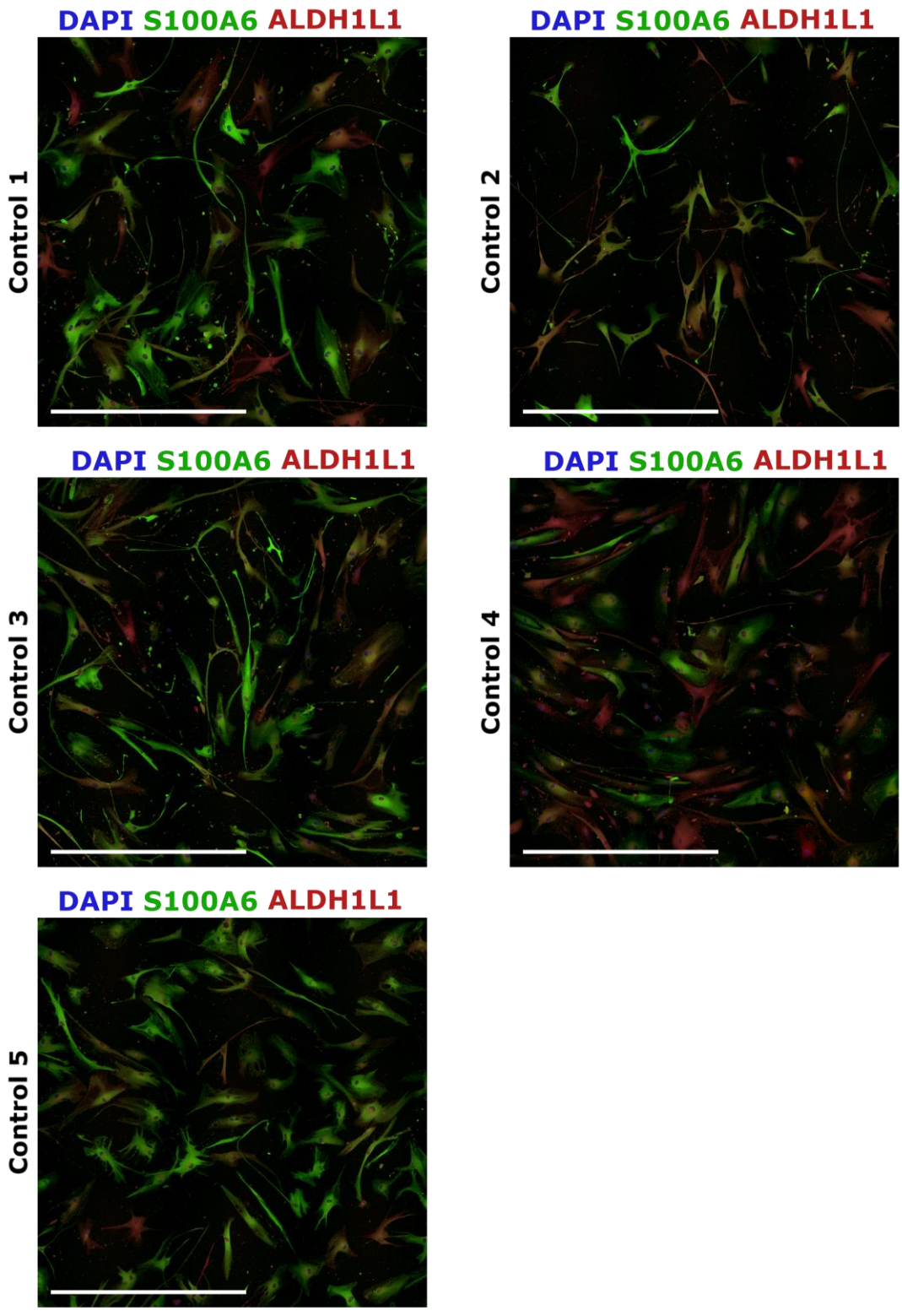


***Figure 3.12 Immature astrocytes derived from control iPSCs***

Astrocytes derived from control iPSCs were fixed on day 35 of differentiation and probed for the astrocyte protein ALDH1L1 (red) and the calcium-binding protein S100A6 (green). Astrocytes were imaged with the Opera Phenix® High-Content Screening System. Scale bars represent 1mm.

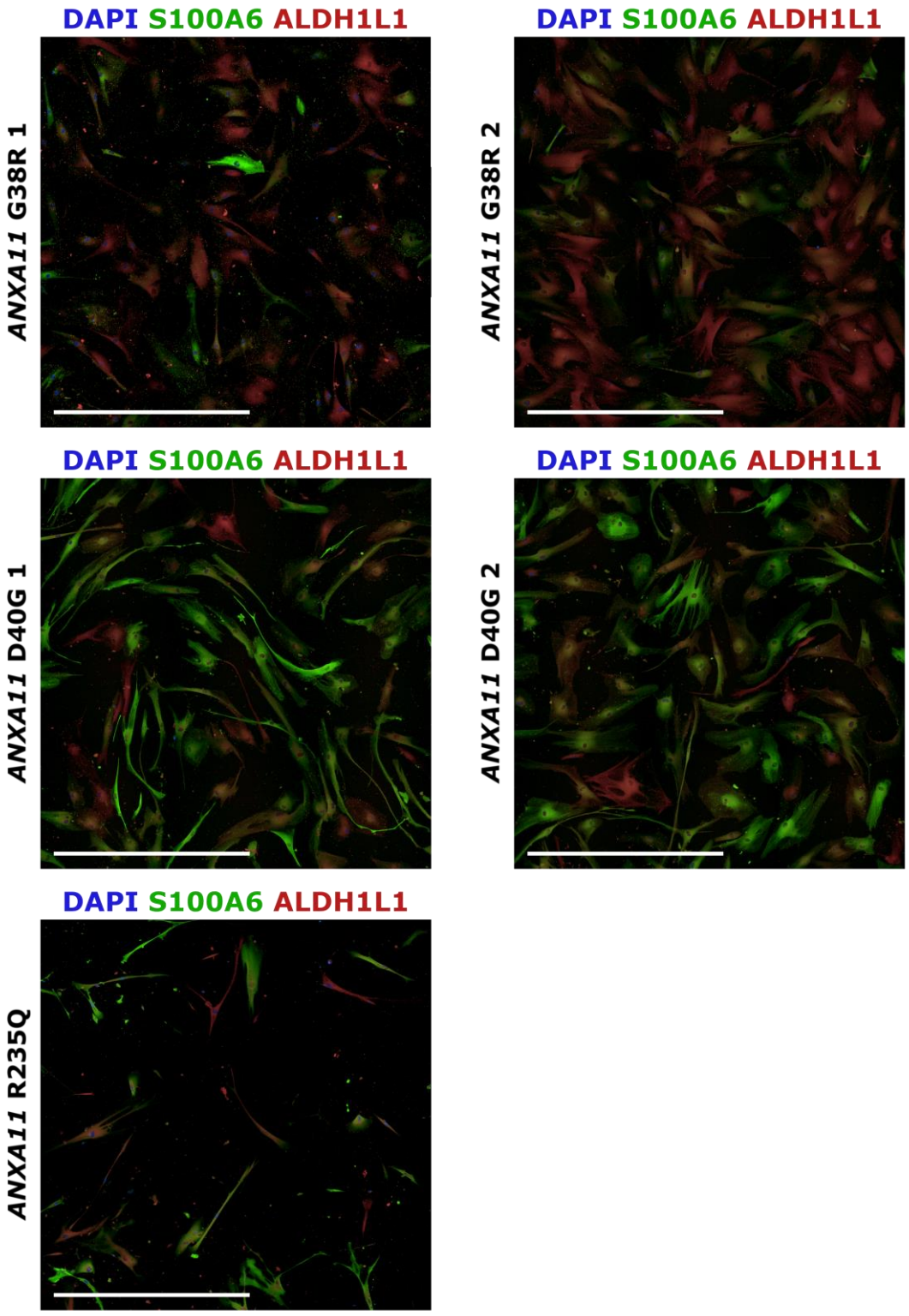


***Figure 3.13 Immature astrocytes derived from ANXA11mut iPSCs***

Astrocytes derived from *ANXA11* ALS patient iPSCs were fixed on day 35 of differentiation and probed for the astrocyte protein ALDH1L1 (red) and the calcium-binding protein S100A6 (green). Astrocytes were imaged with the Opera Phenix® High-Content Screening System. Scale bars represent 1mm.

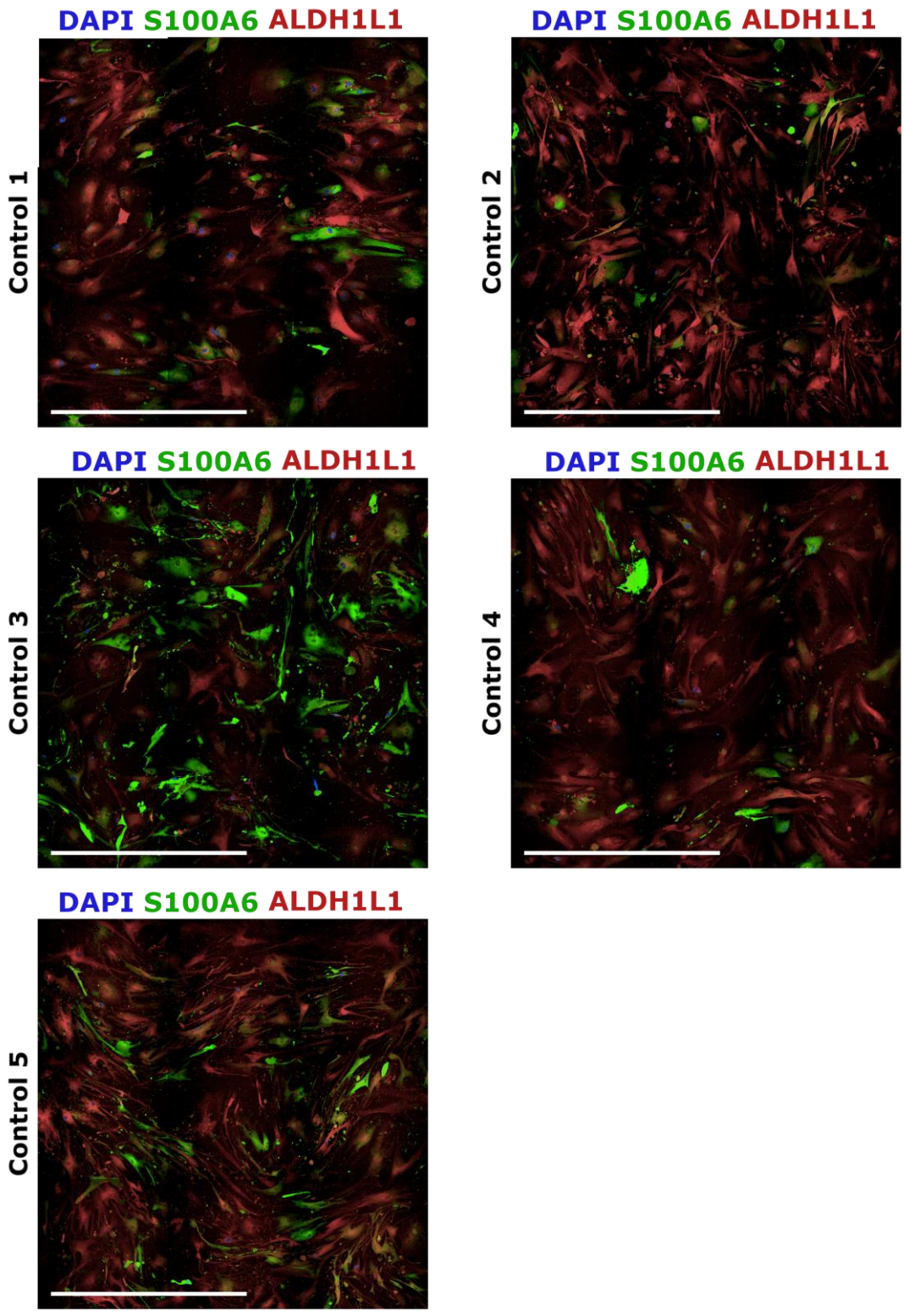


***Figure 3.14 Aged astrocytes derived from control iPSCs***

Astrocytes derived from control iPSCs were fixed on day ~50 of differentiation and probed for the astrocyte protein ALDH1L1 (red) and the calcium-binding protein S100A6 (green). Astrocytes were imaged with the Opera Phenix® High-Content Screening System. Scale bars represent 1mm.

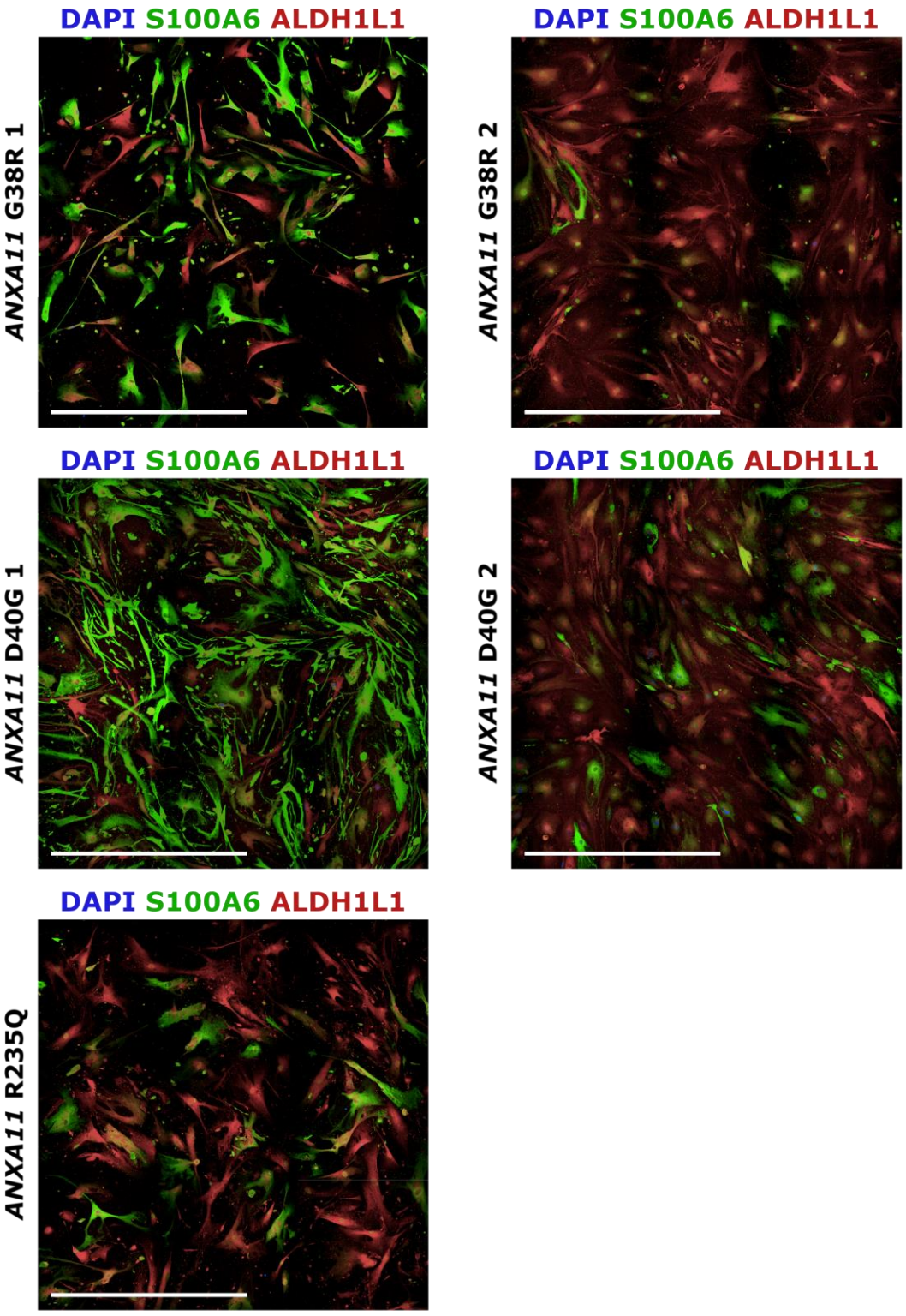


***Figure 3.15 Aged astrocytes derived from ANXA11mut iPSCs***

Astrocytes derived from *ANXA11* ALS patient iPSCs were fixed on day ~50 of differentiation and probed for the astrocyte specific marker ALDH1L1 (red) and the calcium-binding protein S100A6 (green). Astrocytes were imaged with the Opera Phenix® High-Content Screening System. Scale bars represent 1mm.

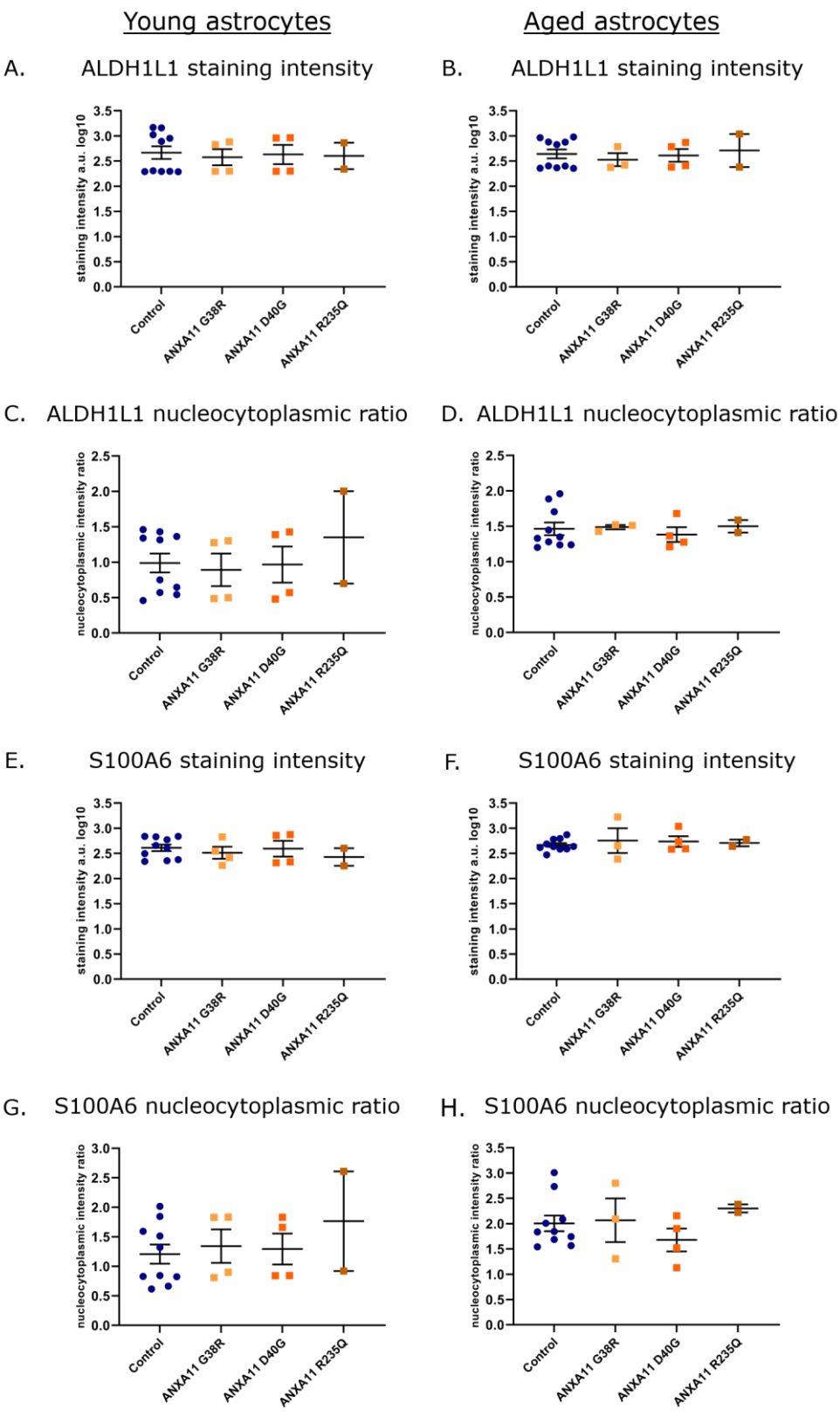


***Figure 3.16 Expression of astrocytic markers in iPSC-derived astrocytes***

Quantification of images represented in Figure 3.12, Figure 3.13, Figure 3.14, and Figure 3.15. Images were quantified in Harmony®. Young astrocytes were analysed on day 35 of differentiation, and aged astrocytes were analysed at day ~50. Data are represented as mean ± SEM, *n* = 2 for each time point.

Each data point represents one cell line in one experimental replicate, where astrocytes were cryorecovered and plated in separate instances, with each replicate comprised of three technical replicates. Control lines are grouped and *ANXA11* ALS patient lines are grouped by mutation. Statistical analyses: (A-B, D-H) Ordinary one-way ANOVA, (C) Brown-Forsythe one-way ANOVA, both with Dunnett's multiple comparisons test ($p > 0.05$).

### *3.3.6 Motor neuron-astrocyte co-culture*

Optimisation of motor neuron-astrocyte co-culture included analysis of direct co-culture of motor neurons on astrocytes, resting motor neurons attached to coverslips on top of cultured astrocytes such that media was shared between the two cell types, and maintaining neurons in culture with well-inserts containing astrocytes, again so that media was conditioned by astrocytes. A schematic of these co-culture designs is included in Figure 3.17. In both instances where astrocytic support was relying on conditioned media (Figure 3.17.B and Figure 3.17.C), fragmentation of neurites occurred and detachment of neurons from glass coverslips was observed in long-term culture, indicating that trophic support alone is not sufficient to extend motor neuron longevity (data not shown). In the direct co-culture condition (Figure 3.17.A), neuronal survival was markedly increased, and neurons remained attached to astrocytes, which attached more-readily to glass coverslips than their neuronal counterparts. An example of direct motor neuron-astrocyte co-culture maintained until day 42 of motor neuron differentiation is included in Figure 3.18, with GFAP positive astrocytes growing alongside motor neurons immunolabelled with the neuronal marker $\beta$3-Tubulin. When reporting data collected from motor neuron-astrocyte co-culture throughout this thesis, reference is made to the neuronal age of cultures.

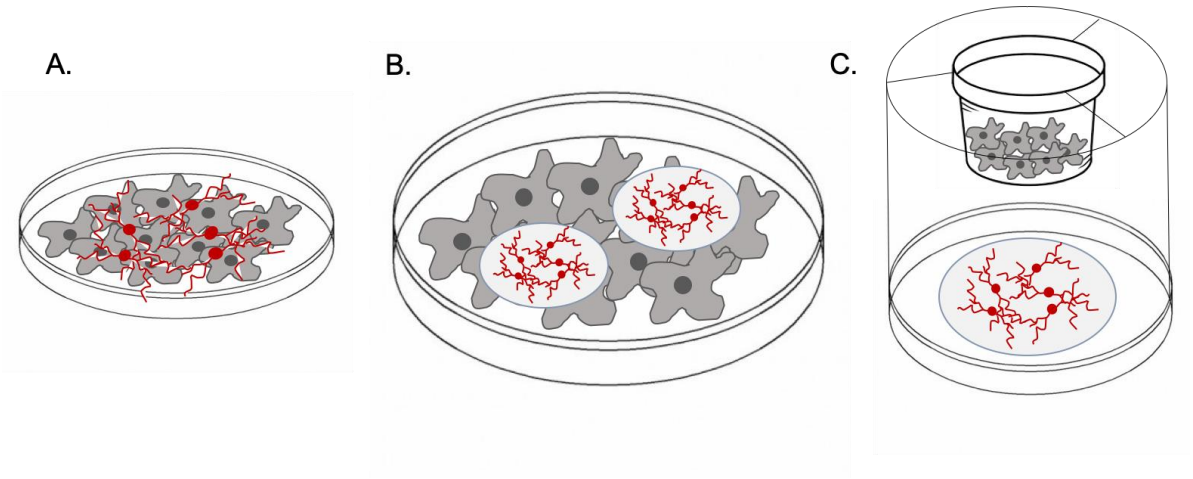


***Figure 3.17 Methods for motor neuron-astrocyte co-culture***

(A) Direct co-culture of motor neurons with astrocytes included direct attachment of neurons onto plated astrocytes; used throughout this thesis. (B) "Resting co-culture" was attempted, whereby motor neurons were plated on coverslips, which were then placed on astrocytes such that the different cell types were sharing the same media. (C) Conditioned media was applied to motor neurons by plating astrocytes in a well insert that was in contact with the neuronal medium. The most effective method of co-culture for increasing the longevity of motor neurons here was (A), indicating that direct contact with astrocytes was important for neuronal survival, as opposed to metabolic support from conditioned media as seen in (B) and (C).

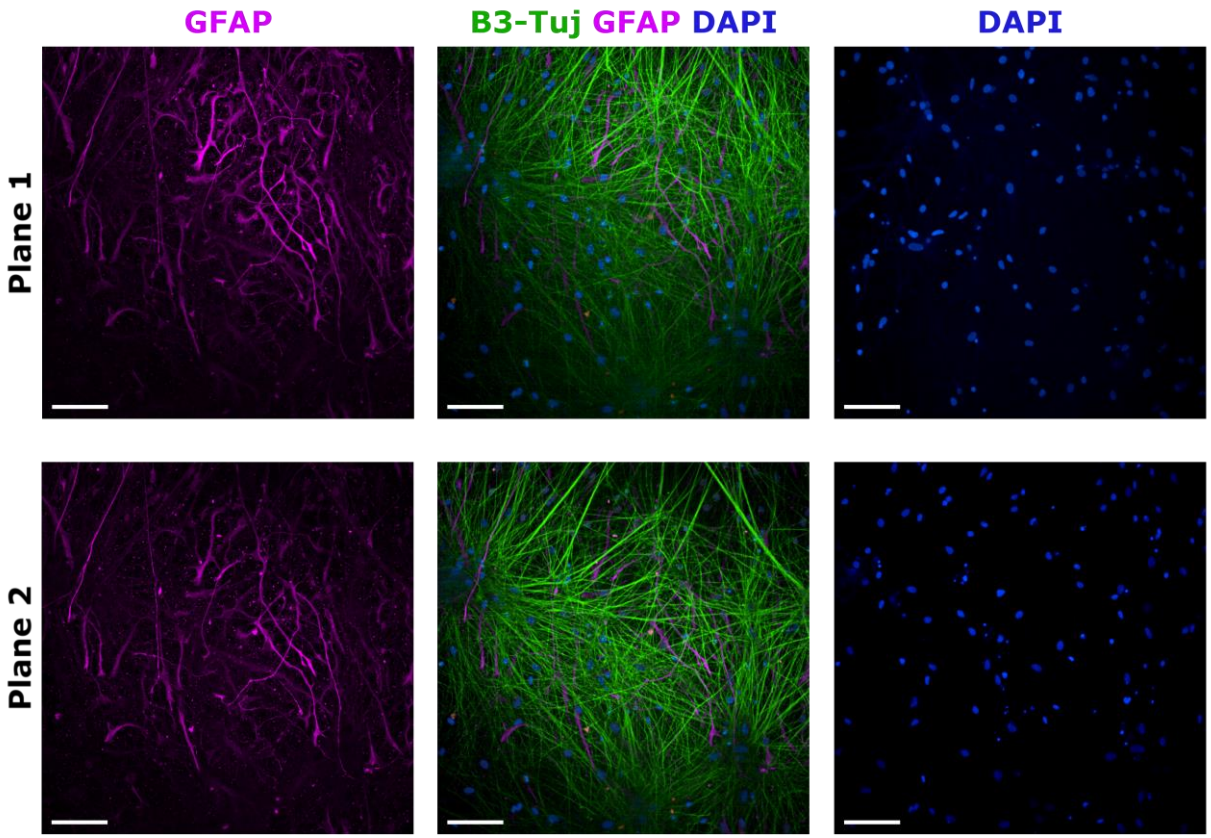


***Figure 3.18 Motor neuron-astrocyte co-culture***

Direct co-culture of motor neurons with astrocytes was established and carried forward in this project. Cultures in this example were fixed on day 42 of motor neuron differentiation, and subject to immunocytochemistry with antibodies targeting the astrocyte protein GFAP (magenta) and the neuronal marker $\beta$3-Tubulin (B3-Tuj, green), and were co-stained with DAPI (blue). Cultures were imaged with the Opera Phenix® High-Content Screening System. The top and bottom panel represent two *z*-planes of the same *XY* image. Scale bars represent 100µm.

## *3.4 Discussion*

ALS is extremely heterogeneous, with many ALS associated SNPs accounting for a small percentage of the ALS patient population. Experimental models of many of these genes are lacking, and investigation of novel mutations can shed new light on disease aetiology. Hence, iPSC lines were derived from patient cells harbouring ALS causing mutations in *ANXA11*, alongside controls. iPSCs were characterised to ensure pluripotency and genomic stability, and differentiated into motor neurons and astrocytes, providing a novel platform for investigation into *ANXA11* associated ALS.

### *3.4.1 Methods for iPSC production*

Introduction of reprogramming factors into LCLs to cause iPSC reprogramming was completed using either SeV or electroporation of episomal plasmids. In the initial stages of this project, commercially available CytoTune 2.0 Sendai virus was used to reprogram LCLs into iPSCs. This proved to have low efficiency, and so episomal plasmid driven reprogramming was used in later instances, resulting in higher success rates in reprogramming experiments and generation of increased numbers of individual iPSC clones in each attempt (data not shown). Loss of residual reprogramming material was not tested for, however both SeV and episomal plasmids are non-integrating, hence the resulting iPSC lines were deemed comparable in downstream experiments. The method used for each cell line included in this project is included in Table 3.1.

### *3.4.2 iPSC characterisation*

The overall aim of iPSC characterisation is to confirm that the cells are pluripotent and that no genomic perturbations have occurred during the reprogramming or culturing process. Proof of pluripotency here includes immunocytochemistry (Figure 3.1; Figure 3.2) and embryoid body assay (Figures 3.3; Figure 3.4). Tests such as PluriTest include hundreds of markers of pluripotency and differentiation, and are a more robust measure of pluripotency than probing for individual proteins or genes (Müller et al., 2011). Limitations with costs and/or equipment are generally the limiting factor for characterisation protocols, and staining is often utilised in lieu of more extensive characterisation. Newly derived iPSCs were positive for the pluripotency marker Oct-3/4 via immunocytochemistry (Figure 3.1; Figure 3.2) and the embryoid body assay indicated tri-lineage potential of iPSCs (Figure 3.3; Figure 3.4). Collectively these data indicate that newly derived iPSCs from control and *ANXA11* ALS patients are pluripotent and therefore suitable for use as an experimental model of ALS.

It is a well-established phenomenon that major chromosomal events can occur in cultured stem cells, which can lead to altered cellular behaviours and misleading experimental readouts. Major chromosomal changes include insertions and deletions, translocations, and duplications of genetic material. Genomic aberrations might occur during iPSC reprogramming and can also arise in prolonged cell culture. Approximately 12.5% of iPSCs may have abnormal karyotypes, such as trisomies, large insertions or deletions, and translocations (Taapken et al., 2011). Random chromosomal abnormalities in cultured cells can confer a proliferative advantage or reduce cell death and apoptosis (Zhang et al., 2019). Consequently, cells harbouring abnormalities can divide and survive more easily, giving rise to mosaic cultures. Additionally, smaller genomic alterations such as SNPs can arise, resulting in similar consequences for cultures. This is supported by the recurrence of abnormalities at specific genomic loci in multiple stem cell lines, indicating that certain genomic regions are susceptible to culture advantageous alterations (Assou et al., 2020; Baker et al., 2016; Merkle et al., 2017; Nikitina et al., 2019; Oliveira et al., 2014; Rebuzzini et al., 2015; Zhang et al., 2019). Assessment of iPSC genomic integrity with whole genome sequencing revealed that 3.5±0.5 base substitutions occur per population doubling, highlighting the necessity to maintain low passage stocks (Kuijk et al., 2020).

Gross genomic integrity is traditionally measured by G-band karyotyping, where dividing cells are fixed during metaphase and chromosomes are spread, visualised, and aligned to a typical karyotype structure. A normal karyotype was seen in all iPSC lines, excluding the ALS patient line *ANXA11* D40G 2 (Figure 3.5), which had a balanced translocation between chromosome 4 and chromosome 22. To investigate whether this translocation was clone specific or due to a generalised karyotypic abnormality in the parent LCL, a second iPSC clone from the same individual was submitted for G-band karyotyping. However, this assay failed multiple times and unfortunately results could not be reported in the present thesis. Due to technical issues encountered whilst completing karyotype analysis, experimental interrogation of cell lines was started before complete karyotype data was collected. The visualisation of an abnormal karyotype in *ANXA11* D40G 2 highlights the importance

of thorough characterisation of cell lines before they are used in experiments. As balanced translocations often occur in healthy adults, without major consequences to adult health, it was decided that the *ANXA11* D40G 2 iPSC line would still be included in analyses.

Although G-band karyotyping is often implemented as the gold standard for genomic analysis, it can be technically challenging, evidenced here by fewer than 20 metaphases being analysed for some cell lines (Figure 3.5). Newer technologies for assessing chromosomal changes include digital karyotyping (Baker et al., 2016; Leary et al., 2007), and genomic tests such as comparative genomic hybridisation (CGH) can give additional insight into genomic stability such as identification of small deletions and duplications. Guidelines for best practice in maintaining genomic stability in iPSC lines have been put forward but are yet to be widely implemented in many instances of iPSC research (McIntire et al., 2020; Rossi et al., 2022). Large-scale stem cell initiatives aim to standardise iPSC technology, increasing the number of cell lines available, alongside thorough characterisation of lines which can often be beyond the scope of smaller laboratories (Ohlemacher et al., 2021; Ramos et al., 2021). Additionally, it has been posited that genomic screening of hESC lines should be implemented prior to their utilisation, to exclude lines with abnormal traits including hidden disease-associated single nucleotide variants, which is also applicable to iPSC technology (Merkle et al., 2022). Mitochondrial DNA variants can fluctuate between parent fibroblasts and corresponding iPSCs and NPCs, which can lead to altered experimental readouts (Palombo et al., 2021). This phenomenon was identified relatively recently in iPSC lines and should be considered in future studies.

An unexpected and time-consuming aspect of this project was the continued presence of EBV genes in LCL-derived iPSCs (Figure 3.7). EBV causes infectious mononucleosis and is associated with lymphomas, other cancers, autoimmune diseases, and multiple sclerosis (Bjornevik et al., 2022; Houen & Trier, 2021; Nociti et al., 2010). To circumvent cell senescence in cell culture, blood cells are transduced with EBV genes to provide a continuously dividing culture (Hui-Yuen et al., 2011). LCLs have been largely utilised for genomic studies, where it is necessary to procure substantial amounts of DNA and maintain a continuous source of patient cellular material. The UK MND

Collections is home to many LCLs from a wide range of ALS patients and controls, which have been extremely useful for identification of ALS causing mutations, including those in *ANXA11* which are the focus of this thesis (Smith et al., 2017). The development of protocols for derivation of iPSCs from LCLs enabled The UK MND Collections to be repurposed as a resource for the production of iPSCs (Barrett et al., 2014; Kumar et al., 2016; Rajesh et al., 2011). In instances where no primary patient cells are available, LCLs are a useful resource, and publications describing LCL reprogramming report the loss of EBV from established iPSC lines (Barrett et al., 2014; Rajesh et al., 2011). However, throughout this project approximately 25% of iPSC clones did not lose EBV genes after multiple passages. In these instances, iPSCs that were positive for EBV genes by PCR at passage 35 were discarded, and a new clone was selected for characterisation and inclusion in experiments. The consequence of EBV DNA persistence in iPSCs is unknown, and characterisation of the effect of EBV DNA on cellular phenotypes should be determined in future studies. Serial iPSC passaging to induce loss of EBV DNA is costly and time-consuming and should be considered when utilising LCLs for iPSC derivation. In future studies, subcloning new LCL-derived iPSCs may enhance the loss of EBV genomic material more efficiently than serial passaging. It should be noted that iPSCs lost EBV DNA at various passages, although all lines were cultured in the same way (Table 3.1). This could lead to variability in experiments, however all lines lost their EBV signal by passage 30, and seeding and working stocks were prepared immediately after the loss of EBV DNA, so it is assumed that lines are comparable. All other pluripotency and genomic characterisation experiments were completed after the loss of EBV to ensure that serial passaging did not introduce cell line abnormalities detected by other characterisation experiments.

### *3.4.3 Establishing reliable experimental design to reduce variability*

Derivation of neuronal cultures from iPSCs has provided an unmatched *in vitro* human model for ALS research. However, as with any biological model there are limitations, including the lack of system biology that is achieved with animal models and the high variability that can be observed in iPSC

derived cultures. The use of different donor material to produce iPSCs may result in different iPSC characteristics (Efrat, 2021), however evidence suggests that the downstream effects on differentiated cells are minimal (Sanchez-Freire et al., 2014). The reversal of epigenetic signatures during iPSC reprogramming is a well-recognised phenomenon, however instances of incomplete resetting of epigenetic modifications have been reported (Zhou et al., 2013). This and other genomic changes that might occur in reprogramming can lead to clonal variability, where iPSCs that have arisen from separate reprogramming events in separate cells from the same starting culture can display different characteristics in later experiments. Extensive characterisation aims to reduce this variability, but in the absence of whole genome sequencing and complete epigenetic profiling of every iPSC line produced, some unknown variability may exist. Traditional reprogramming methods such as retroviral insertion of pluripotency factors into random points in the genome might increase this variability as the random insertion of genes may affect genomic function. Methods such as SeV and transfection with episomal plasmids avoid this and produce iPSCs that are "foot-print free". To avoid attributing clone-specific phenotypes to a wider population, multiple different cell lines should be used in experiments, or if this is not possible multiple clones from the same donor should highlight clonal variation which can then be considered when interoperating results.

Differences in the genetic makeup of donors can cause variability; in instances where two patients have the same genetic mutation the background genetic landscape of each patient will vary, which has consequences for the observed cell cultures. This is equally relevant for control lines, where the absence of disease does not negate differences in cell culture. This raises an important point in the need for good, reliable control lines for experiments. Control lines are collected at moments in time where the donor is "disease-free", however it is possible that such donors will go on to develop diseases that are at least in part governed by their genetic make-up. As such, it is possible that control lines in experiments unknowingly represent a prodromal disease population. To avoid these circumstances, it is necessary to include multiple control lines in experiments, and multiple mutant lines. This will reduce the probability that any results are simply a result of person-to-person

variability and support the notion that they are due to the disease being modelled. Sets of control lines can be further improved by careful selection of control donors. Producing iPSC lines from persons of “extremely healthy ageing” might offer a faithful model for absence of disease. Collections of healthy control iPSC lines have been produced and reported, and inclusion of whole genome sequencing of these lines increases their reliability as experimental controls (Schaniel et al., 2021). The controls used here were derived from blood samples collected between ages 61-84, and the selection of these lines for reprogramming was based on biological sex-and age-matching of control lines to patient lines. At the time of line selection, it was posited that donor age might have unknown influence on the characteristics of iPSCs, such as differentiation potential or culture senescence. Similar effects are seen in fibroblast cultures, where reduced reprogramming efficiency is associated with older donor age (Trokovic et al., 2015). Since then, however, evidence suggests that this is not the case for iPSCs, which show similar differentiation potential and extended culture characteristics independent of donor age (Strässler et al., 2018). This might suggest that in future studies the utilisation of lines from those of “extremely healthy ageing” will provide better control conditions than age-matched controls. The oldest reported donor for iPSC reprogramming was 114 years old, and these iPSCs showed reversal of age characteristic telomere shortening, indicating that even in extreme circumstances age signatures are lost with reprogramming (Lee et al., 2020). A limitation with such study design is that signs of normal aging in disease models might then appear as disease-associated phenotypes, and it may in fact be misleading to compare disease lines to models of extremely healthy ageing. An alternative is to increase the number of control lines to circumvent any misleading data that might arise from individual variability among controls, as has been included here.

Variability can also arise in the differentiation process. Current protocols inevitably yield a mixture of cell types, however protocols are being continuously optimised to reduce this type of variability. As with any experiment, multiple repeats are necessary, and in the case of iPSC derived cultures it is necessary that these repeats are produced from separate rounds of differentiation. Recent single-

cell RNA sequencing data suggest that genetic background can influence *in vitro* differentiation capacity of iPSCs, and so it may be possible to select lines with a high likelihood of producing a desired cell type in future studies (Cuomo et al., 2020). Methods for iPSC maintenance will vary from person-to-person, and laboratory-to-laboratory, and this might translate to variable results. Regular screening for the absence of mycoplasma infections is also important as extensive data indicate that infection can have "virtually unlimited" effects on cultures (Drexler & Uphoff, 2002). Mycoplasma screening was implemented throughout iPSC derivation and maintenance, ensuring the absence of infection. In line with this, antibiotics should be excluded from iPSC culture media as their inclusion can result in low level, yet persistent, bacterial contamination and increased mycoplasma infection as poor aseptic technique is masked. In addition, inclusion of antibiotics can have a negative effect on differentiating stem cells (Varghese et al., 2017), and can alter gene expression (Ryu et al., 2017), and so thorough sterile technique should be employed as the means to prevent contamination.

The limiting factor when addressing these opportunities for variability to arise is often time and workload. As robot and laboratory capacities increase, it might be possible to execute experiments with many conditions so that fewer false positives and negatives are present. Potential avenues for introduction of variability, and experimental design that would reduce variability, are summarised in Figure 3.19.

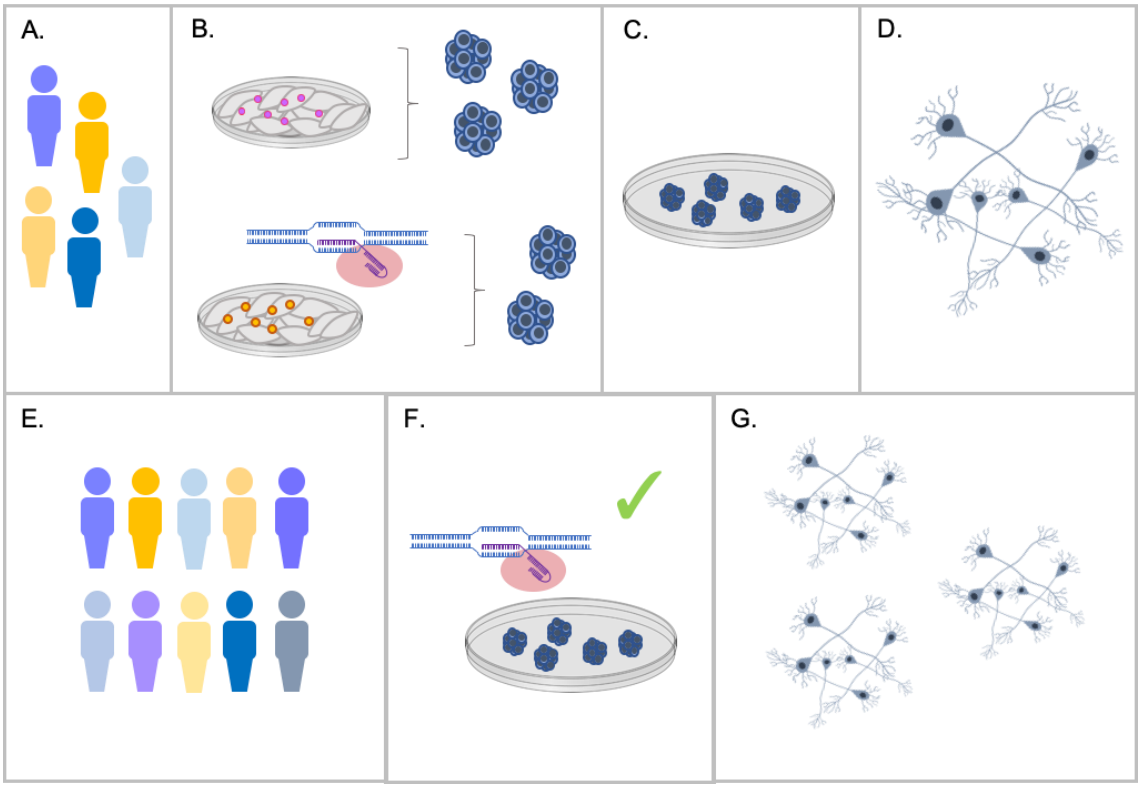


***Figure 3.19 Introduction of variability in iPSC culture and rational study design***

(A) Individual genetic differences in patients and controls will result in variable iPSC characteristics. (B) Different methods for reprogramming and gene editing may affect iPSCs. (C) Differences in iPSC culturing and maintenance can alter pluripotency and genomic stability of cell lines. (D) Separate instances of differentiation can yield different results. Study design to avoid these sources of variability include generating iPSC lines from multiple individuals and including as many lines as possible in experiments (E), using best practice for reprogramming and editing lines to avoid DNA damage including thorough and frequent characterisation tests (F), and including multiple separate rounds of differentiation in each experiment (G).

### *3.4.4 iPSC-derived motor neurons*

The motor neuron differentiation protocol used here yields cultures that are 70-80% positive for the motor neuron marker Islet 1 by day 17 of differentiation (Figure 3.8; Figure 3.9; Figure 3.10). Neurons derived from *ANXA11* patients displayed 70-74% Islet 1 positive nuclei, compared to 79% Islet 1 positive nuclei in control lines, but no significant difference between control lines or each of the three *ANXA11mut* groups was identified by Brown-Forsythe one-way ANOVA. Reduced propensity for neuronal differentiation has been reported in iPSC lines harbouring ALS genetic mutations in *FUS*

(Stronati et al., 2021), and reduced numbers of neurons derived from *TARDBP* mutant iPSCs are positive for the motor neuron marker HB9 (Bossolasco et al., 2018). Additionally, FTD iPSC models with mutations in *PGRN* display reduced corticogenesis (Raitano et al., 2014). The slightly reduced number of motor neurons in *ANXA11* ALS lines seen here could be disease relevant, however the lack of a statistically significant difference suggests that comparable numbers of motor neurons are present in all cell lines. Motor neurons were positive for ChAT as detected by immunocytochemistry at days 17 and 42 of differentiation (Figure 3.11), and neuronal cultures were probed for the motor neuron specific genes ChAT and HB9 by RT-PCR, which were detected in motor neurons on day 21 and 17 of differentiation, respectively, but were not detected in LCL cDNA (Appendix Figure 9.4). Overall, these data show that neuronal cultures included in this thesis include a high proportion of motor neurons and that a phenotype of *ANXA11* ALS patient-derived lines is a small but statistically insignificant reduction in the ability of stem cells to differentiate into Islet 1 positive motor neurons.

In aged cell cultures, residual progenitors present at the time of motor neuron plating can continue to divide, resulting in neuronal cultures becoming diluted by the expansion of undifferentiated cells. This can vary between differentiation instances, highlighting the necessity to include multiple rounds of differentiation for each experiment, and the importance of maintaining stocks of high-quality iPSCs and small molecules for differentiation. Multiple experiments in this thesis include co-culture of motor neurons with astrocytes, presenting a challenge with identification of appropriate cells and exclusion of non-neuronal cells in image quantification. In experiments where high power magnification is used for data acquisition, neurons can be selected for analysis based on neuronal markers and cell morphology. In cases of high-throughput image acquisition (see Chapter 4), protocols were established to exclude non-neuronal cells from quantification (2.4.2). This was established to exclude astrocytes from analysis where neuronal quantification was being performed, but also has application in exclusion of unspecific cells and debris if present. The inclusion of unspecific cells is not desirable, and differentiation protocols are continuously being improved: Efforts to sort cells with MACs or FACs, or to use forced differentiation by inserting cell-type-specific

differentiation drivers into “safe-harbour” genomic sites, might alleviate some random differentiation (Hulme et al., 2021; Nehme et al., 2018). Optimisation of such methods was beyond the scope of this project due to time restraints, equipment limitations, and project aims. However, the yield of motor neurons and the thorough filtering applied here ensure that the results reported in this thesis are both reliable and meet the current standards of motor neuron cultures. In addition, visual inspection of neuronal cultures was consistently applied to exclude any non-neuronal cultures. This was particularly relevant for neurons collected for western blotting, where only clearly neuronal cultures were included (Appendix Figure 9.5).

### *3.4.5 Motor neuron-astrocyte co-culture*

Single cell-type cultures offer a brilliant platform for looking at cell-specific changes, however they don’t accurately represent the complex multicellular nature of the CNS. The function of neurons is heavily influenced by surrounding cells, and establishment of co-culture is increasingly utilised as a means to improve culture quality.

The decision to include astrocytes in co-culture with motor neurons in this project was multifactorial. Motor neuron cultures tend to bundle together and form axon fascicles, which lift off from glass coverslips when maintained in culture for extended periods of time. Efforts were made to avoid this, including amending coverslip coating, washing glass coverslips with hydrochloric acid, and plating different numbers of motor neurons. The optimised procedures are detailed in 2.1, however culture clumping and lifting can persist in aged cultures. This is a widely observed phenomenon, and efforts have been made to produce substrates that discourage motor neurons from lifting when included in basement coating protocols (Thiry et al., 2021). Notably, cell lifting was not observed as drastically when neurons were cultured on plastic culture plates. When attempting to age pure populations of neurons at lower densities, neurites in both control and *ANXA11mut* lines would start to fragment, suggesting that purely neuronal populations are vulnerable to cell death. In addition, increasing evidence suggests that more complex iPSC derived cultures yield “faster-maturing” neurons. This is

evidenced by 3D organoids, for example in Alzheimer's Disease research, where organoids express adult tau isoforms at a much earlier time point than their monolayer neuron counterparts (Lovejoy et al., 2022). Further, co-culturing iPSC-derived motor neurons with iPSC-derived astrocytes enhances the electrophysiological maturation of neurons in a time-dependent manner, and the neurons exhibit structural and protein expression profiles associated with mature cells (Kuijlaars et al., 2016; Taga et al., 2019). One role of astrocytes is the re-uptake of glutamate and subsequent conversion into glutamine, and transfer of glutamine to neurons to restore glutamate levels, indicating that neuronal homeostasis and function may be improved when maintained with astrocytes. For these reasons astrocytes were included in culture: 1. To enable long term maintenance of neurons via preventing neurons from lifting; 2. To give trophic and structural support to neurons, preventing neurite fragmentation; 3. To yield more "mature" motor neurons; 4. To recapitulate the multicellular structure of the CNS more faithfully.

Multiple methods for motor neuron-astrocyte co-culture were tested and are detailed in Figure 3.17. Direct co-culture of motor neurons plated on top of astrocytes was carried forward as this system resulted in better long-term culture survival, was feasible in terms of experimental workload, and was better suited to miniaturised culture formats such as 96-well plates. Co-cultures fixed on day 42 of motor neuron differentiation were probed for cell-type specific markers, revealing networks of GFAP positive astrocytes and $\beta$3-Tubulin positive motor neurons (Figure 3.18). Representative images show the same *XY* region of cells at two *z*-planes, highlighting astrocytes interspersed between neurites, giving rise to cultures with increased complexity compared to monolayer neuronal cultures. Due to limitations with time and prioritisation of neuronal phenotyping, quantification of astrocytes in extended cultures was not directly measured and could be important for future studies. Treatment of astrocytes with mitomycin C was included to prevent overpopulation in cultures that were maintained for extended periods, in part to enable visualisation of post-mitotic neurons in imaging experiments. It is possible that treatment with mitomycin C influences astrocytic function beyond inhibiting cell division, and so the effect of iPSC-derived astrocytes in this system should be

interoperated with caution. The focus of this body of work is the assessment of neurons in the context of *ANXA11* ALS, and so although astrocytes may influence neuronal health and function, it was deemed appropriate to utilise pre-treated non-dividing astrocytes in co-culture in this context. In addition to the influence of reactive astrocytes in co-culture (Tripathi et al., 2017), evidence points towards heterogeneity in astrocytes from different parts of the CNS (Clarke et al., 2020; Yoon et al., 2017). These are important considerations and in future studies it may be necessary to characterise subtle differences in astrocyte phenotypes when assessing their influence on neuronal health.

## *3.5 Conclusions*

To address the lack of iPSCs available for *ANXA11* ALS research, five *ANXA11* ALS patient-derived lines were produced. Five control lines were produced based on matched sex and age proximity. iPSCs were subject to pluripotency and genomic stability characterisation experiments, were routinely tested for the absence of mycoplasma infection, had matched STR profiles to donor LCLs, and were passaged to become EBV negative. The importance of iPSC characterisation was highlighted by an abnormal karyotype in line *ANXA11* D40G 2, and the unexpected nature of EBV persistence in LCL derived iPSCs should be considered in future studies utilising this cell resource for stem cell derivation.

High-yield motor neurons were produced from iPSCs, and motor neuron differentiation capacity was comparable across cell lines. When co-cultured with astrocytes, long-term cell culture was achieved. The characterised cell lines and optimised motor neuron-astrocyte co-cultures provide a unique model for the study of *ANXA11* ALS, which is discussed further in Chapters 4, 5, and 6.

# Chapter 4 Characterisation of *ANXA11* ALS patient motor neurons

## *4.1 Overview*

Protein aggregation and mislocalisation are commonly associated with ALS pathology; many ALS associated proteins form inclusions which can sequester other proteins, often resulting in the formation of insoluble protein aggregates (1.12). In addition to the development of large protein aggregates, many ALS associated proteins mislocalise to atypical cellular compartments. For example, TDP-43, FUS, and many other RBPs are found predominantly in the nucleus in healthy neurons, and their relative abundance in the cytoplasm increases with disease progression (Dormann et al., 2010; Liu et al., 2015, 2021; Tyzack et al., 2019, 2021). TDP-43 mislocalises or aggregates in over 95% of ALS cases, the majority of which do not harbour mutations in the corresponding *TARDBP* gene (Ling et al., 2013; Mackenzie et al., 2007; Neumann et al., 2006). Screening assays utilising cytoplasmic mislocalisation of TDP-43 and FUS have been established as a means to screen newly identified genetic mutations in order to prioritise further experiments, highlighting the usefulness of cell-based protein localisation assays in ALS (Oyston et al., 2021).

Post-mortem histological analyses of patient tissue with G38R or D40G *ANXA11* mutations show Annexin A11, pTDP-43, and TDP-43 positive aggregates in the spinal cord and/or brain of *ANXA11* ALS patients (Smith et al., 2017; Teyssou et al., 2020). This exemplifies the relevance of protein aggregation in *ANXA11* associated ALS. In addition, overexpression of *ANXA11* constructs indicates an altered vesicular like staining pattern of R235Q Annexin A11 in mouse cortical neurons (Smith et al., 2017), indicating a potential early alteration in protein localisation as a consequence of ALS associated mutations, however this hasn't been demonstrated at endogenous protein levels. To address this, the initial characterisation of *ANXA11* ALS patient-derived motor neurons included broad analyses of protein localisation and abundance, which was completed in *ANXA11mut* and

control motor neurons at multiple time points to assess any culture maturity associated protein characteristics.

## *4.2 Methods*

### *4.2.1 High-throughput image analysis and quantification in patient-derived motor neurons*

iPSCs derived from five control and five *ANXA11* ALS patients (2x G38R, 2x D40G, 1x R235Q) were differentiated into motor neurons (2.1.7) and in some instances maintained in co-culture with astrocytes differentiated from the same iPSC lines (2.1.10). iPSC-derived cultures were fixed and subject to immunocytochemistry (2.4.1), and high-throughput characterisation of motor neurons was performed using the Opera Phenix® High-Content Imaging System and Harmony® analysis software (2.4.2). This was completed for motor neuron monocultures on day 17 of differentiation, 17-day old motor neurons maintained in co-culture with astrocytes, and 42-day old motor neurons maintained in co-culture with astrocytes (Table 2.4). High-throughput image analysis was implemented to characterise Annexin A11, TDP-43, and pTDP-43 protein. Quantified characteristics include gross protein localisation in the nucleus and cytoplasm of motor neurons, giving rise to a measure of nucleocytoplasmic ratio, and spot characteristics including spot size and spot count, which were normalised to the nuclear or cytoplasmic area.

To aid visualisation of large amounts of data from high-throughput analyses, spot characteristics and the nucleocytoplasmic ratio of target proteins are presented in a grouped format so that control and *ANXA11mut* characteristics can be concurrently visualised in different culture conditions. Data are grouped by *ANXA11* mutation status in the following groups; control, *ANXA11* G38R, *ANXA11* D40G, and *ANXA11* R235Q. When data from multiple culture paradigms are presented together, data are shown as the mean value for each *ANXA11* mutation status group with error bars showing SD, indicating the variability seen between separate motor neuron inductions (biological replicates).

These data were analysed with a two-way ANOVA with Tukey's multiple comparisons test to compare *ANXA11mut* groups to control across different culture paradigms.

In addition, results from individual experiments (assessment of each target protein in each culture condition) are presented separately in the Appendix, alongside additional measurements from high-throughput analyses that cannot be reliably compared across culture conditions. These are generally arbitrary measures of fluorescent intensity that have not been directly compared across culture paradigms due to the completion of imunocytochemistry and image acquisition at different times, including inconsistent image collection settings. This means that experimental readout is likely to be influenced by confounding variables in addition to the measured variables (i.e. mutation status and culture paradigm). In addition, the number of neurons included for high-throughput analyses are included with the relevant Appendix data to demonstrate the large number of cells included in analyses.

### *4.2.2 High-resolution imaging*

To demonstrate Annexin A11 subcellular localisation and granule characteristics, motor neurons were fixed and probed for Annexin A11 with immunocytochemistry (2.4.1), and imaged with super-resolution microscopy (2.4.3).

### *4.2.3 Protein abundance in iPSC-derived models of ALS*

Annexin A11 and TDP-43 protein was further assessed in iPSCs, motor neurons, and astrocytes with western blotting (2.5.1), with levels of endogenous protein normalised to total protein in different cell types.

## *4.3 Results*

### *4.3.1 High-throughput characterisation of Annexin A11 in ANXA11mut and control motor neurons*

Representative data from high-throughput imaging of Annexin A11 in pure populations of motor neurons fixed at day 17 of differentiation (Figure 4.1; Figure 4.3), 17-day old motor neurons in co-culture with astrocytes (Figure 4.3; Figure 4.4), and 42-day old motor neurons in co-culture with astrocytes (Figure 4.5; Figure 4.6) are shown. The nucleocytoplasmic ratio was calculated by dividing mean nuclear intensity by mean cytoplasmic intensity, a higher value therefore indicating a more nuclear localisation, and a value of 1 indicating equal distribution between the two cellular regions. The mean nucleocytoplasmic ratio of Annexin A11 across all conditions suggests that it resides predominantly in the nucleus, and large measures of error indicate that the localisation is dynamic (Figure 4.7.A; Appendix Figure 9.7; Appendix Figure 9.9; Appendix Figure 9.11). Annexin A11 localisation in neurons showed a slight trend towards increased cytoplasmic localisation when in co-culture with astrocytes, suggesting that neuronal protein localisation is affected by non-cell-autonomous mechanisms, or that neuronal health or metabolic/trophic support was altered in the presence of astrocytes such that Annexin A11 localisation was different compared to motor neuron monocultures. Although the nucleocytoplasmic ratio of Annexin A11 was variable and fluctuated within cell lines, as evidenced by sometimes large standard deviations, the mean nucleocytoplasmic ratio was not significantly different across culture paradigms (Figure 4.7.A).

Annexin A11 spot analysis was completed in the nucleus and cytoplasm of motor neurons in different culture paradigms. This included a measure of spot size and spot count normalised to the region of interest (ROI) (nucleus or cytoplasm). No statistically significant differences in spot characteristics were observed between control and *ANXA11mut* groups in any culture condition. Annexin A11 nuclear spot size was increased in day-17 co-cultured neurons compared to the day-17 motor neuron only and day-42 co-cultured neuron groups (Figure 4.7.C), and Annexin A11 cytoplasmic spot size

was increased in day-42 co-cultured neurons compared to both day 17 groups (Figure 4.7.D). The number of Annexin A11 nuclear and cytoplasmic spots was increased in day-17 co-cultured motor neurons compared to day-17 motor neuron monocultures and day-42 co-cultured motor neurons, and the nuclear and cytoplasmic spot counts were slightly increased in day-17 motor neuron only cultures compared to day-42 co-cultured motor neurons (Figure 4.7.E; Figure 4.7.F).

The total intensity of Annexin A11 was consistent across mutation groups indicating no obvious change in Annexin A11 protein amount caused by endogenous mutations in *ANXA11* (Appendix Figure 9.7; Appendix Figure 9.9; Appendix Figure 9.11). The advantage of utilising high-throughput analysis is the quantification of cellular characteristics in large numbers of cells, reducing bias through automated analysis, and dilution of false effects present in small sample sizes. Over 1,700 neurons were included per cell line in the analysis of Annexin A11 protein distribution in pure populations of young motor neurons (Appendix Figure 9.7), over 3,000 neurons in day-17 neurons maintained in co-culture with astrocytes (Appendix Figure 9.9), and over 2,500 neurons per cell line in day-42 co-cultured motor neurons (Appendix Figure 9.11). In each instance three separate motor neuron inductions were included, each with three technical replicates, indicating increased neuron count in the presence of astrocytes in young motor neurons, and reduced neuron count with culture maturity.

Motor neurons immunolabelled for Annexin A11 were imaged with super-resolution microscopy, revealing widespread Annexin A11 throughout neurons with dynamic localisation (Figure 4.8; Appendix Figure 9.12). Some control and *ANXA11mut* neurons displayed increased cytoplasmic localisation of Annexin A11 and some a more nuclear localisation, which appeared to be independent of *ANXA11* mutation status. Annexin A11 is punctate throughout the nucleus and cytoplasm of neurons, with small bright puncta of various sizes present throughout cells including in neurites (Figure 4.8).

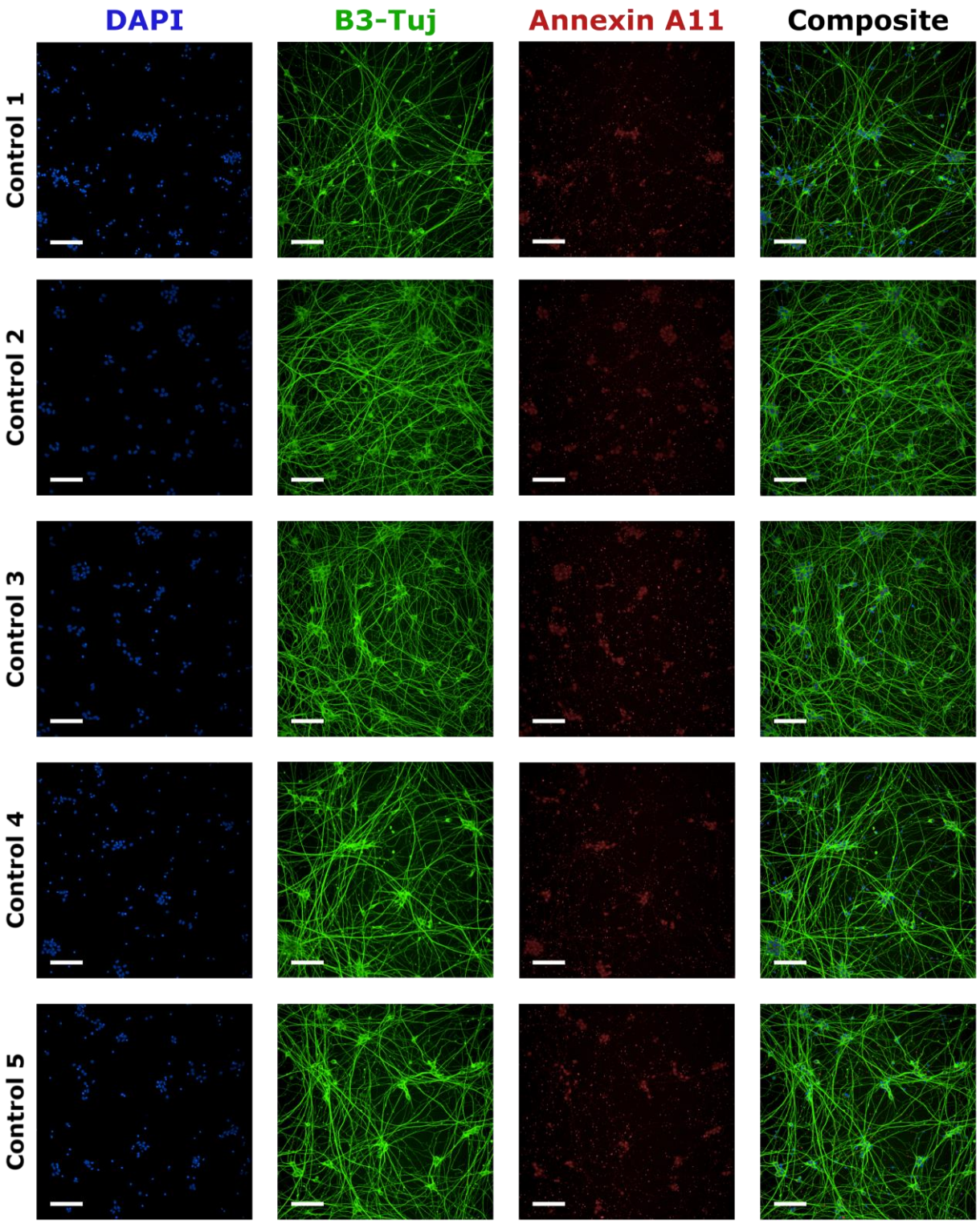


***Figure 4.1 Annexin A11 in young control motor neurons***

Representative images of control motor neurons fixed on day 17 of differentiation. Cultures were probed for $\beta$3-Tubulin (B3-Tuj, green) and Annexin A11 (red), and co-stained with DAPI (blue), and imaged with the Opera Phenix® High-Content Screening System. Scale bars represent 100µm.

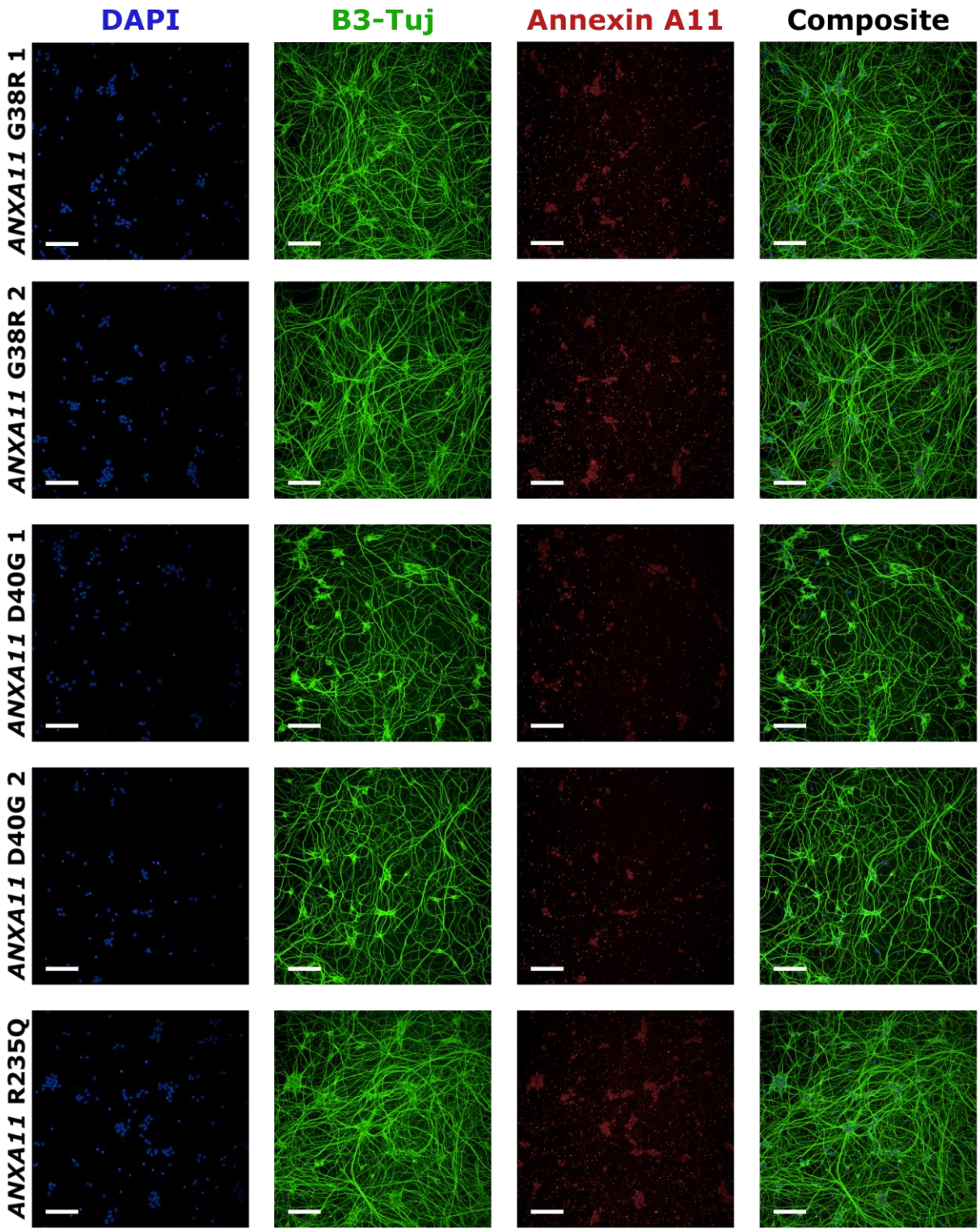


***Figure 4.2 Annexin A11 in ANXA11mut young motor neurons***

Representative images of *ANXA11mut* motor neurons fixed on day 17 of differentiation. Cultures were probed for $\beta$3-Tubulin (B3-Tuj) and Annexin A11 (red), co-stained with DAPI (blue), and imaged with the Opera Phenix® High-Content Screening System. Scale bars represent 100µm.

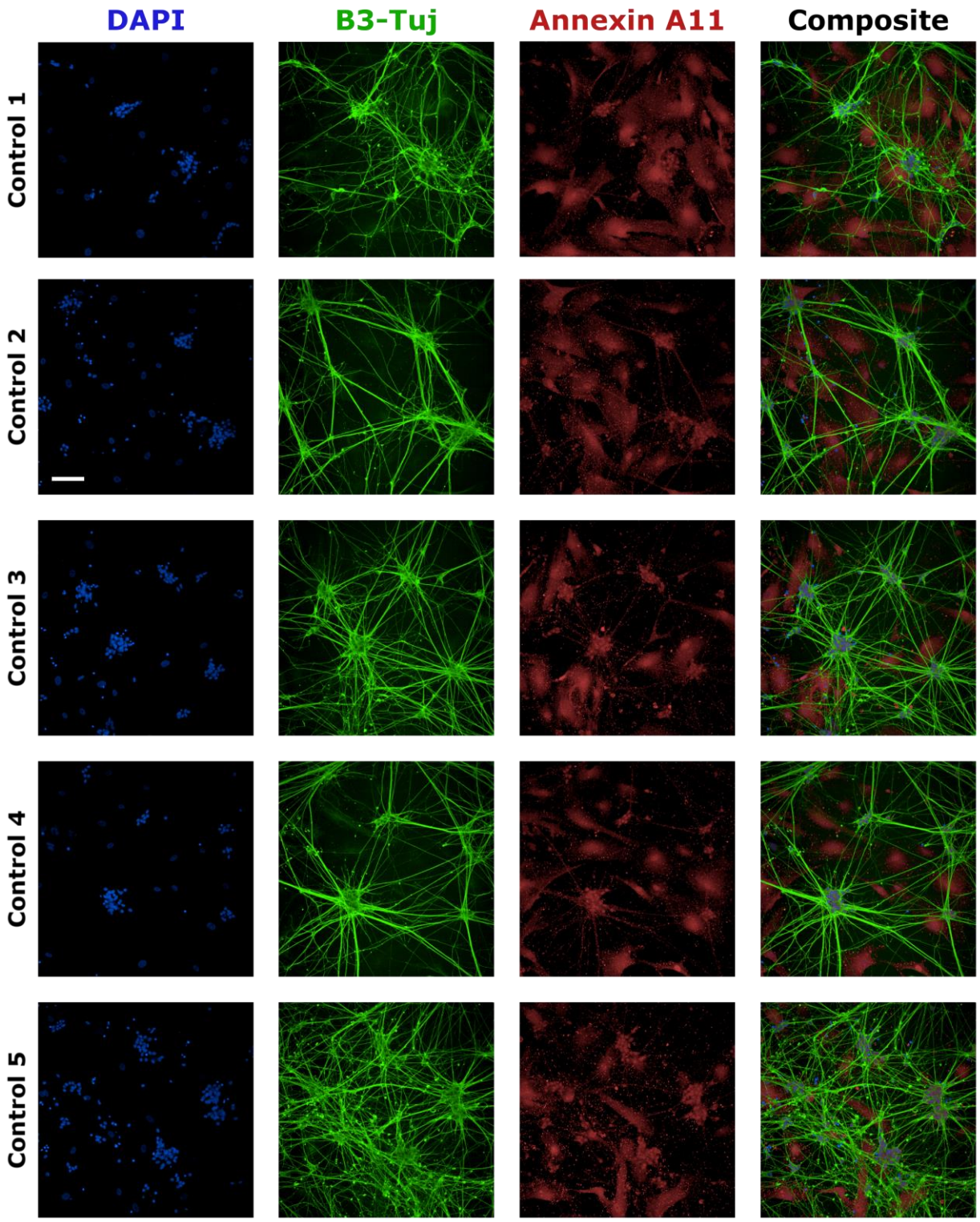


***Figure 4.3 Annexin A11 in young control motor neurons maintained in co-culture with astrocytes***

Representative images of control motor neurons maintained in co-culture with astrocytes, fixed on day 17 of motor neuron differentiation. Cultures were probed for $\beta$3-Tubulin (B3-Tuj) and Annexin A11 (red), co-stained with DAPI (blue), and imaged with the Opera Phenix® High-Content Screening System. Scale bars represent 100µm.

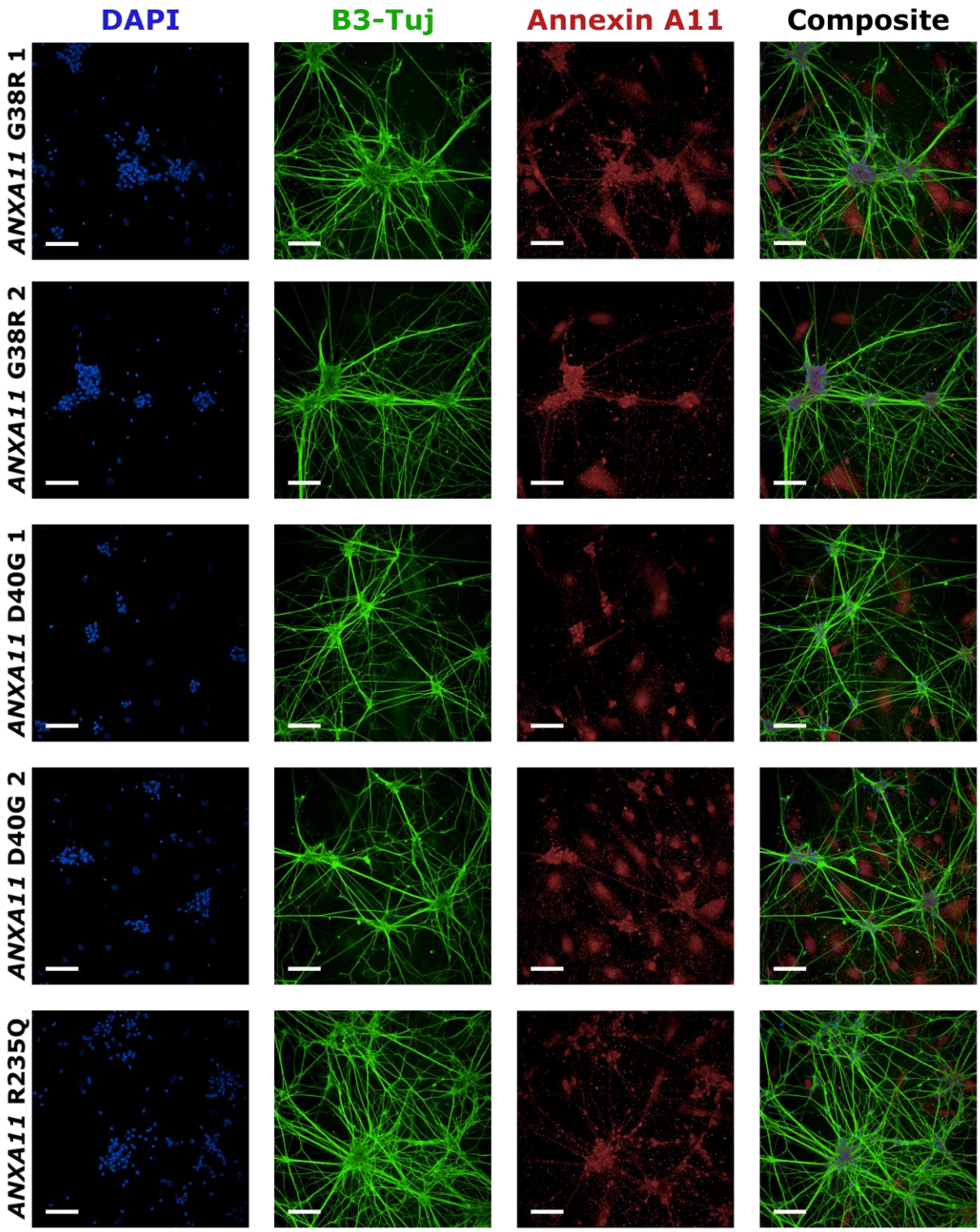


***Figure 4.4 Annexin A11 in young ANXA11mut motor neurons maintained in co-culture with astrocytes***

Representative images of *ANXA11mut* motor neurons maintained in co-culture with astrocytes, fixed on day 17 of motor neuron differentiation. Cultures were probed for $\beta$3-Tubulin (B3-Tuj) and Annexin A11 (red), co-stained with DAPI (blue), and imaged with the Opera Phenix® High-Content Screening System. Scale bars represent 100µm.

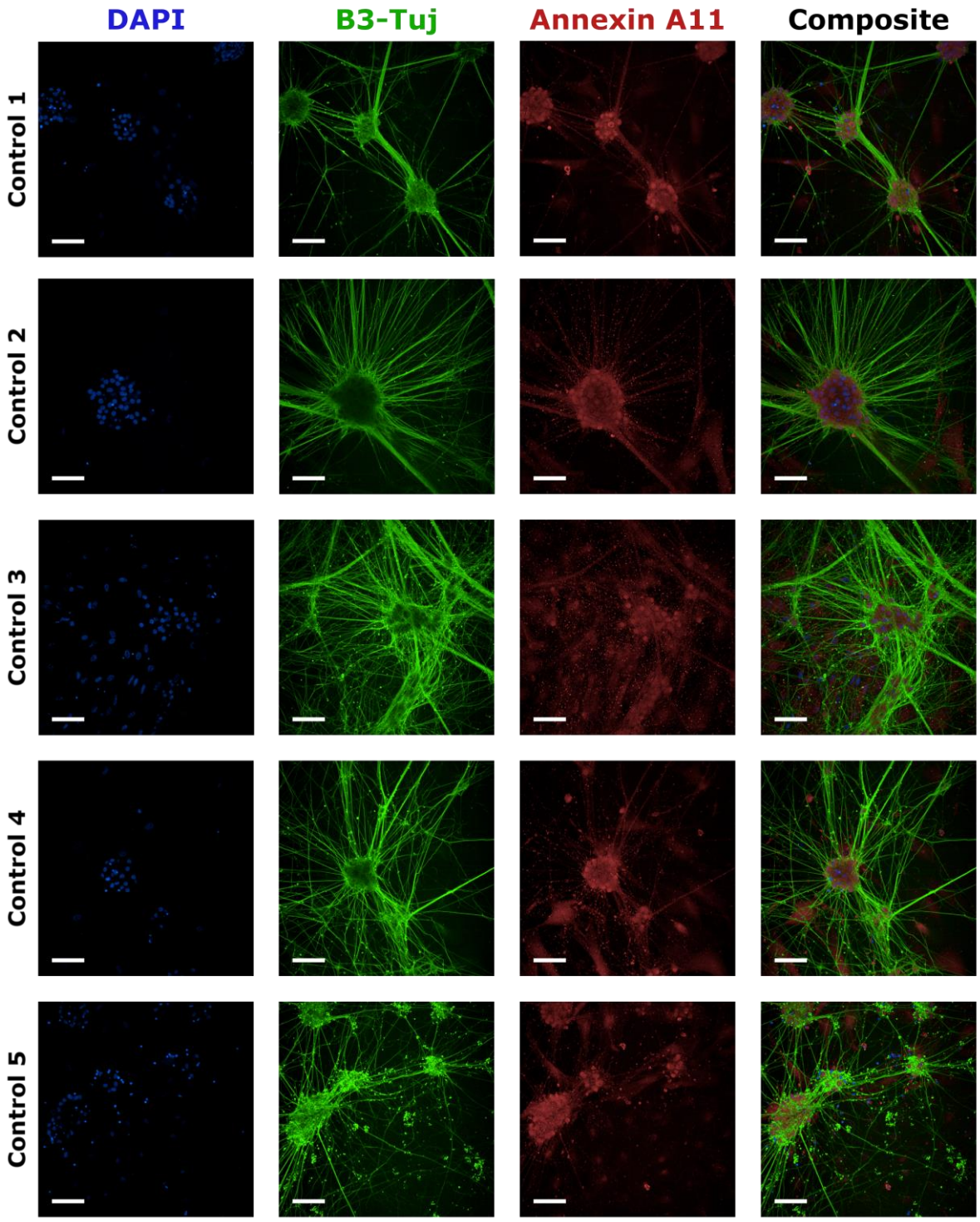


***Figure 4.5 Annexin A11 in aged control motor neurons maintained in co-culture with astrocytes***

Representative images of control motor neurons maintained in co-culture with astrocytes, fixed on day 42 of motor neuron differentiation. Cultures were probed for $\beta$3-Tubulin (B3-Tuj, green) and Annexin A11 (red), co-stained with DAPI (blue), and imaged with the Opera Phenix® High-Content Screening System. Scale bars represent 100µm.

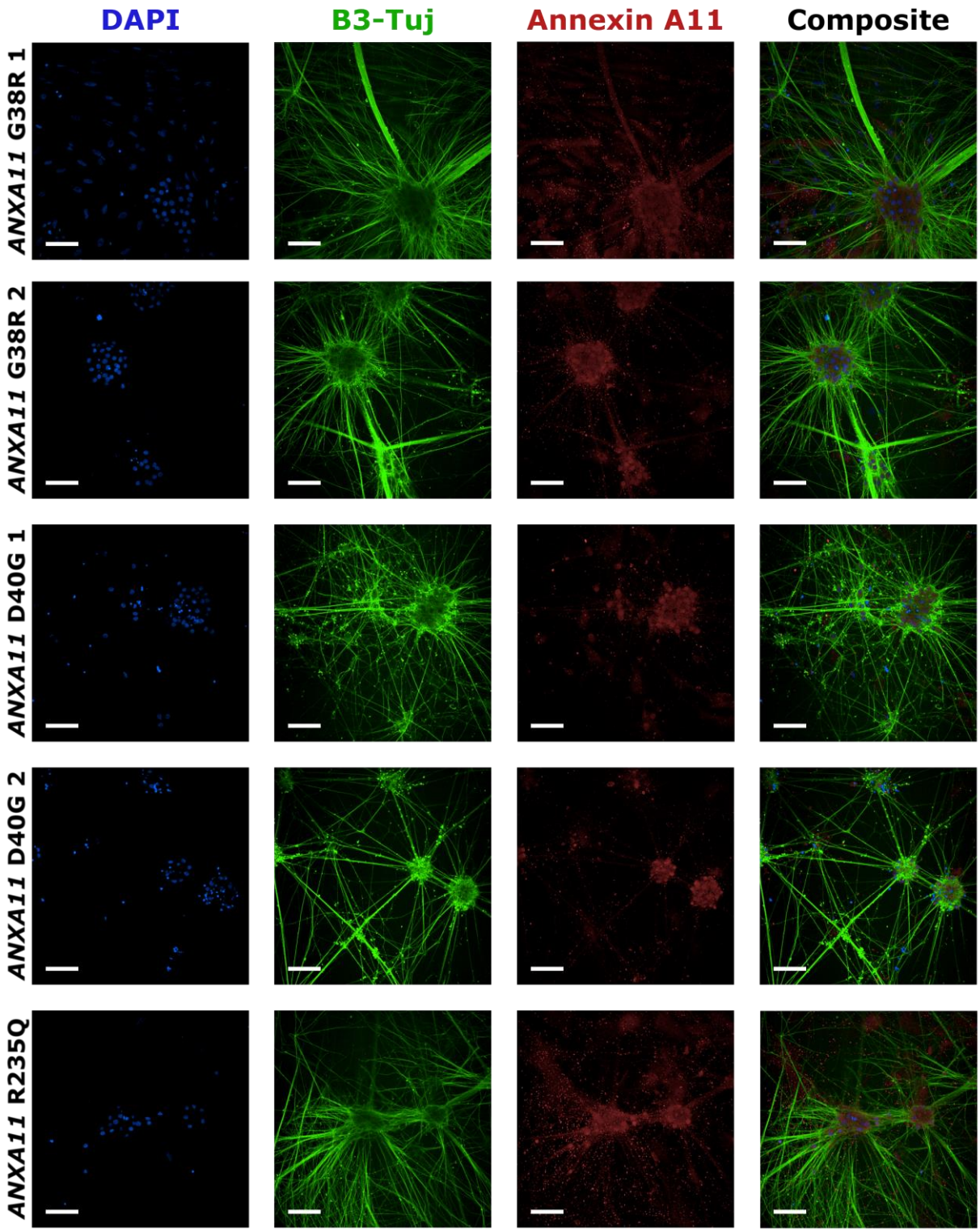


***Figure 4.6 Annexin A11 in aged ANXA11mut motor neurons maintained in co-culture with astrocytes***

Representative images of *ANXA11mut* motor neurons maintained in co-culture with astrocytes, fixed on day 42 of motor neuron differentiation. Cultures were probed for $\beta$3-Tubulin (B3-Tuj, green) and Annexin A11 (red), and co-stained with DAPI (blue), and imaged with the Opera Phenix® High-Content Screening System. Scale bars represent 100µm.

A. Annexin A11 nucleocytoplasmic ratio

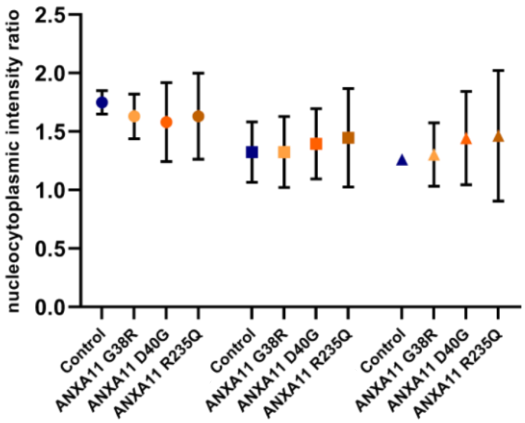


B.

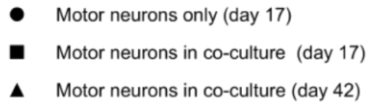


Nucleus

Cytoplasm

C. Annexin A11 spot size

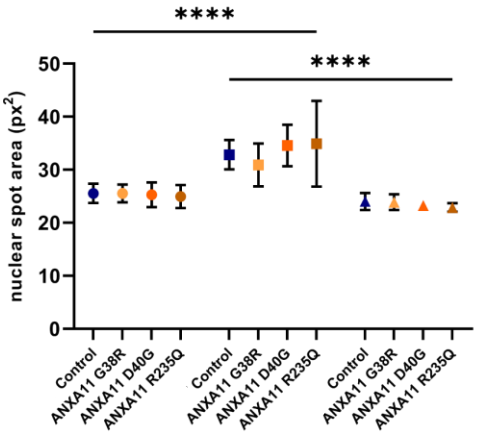


D. Annexin A11 spot size

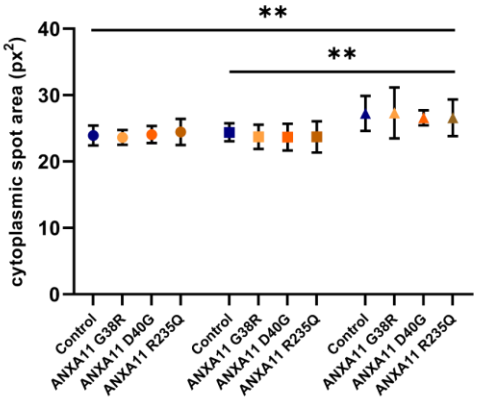


E. Annexin A11 spot count

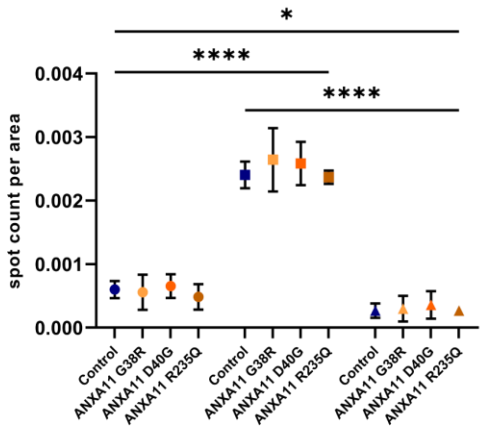


F. Annexin A11 spot count

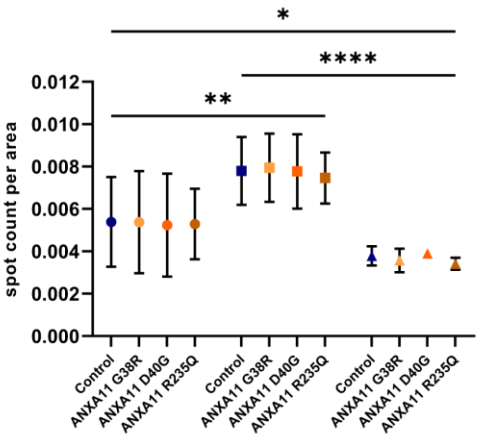

***Figure 4.7 Annexin A11 nucleocytoplasmic ratio and spot analysis across culture paradigms***

Quantification of data represented in Figures 4.1-4.6. (A) The nucleocytoplasmic ratio of Annexin A11 in motor neurons on day 17 of differentiation with and without co-culture with astrocytes, and motor neurons on day 42 of differentiation maintained in co-culture with astrocytes. (B) Culture paradigm key, relevant to A, C, D, E, F. (C) Annexin A11 nuclear spot size was increased in day-17 co-cultured neurons compared to day-17 motor neuron only cultures ($p \leq 0.0001$) and day-42 co-cultured motor neurons ($p \leq 0.0001$). (D) Annexin A11 cytoplasmic spot size was increased in day-42 co-cultured neurons compared to day-17 co-cultured neurons ($p = 0.0048$) and day-17 motor neurons ($p = 0.0070$). (E) Annexin A11 nuclear spot count was increased in day-17 co-cultured neurons compared to day-17 motor neuron only cultures ($p \leq 0.0001$), and day-42 co-cultured neurons ($p \leq 0.0001$), and nuclear spot count was reduced in day-42 co-cultured neurons compared to day-17 motor neuron only cultures ($p = 0.0252$). (F) Annexin A11 cytoplasmic spot count was increased in day-17 co-cultured neurons compared to day-17 motor neuron only cultures ($p = 0.0024$), and day-42 co-cultured neurons ($p \leq 0.0001$), and nuclear spot count was reduced in day-42 co-cultured neurons compared to day-17 motor neuron only cultures ($p = 0.0408$). Data are presented as mean ± SD, number of motor neuron inductions = 3; each data point represents the mean value from all cell lines in control and *ANXA11mut* groups across three motor neuron inductions, with each inducation comprised of three technical replicates. Statistical analysis: Ordinary two-way ANOVA with Tukey's multiple comparisons test (*$p \leq 0.05$; ** $p \leq 0.01$; ****$p \leq 0.0001$).

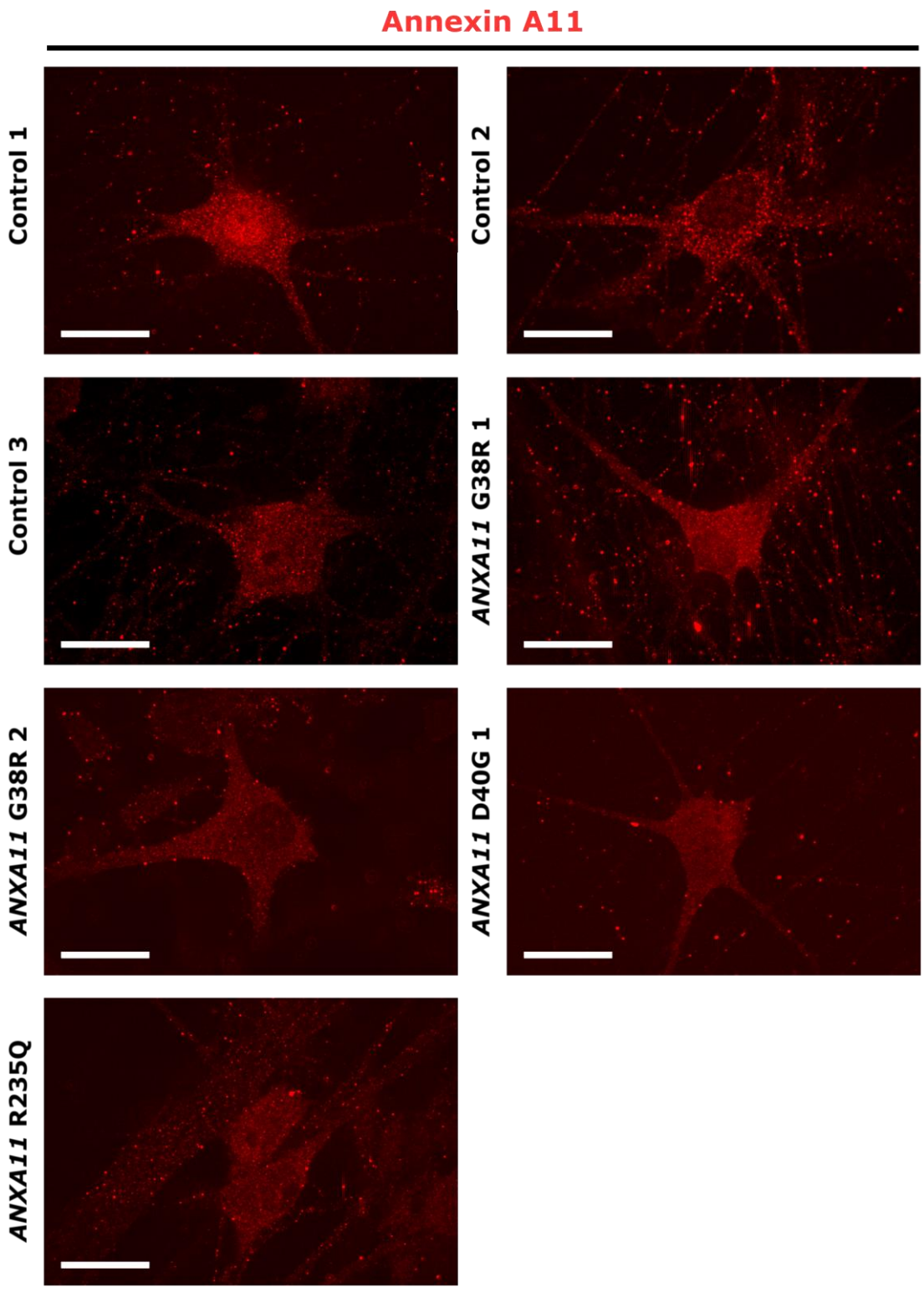


***Figure 4.8 Annexin A11 is punctate in human iPSC-derived motor neurons***

Control and *ANXA11* patient iPSCs were differentiated into motor neurons and maintained in co-culture with control astrocytes until day 42 of motor neuron differentiation. Neurons were immunolabelled for endogenous Annexin A11 (red). Scale bars represent 20µm. See Appendix Figure 9.12 for multi-channel images with the motor neuron marker ChAT, TDP-43, and DAPI.

### *4.3.2 Quantification of Annexin A11 protein in control and ANXA11 ALS patient stem cell models*

RIPA-soluble Annexin A11 abundance was not significantly different in control and *ANXA11mut* motor neurons, however a slight trend towards reduced Annexin A11 was seen in *ANXA11* D40G and R235Q motor neurons compared to control (Figure 4.9). Levels of RIPA-soluble Annexin A11 were consistent across control and *ANXA11* G38R, D40G, and R235Q groups in iPSC-derived astrocytes (Figure 4.10) and undifferentiated iPSCs (Figure 4.11). The normalisation of Annexin A11 to total protein stain enables the comparison of relative protein abundance across multiple cell types as normalisation is completed in the absence of housekeeping proteins that might alter in relative abundance between cell types. Comparison of Annexin A11 abundance across cell types indicated a relative increase in astrocytes and undifferentiated iPSCs compared to motor neurons (Figure 4.12).

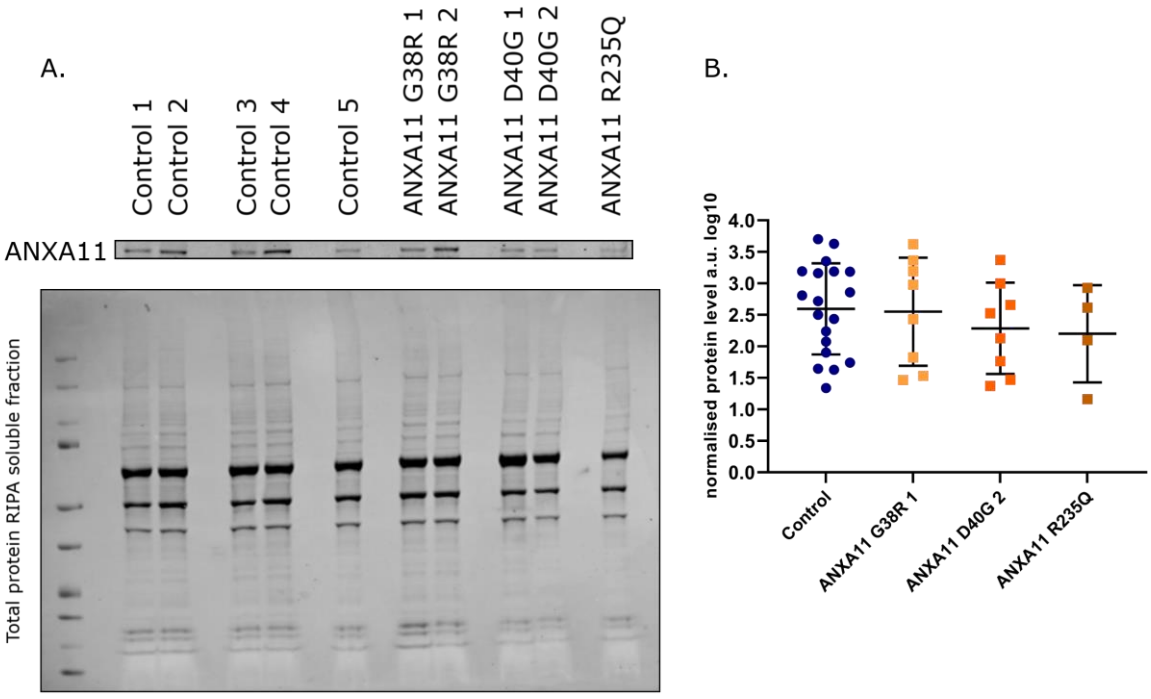


***Figure 4.9 Annexin A11 protein abundance in iPSC-derived motor neurons***

(A) Representative western blot with RIPA-soluble protein harvested from motor neurons on day 17 of differentiation, probed for Annexin A11 and total protein stain. (B) Annexin A11 protein was measured and normalised to total protein. Data are presented as mean ± SEM, *n* = 4. Each data point represents relative Annexin A11 protein abundance in one cell line in one motor neuron induction,

control lines are grouped and *ANXA11* ALS patient lines are grouped by mutation. Statistical analysis: Ordinary one-way ANOVA with Dunnett's multiple comparisons test ($p > 0.05$).

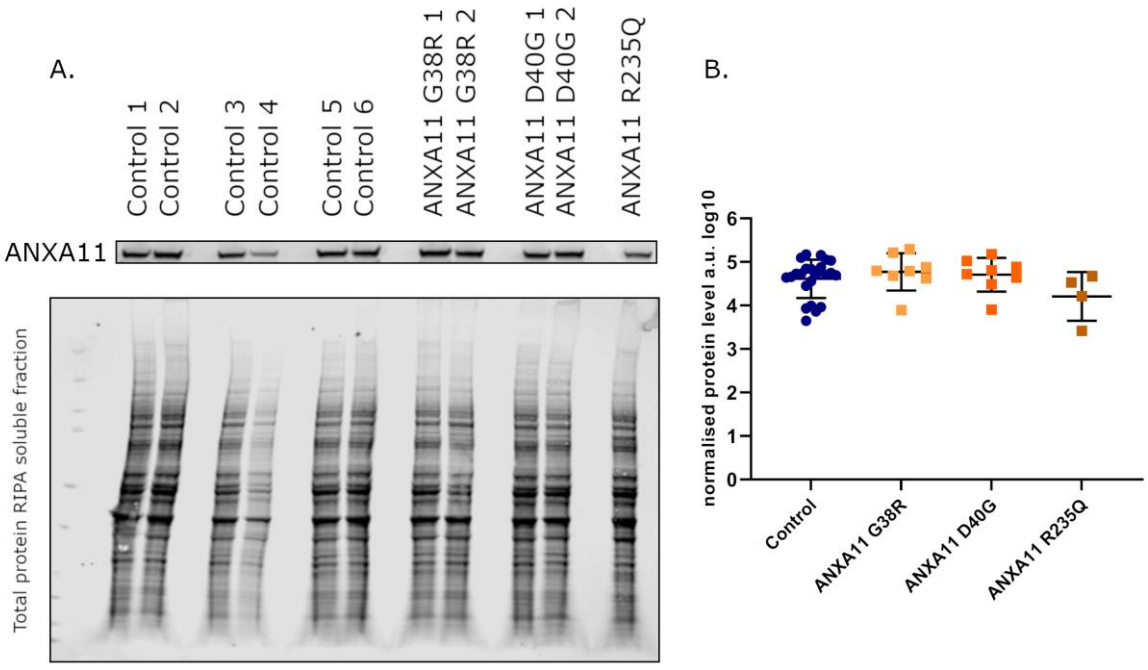


***Figure 4.10 Annexin A11 protein abundance in iPSC-derived astrocytes***

(A) Representative western blot with RIPA-soluble protein harvested from iPSC-derived astrocytes on day ~35 of differentiation, probed for Annexin A11 and total protein stain. (B) Annexin A11 protein was measured and normalised to total protein. Data are presented as mean ± SEM, $n = 4$. Each data point represents relative Annexin A11 protein abundance in one cell line in one biological replicate, control lines are grouped and *ANXA11* ALS patient lines are grouped by mutation. Statistical analysis: Ordinary one-way ANOVA with Dunnett's multiple comparisons test ($p > 0.05$).

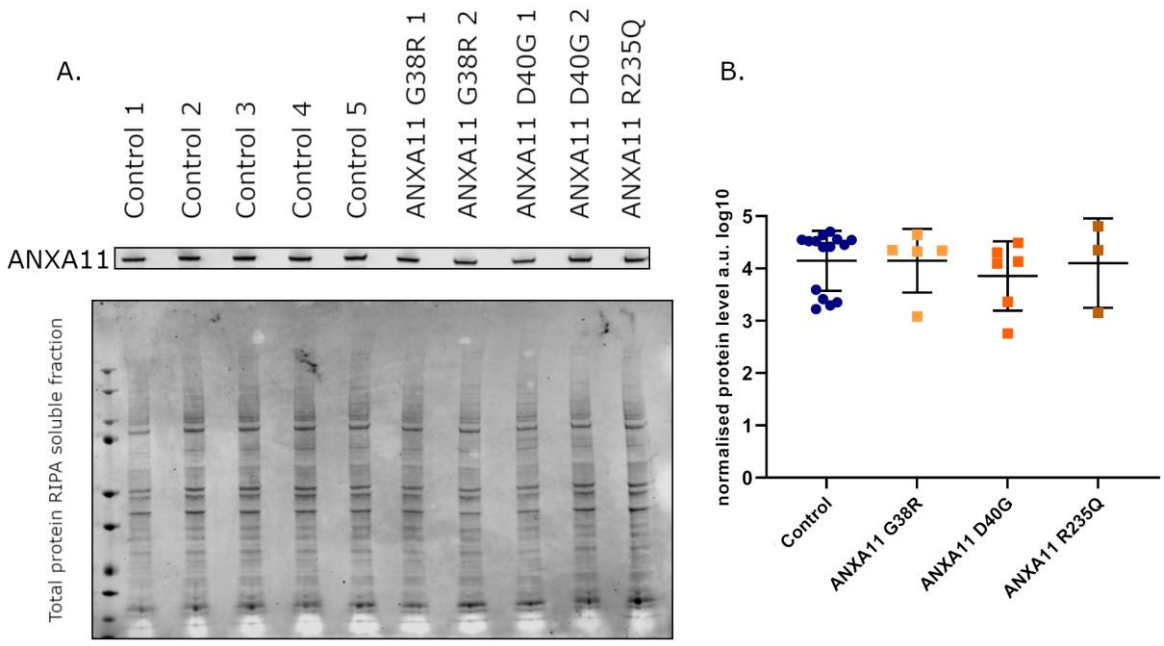


***Figure 4.11 Annexin A11 protein abundance in iPSCs***

(A) Representative western blot loaded with RIPA-soluble protein harvested from iPSCs, probed for Annexin A11 and total protein stain. (B) Annexin A11 protein was measured and normalised to total protein. Data are presented as mean ± SEM, $n$ = 3. Each data point represents relative Annexin A11 protein abundance in one cell line in one biological replicate, control lines are grouped and *ANXA11* ALS patient lines are grouped by mutation. Statistical analysis: Ordinary one-way ANOVA with Dunnett's multiple comparisons test ($p > 0.05$).

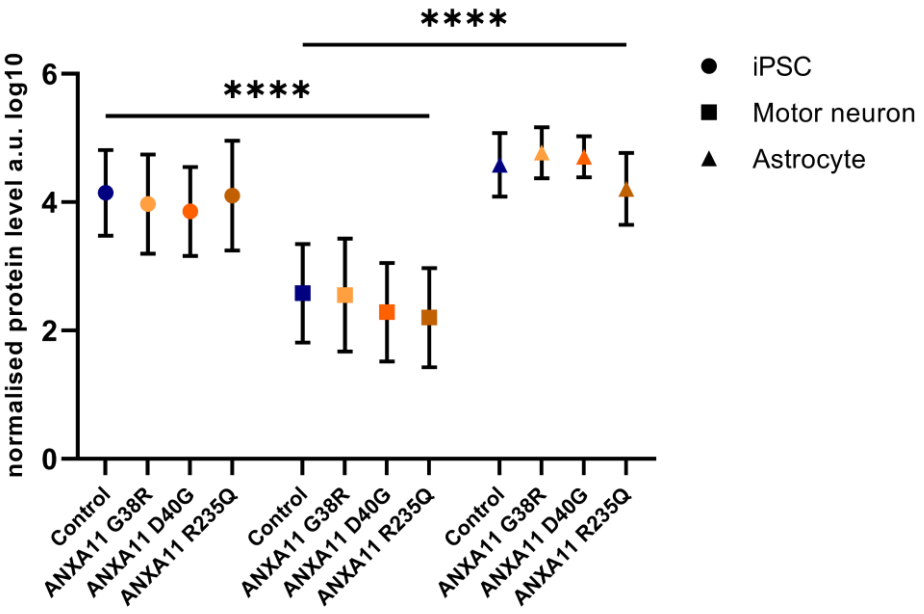


***Figure 4.12 Annexin A11 relative protein abundance is reduced in motor neurons compared to iPSCs and astrocytes***

Annexin A11 protein abundance was measured in iPSCs, motor neurons, and astrocytes, and was normalised to total protein in each instance. Relative Annexin A11 protein abundance was reduced in 17-day old motor neurons compared to iPSCs and astrocytes at day ~35 of differentiation ($p \leq 0.0001$). Data are presented as mean ± SD, $n$ = 3-4. Statistical analysis: Ordinary two-way ANOVA with Tukey's multiple comparisons test (****$p \leq 0.0001$). (Related to Figure 4.9, Figure 4.10, and Figure 4.11.)

### *4.3.3 High throughput characterisation of TDP-43 in ANXA11 patient and control motor neurons*

Motor neurons derived from control and *ANXA11mut* ALS patient iPSCs were probed for TDP-43 localisation and spot characteristics in motor neurons in co-culture with astrocytes on day 17 and 42 of motor neuron differentiation. Detailed analysis of TDP-43 localisation in motor neuron monocultures on day 17 of differentiation is not reported due to corruption of image data files before image quantification, and experiments could not be repeated due to limitations with time. The nucleocytoplasmic ratio was quantified before data files became corrupt and is included in the comparison of nucleocytoplasmic ratio across culture conditions (Figure 4.17.A). Equally, representative images could not be collected from corrupted data files and are not included. Representative images of TDP-43 localisation in day-17 motor neurons in co-culture with astrocytes

are included in Figure 4.13 and Figure 4.14, and representative images of day-42 motor neurons in astrocyte co-culture are included in Figure 4.15 and Figure 4.16.

TDP-43 nucleocytoplasmic ratio was increased in day-17 co-cultured motor neurons compared to day-17 motor neuron only cultures and day-42 co-cultured neurons, with no difference observed between control and any *ANXA11mut* group in any culture paradigm (Figure 4.17.A). TDP-43 localisation was dynamic, particularly in aged neurons, where large SDs indicate that nucleocytoplasmic localisation is variable in both control and *ANXA11mut* lines. The mean TDP-43 nucleocytoplasmic ratio of day-42 co-cultured neurons was increased compared to day-17 motor neuron only cultures, which was not statistically significant, likely due to the large variability across biological replicates in day-42 neurons.

In co-cultured neurons, nuclear TDP-43 spot size was increased in day-17 motor neurons compared to day-42 (Figure 4.17.C), with no difference observed between cytoplasmic spot size (Figure 4.17.D). Additionally, an increase in the number of nuclear spots was observed in day-17 co-cultured motor neurons compared to day-42, and a significant increase in TDP-43 nuclear spot count was observed in *ANXA11* G38R and *ANXA11* R235Q groups compared to control (Figure 4.17.E). No change was detected in the number of cytoplasmic spots across any condition, and considerable variability was seen in this measurement (Figure 4.17.F).

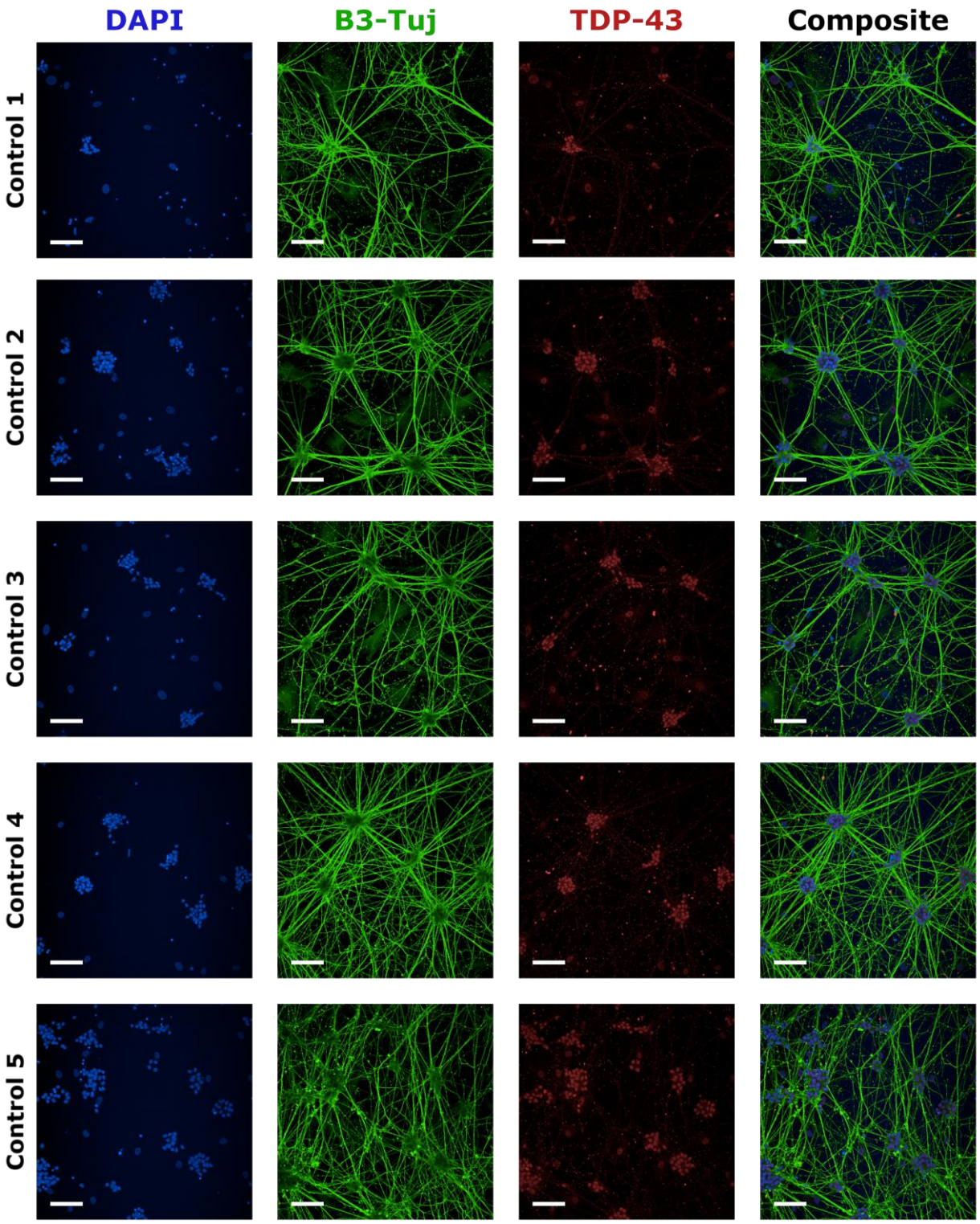


***Figure 4.13 TDP-43 in young control motor neurons maintained in co-culture with astrocytes***

Representative images of control motor neurons maintained in co-culture with astrocytes, fixed on day 17 of motor neuron differentiation. Cultures were probed for $\beta$3-Tubulin (B3-Tuj, green) and TDP-43 (red), co-stained with DAPI (blue), and imaged with the Opera Phenix® High-Content Screening System. Scale bars represent 100µm.

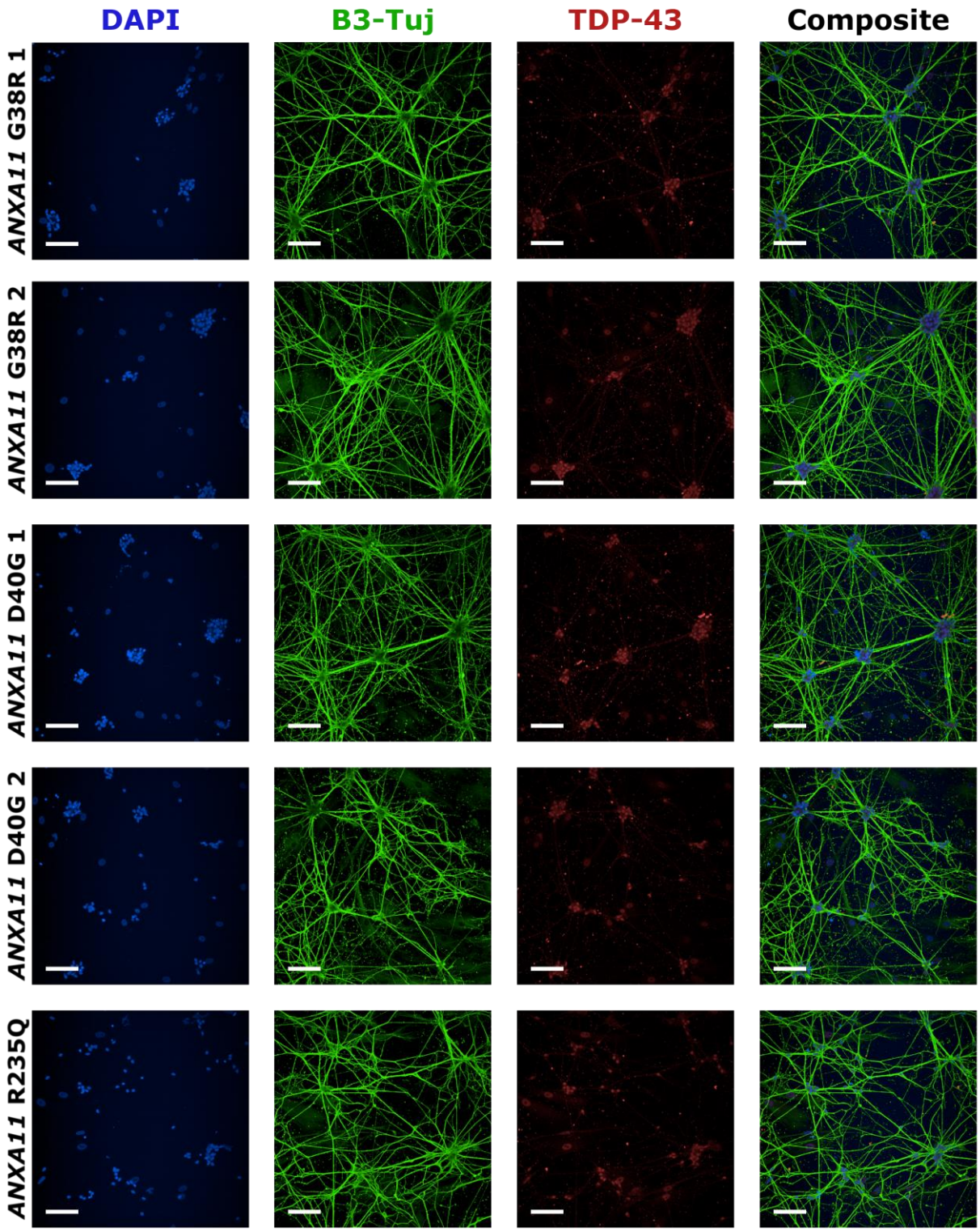


***Figure 4.14 TDP-43 in young ANXA11mut motor neurons maintained in co-culture with astrocytes***

Representative images of *ANXA11mut* motor neurons maintained in co-culture with astrocytes, fixed on day 17 of motor neuron differentiation. Cultures were probed for $\beta$3-Tubulin (B3-Tuj, green) and TDP-43 (red), co-stained with DAPI (blue), and imaged with the Opera Phenix® High-Content Screening System. Scale bars represent 100µm.

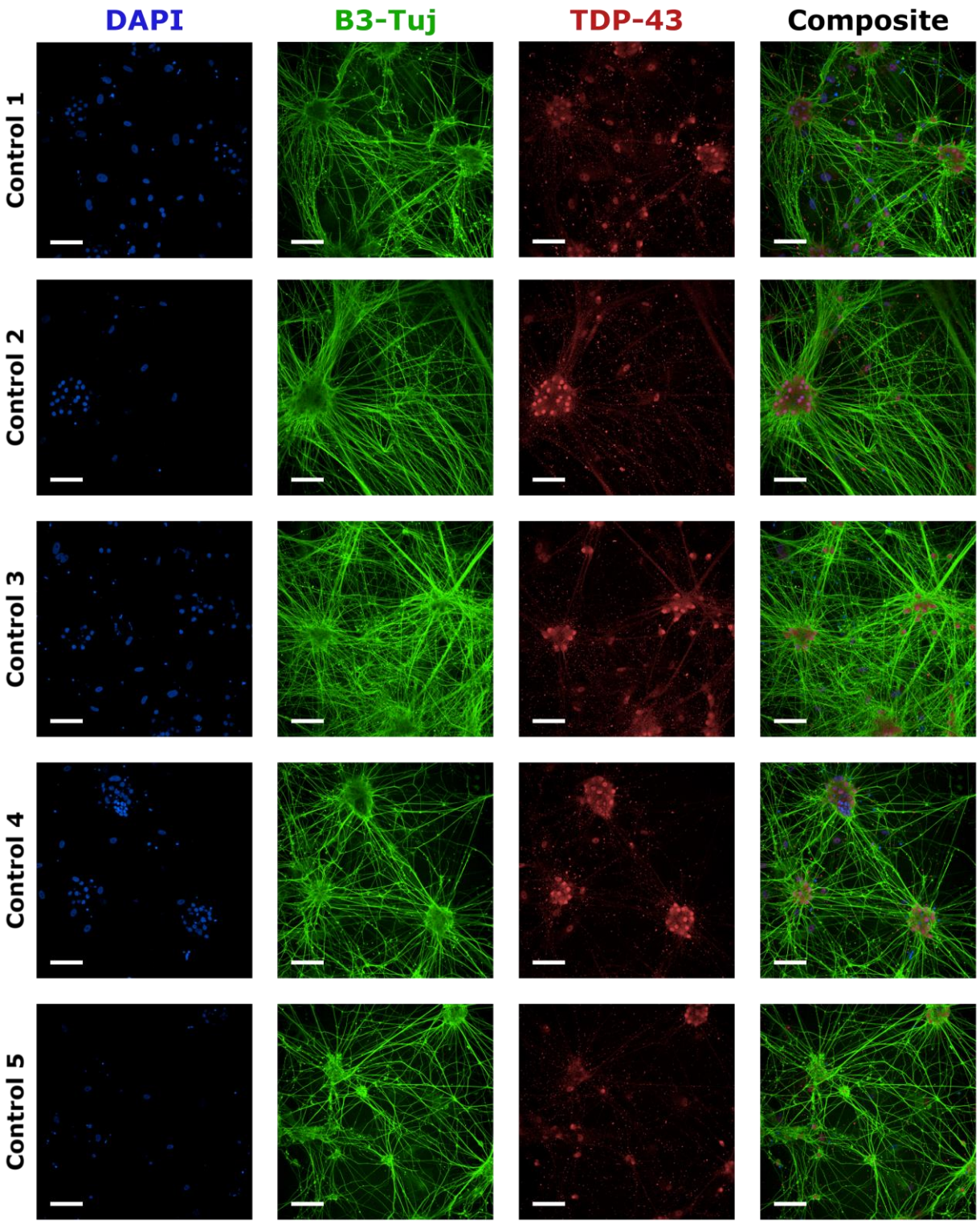


***Figure 4.15 TDP-43 in aged control motor neurons maintained in co-culture with astrocytes***

Representative images of control motor neurons maintained in co-culture with astrocytes, fixed on day 42 of motor neuron differentiation. Cultures were probed for $\beta$3-Tubulin (B3-Tuj, green) and TDP-43 (red), co-stained with DAPI (blue), and imaged with the Opera Phenix® High-Content Screening System. Scale bars represent 100µm.

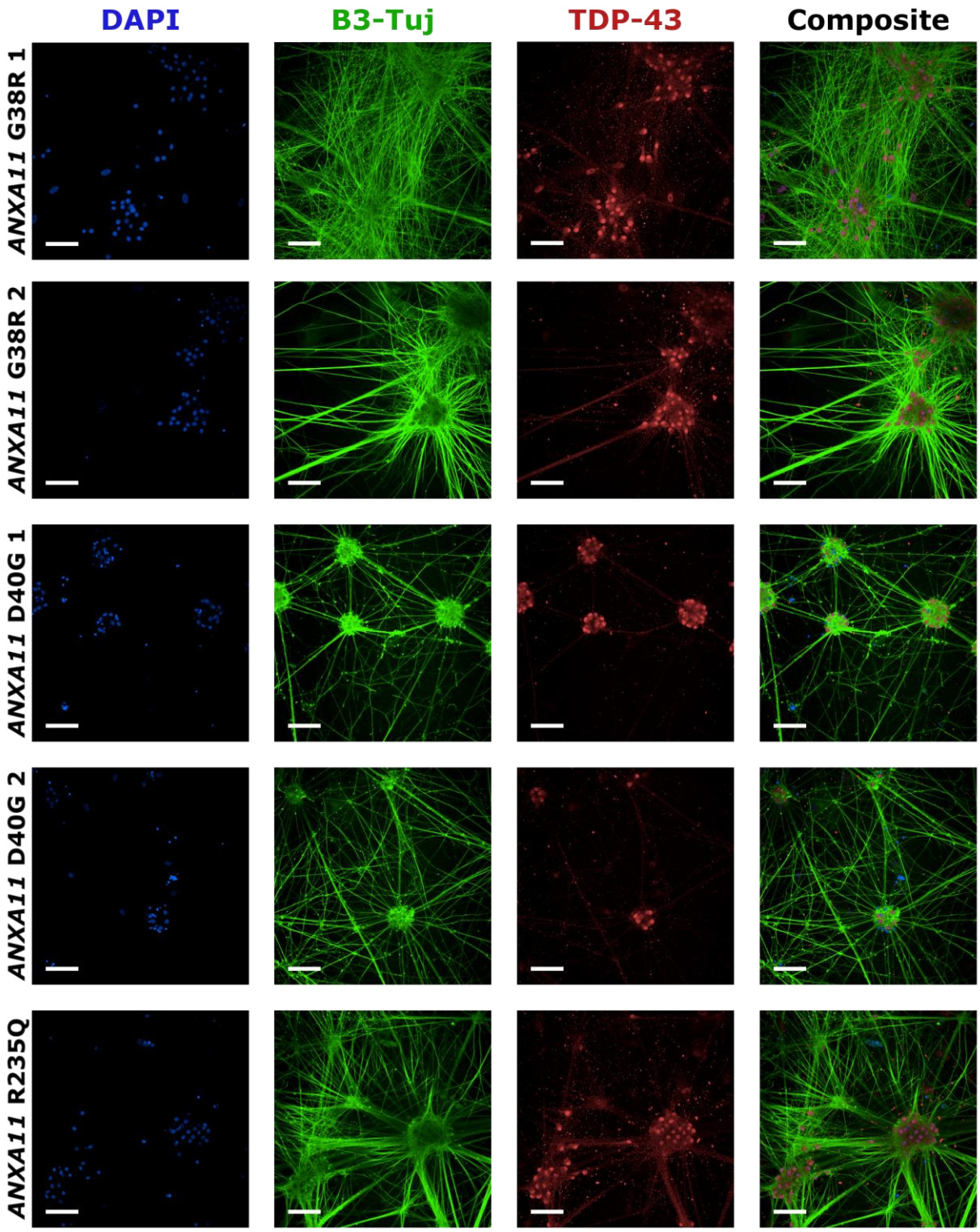


***Figure 4.16 TDP-43 in aged ANXA11mut motor neurons maintained in co-culture with astrocytes***

Representative images of *ANXA11mut* motor neurons maintained in co-culture with astrocytes, fixed on day 42 of motor neuron differentiation. Cultures were probed for $\beta$3-Tubulin (B3-Tuj, green) and TDP-43 (red), co-stained with DAPI (blue) and imaged with the Opera Phenix® High-Content Screening System. Scale bars represent 100µm.

A. TDP-43 nucleocytoplasmic ratio

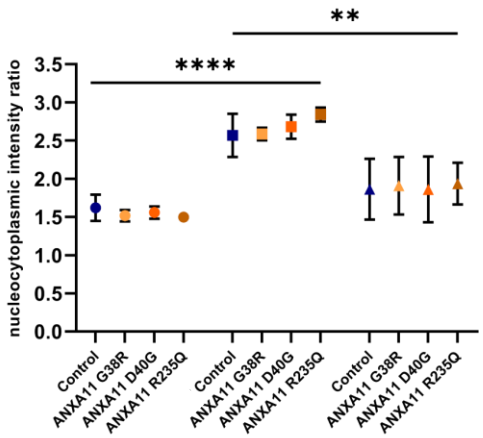


B.

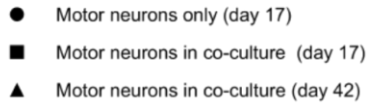


Nucleus

Cytoplasm

C. TDP-43 spot size

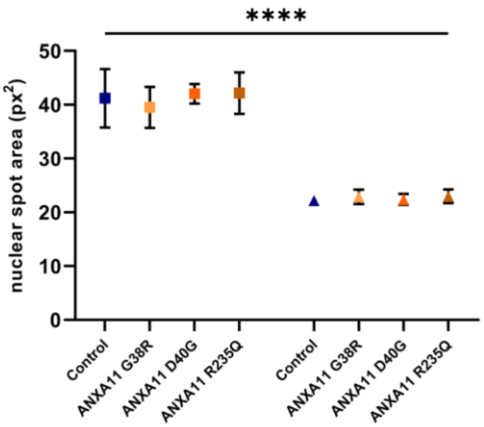


D. TDP-43 spot size

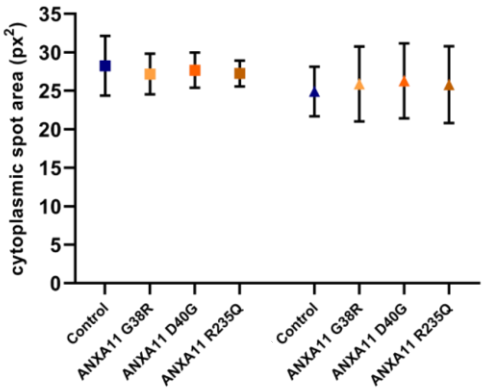


E. TDP-43 spot count

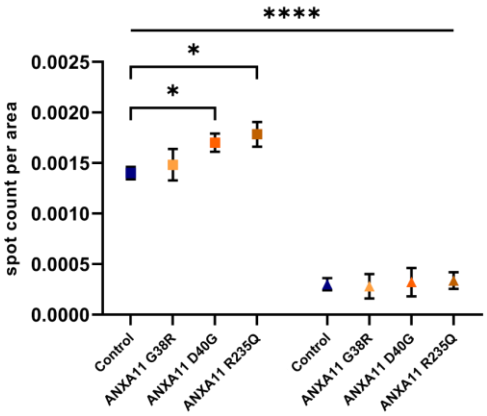


F. TDP-43 spot count

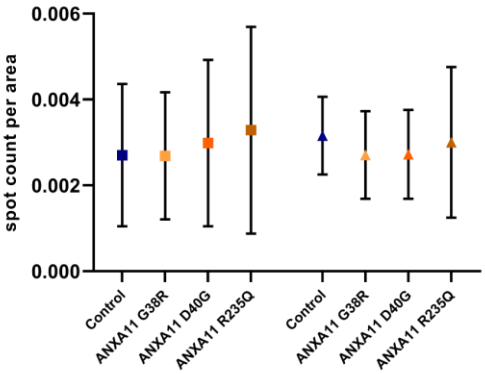

***Figure 4.17 TDP-43 nucleocytoplasmic ratio and spot analysis across culture paradigms***

Quantification of data represented in Figures 4.13-4.16. (A) The nucleocytoplasmic ratio of TDP-43 in motor neurons on day 17 of differentiation with and without co-culture with astrocytes, and motor neurons at day 42 of differentiation maintained in co-culture with astrocytes. TDP-43 was more nuclear in day-17 motor neurons maintained in co-culture compared to motor neuron only cultures ($p \leq 0.0001$) and day-42 co-cultured motor neurons ($p = 0.0011$). (B) Culture paradigm key, relevant to A, C, D, E, F. (C) TDP-43 nuclear spot size was increased in day-17 co-cultured neurons compared to day-42 co-cultured motor neurons ($p \leq 0.0001$). (D) TDP-43 cytoplasmic spot size was consistent across groups. (E) TDP-43 nuclear spot count was increased in day-17 co-cultured neurons compared to day-42 co-cultured neurons ($p \leq 0.0001$) and was increased in *ANXA11* D40G ($p = 0.0417$) and *ANXA11* R235Q ($p = 0.0105$) groups compared to control in day-17 co-cultured motor neurons. (F) TDP-43 cytoplasmic spot count was variable, with no significant differences across groups. Data are presented as mean ± SD, number of motor neuron inductions = 2-3; each data point represents the mean value from all cell lines in control and *ANXA11mut* groups across two-three motor neuron inductions, each comprised of three technical replicates. Statistical analysis: Ordinary two-way ANOVA with Tukey's multiple comparisons test (*$p \leq 0.05$; **$p \leq 0.01$; ****$p \leq 0.0001$).

### *4.3.4 Quantification of TDP-43 protein in control and ANXA11 ALS patient-derived stem cell models*

Relative TDP-43 protein abundance was unchanged across control and *ANXA11mut* groups in day-17 motor neurons (Figure 4.18) and astrocytes (Figure 4.19). An increase in RIPA-soluble TDP-43 was detected in *ANXA11* R235Q iPSCs compared to control (Figure 4.20). However, it should be noted that this appears to be driven by a single data point, and significance was lost when all TDP-43 western blot data were compared using two-way ANOVA (Figure 4.21). A comparison of relative TDP-43 abundance across different cell types revealed reduced TDP-43 in motor neurons compared to iPSCs (Figure 4.21).

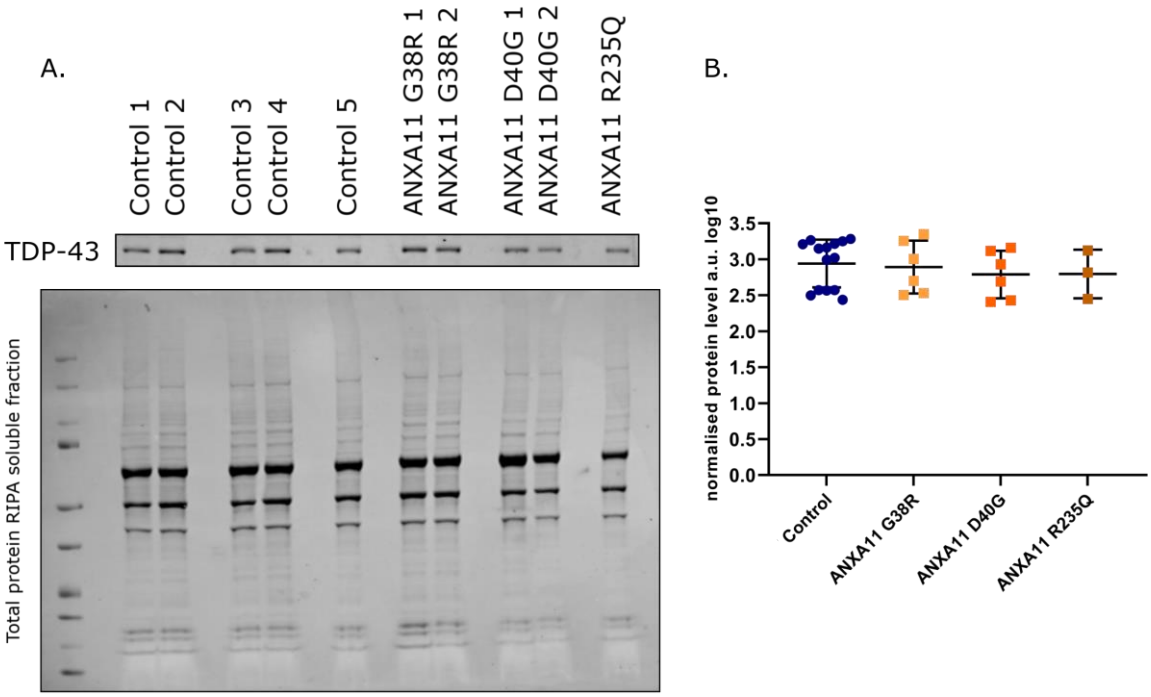


***Figure 4.18 TDP-43 protein abundance in iPSC-derived motor neurons***

(A) Representative western blot with RIPA-soluble protein harvested from motor neurons on day 17 of differentiation, probed for TDP-43 and total protein stain. (B) TDP-43 protein was measured and normalised to total protein. Data are presented as mean ± SEM, number of motor neuron inductions = 3. Each data point represents relative TDP-43 protein abundance in one cell line in one motor neuron induction, control lines are grouped and *ANXA11* ALS patient lines are grouped by mutation. Statistical analysis: Ordinary one-way ANOVA with Dunnett's multiple comparisons test ($p > 0.05$).

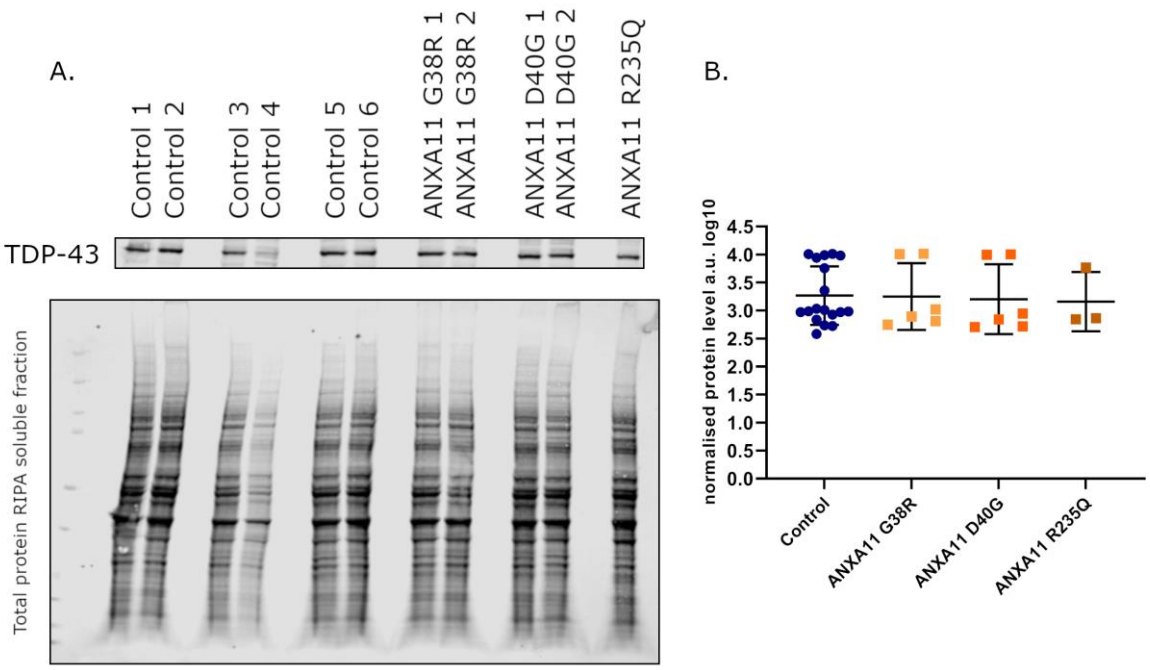


***Figure 4.19 TDP-43 protein abundance in iPSC-derived astrocytes***

(A) Representative western blot loaded with RIPA-soluble protein harvested from iPSC-derived astrocytes on day ~35 of differentiation, probed for TDP-43 and total protein stain. (B) TDP-43 protein was measured and normalised to total protein. Data are presented as mean ± SEM, *n* = 3. Each data point represents relative TDP-43 protein abundance in one cell line in one biological replicate, control lines are grouped and *ANXA11* ALS patient lines are grouped by mutation. Statistical analysis: Ordinary one-way ANOVA with Dunnett's multiple comparisons test ($p > 0.05$).

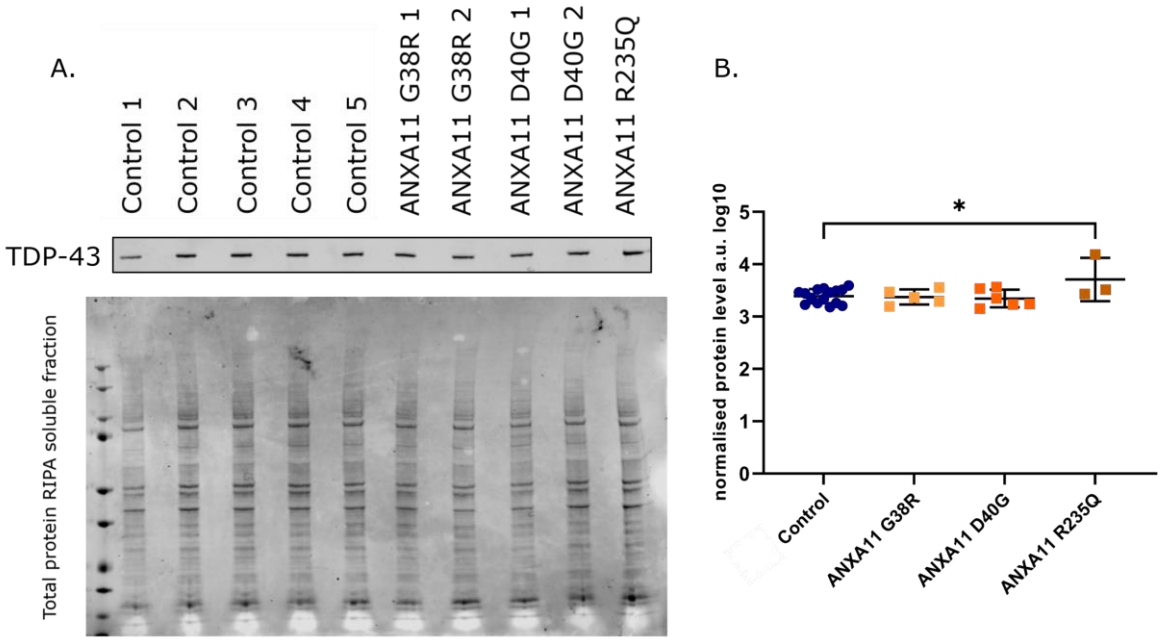


***Figure 4.20 TDP-43 protein abundance in iPSCs***

(A) Representative western blot loaded with RIPA-soluble protein harvested from iPSCs, probed for TDP-43 and total protein stain. (B) TDP-43 protein was measured and normalised to total protein and was increased in *ANXA11* R235Q iPSCs compared to control ($p = 0.0301$). Data are presented as mean ± SEM, $n = 3$. Each data point represents relative TDP-43 protein abundance in one cell line in one biological replicate, control lines are grouped and *ANXA11* ALS patient lines are grouped by mutation. Statistical analysis: Ordinary one-way ANOVA with Dunnett's multiple comparisons test (*$p \leq 0.05$).

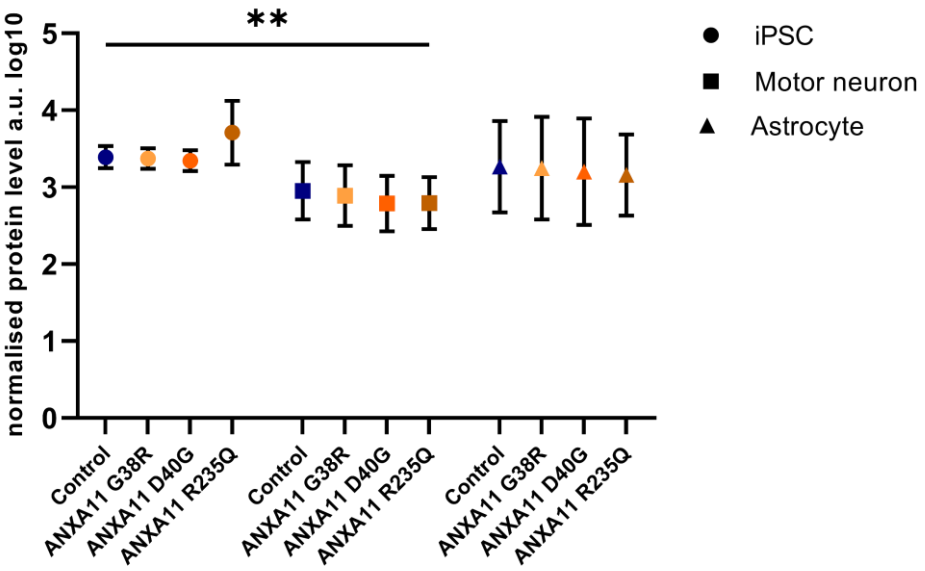


***Figure 4.21 TDP-43 relative protein abundance is reduced in motor neurons compared to iPSCs***

Related to Figure 4.18, Figure 4.18, and Figure 4.20. TDP-43 protein abundance was measured in iPSCs, motor neurons, and astrocytes, and was normalised to total protein in each instance. TDP-43 relative protein expression was reduced in day-17 motor neurons compared to iPSCs ($p$ = 0.0076). Astrocyte protein was collected on day ~35 of differentiation. Data are presented as mean ± SD, $n$ = 3. Statistical analysis: Ordinary two-way ANOVA with Tukey's multiple comparisons test (**$p \leq 0.01$).

### *4.3.5 High-throughput characterisation of pTDP-43 in ANXA11 patient and control motor neurons*

pTDP-43 signal was consistently detected in motor neurons (Figure 4.22; Figure 4.23; Figure 4.24; Figure 4.25; Figure 4.26; Figure 4.27). The nucleocytoplasmic ratio of pTDP-43 was consistent between control and *ANXA11* mutation groups, and across various cell culture paradigms, with no statistically significant differences observed in any condition (Figure 4.28.A).

High-throughput spot analysis indicates increased pTDP-43 nuclear spot size in day-42 compared to day-17 co-cultured motor neurons (Figure 4.28.C). The cytoplasmic spot size was increased in day-42 co-cultured neurons compared to both day 17 culture conditions (Figure 4.28.D). The number of nuclear pTDP-43 spots was highly variable, and no statistically significant differences were observed between *ANXA11* mutation groups and control, or between culture conditions (Figure 4.28.E). The

number of cytoplasmic pTDP-43 spots was also variable, with the total number of spots decreasing in the day-42 co-cultured neurons compared to other culture conditions (Figure 4.28.F). A trend toward increased pTDP-43 spot count in *ANXA11* D40G neurons was observed in nuclear and cytoplasmic spot count in day-17 motor neuron only cultures, which was not significant in two-way analysis (Figure 4.28.E; Figure 4.28.F).

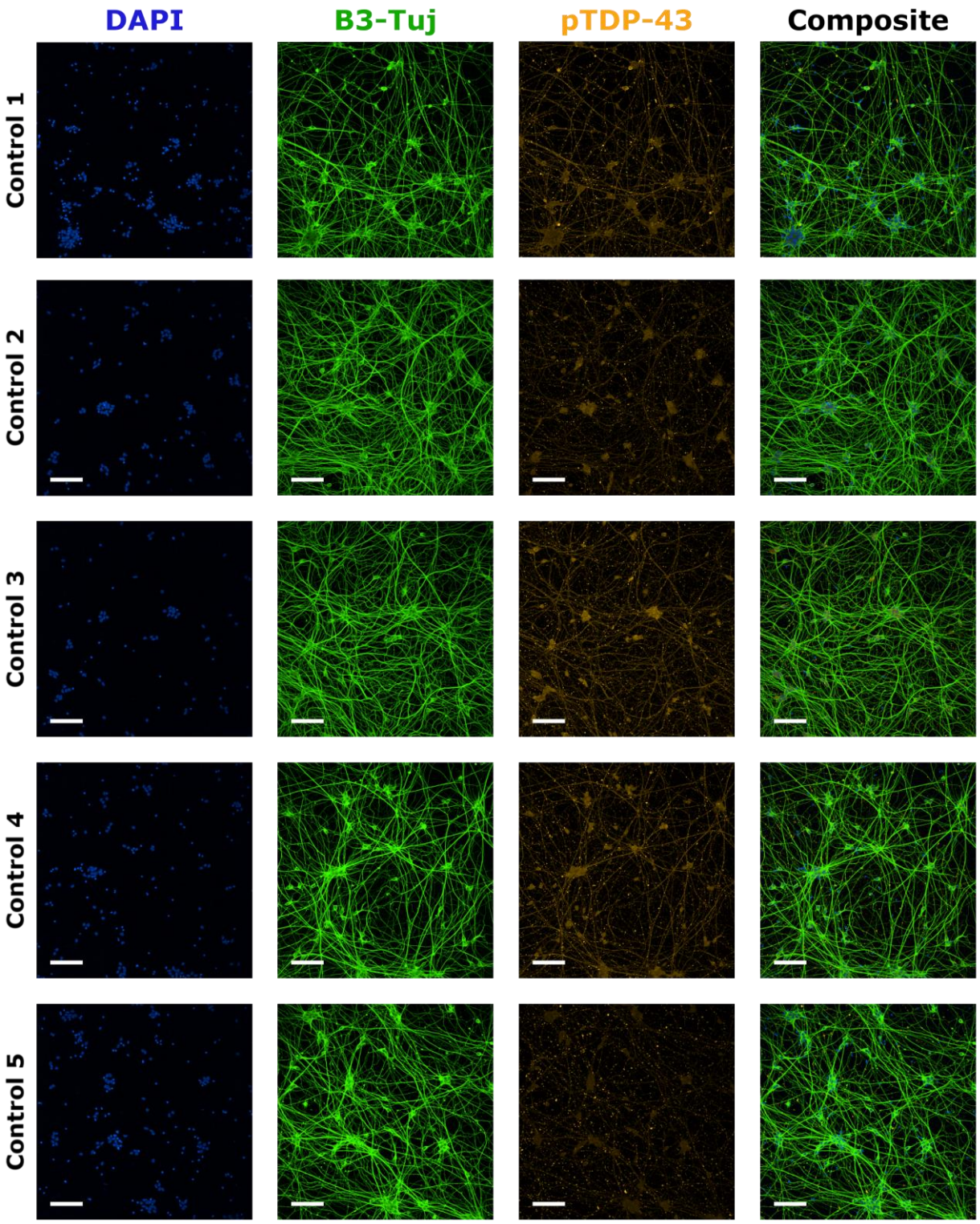


***Figure 4.22 pTDP-43 in young control motor neurons***

Representative images of control motor neurons fixed on day 17 of differentiation. Cultures were probed for $\beta$3-Tubulin (B3-Tuj, green) and pTDP-43 (orange), co-stained with DAPI (blue) and imaged with the Opera Phenix® High-Content Screening System. Scale bars represent 100µm.

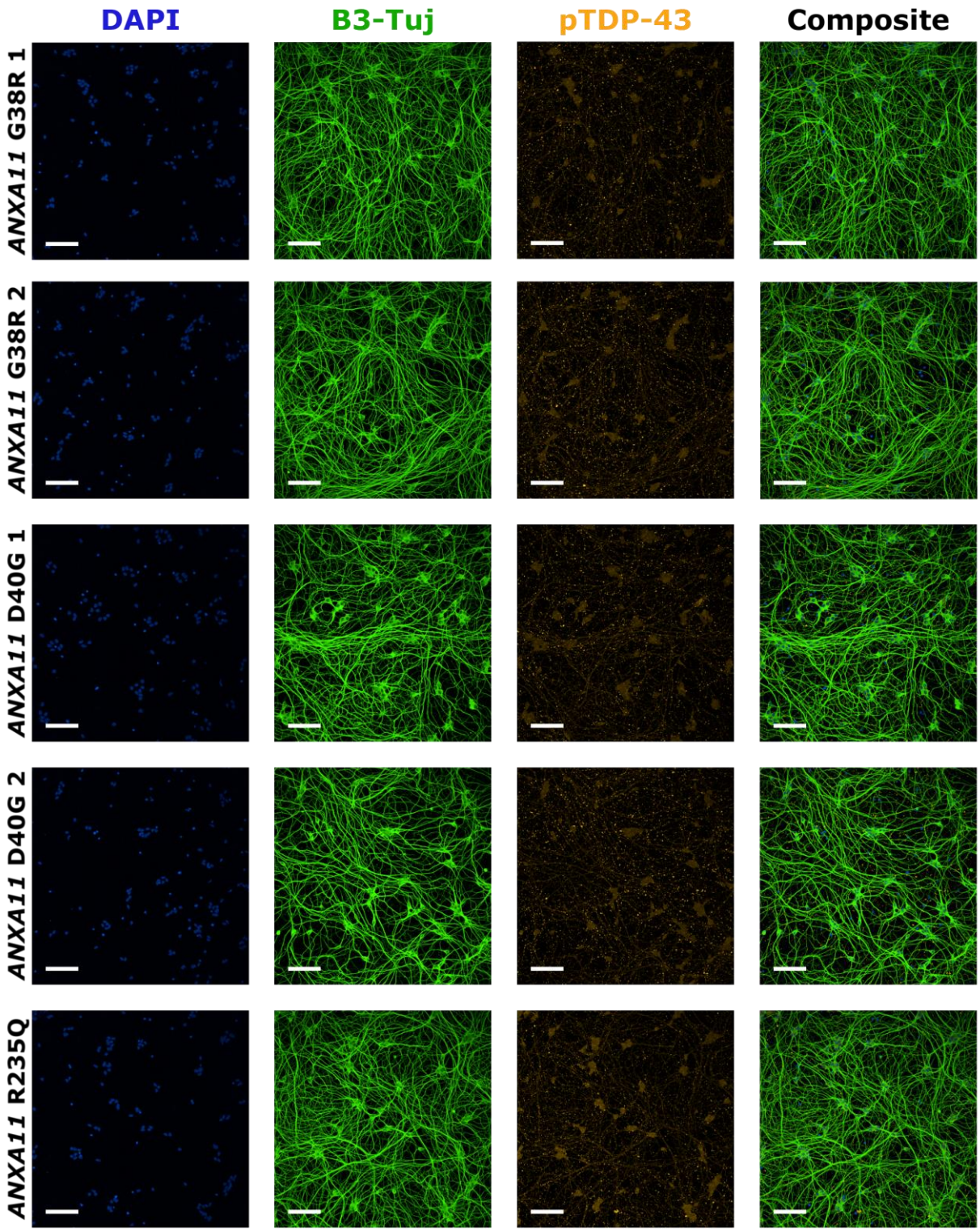


***Figure 4.23 pTDP-43 in young ANXA11mut patient motor neurons***

Representative images of *ANXA11mut* motor neurons fixed on day 17 of differentiation. Cultures were probed for $\beta$3-Tubulin (B3-Tuj, green) and pTDP-43 (orange), and imaged with the Opera Phenix® High-Content Screening System. Scale bars represent 100µm.

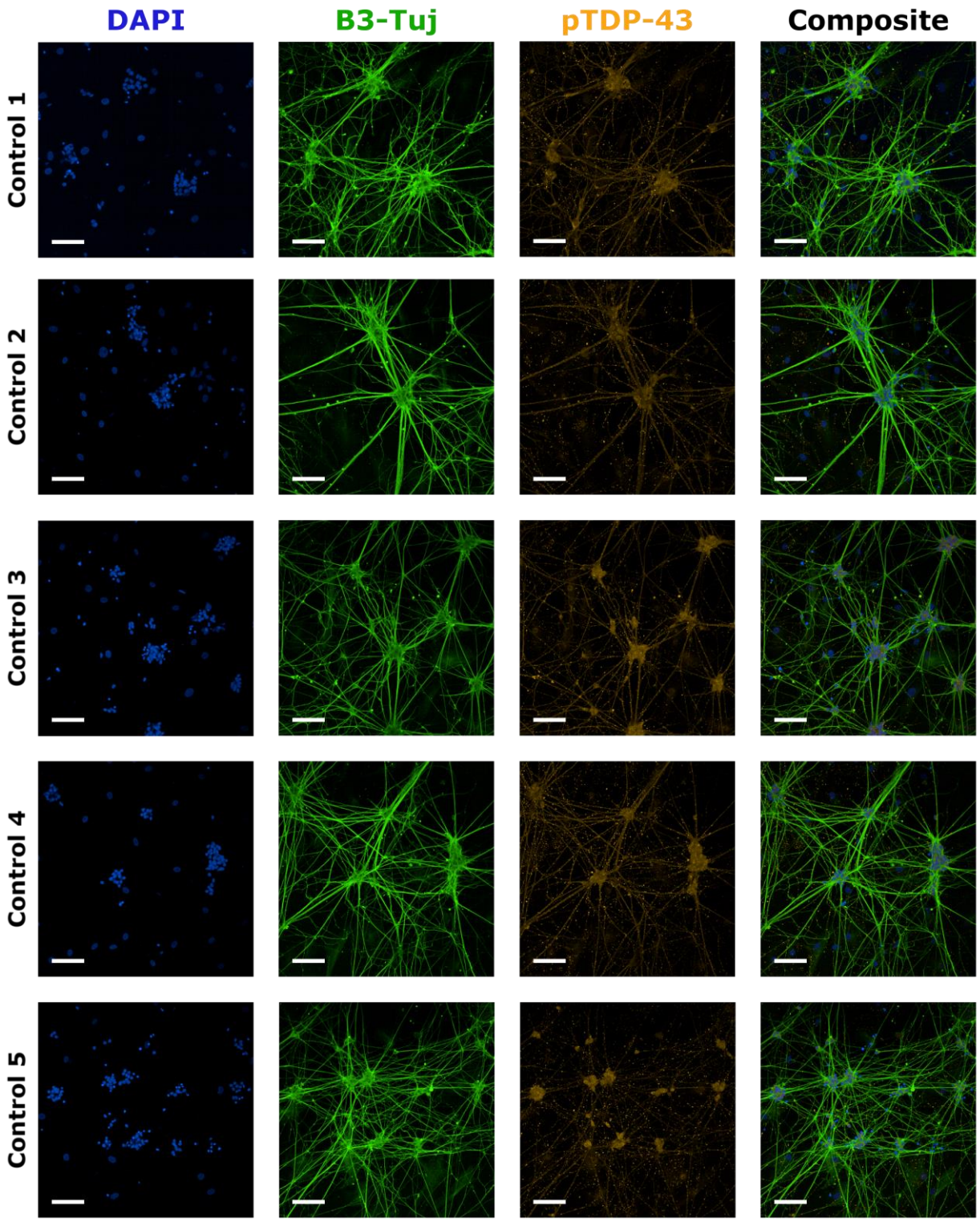


***Figure 4.24 pTDP-43 in young control motor neurons maintained in co-culture with astrocytes***

Representative images of control motor neurons maintained in co-culture with astrocytes, fixed on day 17 of motor neuron differentiation. Cultures were probed for $\beta$3-Tubulin (B3-Tuj, green) and pTDP-43 (orange), co-stained with DAPI (blue) and imaged with the Opera Phenix® High-Content Screening System. Scale bars represent 100µm.

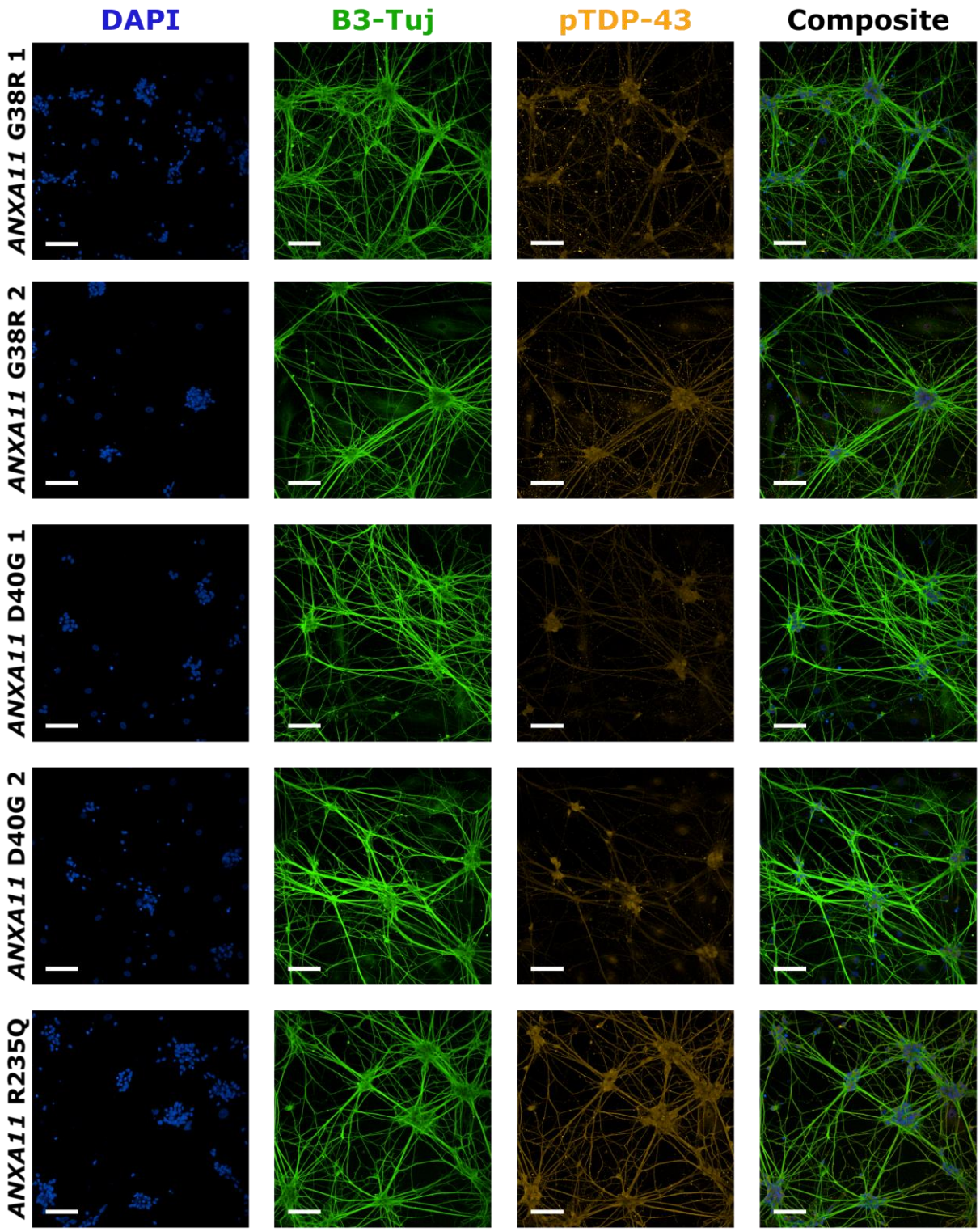


***Figure 4.25 pTDP-43 in young ANXA11mut motor neurons maintained in co-culture with astrocytes***

Representative images of *ANXA11mut* motor neurons maintained in co-culture with astrocytes, fixed on day 17 of motor neuron differentiation. Cultures were probed for $\beta$3-Tubulin (B3-Tuj, green) and pTDP-43 (orange), co-stained with DAPI (blue) and imaged with the Opera Phenix® High-Content Screening System. Scale bars represent 100µm.

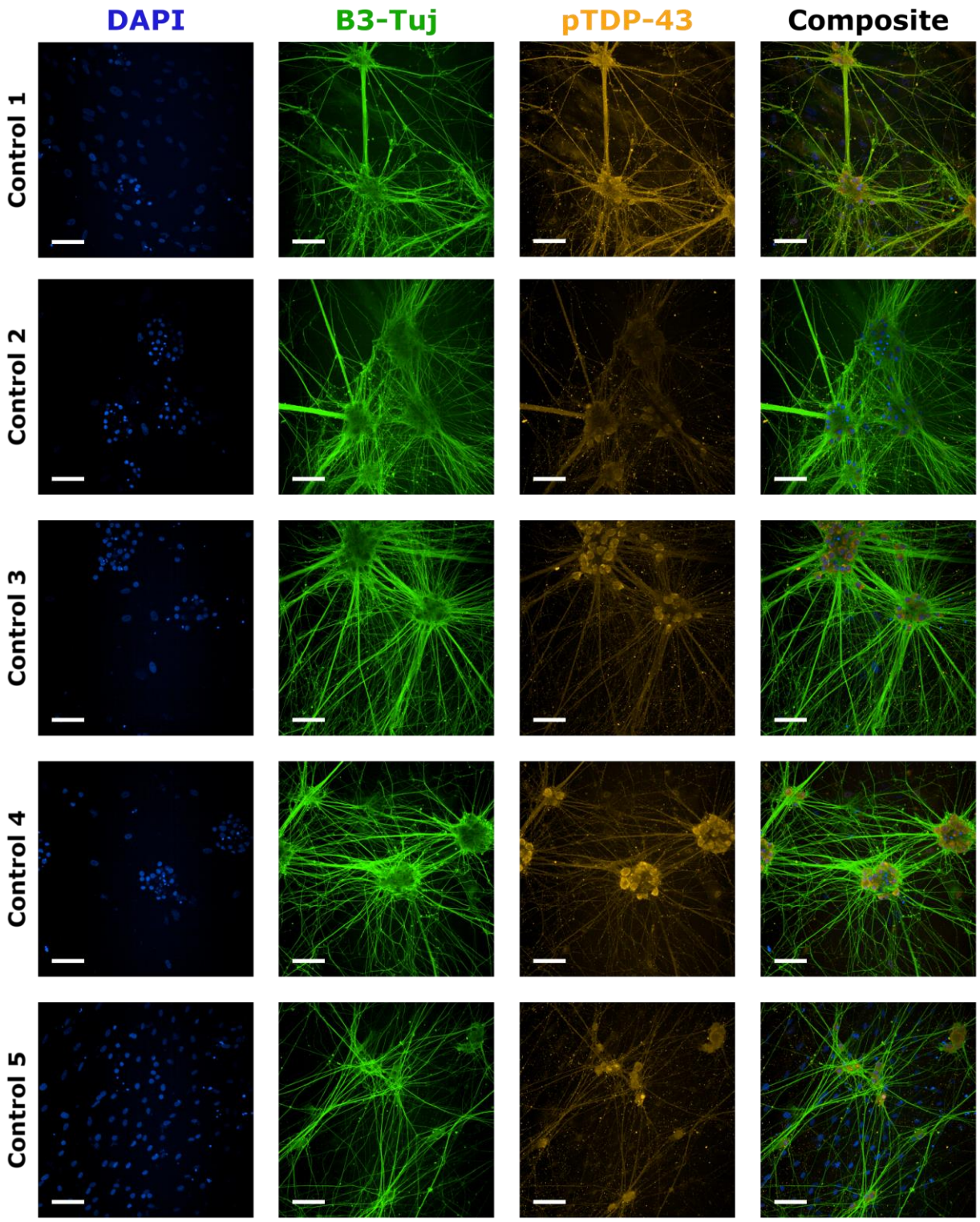


***Figure 4.26 pTDP-43 in aged control motor neurons maintained in co-culture with astrocytes***

Representative images of control motor neurons maintained in co-culture with astrocytes, fixed on day 42 of motor neuron differentiation. Cultures were probed for $\beta$3-Tubulin (B3-Tuj, green) and pTDP-43 (orange), co-stained with DAPI (blue) and imaged with the Opera Phenix® High-Content Screening System. Scale bars represent 100µm.

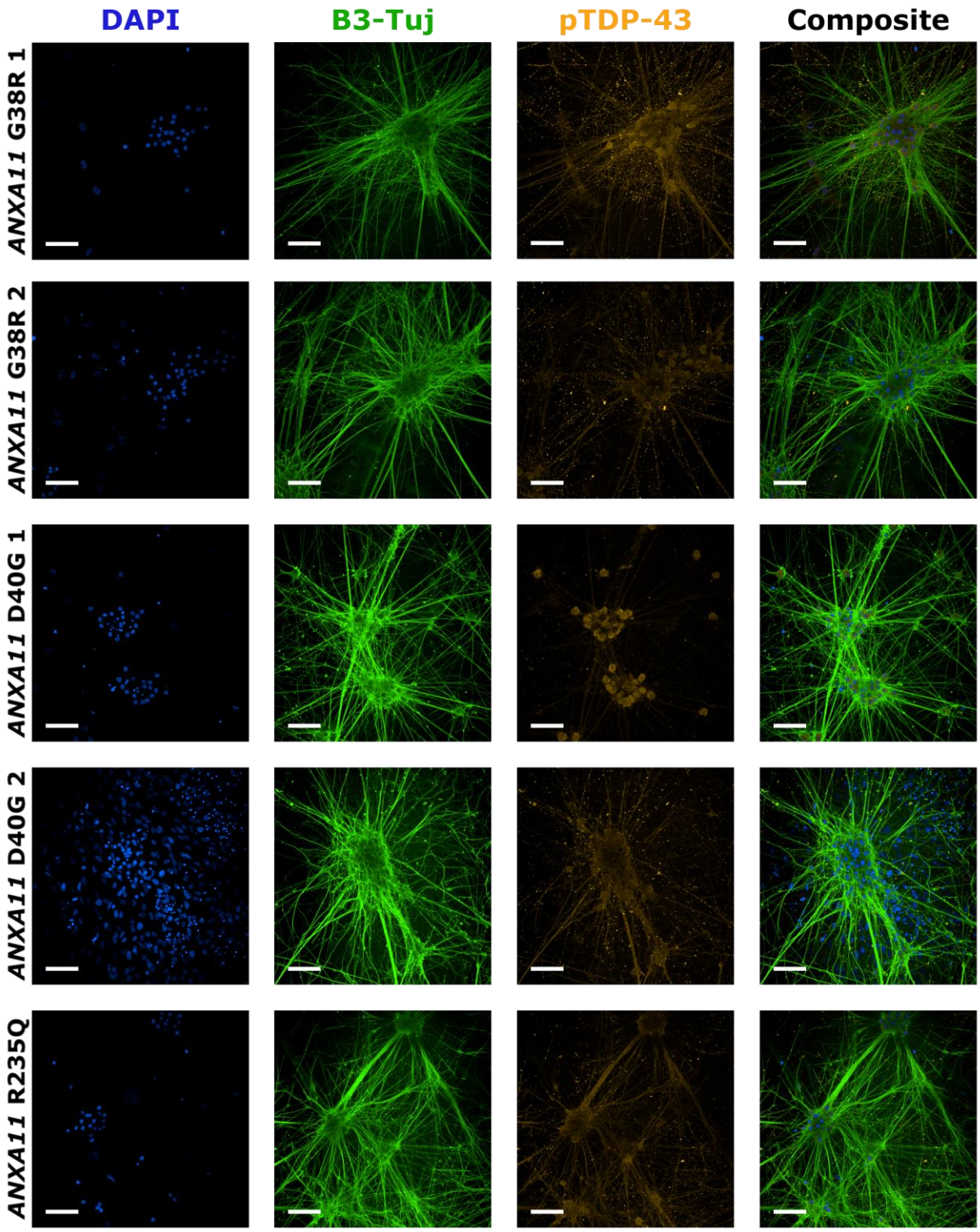


***Figure 4.27 pTDP-43 in aged ANXA11mut motor neurons maintained in co-culture with astrocytes***

Representative images of *ANXA11mut* motor neurons maintained in co-culture with astrocytes, fixed on day 42 of motor neuron differentiation. Cultures were probed for $\beta$3-Tubulin (B3-Tuj, green) and pTDP-43 (orange), co-stained with DAPI (blue) and imaged with the Opera Phenix® High-Content Screening System. Scale bars represent 100µm.

A. pTDP-43 nucleocytoplasmic ratio

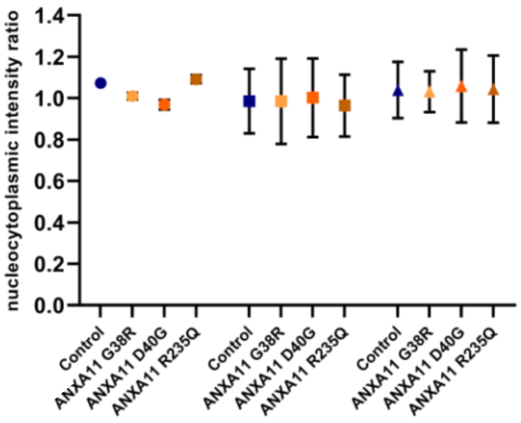


B.

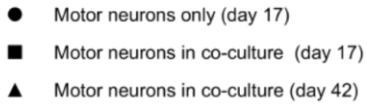


Nucleus

Cytoplasm

C. pTDP-43 spot size

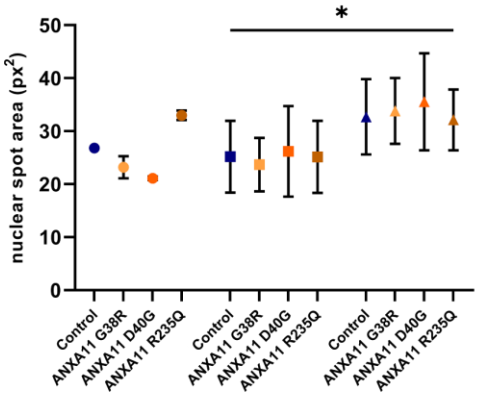


D. pTDP-43 spot size

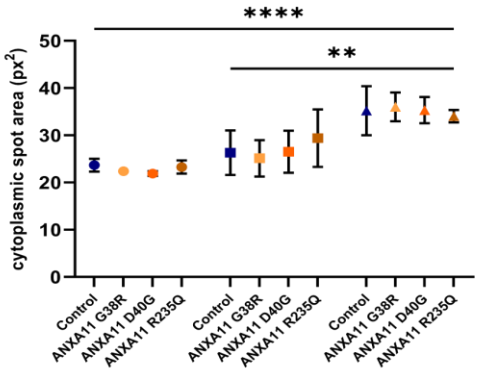


E. pTDP-43 spot count

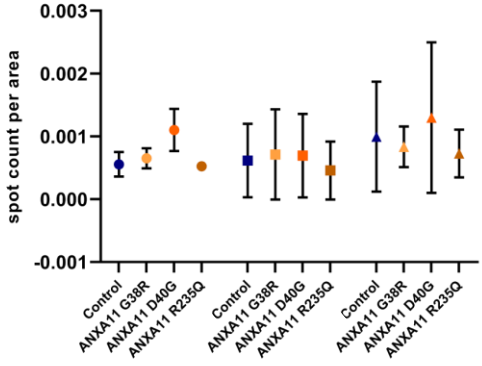


F. pTDP-43 spot count

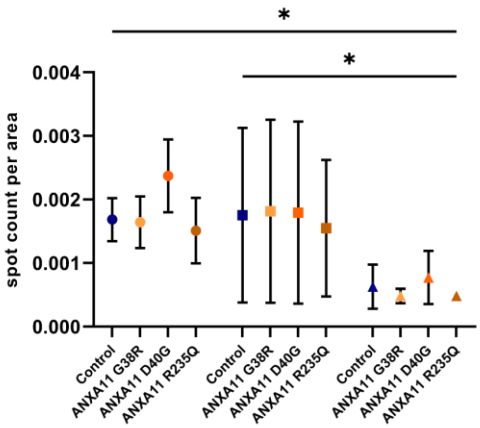

***Figure 4.28 pTDP-43 nucleocytoplasmic ratio and spot characteristics across culture paradigms***

Quantification of data represented in Figures 4.22-4.27. (A) The nucleocytoplasmic ratio of pTDP-43 in motor neurons on day 17 of differentiation with and without co-culture with astrocytes, and motor neurons on day 42 of differentiation maintained in co-culture with astrocytes. (B) Culture paradigm key, relevant to A, C, D, E, F. (C) pTDP-43 nuclear spot size was increased in day-42 co-cultured neurons compared to day-17 co-cultured motor neurons ($p = 0.0309$). (D) pTDP-43 cytoplasmic spot size was increased in day-42 co-cultured neurons compared to day-17 motor neuron only cultures ($p < 0.0001$) and day-17 neurons in co-culture ($p = 0.0012$). (E) pTDP-43 nuclear spot count was comparable across all groups. (F) Cytoplasmic pTDP-43 spot count was reduced in day-42 co-cultured neurons compared to day-17 neurons in monoculture ($p = 0.0329$) and in co-culture ($p = 0.0452$). Data are presented as mean ± SD, number of motor neuron inductions = 2; each data point represents the mean value from all cell lines in control and *ANXA11mut* groups across two motor neuron inductions, each comprised of three technical replicates. Statistical analysis: Ordinary two-way ANOVA with Tukey's multiple comparisons test (*$p \leq 0.05$; **$p \leq 0.01$; ****$p \leq 0.0001$).

## *4.4 Discussion*

Altered protein characteristics are observed in many instances of ALS and can manifest as a range of cellular pathologies including protein mislocalisation, aggregation, altered protein abundance, and post-translational modifications. Therefore, the initial characterisation of newly derived *ANXA11* patient iPSC motor neurons included analysis of Annexin A11 and TDP-43 protein in high-content imaging assays, and quantification of relative protein abundance with western blotting.

### *4.4.1 Annexin A11 characteristics in ANXA11 ALS motor neurons*

Data from The Human Protein Atlas shows that Annexin A11 is expressed ubiquitously across many tissue types with low tissue specificity, and is of relatively low abundance in the CNS compared to other tissue types (https://www.proteinatlas.org/ENSG00000122359-ANXA11/tissue). Immunohistochemically stained human cerebral cortex tissue from healthy individuals indicates that Annexin A11 is predominantly cytoplasmic and membranous in glia and neurons in adult tissue, but is nuclear in multiple other tissue types and cell lines such as U2OS cells

(https://www.proteinatlas.org/ENSG00000122359-ANXA11/subcellular). Histological staining in motor neurons in healthy spinal tissue indicates a predominantly cytoplasmic localisation (Smith et al., 2017), however overexpression studies in primary mouse motor neurons showed a nucleocytoplasmic ratio of approximately 1.5, indicating an increased abundance of Annexin A11 in the nucleus compared to the cytoplasm (Smith et al., 2017). This suggests that the localisation of Annexin A11 is variable, and little is known about the normal function of Annexin A11 in neurons. An initial aim of this project was to characterise normal Annexin A11 localisation in iPSC-derived motor neurons. In control lines, the nucleocytoplasmic ratio of Annexin A11 was 1.75±0.47 in day-17 motor neurons, 1.32±0.23 in day-17 co-cultured motor neurons, and 1.26±0.43 in day-42 co-cultured motor neurons (Appendix Figure 9.7; Appendix Figure 9.9; Appendix Figure 9.11). There appeared to be a slight trend towards increased cytoplasmic localisation of Annexin A11 in co-cultured neurons compared to monocultures, indicating a more mature neuronal phenotype in line with cytoplasmic staining seen in healthy post-mortem tissue. The predominantly nuclear signal indicates a somewhat immature neuronal phenotype, and the increase in cytoplasmic localisation associated with culture maturity did not reach statistical significance.

The nucleocytoplasmic ratio of Annexin A11 was reduced in *ANXA11* R235Q overexpression studies, with the protein becoming more cytoplasmic in the mutant condition (Smith et al., 2017). The nucleocytoplasmic ratio of Annexin A11 measured using high-throughput image analysis showed no difference in any of the mutant groups vs. the control group (Figure 4.7). This was true in day-17 motor neurons (Appendix Figure 9.7), day-17 motor neurons in co-culture with astrocytes (Appendix Figure 9.9), and in day-42 motor neurons (Appendix Figure 9.11). The gross localisation of Annexin A11 in individual cells was variable, as evidenced in high-resolution imaging (Figure 4.8): In some motor neurons Annexin A11 is more nuclear in localisation, and in other cells it is more cytoplasmic, which is not associated with *ANXA11* mutation status. This phenomenon is not as striking in representative images from high-throughput imaging studies (Figure 4.1; Figure 4.2; Figure 4.3; Figure 4.5; Figure 4.6) likely due to the reduced resolution of these images. However, this perhaps

explains some of the variability seen in high-throughput quantification. Large data spread seen across repeats and within biological replicates for nucleocytoplasmic ratio might be partly explained by highly dynamic protein localisation. Annexin A11 is a calcium-binding protein and so is under the influence of highly dynamic processes, and variable localisation could be a consequence of specific intracellular conditions in individual cells, such as altered calcium concentration, which can fluctuate in developing neurons. Subtle differences among cell types within cultures can also introduce variability, however motor neurons positive for ChAT show a range of Annexin A11 expression patterns (Appendix Figure 9.12).

Overexpression studies indicate punctate Annexin A11 in the cytoplasm in primary mouse motor neurons (Smith et al., 2017), consistent with the punctate Annexin A11 staining pattern seen in high-resolution imaging of iPSC-derived motor neurons (Figure 4.8; Appendix Figure 9.12). The functional relevance of punctate Annexin A11 structure is not well defined in motor neurons. Annexin A11 binds to multiple phospholipids in a calcium-dependent manner (Lecona et al., 2003), and its propensity to bind to phospholipid membranes suggests a function in binding membrane-bound vesicles. Indeed, Annexin A11 has been shown to bind to lysosomes with consequences for RNA transport in axons (Liao et al., 2019). Membrane-bound vesicles are involved in many pathways implicated in ALS, including lysosomal, exosomal, endosomal, autophagic, and synaptic processing and function. Thorough characterisation of whether Annexin A11 puncta are vesicular in nature will be important for elucidating *ANXA11* pathology.

Annexin A11 is aggregated in post-mortem spinal cord from patients harbouring G38R or D40G *ANXA11* mutations (Smith et al., 2017; Teyssou et al., 2020). Protein aggregation abnormalities are common across many instances of ALS, and this is often associated with phase-separating proteins. Disruption of low-complexity domain function can increase the propensity of proteins to aggregate as phase-separated protein structures become less likely to disassemble, leading to seeding events for large protein aggregates to form (Babinchak & Surewicz, 2020). Annexin A11 contains a low-complexity domain, in which both the G38R and D40G mutations are located (Figure 1.4), and

multiple studies have demonstrated the ability of Annexin A11 to undergo phase-separation (Krainer et al., 2021; Liao et al., 2019; Nahm et al., 2020). *ANXA11* G38R and D40G mutations were shown to increase the phase-separation propensity of Annexin A11, leading to the formation of fibrous like droplets rather than typical round droplet structures (Nahm et al., 2020). Protein aggregates in ALS are also linked to disruption of protein degradation pathways including autophagy and the ubiquitin-protein system (Blokhuis et al., 2013; S. Chen et al., 2012; Farrawell et al., 2015, 2020; Imamura et al., 2017; Ramesh & Pandey, 2017).

As a proxy to measure altered protein characteristics, high-throughput spot analysis was completed in the cytoplasm and nuclei of iPSC-derived motor neurons. Nuclear and cytoplasmic spots were interrogated independently as cellular studies of ALS proteinopathies often reveal pathology in specific cellular compartments, including in *ANXA11* overexpression studies where altered punctate staining was identified predominantly in the cytoplasm (Smith et al., 2017). Although Annexin A11 displays a punctate staining pattern with super-resolution microscopy (Figure 4.8) it is unlikely that all puncta were detected in the high-throughput parameters used here as image resolution is too low to detect very small structures, and representative images of motor neurons immunolabelled for Annexin A11 support this. Annexin A11 appears to be somewhat diffuse in both the nucleus and cytoplasm, with visible spots present in both cell regions. Neurons on day 17 of differentiation (Figure 4.1; Figure 4.2; Figure 4.3; Figure 4.4) and on day 42 of differentiation (Figure 4.5; Figure 4.6) show similar spot patterns. Spot size and count were unchanged between control and *ANXA11* mutation groups, however fluctuated between culture conditions. As discussed in Chapter 3, functional maturity is accelerated when neurons are maintained in co-culture with astrocytes, for example through earlier electrophysiological maturation and expression of proteins associated with mature neurons (Kuijlaars et al., 2016; Taga et al., 2019). Differences between day-17 motor neuron monocultures and day-17 motor neurons in co-culture might be indicative of a more mature phenotype in co-cultured neurons, namely larger nuclear spots and increased numbers of both nuclear and cytoplasmic spots. Spot characteristics were altered again in day-42 co-cultured

neurons, with fewer nuclear spots compared to day-17 co-cultured neurons, and fewer cytoplasmic spots compared to both day-17 groups. This is associated with altered spot size, revealing fewer but larger cytoplasmic spots in aged neurons and fewer and smaller nuclear spots in day-42 motor neurons. Such an alteration to cytoplasmic spot characteristics in aged motor neurons might indicate an age-associated localisation pattern that increases vulnerability toward aggregation propensity in ageing neurons, whereby large cytoplasmic spots in aged neurons render Annexin A11 more susceptible to aggregation when additional factors are present under disease conditions. This is speculative, but it is interesting to observe a culture age-associated change in Annexin A11 spot characteristics that precedes the aggregation seen in post-mortem tissue. Comparable protein localisation was seen between control and *ANXA11mut* motor neurons in all cell culture paradigms, indicating no overt change in Annexin A11 cellular location as an early pathology in this system.

Intensities in high-throughput imaging experiments were unchanged between control and *ANXA11mut* groups in all culture types, indicating that the amount of endogenous Annexin A11 protein is not changed in motor neurons as a consequence of the *ANXA11* point mutations studied here (Appendix Figure 9.7; Appendix Figure 9.9; Appendix Figure 9.11). To more precisely measure the amount of Annexin A11 protein, RIPA-soluble Annexin A11 was quantified by western blot in iPSCs (Figure 4.11), motor neurons at day 17 of differentiation (Figure 4.9), and astrocytes (Figure 4.10), normalised to total protein. There were no statistically significant differences between control and *ANXA11mut* groups in these cell types, however a slight trend towards reduced protein in *ANXA11* D40G and R235Q motor neurons and *ANXA11* R235Q astrocytes compared to control might be seen (Figure 4.9; Figure 4.10; Figure 4.12). Haploinsufficiency may play a role in a small number of genetic forms of ALS and FTD including *C9ORF72* (Ciura et al., 2013; Shao et al., 2019; Shi et al., 2018), *TBK1* (Freischmidt et al., 2015; Gijselinck et al., 2015; Pottier et al., 2015), and *PGRN* (Arrant et al., 2018; Filiano et al., 2013; Nguyen et al., 2018), however, based on the data presented here it is unlikely that *ANXA11* associated ALS is caused by a loss of Annexin A11 protein, and instead altered function of the protein or associated pathways may be affected.

As Annexin A11 was normalised to total protein there is no reliance on house-keeping proteins (e.g. GAPDH) which can vary in disease state and in different cell types. Normalisation to total protein means that the relative amount of Annexin A11 in different cell types can be compared (Figure 4.12). Annexin A11 is more highly expressed in iPSCs and astrocytes than in young motor neurons, which is in line with transcriptomic brain profiling data indicating increased expression of *ANXA11* in astrocytes compared to neurons (Zhang et al., 2016). *ANXA11* expression is also increased in astrocytes compared to neurons in mouse cells (Zhang et al., 2014), and both datasets suggest increased expression in microglia/macrophages compared to neurons and astrocytes. The relevance of astrocytes in ALS pathology is becoming increasingly recognised, and the potential involvement of glia in *ANXA11* ALS pathology, based partially on expression data from *ANXA11* iPSC models, should be investigated in future analyses. Additionally, the Annexin A11 binding partner S100A6 is upregulated in ALS spinal cord astrocytes (Hoyaux et al., 2000, 2002), although expression levels are comparable in *ANXA11mut* and control iPSC-derived astrocytes (Figure 3.17). The focus of the present body of work is to investigate the function of Annexin A11 in motor neurons; however, culturing motor neurons with astrocytes might aid elucidation of pathology given that cell-to-cell communication and non-cell-autonomous functions can occur in co-culture.

Results from high-throughput imaging and western blot analysis of endogenous Annexin A11 protein in *ANXA11* ALS patient motor neurons imply that Annexin A11 localisation or relative abundance are not early driving forces of disease. Neuronal functions of Annexin A11 are discussed in later chapters and may give insight into disease events that precede the overt protein aggregation that is seen at the end stage of disease.

### *4.4.2 TDP-43 characteristics in ANXA11 ALS motor neurons*

TDP-43 pathology is seen in over 95% of ALS cases and manifests as a range of cellular disruptions including altered cellular localisation, post-translational modifications, and perturbed function (Keating et al., 2022). pTDP-43 aggregates were identified in post-mortem spinal cord from both

*ANXA11* G38R and D40G patients (Smith et al., 2017; Teyssou et al., 2020) and in multiple brain regions in *ANXA11* G38R tissue (Teyssou et al., 2020). Further, TDP-43 was found localised to the cytoplasm in some post-mortem brain regions in an *ANXA11* G38R patient (Teyssou et al., 2020). The characteristics of TDP-43 in iPSC-derived motor neurons were therefore investigated, and control and *ANXA11* patient lines were probed for TDP-43 and pTDP-43 in various cell culture parameters.

In control and *ANXA11mut* lines, TDP-43 was predominantly nuclear and no change in nucleocytoplasmic ratio was identified between control and *ANXA11mut* groups in any paradigm with high-throughput analysis (Figure 4.17.A). TDP-43 nucleocytoplasmic ratio in 17-day old motor neurons was 1.58±0.25 (Figure 4.17), and was significantly increased in day-17 co-cultured motor neurons, which had a TDP-43 nucleocytoplasmic ratio of 2.62±0.27 (Figure 4.17.A; Appendix Figure 9.14). The assumed "normal" condition of TDP-43 is to be predominantly nuclear, and so the higher nucleocytoplasmic ratio of TDP-43 in motor neurons when in co-culture with astrocytes might be indicative of increased neuronal health or reduced neuronal stress in the co-culture paradigm, as astrocytes offer well-characterised trophic and structural support to neurons in culture (Aebersold et al., 2018; Kuijlaars et al., 2016; Taga et al., 2019). The nucleocytoplasmic ratio of TDP-43 in day-42 co-cultured motor neurons was 1.88±0.57, which was significantly reduced compared to day-17 co-cultured neurons, indicating that TDP-43 becomes more cytoplasmic in aged culture conditions. The culture age-associated increase in cytoplasmic TDP-43 might suggest a universal age mediated increase in cytoplasmic TDP-43, which could lead to proteinopathy in those with additional genetic and environmental vulnerability.

Increased cytoplasmic localisation of TDP-43 has been associated with loss of nuclear function and toxic gain of function in the cytoplasm, and disease-associated alterations to nucleocytoplasmic transport and proteostasis have been linked to altered nucleocytoplasmic ratios in ALS. Insoluble TDP-43 sequesters nuclear pore complexes leading to improper import/export (Chou et al., 2018), suggesting that a negative feedback loop might occur, whereby pathological TDP-43 affects nucleocytoplasmic homeostasis, leading to increased TDP-43 in the cytoplasm and further damage

to the nuclear pore. Nuclear pore dysfunction is well established in *C9ORF72* ALS/FTD (Freibaum et al., 2015; Zhang et al., 2015), and increasing evidence indicates that it is also dysfunctional in other forms of the disease including *PFN1* (Giampetruzzi et al., 2019), *FUS* (Lin et al., 2021), and *MAPT* (Paonessa et al., 2019). Interestingly, Annexin A11 has a role in rebuilding the nuclear membrane during mitosis (Tomas & Moss, 2003). Although this may be of reduced relevance for post-mitotic neurons, the role of Annexin A11 in nuclear membrane structure might be an important avenue for further investigation. Network analysis implicated dysfunctional nucleocytoplasmic transport and RBPs as critical factors in ALS/FTD pathology, and implied that disrupted nucleocytoplasmic transport is crucial for disease initiation (Boeynaems et al., 2016), warranting investigation into a potential nucleocytoplasmic disturbance in *ANXA11* ALS. Increased cytoplasmic localisation of TDP-43 in aged cultures cannot be attributed to nuclear pore function without further investigation, and analysis of temporally mediated TDP-43 localisation in iPSC-derived motor neurons may be useful in future investigation of nuclear membrane dynamics in ALS.

It was hypothesised that variable signal from TDP-43 staining might be due to inconsistencies in motor neuron differentiation as less than 100% motor neurons was achieved in differentiation (Figure 3.10). Motor neurons harbouring endogenously tagged TDP-43-mScarlet-I were probed for Islet 1 to assess whether TDP-43 nuclear signal was associated with motor neurons specifically. This indicated the presence of TDP-43 in neurons both positive and negative for Islet 1 (Appendix Figure 9.24), suggesting that additional factors are influencing the variable TDP-43 signal detected here.

High-throughput TDP-43 spot analysis revealed culture paradigm associated changes in spot characteristics, including smaller and fewer nuclear spots in day-42 co-cultured neurons compared to day-17 co-cultured neurons (Figure 4.17.C; Figure 4.17.E), with no change in cytoplasmic spots (Figure 4.17.D; Figure 4.17.F) despite an increase in cytoplasmic localisation of TDP-43 in day-42 cultures (Figure 4.17.A). An increase in TDP-43 nuclear spots was seen in *ANXA11* D40G and R235Q day-17 motor neurons compared to control (Figure 4.17.E), which was not seen in day-42 neurons. Pathological TDP-43 aggregates in post-mortem tissue are typically cytoplasmic, suggesting that if an

altered TDP-43 localisation pattern were identified it might be presumed to be in the cytoplasm. A novel mechanism for TDP-43 aggregation which occurs in micronuclei, small sections of nuclear material that bud-off from the nucleus in response to cellular stress during mitosis, reveals how sequestration of TDP-43 can occur in nuclear compartments in the context of ALS (Droppelmann et al., 2019). No indication of such pathology was investigated here, but this indicates that TDP-43 aggregation and altered localisation can arise in nuclear regions. Additionally, TDP-43 localisation to nucleoli in response to stress can result in altered TDP-43 staining patterns in the nucleus (Martinez-Macias et al., 2019), however, an increase in nuclear TDP-43 spots is not generally considered a hallmark of ALS. TDP-43 does not localise to P-bodies (Colombrita et al., 2009), and data implicating TDP-43 localisation to stress granules highlights altered cytoplasmic localisation pattern, which is discussed in further detail in Chapter 6. TDP-43 nuclear spot quantification does not measure any specific pathway, however an increase in the number of nuclear spots in *ANXA11* D40G and R235Q motor neurons reveals a potential early alteration in iPSC-derived neurons. The lack of altered spot characteristics in day-42 neurons may result from cell death, as fewer neurons survive to this time point (Appendix Figure 9.14; Appendix Figure 9.16), but the nature of fluctuating spot characteristics remains to be established. Measurements of cytoplasmic TDP-43 spots were particularly variable, and further analysis is necessary for thorough characterisation of TDP-43 subcellular localisation, for example with high-resolution imaging. Examples of TDP-43 localisation in neurons at high resolution are included in Appendix Figure 9.12, revealing punctate TDP-43 in the nucleus and cytoplasm. Notably, these images include motor neurons that are co-labelled with Annexin A11, and do not indicate co-localisation of TDP-43 and Annexin A11, supporting immunoprecipitation data showing that TDP-43 and Annexin A11 do not directly interact (Nahm et al., 2020).

The total intensity of TDP-43 in motor neurons as measured by high-content imaging was unchanged between cell lines in day-17 and day-42 co-cultured motor neurons (Appendix Figure 9.14; Appendix Figure 9.16). Western blots were included to measure TDP-43 protein abundance in motor neurons on day 17 of differentiation, revealing comparable levels of TDP-43 in control and *ANXA11mut*

groups (Figure 4.18). This was also true for iPSC derived astrocytes, where no difference was observed between groups (Figure 4.19). Relative abundance of TDP-43 is not a typical ALS phenotypic marker, and evidence for haploinsufficiency is absent, so it is unsurprising that no differences were detected here. Relative TDP-43 abundance was increased in *ANXA11* R235Q iPSC protein, however the effect size is small and appears to be driven by a single data point. Additionally, fluctuation of fluorescent TDP-43 signal in endogenously tagged TDP-43-mScarlet-I iPSCs is observed (data not shown). This appears to be confluency dependent, suggesting that TDP-43 expression might be difficult to accurately measure in stem cells where relative abundance is dynamic. Comparison of relative TDP-43 abundance across cell types revealed a slight increase in iPSCs compared to motor neurons (Figure 4.21). *TARDBP* knockout is lethal in rodent models and embryos die at day ~7.5 of embryonic development (Kraemer et al., 2010), highlighting the importance of TDP-43 in development, and stem cells by proxy, and suggesting that it might be necessary to investigate TDP-43 in immature cell types in addition to mature motor neurons. In future analyses, it will be important to assess the levels of insoluble TDP-43 and Annexin A11 in *ANXA11mut* motor neurons; this might reveal altered protein dynamics that are not observed when assessing soluble protein abundance alone.

TDP-43 is abnormally phosphorylated in post-mortem ALS tissue (Arai et al., 2006; Neumann et al., 2006) and pTDP-43 aggregates are present in post-mortem spinal cord and brain tissue from patients with *ANXA11* G38R and D40G mutations (Smith et al., 2017; Teyssou et al., 2020). Hyper-phosphorylation of TDP-43 and associated pathology have been demonstrated in cell (Chen et al., 2019; Fazal et al., 2021; Nonaka et al., 2009, 2016; Quek et al., 2022; Wu et al., 2021) and animal models (Choksi et al., 2014; Jeon et al., 2019; Liachko et al., 2010) of ALS. TDP-43 can be phosphorylated by multiple kinases, including CK1, CK2, and GSK3 (Neumann et al., 2006; Neumann, Kwong, et al., 2009; White et al., 2021). Interestingly, phosphorylation of TDP-43 by Casein kinase 1δ or phosphomimic mutations in *TARDBP* reduce phase-separation and aggregation of TDP-43, suggesting that phosphorylation of TDP-43 might be a protective mechanism to prevent TDP-43

aggregation (Gruijs da Silva et al., 2022). High-throughput image analysis indicated no change in pTDP-43 nucleocytoplasmic ratio in any culture condition (Figure 4.28.A), however altered nucleocytoplasmic ratio of pTDP-43 is not typically reported as a disease hallmark. Cell-based studies can show widespread pTDP-43 measured by immunocytochemistry, as is demonstrated here (Figure 4.22; Figure 4.23; Figure 4.24; Figure 4.25; Figure 4.26; Figure 4.27), and the cellular localisation differs to that of TDP-43, which is more nuclear than the phosphorylated species (Figure 4.17; Figure 4.28). pTDP-43 intensity was unchanged between control and *ANXA11mut* groups in all culture conditions, indicating an absence of overriding TDP-43 hyper-phosphorylation as an early indicator of *ANXA11* ALS pathology (Appendix Figure 9.18; Appendix Figure 9.20; Appendix Figure 9.22). Representative images of aged motor neurons appear to have increased fluorescent intensity compared to young motor neurons (Figure 4.22; Figure 4.23; Figure 4.24; Figure 4.25; Figure 4.26; Figure 4.27), however, the completion of immunocytochemistry and image acquisition at different times means that arbitrary units of fluorescent intensity cannot be directly compared in this instance.

pTDP-43 nuclear spot size was increased in day-42 compared to day-17 co-cultured neurons (Figure 4.28.C), and cytoplasmic spot size was increased in day-42 neurons compared to both day-17 monocultures and co-cultured neurons (Figure 4.28.D). An increase in pTDP-43 spot size across both control and *ANXA11mut* groups might indicate increased stress across all lines due to longer time in cell culture, implying the nature of TDP-43 is to become phosphorylated and “aggregated” in response to ageing and/or stress, however no differences were observed between control and *ANXA11mut* groups. Further, no change was detected in the number of nuclear pTDP-43 spots across any culture paradigm (Figure 4.28.E). The number of cytoplasmic spots was reduced in day-42 co-cultures compared to both day-17 conditions (Figure 4.28.F), suggesting pTDP-43 spots become fewer and larger in aged neurons. A trend towards increased pTDP-43 spot count in *ANXA11* D40G day-17 motor neurons was seen but did not reach significance in ordinary two-way ANOVA analysis. In a separate analysis of individual culture paradigms, the number of nuclear pTDP-43 spots was significantly increased in *ANXA11* D40G compared to control in day-17 monoculture neurons, and

nuclear spot size was decreased in *ANXA11* D40G and increased in *ANXA11* R235Q neurons compared to control (Appendix Figure 9.17). Reduced pTDP-43 nucleocytoplasmic ratio was seen in *ANXA11* G38R and D40G compared to control in day-17 motor neurons, indicating an increase in cytoplasmic localisation of pTDP-43 (Appendix Figure 9.18). However, the loss of significance in two-way analysis suggests that these effects are weak.

Collectively these data suggest that although pTDP-43 characteristics alter with culture condition, phosphorylation of TDP-43 is not an early phenotype of *ANXA11* ALS in this system. Phosphorylation of TDP-43 is usually associated with late-stage disease, and so it may not be surprising that no striking difference was seen here. The altered structure and localisation of pTDP-43 spots in aged neurons might indicate that with further culture ageing, robust phenotypic differences might arise between control and *ANXA11* groups, which was unfortunately beyond the scope of this project.

### *4.4.3 High-throughput analysis in iPSC-derived neurons*

The utilisation of high-throughput analysis in the characterisation of iPSC-derived neurons is increasingly employed to quantify thousands of cells for more reliable interrogation of immunocytochemistry data. This is demonstrated here by the large number of cells included in analyses (Appendix Figures 9.7; 9.9; 9.11; 9.14; 9.16; 9.18; 9.20; 9.22; 9.24). High-content image analysis holds great potential for understanding sub-cellular phenotypes in ALS, however occasionally inconsistent iPSC characteristics and technical limitations can influence the validation of such studies.

One caveat of high-throughput image analysis is the reliance on antibodies which can give misleading results if they are unspecific. Annexin A11 was detected with a polyclonal antibody targeting amino acids 147-221, representing the end of the N-terminal near the midpoint of the 505AA protein. Annexin proteins share a core Annexin domain at the C-terminal, so antibodies targeting the unique N-termini differentiate between the family members. There is no evidence of truncated or short Annexin A11 protein excluding this region in the literature, so all Annexin A11 protein should be

detected with this epitope based on current understanding. The Annexin A11 antibody used throughout this thesis is included in The Human Protein Atlas, which reports antibody validation via protein array and capture mass spectrometry (https://www.proteinatlas.org/ENSG00000122359-ANXA11/antibody). Since the completion of experiments, research projects with the sole intention of antibody validation for research have been published, including for Annexin A11 (Alshafie et al., 2022). Unfortunately, this analysis did not include the antibody used in this thesis, but these data should be referred to in future analyses. A representative western blot showing all protein bands detected by this Annexin A11 antibody is included in Appendix Figure 9.23, indicating predominant detection of the 56kDa protein with some unspecific detection.

The manufacturer of the TDP-43 antibody used in high-throughput analyses indicates that it has been knockdown/knockout validated. The TDP-43 antibody is polyclonal and targets the N-terminal, raised against a 1-260AA immunogen of the 414-amino acid protein. Short isoforms of TDP-43 have been recently implicated in ALS (Weskamp et al., 2020), and truncated C-terminal fragments have been previously described (Berning & Walker, 2019; Chhangani et al., 2021; Feneberg, Charles, et al., 2020; Wang et al., 2013). The antibody used here should detect short TDP-43 proteins which include the N-terminal, however many C-terminal fragments do not contain the majority of the immunogen sequence (Berning & Walker, 2019). As the antibody is polyclonal it is possible that certain C-terminal fragments will be detected depending on the site of fragmentation, and further investigation of *ANXA11* ALS motor neurons with a panel of antibodies specifically detecting subtypes of TDP-43 will be important in fully elucidating the role of TDP-43 in *ANXA11* mediated pathology. Additional antibodies such as the pTDP-43 antibody were included based on historic validation completed by multiple individuals.

The number of cells included for high-throughput analyses varied in this project due to batch-to-batch differences in neuronal survival. This was not associated with a particular control or *ANXA11mut* group, but fluctuated independently (Appendix Figures 9.7; 9.9; 9.11; 9.14; 9.16; 9.18; 9.20; 9.22; 9.24). Although careful optimisation of analysis pipelines meant that neurons alone were

included in analyses, it is possible that altered cell density at the time of fixation in different experiments affected read-out. In many instances of high-throughput analysis there is a spread of data, with large SEM across all mutation groups or large SD across biological replicates. Although this doesn't occur in every instance, it is seen across multiple examples of quantification. Examples include TDP-43 cytoplasmic spot count (Figure 4.17.F) and Annexin A11 nucleocytoplasmic ratio analysis (Figure 4.7.A). In these examples, it is observed that large data spread is often caused by one experimental repeat: Although the relationship between different mutation groups remains consistent, data varies from one biological repeat to another. For example, in quantification of the nucleocytoplasmic ratio of TDP-43 in aged motor neurons there is a clear separation of data, where the nucleocytoplasmic ratio of TDP-43 varies from approximately 1 to >2. Data points from one biological replicate across all ten cell lines have a value of approximately 1, and two biological replicates display a TDP-43 nucleocytoplasmic ratio of >2 (Appendix Figure 9.1). Therefore, large SEM is not due to an inconsistency among cell lines, but rather is due to the readout from one biological replicate, which is consistent across all cell lines. This could be due to an unknown culture artefact present at the time of fixation, such as the level of cellular stress due to fluctuations in the incubator environment. This highlights the variable nature of iPSC biology and perhaps indicates that more biological and technical replicates are necessary to elucidate neuronal characteristics in iPSC-derived models. Interestingly, a variable nucleocytoplasmic ratio is seen in both TDP-43 and Annexin A11 (Figure 4.17.A; Figure 4.7.A), emphasising the dynamic nature of protein localisation in neuronal cultures.

High-content imaging has proven useful for the characterisation of neurodegenerative diseases. It has been used to identify compounds affecting tau phosphorylation and therefore discovery of novel therapeutics for neurodegenerative diseases (Cheng et al., 2021). Robust disease-associated profiles were identified in fibroblasts from Parkinson's disease patients in an impressive cell profiling study utilising deep learning (Schiff et al., 2022). Deep learning has also been applied to ALS iPSC-derived neurons and was able to predict disease status based on neuronal profile (Imamura et al., 2021;

Verzat et al., 2022). These examples demonstrate that early changes representing prodromal stages of disease can be detected with non-biased approaches, however evaluation of specific processes with hypothesis led research design may be more challenging.

Many studies utilise drugs to induce stress or manipulate specific pathways so that endogenous phenotypes are exaggerated, and "cell-senescence cocktails" have been optimised to accelerate neuronal ageing in the absence of DNA damage to induce ALS phenotypes at earlier time points (Fathi et al., 2022). Alternatively, cell cultures can be maintained for extended periods such that the cultures are "aged", becoming more mature and allowing more time for the consequences of disrupted biology to become apparent. Data suggests that differentiating iPSCs into organoids or employing co-cultures leads to faster maturation of neurons and, therefore, earlier identification of phenotypes. For example, FTD associated adult tau isoforms can be detected in cortical neurons cultured for 365 days (Sposito et al., 2015), and can be detected in organoids after 100 days in culture (Lovejoy et al., 2022). Motor neuron-astrocyte co-cultures were optimised in this project in attempt to enhance neuronal maturity, and high-throughput quantitative assays were completed at multiple time points. However, it should be noted that although cultures were aged to day 42, cultures fixed at this time point likely contain immature neurons, and substantially longer maintenance in culture might be necessary to identify any striking endogenous in Annexin A11 and TDP-43 protein phenotypes. Unfortunately, this was beyond the scope of this body of work due to time restraints, but it would be an interesting prospect to investigate.

Some evidence of endogenous TDP-43 mislocalisation without additional stress in iPSC derived neurons harbouring *TARDBP* mutations exists (Fazal et al., 2021; Smith et al., 2021), however this has not been reported in the context of multiple ALS mutations including *ANXA11*. Annexin A11 is poorly characterised in iPSC-derived motor neurons as no such models are yet to be published. Multiplexed imaging will further increase the power of high-throughput analyses, and many different characteristics can be analysed in a single culture, including in multiple cell types maintained in co-culture (Guo et al., 2019; Schiff et al., 2022; Tomov et al., 2021).

One factor that limited the high-throughput imaging here was the tendency of iPSC motor neurons to “clump up”, which meant that imaging at high magnification in an automated system could result in the collection of large amounts of data where no cell bodies were included in images. Increasing the number of images in data collection was prohibited by the size of data files produced, and the time taken for analysis of such large files. Further optimisation of imaging and analysis methods, and the removal of logistical restraints such as time, research costs, and size of data files associated with collecting data at higher magnifications would give better insight into early endogenous changes in protein localisation studies. The study design here focused on the gross localisation of proteins, and more subtle characteristics that might be evident in higher resolution data may have been missed. When utilising patient-derived neurons, including multiple cell lines is important to reduce false positives arising from line-to-line variability. However, this comes with the caveat that data collection can become limited. Additionally, characterisation of individual cells rather than comparing mean values in cell line analysis might reveal subgroups of neurons in ALS cultures missed by pooling data. As technologies progress these issues will diminish, and future studies will be more readily able to analyse multiple cell lines in both a high-throughput and a high-resolution manner.

## *4.5 Conclusion*

High-throughput quantification revealed subtle changes in *ANXA11* patient motor neurons compared to control, namely altered nuclear TDP-43 spot dynamics in day-17 co-cultured motor neurons. However, comparable protein profiles of Annexin A11, TDP-43, and pTDP-43 were observed in most instances, including in nucleocytoplasmic ratio, spot analysis, and relative protein abundance. Altered protein characteristics were commonly observed between different culture paradigms and showed varying protein localisation and abundance in different cell types and cultures. Collectively these data highlight the dynamic nature of ALS-associated proteins in different model systems, emphasising the need to study non-cell-autonomous and age-associated effects on protein characteristics in iPSC-derived models. The absence of any overt protein mislocalisation

suggests that it is necessary to interrogate specific functions of ALS proteins and pathways to determine early disease events, and that immature neurons do not recapitulate late-stage aggregation events without the addition of cellular stressors.

High-throughput imaging might be better applied to unbiased analyses whereby deep learning algorithms can be implemented to identify early changes instead of targeted analysis of specific proteins. Identifying altered cellular phenotypes in *ANXA11* ALS motor neurons where there is an absence of any overt proteinopathy would indicate that protein aggregation is downstream in neuronal dysfunction. Examples of altered cellular characteristics in *ANXA11* ALS motor neurons are discussed in following chapters.

# Chapter 5 Neurite outgrowth and calcium dynamics – connectivity and signalling in ALS motor neurons

## *5.1 Overview*

Although neurodegeneration is typically late-onset, deficits in neurite outgrowth have been observed in cellular models of ALS (Egawa et al., 2012; Fiesel et al., 2011; Kiskinis et al., 2014) and other neurodegenerative diseases (Capizzi et al., 2022; Pourtoy-Brasselet et al., 2021; Van Damme et al., 2008). Neurite outgrowth abnormalities can indicate several cellular dysfunctions; it is controlled by multiple cellular processes including growth cone dynamics, actin polymerisation, and transport (Miller & Suter, 2018). The polarised and post-mitotic nature of neurons presents a potential cell-specific vulnerability in that tightly regulated cellular compartments with highly specific functions generate multiple levels at which dysfunction can occur. Motor neurons are particularly large, reaching up to one meter in length (Stifani, 2014). As such, distal axons and neuritic branches may be more challenging to repair if damaged, and more susceptible to problems with processes such as intracellular transport or metabolic challenges. As neurite outgrowth can give insight into a range of cellular pathologies, *ANXA11mut* and control iPSC lines were differentiated into motor neurons, and neurite outgrowth was measured at multiple time points. This was completed in immature neurons in a high-throughput system, and a subset of three control and three *ANXA11mut* lines were selected for analysis in microfluidic devices.

Through neurite outgrowth and maturation, individual neurons form connections through chemical synapses and gap junctions, developing into functional networks of cells that communicate via complex signalling pathways (Pereda, 2014). Neuron-to-neuron communication via chemical synapses relies on the influx of calcium ions into post-synaptic neurons to induce action potentials. Additionally, intracellular calcium stores mediate cytosolic calcium levels with consequences for multiple cellular functions. Dysregulation of calcium in ALS is widespread, and both inter-neuronal

signalling (e.g. excitotoxicity) and intra-neuronal calcium homeostasis (e.g. mitochondrial function) are affected (Armada-Moreira et al., 2020). Quantification of spontaneous calcium fluctuations in iPSC-derived neuronal cultures is frequently employed to measure culture maturity, as calcium waves across neuronal networks can be taken as a proxy of cell-to-cell communication. *ANXA11mut* and control iPSC-derived motor neuron-astrocyte co-cultures were aged until day 40 and day 64 of differentiation and probed for spontaneous calcium fluctuations; initially as a measure of culture maturity, and further to compare the calcium activity profiles of ALS patient and control motor neurons. Additionally, the function of Annexin A11 is calcium-dependent, and so acknowledging the presence of calcium signalling in cultured neurons might be important when considering the localisation and function of Annexin A11.

To further measure neuronal activity, motor neuron-astrocyte co-cultures from two *ANXA11mut* and two control lines were subject to patch-clamp analysis to measure resting membrane potential, firing frequency, and number of firing events in motor neurons. This was completed in motor neurons on day 40 of differentiation, which were maintained in co-culture with astrocytes. These cell lines were subject to immunocytochemistry with antibodies targeting synaptic proteins as an additional demonstration of culture maturity.

## *5.2 Methods*

### *5.2.1 Neurite outgrowth analysis*

Motor neurons (2.1.7) were subject to high-throughput neurite outgrowth analysis with the Opera Phenix® High-Content Screening System and Harmony® (2.4.2). Motor neurons were fixed 16 hours after dissociation of embryoid bodies (day 12 of differentiation), and on day 17 of motor neuron differentiation. A subset of three control and three *ANXA11mut* lines were maintained in microfluidic devices to assess distal axon outgrowth (2.1.11) and were fixed on day 25 of motor neuron differentiation. In all instances, immunocytochemistry was used to identify neurites (2.4.1), and

motor neurons grown in microfluidic devices were imaged with a Nikon Spinning Disk Scanning Confocal Microscope (2.4.3).

### *5.2.2 Assessment of neuronal activity in ALS motor neurons*

Motor neuron-astrocyte co-cultures (2.1.10) were aged for 40 and 64 days and probed for spontaneous calcium fluctuations using the fluorescent dye Fluo-4 AM; live imaging data were collected with a Nikon Spinning Disk Scanning Confocal Microscope (2.4.4). For each image set, five ROIs were determined, each within a different cell, and fluorescent signal over time was normalised to three background ROIs to calculate ΔF/F0. This aided visualisation and categorisation of calcium signals by removing background and clarifying whether separate neurons were following the same calcium fluctuation pattern. Data were collected from five control and five *ANXA11mut* lines, two separate motor neuron inductions were completed for each time point, and eight recordings were taken per cell line in each instance.

A subset of four lines (two control and two *ANXA11mut*) were subject to electrophysiological patch-clamp analysis to measure action potential, firing frequency, and number of firing events, courtesy of Dr Seung Chan Kim. Motor neuron-astrocyte co-cultures at day 40 of differentiation were subject to immunocytochemistry with antibodies targeting synaptic proteins (2.4.1) and were imaged with super-resolution microscopy (2.4.3).

## *5.3 Results*

### *5.3.1 Neurite outgrowth analysis of ANXA11 ALS patient motor neurons*

Neurite analysis included measures of neurite length and complexity: Analyses representing the size of outgrowing neurites included total neurite length (combined neurite length per cell) and maximum neurite length (longest neurite per cell). Measures of neurite complexity included the number of neurite roots and the number of neurite extremities. The number of neurite extremities

describes the number of neurite endpoints, and a neurite root is the point at which a neurite begins to grow out from the soma. Harmony® software offers two methods to calculate the number of nodes: (1) represents the number of branching points, and (2) represents the number of neurite segments/the number of roots. A schematic of neurite outgrowth measurement parameters is included in Figure 5.1.

Representative images of control and *ANXA11mut* motor neurons 16 hours after embryoid body dissociation are included in Figure 5.2, and examples of neurite tracing on day 16 are included in Figure 5.3. Neurite outgrowth quantification did not reveal any differences between control neurons and any of the *ANXA11mut* groups in any measurement parameter (Figure 5.4).

Examples of day-17 neuronal cultures and subsequent neurite detection with Harmony®, including detection of nuclei, cytoplasm, and neurites, are included in Figure 5.5. At this time-point neurites were more complex than on day 12, and significant overlap across cells was seen. This may have interfered with delineation of which neurites belonged to each cell, leading to inaccurate readouts from Harmony®. Additionally, neurites often extended beyond the limitations of the field of view by day 17 of differentiation, which will have implications for parameters such as maximum neurite length and number of extremities. Quantification of neurite length (maximum and total neurite length), and neurite complexity (number of roots, nodes, and extremities) yielded no significant differences in these cultures (Figure 5.6).

Lastly, three control and three *ANXA11mut* lines were cultured in microfluidic devices (Figure 5.7), fixed on day 25 of motor neuron differentiation, and subject to immunocytochemistry and imaging. Qualitative analysis implies a perturbed neurite outgrowth phenotype in distal axons in *ANXA11mut* lines as fewer neurites grow through the microfluidic microgrooves (Figure 5.8). In control lines, varying confluency of neurites was observed, however successful outgrowth was seen in all instances. In *ANXA11* G38R neurons, extremely perturbed outgrowth was seen in Experiments 2 and 3, and somewhat perturbed outgrowth was seen in Experiment 1. In *ANXA11* D40G neurons, reduced neurite outgrowth was seen Experiments 1 and 3. In *ANXA11* R235Q neurons, extremely reduced

outgrowth was seen in Experiment 1, yet Experiments 2 and 3 showed successful neurite outgrowth with high confluency of neurites.

It should be noted that in some instances neurite networks lifted off from devices during fixation or immunocytochemistry (Figure 5.8; far left control line in Experiment 2 and Experiment 3, *ANXA11* R235Q in Experiment 3). In these instances, successful neurite outgrowth was observed prior to cell fixation, and networks of lifted neurites can be seen in the images. To evaluate whether equivalent numbers of neurons were present in cultures at fixation in Experiment 1, proximal neurites were imaged (the collection of neurites growing before reaching the microgrooves) and an estimate of cell count in the cell-plating wells was completed. Cell counts from cell-plating wells are comparable (Appendix Figure 9.25), and total neurite intensity in pre-microgroove neurites indicates comparable proximal neurite outgrowth across lines (Appendix Figure 9.26). These analyses were completed only in Experiment 1. Together these results indicate that although there is no initial perturbation to neurite outgrowth in newly plated *ANXA11* patient-derived motor neurons, there may be dysfunctional distal axon outgrowth, reduced axon survival, or impaired axon maintenance in *ANXA11* ALS motor neurons.

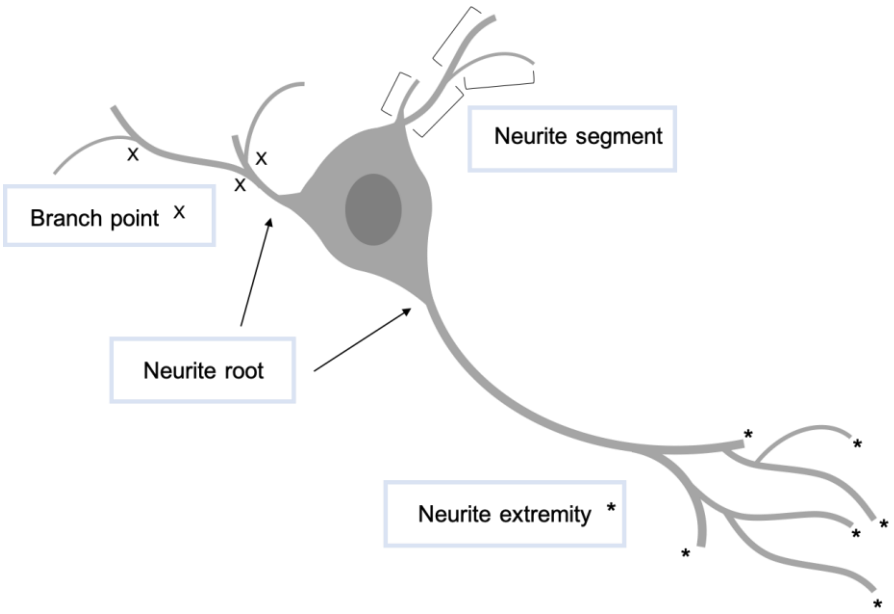


***Figure 5.1 Neurite characteristics in Harmony®***

Characteristics of neurites quantified in Harmony® are shown in the schematic. In addition to measures of neurite length, neurite complexity is represented by the number of roots, branch points, segments, and extremities.

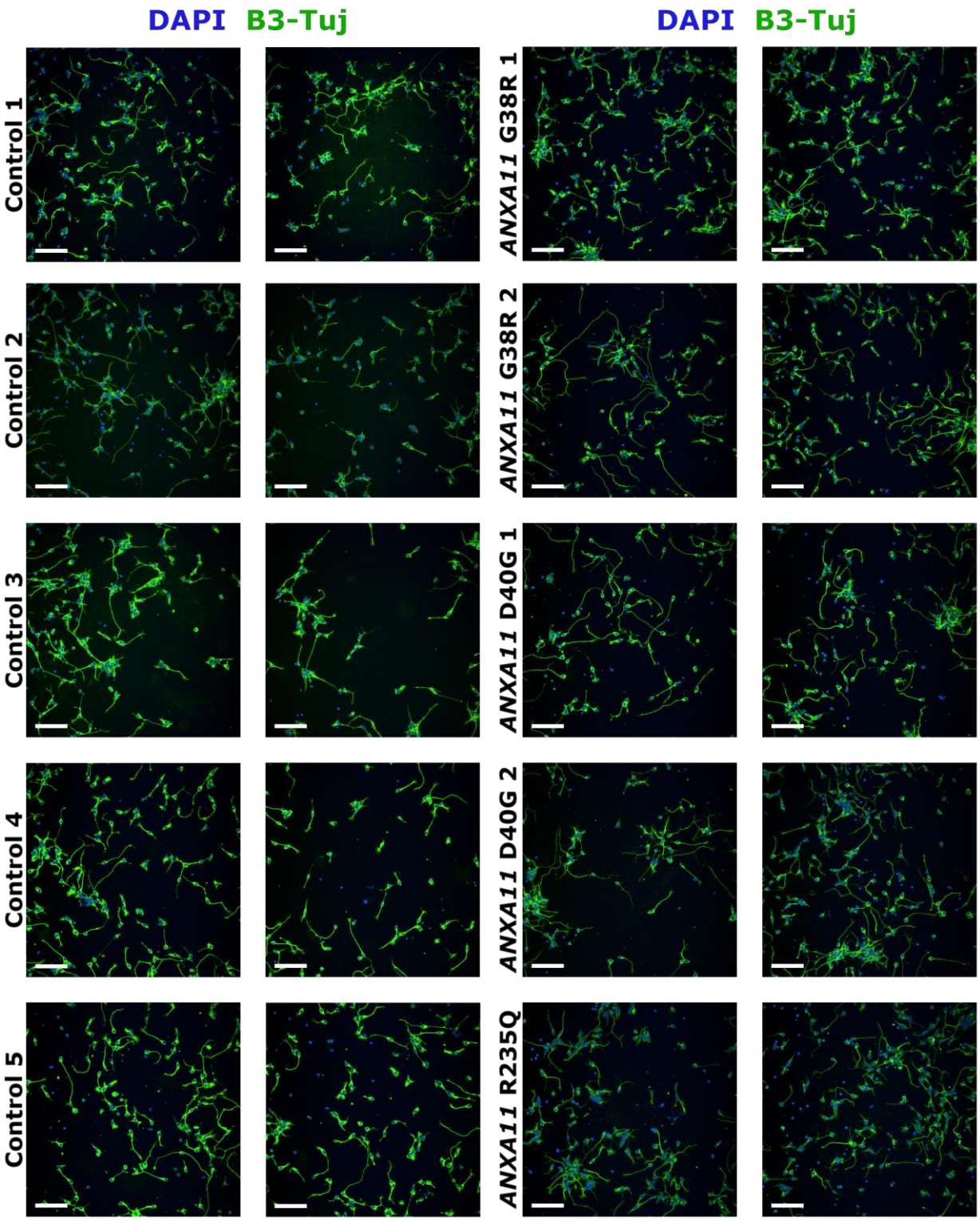


***Figure 5.2 Neurite outgrowth in motor neurons 16 hours post-plating***

Representative images of motor neurons fixed on day 12 of differentiation, imaged with the Opera Phenix® High-Content Screening System. Neurons were probed for $\beta$3-Tubulin (B3-Tuj, green) and co-stained with DAPI (blue). Scale bars represent 100µm.

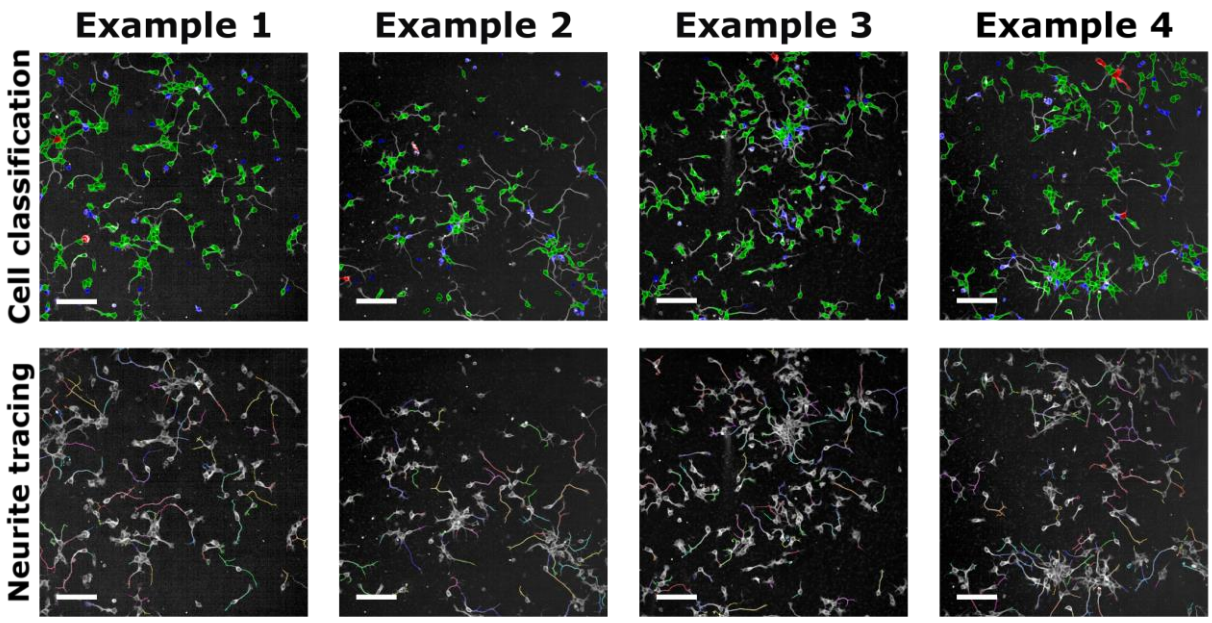


***Figure 5.3 Cell classification and neurite tracing in motor neurons 16 hours post-plating***

Representative images of neurite tracing (multi-coloured) using linear classification in Harmony®. Motor neuron cell bodies are highlighted in green, and large and small debris (red and blue, respectively) were excluded from analyses. Scale bars represent 100µm.

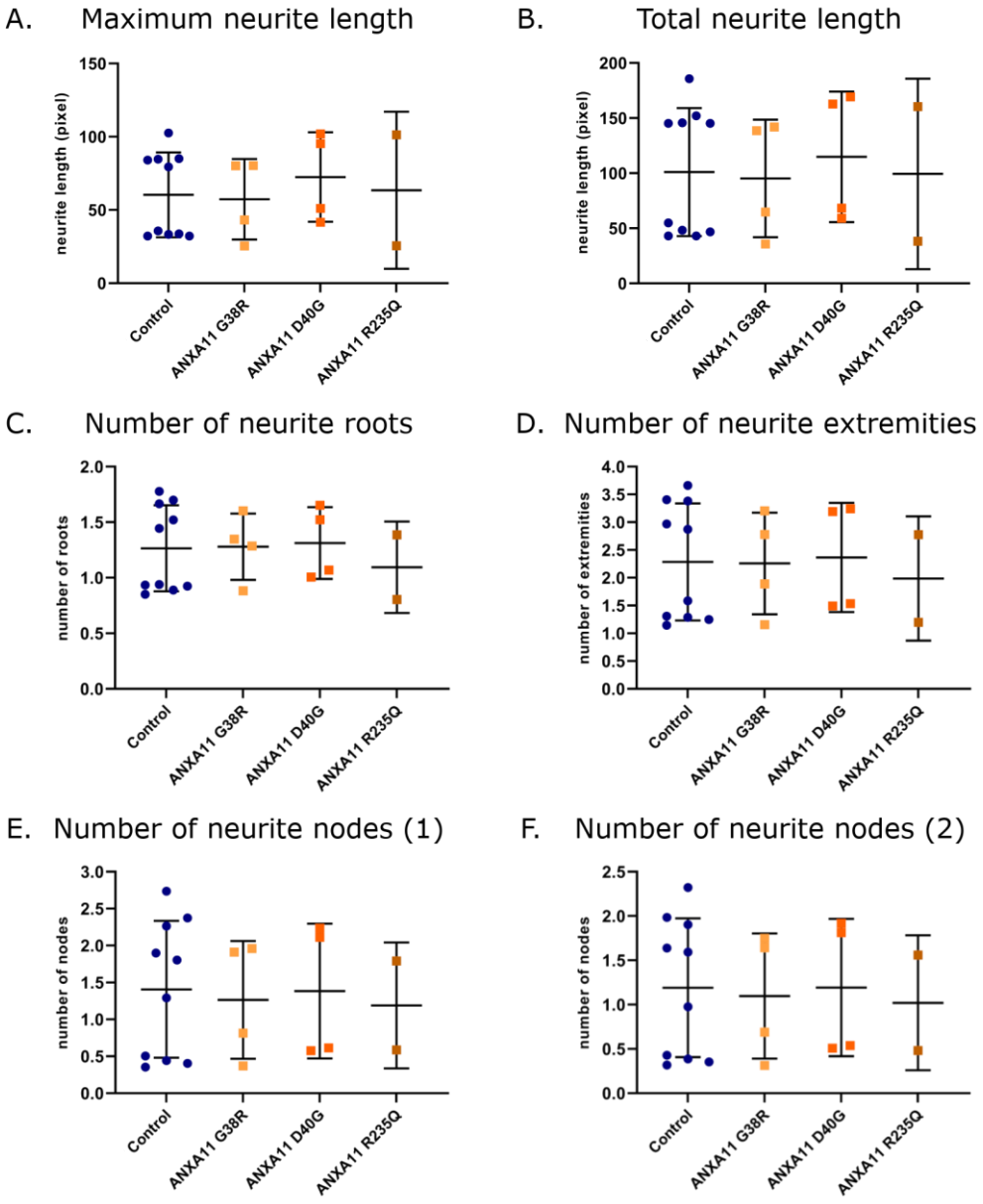


***Figure 5.4 Quantification of neurite outgrowth in motor neurons 16 hours post-plating***

(A) Maximum neurite length and (B) total neurite length represent the length of outgrowing neurites. (C) Number of neurite roots growing out from the cell body. (D) Number of extremities represents the number of neurite endpoints. (E) Number of neurite nodes (1) measures the number of branch points. (F) Number of neurite nodes (2) represents the number of neurite segments/the number of neurite roots. Data are presented as mean ± SEM, number of motor neuron inductions = 2; each data point represents one cell line in one motor neuron induction, with each comprising three technical replicates. Control lines are grouped and *ANXA11* ALS patient lines are grouped by mutation. Statistical analysis: Ordinary one-way ANOVA with Dunnett's multiple comparison test ($p > 0.5$).

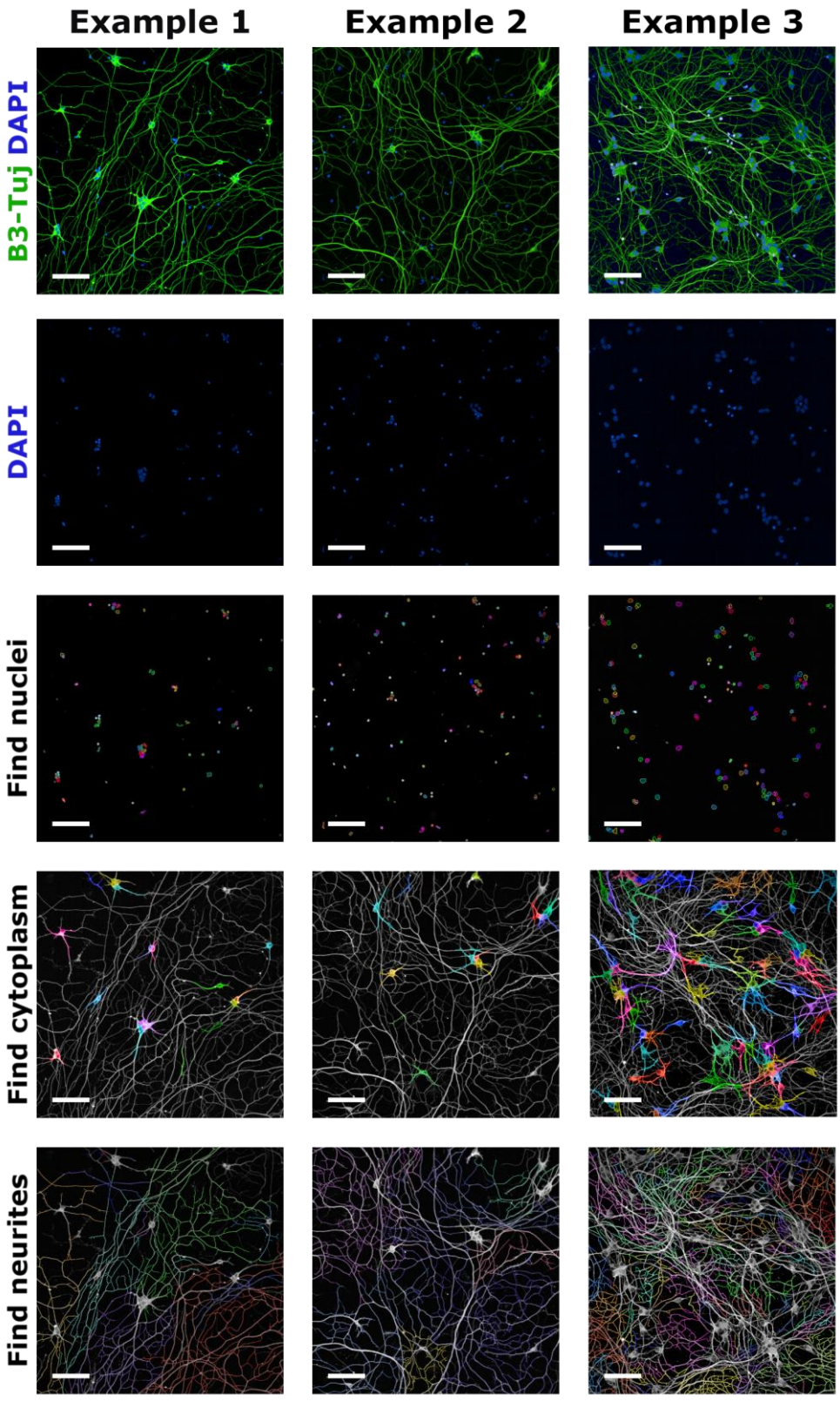


***Figure 5.5 Representative neurite tracing in motor neurons on day 17 of differentiation***

Motor neurons were fixed on day 17 of motor neuron differentiation and stained with $\beta$3-Tubulin (B3-Tuj, green) and DAPI (blue). Images were collected with the Opera Phenix® High-Content Screening Platform and analysed in Harmony®. Scale bars represent 100µm.

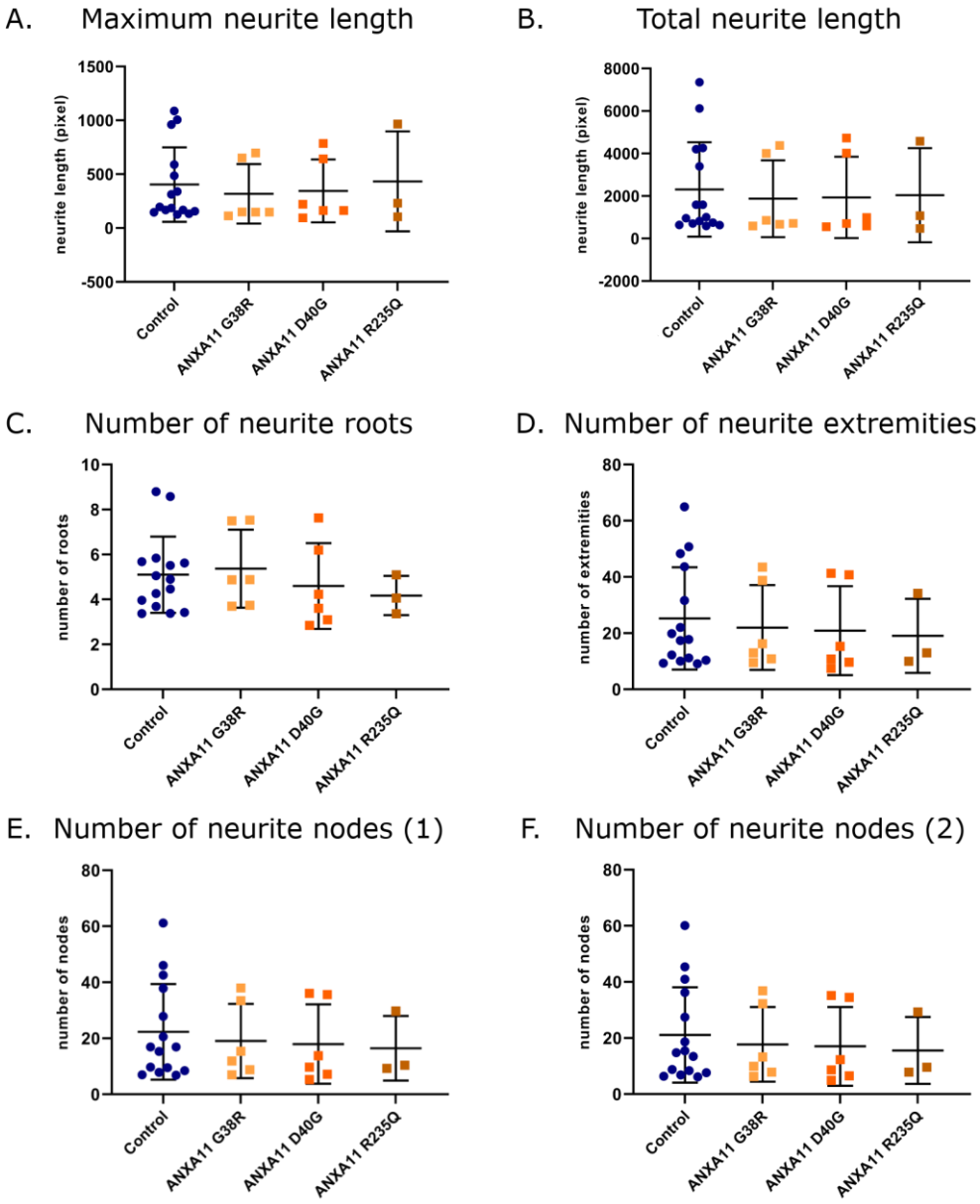


***Figure 5.6 Quantification of neurite outgrowth in motor neurons on day 17 of differentiation***

(A) Maximum neurite length and (B) total neurite length represent the length of outgrowing neurites. (C) The number of neurites growing out from the cell body. (D) The number of neurite endpoints is calculated as number of neurite extremities. (E) Number of neurite nodes (1) measures the number of branch points. (F) Number of neurite nodes (2) represents the number of neurite segments/the number of neurite roots. Data are presented as mean ± SEM, number of motor neuron inductions = 3; each data point represents one cell line in one motor neuron induction, with each comprising three technical replicates. Control lines are grouped and *ANXA11* ALS patient lines are grouped by mutation. Statistical analysis: Ordinary one-way ANOVA with Dunnett's multiple comparison test ($p > 0.5$).

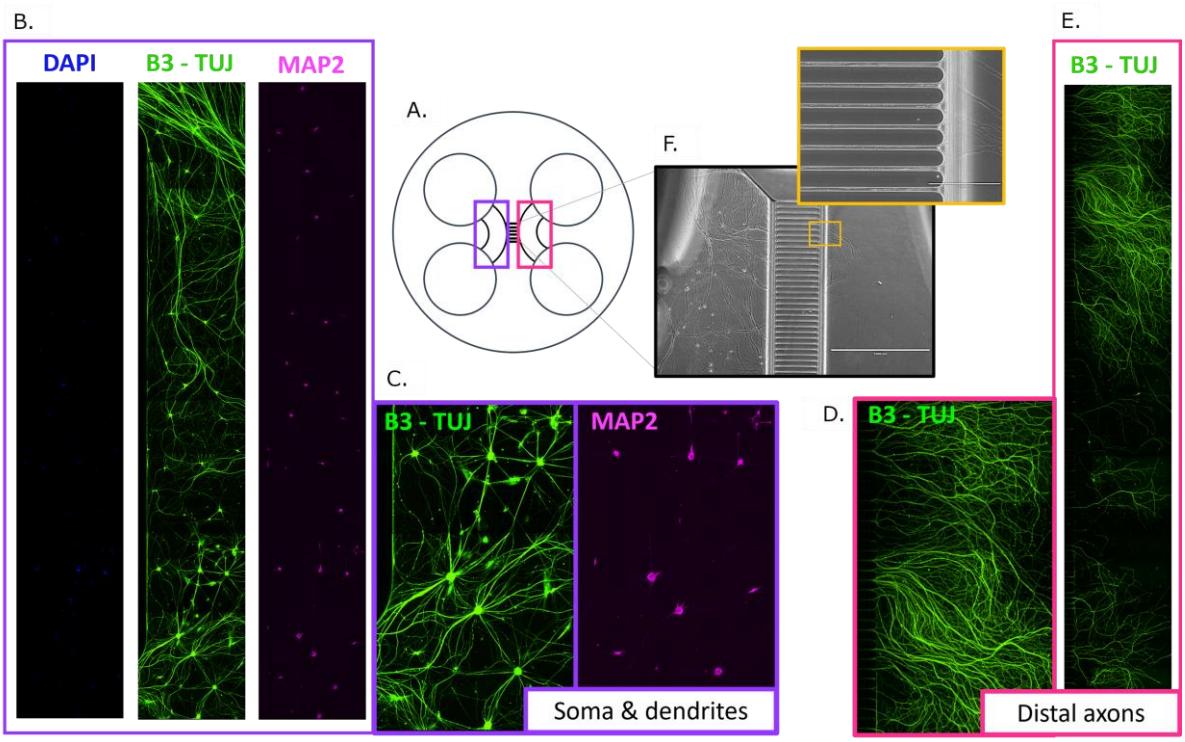


***Figure 5.7 Microfluidic devices***

An example of microfluidic layout and cell placement within the device. (A) The cartoon in the centre shows the microfluidic device layout. Motor neurons and astrocytes are plated in circular chambers on one side of the device (B,C; highlighted with purple), and neurites extend to the centre of the device, such that DAPI (blue) stained nuclei, MAP2 (magenta) positive cell bodies and dendrites, and $\beta$3-Tubulin positive proximal neurites (B3-TUJ, green) can be detected. Distal neurites are detected in the opposite side of the device (D, E; highlighted in pink) and have grown through the microgrooves in the centre of the device (F; highlighted in orange). Scale bars in (F) represent 1000µm and 500µm (inset).

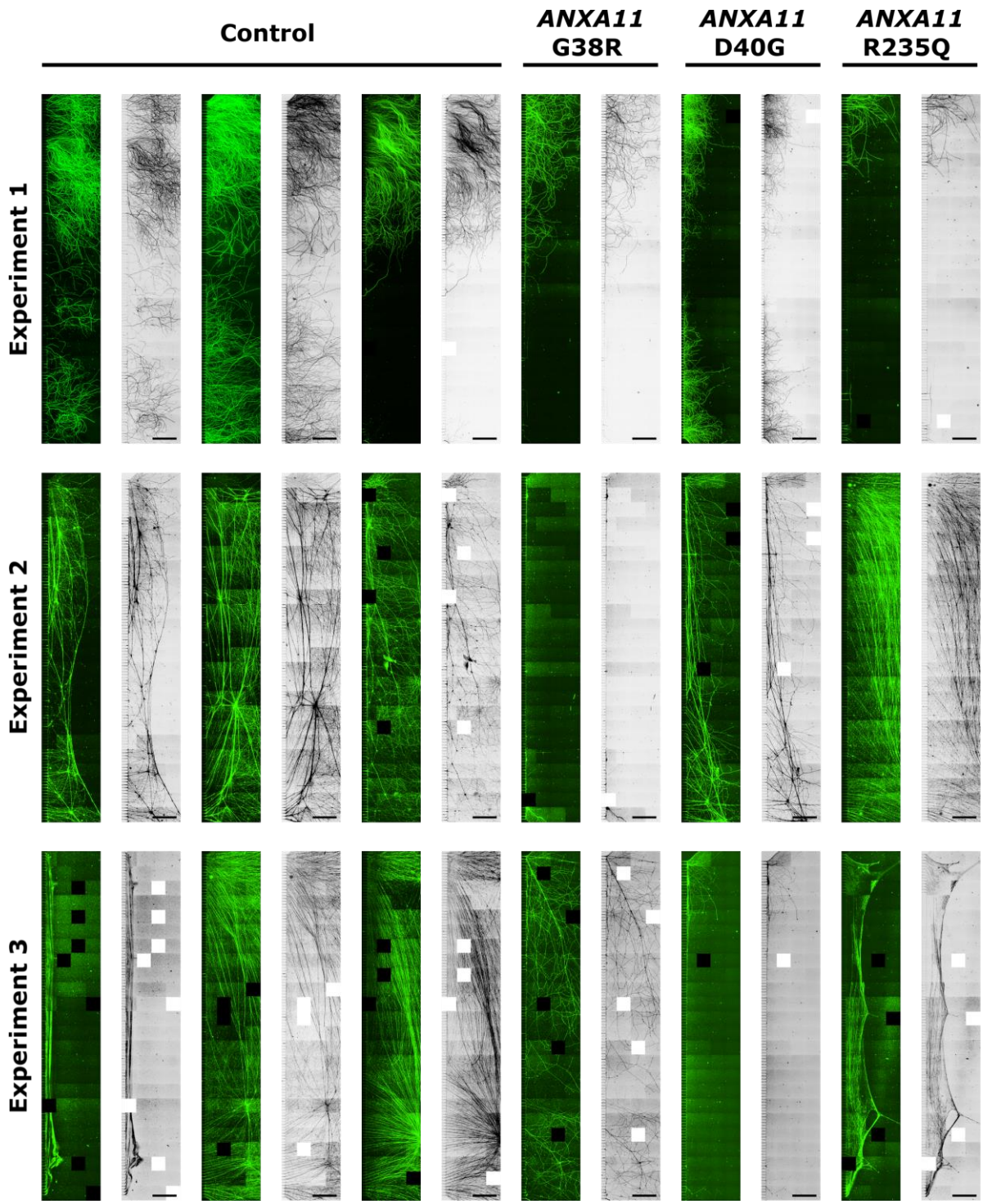


***Figure 5.8 Neurite outgrowth is perturbed in microfluidic devices***

Motor neurons derived from three control and three *ANXA11* ALS patient iPSC lines were cultured with astrocytes in microfluidic devices (see Figure 5.7) and maintained in culture for 25 days. Each image shows the post-microgroove section of the microfluidic chamber (Figure 5.7.F), with axons that have successfully grown through the middle of each device. Large images were collected with a Nikon Spinning Disk Confocal Microscope by stitching multiple fields of view with the Large Image function (empty squares within images are due to failed image collection). Each example is shown in

both fluorescent and greyscale form to aid visualisation. Scale bars represent 500µm. In some instances, neurite networks lifted off from devices during fixation or immunocytochemistry (far left control line in Experiment 2 and Experiment 3, *ANXA11* R235Q in Experiment 3).

### *5.3.2 Characterisation of spontaneous calcium fluctuations in motor neuron-astrocyte co-cultures*

Spontaneous calcium fluctuations were detected in motor neuron-astrocyte co-cultures on day 40 and day 64 of motor neuron differentiation, and changes in Fluo-4 AM intensity fell into various categories. Each time-lapse image was recorded for 60 seconds, and the pattern of calcium fluctuation in this time frame was used to stratify the calcium signals into groups. In some instances, a large synchronous increase in calcium signal was observed one or more times in the recording period (Figure 5.9), which was characterised by all neurons in the field of view and all ROIs increasing and decreasing in fluorescent signal in synchrony. In some instances, rapid, repetitive, and synchronous fluctuations were observed (Figure 5.10). In these cases, fluctuations occurred in quick succession and were smaller in nature. In some image sets no synchronous calcium fluctuations were observed and signal was detected in stand-alone cells or neurites (Figure 5.11). Lastly, in some instances no calcium fluctuations were detected in the 60 second recording period (Figure 5.12).

Recordings were categorised and grouped by mutation status; control, *ANXA11* G38R, *ANXA11* D40G, and *ANXA11* R235Q. Stacked bar charts show the calcium fluctuation patterns detected in each group (Figure 5.13.A; Figure 5.13.B). Visual inspection suggests that rapid and repetitive calcium fluctuations (Figure 5.10) are more present in *ANXA11* G38R compared to control motor neurons on both day 40 and day 64 of culture maturation. On day 64, *ANXA11* R235Q neurons displayed an increased number of large, synchronised calcium fluctuations compared to control. In both instances *ANXA11* D40G neurons show a similar fluctuation pattern to control, however the day 64 *ANXA11* D40G group includes a higher proportion of recordings where no calcium fluctuations were detected, suggesting that altered calcium dynamics may be mutation specific in *ANXA11* ALS.

To statistically compare control and *ANXA11mut* groups, data from day 40 and day 64 motor neurons and *ANXA11mut* groups were combined. The comparison of categorised data with a chi-squared test necessitates that no more than 20% of the expected frequencies can have a value of less than 5, and that no expected frequencies can have a value of less than 1. This was not met when assessing each time point or when comparing every *ANXA11mut* group individually. Alternative statistical tests for comparison of small categorical datasets include Fisher's exact test, which can only be applied when there are two categories, which does not apply here (Kim, 2017). Additional tests have been developed however are not included in the statistical analysis tools that were available throughout this project. Therefore, although *ANXA11mut* groups showed different activity profiles to one another, and data from different time points should not typically be combined, no statistical analysis could be applied to the original groups. Analysis of grouped data indicates a statistically significant difference between control and *ANXA11mut* groups (Figure 5.13.C), suggesting that calcium activity is altered in *ANXA11* ALS motor neurons. For the reasons discussed here, this result should be taken as a preliminary indication of altered calcium dynamics and is not conclusive.

Once calcium experiments were complete, cells were fixed and probed for the cholinergic neuron marker ChAT and the glutamatergic neuronal marker vGLUT2 to ensure appropriate cell types were present in cultures (Appendix Figure 9.27; Appendix Figure 9.28). Subsequent imaging revealed diverse neuronal cell populations with evidence of both ChAT and vGLUT2 positive neurons in cultures that had been probed for spontaneous calcium fluctuations.

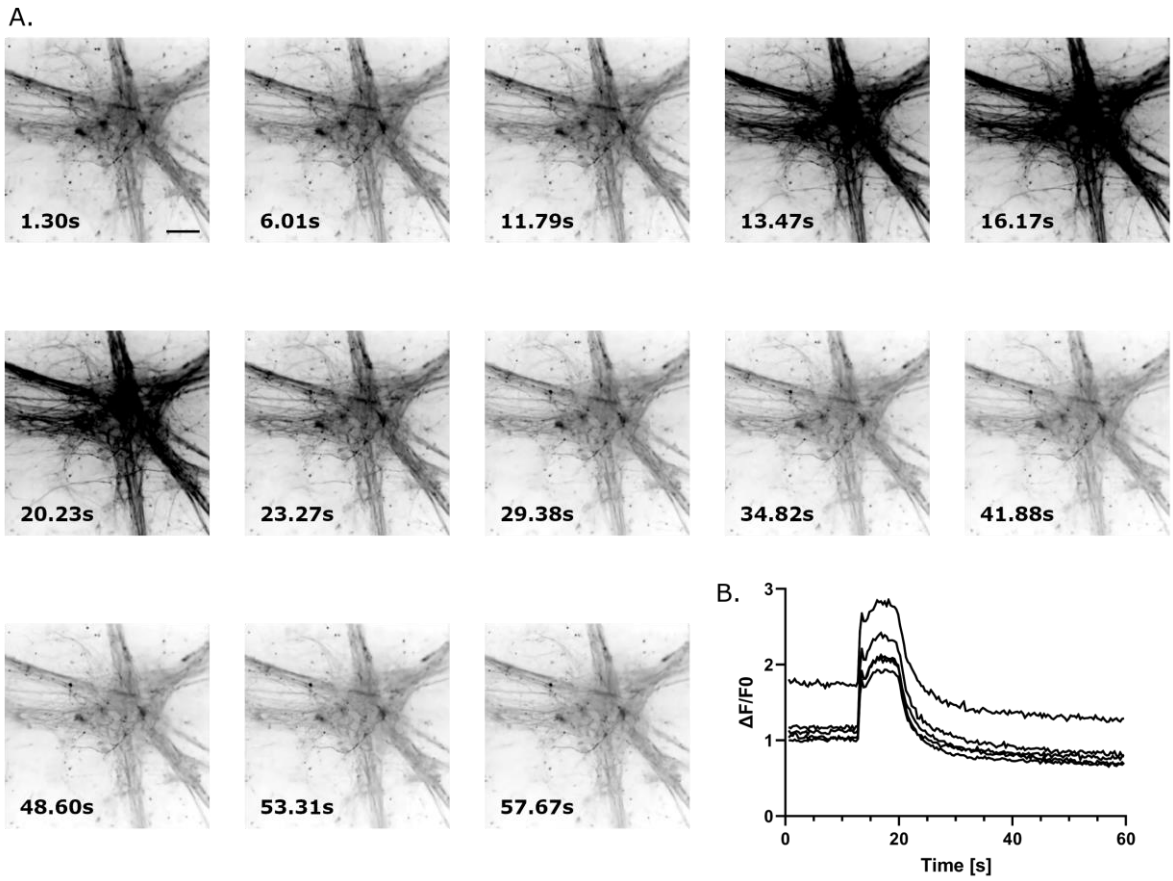


***Figure 5.9 Large synchronised calcium fluctuations in motor neurons***

Motor neurons were maintained in co-culture with astrocytes for 40 or 64 days from motor neuron induction, incubated with Fluo-4 AM, and imaged with a Nikon Spinning Disk Confocal Microscope. (A) Example stills from time-lapsed imaging of day-40 motor neurons exhibiting a large and synchronised fluctuation in calcium concentration within the 60 second recording time, as indicated by increased intensity of Fluo-4 AM (greyscale). Time is indicated in the bottom left corner of each frame, scale bar represents 50µm (top left image). (B) Fluorescent signal from Fluo-4 AM from five ROIs was normalised to background using ΔF/F0 and plotted against time. Simultaneous increase in Fluo-4 AM signal in all ROIs indicates synchronised calcium fluctuations in neighbouring cells. The cell line included in the example is *ANXA11* G38R 1 on day 40 of differentiation.

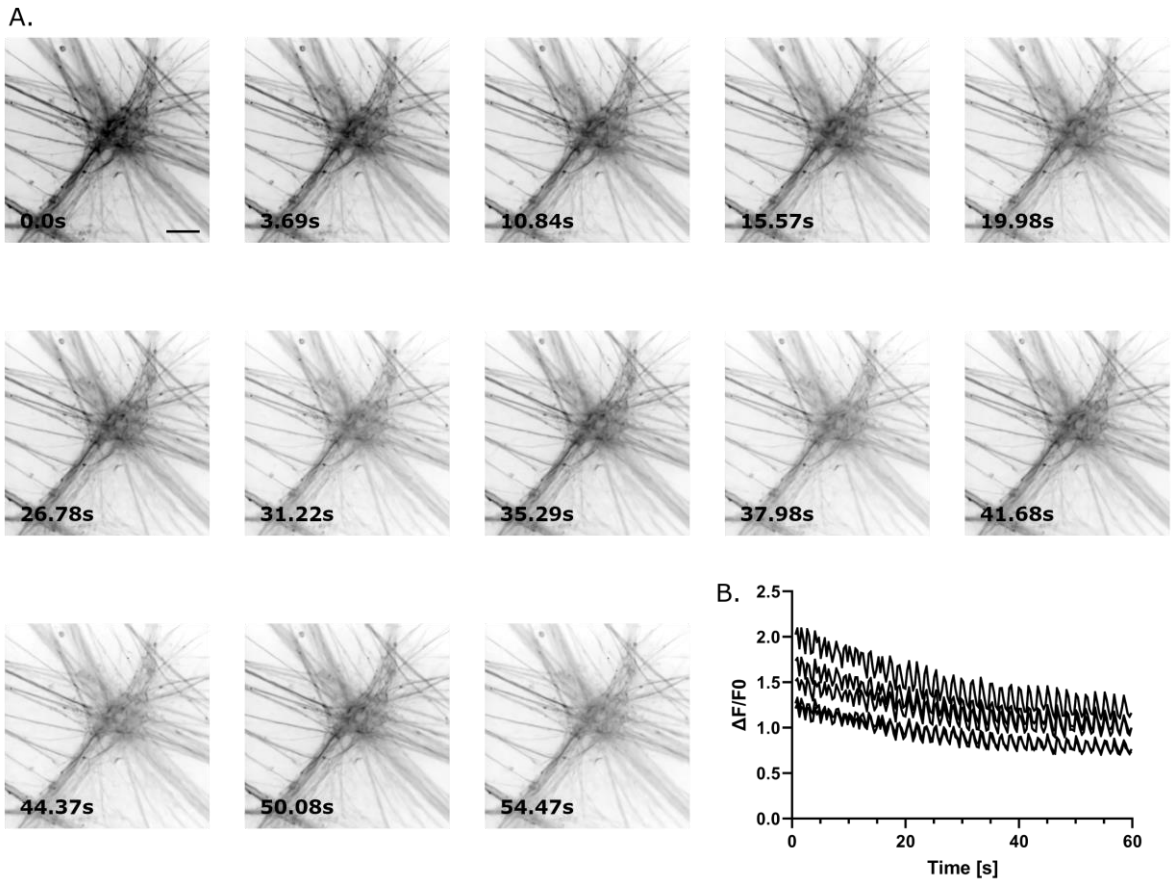


***Figure 5.10 Continuous repetitive calcium fluctuations in motor neurons***

Motor neurons were maintained in co-culture with astrocytes for 40 or 64 days from motor neuron induction, incubated with Fluo-4 AM, and imaged with a Nikon Spinning Disk Confocal Microscope. (A) Example stills from time-lapsed imaging of day-40 motor neurons exhibiting multiple spontaneous and synchronised increases in calcium concentration within the 60 second recording time, as indicated by increased intensity of Fluo-4 AM (greyscale). Time is indicated in the bottom left corner of each frame, scale bar represents 50µm (top left image). (B) Fluorescent signal from Fluo-4 AM from five ROIs was normalised to background using ΔF/F0 and plotted against time. Simultaneous increase in Fluo-4 AM signal in all ROIs indicates repetitive synchronous calcium fluctuations in neighbouring cells. The cell line included in the example is *ANXA11* G38R 2 on day 40 of differentiation.

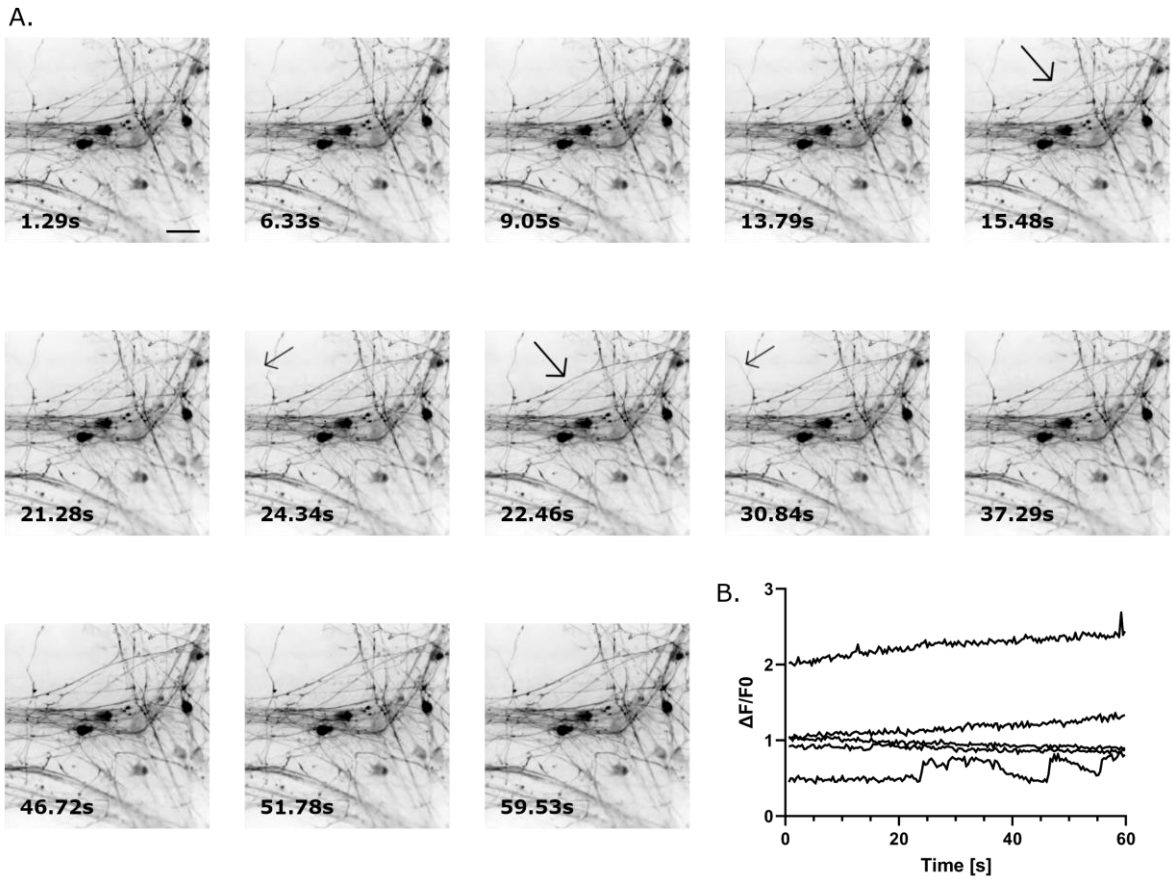


***Figure 5.11 Unsynchronised calcium activity in motor neurons***

Motor neurons were maintained in co-culture with astrocytes for 40 or 64 days from motor neuron initiation, incubated with Fluo-4 AM, and imaged with a Nikon Spinning Disk Confocal Microscope. (A) Example stills from time-lapsed imaging of day-40 motor neurons exhibiting calcium fluctuations in individual neurites as indicated by increased intensity of Fluo-4 AM (greyscale). Black arrows (paired by arrow size and location) indicate neurites with fluctuating Fluo4 intensity. Time is indicated in the bottom left corner of each frame, scale bar represents 50µm (top left image). (B) Fluorescent signal from Fluo-4 AM from five ROIs was normalised to background using ΔF/F0 and plotted against time. The cell line included in the example is control 5 on day 40 of differentiation.

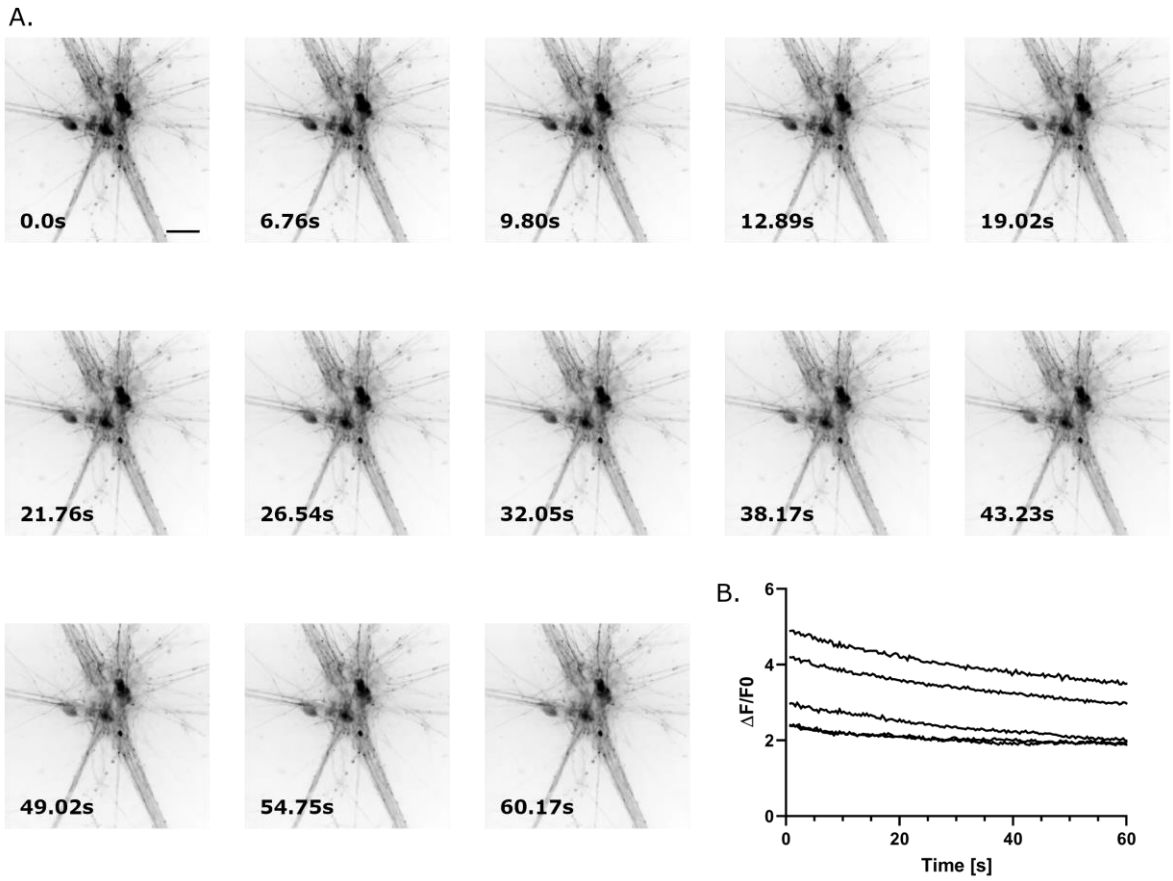


***Figure 5.12 No calcium fluctuations detected in motor neurons***

Motor neurons were maintained in co-culture with astrocytes for 40 or 64 days from motor neuron initiation, incubated with Fluo-4 AM, and imaged with a Nikon Spinning Disk Confocal Microscope. (A) Example stills from time-lapsed imaging of day-40 motor neurons with no detectable fluctuations in Fluo-4 AM intensity within the 60 second recording time, as indicated by unchanged intensity of Fluo-4 AM (greyscale). Time is indicated in the bottom left corner of each frame, scale bar represents 50µm (top left image). (B) Fluorescent signal from Fluo-4 AM from five ROIs was normalised to background using ΔF/F0 and plotted against time. The cell line included in the example is control 4 on day 40 of differentiation.

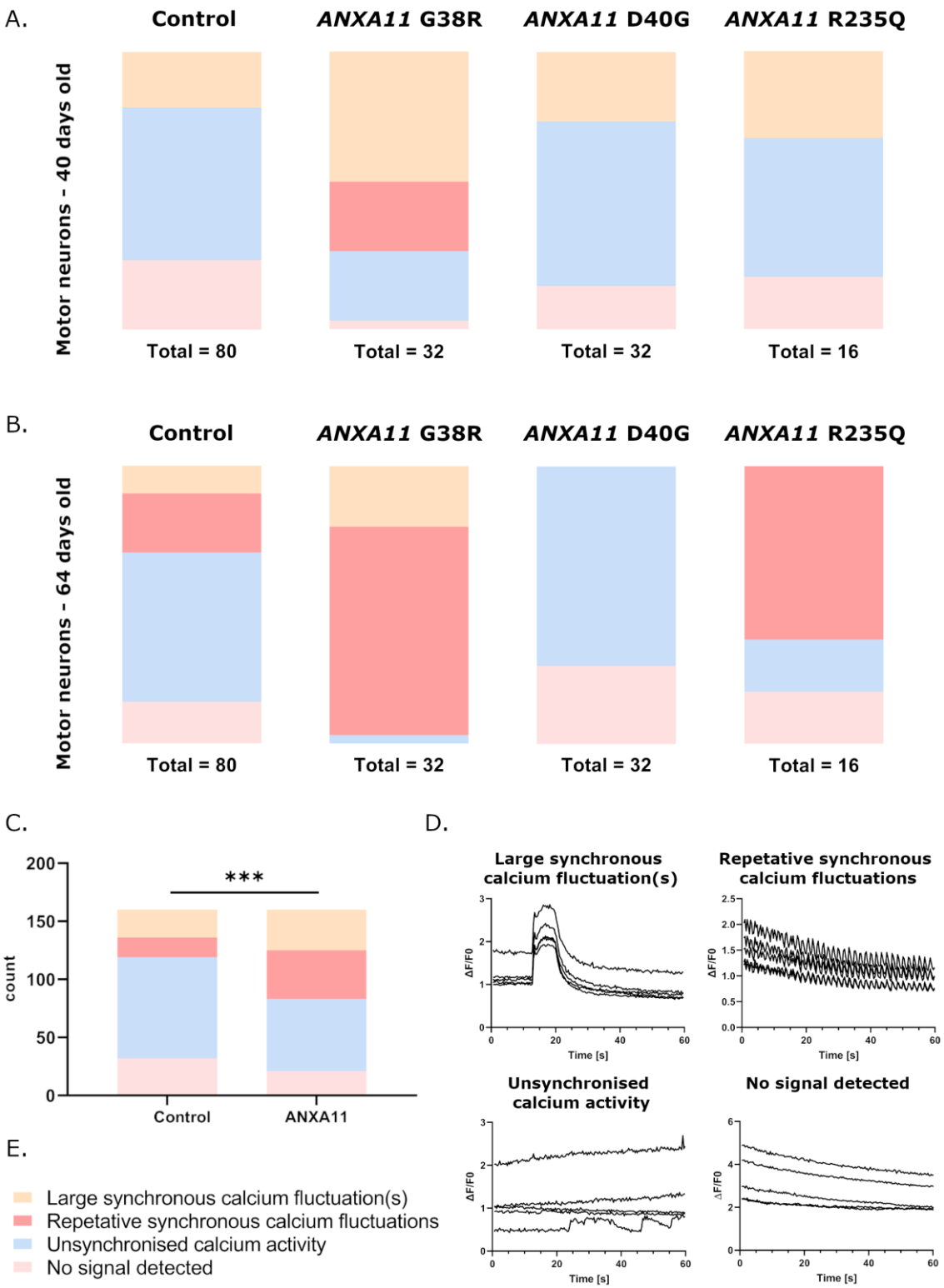


***Figure 5.13 Categorisation of calcium activity in motor neurons***

Spontaneous calcium activity was categorised for control and *ANXA11mut* co-cultured motor neurons on (A) day 40 and (B) day 64 of differentiation, the total number of time lapse images quantified for each group is included under the relevant graph section, number of motor neuron inductions = 2 for each time point. (C) Data from day-40 and day-64 neurons were combined so that

control and *ANXA11mut* could be statistically compared, revealing a difference between the two groups ($p$ = 0.0003). Statistical analysis; chi-squared test (***$p \leq 0.001$). (D) Example activity traces of each of the four categories, as shown in Figures 5.9-12. (E) Key for (A, B, and C).

### *5.3.3 Electrophysiology and synapse analysis*

To further assess activity in control and *ANXA11mut* motor neurons, a subset of lines was subject to patch-clamp analysis, courtesy of Dr Seung Chan Kim. Four cell lines (2x control, 1x *ANXA11* G38R, 1x *ANXA11* D40G) were included for analysis. The reduction in cell line number compared to other analyses was due to technical limitations. Quantification included the number of firing events in response to increasing current injection, the frequency of firing events (calculated from the inter-event interval), and resting membrane potential (Figure 5.14). Some separation occurred between control and *ANXA11mut* lines, with an increased number of firing events and increased frequency observed in control lines, however no statistical significance was observed. Resting membrane potential was similar across cell lines (control 4, -44.30±2.71; control 5, -46.66±2.41; *ANXA11* G38R 2, -47.33±3.15; *ANXA11* D40G 2, -51.00±2.84 (mV)).

To assess synaptic maturity of cultures, the same cell lines used in electrophysiological experiments were fixed on day 40 of motor neuron differentiation and probed for the synaptic markers Synapsin 1 and bassoon. Synapsin 1 and bassoon localise to the pre-synapse: Synapsin 1 is a synaptic vesicle-associated protein (Baldelli et al., 2013), and bassoon is a scaffolding protein that assembles the active zone (Gundelfinger et al., 2016). High-resolution imaging of neurites from day-40 motor neurons showed abundant Synapsin 1 and bassoon in control and *ANXA11mut* motor neurons (Figure 5.15). Additionally, due to evidence that aged cultures were comprised of a combination of ChAT positive and vGLUT2 positive neurons (Appendix Figure 9.27; Appendix Figure 9.28), vGLUT2 and Annexin A11 were probed for in day-50 control motor neurons, revealing potential localisation of Annexin A11 to vGLUT2 positive synaptic vesicles (Figure 5.16).

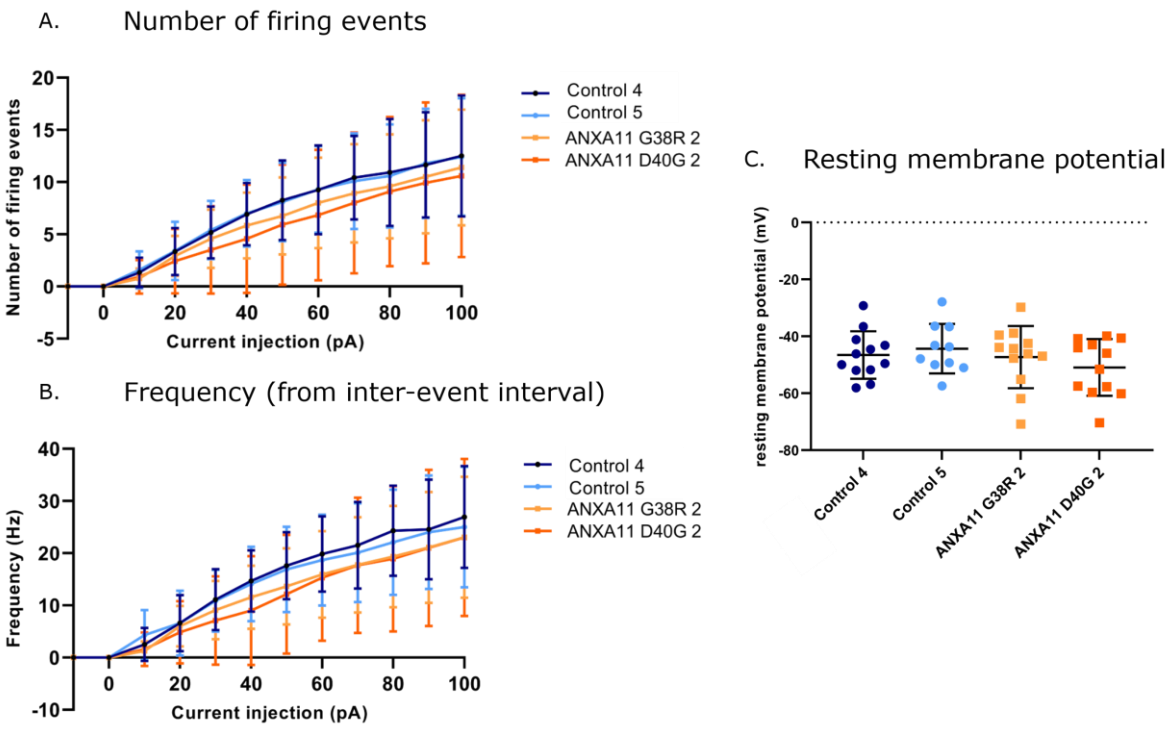


***Figure 5.14 Electrophysiological analysis of motor neurons***

Two control and two *ANXA11* patient iPSC lines were differentiated into motor neurons and maintained in co-culture with astrocytes until day 40 of motor neuron differentiation. (A) The number of firing events per 500ms was measured with a current injection step size of 10pA (-10 to 100pA). The two control lines showed a slight trend toward increased firing, which was not significant. (B) The firing frequency, calculated from the inter-event interval, showed a slight separation between control and *ANXA11mut* lines, which was not statistically significant. (C) The resting membrane potentials were; control 4, -44.30±2.71; control 5, -46.66±2.41; *ANXA11* G38R 2, -47.33±3.15; *ANXA11* D40G 2, -51.00±2.84 (mV). The data sets for each cell line are comprised of measurements from 10-12 neurons collected across three motor neuron inductions (control 4, $n$ = 12; control 5, $n$ = 10, *ANXA11* G38R 2, $n$ = 12; *ANXA11* D40G, $n$ = 12). (C) Statistical analysis: Ordinary one-way ANOVA with Tukey's multiple comparisons test ($p > 0.05$).

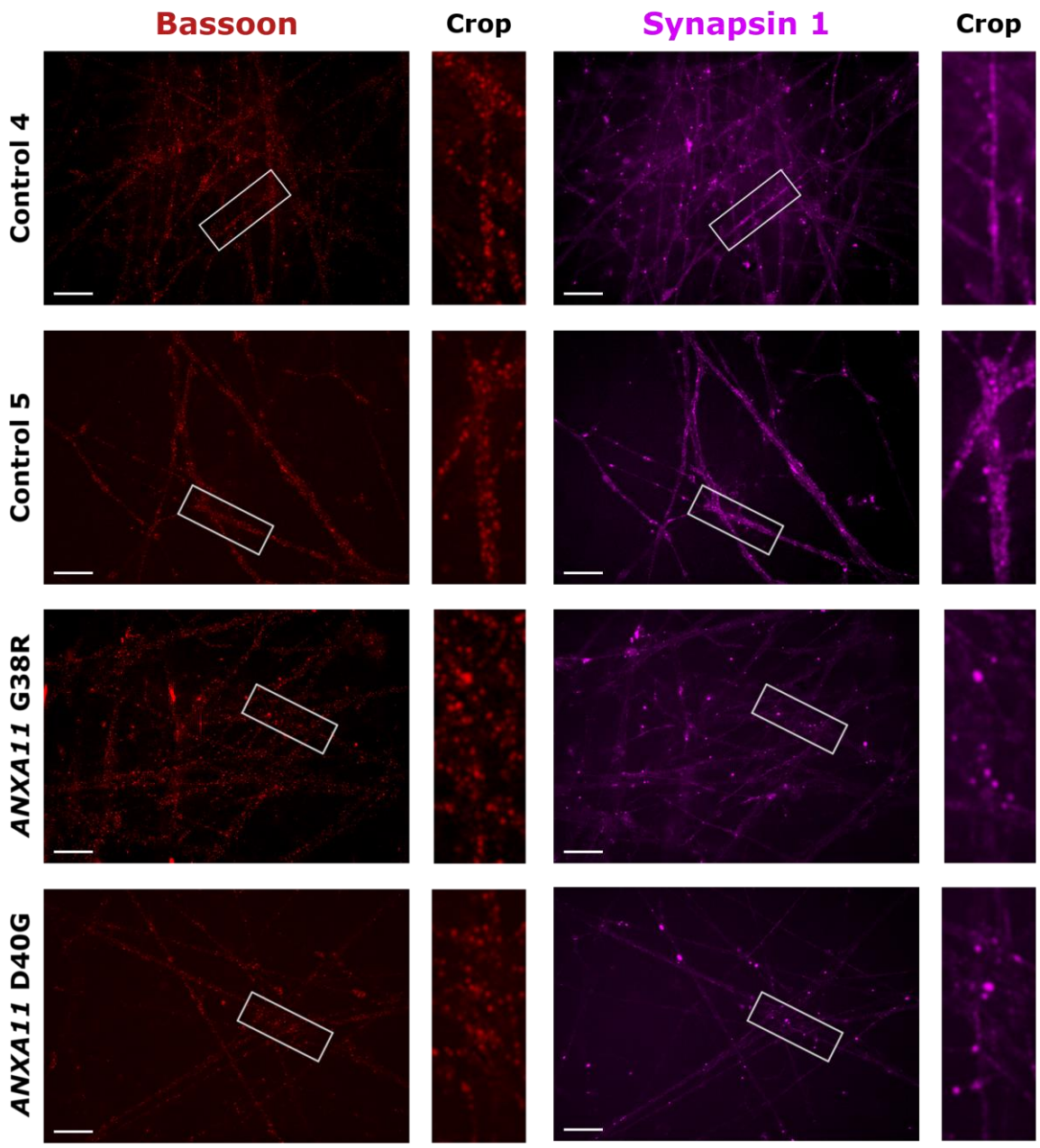


***Figure 5.15 Synaptic proteins bassoon and Synapsin 1 are expressed in iPSC-derived motor neurons***

iPSC-derived motor neurons were maintained in co-culture with astrocytes and fixed on day 40 of motor neuron differentiation. Immunocytochemistry using antibodies targeting the pre-synaptic proteins bassoon (red) and Synapsin 1 (magenta) revealed the presence of synapses in motor neuron neurites. Images were taken with a Nikon iSIM system. Scale bars represent 10µm.

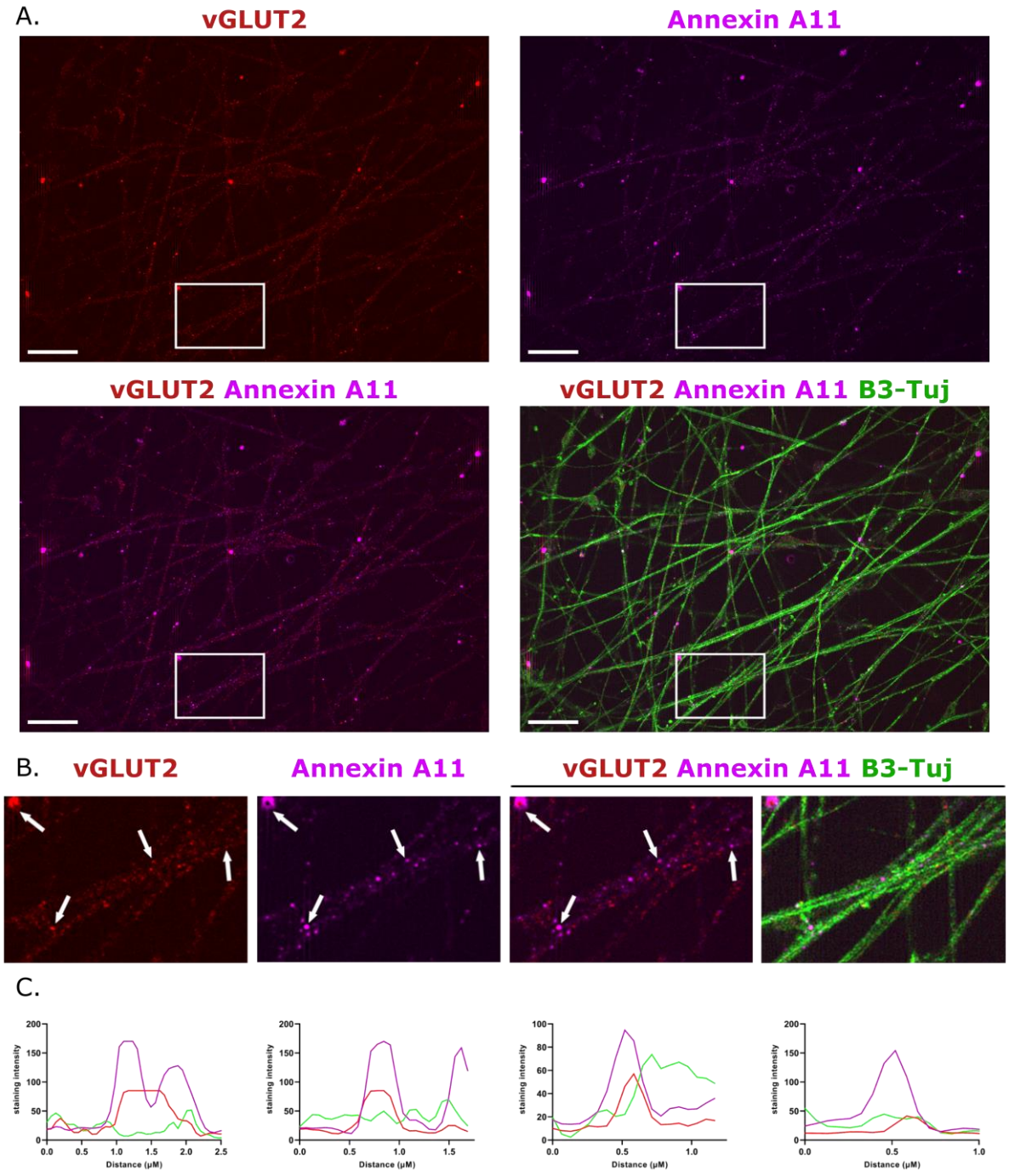


***Figure 5.16 Annexin A11 localises to vGLUT2 positive puncta in neurites***

(A) Immunocytochemistry with antibodies targeting the neurite marker $\beta$3-Tubulin (B3-Tuj, green), Annexin A11 (magenta), and the glutamatergic synaptic vesicle protein vGLUT2 (red) in day-50 control 1 motor neurons. (B) Magnified regions show co-localisation of Annexin A11 and vGLUT2, indicated with white arrows. (C) Intensity traces represent puncta indicated from left to right by white arrows in (B). Colours included in intensity traces represent Annexin A11 (magenta), vGLUT2 (red), and $\beta$3-Tubulin (green). Scale bar represents 10µm.

## *5.4 Discussion*

The utilisation of stem cell-derived neuronal cultures to model neurological disease allows assessment of neurite specific processes, including initial outgrowth of neurites and the subsequent formation of connections between axons and dendrites. Perturbation to neurite outgrowth can indicate multiple dysregulated cellular pathways, and assessment of neuronal activity can indicate altered signalling or homeostatic imbalance. Here, initial neurite outgrowth was unchanged in *ANXA11mut* motor neurons on day 12 and day 17 of motor neuron differentiation (Figure 5.4; Figure 5.6). Intriguingly, distal axon integrity appeared to be affected in patient lines, indicating that although primary neurite formation was successful, the maintenance of cellular compartments distant from cell bodies was affected (Figure 5.8).

To assess whether spontaneous activity and functional connections had been established in iPSC-derived neuronal cultures, live calcium imaging and electrophysiological recordings were implemented. This revealed that cultures were indeed active and often synchronous, and implied altered states of calcium activity across control and *ANXA11mut* groups (Figure 5.13). Patch-clamp analysis did not reveal differences in action potential firing frequency or resting membrane voltage (Figure 5.14). Evidence of synaptic proteins in motor neurons on day 40 of differentiation indicated that neurons were expressing proteins necessary for intercellular communication, with some evidence that Annexin A11 is localised to synaptic regions in glutamatergic neurons (Figure 5.15; Figure 5.16).

### *5.4.1 Neurite outgrowth in ANXA11 ALS motor neurons*

The highly polarised nature of neurons is necessary for their function. Neuronal polarity is under the tight control of initial neurogenesis and is maintained in mature neurons in part by the axon initial segment (Barnes & Polleux, 2009; Ho & Rasband, 2011). Neurite outgrowth is the process by which young neurons extend out, led by growth cones at the tip of spindle-like protrusions, forming

structures that develop into axons and dendrites. The cytoskeleton mediates this process, and an array of transcription factors are involved in neurite extension including neurogenin1 (Kim et al., 2002), neurogenin2 (Liu et al., 2013), Pea3 (Kandemir et al., 2020), STAT3 (L. Zhou & Too, 2011), and the Neurod family (Lee et al., 2020; Tutukova et al., 2021), to name a few. This enables neurons to create networks of highly specific and complex interactions. These interactions are mediated by chemical synapses, where neurotransmitters are released into the synaptic cleft from the presynaptic compartment and bind to the post-synaptic compartment, causing an influx of ions, depolarisation of the membrane, and induction of action potentials (Bean, 2007).

Alterations in axons and dendrites have been identified in multiple cellular and animal models of neurodegenerative diseases, including ALS/FTD (Akiyama et al., 2019; Genç et al., 2017; Harjuhaahto et al., 2020; Sasaki & Iwata, 1999). Additionally, many studies show perturbation at the synaptic, axonal, or NMJ level prior to soma pathology or neuronal loss (Fischer et al., 2004; Juan et al., 2022; López-Erauskin et al., 2018; Ozdinler et al., 2011; Shahidullah et al., 2013; So et al., 2018; Zhang et al., 2022). Some ALS/FTD associated proteins have been shown to mediate neurite outgrowth including progranulin (Van Damme et al., 2008), TDP-43 (Atkinson et al., 2021; Fiesel et al., 2011; Mitsuzawa et al., 2021), and FUS (Stoklund Dittlau et al., 2021). The initially unaffected neurite outgrowth observed here (Figure 5.4) might suggest that transcriptional regulation and cytoskeletal dynamics that initiate neurite outgrowth are not primarily perturbed, but instead there is a failure to support distal axon function. It should be noted that these early neurites include axons and dendrites, and it may be informative in future analysis to include specific markers such as Map2 and Tau to differentiate between the two. Overlap of pan-neuronal $\beta$3-Tubulin with dendrite specific Map2 was assessed in control cells on day 12 of differentiation, indicating that most neurites are Map2 positive, however some $\beta$3-Tubulin positive neurites where Map2 is absent are highlighted (Appendix Figure 9.29). This suggests that many of the neurites quantified in day-12 analysis are early dendrites, and in future investigation it will be important to specifically assess axons to identify the time point at which they become affected.

Substantial evidence exists for the “dying back” hypothesis, where initial insult at the NMJ leads to gradual degeneration of the motor neuron in a retrograde fashion (Arbour et al., 2015; Fischer et al., 2004; Genin et al., 2019; Mejia Maza et al., 2021; Narai et al., 2009; Picchiarelli et al., 2019; So et al., 2018; Tremblay et al., 2017). The reduced distal axon health seen here (Figure 5.8) cannot be attributed to dysfunctional NMJs as without co-culture with muscle cells NMJ function cannot be assessed. Microfluidic systems with muscle cells and iPSC derived motor neurons enable inspection of NMJ formation and function, and would be a valuable tool in elucidating distal axonopathy in *ANXA11* ALS. Implementation of such cultures has revealed reduced formation of NMJs in mutant *FUS* conditions, which was rescued with HDAC6 inhibition (Stoklund Dittlau et al., 2021).

Axon degeneration independent of initial outgrowth is mediated by multiple neuronal pathways. For example, degeneration of iPSC derived mutant *SOD1* motor neuron axons is linked to aggregation of neurofilament proteins (Chen et al., 2014). Contrastingly, axon destruction can occur in response to injury, which is mediated by metabolic sensors and the SARM1 protein (Figley et al., 2021), which is implicated in ALS (Bloom et al., 2022; Gilley et al., 2021). It was beyond the scope of this project to investigate specific degeneration pathways and additional analysis will be necessary: Time-lapse imaging of neurite outgrowth in iPSC derived neurons will be useful for assessing at which point axon integrity is lost in *ANXA11* ALS, to confirm whether axons grow and degenerate, or whether distal axon formation is perturbed. Implementation of axonopathy experiments, where axons are severed and regrowth is assessed (Stoklund Dittlau et al., 2021), will be informative in assessing *ANXA11mut* motor neuron response to injury. In conjunction, specially optimised axon interrogation allows RNA sequencing of distal axons (Nijssen et al., 2019) and it will be important to assess the axonal transcriptomic profiles of *ANXA11* ALS motor neurons in future studies.

Distal axons were not quantified here as different antibodies were used in immunocytochemistry, and so quantification could be misleading (Figure 5.8). In Experiments 2 and 3, neurites were immunolabelled for FUS, Annexin A11, and puromycin, as the motor neurons were assessed for local translation (6.3.3). The representative images in Figure 5.8 show FUS with increased contrast to

highlight neurites. Experiment 1 includes neurites immunolabelled for $\beta$3-Tubulin, and, due to time restraints, it was not possible to repeat this experiment multiple times. For Experiment 1, quantification of total fluorescent intensity from neurites before and after the microgroove region supports a reduction in distal axon outgrowth in *ANXA11mut* lines (Appendix Figure 9.26). It will be important to confirm and quantify distal axon outgrowth using consistent experimental parameters, and data shown here should serve only as an initial indication that distal axon density is reduced in *ANXA11mut* lines. Bright-field imaging was attempted to visualise distal axons without the inclusion of different antibodies, but image quality was poor and so neurites were visualised as described.

To ensure that the observed reduced axon outgrowth seen here was due to neurite instability instead of reduced motor neuron count, neuronal plating compartments of microfluidic devices were stained with DAPI and neuronal nuclei were counted (Appendix Figure 9.25). This revealed apparently comparable numbers of neurons present in devices at the point of fixation, however was only included for Experiment 1. One culture condition that was not applied here was a differential concentration of growth factors across microfluidic devices. In many instances in the literature, growth factors are added at a higher concentration on the distal side of the device to encourage neurite growth through to the compartment where growth factors are more abundant. Microfluidic devices in this instance were not maintained in this way, and complete motor neuron media was applied to the entire culture. This may have resulted in an exaggerated phenotype in *ANXA11mut* lines, and the inclusion of a growth factor gradient may have encouraged more successful outgrowth (Spijkers et al., 2021). Additionally, the inclusion of muscle cells, or other supportive cell types such as glial cells, in distal axon compartments would be an informative way to assess the role of non-cell-autonomous mechanisms in axon maintenance. An absence of glia from iPSC neuron derived co-cultures has been shown to cause motor neuron-specific axon degeneration (Chen et al., 2014). In this project, astrocyte co-culture was partly included to maintain culture longevity due to fragmentation of neurites in aged neurons (3.3.6). This suggests that axon integrity is partially

dependent on extracellular support, and it would be useful for therapeutic targeting to assess the functional consequences of non-neuronal cells in axon stability.

Collectively these data indicate an early dysfunction in axons, however mechanistic insight into the cause of axon instability remains to be explored. Axon specific functions of Annexin A11 are not well defined. Recent evidence shows that Annexin A11 acts as a tether between lysosomes transported along axons and RNA granules that "hitch-hike" on lysosomes (Liao et al., 2019). The highly polarised and exceptional length of neurons, particularly long lower motor neurons, means that many cellular components need to be transported a substantial distance to synaptic terminals. RNA is an essential cargo, and local translation throughout the axon relies on the delivery of RNA, highlighting RNA dynamics as an essential avenue for investigation in *ANXA11* associated ALS. Axonal RNA transport and local translation in *ANXA11* ALS motor neurons are explored in Chapter 6.

### *5.4.2 Spontaneous calcium activity and action potentials*

Once initial neurite outgrowth has occurred, synapses form between neurons, and synaptic plasticity orchestrates the network of cells that make up the CNS. Once synaptic connections are made, random firing events stimulate connectivity between cells and aid the maturation of functional networks (Ben-Ari, 2001; Cohen et al., 2008; Zhang & Poo, 2001). The synaptic connections between neurites that determine cell-to-cell communication have been associated with early disease events in many neurodegenerative diseases. Multiple ALS related genes and proteins have recently been implicated at the synaptic level, including *TARDBP* and *FUS* (Dyer et al., 2021; Ling, 2018; Markert et al., 2020; Mejia Maza et al., 2021; Picchiarelli et al., 2019; Sahadevan et al., 2021; Salam et al., 2021; Wong et al., 2021), *C9ORF72* (Butti et al., 2021; Catanese et al., 2021; Jensen et al., 2020; Nishimura & Arias, 2021; Perkins et al., 2021; Xiao et al., 2019) and *SOD1* (Song, 2020). Loss of synaptic function of dynactin subunit 1 leads to loss of synaptic stability and impaired growth of motor neurons (Bercier et al., 2019), highlighting the importance of synapse integrity in axon outgrowth. Although evidence of synaptic proteins was included here (Figure 5.15), limitations in time and antibody

availability meant that in-depth analyses of synaptic composition and structure were not feasible within this project, and notably no post-synaptic markers were included. The potential localisation of Annexin A11 to vGLUT2 positive synaptic vesicles implies Annexin A11 may have a role at synapses (Figure 5.16), and this would be an intriguing avenue for further investigation.

Disease-associated altered synaptic connections can manifest as dysregulated calcium signalling, and calcium fluctuations can be utilised to measure culture activity in iPSC derived neurons, indicating the presence of functional ion channels or release of calcium from endogenous stores (Burley et al., 2022; Sharma et al., 2020). There are multiple arguments for assessment of calcium activity in iPSC derived neurons; as an indication of culture maturity, and to recognise disease associated calcium activity profiles. Of relevance to this thesis is the role of calcium-dependent protein function: Annexin A11 binds to phospholipid membranes in the presence of calcium, so evidence of calcium signalling in iPSC derived neurons might be necessary to accurately assess the characteristics of Annexin A11 protein. In most instances, some level of spontaneous calcium activity was observed in control and *ANXA11mut* groups on days 40 and 64 of differentiation. In all groups, some recordings showed an absence of calcium activity, with the exception of day-64 *ANXA11* G38R neurons which showed consistent activity (Figure 5.13). This indicates that iPSC-derived neurons were mature and confirms that cultures are functionally active, which is important when considering experimental results.

Calcium activity was categorised based on observed fluctuation patterns, including large synchronous bursts at varying frequencies, unsynchronised activity in individual cells or neurites, and no observable activity. In the absence of more stringent quantification options, ΔF/F0 was implemented to normalise fluorescent signal to the background and enable data visualisation of signal over time (Figure 5.9 – Figure 5.13). ΔF/F0 is commonly used to measure calcium signals in biological research and is often included in automated analysis tools such as EZCalcium (Cantu et al., 2020), or implementation of quantification algorithms (Cornelissen et al., 2013; Kuijlaars et al., 2016). Unfortunately, the optimisation of these tools was beyond the scope of this project, but would

be useful for further investigation into the calcium dynamics of *ANXA11* patient motor neurons. Qualitative analysis of calcium fluctuations suggests a relative increase in the amount of rapid, repetitive, synchronous bursts in *ANXA11* G38R neurons compared to the control group on day 40 and day 64 of motor neuron differentiation, and an increase in large, synchronous fluctuations in day-64 *ANXA11* R235Q neurons (Figure 5.13). A more marked difference between control and *ANXA11mut* lines was observed in day-64 neurons, suggesting that calcium alterations are progressive and exacerbated with culture maturity.

iPSC-derived neurons have been shown to exhibit synchronous firing as they form functional networks, which is increased in the presence of astrocytes which improve the maturation of network functionality (Kuijlaars et al., 2016). This suggests that the observed synchronous activity is expected in iPSC-derived neuronal cultures. The differential presence of such activity in control and *ANXA11mut* groups indicates altered calcium homeostasis in mutant groups. Interestingly, the *ANXA11* D40G group showed a different calcium fluctuation pattern and displayed decreased calcium fluctuations in day-64 neurons compared with day-40, suggesting altered calcium dynamics are mutation specific in *ANXA11* ALS (Figure 5.13). Recent analysis of *C9ORF72* expansion iPSC-derived motor neurons highlighted hyperexcitability in mutant neurons on day 40 of differentiation, which was associated with increased release of calcium from internal stores in the absence of altered electrophysiological profile (measured by patch-clamp) (Burley et al., 2022). This hyperexcitability was transient, and more mature cultures (day 47 of differentiation) showed a reduction in excitability, reflecting the age-associated reduction in activity seen in *ANXA11* D40G neurons (Figure 5.13). This highlights the need to assess multiple time points and suggests a developmental aspect in ALS hyperexcitability. Further, the data from *C9ORF72* motor neurons (Burley et al., 2022) reflect results from *ANXA11mut* motor neurons, which displayed increased calcium activity compared to control (Figure 5.13) in the absence of alterations to electrophysiological profile (Figure 5.14). A culture maturity dependent decrease in calcium activity does not apply to *ANXA11* G38R and R235Q motor neurons in qualitative analysis, and further culture aging would be useful for clarification of

temporally mediated calcium activity in *ANXA11* motor neurons. Identification of similar activity profiles in *C9ORF72* and *ANXA11mut* motor neurons indicates a common phenotype, and a direct comparison of ALS genetic subtypes in the context of neuronal activity may be important for elucidation of shared cellular pathologies and disease targeting.

Calcium homeostasis is affected in multiple instances of ALS, including *ANXA11*. Calcium-dependent translocation of Annexin A11 was altered in HeLa cells expressing *ANXA11-GFP* constructs harbouring ALS associated mutations in response to treatment with ionomycin. Further, *ANXA11* patient fibroblasts had increased basal calcium levels compared to controls and showed reduced calcium release in response to thapsigargin treatment. Knockdown of *ANXA11* in patient mesenchymal stem cells resulted in the same features, which were rescued by WT *ANXA11* expression, but not mutant *ANXA11* (Nahm et al., 2020). The observed increase in basal calcium in patient fibroblasts might reflect the increased calcium fluctuation propensity seen here in *ANXA11* G38R and R235Q neurons (Figure 5.13).

Measurement of spontaneous calcium fluctuations without stimulation is useful for assessing endogenous neuronal profile and can indicate whether altered calcium dynamics are involved in pathology. However, the nature of calcium fluctuations remains unidentified. The utilisation of drugs influencing calcium release from internal stores, such as ionomycin and thapsigargin, would clarify whether intracellular calcium buffering is dysfunctional. Similarly, calcium channel blockers such as AMPA antagonists or action potential mediators such as potassium chloride can be used to assess whether changes to calcium activity are caused by altered regulation of calcium influx into neurons from the extracellular space. This, alongside profiling a range of channels associated with calcium homeostasis, such as AMPA receptor subunits, would shed light on *ANXA11* ALS and excitotoxicity. AMPA receptors are post-synaptic calcium-permeable glutamate receptors which alter in permeability depending on subunit inclusion (GluA1-GluA4). Alterations to calcium dynamics in iPSC-derived models of ALS are associated with glutamate receptor properties, with mutation specific nuances (Bursch et al., 2019). Studies evaluating *C9ORF72* neurons indicate upregulation of GluA1

AMPA receptor subunits in motor neurons but not cortical neurons, resulting in enhanced vulnerability to excitotoxicity as a consequence of increased calcium permeability (Selvaraj et al., 2018). NMDA receptors are also implicated in excitotoxicity (Gerber et al. 2013; Paul & de Belleroche, 2014; Sasabe et al., 2007; Spalloni et al., 2013), indicating it may be informative to interrogate a range of glutamatergic receptors in *ANXA11mut* motor neurons.

It may be true that both intracellular calcium and external calcium influx are affected. Evidence from hippocampal neurons reveals a link between ER calcium store release into the synaptic cytoplasm and enhanced spontaneous neurotransmission (Chanaday et al., 2021). This highlights a relationship whereby fluctuations in intracellular calcium, including as a result of ER stress, can modulate neurotransmission. Additionally, iPSC-derived motor neurons harbouring mutations in *C9ORF72* or *TARDBP* showed upregulation of calcium-permeable receptor subunits and impaired mitochondrial calcium buffering capacity, resulting in altered glutamate-mediated calcium release (Dafinca et al., 2020). Although the calcium fluctuations seen in *ANXA11* ALS motor neurons cannot be specifically attributed to the release of calcium from internal stores or calcium influx through calcium channels, the synchronised nature of calcium fluctuations in neighbouring neurons indicates that cell-to-cell signalling is occurring.

As well as chemical synapses, gap junctions, or electrical synapses, exist between neurons and mediate ion gradients across neuronal membranes. Connexin 40 gap junctions exist between developing spinal neurons and have a role in mediating NMJ formation. Knockdown of connexin 40 in mice leads to reduced electrical coupling between lumbar motor neurons and fewer neuromuscular synapses, highlighting the importance of neuronal gap junctions in motor neuron function (Personius et al., 2007). Gap junctions between glial cells support glutamate buffering, and are mediated by connexins, including connexin 43. Astrocyte specific knockdown of connexin 43 slowed disease progression and protected motor neurons in ALS mice (Almad et al., 2020), and connexin 43 was shown to be upregulated in patient brain and spinal cord, and in iPSC-derived astrocytes (Almad et al., 2016). Increased levels of connexin 43 were associated with increased

cellular calcium levels in astrocytes expressing mutant *SOD1* (Almad et al., 2016), indicating that it may be necessary to assess the function of astrocytes when investigating calcium dysregulation in patient-derived co-cultures. Astrocytes alter GluA2 expression in motor neurons, and consequently influence motor neuron vulnerability to excitotoxicity (Van Damme et al., 2007), and *C9ORF72* astrocytes cause loss of action potential and reduced magnitude of voltage-activated ion currents in co-cultured motor neurons (Zhao et al., 2020). Further evaluation of calcium fluctuations in mixed co-cultures, with control neurons in culture with mutant astrocytes and vice versa, would elucidate whether calcium alterations in *ANXA11mut* motor neurons are caused by endogenous neuronal changes or non-cell-autonomous events.

Calcium activity in neurons is complex, and dysregulation of multiple organelles and pathways mediating neuronal calcium has been associated with ALS. Examples include lysosome function (Tedeschi et al., 2019), autophagy (Bootman et al., 2018), apoptosis (Sukumaran et al., 2021) mitochondrial dysfunction (Jaiswal, 2014), and mitochondrial-ER tethering (Chen et al., 2021; Gomez-Suaga et al., 2022; Peggion et al., 2021). Many proteins whose genes are mutated in ALS are somehow related to calcium signalling, including *VAPB*, *ALS2*, and *MATR3* (Leal & Gomes, 2015). To assess the affect of intracellular calcium accumulation on ALS associated proteins, multiple WT cell lines were treated with ionomycin or thapsigargin, which caused a decrease in the abundance of the ALS-associated proteins TDP-43, C9ORF72, Matrin3, VCP, FUS, SOD1, and profilin-1, and an increase in p62 (De Marco et al., 2022). This suggests a shared vulnerability of ALS-associated proteins to fluctuating calcium levels, indicating that hyperexcitability might exacerbate dysregulated protein function in ALS. The heterogeneous nature of calcium dynamics in ALS highlights the necessity to investigate specific calcium-mediated pathways in *ANXA11* ALS patient motor neurons.

As discussed above, multiple studies implicating dysregulated calcium dynamics in ALS focus on the dynamics of glutamatergic signalling. vGLUT2 is present in excitatory neurons and spinal interneurons (Wang et al., 2018), and a small subset of spinal motor neurons have been shown to express both vGLUT2 and ChAT (Herzog et al., 2004). ChAT is present in lower motor neurons where

it functions at the NMJ as spinal motor neurons synapse onto muscle, and is present in other brain regions including subcortical regions (Li et al., 2018). Recent evidence from rodents indicates that in addition to individual neurons expressing multiple neurotransmitters, a small percentage (2%) of synaptic vesicles can contain more than one type of vesicular transporter, including a small subset expressing both vGLUT2 and VAChT (Upmanyu et al., 2022). Additionally, spinal cholinergic interneurons have been shown to modulate motor neurons and locomotor behaviour in zebrafish (Bertuzzi & Ampatzis, 2018), indicating that although ChAT is present in motor neurons, confirmation of ChAT expression will not identify motor neurons exclusively. The motor neuron differentiation protocol used here was based on published data reporting the production of spinal motor neurons (Maury et al., 2015), however current culture standards mean that mixed motor neuron populations are usually achieved. The presence of both vGLUT2 and ChAT in motor neuron cultures indicates a diverse population of neurons (Appendix Figure 9.27; Appendix Figure 9.28). Some non-motor specific neurons likely persist in culture as the percentage of Islet 1 positive nuclei in young neurons was between 70-80% (Figure 3.10), and it will be informative to assess the presence of additional neuronal subtypes, including interneurons. Due to limited antibody availability, ChAT and vGLUT2 were probed for in neurons from the same motor neuron induction, rather than in a co-stain in the same cells. The presence of both vGLUT2 and ChAT positive neurons means that delineation of specifically vulnerable sub-populations of neurons was not achieved in this project. It may be the case that vGLUT2 and ChAT positive neurons are both affected, or that interaction between neuronal subtypes leads to altered calcium signalling. Co-localisation of Annexin A11 to vGLUT2 positive synaptic vesicles indicates a potential function of Annexin A11 in excitatory synaptic function (Figure 5.17). This, alongside evidence that calcium signalling is disrupted in *ANXA11* ALS, warrants further investigation into the role of *ANXA11* mutations in excitotoxicity and calcium homeostasis.

Altered calcium fluctuations can be associated with altered electrophysiological properties, and so a subset of motor neurons was subject to electrophysiological readings by patch-clamp analysis. Two control and two *ANXA11mut* lines, one with a G38R mutation and one with a D40G mutation, were

included for analysis. These were selected based on apparently altered calcium dynamics in *ANXA11* G38R neurons (5.13), and D40G was included as it is the most commonly reported mutation in *ANXA11* ALS. Control lines were selected based on the closest age and sex match of the original LCLs selected for iPSC derivation (Table 3.1). Patch-clamp analysis was implemented to measure firing frequency, inter-firing event, and resting membrane potential. There was a slight trend towards reduced firing rate and frequency in the patient-derived lines, however no significant difference was observed. The resting membrane potential was broadly consistent across control and *ANXA11mut* cell lines, with no statistically significant difference observed (Figure 5.14).

Both hyperexcitability and hypoexcitability have been observed in cellular models of ALS and vary depending on mutation status and culture maturation of iPSC-derived neurons. Mutations in *FUS* (R495QfsX527, R521C, R521H, R521L, P525L) can result in hypoexcitability (Guo et al., 2017; Naujock et al., 2016), as can mutations in *SOD1* (D90A, R115G) (Naujock et al., 2016). Conversely, hyperexcitability has been detected in iPSC-derived motor neurons harbouring *FUS* (M511fs, H517Q), *C9ORF72*, and *SOD1* (A4V, G85S, D90A) mutations (Wainger et al., 2014), which was rescued when the genetic mutation in the A4V *SOD1* line was corrected. Although these data are seemingly contradictory, they include mostly different mutations, suggesting that within one gene separate mutations can have vastly different effects on neuronal activity. The time at which activity measurements are taken may also affect whether neurons are hyper- or hypo- excitable, and it has been demonstrated that iPSC-derived cortical cultures display an initial phase of increased activity, followed by a decrease in activity, with eventual establishment of non-synchronous and ordered activity patterns (Kirwan et al., 2015). However, the three studies referenced above all perform recordings around day 50 of motor neuron differentiation (Guo et al., 2017; Naujock et al., 2016; Wainger et al., 2014). Motor neuron differentiation protocols often differ subtly between research institutions and groups, and as such reproducibility of experimental results can be challenging. This reflects of a larger issue in medical research and highlights the necessity of repeated measurements for faithful elucidation of disease phenotypes.

Axonal excitability is measurable in patients and is increased in individuals with ALS (Park et al., 2017), as is cortical excitability (Higashihara et al., 2021). This implies that models displaying hyperexcitability are more closely representing the human pathology, however it should be noted that measurements collected in patients are predominantly taken after disease onset, and it is possible that hypoexcitability occurs at a different stage of disease. In the case of *ANXA11mut* motor neurons where no statistically significant differences were detected between control and patient derived lines in patch-clamp analysis (Figure 5.14), it may be that motor neurons at day 40 of differentiation were too immature for such alterations to appear. The suggestion of altered calcium fluctuations in the absence of altered electrophysiological abnormalities is intriguing and raises further questions as to the nature of calcium fluctuations in motor neuron-astrocyte cultures, as discussed above.

## *5.5 Conclusions*

Initial neurite outgrowth in *ANXA11* ALS motor neurons was not affected in this study, however distal axons appear to be vulnerable. This may indicate that pathology arises in the axon, indicative of the dying back hypothesis, or that there is a failure to generate or maintain distal neurites. This may be particulary relevant for long motor axons where, for example, the bioenergitc demand, delivery of cargos, and relay of signals may be influcenced by the additional pressure of supporting long axons. The role of axon specific functions of Annexin A11 remain to be fully elucidated, and it is possible that such processes mediate disease. Some of the axonal functions of Annexin A11 are explored in Chapter 6.

An apparent alteration in calcium homeostasis or signalling in *ANXA11mut* neurons alludes to an overlapping pathology in multiple instances of ALS, as evidence exists for calcium dysregulation in the context of multiple ALS associated genes. Further investigation into the role of calcium in *ANXA11* pathology is necessary, however novel data for calcium alterations in patient-derived motor neurons

offers preliminary evidence that calcium dysregulation is an early pathology in *ANXA11* associated ALS.

# Chapter 6 RNA biology in *ANXA11* patient motor neurons

## *6.1 Overview*

Multiple steps of RNA processing are affected in ALS, and the role of Annexin A11 in these processes is largely unexplored. RNA metabolism describes a broad range of cellular processes: Initial transcription of genes, mRNA processing including splicing and transcript regulation, mRNA trafficking, mRNA regulation in response to stress, and translation of mRNA into protein (1.10). RNA biology is an attractive target for understanding ALS pathology; incorrect transcription or processing of RNA species specific to motor neuron function could explain the cell-specific pathology seen in the disease. Further, the intricate orchestration of RNA processing in specific neuronal compartments including the soma, axon, synapses, and dendrites means that there are multiple levels at which the delicate balance of RNA biology can be disrupted.

Stress granules are small membraneless organelles that form in response to stress, transiently sequestering non-translating mRNA to enable rapid return to neuronal homeostasis when stressful stimuli are removed (Protter & Parker, 2016). As discussed in 1.10.5, evidence for a stress granules pathology in ALS is substantial, with data suggesting that dysfunctional stress granule assembly and/or disassembly act as seeding events for pathological protein aggregation. Annexin A11 was first implicated in stress granule biology in a large proximity labelling screen (Markmiller et al., 2018) and has been shown to localise to stress granules in fibroblasts and cell line overexpression models (Liao et al., 2019; Nahm et al., 2020). The localisation of Annexin A11 to stress granules in patient-derived motor neurons has not yet been reported. Therefore, the inclusion of Annexin A11 to G3BP1 positive stress granules was explored in response to a range of stress-inducing stimuli. This was further explored through a comparison of Annexin A11 overlap with G3BP1 positive stress granules in *ANXA11mut* and control motor neurons.

Annexin A11 is ubiquitously expressed throughout the body, and prior to the association of mutations in *ANXA11* with ALS, neuron specific Annexin A11 functions were poorly established. One of the first reported neuron specific functions of Annexin A11 is a role in axonal RNA trafficking (Liao et al., 2019). Annexin A11 was shown to act as a tether between RBPs and lysosomes, which are transported by motor proteins, such that RBPs use Annexin A11 to "hitch-hike" on lysosomes. The transport of fluorescently labelled RBPs and axon-abundant actin mRNA was shown to be perturbed in the presence of *ANXA11* mutations in overexpression models in the same study. Quantification of anterograde and retrograde RNA trafficking was included here to evaluate whether any gross change in RNA transport is detectable in *ANXA11* ALS patient-derived motor neurons.

One of the essential functions of axonal transport is the delivery of cargos to support translation throughout neurons. Local protein translation is a means for highly polarised cells such as neurons to respond rapidly to changes in the local environment, enabling neuronal plasticity in response to intracellular and intercellular cues (Biever et al., 2019; Monday et al., 2022). Local translation has recently been implicated in ALS pathology (Altman et al., 2021; Birsa et al., 2021; Briese et al., 2020; Burguete et al., 2015; Chu et al., 2019; Ishiguro et al., 2016; Lehmkuhl et al., 2021; López-Erauskin et al., 2018; Majumder et al., 2016; Murakami et al., 2015; Nagano et al., 2020; Sephton et al., 2014; Wong et al., 2021), and multiple studies have demonstrated altered global protein translation in cell and animal models (Charif et al., 2020; Gao et al., 2021; Lehmkuhl et al., 2021; MacNair et al., 2016; Majumder et al., 2016; Marques et al., 2020; Neelagandan et al., 2019; Russo et al., 2017). Interestingly, Rab7-positive late endosomes were shown to act as sites of local protein translation in neurons (Cioni et al., 2019). The unique structure of Annexin A11 as a phospholipid membrane-binding protein with a low-complexity domain (Figure 1.3) make it an attractive target for understanding how RBP and vesicle interactions might be stabilised in this process. In line with this, ribopuromycylation was used to determine Annexin A11 inclusion to sites of local translation in axons, and protein translation in distal axons in *ANXA11mut* and control motor neurons were compared. Annexin A11 interacts directly with FUS (Nahm et al., 2020), which is implicated in

translation (Birsa et al., 2021; López-Erauskin et al., 2018; Murakami et al., 2015; Salam et al., 2021; Sévigny et al., 2020), and Annexin A11 was upregulated in post-mortem brain tissue from an ALS patient with a *FUS* p.G504Wfs*12 mutation (Nahm et al., 2020). Hence, FUS protein level in *ANXA11* ALS patient motor neurons was measured. Finally, global protein translation was measured by puromycin incorporation in neurons with quantitative imaging.

## *6.2 Methods*

### *6.2.1 Annexin A11 and stress granules*

G3BP1 positive stress granules were probed for Annexin A11 in response to multiple stressors. These included sodium arsenite, puromycin, and sorbitol. Co-cultured motor neurons at day 21 of differentiation (2.1.7) were subject to various drug treatment conditions (2.3.1), fixed, and immunolabelled with antibodies detecting the stress granule protein G3BP1 and Annexin A11 (2.4.1). Imaging was completed with a Nikon Spinning Disk confocal microscope before processing and quantification with Nikon NIS-Elements (2.4.3). In some instances, stress granules were imaged with super-resolution microscopy (2.4.3). For comparison of control vs. *ANXA11mut* groups, motor neurons were treated with sodium arsenite (2.3.1) and eight images were taken for each cell line for each technical repeat with a Nikon Spinning Disk confocal microscope. Thresholding and quantification were performed on individual image *z*-planes, and the mean of these was taken as the result for each image. Two biological repeats were included, with each comprised of two technical repeats where neurons from the same batch of iPSC differentiation were maintained separately. Five control and five *ANXA11mut* lines were included and were separated into control, *ANXA11* G38R, *ANXA11* D40G, and *ANXA11* R235Q groups for analysis.

### *6.2.2 RNA transport in iPSC-derived motor neurons*

Motor neurons (2.1.7) were maintained in microfluidic devices (2.1.11) with astrocytes (2.1.10) until day 26 of differentiation and incubated with SYTO™ RNASelect™ which increases in fluorescent intensity when bound to RNA (2.4.5). Live imaging of RNA particles was completed with a Nikon Spinning Disk microscope (2.4.5), and time-lapse images were quantified with KymographClear and KymographSelect (Mangeol et al., 2016).

### *6.2.3 Local translation in iPSC-derived motor neurons*

Motor neuron-astrocyte co-cultures (2.1.10) were maintained on glass coverslips or in microfluidic devices (2.1.11). Translational hotspots were identified by ribopuromycylation which includes co-treatment with emetine and puromycin (2.3.2), and cells were fixed and subject to immunocytochemistry with antibodies targeting puromycin and endogenous proteins (2.4.1). Neurites were imaged with super-resolution microscopy (2.4.3) and images were quantified in Nikon NIS-Elements and Fiji. Puromycin labelled hotspots of axonal translation were detected by the 'Bright spot detection' tool with the 'Different sizes' parameter selected in Nikon NIS-Elements, and fluorescent intensities of target proteins were measured within these spots. The correlation of fluorescent intensities was measured by Pearson's correlation coefficient in GraphPad, and the line of best fit was added with the linear regression tool. To measure the number of hotspots per neurite length, neurites were traced in Fiji to yield the total neurite length per image, and puromycin spot counts from Nikon NIS-Elements were normalised to these values.

### *6.2.4 Global translation and protein abundance*

Twenty-one-day old motor neurons maintained in co-culture with astrocytes were incubated with puromycin to detect newly synthesised peptides (2.3.3), fixed, and subject to immunocytochemistry with antibodies targeting puromycin and $\beta$3-Tubulin to detect neurons (2.4.1). Cultures were imaged

with the Opera Phenix® High Content Screening System and mean puromycin intensity in neurons was measured using Harmony® (2.4.2).

The relative abundance of FUS protein was measured in day-17 motor neurons by western blot, by normalising the signal from FUS to total protein stain (2.5.1).

## *6.3 Results*

### *6.3.1 Annexin A11 and stress granules*

Initial investigation of Annexin A11 stress granule dynamics included the interrogation of puromycin-treated motor neurons with super-resolution microscopy, revealing modest localisation of Annexin A11 to G3BP1 stress granules (Figure 6.1). As TDP-43 is known to localise to stress granules, and TDP-43 inclusions have been identified in post-mortem tissue from *ANXA11* ALS patients, overlap of Annexin A11, TDP-43, and G3BP1 in response to stress was assessed, again with puromycin treatment in control motor neurons, and super-resolution imaging. This revealed no overlap of Annexin A11 and TDP-43 in the same stress granules in qualitative analysis and fluorescent intensity tracing (Figure 6.2), however indicated successful stress granule formation. Additionally, a marked localisation of TDP-43 to G3BP1 stress granules was seen, indicating that localisation of ALS-associated proteins to stress granules is observable in this system. In this instance, although the treatment conditions were consistent, little if any overlap of Annexin A11 to stress granules in response to puromycin treatment was observed in fluorescent intensity tracing (Figure 6.2).

To further explore Annexin A11 stress granule dynamics, control motor neurons were exposed to a range of stressful stimuli and probed for G3BP1 stress granules. Motor neurons were imaged with normal confocal microscopy, with the aim to interrogate an increased number of neurons compared to super-resolution microscopy. Various methods for the induction of stress granules have been reported in the literature; puromycin (Figure 6.3), sodium arsenite (Figure 6.4), and sorbitol (Figure 6.5) are shown here. Successful induction of the stress granule response was seen in all treatment

conditions, demonstrated by G3BP1 localisation to focal granules throughout neurons (Figure 6.3; Figure 6.4; Figure 6.5). Treatment with sodium arsenite or puromycin resulted in large G3BP1 cytoplasmic aggregates, and osmotic stress induced by sorbitol resulted in smaller stress granules throughout the nucleus and cytoplasm. Qualitative analysis indicates that Annexin A11 is poorly detected in puromycin-induced G3BP1 stress granules with the image acquisition settings used here as fluorescent intensity tracings do not indicate an increase in Annexin A11 intensity in parallel with G3BP1 intensity changes (Figure 6.3). Intensity tracings across sodium arsenite induced G3BP1 stress granules revealed an increase in Annexin A11 intensity in some, but not all, stress granules (Figure 6.4). Similarly, stress granules induced by osmotic stress showed a modest increase in Annexin A11 intensity in some cases, with an absence of Annexin A11 fluctuation in others (Figure 6.5). These data indicate that under specific conditions, modest localisation of Annexin A11 to stress granules is a feature of control motor neurons, and that Annexin A11 inclusion to stress granules is dynamic and stressor specific. A more marked stress granule response in terms of Annexin A11 localisation to G3BP1 stress granules was observed with sodium arsenite treatment, which was selected for comparison of stress granule dynamics in control and *ANXA11* ALS patient motor neurons.

Co-cultured motor neurons at day 21 of differentiation were either treated with sodium arsenite or untreated, probed for Annexin A11, the stress granule marker G3BP1, and the neuronal marker $\beta$3-Tubulin, and imaged with a Nikon Spinning Disk Confocal Microscope (Figure 6.6; Figure 6.7; Figure 6.8; Figure 6.9). Images were quantified with Nikon NIS-Elements software which included various thresholding steps whereby fluorescent intensity was used to define cellular regions. For example, the neuronal area was defined by thresholding $\beta$3-Tubulin, DAPI thresholding was used to define nuclei, and G3BP1 thresholding was used to define stress granules (Figure 6.10). Stress granule induction was confirmed by measuring the percentage of G3BP1 granule area normalised to the neuronal area, which was increased in response to sodium arsenite treatment (Figure 6.11.B). Despite an observable difference in G3BP1 pattern in untreated vs. treated neurons in representative images (Figure 6.6; Figure 6.7; Figure 6.8; Figure 6.9), it should be noted that some “stress granules”

were identified in the untreated group (Figure 6.11.B). This is due to the nature of image analysis with thresholding, and the necessity to maintain a consistent threshold across treated and untreated conditions, and across all cell lines, to ensure unbiased quantification. As G3BP1 is present in untreated motor neurons, it was not possible to set a threshold that specifically detected stress granules without some unspecific inclusion of G3BP1 in untreated neurons. However, the increase in relative stress granule area (Figure 6.11.B) and visual confirmation of stress granule formation in representative images indicate that stress granule induction was successful.

A significant difference in stress granule area per neuron was observed in *ANXA11* R235Q compared to control motor neurons, suggesting perturbed stress granule formation in the context of mutations in the *ANXA11* C-terminal (6.11.B). The nucleocytoplasmic ratio of G3BP1 was reduced in sodium arsenite treated compared to untreated neurons (6.11.A) which was mirrored by a significant increase in cytoplasmic intensity (6.11.D), and the nuclear intensity was unchanged (Figure 6.11.C). The mean intensity of Annexin A11 inside G3BP1 stress granules was consistent across cell lines and conditions, indicating no change in Annexin A11 inclusion to stress granules in this model (Figure 6.11.E). Additionally, Annexin A11 was subject to thresholding, and overlap between Annexin A11 and G3BP1 stress granule binary masks was measured as a percentage (6.11.F). A trend towards increased overlap of Annexin A11 and G3BP1 stress granules in sodium arsenite treated neurons was seen, however particularly large data variability across biological replicates meant that this was not statistically significant.

The number of Annexin A11 spots per cell (calculated as the number of bright Annexin A11 spots normalised to the neuronal area as defined by thresholding $\beta$3-Tubulin) was unchanged across treatment and cell line conditions (6.12.C), however the number of Annexin A11 spots per number of DAPI positive nuclei increased in response to sodium arsenite treatment across all cell lines groups (6.12.A), indicating an Annexin A11 stress response. Mean Annexin A11 spot fluorescent intensity (Figure 6.12.B), nucleocytoplasmic ratio (Figure 6.12.E), mean nuclear intensity (Figure 6.12.F), and mean cytoplasmic intensity (Figure 6.12.G) were unaffected by sodium arsenite treatment or

*ANXA11* mutation. The mean Annexin A11 spot size was not changed in response to stress, however a general increase in spot size in *ANXA11* G38R neurons compared to control was observed (Figure 6.12.D). These data suggest Annexin A11 is responsive to stress and that perturbations to stress response are mutation specific, with no altered stress granule dynamics observed in *ANXA11* G38R or D40G neurons, and a reduction in stress granule formation propensity in *ANXA11* R235Q.

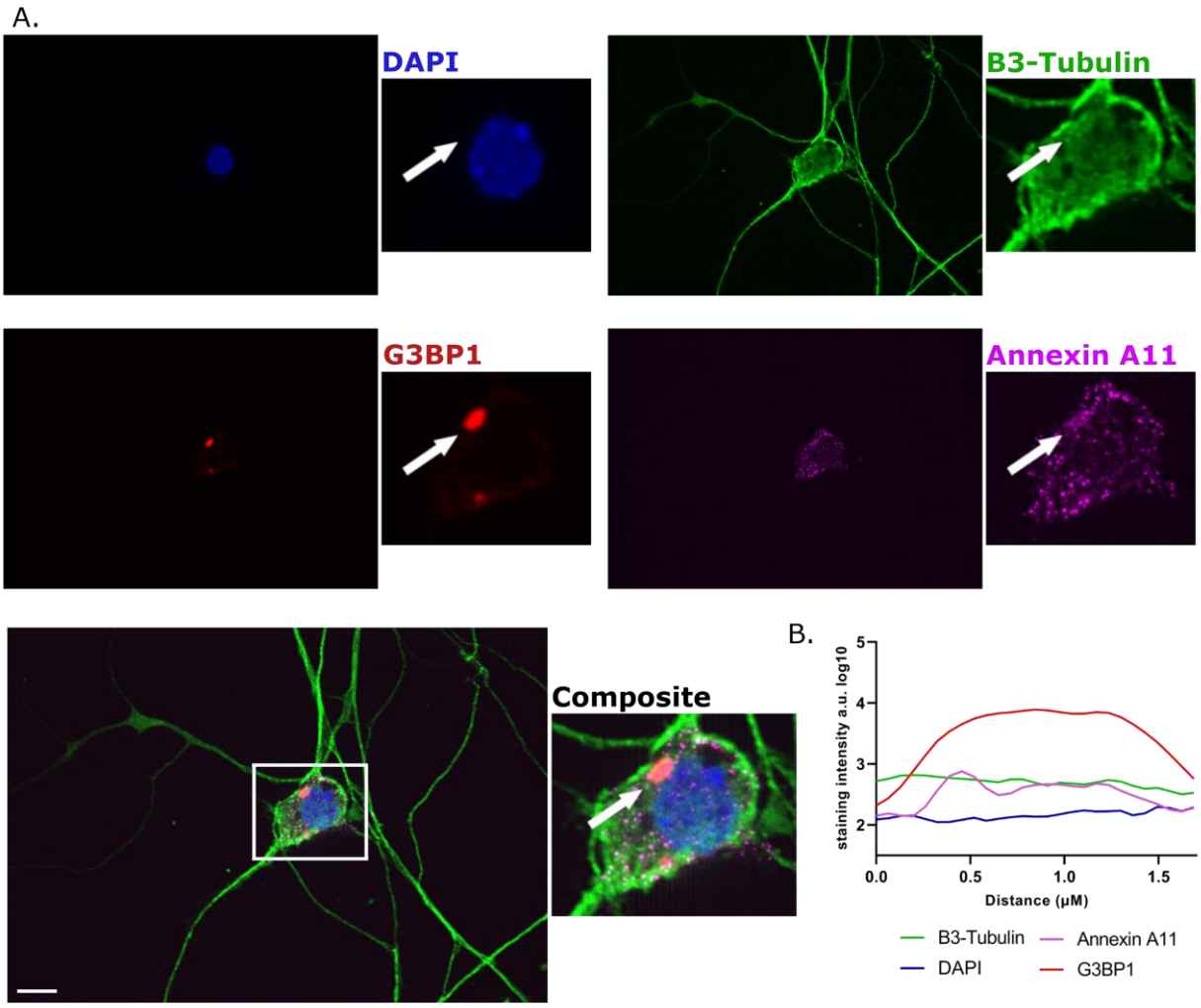


***Figure 6.1 Annexin A11 localisation to puromycin-induced stress granules with high-resolution imaging***

(A) Control motor neurons at day 21 of differentiation were treated with puromycin to induce stress granule formation, fixed, subject to immunocytochemistry with antibodies targeting neuronal marker $\beta$3-Tubulin (green), stress granule marker G3BP1 (red), and Annexin A11 (magenta), co-stained with DAPI (blue), and imaged with super-resolution microscopy (iSIM). (B) A fluorescent intensity trace across a stress granule (indicated with a white arrow in (A) reveals an increase in

G3BP1 intensity across the granule, which is mirrored by a subtle increase in Annexin A11 fluorescent intensity. Scale bar indicates 10µm.

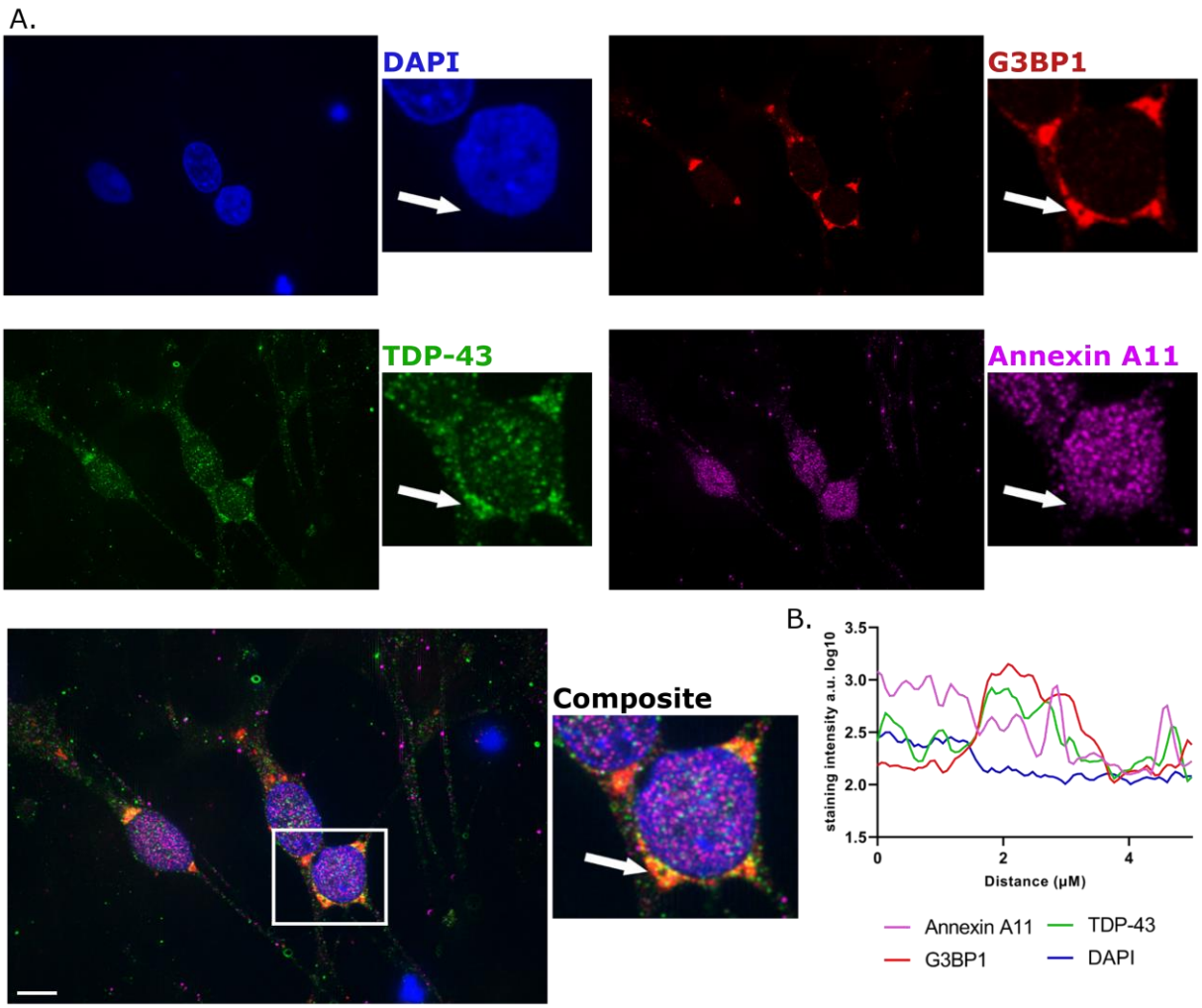


***Figure 6.2 Annexin A11 and TDP-43 do not localise to the same G3BP1 stress granules in response to puromycin treatment***

(A) Control motor neurons at day 21 of differentiation were treated with puromycin to induce stress granule formation, fixed, subject to immunocytochemistry with antibodies targeting stress granule marker G3BP1 (red), TDP-43 (green), and Annexin A11 (magenta), co-stained with DAPI (blue), and imaged with super resolution microscopy (iSIM). (B) A fluorescent intensity trace across a stress granule (indicated with a white arrow in A) reveals an increase in G3BP1 intensity across the granule, which is mirrored by an increase in TDP-43 intensity, but not Annexin A11. Scale bar indicates 10µm.

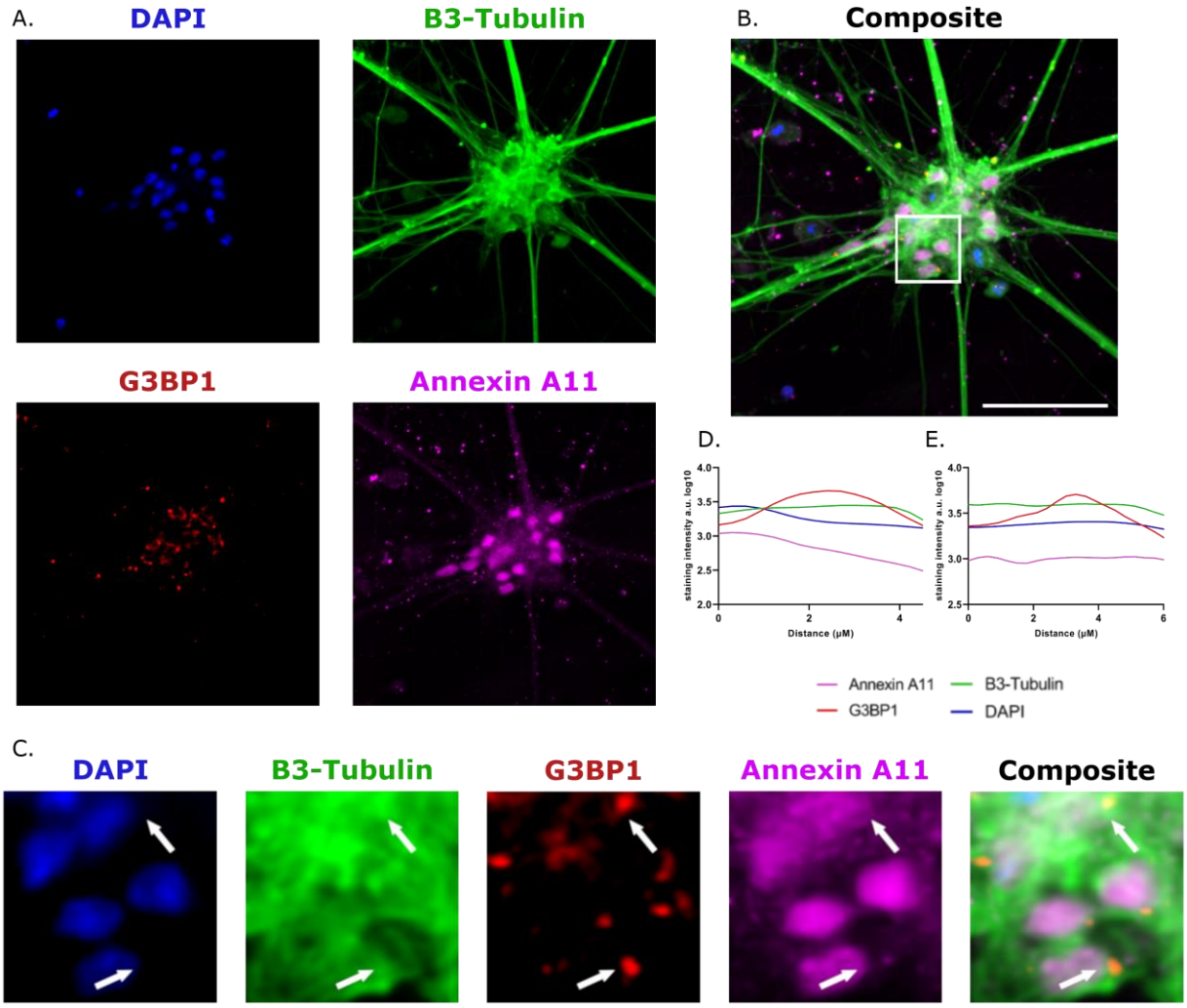


***Figure 6.3 Annexin A11 does not consistently localise to G3BP1 stress granules in response to puromycin treatment***

(A) Control motor neurons were maintained in co-culture with astrocytes until day 21 of motor neuron differentiation, treated with puromycin, fixed, and subject to immunocytochemistry with antibodies targeting the stress granule protein G3BP1 (red), Annexin A11 (magenta), and $\beta$3-Tubulin (green), and were co-stained with DAPI (blue). The white box in (B) highlights the image region included in (C). (C) The formation of stress granules was confirmed by typical stress granule morphology of G3BP1. Annexin A11 did not appear to specifically localise to stress granules (indicated by white arrows). (D, E) Intensity traces across stress granules show focalised intensity of G3BP1 signal, with Annexin A11 intensity showing no paralleled increase in intensity. Scale bar represents 50µm.

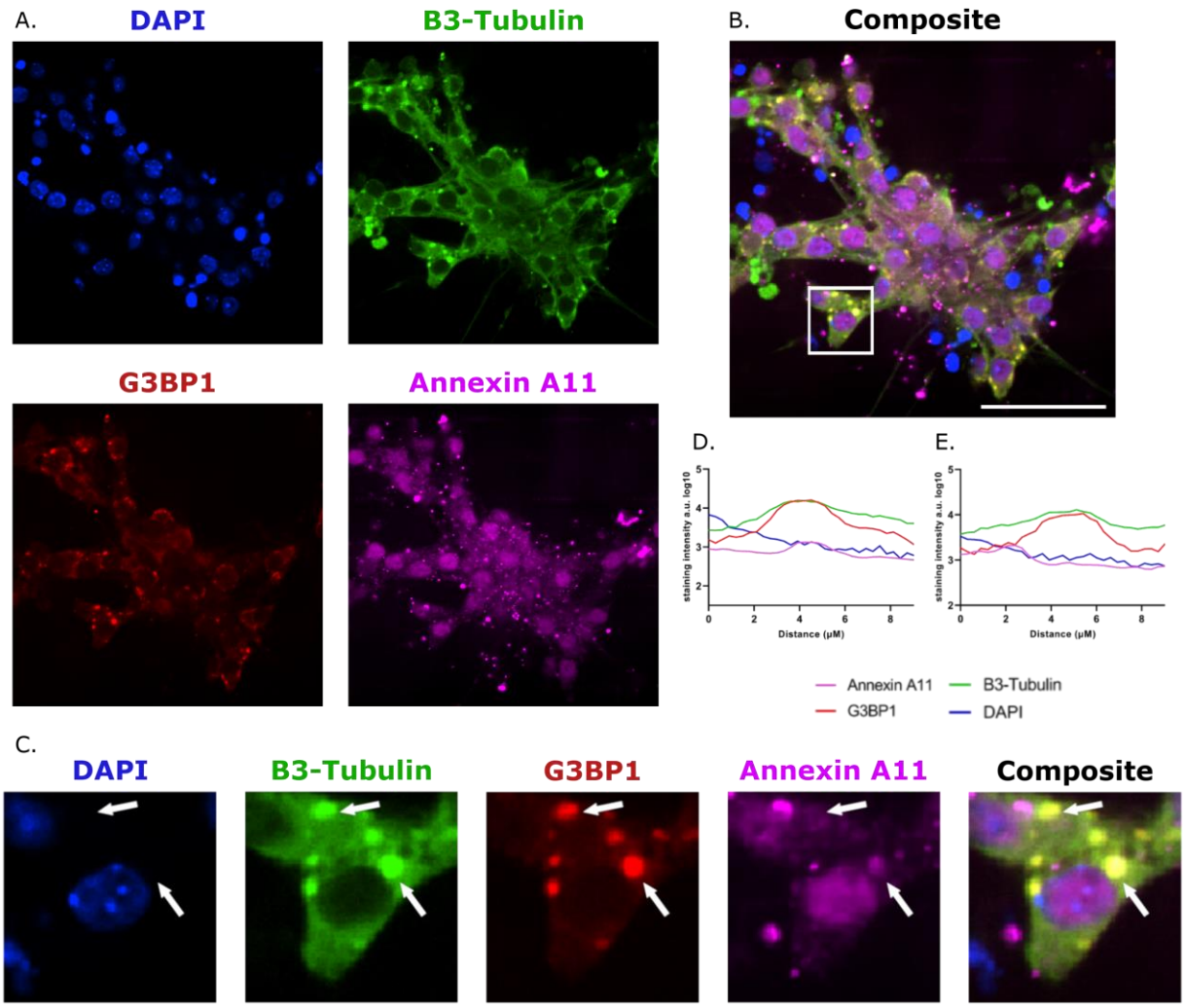


***Figure 6.4 Annexin A11 sometimes localises to G3BP1 stress granules in response to sodium arsenite treatment***

(A) Control motor neurons were maintained in co-culture with astrocytes until day 21 of motor neuron differentiation, treated with sodium arsenite, fixed, and subject to immunocytochemistry with antibodies targeting the stress granule protein G3BP1 (red), Annexin A11 (magenta), and $\beta$3-Tubulin (green), and were co-stained with DAPI (blue). The white box in (B) highlights the image region included in (C). (C) Formation of stress granules was confirmed by typical stress granule morphology of G3BP1. Annexin A11 appeared to localise to some, but not all, stress granules (indicated by white arrows). (D, E) Intensity traces across stress granules show focalised intensity of G3BP1 signal, which was mirrored by a modest increase in Annexin A11 intensity in one example (D), and no associated Annexin A11 signal fluctuation in another (E). Scale bar represents 50µm.

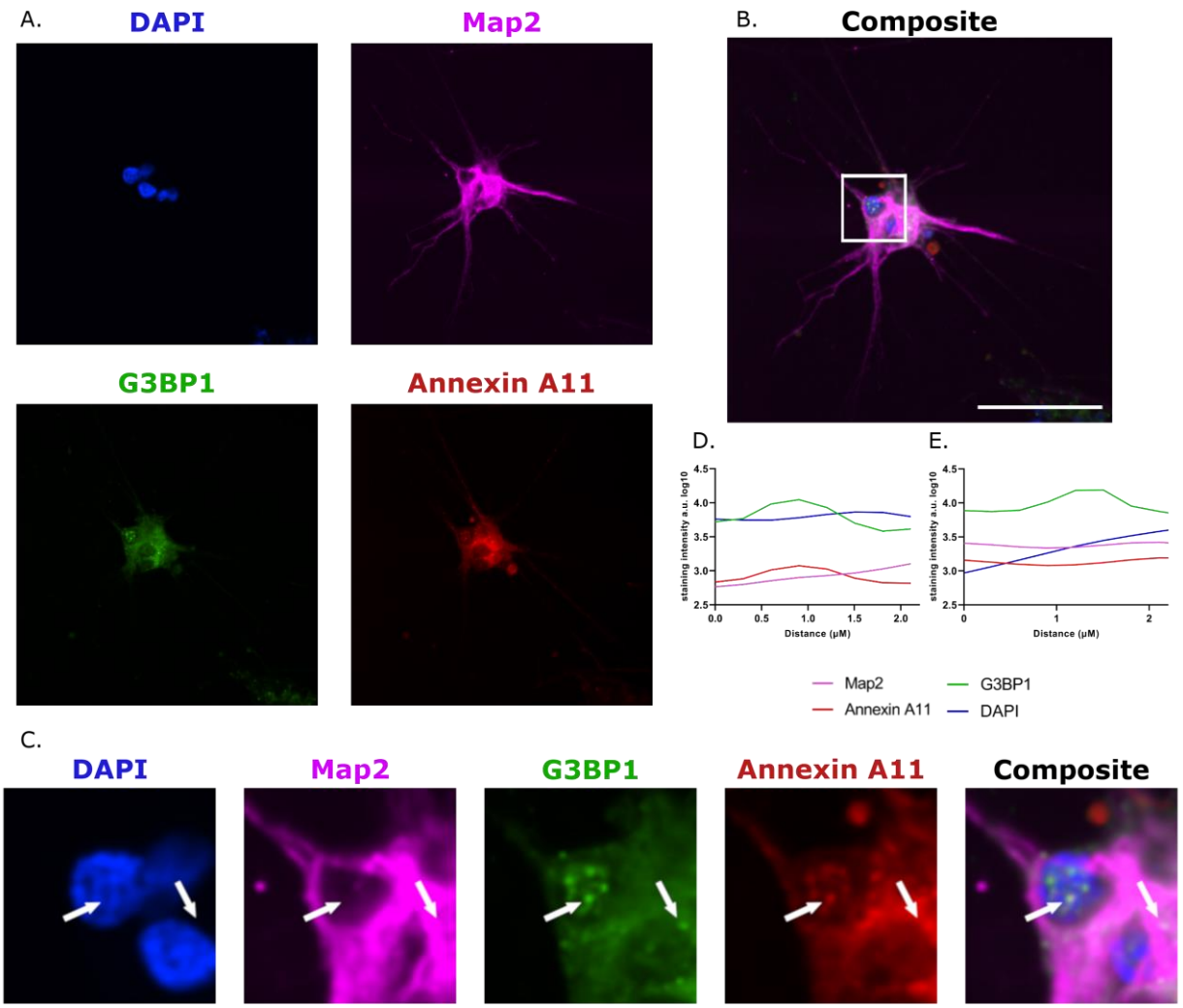


***Figure 6.5 Annexin A11 sometimes localises to G3BP1 stress granules in response to sorbitol treatment***

(A) Control motor neurons were maintained in co-culture with astrocytes until day 21 of motor neuron differentiation, treated with sorbitol, fixed, and subject to immunocytochemistry with antibodies targeting the stress granule protein G3BP1 (green), Annexin A11 (red), and Map2 (magenta), and were co-stained with DAPI (blue). The white box in (B) highlights the image region included in (C). (C) Formation of stress granules was confirmed by the presence of small punctate G3BP1 species. Annexin A11 appeared to localise to some, but not all, stress granules (indicated by white arrows). (D, E) Intensity traces across stress granules show focalised intensity of G3BP1 signal, which was mirrored by a modest increase in Annexin A11 intensity in one example (D), and no associated Annexin A11 signal change in another (E). Scale bar represents 50µm.

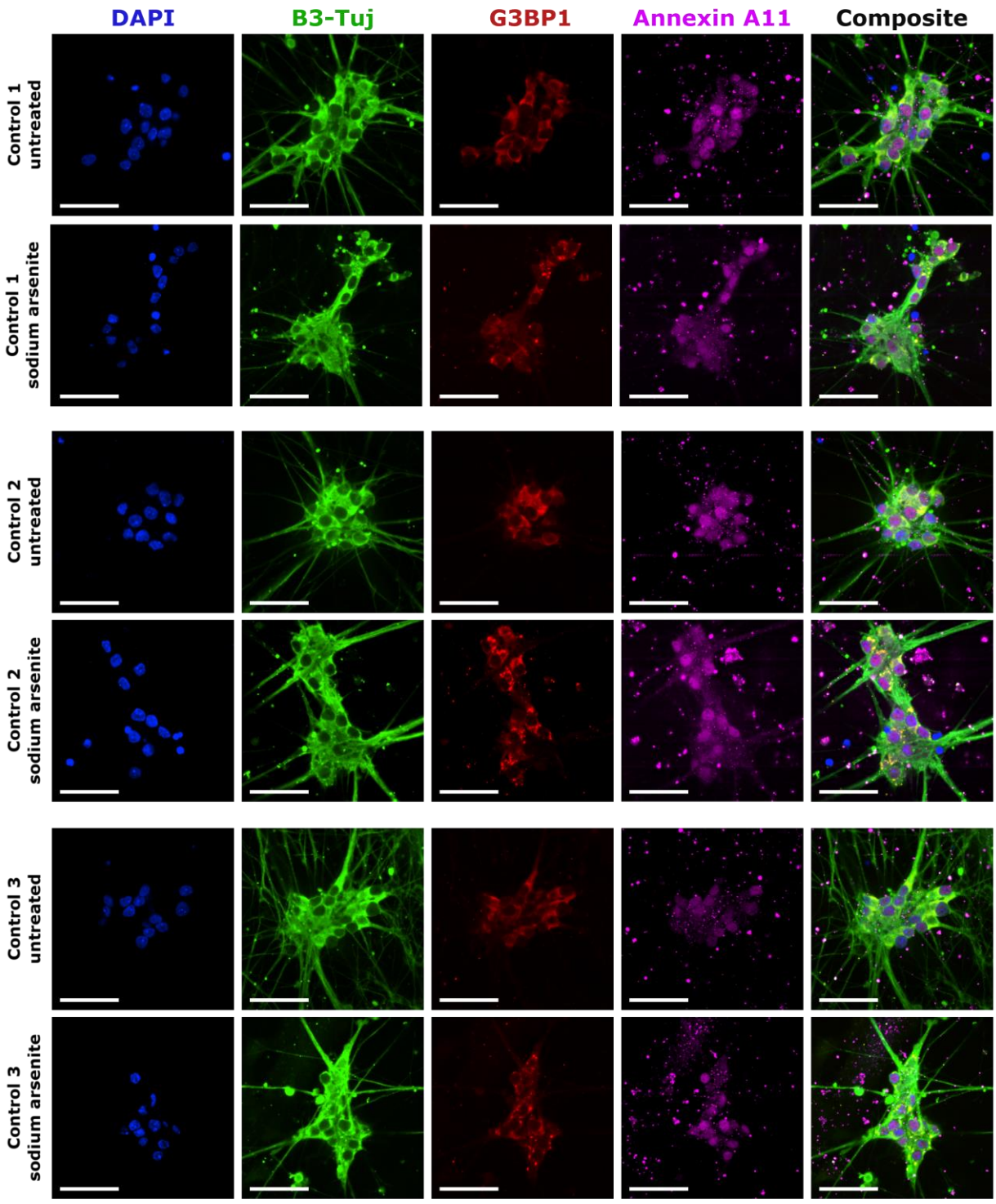


***Figure 6.6 Stress granules in control motor neurons***

Representative images of control motor neurons in untreated vs. sodium arsenite treated conditions. Motor neurons were maintained in co-culture with astrocytes until day 21 of differentiation, treated, fixed, subject to immunocytochemistry with antibodies targeting neuronal marker $\beta$3-Tubulin (B3-Tuj, green), stress granule marker G3BP1 (red), and Annexin A11 (magenta), co-stained with DAPI (blue), and imaged with a Nikon Spinning Disk confocal microscope. Scale bars represent 50µm.

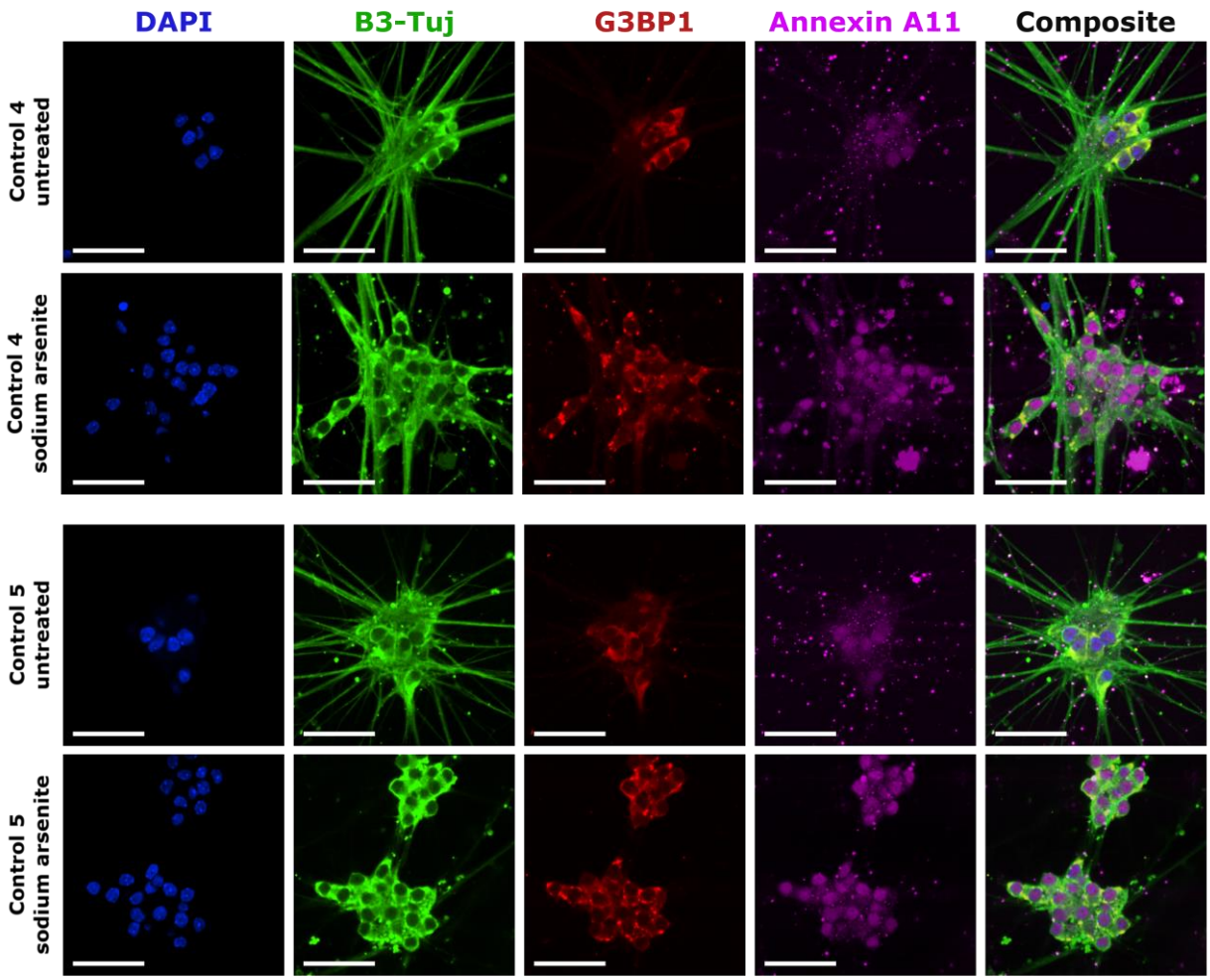


***Figure 6.7 Stress granules in control motor neurons***

Representative images of control motor neurons in untreated vs. sodium arsenite treated conditions. Motor neurons were maintained in co-culture with astrocytes until day 21 of differentiation, treated, fixed, subject to immunocytochemistry with antibodies targeting neuronal marker $\beta$3-Tubulin (B3-Tuj, green), stress granule marker G3BP1 (red), and Annexin A11 (magenta), co-stained with DAPI (blue), and imaged with a Nikon Spinning Disk confocal microscope. Scale bars represent 50µm.

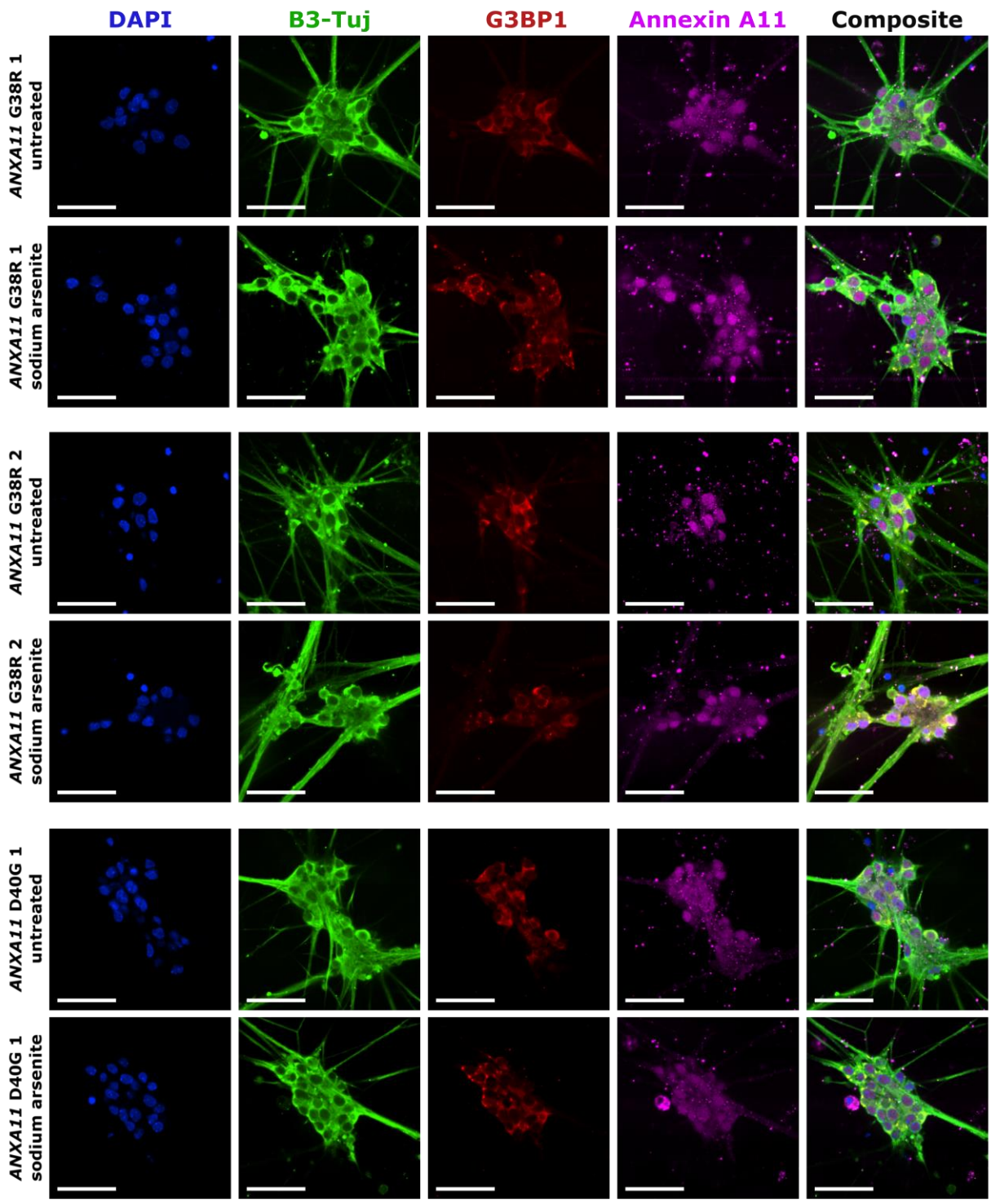


***Figure 6.8 Stress granules in ANXA11mut motor neurons***

Representative images of *ANXA11mut* motor neurons in untreated vs. sodium arsenite treated conditions. Motor neurons were maintained in co-culture with astrocytes until day 21 of differentiation, treated, fixed, subject to immunocytochemistry with antibodies targeting neuronal marker $\beta$3-Tubulin (B3-Tuj, green), stress granule marker G3BP1 (red), and Annexin A11 (magenta),

co-stained with DAPI (blue), and imaged with a Nikon Spinning Disk confocal microscope. Scale bars represent 50µm.

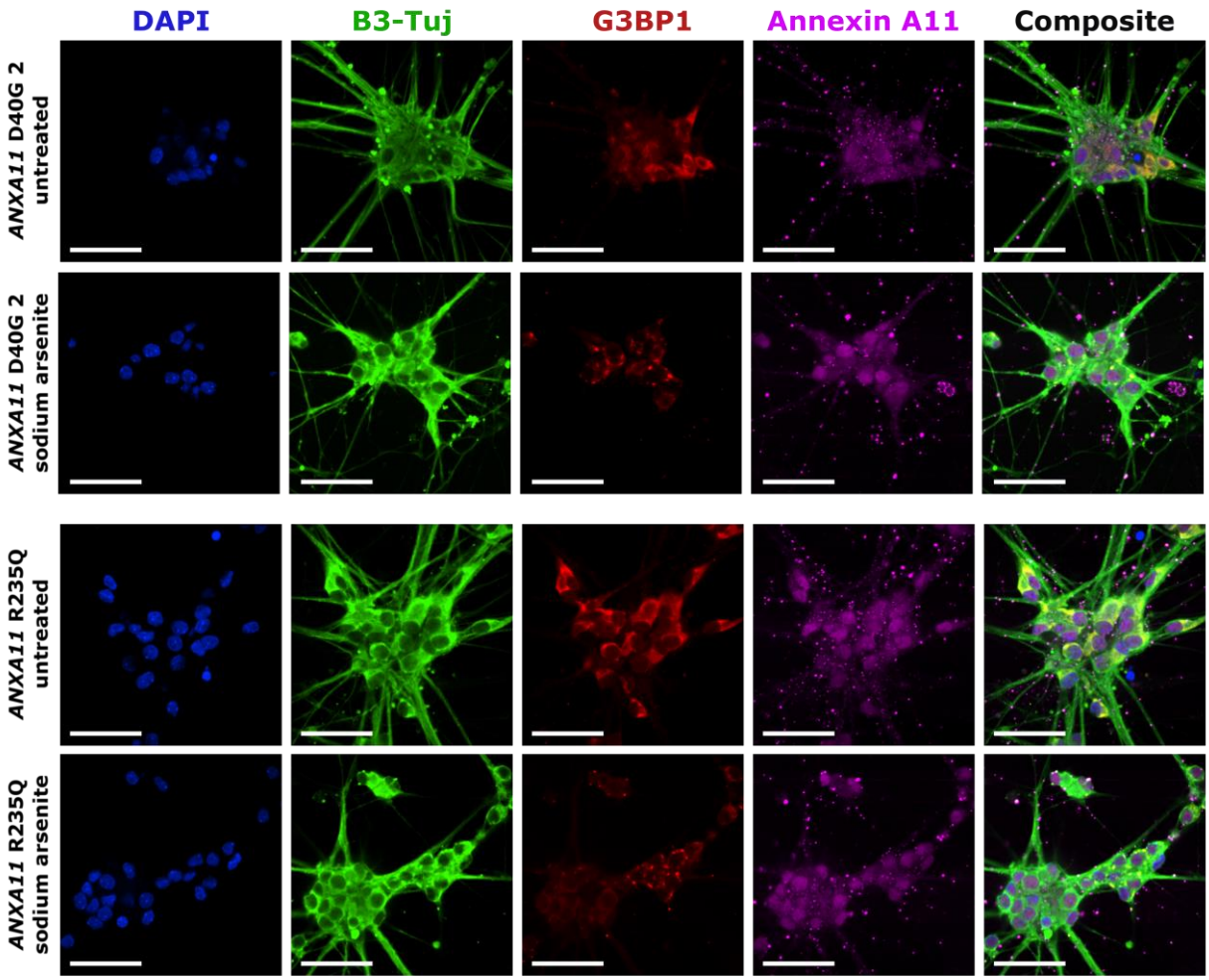


***Figure 6.9 Stress granules in ANXA11mut motor neurons***

Representative images of *ANXA11mut* motor neurons in untreated vs. sodium arsenite treated conditions. Motor neurons were maintained in co-culture with astrocytes until day 21 of differentiation, treated, fixed, subject to immunocytochemistry with antibodies targeting neuronal marker $\beta$3-Tubulin (B3-Tuj, green), stress granule marker G3BP1 (red), and Annexin A11 (magenta), co-stained with DAPI (blue), and imaged with a Nikon Spinning Disk confocal microscope. Scale bars represent 50µm.

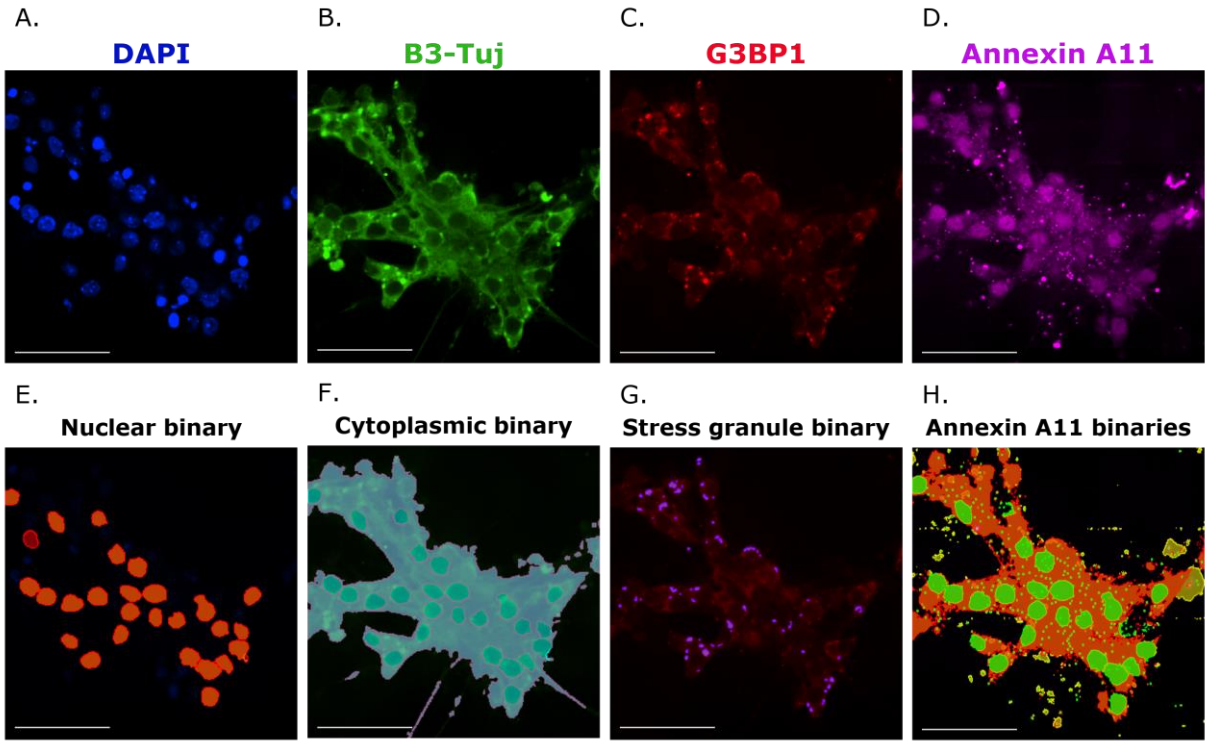


***Figure 6.10 Stress granule quantification with Nikon NIS-Elements***

(A-D) Representative image for stress granule analysis. (E-H) Representative binary masks in Nikon NIS-Elements. (A, E) DAPI staining was used to create the nuclear binary. (B, F) $\beta$3-Tubulin (B3-Tuj, green) was used to define the neuronal and cytoplasmic regions. (C, G) G3BP1 (red) was used to identify stress granules, and the binary mask was adjusted such that bright stress granule regions were isolated from more diffuse G3BP1 signal. (D, H) Annexin A11 (magenta) could be defined by multiple binary masks in multiple regions including the nucleus (H; green), cytoplasm (H; orange), and bright spots which were quantified in spot analysis (H; small green dots). Non-specific staining caused by cell debris or background (for example) were excluded from quantification by incorporating defined neuronal regions into target protein binary mask parameters; see exclusion of non-neuronal Annexin A11 in (H; yellow). Scale bars represent 50µm.

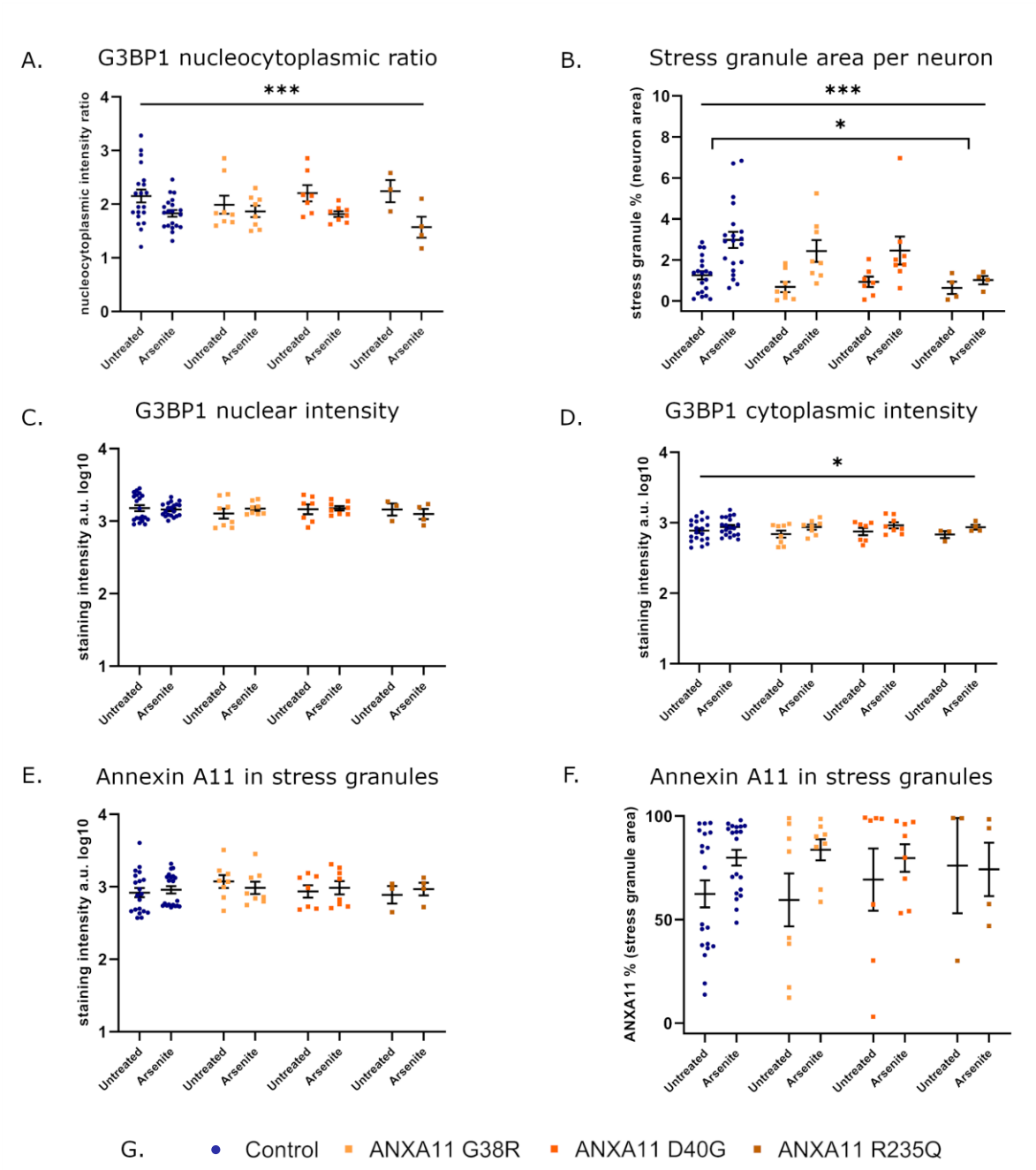


***Figure 6.11 Stress granule analysis in sodium arsenite treated motor neurons***

(A) The nucleocytoplasmic ratio of G3BP1 was reduced in sodium arsenite treated neurons, with no difference between control and any *ANXA11mut* group ($p$ = 0.0010; untreated vs. arsenite groups). (B) Stress granule area per neuronal area was increased in response to sodium arsenite treatment ($p$ = 0.0003; untreated vs. arsenite groups), and was significantly reduced in *ANXA11* R235Q compared to control ($p$ = 0.0407). (C) The intensity of G3BP1 in motor neuron nuclei was unchanged across control and *ANXA11mut* groups, and in response to stress. (D) Increased G3BP1 intensity was observed in the cytoplasm of motor neurons in response to stress, and was not statistically different across control and *ANXA11mut* groups ($p$ = 0.0189; untreated vs. arsenite groups). (E) The average

intensity of Annexin A11 inside stress granules was not changed across groups, or in response to stress. (F) A trend toward increased overlap of Annexin A11 positive regions with G3BP1 stress granules was seen in the arsenite treated group, which was not significant. (G) Key for motor neuron cell line groups. Data are presented as mean ± SD, $n = 4$ (two motor neuron inductions, each with two technical replicates). Each data point represents a control or *ANXA11mut* cell line in one technical replicate. Statistical analysis: Ordinary Two-Way ANOVA with Dunnett's multiple comparisons test (* = $p \leq 0.05$, *** = $p \leq 0.001$).

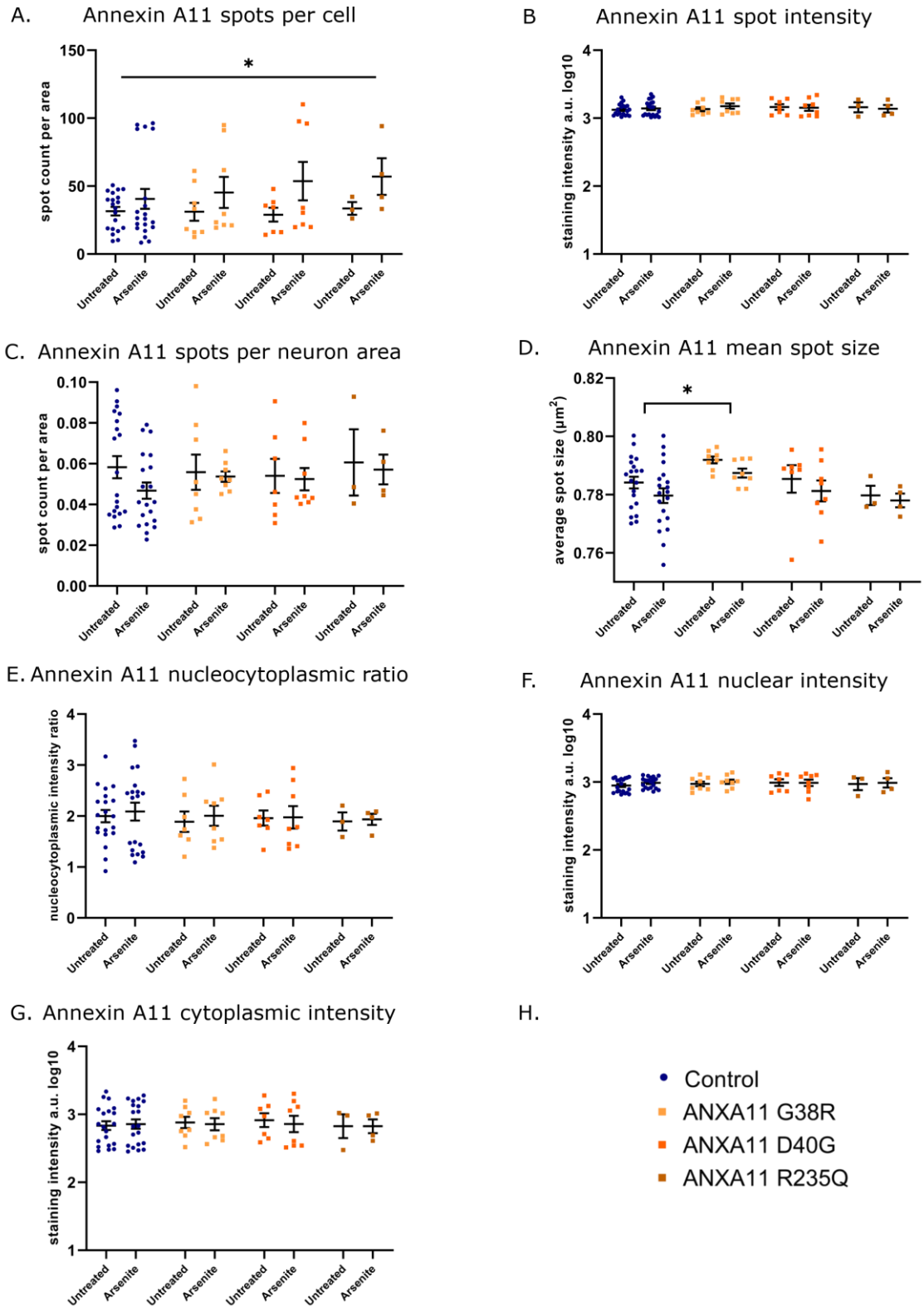


***Figure 6.12 Annexin A11 response to sodium arsenite treatment***

(A) Annexin A11 spot count per DAPI positive nuclei was increased in response to stress ($p$ = 0.0152; untreated vs. arsenite groups). (B) Fluorescent intensity of Annexin A11 spots was consistent across

groups and did not change in response to stress. (C) The number of Annexin A11 spots normalised to $\beta$3-Tubulin area was unchanged across mutation groups and in response to stress. (D) Annexin A11 average spot size was significantly larger in *ANXA11* G38R motor neurons compared to control ($p$ = 0.0172). (E) The nucleocytoplasmic ratio of Annexin A11 was consistent across groups and did not change in response to stress, and the nuclear (F) and cytoplasmic (G) intensity of Annexin A11 was consistent across groups. (H) Key for groups included. Data in are presented as mean ± SD, $n$ = 4 (two motor neuron inductions, each with two technical replicates). Each data point represents a control or *ANXA11mut* cell line in one technical replicate. Statistical analysis: Ordinary Two-Way ANOVA with Dunnett's multiple comparisons test (* = $p \leq 0.05$).

### *6.3.2 Global axonal RNA transport velocity is increased in ANXA11mut motor neurons*

To measure RNA transport, iPSC derived motor neurons were cultured in microfluidic devices to permit quantification of transport in anterograde and retrograde directions (Figure 5.7). Cultures were maintained for 26 days and stained with the dye SYTO™ RNASelect™, revealing transport of RNA in both the anterograde and retrograde direction. Time-lapse images were quantified using the tools KymographClear and KymographDirect (Mangeol et al., 2016). Kymographs were manually traced in Fiji using the KymographClear plugin, and particle velocity was quantified in KymographClear (Figure 6.13). In all control and *ANXA11mut* lines, the number of traceable RNA particles moving in the retrograde direction was higher than in the anterograde direction (Table 6.1, Figure 6.14).

Mean RNA particle velocities for each cell line were; control 1, anterograde 1.103±0.626, retrograde 1.297±0.610; control 2, anterograde 1.257±0.725, retrograde 1.393±0.634; control 4, anterograde 1.154±0.631, retrograde 1.490±0.639; *ANXA11* G38R, anterograde 1.367±0.737, retrograde 1.574±0.714; *ANXA11* D40G, anterograde 1.247±0.731, retrograde 1.572±0.688; *ANXA11* R235Q, anterograde 1.508±0.919, retrograde 1.527±0.618 (data are presented as mean µm/s ± SD). Individual particle velocities were subject to Kruskal-Wallis one-way analysis of variance with Dunn's multiple comparisons test for anterograde and retrograde transport separately. In instances where a significant difference was detected between control and *ANXA11mut* lines, particle velocity was

increased in *ANXA11* patient lines compared to control, in both the anterograde and retrograde direction (Figure 6.15). Results from statistical analysis are displayed in a grid format and show an increase in the number of statistically significant differences between control vs. *ANXA11mut* lines compared to control vs. control and *ANXA11mut* vs. *ANXA11mut* (Figure 6.15). In anterograde velocity analysis, a significant difference was detected between control vs. *ANXA11mut* in 56% of comparisons, 34% of *ANXA11mut* vs. *ANXA11mut*, and 0% of control vs. control. In retrograde analysis, a significant difference was detected between 67% of control vs. *ANXA11mut* pairs, 34% of control vs. control, and 0% of *ANXA11mut* vs. *ANXA11mut*. The abundance of RNA particles was such that counting stationary particles was not possible, and so the percentage of moving particles was not quantified.

In ribopuromycylation experiments (see 6.3.3), control motor neurons were co-labelled with Annexin A11 and Lamp1. Data collection focused on neurites, as opposed to the cell body, as local axonal translation was targeted for quantification. It was observed during data collection that the staining pattern of Lamp1 differed substantially in the soma and neurites, with large vesicle-like Lamp1 positive structures observable only in the soma. Interestingly, a few examples where Lamp1 vesicles co-localised with a single bright spot of Annexin A11 at the vesicle edge were present, mirroring the staining pattern originally identified in the characterisation of Annexin A11 as a lysosome-RBP tether for axonal transport (Liao et al., 2019), an example of this staining pattern is included in Appendix Figure 9.30. Although these structures weren't observed in neurites, it is notable that structures similar to those observed in the identification of the RNA transport function of Annexin A11 are present in iPSC-derived motor neurons (Figure 6.16).

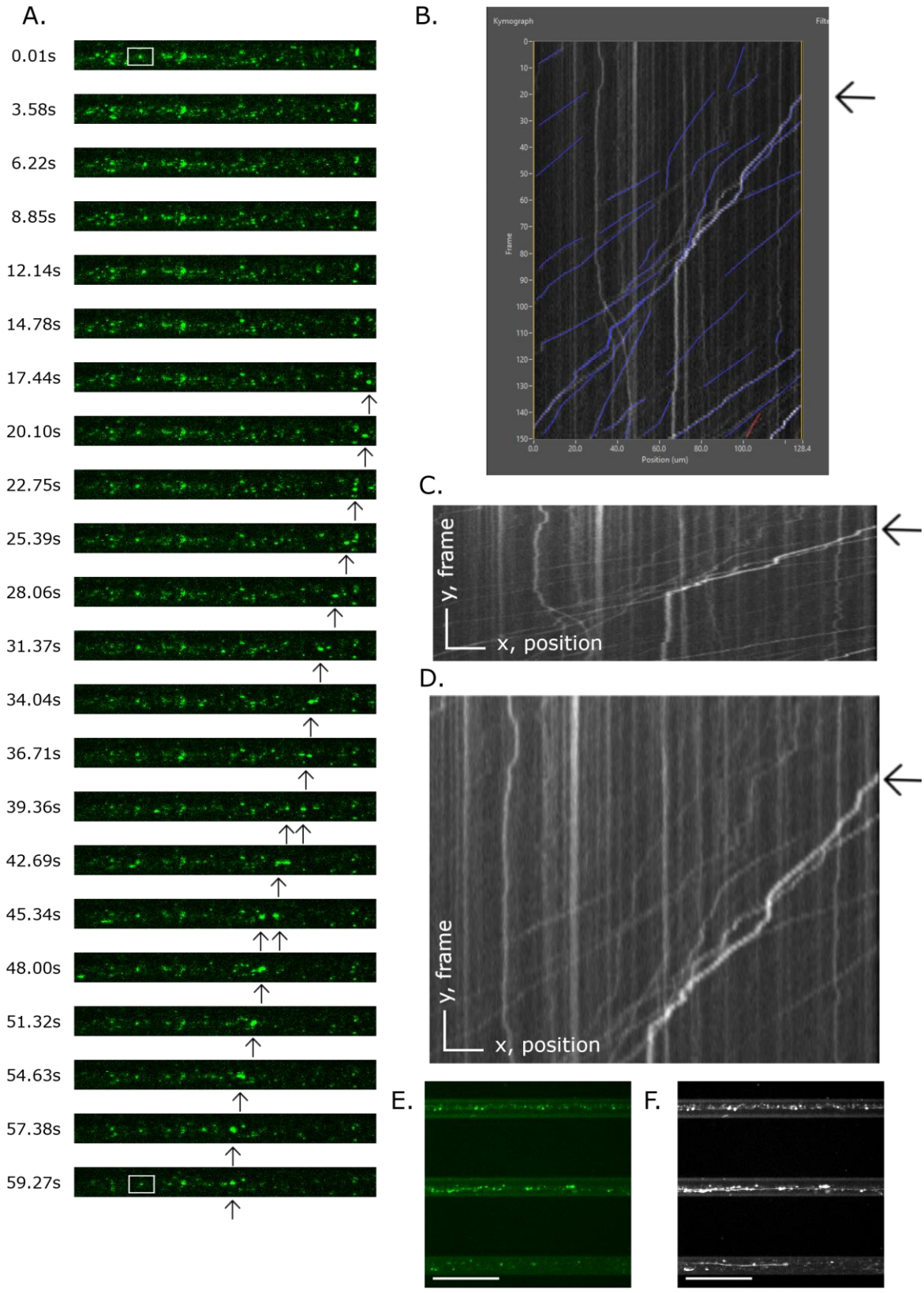


***Figure 6.13 Quantification of RNA granule velocity in motor neuron axons***

(A-D) An example of RNA transport data collected from one microgroove in a microfluidic device. (A) Example images from one microgroove show the movement of RNA granules over a 60 second

period, the collection time of each frame is shown on the left-hand side. Black upwards pointing arrows indicate the movement of an RNA granule, in some cases two arrows are included where the RNA granule in question crosses over another moving granule. A white box in the first and last frame highlight a stationary RNA granule, which is visible across all time frame images. (B) Quantification of particle velocity was completed in KymographDirect, retrograde individual particle traces are highlighted in blue. (C) Kymographs were generated with KymographClear, the example shown corresponds to the full time-lapse image (> 60 seconds) from which the time frames in (A) are taken. The section of the kymograph corresponding only to the still images shown in (A) is included in (D), which has been cropped and elongated to aid the visualisation of kymograph representation of image data. Black arrows in (C) and (D) indicate the point at which the particle indicated by black arrows in (A) comes into the field of view and is traced in the kymograph. (E) An example of a full single time frame image acquired for RNA transport quantification, with three microfluidic microgrooves seen. (F) A max projection image of the entire time series corresponding to (E), dense lines indicate tracks where RNA granules are moving, which were used as a guide for kymograph production in KymographClear. Scale bars represent 50µm.

*Table 6.1 Traceable RNA particle count in transport analysis*

| Cell line | Number of traceable anterograde particles | Number of traceable retrograde particles | Anterograde to retrograde transport ratio |
|---|---|---|---|
| **Control 1** | 218 | 363 | 0.60 |
| **Control 2** | 229 | 408 | 0.56 |
| **Control 4** | 418 | 1408 | 0.30 |
| ***ANXA11* G38R** | 381 | 669 | 0.57 |
| ***ANXA11* D40G** | 312 | 516 | 0.60 |
| ***ANXA11* R235Q** | 391 | 1022 | 0.38 |

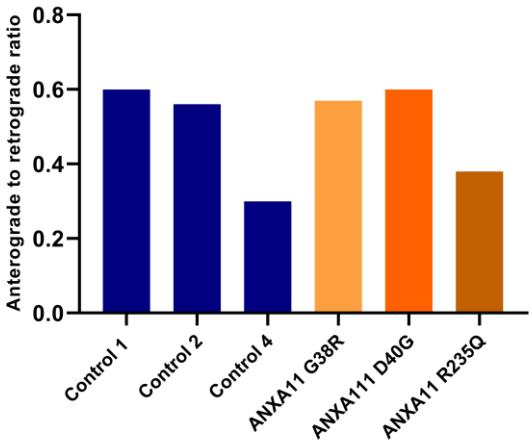


***Figure 6.14 RNA particle anterograde to retrograde transport ratio***

Visualisation of the anterograde to retrograde transport ratio, including all traceable RNA granules from two biological replicates.

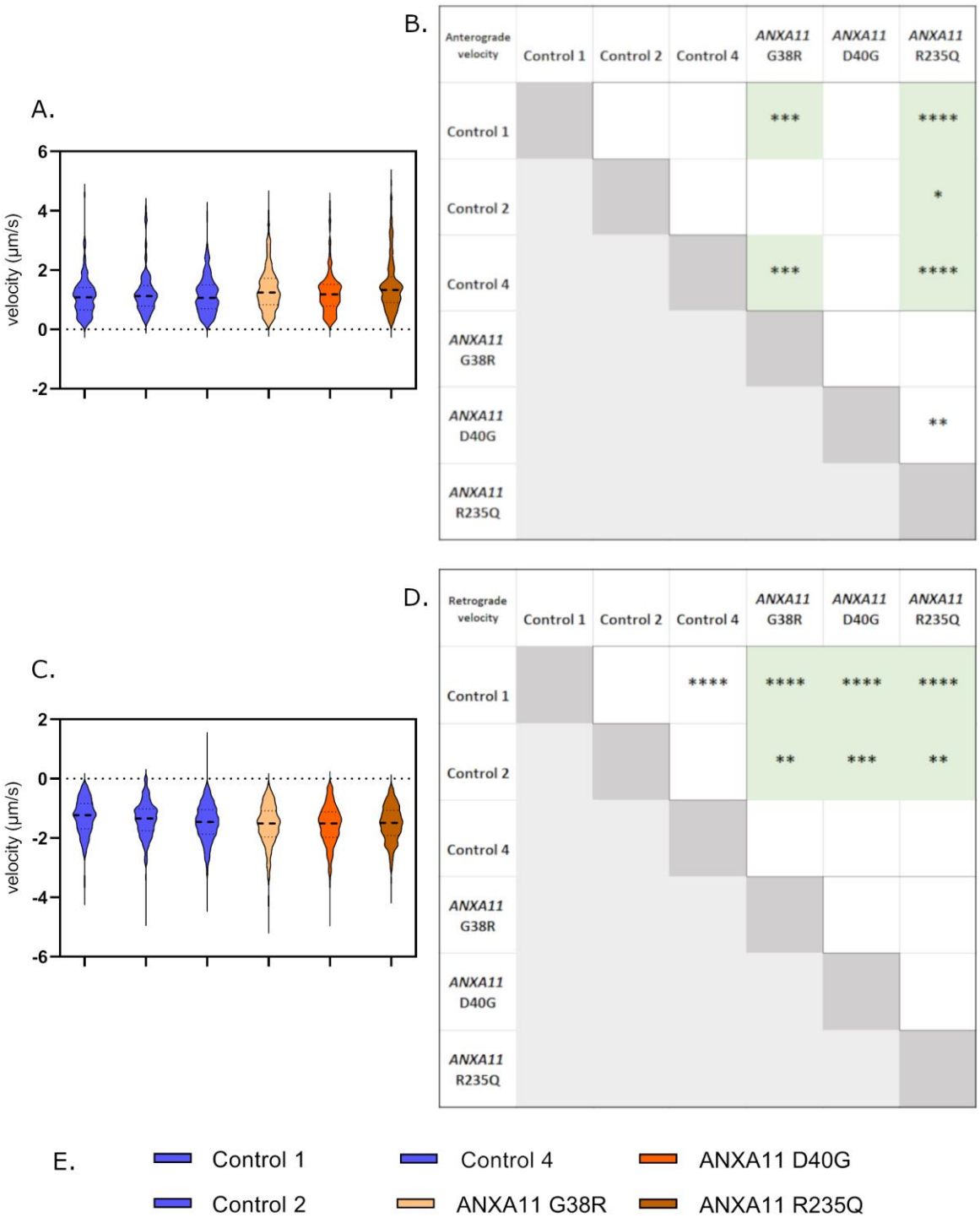


***Figure 6.15 RNA granules display increased velocity in ANXA11mut motor neurons***

(A) Anterograde velocity of individual RNA particles was plotted for each cell line. (B) Anterograde velocity data were subject to Kruskal-Wallis one-way analysis of variance with Dunn's multiple comparisons test, significant differences between cell line comparisons are indicated by asterisks. (C) Retrograde velocity of individual RNA particles was plotted for each cell line and are displayed as negative values reflecting the raw data read out from quantification of velocity in KymographDirect. (D) Retrograde velocity data were subject to Kruskal-Wallis one-way analysis of variance with Dunn's

multiple comparisons test, significant differences between cell line comparisons are indicated by asterisks. (B, D) In instances where a significant difference was detected between a control and *ANXA11mut*, the relevant box is shaded green where the *ANXA11mut* velocity was increased compared to control. (E) Key for (A and C). (** = p < 0.05; ** = p < 0.01; *** = p < 0.001; **** = p < 0.0001;* number of motor neuron inductions = 2).

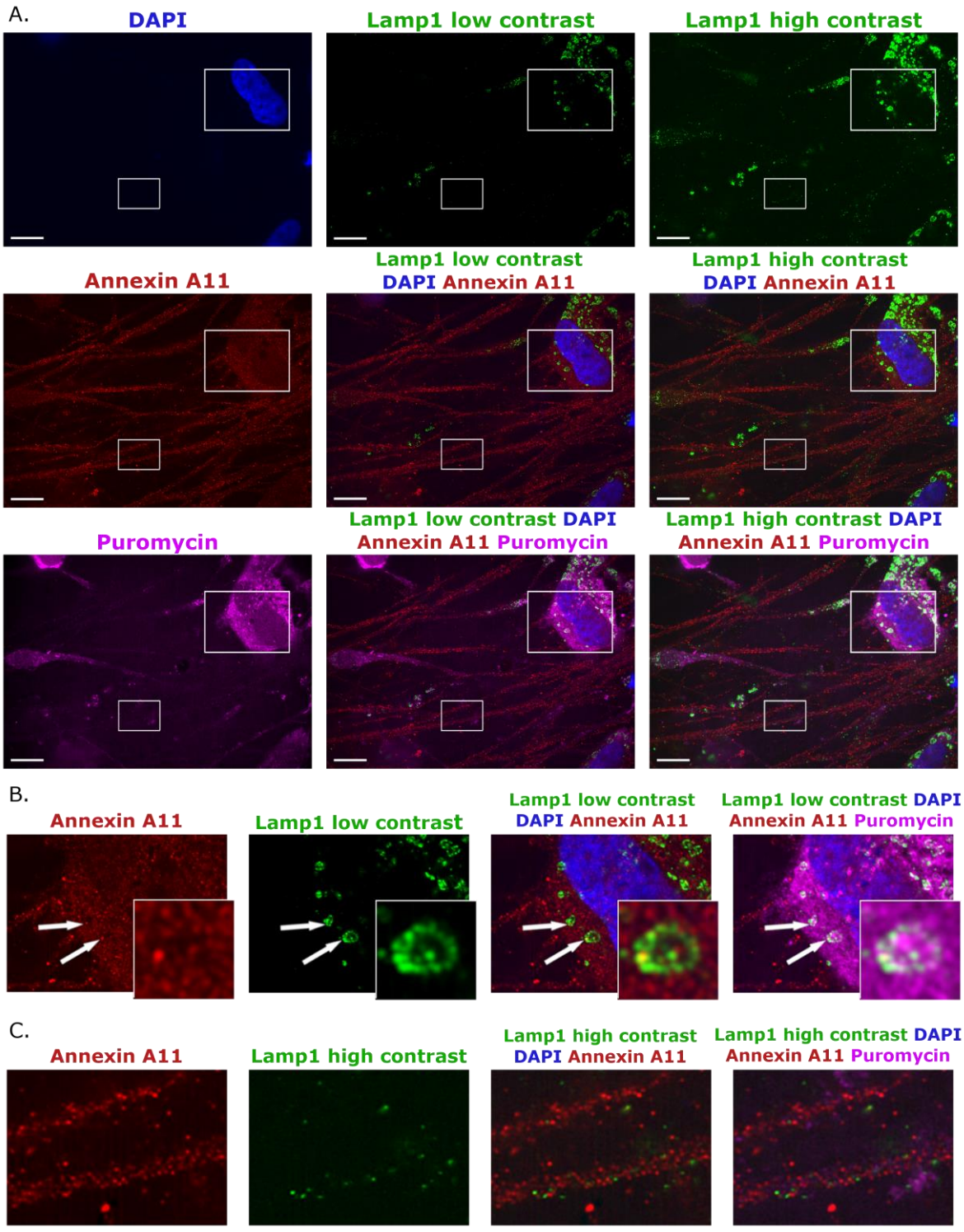


***Figure 6.16 Large Lamp1 vesicles are observed in the soma but not neurites of motor neurons***

control motor neurons from ribopuromycylation analyses were subject to immunochemistry with antibodies targeting Annexin A11 (red), Lamp1 (green), and puromycin (magenta), and were co-stained with DAPI (blue). (A) Lamp1 was present throughout cells, with vesicular like structures present in the soma, and punctate neurite staining observable with increased brightness/contrast. Large and small white boxes in (A) correspond to (B) and (C), respectively. (B) Lamp1 positive vesicles

were present in the soma (indicated by white arrows), with focal points of Annexin A11 observed at the vesicle edge in some instances (inset images). (C) Annexin A11 is abundant in proximal neurites alongside some Lamp1 punctate structures, which does not appear to co-localise with Annexin A11. Representative images of puromycin are included for transparency as images were collected from neurons subject to ribopuromycylation. Scale bars represent 10μm.

### *6.3.3 Annexin A11 in local translation*

Local translation was assessed by ribopuromycylation which can be used to visualise hotspots of translation in neurites (David et al., 2013; Graber et al., 2013). Firstly, ribopuromycylation was performed on motor neurons on day 21 of differentiation which were immunolabelled for puromycin, $\beta$3-Tubulin, and Annexin A11. Focal points of local translation were identified by puromycin signal, and Annexin A11 was seen to localise to a subset of these spots (Figure 6.17), suggesting that Annexin A11 is present at sites of local translation in iPSC-derived motor neurons. Untreated motor neurons showed some unspecific staining; however this was of reduced intensity compared with treated neurons (Appendix Figure 9.31).

Next, control motor neurons were subject to ribopuromycylation and immunolabelled for a panel of proteins with potential to co-localise with Annexin A11 at points of local translation. These were imaged with super-resolution microscopy and points of local translation were defined as puromycin labelled “spots”. Thresholding in Nikon NIS-Elements was used to identify bright puromycin spots which were taken as focal points of translation, and fluorescence intensity values from Annexin A11 and proteins of interest were measured in these puromycin spots. Examples of puromycin spot detection are included in Figure 6.18. Analysed proteins include; ribosomal protein S6, FUS, G3BP1, Lamp1, Rab7, TDP-43, FMRP, snRNP70, and ChAT. Markers were selected based on published literature indicating that target proteins are involved in local translation, or that Annexin A11 binds to said proteins, and are discussed in 6.4.3. Examples of ribopuromycylation targeting Annexin A11 and these proteins are included in Figure 6.19, Figure 6.20, and Figure 6.21. Fluorescent intensities of Annexin A11 and target proteins were plotted with linear regression on *XY* graphs and correlation

between the two signals was measured by Pearson's correlation coefficient, a positive measure of correlation indicating that the intensity of each protein at sites of translation is mirrored (Figure 6.22). Results from Pearson's correlation coefficient are included in Table 6.2. Statistically significant positive correlations were detected between Annexin A11 and FUS, G3BP1, S6, and snRNP70, suggesting that there could be a functional link between these proteins in translation. No correlation was detected between Annexin A11 and Lamp1, Rab7, TDP-43, FMRP, or ChAT, indicating that although some of these proteins have a role in protein translation, they might be comparatively less associated with Annexin A11 function.

To compare local translation across control and *ANXA11* ALS patient motor neurons, a subset of lines including three control and three *ANXA11mut* lines were grown in microfluidic chambers so that distal neurites could be assessed (Figure 5.7). Neurons were subject to ribopuromycylation and immunolabelled for puromycin and Annexin A11. FUS was included as a co-label due to its apparent correlation with Annexin A11 at points of local translation (Figure 6.22; Table 6.1). Representative images show that Annexin A11 and FUS localise to the same translational hotspots in distal neurites (Figure 6.23). Fluorescent intensities of Annexin A11 and FUS were measured as described above and subject to Pearson's correlation coefficient, revealing significant correlation in all cell lines (Figure 6.24; Table 3). To enable visualisation of the strength of Annexin A11 and FUS correlation across cell lines, *r* values from correlation analysis are included in a bar chart, indicating a stronger correlation in control 1 and control 2 compared to the other cell lines (Figure 6.25).

The intensity of Annexin A11 and FUS at sites of local translation were compared separately and subject to Kruskal-Wallis analysis of variance with Dunn's multiple comparisons test (Figure 6.26). Significant differences were detected between most cell line pairings. For Annexin A11, significant differences between control and *ANXA11mut* lines were detected in four out of nine cell line pairings, and where significant differences were detected the signal in *ANXA11mut* lines was always increased compared to control. For FUS, significant differences were detected in six out of nine control vs. *ANXA11mut* cell line pairings. Reduced FUS signal was detected in *ANXA11mut* lines

compared to control in instances where significance was reached, excluding the comparison of control 2 and *ANXA11* D40G, where FUS signal was increased in the *ANXA11* D40G line.

To measure the overall amount of local translation, the number of puromycin spots was normalised to neurite length. Results from individual images were included in analysis, as opposed to mean values from each cell line, to highlight the large variability observed within each cell line. Data were subject to Kruskal-Wallis one-way analysis with Dunn's multiple comparisons test, revealing a significant increase in the number of puromycin spots per neurite length in *ANXA11* G38R compared to control 1 and *ANXA11* R235Q (Figure 6.27). Distal axons were sparser in some cell lines and acquired images included a range of total neurite lengths; the total length of distal axons quantified for each cell line is included in Figure 6.27 to demonstrate this more clearly.

As a crude measurement of global protein translation, 21-day old motor neurons maintained in co-culture with astrocytes were incubated with puromycin, fixed, and immunolabelled with an antibody detecting puromycin and the neuronal marker $\beta$3-Tubulin (Figure 6.29; Figure 6.30). Cultures were imaged with the Opera Phenix® High-Content Screening System and neurons were quantified in Harmony®. Comparable levels of puromycin intensity were seen across control and *ANXA11mut* groups, indicating no change in global translation under these conditions (Figure 6.31).

Lastly, the relative abundance of FUS protein was measured in iPSC-derived motor neurons. Control and *ANXA11mut* iPSCs were differentiated into motor neurons and RIPA-soluble protein was collected on day 17 of differentiation. Samples were separated by western blot and signal from an antibody detecting endogenous FUS protein was normalised to total protein (Figure 6.32), indicating no change in the amount of FUS protein in *ANXA11mut* motor neurons compared to control.

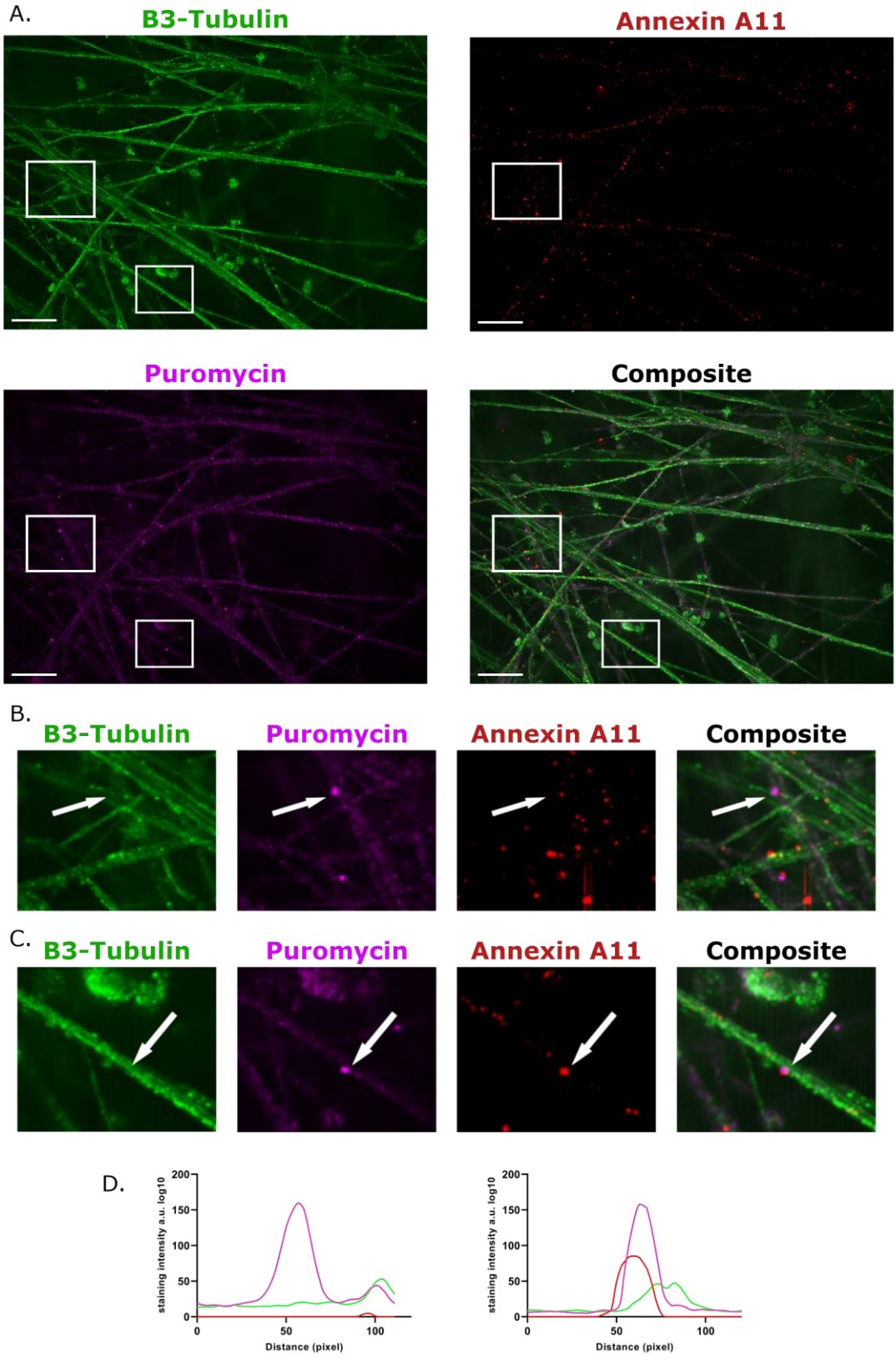


***Figure 6.17 Annexin A11 localises to points of local translation in motor neuron neurites***

(A) Control motor neurons were subject to ribopuromycylation and immunocytochemistry with antibodies detecting $\beta$3-Tubulin (B3-Tubulin, green), Annexin A11 (red), and puromycin (magenta)

to detect sites of local translation. (B, C) Puromycin hotspots are identified in neurites, some with no Annexin A11 (B), and some with Annexin A11 co-localisation (C). White boxes in (A) correspond to (B; large box) and (C; small box). Translational hotspots are indicated by white arrows. (D) Intensity traces across bright puromycin spots indicate translation hotspots where Annexin A11 is absent (corresponding to (B)) and where Annexin A11 is present (corresponding to (C)), colours included in the intensity traces reflect the fluorescent signals in (A-C). Scale bars represent 10µm.

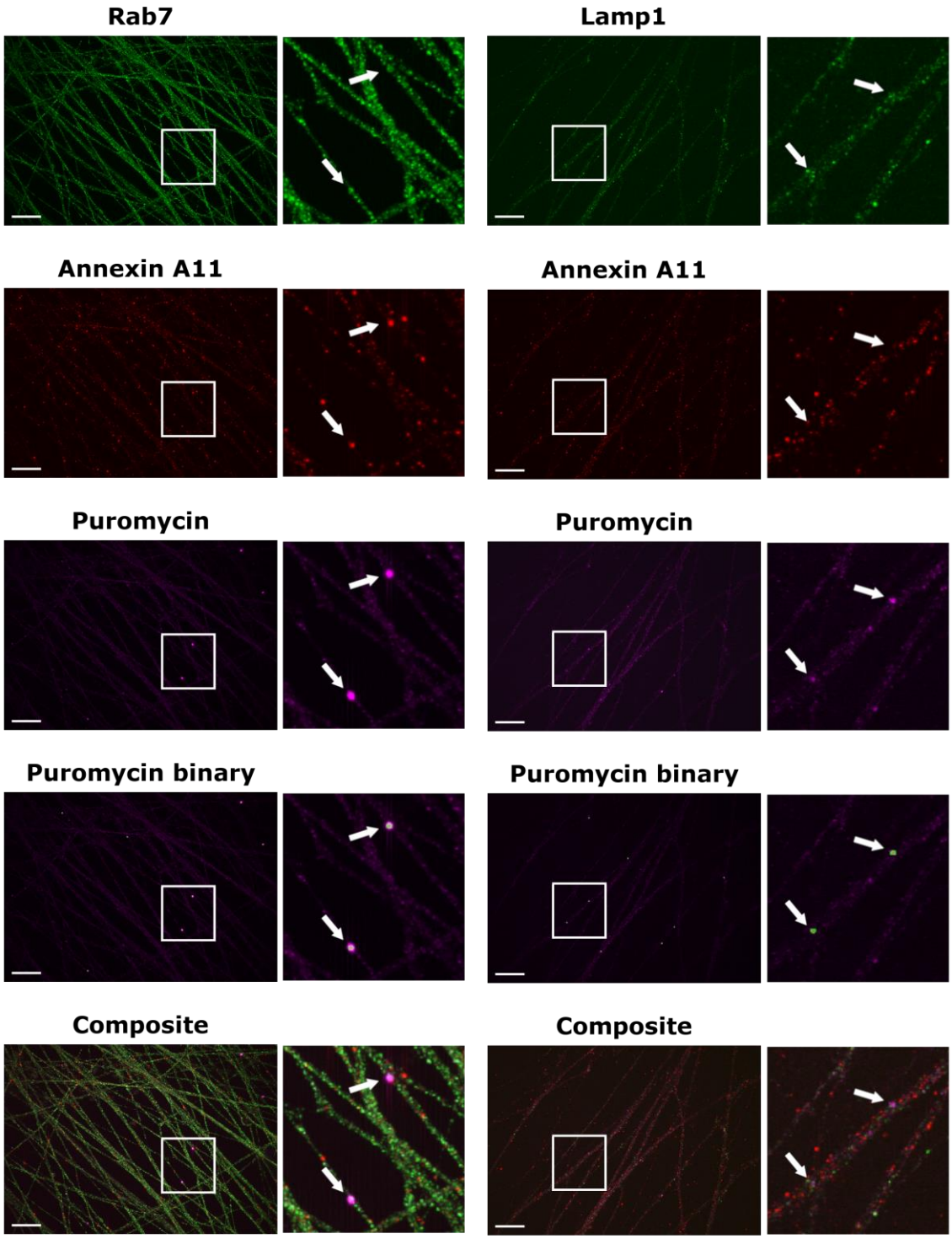


***Figure 6.18 Quantification of translational hotspots in motor neurons***

Analysis of translational hotspots in motor neuron neurites was completed in Nikon NIS-Elements. Ribopuromycylation was completed and bright puromycin spots were detected using "Spot detection – Different sized spots" to localise points of translation. Fluorescent intensities of Annexin A11 and target proteins were measured at these sites. Magnified areas are indicated by white boxes.

The example included in the left-hand panel is Rab7 (green), the right-hand panel shows interrogation of Lamp1 (green). Scale bars represent 10μm.

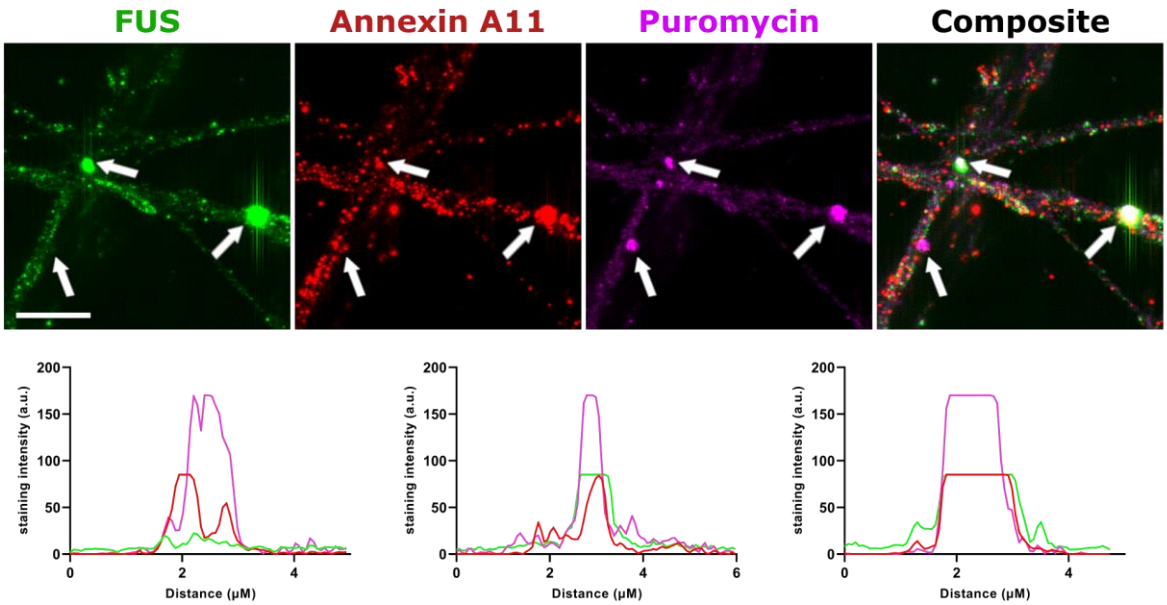
FUS
Annexin A11
Puromycin
Composite
staining intensity (a.u.)
Distance (μM)

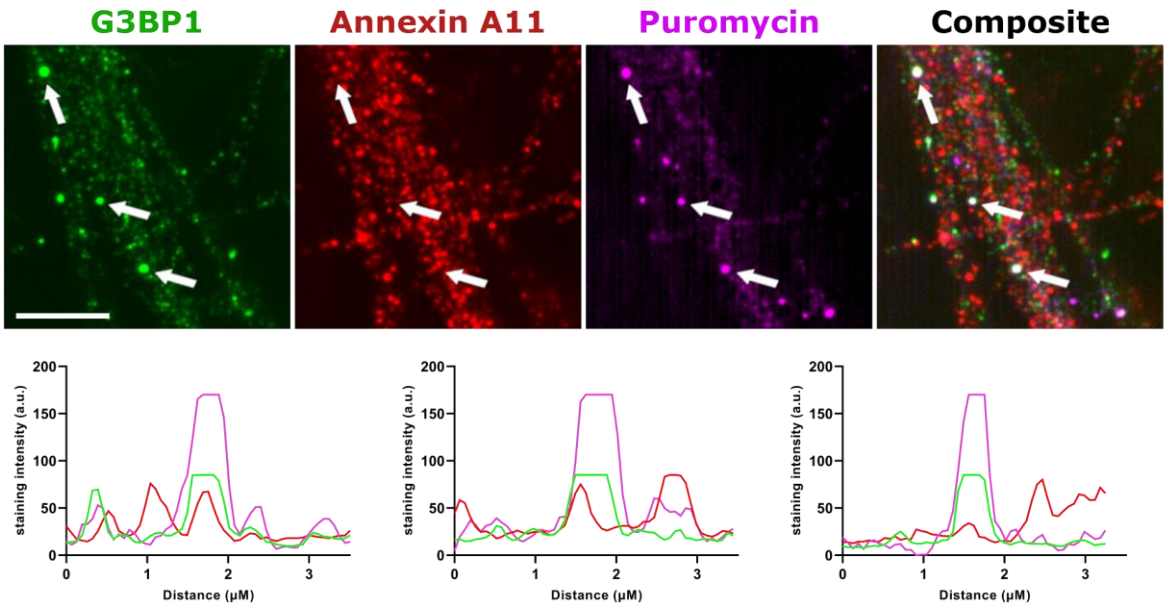
G3BP1
Annexin A11
Puromycin
Composite
staining intensity (a.u.)
Distance (μM)

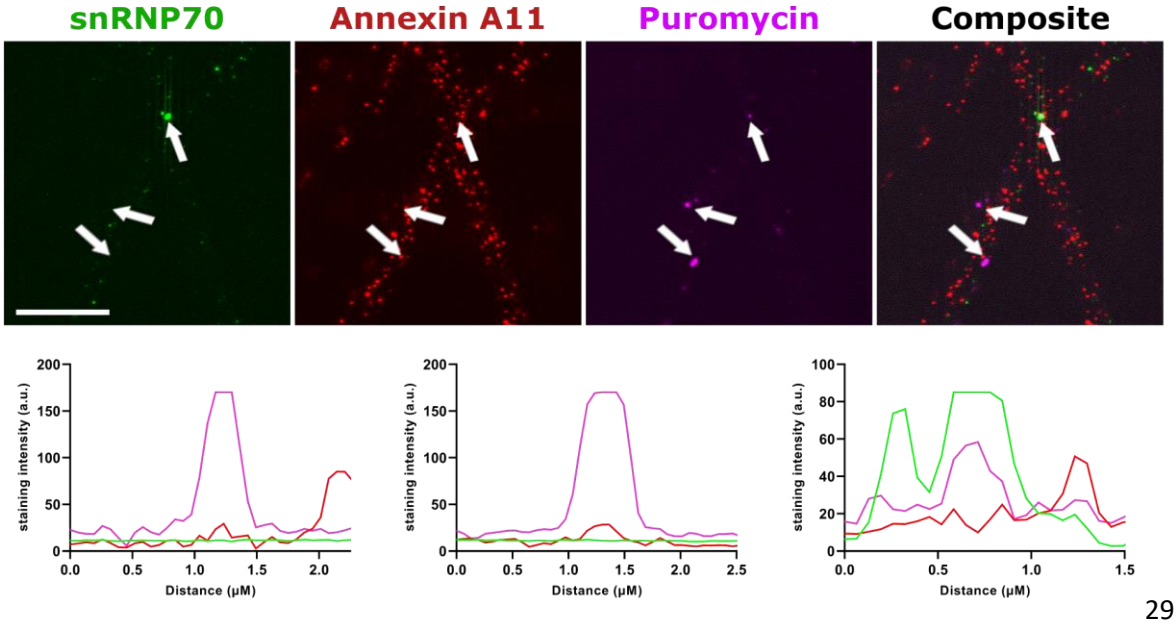
snRNP70
Annexin A11
Puromycin
Composite
staining intensity (a.u.)
Distance (μM)

***Figure 6.19 Localisation of Annexin A11, FUS, G3BP1, and snRNP70 to ribopuromycylation spots***

Examples of neurite translational hotspots detected by ribopuromycylation, including an antibody detecting puromycin (magenta), Annexin A11 (red), and target proteins FUS, G3BP1, and snRNP70 (green). Intensity traces were drawn across puromycin spots (indicated by white arrows) and are represented below each image panel, with the intensity traces representing the indicated puromycin spots from left to right in each instance. The colours used in intensity traces reflect the colours indicated in representative images. Scale bars represent 5µm.

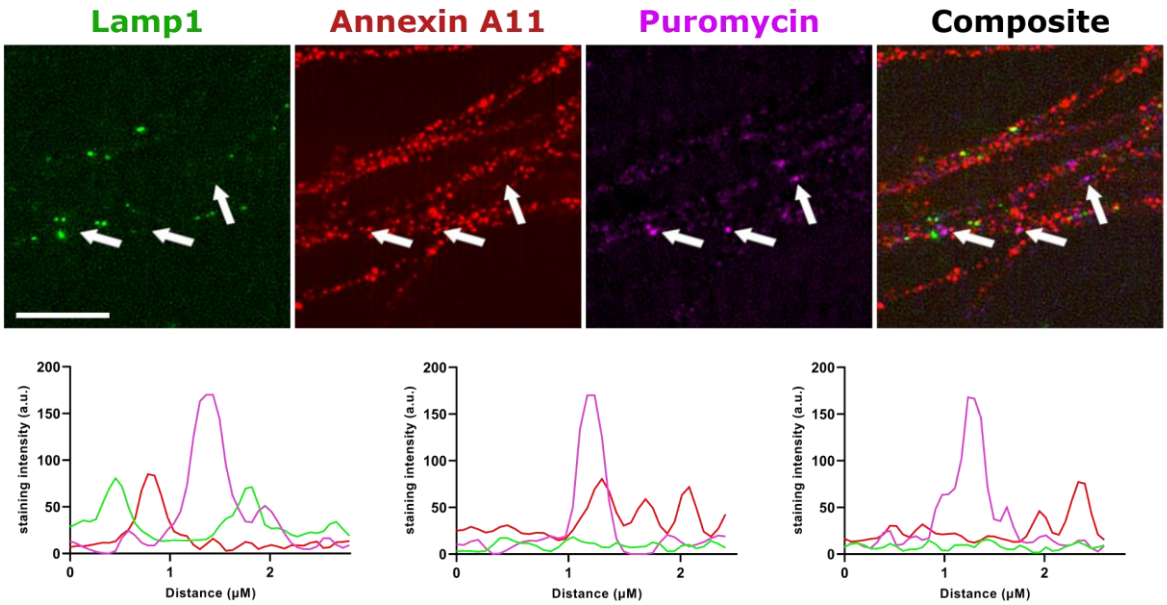
Lamp1
Annexin A11
Puromycin
Composite
staining intensity (a.u.)
Distance (μM)

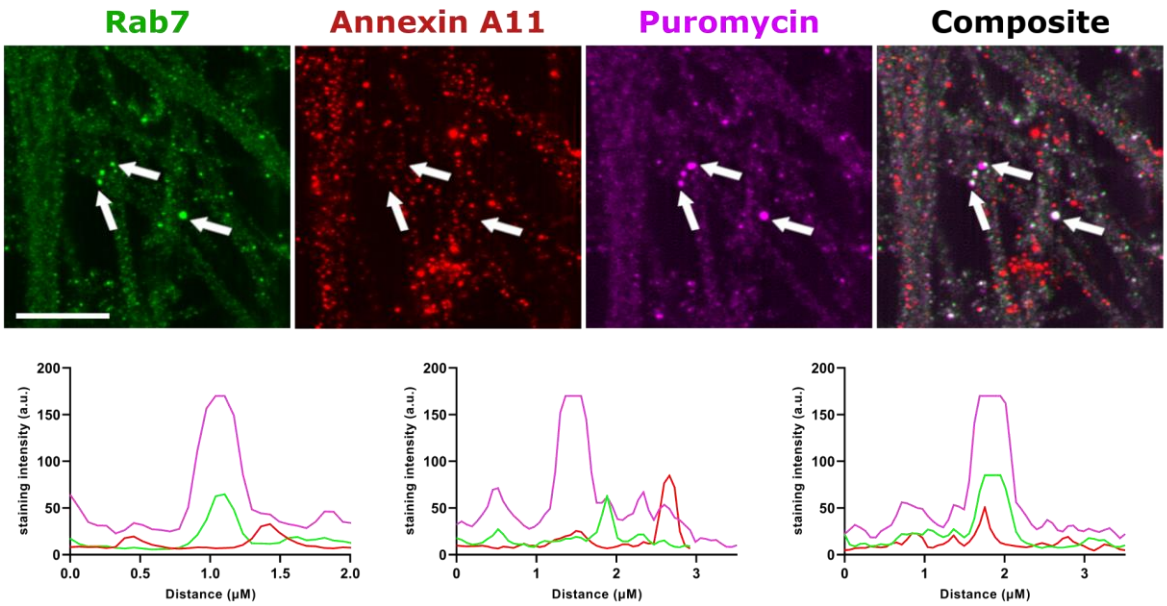
Rab7
Annexin A11
Puromycin
Composite
staining intensity (a.u.)
Distance (μM)

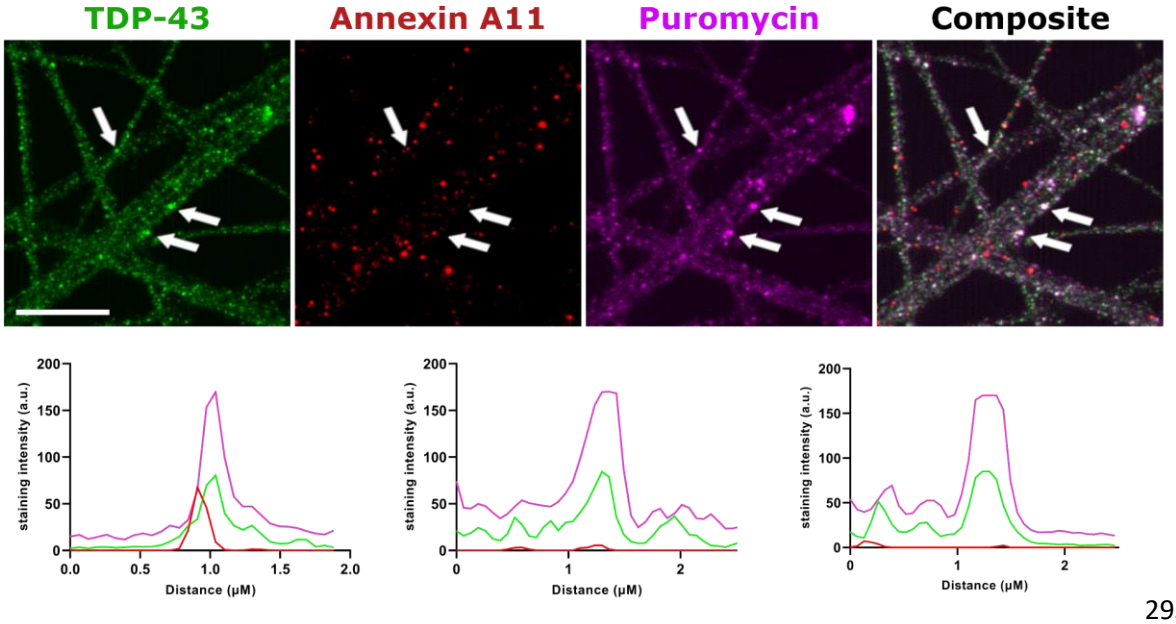
TDP-43
Annexin A11
Puromycin
Composite
staining intensity (a.u.)
Distance (μM)

***Figure 6.20 Localisation of Annexin A11, Lamp1, Rab7, and TDP-43 to ribopuromycylation spots***

Examples of neurite translational hotspots detected by ribopuromycylation, including an antibody detecting puromycin (magenta), Annexin A11 (red), and target proteins Lamp1, Rab7, and TDP-43 (green). Intensity traces were drawn across puromycin spots (indicated by white arrows) and are represented below each image panel, with the intensity traces representing the indicated puromycin spots from left to right in each instance. The colours used in intensity traces reflect the colours indicated in representative images. Scale bars represent 5µm.

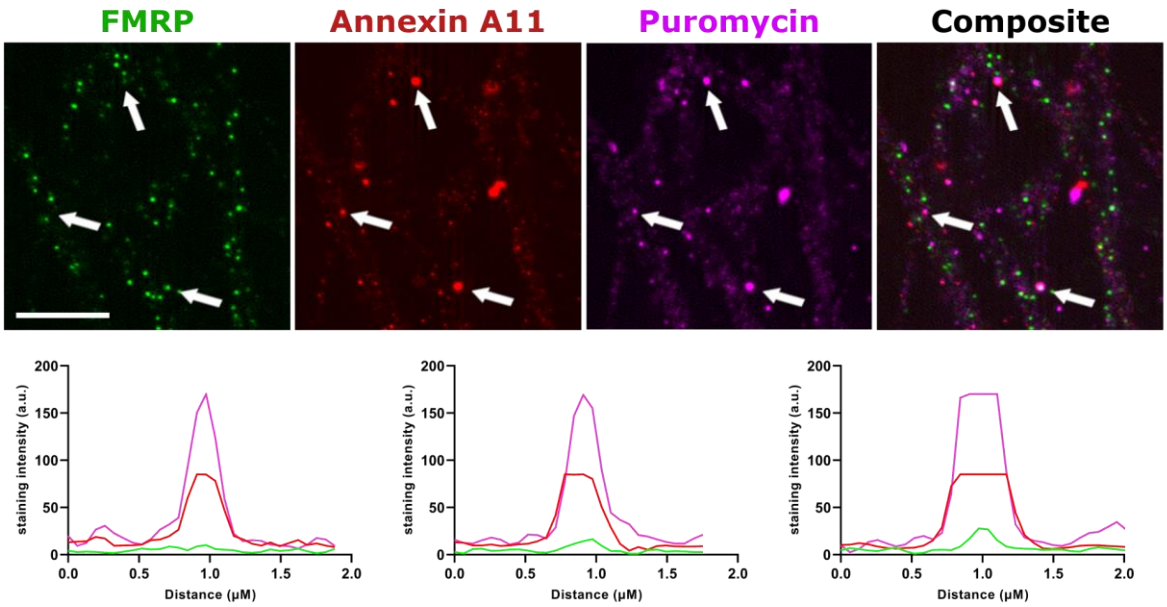
FMRP
Annexin A11
Puromycin
Composite
staining intensity (a.u.)
Distance (μM)

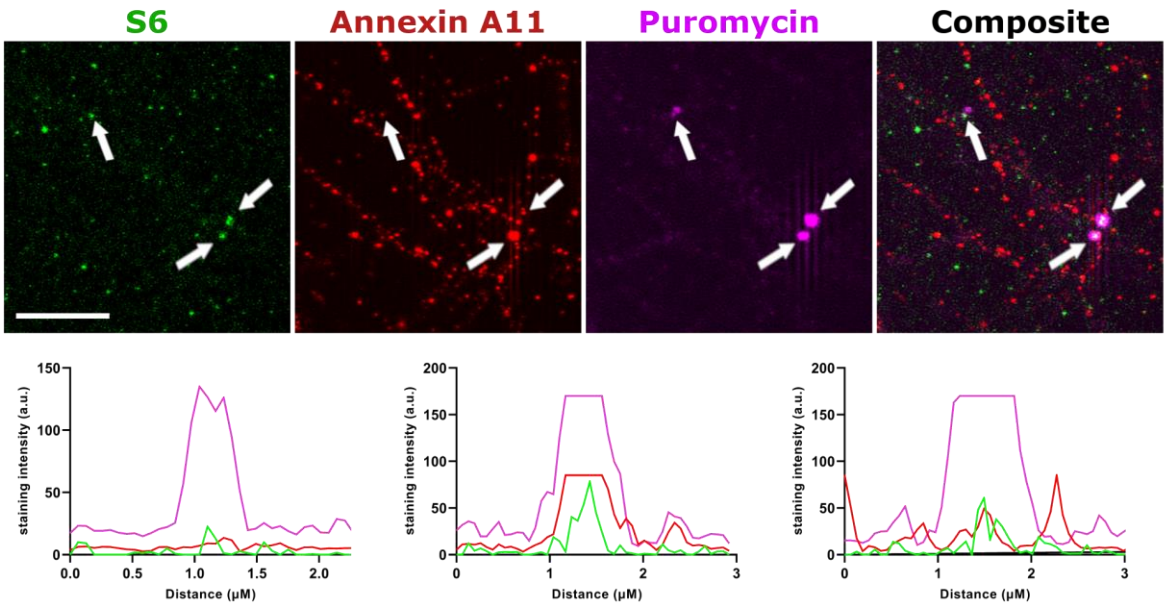
S6
Annexin A11
Puromycin
Composite
staining intensity (a.u.)
Distance (μM)

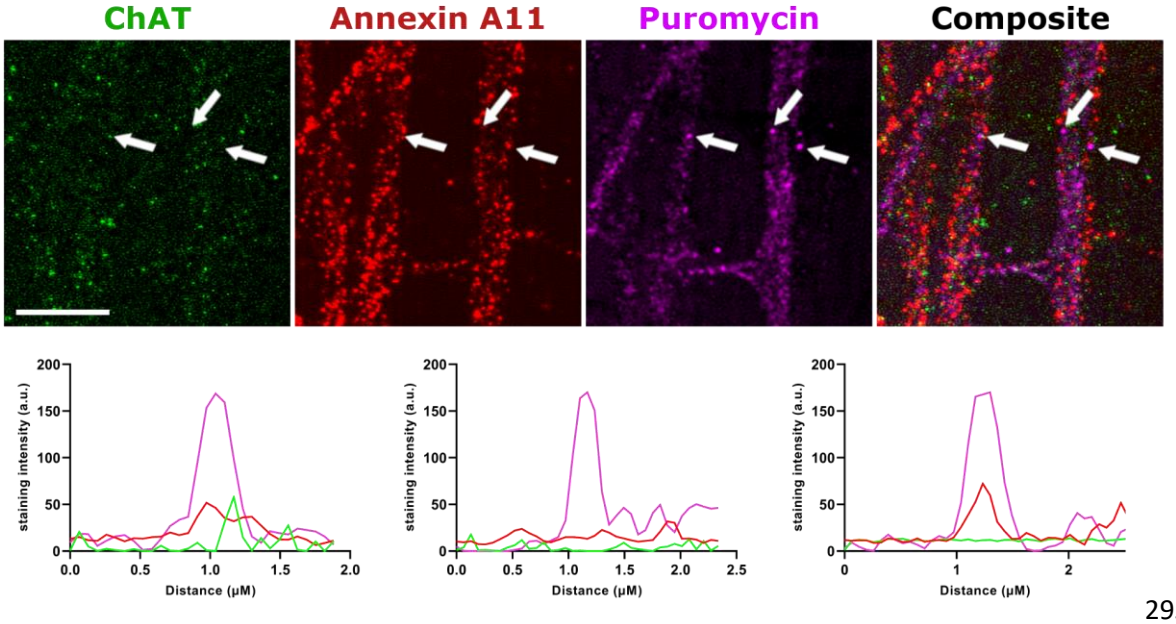
ChAT
Annexin A11
Puromycin
Composite
staining intensity (a.u.)
Distance (μM)

***Figure 6.21 Localisation of Annexin A11, FMRP, S6, and ChAT to ribopuromycylation spots***

Examples of neurite translational hotspots detected by ribopuromycylation, including an antibody detecting puromycin (magenta), Annexin A11 (red), and target proteins FMRP, S6, and ChAT (green). Intensity traces were drawn across puromycin spots (indicated by white arrows) and are represented below each image panel, with the intensity traces representing the indicated puromycin spots from left to right in each instance. The colours used in intensity traces reflect the colours indicated in representative images. Scale bars represent 5µm.

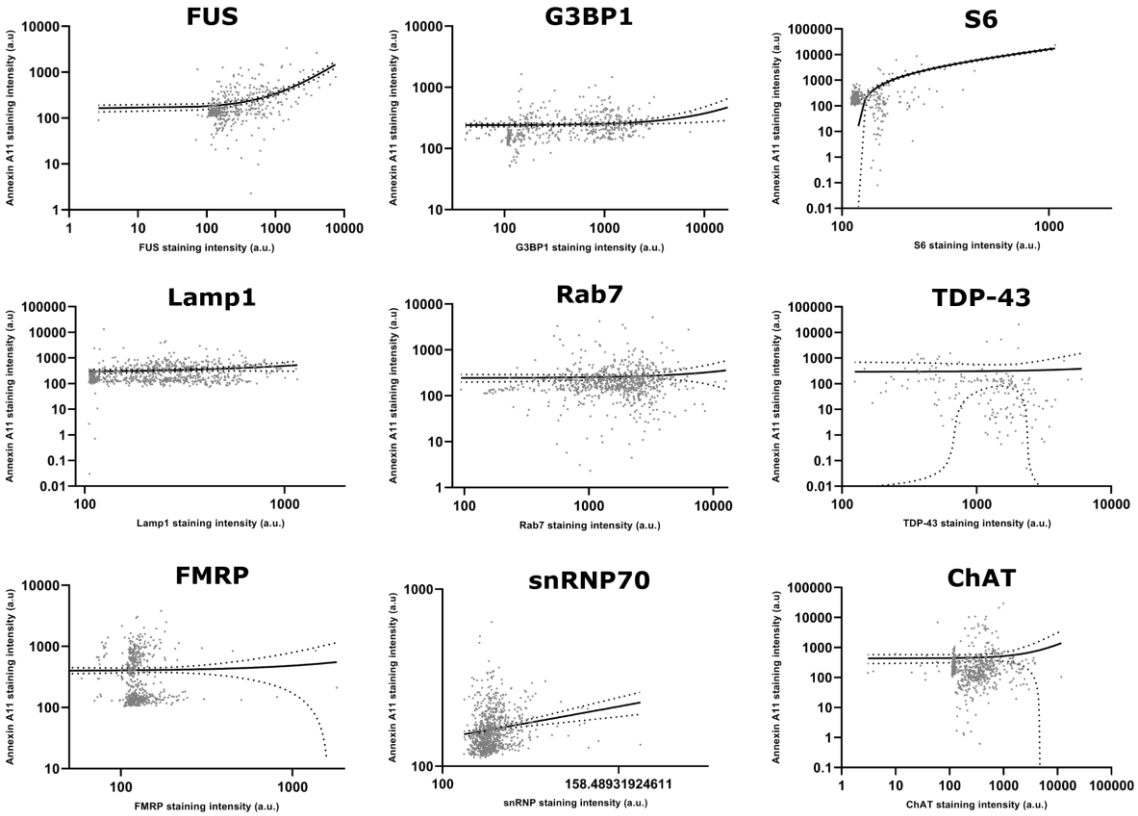


***Figure 6.22 Characterisation of Annexin A11 translational hotspots in control motor neurons***

Fluorescent intensities of Annexin A11 and target proteins at sites of local translation were plotted on *XY* graphs in GraphPad Prism, with each data point representing an individual translational hotspot as defined by puromycin labelling. Linear regression lines were included to represent the line of best fit with 95% confidence intervals. Annexin A11 fluorescent intensity is included on the *y* axis, and target proteins are in *x*.

***Table 6.2 Pearson's correlation coefficient of Annexin A11 and target proteins at sites of local translation***

| Target protein | Pearson *r* | 95% confidence interval | $r^2$ | *P* (two-tailed) | # *XY* pairs |
|---|---|---|---|---|---|
| **FUS** | 0.4171 | 0.3389 to 0.4896 | 0.174 | <0.0001 (****) | 463 (*n* = 3) |
| **G3BP1** | 0.1073 | 0.01913 to 0.1937 | 0.01151 | 0.0172 (*) | 493 (*n* = 2) |
| **S6** | 0.8035 | 0.7603 to 0.8396 | 0.6456 | <0.0001 (****) | 312 (*n* = 3) |
| **Lamp1** | 0.06337 | -0.009285 to 0.1354 | 0.004016 | 0.0873 (ns) | 729 (*n* = 3) |
| **Rab7** | 0.03114 | -0.03950 to 0.1015 | 0.00097 | 0.3875 (ns) | 772 (*n* = 2) |
| **TDP-43** | 0.00902 | -0.1350 to 0.1527 | 0.00008136 | 0.9027 (ns) | 186 (*n* = 1) |
| **FMRP** | 0.01969 | -0.06161 to 0.1007 | 0.0003879 | 0.6351 (ns) | 583 (*n* = 2) |
| **snRNP70** | 0.1332 | 0.06889 to 0.1965 | 0.01775 | <0.0001 (****) | 911 (*n* = 1) |
| **ChAT** | 0.0318 | -0.04219 to 0.1054 | 0.001011 | 0.3995 (ns) | 704 (*n* = 2) |

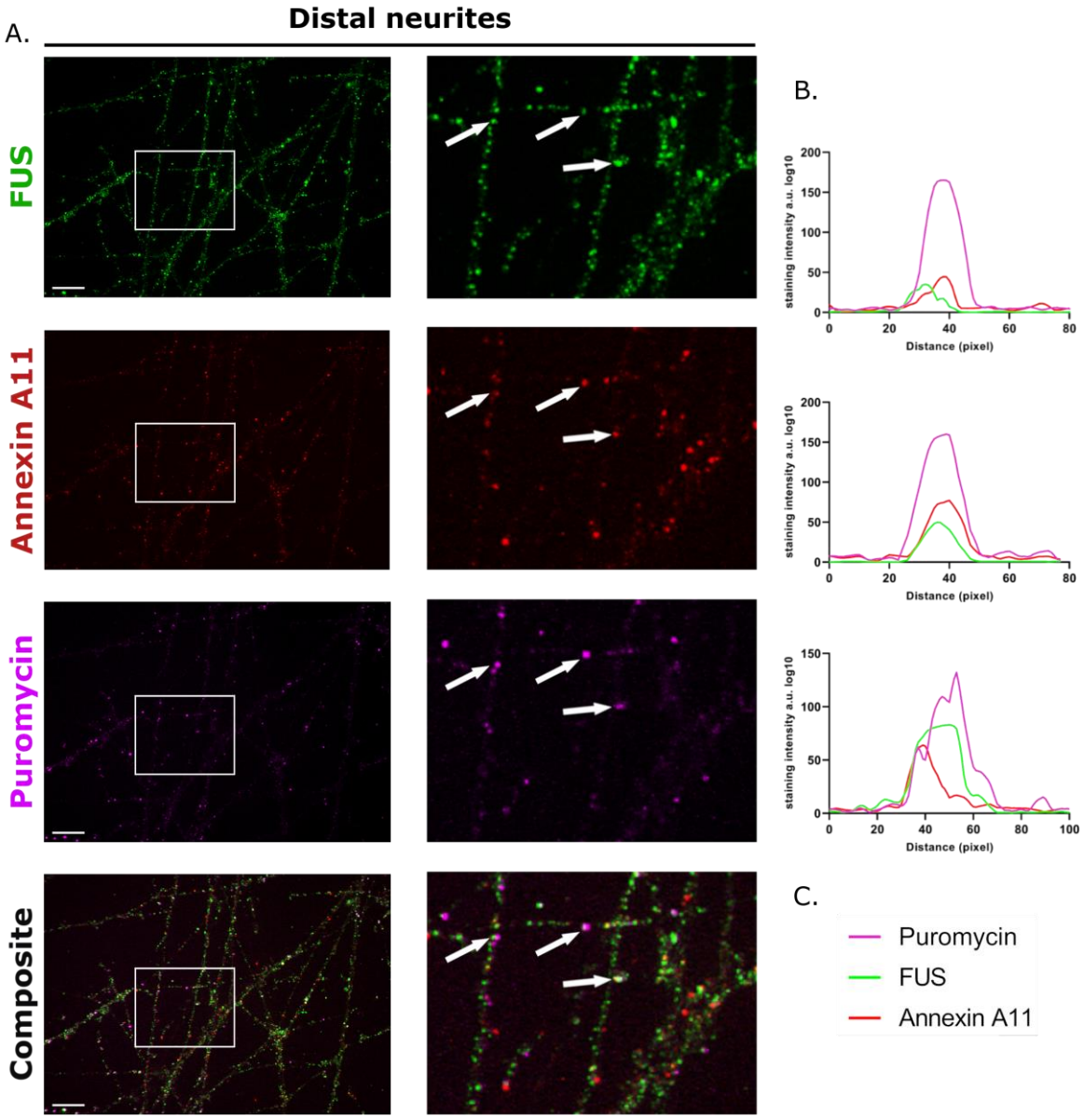


***Figure 6.23 Annexin A11 and FUS localise to the same translational hotspots in distal neurites***

(A) Motor neurons grown in microfluidic devices to compartmentalise distal neurites were subject to ribopuromycylation and immunocytochemistry targeting FUS (green), Annexin A11 (red), and puromycin (magenta) to detect translational hotspots. The white boxes in the left-hand panel indicate the region magnified in the right-hand panel. White arrows indicate translational hotspots where both Annexin A11 and FUS are localised. (B) Intensity traces across the spots indicated with white arrows in (A) show mirrored increase in puromycin, Annexin A11, and FUS signal, and represent the white arrows from left to right in (A) from top to bottom in (B). (C) Key for (B). Scale bars represent 10µm.

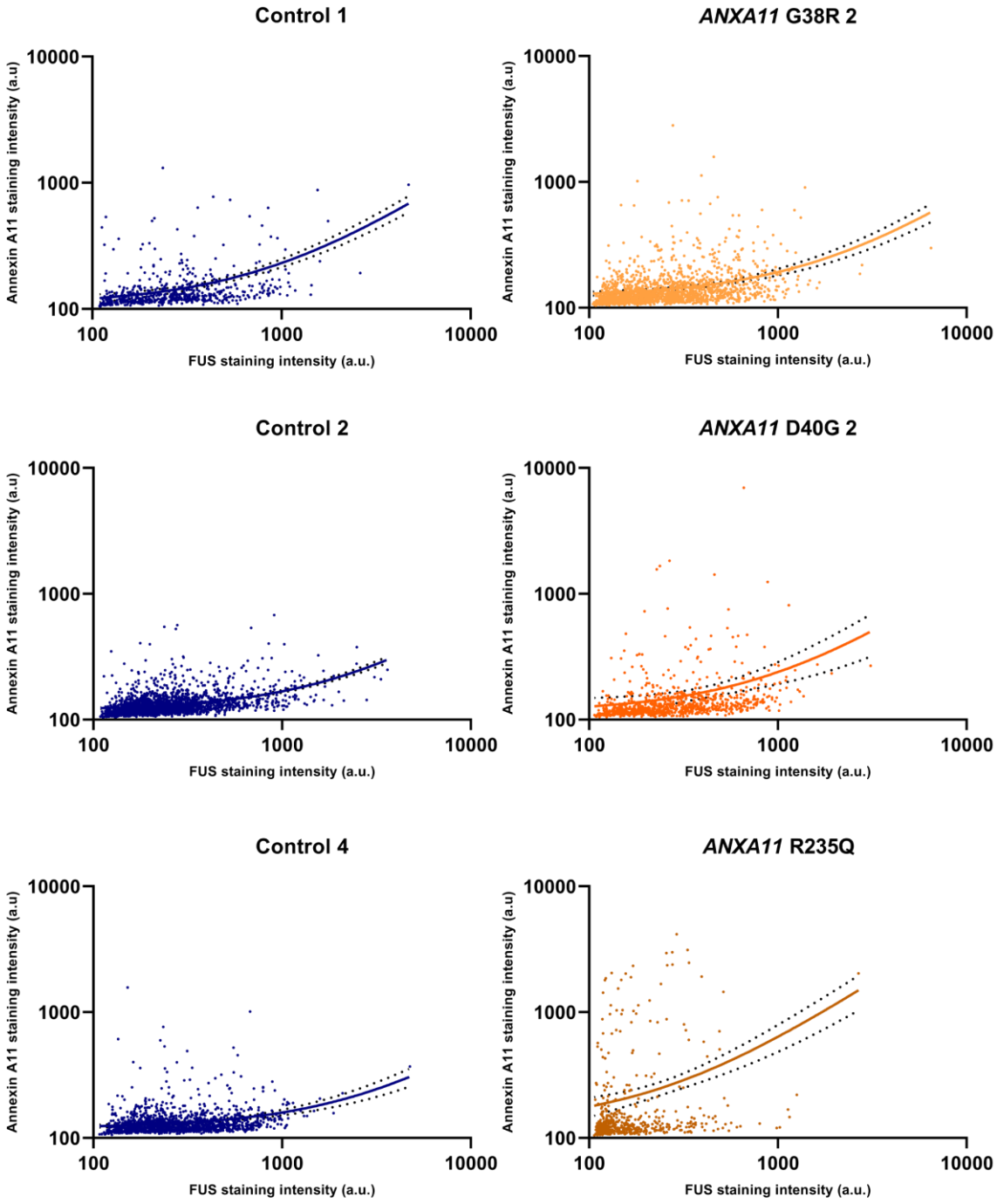


***Figure 6.24 Correlation of Annexin A11 and FUS at sites of local translation in distal neurites***

Fluorescent intensities from ribopuromycylation in distal neurites were plotted on *XY* graphs in GraphPad Prism for each cell line, each data point represents an individual translational hotspot as defined by puromycin labelling. Annexin A11 fluorescent intensity is included on the *y* axis, and FUS fluorescent intensity is in *x*. Linear regression lines with 95% confidence intervals are included to represent the line of best fit. Number of motor neuron inductions = 2.

***Table 6.3 Correlation of Annexin A11 and FUS at sites of local translation in control and ALS patient motor neurons***

| Cell line | Pearson *r* | 95% confidence interval | $r^2$ | *P* (two-tailed) | # *XY* pairs |
|---|---|---|---|---|---|
| **Control 1** | 0.3862 | 0.3175 to 0.4508 | 0.1491 | <0.0001 | 627 |
| **Control 2** | 0.3456 | 0.3118 to 0.3785 | 0.1194 | <0.0001 | 2687 |
| **Control 4** | 0.1545 | 0.1107 to 0.1978 | 0.02388 | <0.0001 | 1932 |
| ***ANXA11* G38R** | 0.1926 | 0.1508 to 0.2338 | 0.03711 | <0.0001 | 2072 |
| ***ANXA11* D40G** | 0.1176 | 0.05550 to 0.1789 | 0.01384 | 0.0002 | 982 |
| ***ANXA11* R235Q** | 0.2001 | 0.1286 to 0.2695 | 0.0405 | <0.0001 | 714 |

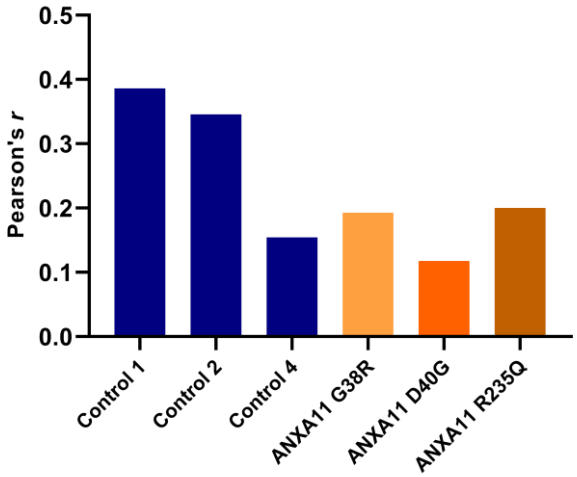


***Figure 6.25 Visualisation of r values from Pearson's correlation coefficient in ribopuromycylation analysis***

*R* values from Pearson's correlation coefficient are shown side by side to aid visualisation of the strength of correlation between Annexin A11 and FUS at puromycin spots across cell lines.

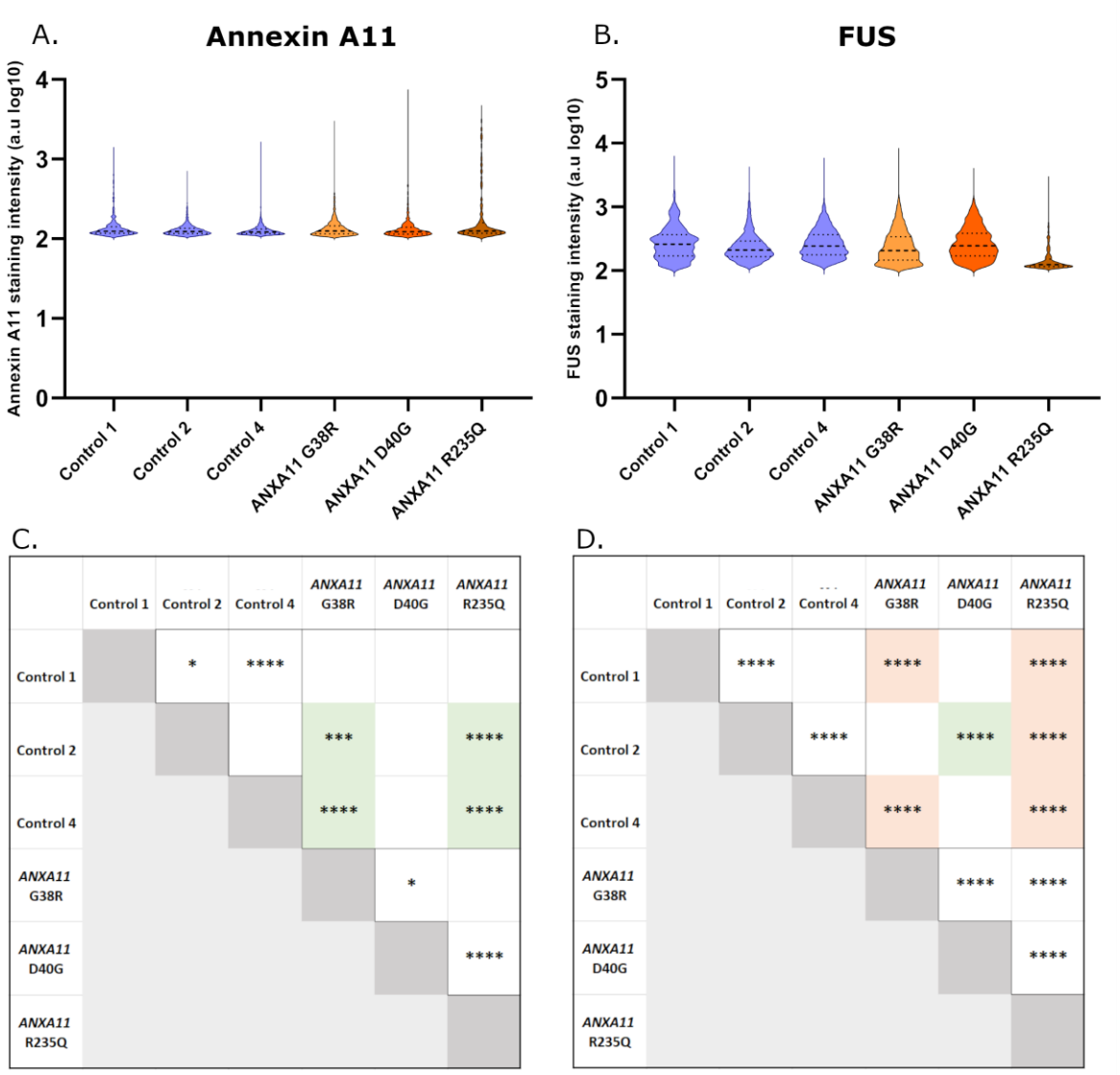


***Figure 6.26 Intensity of Annexin A11 and FUS at sites of local translation in distal neurites***

The fluorescent intensity of Annexin A11 (A) and FUS (B) at sites of local translation are shown for control and *ANXA11mut* motor neuron distal axons. Data were subject to Kruskal-Wallis one-way analysis of variance with Dunn's multiple comparisons test, and significant differences between each cell line pair are indicated for Annexin A11 (C) and FUS (D). Where significant differences were detected in control and *ANXA11mut* pairwise comparisons, an increase in fluorescent intensity in the *ANXA11mut* line compared to control is shaded green, and where significant difference is associated with reduced intensity in the *ANXA11mut* line compared to control, orange shading is included (* = *p < 0.05, *** p < 0.001, **** = p < 0.0001;* number of motor neuron inductions = 2).

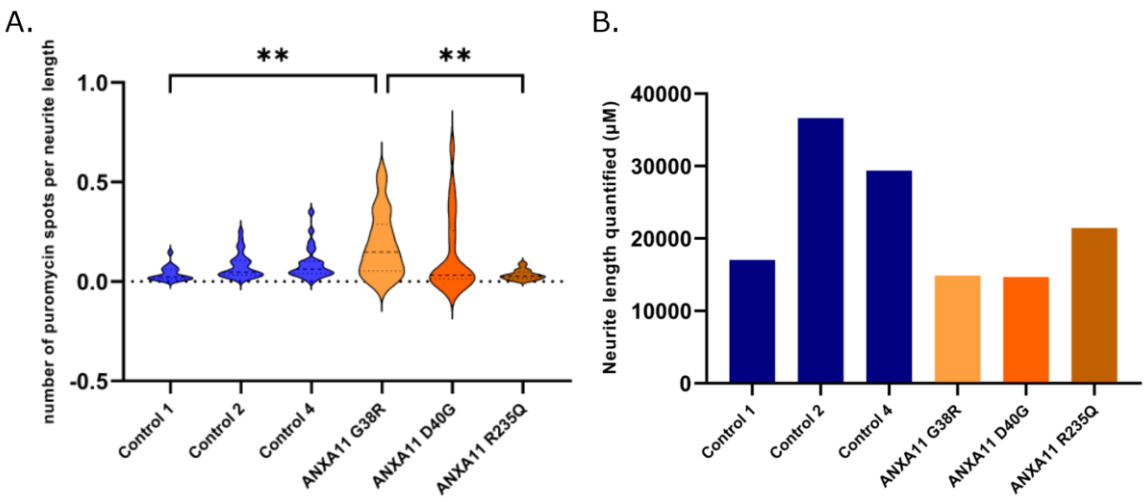


***Figure 6.27 Density of translational hotspots in distal neurites***

(A) The number of puromycin labelled translational hotspots was normalised to the total neurite length per image (µm) and the value for each image is included in the violin plot. Data were subject to Kruskal-Wallis one-way analysis of variance with Dunn's multiple comparisons test, and significant differences are indicated (*** = $p < 0.01$;* number of motor neuron inductions = 2). (B) The total length of neurites in images used for quantification of local translation in distal neurites was inconsistent across cell lines due to differences in distal axon density. A bar chart with the total neurite length quantified per cell line is included to demonstrate this.

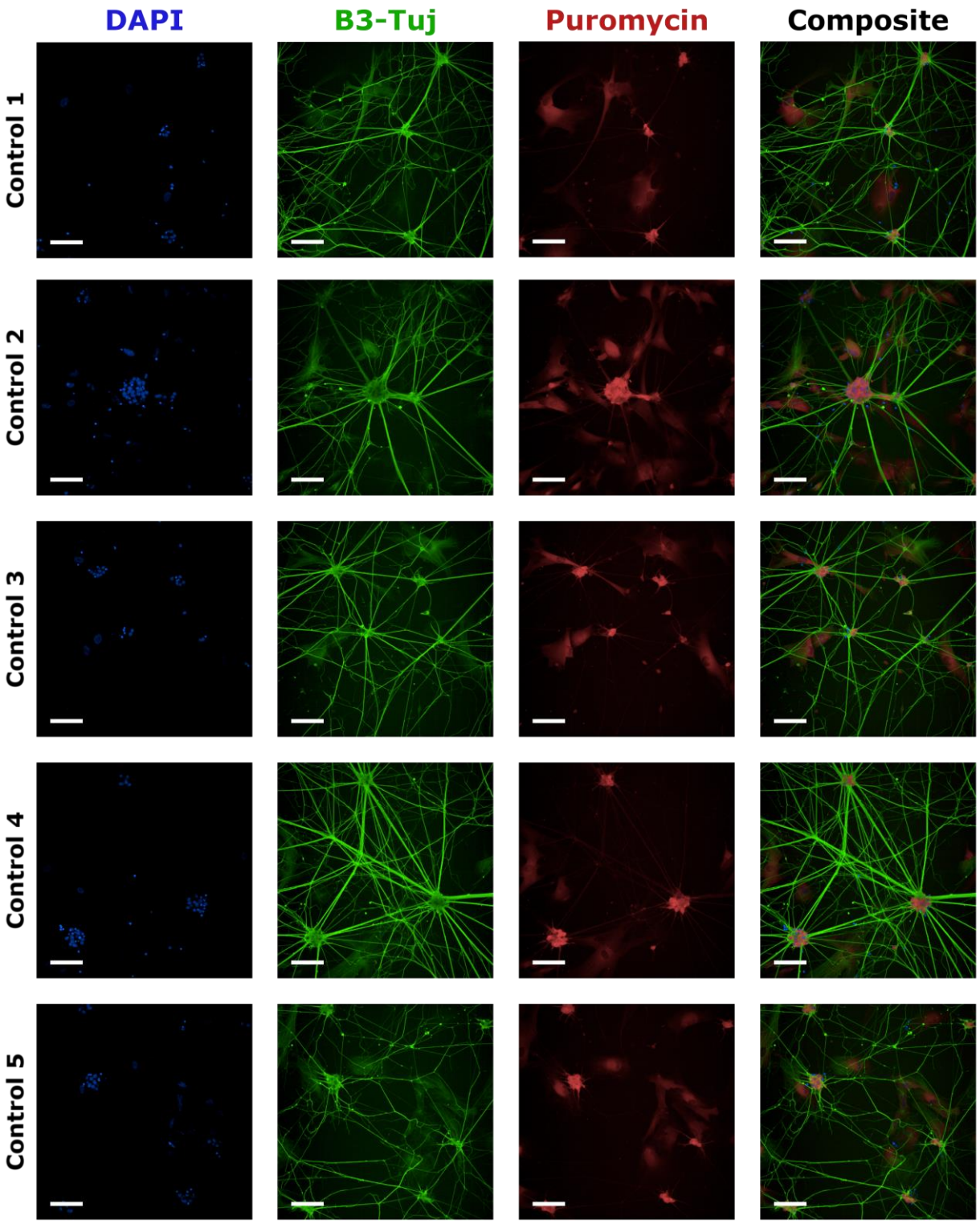


***Figure 6.28 Global translation in control motor neurons***

Control motor neurons were maintained in co-culture with astrocytes until day 21 of motor neuron differentiation, treated with puromycin, fixed, and subject to immunocytochemistry with antibodies targeting puromycin (red) and the neuronal marker $\beta$3-Tubulin (B3-Tuj, green), nuclei were stained with DAPI (blue). Scale bars represent 100µm.

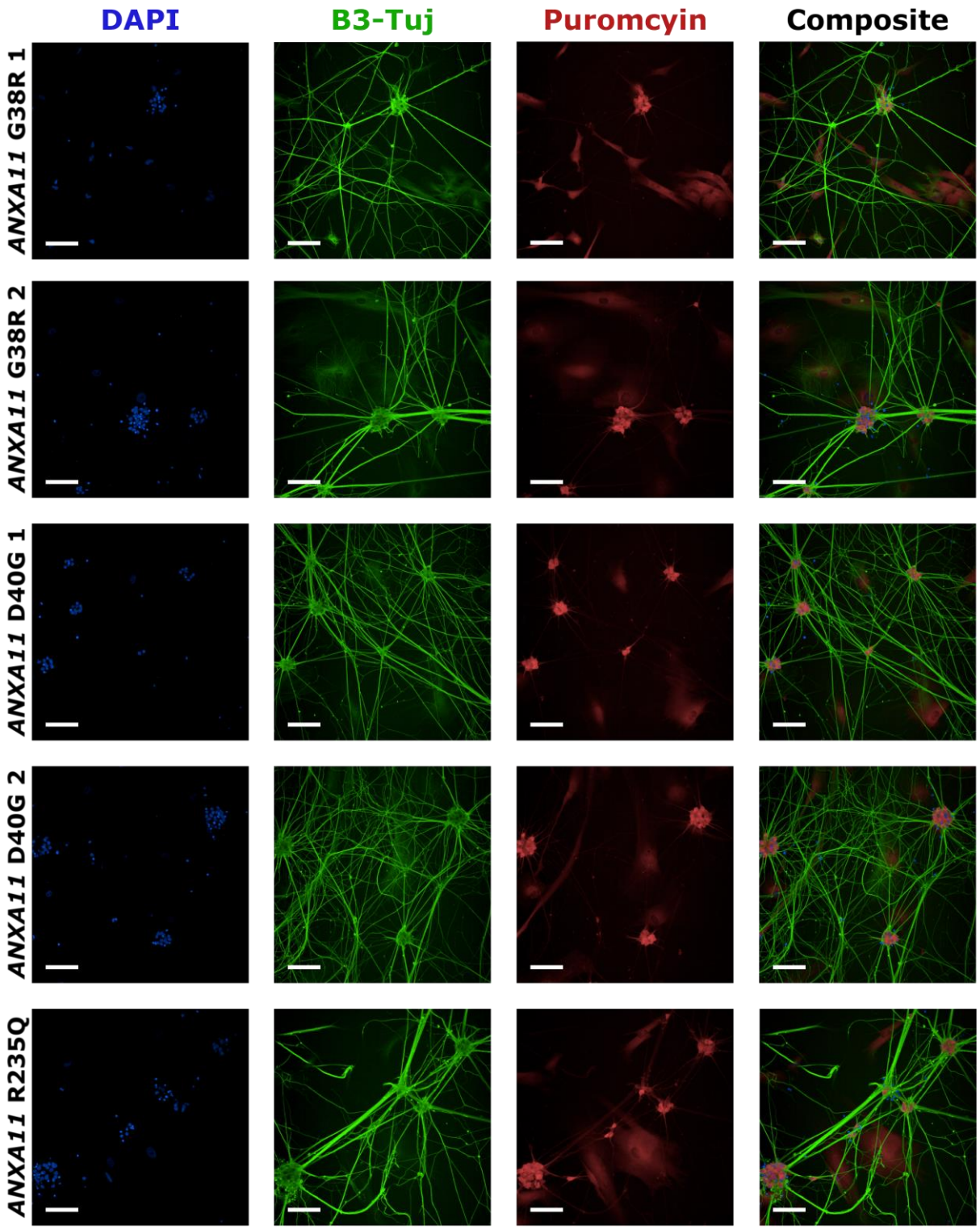


***Figure 6.29 Global translation in ANXA11mut motor neurons***

*ANXA11* patient derived motor neurons were maintained in co-culture with astrocytes until day 21 of motor neuron differentiation treated with puromycin, fixed, and subject to immunocytochemistry with antibodies targeting puromycin (red) and the neuronal marker $\beta$3-Tubulin (B3-Tuj, green), nuclei were stained with DAPI (blue). Scale bars represent 100µm.

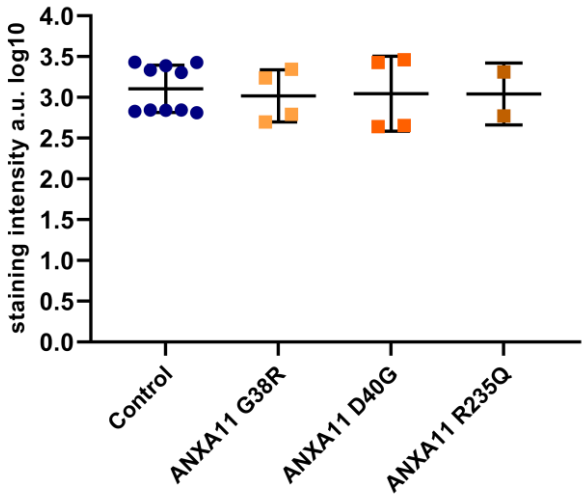


***Figure 6.30 Global protein translation is unaffected in ANXA11 ALS patient motor neurons***

Quantification of data represented in Figure 6.28 and Figure 6.29. Total intensity of puromycin in neurons was used as a measure of total protein translation and was not changed in any *ANXA11* mutation group compared to control. Data are presented as mean ± SEM, number of motor neuron inductions = 2. Each data point represents one cell line in one motor neuron induction, with each comprised of three technical replicates. Control lines are grouped and *ANXA11* ALS patient lines are grouped by mutation. Statistical analysis: Brown-Forsythe one-way ANOVA with Dunnett's multiple comparisons test ($p > 0.05$).

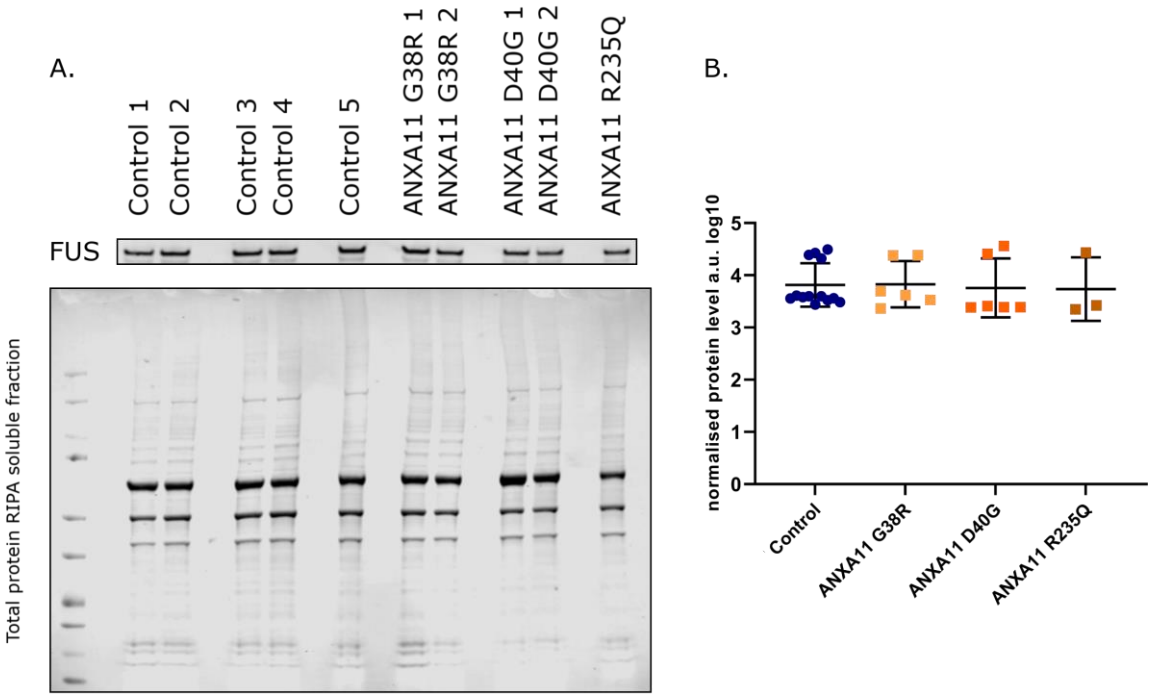


***Figure 6.31 FUS protein levels are consistent across control and ANXA11mut motor neurons***

(A) Representative western blot loaded with RIPA-soluble protein harvested from motor neurons on day 17 of differentiation, probed for FUS and total protein stain. (B) FUS protein was measured and normalised to total protein. Data are presented as mean ± SEM, number of motor neuron inductions = 3. Each data point represents relative FUS protein abundance in one cell line in one motor neuron induction, control lines are grouped and *ANXA11* ALS patient lines are grouped by mutation. Statistical analysis: Ordinary one-way ANOVA with Dunnett's multiple comparisons test ($p > 0.05$).

## *6.4 Discussion*

RNA processing is dysregulated in ALS, and multiple RNA pathways are implicated in pathology. Annexin A11 has been associated with stress granule dynamics (Markmiller et al., 2018; Nahm et al., 2020), RNA transport (Liao et al., 2019), and global protein translation (Nahm et al., 2020). These processes were explored in *ANXA11* ALS patient and control motor neurons to elucidate the role of endogenous Annexin A11 in cell-type specific RNA biology, and to establish the influence of ALS associated *ANXA11* point mutations on these functions.

### *6.4.1 Annexin A11 and stress granules*

Annexin A11 was first implicated in stress granule biology through APEX proximity labelling to identify proteins in close contact with the stress granule marker G3BP1; Annexin A11 was shown to localise to stress granules in HEK293 cells, but not in neural progenitors (Markmiller et al., 2018). A separate study showed that Annexin A11 localised to sodium arsenite-induced TIA1 positive stress granules in fibroblasts from controls and patients harbouring G38R, H390P, and R456H mutations in *ANXA11* (Nahm et al., 2020). Overexpression of *ANXA11* constructs in HeLa cells showed reduced dissociation of mCherry-TIA1 and Annexin-GFP stress granules harbouring *ANXA11* mutations (G38R, D40G, H390P, R456H), compared to WT *ANXA11,* in the recovery time after stress exposure (Nahm et al., 2020). The same study showed Annexin A11 co-aggregation with FUS in response to osmotic stress. Overexpression of mEmerald-tagged *ANXA11* constructs in U2OS cells subject to heat-shock showed significant overlap of WT Annexin A11 with G3BP1 and Oligo-dT positive stress granules, which was not significantly reduced in *ANXA11* D40G expressing cells, but was reduced in *ANXA11* R235Q or R346C expressing cells (Liao et al., 2019). Collectively these data indicate that Annexin A11 has a role in stress granule biology, but do not measure stress granule assembly or Annexin A11 inclusion to stress granules in motor neurons with endogenous protein expression levels.

Initially, control motor neurons were subject to known stressors to interrogate the inclusion of Annexin A11 to G3BP1 positive stress granules in iPSC-derived motor neurons. Puromycin is typically used as a protein translation inhibitor and works by destabilising polysomes by promoting termination. Puromycin has been shown to exacerbate stress granule formation in co-treatment with drugs such as sodium arsenite, and prolonged treatment of motor neurons with puromycin is thought to lead to stress granule induction by increasing the pool of cytoplasmic mRNA thus lowering the threshold for stress granule formation (Aulas et al., 2017; Bounedjah et al., 2014; Kedersha et al., 2000; Markmiller et al., 2018; Wolozin & Ivanov, 2019). Assessment of puromycin induced stress granules with super resolution microscopy revealed a modest increase in Annexin A11 intensity across G3BP1 positive stress granules (Figure 6.1), however these results were inconsistent (Figure

6.2). Additionally, striking inclusion of endogenous TDP-43 to puromycin induced stress granules in the absence of Annexin A11 localisation to the same region suggests that Annexin A11 is not consistently recruited to stress granules in response to puromycin treatment in iPSC derived motor neurons (Figure 6.2).

Differential inclusion of proteins to stress granules depending on the nature of the stress inducing event have been reported (Frydrýšková et al., 2020; Markmiller et al., 2018), and so additional stressors were investigated in control motor neurons. Motor neurons were treated with puromycin, sodium arsenite, and sorbitol, and were imaged with confocal microscopy with a view to increase the number of neurons in later quantification, compared to low-throughput super resolution microscopy. Motor neurons treated with puromycin did not display inclusion of Annexin A11 to stress granules at lower resolution (Figure 6.3). Sodium arsenite is well reported to induce stress granules in cellular systems and was shown to induce the stress granule response in control motor neurons, resulting in localisation of Annexin A11 to some G3BP1 stress granules (Figure 6.4). Induction of stress granule formation with the osmotic stressor sorbitol resulted in formation of small stress granules throughout the nucleus and cytoplasm, which appeared to occasionally co-localise with Annexin A11 (Figure 6.5). Induction of the stress granule response with heat-shock has been reported in many cell line studies and was attempted here but was unsuccessful as no stress granules could be detected (data not shown). These data show that localisation of Annexin A11 to stress granules is context-dependent and subtle. To investigate this further, stress granule characteristics were assessed in control and *ANXA11mut* motor neurons. Due to the detection of Annexin A11 in stress granules in response to sodium arsenite treatment, this stressor was selected for a full comparison of stress granule dynamics in control and *ANXA11mut* motor neurons.

Stress granule analysis was completed in five control and five *ANXA11* ALS patient-derived cell lines (Figure 6.6; Figure 6.7; Figure 6.8; Figure 6.9). As quantification was performed by thresholding entire images (Figure 6.10), reported data are representative of stress granule characteristics in multiple cells, as opposed to the interrogation of individual stress granules. Such quantification can dilute

signal seen in individual stress granules, but instead represents protein localisation across multiple cells, giving a broad analysis of stress granule characteristics. The effectiveness of threshold-based quantification is evidenced by the statistically significant decrease in G3BP1 nucleocytoplasmic ratio and increase in G3BP1 granule area per neuron in response to sodium arsenite treatment (Figure 6.11.A, Figure 6.11.B, respectively). The stress granule area per neuronal area was reduced in *ANXA11* R235Q neurons compared to control, suggesting that stress granule induction is impaired in this instance (Figure 6.11.B). No similar reduction was observed in *ANXA11* G38R or D40G motor neurons, indicating a C-terminal mutation specific event. This might be unexpected as the G38R and D40G mutations reside in the low-complexity RBP binding domain, and so it might be assumed that mutations in this region are more likely to affect stress granule dynamics. Interestingly, evidence that folded domains in hnRNPA1 affect the liquid-liquid phase-separation of the low-complexity region implicate that phase-separation events are not mediated solely by disordered regions (Martin et al., 2021). Therefore, if stress granule formation is affected by the low-complexity region of Annexin A11, it may be the case that C-terminal mediated tertiary structure of Annexin A11 is necessary for the proper functioning of the disordered region, and thus stress granule formation. Alternatively, formation of stress granules might be unrelated to the Annexin A11 disordered region, and altered phospholipid and calcium interactions might be responsible for reduced stress granule formation in *ANXA11* R235Q motor neurons. Importantly, a similar phenotype was seen in U2OS overexpression studies, where mutations in the Annexin core domain specifically reduced Annexin A11 localisation to stress granules, whereas the D40G mutation did not (Liao et al., 2019).

The same image thresholding method was used to measure overlap of Annexin A11 with G3BP1, which revealed no statistically significant difference in control and *ANXA11mut* neurons (Figure 6.11.F), however mean values did suggest an increase in overlap in response to treatment in all groups. This measurement showed a large spread of data evidenced by large SDs, highlighting the variable and dynamic nature of Annexin A11 localisation. This variability can be seen when assessing individual cells, where intensity traces across stress granules reveal different amounts of Annexin

A11 inclusion to separate stress granules within one cell (Figure 6.4). The variable nature of protein inclusion to stress granules is well established, often focused on the inclusion of proteins to specifically labelled stress granules (e.g. G3BP1, TIA1, PABP), or localisation of proteins to stress granules in specific cell types or in response to specific stressors (Aulas et al., 2017; Markmiller et al., 2018). In addition to recognition of these types of variability, it may be important to consider variability within cell-type and protein-specific stress granules, and the large data spread seen here indicates the inclusion of proteins (i.e. Annexin A11) to specific stress granules (i.e. G3BP1 stress granules in iPSC-derived motor neurons) is also highly variable.

Fluorescent intensity of Annexin A11 inside G3BP1 stress granules indicated no difference between control and *ANXA11mut* lines (Figure 6.11.E). Due to the nature of thresholding for image quantification, "stress granules" were also detected in the untreated condition and represent brighter regions of diffuse G3BP1 fluoresence, rather than focal stress granules, which is evident in representative images where G3BP1 signal is present in untreated neurons (Figure 6.6; Figure 6.7; Figure 6.8; Figure 6.9). Annexin A11 intensity was unchanged between "stress granules" detected in untreated cells and stress granules in the sodium arsenite condition, suggesting that overlap of Annexin A11 and G3BP1 is not stress specific. These data suggest that although Annexin A11 occasionally localises to stress granules in young iPSC-derived motor neurons, this is a subtle characteristic. The disparity seen between these data and published investigation into Annexin A11 inclusion into stress granules may be due to overexpression artefact, as most evidence comes from expression of constructs with fluorescently labelled Annexin A11. This could result in an exaggerated phenotype compared to endogenous events and might explain why Annexin A11 signal in stress granules is so much higher in cell line studies than has been seen in the present body of work. Sodium arsenite induced stress in fibroblasts resulted in endogenous Annexin A11 localisation to TIA1 stress granules, which was comparable in control and *ANXA11mut* fibroblasts. In this study the inclusion of mutant, but not WT, Annexin A11 to stress granules was affected by the addition of an intracellular calcium chelator prior to sodium arsenite treatment, indicating that altered stress granule inclusion

of Annexin A11 in overexpression studies could be a consequence of impaired calcium response, as opposed to a direct affectation of Annexin A11 stress granule inclusion (Nahm et al., 2020). Annexin A11 has been shown to bind to RBPs (Liao et al., 2019), and it is plausible that inclusion of Annexin A11 to stress granules is a by-product of interaction with other RBPs, localising Annexin A11 to stress granules as a consequence of these interactions, as opposed to Annexin A11 having an important role in stress granule biology. This could lead to an exaggerated Annexin A11 stress granule signal in over-expression models, and might explain the often weak Annexin A11 stress granule signal seen in motor neurons.

Disease-associated disruption of the nucleocytoplasmic ratio of ALS-associated proteins and RBPs is well documented and may be associated with stress inducing events. ALS-associated proteins (TDP-43, FUS, SFPQ, hnRNPA1, hnRNPK) localise to the cytoplasm in response to osmotic stress in iPSC-derived neurons, and some RBPs become more cytoplasmic in response to oxidative (TDP-43) or heat (TDP-43, FUS) stress (Harley & Patani, 2020). The RNA binding capacity of Annexin A11 is not well defined, however its role in binding RBPs has been described (Liao et al., 2019). Additionally, the Annexin A11 low-complexity N-terminal mirrors disordered regions that are frequently present in proteins associated with ALS and other neurodegenerative diseases (March et al., 2016), and these regions are often implicated in phase-separation and RNA binding. The nucleocytoplasmic ratio of Annexin A11 was unchanged in response to sodium arsenite induced stress (Figure 6.12.E) which may be expected as altered nucleocytoplasmic ratio of RBPs does not to appear to be a robust feature of sodium arsenite induced stress specifically (Harley & Patani, 2020). Interestingly, the nucleocytoplasmic ratio of G3BP1 was decreased in response to sodium arsenite treatment (Figure 6.11.A), reiterating that this phenotype is both detectable and present in iPSC-derived motor neurons when assessing appropriate target proteins.

Annexin A11 nucleocytoplasmic ratio was highly variable in all cell lines and across treatment conditions, which was also seen in high-throughput analyses (Figure 4.7), emphasising the fluid nature of Annexin A11 localisation and supporting the notion that Annexin A11 is not fixed to one

cellular compartment in either homeostatic or stressed conditions. Most spot characteristics of Annexin A11 in untreated neurons were not statistically different, including spot fluorescent intensity (Figure 6.12.B) and the number of Annexin A11 spots normalised to neuronal area (Figure 6.12.C). These data are in conjunction with high-throughput analyses of Annexin A11 in unstressed cells, where no discernible differences in Annexin A11 localisation or spot characteristics were identified in motor neurons on day 17 and day 42 of differentiation (Figure 4.7; Appendix Figure 9.13; Appendix Figure 9.15). However, the mean Annexin A11 spot size was increased in *ANXA11* G38R compared to control motor neurons (Figure 6.12.D), indicating that some spot characteristics may not have been recognised in high-throughput analyses. Although increased spot size in this instance cannot be attributed to an aggregation event, altered spot characteristics may be indicative of early altered Annexin A11 self-interaction or processing. An increase in Annexin A11 spot count per DAPI positive nuclei was observed in response to sodium arsenite treatment (Figure 6.12.A), however the same trend was not seen when Annexin A11 spot count was normalised to $\beta$3-Tubulin area (Figure 6.12.C), indicating that further analysis of Annexin A11 response to stress is necessary. Post-mortem analysis of patient tissue revealed large Annexin A11 positive inclusions (Smith et al., 2017; Teyssou et al., 2020), and an increase in Annexin A11 spots in response to sodium arsenite treatment could be indicative of a stress response that is upstream of later aggregation events if recovery after stress is perturbed.

Exposure to cellular stress did not cause alterations in Annexin A11 inclusion to stress granules, which may argue against a stress granule hypothesis for Annexin A11; instead of aberrant stress granules acting as seeding events for aggregate formation, another cellular dysfunction may be the root cause of end-stage aggregation. It may be the case that the neurons assessed here are too immature for alterations in endogenous Annexin A11 localisation to be readily observed, or that higher power magnification would be necessary for identification of subtle changes. Alternatively, assessment of stress granule characteristics in the recovery period after stress exposure might reveal stress granule associated perturbations that are not identified when interrogating neurons

immediately after the stressful event. The recovery of neurons after exposure to stress could not be measured here due to technical and time limitations. Additionally, heat stress has been shown to more accurately mimic ALS pathology compared to drug induced stress, including sodium arsenite treatment, and it may be important in future studies to carefully consider the translation of artificial stressful conditions to disease processes (Verzat et al., 2022). The potential localisation of Annexin A11 to sorbitol induced G3BP1 stress granules also warrants further investigation (Figure 6.5), and whether *ANXA11* mutations cause altered response to osmotic stress in patient derived motor neurons remains to be established.

One noteworthy observation was the apparent increase in $\beta$3-Tubulin across G3BP1 stress granules in sodium arsenite treated neurons (Figure 6.4; Figure 6.6; Figure 6.7; Figure 6.8; Figure 6.9). Literature review does not indicate localisation of microtubule proteins to stress granules, however pan-neuronal markers such as $\beta$3-Tubulin are not often included in representative images. Some evidence exists for a role of microtubules in stress granule formation, namely fusion of small stress granules into large granules via transport of RBPs (Chernov et al., 2009; Fujimura et al., 2009; Ivanov et al., 2003; Loschi et al., 2009), and a role in cancer stress granule biology (Franchini et al., 2019), but direct evidence for inclusion to neuronal stress granules is absent. Interestingly, microtubule associated proteins co-aggregate with TDP-43 via a distinct mechanism compared with TDP-43 aggregation with RBPs, indicating that subsets of aggregates occur in ALS, and some may be associated with microtubule proteins (Watanabe et al., 2020). Additionally, RBP delivery to stress granules could result in increased signal from $\beta$3-Tubulin across the surface of granules rather than from within. Microtubule regulation of stress granules in the context of ALS is not well reported, and it would be interesting to investigate this further as both stress granule and microtubule dysfunction are implicated in ALS/FTD.

### *6.4.2 RNA trafficking in ANXA11 ALS*

Axonal transport is predominantly mediated by motor proteins that bind to and move along microtubule subunits, transporting cargos that are bound at the opposite end of the transport machinery. Kinesins are responsible for moving cargos in the anterograde direction, and dyneins and dynactin mediate retrograde transport. Axonal transport is perturbed in ALS, and mutations have been identified in genes mediating transport machinery including the motor protein subunit KIF5A (Baron et al., 2022; Faruq et al., 2019; Nicolas et al., 2018). ALS associated mutations have also been identified in the microtubule protein *TUBA4A* (Pensato et al., 2015; Smith et al., 2014), and are associated with trafficking defects (Buscaglia et al., 2020).

Evidence for the role of Annexin A11 in axonal transport is predominantly RBP-lysosome tethering mediated transport (Liao et al., 2019), and detailed exploration of the consequences of such transport are likely underway. This function of Annexin A11 is intriguing as it is potentially neuron specific, and so could help explain targeted motor neuron degeneration in *ANXA11* ALS. To investigate axonal transport in *ANXA11* ALS patient-derived motor neurons, a broad measurement of RNA transport was completed to assess global movement of RNA species in the anterograde and retrograde directions.

Global RNA transport was measured in motor neurons in microfluidic devices and average velocity of RNA granules was calculated. In all control and *ANXA11mut* motor neurons there was an increase in retrograde compared to anterograde transport (Table 6.1, Figure 6.14). An analysis of axonal transport deficits across neurodegenerative diseases found that regardless of the cause of transport defects, the main central impairment is a disrupted ratio between retrograde and anterograde transport (Mitchell et al., 2012). However, this ratio fluctuated independently of disease status in the parameters included here (Table 6.1, Figure 6.14). The microfluidics paradigm used here did not include any supporting cell types at the distal axon side of the microfluidic chambers, and it would

be interesting to evaluate whether predominantly retrograde mRNA transport is observed as a consequence of reduced input at the distal axon.

The total number of moving particles could not be measured here as in many instances it was clear that multiple axons were growing through microfluidic microgrooves, and in others only one or two. It was not possible to measure the total number of neurites per microgroove, hence the number of moving particles could not be normalised in this way. The use of SYTO™ RNASelect™ to measure RNA transport resulted in an extremely high signal from axons, due to the global staining and high abundance of RNA in axons. This meant that quantification of every particle was impossible, and equally meant that measurement of stationary particles was rendered unachievable. The comparison of moving vs. stationary RNA particles is an important measurement in the assessment of disease associated changes to RNA transport, and so it is unfortunate that this could not be reliably measured in the current dataset. Efforts were made to increase magnification and resolution, however this led to bleaching of the SYTO™ RNASelect™ dye. Further, quantification of individual particle dynamics using particle trafficking functions in image analysis software was attempted, but the abundant signal and often low signal-to-noise ratio of small particles meant that the results from such analysis were not reliable. In future studies, bleaching could be utilised to remove the signal from neurite regions prior to recording, so that RNA particles entering the field of view post bleaching could be specifically measured. This was beyond the scope of this project but might enhance detection of moving particles in future analysis.

Measurement of RNA transport characteristics in motor neurons indicates that ALS-associated mutations in *ANXA11* result in increased mean RNA particle velocity. In both anterograde and retrograde transport groups, there is an increase in the number of statistically significant differences between control and *ANXA11mut* cell line parings compared to control vs. control and *ANXA11mut* vs. *ANXA11mut* (Figure 6.15). In all instances of statistical significance between a control line and an *ANXA11mut* line, RNA particle velocity is increased in the *ANXA11mut* line compared to the control. The increased velocity of RNA transport in *ANXA11mut* lines may seem counter-intuitive, as multiple

studies have shown axonal transport to be perturbed in ALS (Akiyama et al., 2019; Alami et al., 2014; Mehta et al., 2021; Sleigh et al., 2020). Data on the effect of *ANXA11* mutations on RNA transport has focused on association with lysosomes and RNPs, rather than direct measurement of transport velocity. Quantification of *CAPRIN1* positive RNA granule transport in zebrafish expressing fluorescently labelled *CAPRIN1*, Annexin A11, and lysosomes showed a reduced number of moving *CAPRIN1* positive vesicles in D40G and R235Q *ANXA11* overexpressing axons vs. WT. Analysis of *CAPRIN1* RNA granule velocity showed no difference between axons expressing WT or mutant *ANAX11*. However, both WT and D40G *ANXA11* overexpression were associated with significantly faster retrograde *CAPRIN1* RNA transport compared to untransfected axons (Liao et al., 2019). Other than this, no measurement of RNA transport velocity in *ANXA11* ALS has been reported.

Although it remains to be explored, one explanation might be that a reduction in Annexin A11 mediated transport results in an increased average RNA transport velocity. Multiple mechanisms for RNA transport exist, each with specific cargos. Annexin A11 associated transport involves a large cargo consisting of a membrane-bound vesicle, Annexin A11 tether, and RNP likely containing multiple RBPS. Direct interaction of transport machinery with RBPs, which occurs in the case of mRNA bound SFPQ and KIF5A (Fukuda et al., 2021), for example, may be less cumbersome compared with Annexin A11 mediated RNA transport. It might therefore be logical that reduced slow transport leads to an unexpected increase in overall RNA transport velocity. As different mechanisms are involved in separate branches of transport control, it may be necessary to separate transport for analyses, for example into fast and slow axonal transport categories, to identify any reduction in Annexin A11 mediated transport. It should be noted that RNA species that are mediated by Annexin A11 tethering account for a small percentage of overall transport (Liao et al., 2019) which may suggest that reduced Annexin A11 function would not be sufficient to present as an overall increase in RNA transport velocity. Alternatively, the reduced distal axon growth observed in microfluidic experiments (Figure 5.8) indicates that distal axons are abnormal in *ANXA11mut* lines: Increased retrograde transport velocity could indicate an upregulated signalling pathway that is relaying

distress signals to the nucleus and soma, or increased transport of faulty cargo for degradation. This is speculative and it would be necessary to explore these hypotheses further to understand the true impact of *ANXA11* mutations on RNA transport. Live imaging of RNA and fluorescently tagged endogenous *ANXA11* would be useful for visualisation of RNA that is co-trafficking with Annexin A11 specifically. Further, identification of which RNA species are associated with Annexin A11 mediated transport by proximity assay, and targeted transport assays such as RNA beacons would reveal whether certain RNA is vulnerable to Annexin A11 transport defects. The selective loss of motor neurons in ALS hint that dysregulation is not global, and so the identification of motor neuron specific RNA might shed light on why these cells are affected in disease, and might present a target for therapeutic intervention.

Individual particle velocities were calculated by KymographDirect based on tracing lines in kymographs. Therefore, average velocity of particles does not give an indication of whether particles tend to fluctuate in velocity, as each velocity measurement is the average velocity for that line trace. The standard deviation of each individual particle velocity gives a measure of velocity fluctuation for individual particles, however kymographs were not drawn over vertical sections of traces (i.e. stationary particles), and so measurements represent velocity only when particles are moving, and do not consider whether particles are pausing. In cases where RNA granules were moving, paused, and moved again, individual velocity readings were taken for each period of movement. The data shown here therefore focus on the function of transport machinery when in motion. Insight into the intricacies of transport such as the amount of time particles pause vs. time spent moving, and the number of times particles pause during transport through the axon, could be important in elucidating the consequences of *ANXA11* mutations. As RNPs bind to lysosomes that are being transported by Annexin A11 tethering (Liao et al., 2019) it is possible that mutations in *ANXA11* result in perturbed interaction between Annexin A11 and RNPs or lysosomes, which could manifest as altered cargo dissociation and pausing characteristics.

Although differences in RNA velocity were observed in transport analyses, this has not been directly associated with the function of Annexin A11 as a lysosome-RBP tether. In motor neurons that were included in local translation analysis, which is discussed in the next section, vesicular Lamp1 positive structures were seen in the soma of control motor neurons (Figure 6.16). A staining pattern was observed whereby a bright point of Annexin A11 was present at the edge of some Lamp1 positive vesicles, which was originally observed in work detailing the tethering function of Annexin A11 (Liao et al., 2019) (Appendix Figure 9.30). This is an important observation as it indicates that a similar interaction is occurring in iPSC-derived motor neurons. Lamp1 vesicle-like structures are not observed in neurites (Figure 6.16), which is consistent with other instances of neuronal characterisation of Lamp1 structures (Cheng et al., 2018). The specific function of Annexin A11 in RNA transport in motor neurons remains to be fully established, however the results presented here support the hypothesis *ANXA11* ALS is associated with RNA transport.

### *6.4.3 Protein translation and Annexin A11*

Localised protein translation is an essential function of neurons, whose long axons need to be reactive to local signals, and the ability of neurons to translate proteins quickly and locally accounts for neuronal plasticity. Annexin A11 was shown to localise to puromycin spots in ribopuromycylation experiments (Figure 6.17), suggesting it may have a role in local translation in motor neurons. Global translation was reduced in patient fibroblasts harbouring *ANXA11* G38R, H390P, or R456H mutations, however was unaffected when *ANXA11* was knocked down by siRNA in HeLa cells (Nahm et al., 2020), indicating that there may be a gain of function associated with *ANXA11* mutations and repressed translation.

To explore whether Annexin A11 is associated with other proteins of interest at sites of local translation in axons, motor neurons were subject to immunocytochemistry co-labelling targeting Annexin A11 and a panel of proteins in the context of ribopuromycylation (Figure 6.19; Figure 6.20; Figure 6.21; Figure 6.22; Table 6.2). Proteins whose fluorescent intensity correlated with that of

Annexin A11 at sites of local translation included FUS, S6, G3BP1, and snRNP70. Correlation of Annexin A11 and S6 further implicates Annexin A11 in local translation as it indicates an increase of Annexin A11 to sites of translation with increased ribosomal signal. The presence of multiple data points with very low Annexin A11 fluorescent intensities (<100 a.u.) and corresponding S6 signals of >100 a.u indicate that many translational hotspots that are positive for S6 do not include Annexin A11, indicating a diverse population of translational spots with Annexin A11 included in a subset. Additionally, in Pearson's coefficient, the *r* value for correlation between Annexin A11 and S6 was higher than any other significant correlation, and at 0.8035 indicated an extremely strong correlation between Annexin A11 and S6 at sites of translation (Table 6.2).

It should be noted that only one biological repeat was included for snRNP70 in ribopuromycylation analysis, and it would be necessary to repeat this experiment before drawing conclusions from correlation of Annexin A11 and snRNP70 at translational hotspots. snRNP70 is a small ribonucleoprotein subunit of the U1 major spliceosome. FUS has been shown to regulate snRNP70 transcript and protein abundance (Nakaya, 2020), and snRNP70 protein is enriched in protein fractions that immunoprecipitate with ALS associated FUS, EWSR1, and TAF15 (Chi et al., 2018). With particular relevance to the present ribopuromycylation analysis is evidence that snRNP70 localises to RNA-associated granules in zebrafish axons: snRNP70 regulates motor axon growth, generation of NMJs, and acetylcholine receptor clustering, with an additional role in the regulation of splice isoforms at axonal locations (Nikolaou et al., 2020). This work is yet to be peer-reviewed, however is interesting in the context of axonal functions of snRNP70. Recent data indicate that alternative *snRNP70* RNA splicing events are associated with a subtype of ALS (Nakaya, 2022), and that U7 snRNP is required for NMJ integrity (Tisdale, 2022). These studies, alongside potential correlation between Annexin A11 and snRNP70 at sites of translation, suggest that this relatively underexplored gene/protein should be further investigated in the context of ALS and in *ANXA11* ALS specifically.

A weak correlation was identified between Annexin A11 and G3BP1 at translation hotspots (Figure 6.22; Table 6.2). G3BP1 is well characterised as a stress granule protein, and sequestration of mRNA

by RBPs can inhibit their translation. Axonal regrowth after axotomy is mediated by G3BP1 as it sequesters mRNA into stress granule-like structures which dissociate as G3BP1 becomes phosphorylated, and overexpression of dominant negative G3BP protein increases axonal mRNA translation and axonal regrowth, highlighting negative translational control by G3BP1 (Sahoo et al., 2018). G3BP1 has additional roles in ribosomal quality control and turnover by prevention of ribosomal degradation (Meyer et al., 2020), and mediation of mRNA degradation (Fischer et al., 2020), emphasising the diverse functions of G3BP1 as a regulator of RNA biology. In stress granule analysis, the localisation of Annexin A11 to G3BP1 positive granules was unchanged across *ANXA11mut* and control groups (Figure 6.11), however indicated that there is overlap of Annexin A11 and G3BP1 granules. The apparent correlation of Annexin A11 with G3BP1 at sites of local translation is an important target for future validation and may have broad implications for ALS pathology as G3BP1 stress granules have been assessed in the context of multiple ALS associated mutations.

Correlation between Annexin A11 and FUS was highly significant in ribopuromycylation analysis (Figure 6.22; Table 6.2), and the role of FUS in localised translation has been acknowledged since at least 2013 (Yasuda et al., 2013). ALS associated mutations in FUS reduce axonal protein synthesis which is associated with reduced expression of ion channels and transporters, leading to altered synaptic function in the absence of cytoplasmic aggregation or nuclear loss of FUS (López-Erauskin et al., 2018). The same study found that mutant FUS accumulation causes axon specific stress granule formation which reduces the rate of local translation. This may have implications for the stress granule analysis reported here (6.3.1): In addition to assessing stress granules in the soma, it may be essential to assess axonal stress granules, which was not included here. Mutations in FUS lead to improper phase-separation propensity and reduced solubility, causing RNP granule dysfunction which impairs protein synthesis at axon terminals (Murakami et al., 2015). Mutant FUS further affects phase-separation of FMRP resulting in translational repression of FMRP bound mRNA (Birsa et al., 2021). Proteomic analysis of FUS aggregates collected from N2a overexpression models of

mutant *FUS* revealed sequestration of proteins involved in translation (Kamelgarn et al., 2018). Interestingly multiple importins and exportins were also found to be sequestered in this analysis, as were Annexins A2, A5, and A6, but not Annexin A11. Reduced transcription of genes associated with translation and ribosomal localisation and biogenesis were identified in actinomycin D treated *FUSΔNLS* mice compared to WT *FUS* mice (Sahadevan et al., 2021), suggesting that the effect of FUS on translation is multi layered, through affecting transcription of translation-mediating genes and by direct interaction with translation machinery. Mutant FUS mediated repression of translation and the importance of localised stress granules in this process, in addition to direct interaction of Annexin A11 and FUS (Nahm et al., 2020), are intriguing in the context of Annexin A11 correlation with both FUS and G3BP1 at sites of translation.

Proteins selected for ribopuromycylation experiments that did not appear to correlate with Annexin A11 include Lamp1, Rab7, TDP-43, FMRP, and ChAT (Figure 6.22). As with snRNP70, only one experimental repeat was completed for TDP-43 and so results should be interoperated with caution, and multiple lines of evidence for TDP-43 function in local translation exist (Altman et al., 2021; Briese et al., 2020; Chu et al., 2019; Coyne et al., 2015; Gao et al., 2021; Lehmkuhl et al., 2021; Majumder et al., 2016). In addition to a role in local protein synthesis, overexpression of ΔNLS cytoplasmic TDP-43 leads to reduced global protein synthesis (Charif et al., 2020), indicating that pathology might not be restricted to specific cellular regions.

FMRP has a well characterised role in local translation (Brackett et al., 2013; Brown et al., 2001; Chen et al., 2014; Chu et al., 2019; Coyne et al., 2015; Miyashiro et al., 2003), including through interactions with TDP-43 (Majumder et al., 2016) and FUS (Birsa et al., 2021). FMRP has been recently implicated in ALS and FMRP aggregates are detected in lumbar motor neurons in both fALS and sALS (Freischmidt et al., 2021). The role of FMRP in the context of Annexin A11 local translation should not be disregarded despite the lack of evidence in correlation analyses, particularly as subsequent western blot data using the same FMRP antibody resulted in extremely weak protein detection (Appendix Figure 9.31), indicating that the results from FMRP ribopuromycylation experiments may

be unreliable. Additionally, due to limited antibody species availability, the Annexin A11 antibody used in co-stain with FMRP was different to other experiments, and the characterisation of this antibody is less well documented compared with the Annexin A11 antibody that was used throughout the rest of this thesis.

One caveat of puromycin based techniques is that identification of proteins at translational sites could indicate involvement of these proteins in the process of translation, or that said proteins are being translated locally and therefore overlap with the signal from translational machinery. It will be necessary to distinguish these events in future analyses, and ChAT was in part included to explore whether Annexin A11 is associated with translational spots where ChAT was being locally produced, as there is no indication in the literature that ChAT has a role in local translation. A fluorescent signal from ChAT was observed in some puromycin spots which suggests that ChAT is locally translated, however this did not correlate with the Annexin A11 signal. Despite this, ChAT was an interesting target to investigate as it could be hypothesised that Annexin A11 is involved with the protein turnover of motor neuron-specific proteins. Subtypes of cholinergic neurons exist in addition to motor neurons, and so global analysis of protein abundance in axons, for example by mass-spectrometry, might present better targets for investigating specific proteins affected by local translation in distal axons in ALS.

The function of Annexin A11 as a tether between RBPs and membrane-bound vesicles, namely Lamp1 positive lysosomes, has a proven role in RNP axonal transport (Liao et al., 2019), and local protein translation occurs at Rab7 endosomes (Cioni et al., 2019). It is an attractive proposition that Annexin A11 has a function in stabilising protein translation at the surface of membrane-bound vesicles by facilitating interaction between endosomes and RNPs containing translating mRNA. In ribopuromycylation analysis no correlation was detected between Annexin A11 and either Lamp1 or Rab7. It is probable that many subsets of translational points exist, and that groups of mRNAs are mediated by sometimes disparate groups of translational mediators; it may be the case that late endosome-mediated neuronal translation is separate from Annexin A11 function. Evidence for Rab7

vesicle-mediated translation comes from retinal ganglion cells, so it could be suggested that this is a neuron subtype-specific function, however Rab7 was detected in puromycin spots in iPSC-derived motor neurons (Figure 6.18; Figure 6.20). Alternatively, it may be true that the ribopuromycylation technique implemented here is not sensitive enough to accurately quantify small but functionally significant interactions. Indeed, although Lamp1 vesicles were shown to co-transport with G3BP1 more so than other organelles, Lamp1 vesicles co-localised with <30% of G3BP1 granules and co-transported with only ~5% (Liao et al., 2019), and so broad analysis of a large number of translational spots might dilute the signal from similar interactions. Further, lack of correlation does not negate the localisation of Annexin A11 and other proteins to the same ribopuromycylation labelled spots; instead strengthens the prioritisation of those that do correlate. The involvement of Rab7- and Lamp1-positive vesicles in Annexin A11 function remain to be fully elucidated and represent an important avenue for further investigation. The observation that Lamp1 is inconsistent in the soma and proximal neurites suggests that Lamp1-positive species are diverse (Figure 6.16), and it may be useful to create a distinction between these structures in future analysis of the role Lamp1 might play in axonal transport and local translation.

Correlation of target proteins was completed in neuronal cultures on coverslips and so diverse axonal and dendritic regions are likely included in images; further analysis in specific compartments such as distal axons might reveal more subtle local translation characteristics. As thresholding puromycin spots was implemented to identify translation hotspots, it may be the case that functionally relevant protein interactions, where proteins are adjacent but not directly overlapping, will be missed. In representative traces demonstrating Annexin A11 and FUS localisation to the same translation hotspots in distal neurons, Annexin A11 and FUS appear to be side-by-side within the region defined by puromycin in some cases (Figure 6.24). Such microscopic features of protein localisation might be better defined with alternative super resolution systems, and subtle localisation characteristics may be better visualised and quantified with 3D image analysis: Although this was initially included in this project, thresholding in image analysis software for 3D quantification was insufficiently sensitive

compared with thresholding in 2D analysis, and time limitations meant that further optimisation of 3D analysis could not be achieved.

Three control and three *ANXA11mut* cell lines were cultured in microfluidic devices so that local translation could be assessed at the distal axon. Perturbed neurite outgrowth in distal axons indicates a region-specific vulnerability (Figure 5.8), so analysis of localised translation here may be more informative. Motor neurons were subject to ribopuromycylation and co-labelled for puromycin, Annexin A11, and FUS. Correlation analysis of Annexin A11 and FUS at sites of local translation revealed sustained correlation across all control and *ANXA11mut* motor neurons, which was slightly reduced in significance in *ANXA11* D40G (Figure 6.24). Pearson's correlation results are included in Table 6.3 with *r* values indicating a stronger correlation between control 1 and control 2 compared to other cell lines, which can be visualised more readily in Figure 6.22. This trend was not observed in control 4, highlighting individual differences in iPSC lines and indicating that further analysis will be necessary to fully characterise whether the correlation of Annexin A11 and FUS at sites of local translation is associated with *ANXA11* ALS.

The fluorescent intensity of Annexin A11 and FUS at sites of translation were separately measured and subject to Kruskal-Wallis one-way analysis with Dunn's multiple comparisons test (Figure 6.26). Significant differences in fluorescent signal were detected between most cell lines, however where control and *ANXA11mut* lines were significantly different, Annexin A11 signal was consistently increased in *ANXA11mut* lines. Conversely, where significant differences were detected in FUS signal, this was reduced in *ANXA11mut* lines compared to control, with the exception of control 2 and *ANXA11* D40G, where FUS signal was higher in the ALS line. Collectively these data indicate that mutations in *ANXA11* impact the localisation of Annexin A11 and FUS to sites of translation in distal neurons. Direct interaction of Annexin A11 and FUS has been demonstrated (Nahm et al., 2020) however has not been reported in the context of *ANXA11* mutations. Whether altered interaction between these proteins is associated with altered localisation to sites of translation would be an important step in understanding the role of Annexin A11 and FUS in local translation. As differences

were also detected between control vs. control and *ANXA11mut* vs. *ANXA11mut* it is apparent that fluctuations in intensities are not only disease specific, however the sustained direction of significance (i.e. reduced or increased signal intensity) in control vs. *ANXA11mut* pairings suggests a disease specific event.

The function of Annexin A11 at sites of translation remains to be elucidated, however an increase in localisation could be a compensatory mechanism for reduced function, or as a consequence of altered interaction with binding partners. As discussed above, the role of FUS in local translation is better established, and in the context of ALS, mutant FUS is most often associated with translational repression. Reduced FUS signal at sites of local translation in *ANXA11mut* motor neurons could have similar consequences, and reduced distal axon outgrowth (Figure 5.8) may be associated with impaired translation as a result of reduced FUS localisation to translational spots. If the direct interaction between Annexin A11 and FUS has a role in local translation and is affected by mutations in *ANXA11,* this could result in reduced FUS at sites of translation, and upregulation of Annexin A11 at these sites may be compensatory as the neurons cope with perturbed protein turnover. These preliminary data are in no way sufficient to support these hypotheses, but justify further investigation into the role of Annexin A11 and FUS in local translation. In addition, it will be important to determine whether Annexin A11 and FUS are altered in distal axons without drug treatment, as it may be the case the altered protein abundance is not only associated with sites of local translation but is dysregulated under normal conditions. The total abundance was not measured in the current dataset as without a neuronal marker, signal from target proteins could not be normalised, and it could be misleading to measure fluorescent intensity without normalisation, particularly as the density of axons in images was variable (Figure 6.27). The relative abundance of FUS and Annexin A11 protein was unchanged between control and *ANXA11mut* motor neurons in western blot analysis (Figure 4.9; Figure 6.32), and it would be informative to measure this in axons specifically. Both proteins are abundant in the nucleus and it is likely that a large proportion of signal from total protein extracts represents non-axonal protein.

The number of translational hotspots in control and *ANXA11mut* distal axons was measured by normalising the number of puromycin spots to neurite length. Puromycin spots were detected by thresholding as described, and neurites were measured by tracing neurites with the measure tool in Fiji. No pan-neuronal marker was included due to experimental limitations. It will be important to repeat this experiment with more thorough measurement parameters so that data can be more accurately normalised, for example by neurite volume. Neurite length was utilised to achieve a crude preliminary measure of the number of translational spots in distal axons, and revealed an increase in *ANXA11* G38R compared to control 1 and *ANXA11* R235Q (Figure 6.27). An increase in translational spots could indicate an attempt to upregulate the turnover of new proteins if distal neurites are dysfunctional. Although no significant difference was detected between *ANXA11* D40G or *ANXA11* R235Q and control lines, graphical representation of densities highlight a trend toward increased puromycin spot density in *ANXA11* D40G and reduced density in *ANXA11* R235Q compared to controls, and it is noteworthy that mutations residing in different functional domains could have opposing effects on local translation. *ANXA11* R235Q resides in the phospholipid binding domain and interferes with membrane binding including to Lamp1 vesicles (Liao et al., 2019). On the other hand, *ANXA11* G38R and D40G sit in the low-complexity domain which is associated with phase-separation and interaction with RBPs and other proteins. It could be postulated that if Annexin A11 does have a role in stabilising interactions in local translation, that a reduced interaction with membranes (R235Q) could diminish the number of these focal points, whereas reduced interaction with RBPs (G38R, D40G), and therefore reduced availability of RNA for translation, could result in upregulation of these sites. Both scenarios could be associated with an overall reduction in local protein translation. The reduced neurite outgrowth phenotype was observed consistently for *ANXA11* G38R and D40G. However, it was only present in 1 out of 3 biological repeats for *ANXA11* R235Q, suggesting that local translation abnormalities could be mutation-specific if they are indeed associated with perturbed distal axon growth (Figure 5.8). Despite comparable numbers of images being included for analysis, axon density per image was inconsistent meaning that the total neurite length measured per cell line was uneven. The total neurite length measured per cell line is included

in Figure 6.27 to demonstrate this. To more thoroughly measure the number of translational spots in axons at different distances from the soma, alternative microfluidic devices could be utilised whereby microgrooves are directly adjacent to the cell body compartment, allowing a direct measure of axon length. Such experiments in iPSC-derived motor neurons revealed an increase in the relative number of puromycin spots in long axons compared to short axons, and importantly showed that TDP-43 and FUS are differentially dispersed throughout axons depending on whether axons are long or short, which could have implications for translational hotspots assessed here (Hagemann et al., 2022).

Although puromycin has been historically used in the interrogation of translation (Aviner, 2020) there is some evidence that even with the inclusion of elongation inhibitors, nascent peptides diffuse prior to fixation, and detection of puromycin spots may not specifically represent translational hotspots in every instance (Enam et al., 2020; Hobson et al., 2020). Additionally, the use of puromycin in SUnSET assays which measure the rate of protein synthesis (Schmidt et al., 2009) has been subsequently shown to be unreliable when assessing protein synthesis in energy-starved cells (Marciano et al., 2018), highlighting that specific cellular conditions might be necessary for accurate interpretation of puromycin based experiments. Alternative methods for translation analysis include live translational reporters (Biswas et al., 2019), however these often rely on overexpression and fluorescent tags which can introduce additional variability. Another caveat with the interrogation of puromycin spots is that delineating whether co-localised proteins constitute part of the translational machinery or are themselves being translated is unclear. It will be necessary to complete further experiments to elucidate whether alterations in Annexin A11 and FUS abundance at translational spots are a consequence of increased and reduced translation of these proteins, respectively, or whether the observed fluctuations are associated with altered function of these proteins at translational sites.

As with any antibody-based technique, validation of specific protein detection is paramount for producing reliable data. As discussed in 4.4.3, the Annexin A11 antibody used here has been well

characterised. The FUS antibody utilised in ribopuromycylation analysis was included in broad characterisation of FUS antibodies (Alshafie et al., 2021), and was shown to have good specificity in immunocytochemistry in HEK293 cells, with some unspecific banding in western blot detection of FUS. Some unspecific bands were also detected by western blot in iPSC motor neuron protein, however were easily excluded from quantification (Appendix Figure 9.32). Due to antibody species availability, the TDP-43 antibody used here differed from that used in Chapter 4. This and some other antibodies included in ribopuromycylation analysis here are less well characterised, and selection was based on use in literature and observation of expected cellular localisation. It was beyond the scope of this project to include thorough characterisation of all antibodies, and it is essential to acknowledge that antibody specificity can impact experimental readout. As previously discussed, the FMRP antibody was shown to be unreliable in western blot analysis (Appendix Figure 9.31), and the results from ribopuromycylation experiments with this antibody may be unreliable.

Global translation was unaffected in motor neurons (Figure 6.29; Figure 6.30; Figure 6.31), however mutations in *ANXA11* were shown to reduce global protein synthesis in patient fibroblasts with SUnSET assay (Nahm et al., 2020). More sensitive techniques such as SUnSET (Schmidt et al., 2009) or optimised AHA assays might reveal translation phenotypes that are missed with global puromycin labelling. Despite this, apparent alterations at sites of local synthesis hint toward an axon-specific dysfunction, and it may be the case that global translation deficiencies seen in fibroblasts do not persist in neurons.

Together these data constitute preliminary evidence that Annexin A11 has a role in local translation in motor neurons. Further, Annexin A11 is associated with FUS in local translation, which may be affected in *ANXA11mut* distal axons. Additional validation will be necessary to confirm the functional role of Annexin A11 in translation, and the co-function of Annexin A11 with FUS, G3BP1, and snRNP70 at sites of axonal translation should be explored.

# Chapter 7 General discussion

## *7.1 Motor neuron pathology in ANXA11 associated ALS*

As with many ALS associated genes, *ANXA11* ALS represents a small percentage of the total ALS population. *ANXA11* ALS patients present with a mixed clinical phenotype, with variable site and age of onset as well as disease duration (Smith et al., 2017). The identification of neuronal phenotypes across multiple instances of ALS is useful for the prioritisation of therapeutic discovery, and, as discussed in 1.6, categorisation of genes into functional groups might be useful for patient stratification. The data presented here serve as preliminary characterisation of neuronal phenotypes in *ANXA11* ALS, and lead to generation of hypotheses for future investigation into the consequences of novel mutations.

The aim of this thesis was to explore the neuronal phenotypes associated with ALS-causative mutations in *ANXA11*. To achieve this, iPSC lines derived from *ANXA11* ALS patients were generated and characterised, and motor neuron-astrocyte co-culture was optimised to enable the exploration of *ANXA11* phenotypes in disease relevant cells (Chapter 3). Initial characterisation of motor neurons included high-throughput analysis of Annexin A11, TDP-43, and pTDP-43, revealing that ALS associated protein characteristics are dependent on cell culture dynamics, including culture maturity and the presence of astrocytes (Chapter 4). Some modest alterations were detected between control and *ANXA11mut* neurons, however the characterisation of broad protein localisation and abundance in motor neurons indicated that striking alterations in the subcellular localisation of the interrogated proteins is not an early feature of *ANXA11* ALS. The absence of broad changes in protein localisation is perhaps unsurprising in immature iPSC-derived motor neurons, and in the context of additional phenotypes indicates that Annexin A11 and TDP-43 mislocalisation or aggregation are downstream of cellular perturbation. As is common across multiple forms of ALS, protein inclusions detected at

disease end stage implicate pathological protein aggregation in neuronal death, and in the case of *ANXA11* mutations these may be a consequence of dysregulated calcium or RNA processing.

In summary of the predominant cellular phenotypes identified in this body of work; initial neurite outgrowth was unaffected in motor neurons but was perturbed in distal axons of *ANXA11mut* motor neurons grown in microfluidic devices (5.3.1). Motor neuron-astrocyte co-cultures displayed spontaneous calcium fluctuations, which appeared to be increased in *ANXA11* G38R and R235Q motor neurons compared to control (5.3.2). Annexin A11 was shown to sometimes localise to stress granules, and induction of stress granules was perturbed in *ANXA11* R235Q motor neurons (6.3.1). Global RNA transport velocity was increased in *ANXA11mut* neurons compared to control in both the anterograde and retrograde direction (6.3.2). Annexin A11 localised to focal points of local translation and correlated with FUS at these sites. Correlation between Annexin A11 and FUS may be affected in distal axons in patient derived neurons, and the amount of Annexin A11 and FUS at sites of local translation was altered in motor neurons harbouring *ANXA11* mutations (6.3.3). This somewhat broad phenotyping of newly derived *ANXA11mut* iPSC lines has implicated various cellular pathways in pathology, and how these neuronal phenotypes overlap with one another give rise to a multifactorial hypothesis for the consequences of *ANXA11* mutations.

Evidence that altered calcium signalling is associated with local translation is intriguing and highlights how these cellular processes are intrinsically linked. Comparison of humanised mutant *FUS* and humanised WT *FUS* mice revealed reduction in the expression of ion channels and transporter proteins necessary for synaptic function (López-Erauskin et al., 2018). This was associated with repressed intra-axonal translation and resulted in reduced synaptic activity. No direct measure of synaptic activity was included in this thesis; however, this demonstrates that potentially altered calcium fluctuation phenotypes could be associated with altered expression levels of ion channels or other proteins that mediate calcium activity. A similar phenotype was identified in *C9ORF72* iPSC derived neurons, which revealed hyperexcitability in young motor neurons associated with upregulation of synaptic transcripts, which transitioned to hypoexcitability and reduced synaptic

transcripts in matured neurons (Sommer et al., 2022). This reflects calcium activity of *ANXA11* G38R and R235Q motor neurons, which displayed increased spontaneous calcium fluctuations compared to control (Figure 5.14). These data suggest a common phenotype whereby calcium homeostasis and expression of proteins associated with neuronal activity collectively contribute to disease characteristics in ALS. Future work should assess the hypothesis that altered calcium fluctuations in *ANXA11* ALS motor neurons are related to altered translation of proteins associated with neuronal activity, including synaptic proteins. Additionally, calcium has a role in mediating local translation (Mofatteh, 2020), indicating a bi-directional relationship that could be hypothesised to contribute to a continuous exacerbation of neuronal dysfunction as dysregulated calcium affects protein translation, which affects calcium homeostasis, and so on.

Local translation is reliant on transport of RNA from the nucleus to dendrites and axons, and it might be unsurprising that these processes are together implicated in disease. This is particularly relevant if proteins mediating the transport of RNA are also involved in local translation, as is that case for TDP-43 (Alami et al., 2014; Chu et al., 2019; Gao et al., 2021; Majumder et al., 2016) and FUS (Akiyama et al., 2019; Birsa et al., 2021; Imperatore et al., 2020; López-Erauskin et al., 2018). Although these functions remain to be fully elucidated for Annexin A11, its role in RNA transport has been described (Liao et al., 2019), and preliminary data indicate an additional role in local protein synthesis (6.3.3). An apparent increase in RNA axonal transport velocity is intriguing as it is not in conjunction with studies indicating perturbed axonal transport in ALS (Buscaglia et al., 2020; Clark et al., 2016; Gibbs et al., 2018; Ikenaka et al., 2013; Mehta et al., 2021; Sleigh et al., 2020). It should be noted than in many of these reported cases of axonal transport defects, disease associated perturbations include measures other than velocity, such as altered cargo pausing or relative number of moving cargos, and include a range of cargos such as mitochondria and vesicles: It will be informative to assess these transport dynamics in the context of *ANXA11* mutations.

Liquid-liquid phase-separation of proteins involved in ALS pathology is implicated in many dysfunctional pathways, including those assessed here: RNA transport (Wiedner & Giudice, 2021),

local translation (Gao et al., 2021), protein aggregation (Babinchak & Surewicz, 2020), and stress granule dynamics (Banani et al., 2017; Shin & Brangwynne, 2017) are reliant on phase-separation of proteins. The N-terminal of Annexin A11 is disordered and has been shown to phase-separate, and *ANXA11* mutations result in the formation of fibrous droplets that differ from the WT species (Liao et al., 2019). Some recent lines of evidence indicate a role of calcium in regulation of protein phase-separation (Huang et al., 2022; Mayfield et al., 2021), suggesting that dysregulated calcium homeostasis might influence the wide-range of phase-separation-dependent protein functions, however this remains to be established for ALS-associated proteins in neurons. Further, loss of the stress granule protein G3BP1 can result in abnormal calcium homeostasis (Martin et al., 2013). The reduction in G3BP1 stress granule formation in *ANXA11* R235Q motor neurons (Figure 6.11), occasional localisation of Annexin A11 to G3BP1 stress granules (6.3.1), and the potential co-localisation of Annexin A11 and G3BP1 at sites of local translation (Table 6.2) warrant further investigation into how these processes are linked in disease. In addition, Annexin A11 binding to phospholipids is mediated by calcium and Annexin A11 interaction with RBPs is calcium dependent (Nahm et al., 2020): Calcium dysregulation may have broad consequences for the function of both the phase-separating and phospholipid-binding functions of Annexin A11.

## *7.2 The use of induced pluripotent stem cells in neurodegenerative research*

Increasingly, the inclusion of iPSC-derived neurons in ALS research is considered necessary to measure dysfunction in human derived cells. Their position in modelling specialised cell types affected in disease means they are essential for understanding neuron specific and non-cell-autonomous functions. Evidence of neuronal and glial perturbations collected from iPSC-derived models are referenced throughout this thesis and have vastly benefited the understanding of pathology. The variability often seen with these models is evidenced here, and it will be necessary in future studies to improve the technology to increase reproducibility of data. Increasing complexity in the systems that can be produced with iPSCs, such as high-order co-cultures and organoids, might

increase such variability as more diverse cell types are included in cultures. Looking toward the future of iPSC-based research, it would be incredibly informative to include hundreds of cell lines in automated culture and analysis, so that individual cell line characteristics are minimised, and instead population-based cellular phenotyping becomes the norm. As the feasibility of large-scale studies increases, it will be an exciting time for ALS research. An unpublished meta-analysis incorporating multiple published datasets recently highlighted the potential power in analysing large amounts of ALS iPSC-derived neuron data: Combined analysis encompassing data from 429 donors identified alterations in splicing and genomic instability as predominant disease pathways (Ziff et al., 2022). The relatively underexplored utilisation of iPSCs for population studies may accelerate therapeutic targeting in the near future.

Astrocytes were included in cell cultures used throughout this project primarily to improve neuronal longevity and functional maturity, and it was not feasible to also analyse the impact of control vs. *ANXA11mut* astrocytes on neuronal function. Astrocytes affect neuronal function in control and ALS disease models (1.16.1), and neurons and neuronal activity affect astrocyte gene expression (Hasel et al., 2017). Underpinning the influence of astrocytes on the neuronal phenotypes seen here will be important. Additionally, no direct measurements of astrocyte function or characteristics were included, and further analysis of *ANXA11mut* astrocytes will be important, particularly when considering the translational impact of non-cell-autonomous disease mechanisms.

## *7.3 Conclusions and future direction*

The utilisation of *ANXA11* ALS patient-derived iPSCs has shed light on ALS pathology by recognising alterations in axon integrity and calcium dynamics in patient motor neurons, and through preliminary characterisation of Annexin A11 in local translation. The absence of alterations to gross protein localisation, among other cellular characteristics, highlight the necessity of investigation into specific cellular functions in search of targets for therapeutic intervention in ALS. Throughout this work further hypotheses have arisen, and many questions remain to be answered. The strive to find

a cure for ALS is ongoing, and the consideration of this work alongside evidence of overlapping and disparate disease mechanisms will lead to a better understanding of pathology, to the end that viable therapeutics will eventually be developed.

# 8 Bibliography


Aasen, T., Raya, A., Barrero, M. J., Garreta, E., Consiglio, A., Gonzalez, F., Vassena, R., Bilić, J., Pekarik, V., Tiscornia, G., Edel, M., Boué, S., & Belmonte, J. C. I. (2008). Efficient and rapid generation of induced pluripotent stem cells from human keratinocytes. *Nature Biotechnology*, *26*(11), 1276–1284. https://doi.org/10.1038/nbt.1503

Aebersold, M. J., Thompson-Steckel, G., Joutang, A., Schneider, M., Burchert, C., Forró, C., Weydert, S., Han, H., & Vörös, J. (2018). Simple and Inexpensive Paper-Based Astrocyte Co-culture to Improve Survival of Low-Density Neuronal Networks. *Frontiers in Neuroscience*, *12*, 94. https://doi.org/10.3389/fnins.2018.00094

Aikio, M., Wobst, H. J., Odeh, H. M., Lee, B. L., Class, B., Ollerhead, T. A., Mack, K. L., Ford, A. F., Barbieri, E. M., Cupo, R. R., Drake, L. E., Castello, N., Baral, A., Dunlop, J., Gitler, A. D., Javaherian, A., Finkbeiner, S., Brown, D. G., Moss, S. J., … Shorter, J. (2021). Opposing roles of p38α-mediated phosphorylation and arginine methylation in driving TDP-43 proteinopathy. *bioRxiv*. https://doi.org/10.1101/2021.08.04.455154

Akamatsu, M., Yamashita, T., Hirose, N., Teramoto, S., & Kwak, S. (2016). The AMPA receptor antagonist perampanel robustly rescues amyotrophic lateral sclerosis (ALS) pathology in sporadic ALS model mice. *Scientific Reports*, *6*, 28649. https://doi.org/10.1038/srep28649

Akamatsu, M., Yamashita, T., Teramoto, S., Huang, Z., Lynch, J., Toda, T., Niu, L., & Kwak, S. (2022). Testing of the therapeutic efficacy and safety of AMPA receptor RNA aptamers in an ALS mouse model. *Life Science Alliance*, *5*(4). https://doi.org/10.26508/lsa.202101193

Akiyama, T., Suzuki, N., Ishikawa, M., Fujimori, K., Sone, T., Kawada, J., Funayama, R., Fujishima, F., Mitsuzawa, S., Ikeda, K., Ono, H., Shijo, T., Osana, S., Shirota, M., Nakagawa, T., Kitajima, Y., Nishiyama, A., Izumi, R., Morimoto, S., … Aoki, M. (2019). Aberrant axon branching via Fos-B dysregulation in FUS-ALS motor neurons. *EBioMedicine*, *45*, 362–378. https://doi.org/10.1016/j.ebiom.2019.06.013

Aksu-Menges, E., Balci-Hayta, B., Bekircan-Kurt, C. E., Aydinoglu, A. T., Erdem-Ozdamar, S., & Tan, E. (2021). Two distinct skeletal muscle microRNA signatures revealing the complex mechanism of sporadic ALS. *Acta Neurologica Belgica*. https://doi.org/10.1007/s13760-021-01743-w

Al Khleifat, A., Iacoangeli, A., van Vugt, J. J. F. A., Bowles, H., Moisse, M., Zwamborn, R. A. J., van der Spek, R. A. A., Shatunov, A., Cooper-Knock, J., Topp, S., Byrne, R., Gellera, C., López, V., Jones, A. R., Opie-Martin, S., Vural, A., Campos, Y., van Rheenen, W., Kenna, B., … Al-Chalabi, A. (2022). Structural variation analysis of 6,500 whole genome sequences in amyotrophic lateral sclerosis. *Npj Genomic Medicine*, *7*(1), 8. https://doi.org/10.1038/s41525-021-00267-9

Alami, N. H., Smith, R. B., Carrasco, M. A., Williams, L. A., Winborn, C. S., Han, S. S. W., Kiskinis, E., Winborn, B., Freibaum, B. D., Kanagaraj, A., Clare, A. J., Badders, N. M., Bilican, B., Chaum, E., Chandran, S., Shaw, C. E., Eggan, K. C., Maniatis, T., & Taylor, J. P. (2014). Axonal transport of TDP-43 mRNA granules is impaired by ALS-causing mutations. *Neuron*, *81*(3), 536–543. https://doi.org/10.1016/j.neuron.2013.12.018

Al-Chalabi, A., Andersen, P. M., Nilsson, P., Chioza, B., Andersson, J. L., Russ, C., Shaw, C. E., Powell, J. F., & Leigh, P. N. (1999). Deletions of the heavy neurofilament subunit tail in amyotrophic lateral sclerosis. *Human Molecular Genetics*, *8*(2), 157–164. https://doi.org/10.1093/hmg/8.2.157

Al-Chalabi, A., Fang, F., Hanby, M. F., Leigh, P. N., Shaw, C. E., Ye, W., & Rijsdijk, F. (2010). An estimate of amyotrophic lateral sclerosis heritability using twin data. *Journal of Neurology, Neurosurgery, and Psychiatry*, *81*(12), 1324–1326. https://doi.org/10.1136/jnnp.2010.207464

Allen, M. J., Shan, X., Caruccio, P., Froggett, S. J., Moffat, K. G., & Murphey, R. K. (1999). Targeted Expression of Truncated Glued Disrupts Giant Fiber Synapse Formation in Drosophila. *Journal of Neuroscience*, *19*(21), 9374–9384. https://doi.org/10.1523/JNEUROSCI.19-21-09374.1999

Allison, R. L., Adelman, J. W., Abrudan, J., Urrutia, R. A., Zimmermann, M. T., Mathison, A. J., & Ebert, A. D. (2022). Microglia Influence Neurofilament Deposition in ALS iPSC-Derived Motor Neurons. *Genes*, *13*(2), 241. https://doi.org/10.3390/genes13020241

Allodi, I., Montañana-Rosell, R., Selvan, R., Löw, P., & Kiehn, O. (2021). Locomotor deficits in a mouse model of ALS are paralleled by loss of V1-interneuron connections onto fast motor neurons. *Nature Communications*, *12*(1), 3251. https://doi.org/10.1038/s41467-021-23224-7

Almad, A. A., Doreswamy, A., Gross, S. K., Richard, J.-P., Huo, Y., Haughey, N., & Maragakis, N. J. (2016). Connexin 43 in Astrocytes Contributes to Motor Neuron Toxicity in Amyotrophic Lateral Sclerosis. *Glia*, *64*(7), 1154–1169. https://doi.org/10.1002/glia.22989

Almad, A. A., Taga, A., Joseph, J., Welsh, C., Patankar, A., Gross, S. K., Richard, J.-P., Pokharel, A., Lillo, M., Dastgheyb, R., Eggan, K., Haughey, N., Contreras, J. E., & Maragakis, N. J. (2020). Connexin 43 hemichannels mediate spatial and temporal disease spread in ALS. *BioRxiv*. https://doi.org/10.1101/2020.03.14.990747

Almeida, S., Gascon, E., Tran, H., Chou, H. J., Gendron, T. F., DeGroot, S., Tapper, A. R., Sellier, C., Charlet-Berguerand, N., Karydas, A., Seeley, W. W., Boxer, A. L., Petrucelli, L., Miller, B. L., & Gao, F.-B. (2013). Modeling key pathological features of frontotemporal dementia with C9ORF72 repeat expansion in iPSC-derived human neurons. *Acta Neuropathologica*, *126*(3), 385–399. https://doi.org/10.1007/s00401-013-1149-y

Al-Saif, A., Al-Mohanna, F., & Bohlega, S. (2011). A mutation in sigma-1 receptor causes juvenile amyotrophic lateral sclerosis. *Annals of Neurology*, *70*(6), 913–919. https://doi.org/10.1002/ana.22534

Alshafie, W., Ayoubi, R., Nicouleau, M., Durcan, T. M., McPherson, P. S., & Laflamme, C. (2022). *Antibody Characterization Report for Annexin A11*. https://doi.org/10.5281/zenodo.5903684

Alshafie, W., Fotouhi, M., You, Z., Durcan, T. M., McPherson, P. S., & Laflamme, C. (2021). Antibody Characterization Report for RNA-binding protein FUS. https://doi.org/10.5281/zenodo.5259945

Altman, T., Ionescu, A., Ibraheem, A., Priesmann, D., Gradus-Pery, T., Farberov, L., Alexandra, G., Shelestovich, N., Dafinca, R., Shomron, N., Rage, F., Talbot, K., Ward, M. E., Dori, A., Krüger, M., & Perlson, E. (2021). Axonal TDP-43 condensates drive neuromuscular junction disruption through inhibition of local synthesis of nuclear encoded mitochondrial proteins. *Nature Communications*, *12*(1), 6914. https://doi.org/10.1038/s41467-021-27221-8

Alvarez-Mora, M. I., Podlesniy, P., Riazuelo, T., Molina-Porcel, L., Gelpi, E., & Rodriguez-Revenga, L. (2022). Reduced mtDNA Copy Number in the Prefrontal Cortex of C9ORF72 Patients. *Molecular Neurobiology*, *59*. 1230-1237. https://doi.org/10.1007/s12035-021-02673-7

An, H., Litscher, G., Wei, W., Watanabe, N., Hashimoto, T., Iwatsubo, T., Buchman, V. L., & Shelkovnikova, T. A. (2021). Compositional analysis of ALS-linked stress granule-like structures reveals factors and cellular pathways dysregulated by mutant FUS under stress. *BioRxiv*. https://doi.org/10.1101/2021.03.02.433611

Andrade, N. S., Ramic, M., Esanov, R., Liu, W., Rybin, M. J., Gaidosh, G., Abdallah, A., Del'Olio, S., Huff, T. C., Chee, N. T., Anatha, S., Gendron, T. F., Wahlestedt, C., Zhang, Y., Benatar, M., Mueller, C., & Zeier, Z. (2020). Dipeptide repeat proteins inhibit homology-directed DNA double strand break repair in C9ORF72 ALS/FTD. *Molecular Neurodegeneration*, *15*, 13. https://doi.org/10.1186/s13024-020-00365-9

Andrusiak, M. G., Sharifnia, P., Lyu, X., Wang, Z., Dickey, A. M., Wu, Z., Chisholm, A. D., & Jin, Y. (2019). Inhibition of Axon Regeneration by Liquid-like TIAR-2 Granules. *Neuron*, *104*(2), 290-304. https://doi.org/10.1016/j.neuron.2019.07.004

*ANXA11 protein expression summary—The Human Protein Atlas*. Retrieved 1 January 2022, from https://www.proteinatlas.org/ENSG00000122359-ANXA11

Arai, T., Hasegawa, M., Akiyama, H., Ikeda, K., Nonaka, T., Mori, H., Mann, D., Tsuchiya, K., Yoshida, M., Hashizume, Y., & Oda, T. (2006). TDP-43 is a component of ubiquitin-positive tau-negative inclusions in frontotemporal lobar degeneration and amyotrophic lateral sclerosis. *Biochemical and Biophysical Research Communications*, *351*(3), 602–611. https://doi.org/10.1016/j.bbrc.2006.10.093

Arbour, D., Tremblay, E., Martineau, É., Julien, J.-P., & Robitaille, R. (2015). Early and Persistent Abnormal Decoding by Glial Cells at the Neuromuscular Junction in an ALS Model. *Journal of Neuroscience*, *35*(2), 688–706. https://doi.org/10.1523/JNEUROSCI.1379-14.2015

Armada-Moreira, A., Gomes, J. I., Pina, C. C., Savchak, O. K., Gonçalves-Ribeiro, J., Rei, N., Pinto, S., Morais, T. P., Martins, R. S., Ribeiro, F. F., Sebastião, A. M., Crunelli, V., & Vaz, S. H. (2020). Going the Extra (Synaptic) Mile: Excitotoxicity as the Road Toward Neurodegenerative Diseases. *Frontiers in Cellular Neuroscience*, *14*. https://www.frontiersin.org/article/10.3389/fncel.2020.00090

Arrant, A. E., Onyilo, V. C., Unger, D. E., & Roberson, E. D. (2018). Progranulin Gene Therapy Improves Lysosomal Dysfunction and Microglial Pathology Associated with Frontotemporal Dementia and Neuronal Ceroid Lipofuscinosis. *The Journal of Neuroscience: The Official Journal of the Society for Neuroscience*, *38*(9), 2341–2358. https://doi.org/10.1523/JNEUROSCI.3081-17.2018

Arredondo, C., Cefaliello, C., Dyrda, A., Jury, N., Martinez, P., Díaz, I., Amaro, A., Tran, H., Morales, D., Pertusa, M., Stoica, L., Fritz, E., Corvalán, D., Abarzúa, S., Méndez-Ruette, M., Fernández, P., Rojas, F., Kumar, M. S., Aguilar, R., … Zundert, B. van. (2022). Excessive release of inorganic polyphosphate by ALS/FTD astrocytes causes non-cell-autonomous toxicity to motoneurons. *Neuron*, *100*(10), 16561670. https://doi.org/10.1016/j.neuron.2022.02.010

Arthur, K. C., Calvo, A., Price, T. R., Geiger, J. T., Chiò, A., & Traynor, B. J. (2016). Projected increase in amyotrophic lateral sclerosis from 2015 to 2040. *Nature Communications*, *7,* 12408. https://doi.org/10.1038/ncomms12408

Ash, P. E. A., Bieniek, K. F., Gendron, T. F., Caulfield, T., Lin, W.-L., DeJesus-Hernandez, M., van Blitterswijk, M. M., Jansen-West, K., Paul, J. W., Rademakers, R., Boylan, K. B., Dickson, D. W., & Petrucelli, L. (2013). Unconventional Translation of C9ORF72 GGGGCC Expansion Generates Insoluble Polypeptides Specific to c9FTD/ALS. *Neuron*, *77*(4), 639–646. https://doi.org/10.1016/j.neuron.2013.02.004

Ashary, A. A., Patel, D. N., & Hirsch, A. R. (2020). 101 Amyotrophic Lateral Sclerosis (ALS) - Not Just a Motor Disease? Isolated Bitter and Sweet Taste Loss in ALS. *CNS Spectrums*, *25*(2), 266. https://doi.org/10.1017/S109285292000019X

Assou, S., Girault, N., Plinet, M., Bouckenheimer, J., Sansac, C., Combe, M., Mianné, J., Bourguignon, C., Fieldes, M., Ahmed, E., Commes, T., Boureux, A., Lemaître, J.-M., & De Vos, J. (2020). Recurrent Genetic Abnormalities in Human Pluripotent Stem Cells: Definition and Routine Detection in Culture Supernatant by Targeted Droplet Digital PCR. *Stem Cell Reports*, *14*(1), 1–8. https://doi.org/10.1016/j.stemcr.2019.12.004

Atkinson, R. A. K., Fair, H. L., Wilson, R., Vickers, J. C., & King, A. E. (2021). Effects of TDP-43 overexpression on neuron proteome and morphology in vitro. *Molecular and Cellular Neuroscience*, *114*, 103627. https://doi.org/10.1016/j.mcn.2021.103627

Aulas, A., Fay, M. M., Lyons, S. M., Achorn, C. A., Kedersha, N., Anderson, P., & Ivanov, P. (2017). Stress-specific differences in assembly and composition of stress granules and related foci. *Journal of Cell Science*, *130*(5), 927–937. https://doi.org/10.1242/jcs.199240

Aulas, A., Fay, M. M., Szaflarski, W., Kedersha, N., Anderson, P., & Ivanov, P. (2017). Methods to Classify Cytoplasmic Foci as Mammalian Stress Granules. *Journal of Visualized Experiments : JoVE*, *123*, 55656. https://doi.org/10.3791/55656

Aviner, R. (2020). The science of puromycin: From studies of ribosome function to applications in biotechnology. *Computational and Structural Biotechnology Journal*, *18*, 1074–1083. https://doi.org/10.1016/j.csbj.2020.04.014

Ayala, Y. M., De Conti, L., Avendaño-Vázquez, S. E., Dhir, A., Romano, M., D'Ambrogio, A., Tollervey, J., Ule, J., Baralle, M., Buratti, E., & Baralle, F. E. (2011). TDP-43 regulates its mRNA levels

through a negative feedback loop. *The EMBO Journal*, *30*(2), 277–288. https://doi.org/10.1038/emboj.2010.310

Babinchak, W. M., & Surewicz, W. K. (2020). Liquid–Liquid Phase Separation and Its Mechanistic Role in Pathological Protein Aggregation. *Journal of Molecular Biology*, *432*(7), 1910–1925. https://doi.org/10.1016/j.jmb.2020.03.004

Baker, D., Hirst, A. J., Gokhale, P. J., Juarez, M. A., Williams, S., Wheeler, M., Bean, K., Allison, T. F., Moore, H. D., Andrews, P. W., & Barbaric, I. (2016). Detecting Genetic Mosaicism in Cultures of Human Pluripotent Stem Cells. *Stem Cell Reports*, *7*(5), 998–1012. https://doi.org/10.1016/j.stemcr.2016.10.003

Baldelli, P., Fassio, A., Corradi, A., Valtorta, F., & Benfenati, F. (2013). The Synapsins and the Control of Neuroexocytosis. In *Madame Curie Bioscience Database [Internet]*. Landes Bioscience. https://www.ncbi.nlm.nih.gov/books/NBK6569/

Banani, S. F., Lee, H. O., Hyman, A. A., & Rosen, M. K. (2017). Biomolecular condensates: Organizers of cellular biochemistry. *Nature Reviews Molecular Cell Biology*, *18*(5), 285–298. https://doi.org/10.1038/nrm.2017.7

Bances, P., Fernandez, M.-R., Rodriguez-Garcia, M.-I., Morgan, R. O., & Fernandez, M.-P. (2000). Annexin A11 (ANXA11) Gene Structure as the Progenitor of Paralogous Annexins and Source of Orthologous cDNA Isoforms. *Genomics*, *69*(1), 95–103. https://doi.org/10.1006/geno.2000.6309

Bannwarth, S., Ait-El-Mkadem, S., Chaussenot, A., Genin, E. C., Lacas-Gervais, S., Fragaki, K., Berg-Alonso, L., Kageyama, Y., Serre, V., Moore, D. G., Verschueren, A., Rouzier, C., Le Ber, I., Augé, G., Cochaud, C., Lespinasse, F., N'Guyen, K., de Septenville, A., Brice, A., … Paquis-Flucklinger, V. (2014). A mitochondrial origin for frontotemporal dementia and amyotrophic lateral sclerosis through CHCHD10 involvement. *Brain: A Journal of Neurology*, *137*(8), 2329–2345. https://doi.org/10.1093/brain/awu138

Barbosa, M., Gomes, C., Sequeira, C., Gonçalves-Ribeiro, J., Pina, C. C., Carvalho, L. A., Moreira, R., Vaz, S. H., Vaz, A. R., & Brites, D. (2021). Recovery of Depleted miR-146a in ALS Cortical Astrocytes Reverts Cell Aberrancies and Prevents Paracrine Pathogenicity on Microglia and Motor Neurons. *Frontiers in Cell and Developmental Biology*, *9*. https://doi.org/10.3389/fcell.2021.634355

Barmada, S. J., Serio, A., Arjun, A., Bilican, B., Daub, A., Ando, D. M., Tsvetkov, A., Pleiss, M., Li, X., Peisach, D., Shaw, C., Chandran, S., & Finkbeiner, S. (2014). Autophagy induction enhances TDP43 turnover and survival in neuronal ALS models. *Nature Chemical Biology*, *10*(8), 677–685. https://doi.org/10.1038/nchembio.1563

Barnes, A. P., & Polleux, F. (2009). Establishment of Axon-Dendrite Polarity in Developing Neurons. *Annual Review of Neuroscience*, *32*(1), 347–381. https://doi.org/10.1146/annurev.neuro.31.060407.125536

Barnes, J. A., & Gomes, A. V. (2002). Proteolytic signals in the primary structure of annexins. *Molecular and Cellular Biochemistry*, *231*(1–2), 1–7. https://doi.org/10.1023/A:1014476123120

Baron, D. M., Fenton, A. R., Saez-Atienzar, S., Giampetruzzi, A., Sreeram, A., Shankaracharya, Keagle, P. J., Doocy, V. R., Smith, N. J., Danielson, E. W., Andresano, M., McCormack, M. C., Garcia, J., Bercier, V., Bosch, L. V. D., Brent, J. R., Fallini, C., Traynor, B. J., Holzbaur, E. L. F., & Landers, J. E. (2022). ALS-associated KIF5A mutations abolish autoinhibition resulting in a toxic gain of function. *Cell Reports*, *39*(1), 110598. https://doi.org/10.1016/j.celrep.2022.110598

Barrett, R., Ornelas, L., Yeager, N., Mandefro, B., Sahabian, A., Lenaeus, L., Targan, S. R., Svendsen, C. N., & Sareen, D. (2014). Reliable Generation of Induced Pluripotent Stem Cells From Human Lymphoblastoid Cell Lines. *Stem Cells Translational Medicine*, *3*(12), 1429–1434. https://doi.org/10.5966/sctm.2014-0121

Barton, S. K., Gregory, J. M., Chandran, S., & Turner, B. J. (2019). Could an Impairment in Local Translation of mRNAs in Glia be Contributing to Pathogenesis in ALS? *Frontiers in Molecular Neuroscience*, *12*. https://www.frontiersin.org/article/10.3389/fnmol.2019.00124

Barton, S. K., Lau, C. L., Chiam, M. D. F., Tomas, D., Muyderman, H., Beart, P. M., & Turner, B. J. (2020). Mutant TDP-43 Expression Triggers TDP-43 Pathology and Cell Autonomous Effects on Primary Astrocytes: Implications for Non-cell Autonomous Pathology in ALS. *Neurochemical Research*. *45*, 1451-1459. https://doi.org/10.1007/s11064-020-03048-5

Bashford, J. A., Wickham, A., Iniesta, R., Drakakis, E. M., Boutelle, M. G., Mills, K. R., & Shaw, C. E. (2020). The rise and fall of fasciculations in amyotrophic lateral sclerosis. *Brain Communications*, *2*(1), fcaa018. https://doi.org/10.1093/braincomms/fcaa018

Bashford, J., Wickham, A., Iniesta, R., Drakakis, E., Boutelle, M., Mills, K., & Shaw, C. (2019). SPiQE: An automated analytical tool for detecting and characterising fasciculations in amyotrophic lateral sclerosis. *Clinical Neurophysiology*, *130*(7), 1083–1090. https://doi.org/10.1016/j.clinph.2019.03.032

Baskoylu, S. N., Chapkis, N., Unsal, B., Lins, J., Schuch, K., Simon, J., & Hart, A. C. (2022). Disrupted autophagy and neuronal dysfunction in C. elegans knockin models of FUS amyotrophic lateral sclerosis. *Cell Reports*, *38*(4), 110195. https://doi.org/10.1016/j.celrep.2021.110195

Bastide, A., Yewdell, J. W., & David, A. (2018). The RiboPuromycylation Method (RPM): An Immunofluorescence Technique to Map Translation Sites at the Sub-cellular Level. *Bio-Protocol*, *8*(1), e2669. https://doi.org/10.21769/BioProtoc.2669

Basu, S., Rajendra, K. C., Alagar, S., & Bahadur, R. P. (2022). Impaired nuclear transport induced by juvenile ALS causing P525L mutation in NLS domain of FUS: A molecular mechanistic study. *Biochimica et Biophysica Acta (BBA) - Proteins and Proteomics*, *1870*(4), 140766. https://doi.org/10.1016/j.bbapap.2022.140766

Bean, B. P. (2007). The action potential in mammalian central neurons. *Nature Reviews Neuroscience*, *8*(6), 451–465. https://doi.org/10.1038/nrn2148

Bede, P., Chipika, R. H., Christidi, F., Hengeveld, J. C., Karavasilis, E., Argyropoulos, G. D., Lope, J., Shing, S. L. H., Velonakis, G., Dupuis, L., Doherty, M. A., Vajda, A., McLaughlin, R. L., & Hardiman, O. (2021). Genotype-associated cerebellar profiles in ALS: Focal cerebellar pathology and cerebro-cerebellar connectivity alterations. *Journal of Neurology, Neurosurgery & Psychiatry*, *92*(11), 1197–1205. https://doi.org/10.1136/jnnp-2021-326854

Behzadi, A., Pujol-Calderón, F., Tjust, A. E., Wuolikainen, A., Höglund, K., Forsberg, K., Portelius, E., Blennow, K., Zetterberg, H., & Andersen, P. M. (2021). Neurofilaments can differentiate ALS subgroups and ALS from common diagnostic mimics. *Scientific Reports*, *11*(1), 22128. https://doi.org/10.1038/s41598-021-01499-6

Bellmann, J., Monette, A., Tripathy, V., Sójka, A., Abo-Rady, M., Janosh, A., Bhatnagar, R., Bickle, M., Mouland, A. J., & Sterneckert, J. (2019). Viral Infections Exacerbate FUS-ALS Phenotypes in iPSC-Derived Spinal Neurons in a Virus Species-Specific Manner. *Frontiers in Cellular Neuroscience*, *13*. https://doi.org/10.3389/fncel.2019.00480

Ben-Ari, Y. (2001). Developing networks play a similar melody. *Trends in Neurosciences*, *24*(6), 353–360. https://doi.org/10.1016/s0166-2236(00)01813-0

Bennett, C. L., & La Spada, A. R. (2021). SUMOylated Senataxin functions in genome stability, RNA degradation, and stress granule disassembly, and is linked with inherited ataxia and motor neuron disease. *Molecular Genetics & Genomic Medicine*, *9*(12), e1745. https://doi.org/10.1002/mgg3.1745

Bercier, V., Hubbard, J. M., Fidelin, K., Duroure, K., Auer, T. O., Revenu, C., Wyart, C., & Del Bene, F. (2019). Dynactin1 depletion leads to neuromuscular synapse instability and functional abnormalities. *Molecular Neurodegeneration*, *14*, 27. https://doi.org/10.1186/s13024-019-0327-3

Bereman, M. S., Kirkwood, K. I., Sabaretnam, T., Furlong, S., Rowe, D. B., Guillemin, G. J., Mellinger, A. L., & Muddiman, D. C. (2020). Metabolite Profiling Reveals Predictive Biomarkers and the Absence of β-Methyl Amino-l-alanine in Plasma from Individuals Diagnosed with Amyotrophic Lateral Sclerosis. *Journal of Proteome Research*. *19*(8), 3276-3285. https://doi.org/10.1021/acs.jproteome.0c00216

Berning, B. A., & Walker, A. K. (2019). The Pathobiology of TDP-43 C-Terminal Fragments in ALS and FTLD. *Frontiers in Neuroscience*, *13*. https://www.frontiersin.org/article/10.3389/fnins.2019.00335

Berry, J. D., Cudkowicz, M. E., Windebank, A. J., Staff, N. P., Owegi, M., Nicholson, K., McKenna-Yasek, D., Levy, Y. S., Abramov, N., Kaspi, H., Mehra, M., Aricha, R., Gothelf, Y., & Brown, R. H. (2019). NurOwn, phase 2, randomized, clinical trial in patients with ALS: Safety, clinical, and biomarker results. *Neurology*, *93*(24), e2294–e2305. https://doi.org/10.1212/WNL.0000000000008620

Bersano, A., Bo, R. D., Lamperti, C., Ghezzi, S., Fagiolari, G., Fortunato, F., Ballabio, E., Moggio, M., Candelise, L., Galimberti, D., Virgilio, R., Lanfranconi, S., Torrente, Y., Carpo, M., Bresolin, N., Comi, G. P., & Corti, S. (2009). Inclusion body myopathy and frontotemporal dementia caused by a novel VCP mutation. *Neurobiology of Aging*, *30*(5), 752–758. https://doi.org/10.1016/j.neurobiolaging.2007.08.009

Bersano, E., Sarnelli, M. F., Solara, V., Iazzolino, B., Peotta, L., Marchi, F. D., Facchin, A. P., Moglia, C., Canosa, A., Calvo, A., Chiò, A., & Mazzini, L. (2020). Decline of cognitive and behavioral functions in amyotrophic lateral sclerosis: A longitudinal study. *Amyotrophic Lateral Sclerosis and Frontotemporal Degeneration*, *21*(5-6), 373-379. https://doi.org/10.1080/21678421.2020.1771732

Bertuzzi, M., & Ampatzis, K. (2018). Spinal cholinergic interneurons differentially control motoneuron excitability and alter the locomotor network operational range. *Scientific Reports*, *8*(1), 1988. https://doi.org/10.1038/s41598-018-20493-z

Besnard-Guérin, C. (2020). Cytoplasmic localization of amyotrophic lateral sclerosis-related TDP-43 proteins modulates stress granule formation. *European Journal of Neuroscience*, *52*(8), 3995–4008. https://doi.org/10.1111/ejn.14762

Beyer, F., Lüdje, W., Karpf, J., Saher, G., & Beckervordersandforth, R. (2021). Distribution of Aldh1L1-CreERT2 Recombination in Astrocytes Versus Neural Stem Cells in the Neurogenic Niches of the Adult Mouse Brain. *Frontiers in Neuroscience*, *15*. https://www.frontiersin.org/article/10.3389/fnins.2021.713077

Bhandari, R., Kuhad, A., & Kuhad, A. (2018). Edaravone: A new hope for deadly amyotrophic lateral sclerosis. *Drugs of Today*, *54*(6), 349–360. https://doi.org/10.1358/dot.2018.54.6.2828189

Bhardwaj, A., Myers, M. P., Buratti, E., & Baralle, F. E. (2013). Characterizing TDP-43 interaction with its RNA targets. *Nucleic Acids Research*, *41*(9), 5062–5074. https://doi.org/10.1093/nar/gkt189

Biever, A., Donlin-Asp, P. G., & Schuman, E. M. (2019). Local translation in neuronal processes. *Current Opinion in Neurobiology*, *57*, 141–148. https://doi.org/10.1016/j.conb.2019.02.008

Birger, A., Ben-Dor, I., Ottolenghi, M., Turetsky, T., Gil, Y., Sweetat, S., Perez, L., Belzer, V., Casden, N., Steiner, D., Izrael, M., Galun, E., Feldman, E., Behar, O., & Reubinoff, B. (2019). Human iPSC-derived astrocytes from ALS patients with mutated C9ORF72 show increased oxidative stress and neurotoxicity. *EBioMedicine*, *50*, 274–289. https://doi.org/10.1016/j.ebiom.2019.11.026

Birsa, N., Ule, A. M., Garone, M. G., Tsang, B., Mattedi, F., Chong, P. A., Humphrey, J., Jarvis, S., Pisiren, M., Wilkins, O. G., Nosella, M. L., Devoy, A., Bodo, C., Fuente, R. F. de la, Fisher, E. M. C., Rosa, A., Viero, G., Forman-Kay, J. D., Schiavo, G., & Fratta, P. (2021). FUS-ALS mutants alter FMRP phase separation equilibrium and impair protein translation. *Science Advances*, *7*(30), eabf8660. https://doi.org/10.1126/sciadv.abf8660

Biswas, J., Liu, Y., Singer, R. H., & Wu, B. (2019). Fluorescence Imaging Methods to Investigate Translation in Single Cells. *Cold Spring Harbor Perspectives in Biology*, *11*(4), a032722. https://doi.org/10.1101/cshperspect.a032722

Bjornevik, K., Cortese, M., Healy, B. C., Kuhle, J., Mina, M. J., Leng, Y., Elledge, S. J., Niebuhr, D. W., Scher, A. I., Munger, K. L., & Ascherio, A. (2022). Longitudinal analysis reveals high prevalence of Epstein-Barr virus associated with multiple sclerosis. *Science*, *375*(6578), 296–301. https://doi.org/10.1126/science.abj8222

Blokhuis, A. M., Groen, E. J. N., Koppers, M., van den Berg, L. H., & Pasterkamp, R. J. (2013). Protein aggregation in amyotrophic lateral sclerosis. *Acta Neuropathologica*, *125*(6), 777–794. https://doi.org/10.1007/s00401-013-1125-6

Bloom, A. J., Mao, X., Strickland, A., Sasaki, Y., Milbrandt, J., & DiAntonio, A. (2022). Constitutively active SARM1 variants that induce neuropathy are enriched in ALS patients. *Molecular Neurodegeneration*, *17*, 1. https://doi.org/10.1186/s13024-021-00511-x

Boeynaems, S., Bogaert, E., Damme, P. V., & Bosch, L. V. D. (2016). Inside out: The role of nucleocytoplasmic transport in ALS and FTLD. *Acta Neuropathologica*, *132*(2), 159–173. https://doi.org/10.1007/s00401-016-1586-5

Bogaert, E., Boeynaems, S., Kato, M., Guo, L., Caulfield, T. R., Steyaert, J., Scheveneels, W., Wilmans, N., Haeck, W., Hersmus, N., Schymkowitz, J., Rousseau, F., Shorter, J., Callaerts, P., Robberecht, W., Van Damme, P., & Van Den Bosch, L. (2018). Molecular Dissection of FUS Points at Synergistic Effect of Low-Complexity Domains in Toxicity. *Cell Reports*, *24*(3), 529-537.e4. https://doi.org/10.1016/j.celrep.2018.06.070

Bonifacino, T., Rebosio, C., Provenzano, F., Torazza, C., Balbi, M., Milanese, M., Raiteri, L., Usai, C., Fedele, E., & Bonanno, G. (2019). Enhanced Function and Overexpression of Metabotropic Glutamate Receptors 1 and 5 in the Spinal Cord of the SOD1G93A Mouse Model of Amyotrophic Lateral Sclerosis during Disease Progression. *International Journal of Molecular Sciences*, *20*(18), 4552. https://doi.org/10.3390/ijms20184552

Bootman, M. D., Chehab, T., Bultynck, G., Parys, J. B., & Rietdorf, K. (2018). The regulation of autophagy by calcium signals: Do we have a consensus? *Cell Calcium*, *70*, 32–46. https://doi.org/10.1016/j.ceca.2017.08.005

Bosco, D. A., Lemay, N., Ko, H. K., Zhou, H., Burke, C., Kwiatkowski, T. J., Sapp, P., McKenna-Yasek, D., Brown, R. H., & Hayward, L. J. (2010). Mutant FUS proteins that cause amyotrophic lateral sclerosis incorporate into stress granules. *Human Molecular Genetics*, *19*(21), 4160–4175. https://doi.org/10.1093/hmg/ddq335

Bosco, D. A., Morfini, G., Karabacak, N. M., Song, Y., Gros-Louis, F., Pasinelli, P., Goolsby, H., Fontaine, B. A., Lemay, N., McKenna-Yasek, D., Frosch, M. P., Agar, J. N., Julien, J.-P., Brady, S. T., & Brown, R. H. (2010). Wild-type and mutant SOD1 share an aberrant conformation and a common pathogenic pathway in ALS. *Nature Neuroscience*, *13*(11), 1396–1403. https://doi.org/10.1038/nn.2660

Bossolasco, P., Sassone, F., Gumina, V., Peverelli, S., Garzo, M., & Silani, V. (2018). Motor neuron differentiation of iPSCs obtained from peripheral blood of a mutant TARDBP ALS patient. *Stem Cell Research*, *30*, 61–68. https://doi.org/10.1016/j.scr.2018.05.009

Boucherie, C., Schäfer, S., Lavand'homme, P., Maloteaux, J.-M., & Hermans, E. (2009). Chimerization of astroglial population in the lumbar spinal cord after mesenchymal stem cell transplantation prolongs survival in a rat model of amyotrophic lateral sclerosis. *Journal of Neuroscience Research*, *87*(9), 2034–2046. https://doi.org/10.1002/jnr.22038

Bounedjah, O., Desforges, B., Wu, T.-D., Pioche-Durieu, C., Marco, S., Hamon, L., Curmi, P. A., Guerquin-Kern, J.-L., Piétrement, O., & Pastré, D. (2014). Free mRNA in excess upon polysome dissociation is a scaffold for protein multimerization to form stress granules. *Nucleic Acids Research*, *42*(13), 8678–8691. https://doi.org/10.1093/nar/gku582

Brackett, D. M., Qing, F., Amieux, P. S., Sellers, D. L., Horner, P. J., & Morris, D. R. (2013). Fmr1 Transcript Isoforms: Association with Polyribosomes; Regional and Developmental Expression in Mouse Brain. *PLoS ONE*, *8*(3). https://doi.org/10.1371/journal.pone.0058296

Bradley, W. G., & Mash, D. C. (2009). Beyond Guam: The cyanobacteria/BMAA hypothesis of the cause of ALS and other neurodegenerative diseases. *Amyotrophic Lateral Sclerosis*, *10*(2), 7–20. https://doi.org/10.3109/17482960903286009

Brainstorm-Cell Therapeutics. (2021). *A Phase 3, Randomized Double-Blind, Placebo-Controlled Multicenter Study to Evaluate Efficacy and Safety of Repeated Administration of NurOwn® (Autologous Mesenchymal Stem Cells Secreting Neurotrophic Factors) in Participants With ALS* (Clinical Trial Registration study/NCT03280056). clinicaltrials.gov. https://clinicaltrials.gov/ct2/show/study/NCT03280056

Briese, M., Saal-Bauernschubert, L., Lüningschrör, P., Moradi, M., Dombert, B., Surrey, V., Appenzeller, S., Deng, C., Jablonka, S., & Sendtner, M. (2020). Loss of Tdp-43 disrupts the axonal transcriptome of motoneurons accompanied by impaired axonal translation and mitochondria function. *Acta Neuropathologica Communications*, *8*(1), 116. https://doi.org/10.1186/s40478-020-00987-6

Bright, F., Chan, G., van Hummel, A., Ittner, L. M., & Ke, Y. D. (2021). TDP-43 and Inflammation: Implications for Amyotrophic Lateral Sclerosis and Frontotemporal Dementia. *International Journal of Molecular Sciences*, *22*(15), 7781. https://doi.org/10.3390/ijms22157781

Brooks, B. R., Miller, R. G., Swash, M., Munsat, T. L., & World Federation of Neurology Research Group on Motor Neuron Diseases. (2000). El Escorial revisited: Revised criteria for the diagnosis of amyotrophic lateral sclerosis. *Amyotrophic Lateral Sclerosis and Other Motor Neuron Disorders: Official Publication of the World Federation of Neurology, Research Group on Motor Neuron Diseases*, *1*(5), 293–299. https://doi.org/10.1080/146608200300079536

Brown, A.-L., Wilkins, O. G., Keuss, M. J., Hill, S. E., Zanovello, M., Lee, W. C., Bampton, A., Lee, F. C. Y., Masino, L., Qi, Y. A., Bryce-Smith, S., Gatt, A., Hallegger, M., Fagegaltier, D., Phatnani, H., Newcombe, J., Gustavsson, E. K., Seddighi, S., Reyes, J. F., … Fratta, P. (2022). TDP-43 loss and ALS-risk SNPs drive mis-splicing and depletion of UNC13A. *Nature*, *603*(7899), 131–137. https://doi.org/10.1038/s41586-022-04436-3

Brown, V., Jin, P., Ceman, S., Darnell, J. C., O'Donnell, W. T., Tenenbaum, S. A., Jin, X., Feng, Y., Wilkinson, K. D., Keene, J. D., Darnell, R. B., & Warren, S. T. (2001). Microarray Identification of FMRP-Associated Brain mRNAs and Altered mRNA Translational Profiles in Fragile X Syndrome. *Cell*, *107*(4), 477–487. https://doi.org/10.1016/S0092-8674(01)00568-2

Brugman, F., Wokke, J. H. J., Scheffer, H., Versteeg, M. H. A., Sistermans, E. A., & van den Berg, L. H. (2005). Spastin mutations in sporadic adult-onset upper motor neuron syndromes. *Annals of Neurology*, *58*(6), 865–869. https://doi.org/10.1002/ana.20652

Bruijn, L. I., Houseweart, M. K., Kato, S., Anderson, K. L., Anderson, S. D., Ohama, E., Reaume, A. G., Scott, R. W., & Cleveland, D. W. (1998). Aggregation and Motor Neuron Toxicity of an ALS-Linked SOD1 Mutant Independent from Wild-Type SOD1. *Science*, *281*(5384), 1851–1854. https://doi.org/10.1126/science.281.5384.1851

Brunet, M. A., Jacques, J.-F., Nassari, S., Tyzack, G. E., McGoldrick, P., Zinman, L., Jean, S., Robertson, J., Patani, R., & Roucou, X. (2020). The FUS gene is dual-coding with both proteins contributing to FUS-mediated toxicity. *EMBO Reports*, *22*, e50640. https://doi.org/10.15252/embr.202050640

Buratti, E. (2018). TDP-43 post-translational modifications in health and disease. *Expert Opinion on Therapeutic Targets*, *22*(3), 279–293. https://doi.org/10.1080/14728222.2018.1439923

Burberry, A., Suzuki, N., Wang, J.-Y., Moccia, R., Mordes, D. A., Stewart, M. H., Suzuki-Uematsu, S., Ghosh, S., Singh, A., Merkle, F. T., Koszka, K., Li, Q.-Z., Zon, L., Rossi, D. J., Trowbridge, J. J., Notarangelo, L. D., & Eggan, K. (2016). Loss-of-function mutations in the C9ORF72 mouse ortholog cause fatal autoimmune disease. *Science Translational Medicine*, *8*(347), 347ra93. https://doi.org/10.1126/scitranslmed.aaf6038

Burberry, A., Wells, M. F., Limone, F., Couto, A., Smith, K. S., Keaney, J., Gillet, G., van Gastel, N., Wang, J.-Y., Pietilainen, O., Qian, M., Eggan, P., Cantrell, C., Mok, J., Kadiu, I., Scadden, D. T., & Eggan, K. (2020). C9orf72 suppresses systemic and neural inflammation induced by gut bacteria. *Nature*, *582*, 89–94. https://doi.org/10.1038/s41586-020-2288-7

Burguete, A. S., Almeida, S., Gao, F.-B., Kalb, R., Akins, M. R., & Bonini, N. M. (2015). GGGGCC microsatellite RNA is neuritically localized, induces branching defects, and perturbs transport granule function. *ELife*, *4*, e08881. https://doi.org/10.7554/eLife.08881

Burley, S., Beccano-Kelly, D. A., Talbot, K., Llana, O. C., & Wade-Martins, R. (2022). Hyperexcitability in young iPSC-derived C9ORF72 mutant motor neurons is associated with increased intracellular calcium release. *Scientific Reports*, *12*, 7278. https://doi.org/10.1038/s41598-022-09751-3

Bursch, F., Kalmbach, N., Naujock, M., Staege, S., Eggenschwiler, R., Abo-Rady, M., Japtok, J., Guo, W., Hensel, N., Reinhardt, P., Boeckers, T. M., Cantz, T., Sterneckert, J., Van Den Bosch, L.,

Hermann, A., Petri, S., & Wegner, F. (2019). Altered calcium dynamics and glutamate receptor properties in iPSC-derived motor neurons from ALS patients with C9orf72, FUS, SOD1 or TDP43 mutations. *Human Molecular Genetics*, *28*(17), 2835–2850. https://doi.org/10.1093/hmg/ddz107

Buscaglia, G., Northington, K. R., Moore, J. K., & Bates, E. A. (2020). Reduced TUBA1A Tubulin Causes Defects in Trafficking and Impaired Adult Motor Behavior. *ENeuro*, *7*(2), ENEURO.0045-20.2020. https://doi.org/10.1523/ENEURO.0045-20.2020

Butti, Z., Pan, Y. E., Giacomotto, J., & Patten, S. A. (2021). Reduced C9orf72 function leads to defective synaptic vesicle release and neuromuscular dysfunction in zebrafish. *Communications Biology*, *4*(1), 1–16. https://doi.org/10.1038/s42003-021-02302-y

Caiazzo, M., Giannelli, S., Valente, P., Lignani, G., Carissimo, A., Sessa, A., Colasante, G., Bartolomeo, R., Massimino, L., Ferroni, S., Settembre, C., Benfenati, F., & Broccoli, V. (2015). Direct Conversion of Fibroblasts into Functional Astrocytes by Defined Transcription Factors. *Stem Cell Reports*, *4*(1), 25–36. https://doi.org/10.1016/j.stemcr.2014.12.002

Campbell, D. S., & Holt, C. E. (2001). Chemotropic Responses of Retinal Growth Cones Mediated by Rapid Local Protein Synthesis and Degradation. *Neuron*, *32*(6), 1013–1026. https://doi.org/10.1016/S0896-6273(01)00551-7

Campbell, K. H. S., McWhir, J., Ritchie, W. A., & Wilmut, I. (1996). Sheep cloned by nuclear transfer from a cultured cell line. *Nature*, *380*(6569), 64–66. https://doi.org/10.1038/380064a0

Cantu, D. A., Wang, B., Gongwer, M. W., He, C. X., Goel, A., Suresh, A., Kourdougli, N., Arroyo, E. D., Zeiger, W., & Portera-Cailliau, C. (2020). EZcalcium: Open-Source Toolbox for Analysis of Calcium Imaging Data. *Frontiers in Neural Circuits*, *14*. https://doi.org/10.3389/fncir.2020.00025

Capizzi, M., Carpentier, R., Denarier, E., Adrait, A., Kassem, R., Mapelli, M., Couté, Y., & Humbert, S. (2022). Developmental defects in Huntington's disease show that axonal growth and microtubule reorganization require NUMA1. *Neuron*, *110*(1), 36-50.e5. https://doi.org/10.1016/j.neuron.2021.10.033

Castellanos-Montiel, M. J., Chaineau, M., & Durcan, T. M. (2020). The Neglected Genes of ALS: Cytoskeletal Dynamics Impact Synaptic Degeneration in ALS. *Frontiers in Cellular Neuroscience*, *14*. https://doi.org/10.3389/fncel.2020.594975

Catanese, A., Rajkumar, S., Sommer, D., Freisem, D., Wirth, A., Aly, A., Massa-López, D., Olivieri, A., Torelli, F., Ioannidis, V., Lipecka, J., Guerrera, I. C., Zytnicki, D., Ludolph, A., Kabashi, E., Mulaw, M. A., Roselli, F., & Böckers, T. M. (2021). Synaptic disruption and CREB-regulated transcription are restored by K+ channel blockers in ALS. *EMBO Molecular Medicine*, *13*, e13131. https://doi.org/10.15252/emmm.202013131

Cathcart, S. J., Appel, S. H., Peterson, L. E., Greene, E. P., Powell, S. Z., Arumanayagam, A. S., Rivera, A. L., & Cykowski, M. D. (2021). Fast Progression in Amyotrophic Lateral Sclerosis Is Associated With Greater TDP-43 Burden in Spinal Cord. *Journal of Neuropathology & Experimental Neurology*, *80*(8), 754–763. https://doi.org/10.1093/jnen/nlab061

Chanaday, N. L., Nosyreva, E., Shin, O.-H., Zhang, H., Aklan, I., Atasoy, D., Bezprozvanny, I., & Kavalali, E. T. (2021). Presynaptic store-operated Ca2+ entry drives excitatory spontaneous neurotransmission and augments endoplasmic reticulum stress. *Neuron*, *109*(8), 1314-1332.e5. https://doi.org/10.1016/j.neuron.2021.02.023

Charif, S. E., Luchelli, L., Vila, A., Blaustein, M., & Igaz, L. M. (2020). Cytoplasmic Expression of the ALS/FTD-Related Protein TDP-43 Decreases Global Translation Both in vitro and in vivo. *Frontiers in Cellular Neuroscience*, *14*. https://doi.org/10.3389/fncel.2020.594561

Chatterjee, N., & Walker, G. C. (2017). Mechanisms of DNA damage, repair, and mutagenesis. *Environmental and Molecular Mutagenesis*, *58*(5), 235–263. https://doi.org/10.1002/em.22087

Cheah, B. C., Vucic, S., & Kiernan, A. V. K. and M. C. (2010). *Riluzole, Neuroprotection and Amyotrophic Lateral Sclerosis*. Current Medicinal Chemistry. *17*(18), 1942-1959. http://www.eurekaselect.com/70209/article

Chen, E., Sharma, M. R., Shi, X., Agrawal, R. K., & Joseph, S. (2014). Fragile X Mental Retardation Protein Regulates Translation by Binding Directly to the Ribosome. *Molecular Cell*, *54*(3), 407–417. https://doi.org/10.1016/j.molcel.2014.03.023

Chen, H., Qian, K., Du, Z., Cao, J., Petersen, A., Liu, H., Blackbourn, L. W., Huang, C.-L., Errigo, A., Yin, Y., Lu, J., Ayala, M., & Zhang, S.-C. (2014). Modeling ALS with iPSCs reveals that mutant SOD1 misregulates neurofilament balance in motor neurons. *Cell Stem Cell*, *14*(6), 796–809. https://doi.org/10.1016/j.stem.2014.02.004

Chen, H.-J., & Mitchell, J. C. (2021). Mechanisms of TDP-43 Proteinopathy Onset and Propagation. *International Journal of Molecular Sciences*, *22*(11), 6004. https://doi.org/10.3390/ijms22116004

Chen, H.-J., Mitchell, J. C., Novoselov, S., Miller, J., Nishimura, A. L., Scotter, E. L., Vance, C. A., Cheetham, M. E., & Shaw, C. E. (2016). The heat shock response plays an important role in TDP-43 clearance: Evidence for dysfunction in amyotrophic lateral sclerosis. *Brain: A Journal of Neurology*, *139*(5), 1417–1432. https://doi.org/10.1093/brain/aww028

Chen, H.-J., Topp, S. D., Hui, H. S., Zacco, E., Katarya, M., McLoughlin, C., King, A., Smith, B. N., Troakes, C., Pastore, A., & Shaw, C. E. (2019). RRM adjacent TARDBP mutations disrupt RNA binding and enhance TDP-43 proteinopathy. *Brain: A Journal of Neurology*, *142*(12), 3753–3770. https://doi.org/10.1093/brain/awz313

Chen, J., Bassot, A., Giuliani, F., & Simmen, T. (2021). Amyotrophic Lateral Sclerosis (ALS): Stressed by Dysfunctional Mitochondria-Endoplasmic Reticulum Contacts (MERCs). *Cells*, *10*(7), 1789. https://doi.org/10.3390/cells10071789

Chen, K.-W., & Chen, J.-A. (2020). Functional Roles of Long Non-coding RNAs in Motor Neuron Development and Disease. *Journal of Biomedical Science*, *27*(1), 38. https://doi.org/10.1186/s12929-020-00628-z

Chen, S., Sayana, P., Zhang, X., & Le, W. (2013). Genetics of amyotrophic lateral sclerosis: An update. *Molecular Neurodegeneration*, *8*, 28. https://doi.org/10.1186/1750-1326-8-28

Chen, S., Zhang, X., Song, L., & Le, W. (2012). Autophagy Dysregulation in Amyotrophic Lateral Sclerosis. *Brain Pathology*, *22*(1), 110–116. https://doi.org/10.1111/j.1750-3639.2011.00546.x

Cheng, C., Reis, S. A., Adams, E. T., Fass, D. M., Angus, S. P., Stuhlmiller, T. J., Richardson, J., Olafson, H., Wang, E. T., Patnaik, D., Beauchamp, R. L., Feldman, D. A., Silva, M. C., Sur, M., Johnson, G. L., Ramesh, V., Miller, B. L., Temple, S., Kosik, K. S., … Haggarty, S. J. (2021). High-content image-based analysis and proteomic profiling identifies Tau phosphorylation inhibitors in a human iPSC-derived glutamatergic neuronal model of tauopathy. *Scientific Reports*, *11*(1), 1–21. https://doi.org/10.1038/s41598-021-96227-5

Cheng, X.-T., Huang, N., & Sheng, Z.-H. (2022). Programming axonal mitochondrial maintenance and bioenergetics in neurodegeneration and regeneration. *Neuron*, *110*(12), 1899-1932. https://doi.org/10.1016/j.neuron.2022.03.015

Cheng, X.-T., Xie, Y.-X., Zhou, B., Huang, N., Farfel-Becker, T., & Sheng, Z.-H. (2018). Characterization of LAMP1-labeled nondegradative lysosomal and endocytic compartments in neurons. *The Journal of Cell Biology*, *217*(9), 3127–3139. https://doi.org/10.1083/jcb.201711083

Chernov, K. G., Barbet, A., Hamon, L., Ovchinnikov, L. P., Curmi, P. A., & Pastré, D. (2009). Role of Microtubules in Stress Granule Assembly. *The Journal of Biological Chemistry*, *284*(52), 36569–36580. https://doi.org/10.1074/jbc.M109.042879

Chesi, A., Staahl, B. T., Jovičić, A., Couthouis, J., Fasolino, M., Raphael, A. R., Yamazaki, T., Elias, L., Polak, M., Kelly, C., Williams, K. L., Fifita, J. A., Maragakis, N. J., Nicholson, G. A., King, O. D., Reed, R., Crabtree, G. R., Blair, I. P., Glass, J. D., & Gitler, A. D. (2013). Exome sequencing to identify de novo mutations in sporadic ALS trios. *Nature Neuroscience*, *16*(7), 851–855. https://doi.org/10.1038/nn.3412

Chew, S., & Atassi, N. (2019). Positron Emission Tomography Molecular Imaging Biomarkers for Amyotrophic Lateral Sclerosis. *Frontiers in Neurology*, *10*. https://www.frontiersin.org/article/10.3389/fneur.2019.00135

Chhangani, D., Martín-Peña, A., & Rincon-Limas, D. E. (2021). Molecular, functional, and pathological aspects of TDP-43 fragmentation. *IScience*, *24*(5), 102459. https://doi.org/10.1016/j.isci.2021.102459

Chi, B., O'Connell, J. D., Yamazaki, T., Gangopadhyay, J., Gygi, S. P., & Reed, R. (2018). Interactome analyses revealed that the U1 snRNP machinery overlaps extensively with the RNAP II machinery and contains multiple ALS/SMA-causative proteins. *Scientific Reports*, *8*(1), 8755. https://doi.org/10.1038/s41598-018-27136-3

Chiang, C.-H., Grauffel, C., Wu, L.-S., Kuo, P.-H., Doudeva, L. G., Lim, C., Shen, C.-K. J., & Yuan, H. S. (2016). Structural analysis of disease-related TDP-43 D169G mutation: Linking enhanced stability and caspase cleavage efficiency to protein accumulation. *Scientific Reports*, *6*(1), 21581. https://doi.org/10.1038/srep21581

Chien, H.-M., He, R.-Y., Lee, C.-C., Huang, Y.-A., Hung, I.-J., Hou, K.-T., Hsiao, J.-C., Lu, P.-C., Agnihotri, D., Hwang, E., & Huang, J. J.-T. (2021). Nanoscopic investigation of C9orf72 poly-GA oligomers on nuclear membrane disruption by a photoinducible platform. *Communications Chemistry*, *4*(1), 1–13. https://doi.org/10.1038/s42004-021-00547-6

Chio, A., Logroscino, G., Hardiman, O., Swingler, R., Mitchell, D., Beghi, E., & Traynor, B. G. (2009). Prognostic factors in ALS: A critical review. *Amyotrophic Lateral Sclerosis : Official Publication of the World Federation of Neurology Research Group on Motor Neuron Diseases*, *10*(5–6), 310–323. https://doi.org/10.3109/17482960802566824

Chiu, I. M., Morimoto, E. T. A., Goodarzi, H., Liao, J. T., O'Keeffe, S., Phatnani, H. P., Muratet, M., Carroll, M. C., Levy, S., Tavazoie, S., Myers, R. M., & Maniatis, T. (2013). A Neurodegeneration-Specific Gene-Expression Signature of Acutely Isolated Microglia from an Amyotrophic Lateral Sclerosis Mouse Model. *Cell Reports*, *4*(2), 385–401. https://doi.org/10.1016/j.celrep.2013.06.018

Choksi, D. K., Roy, B., Chatterjee, S., Yusuff, T., Bakhoum, M. F., Sengupta, U., Ambegaokar, S., Kayed, R., & Jackson, G. R. (2014). TDP-43 Phosphorylation by casein kinase Iε promotes oligomerization and enhances toxicity in vivo. *Human Molecular Genetics*, *23*(4), 1025–1035. https://doi.org/10.1093/hmg/ddt498

Chou, C.-C., Zhang, Y., Umoh, M. E., Vaughan, S. W., Lorenzini, I., Liu, F., Sayegh, M., Donlin-Asp, P. G., Chen, Y. H., Duong, D. M., Seyfried, N. T., Powers, M. A., Kukar, T., Hales, C. M., Gearing, M., Cairns, N. J., Boylan, K. B., Dickson, D. W., Rademakers, R., … Rossoll, W. (2018). TDP-43 pathology disrupts nuclear pore complexes and nucleocytoplasmic transport in ALS/FTD. *Nature Neuroscience*, *21*(2), 228–239. https://doi.org/10.1038/s41593-017-0047-3

Chow, C. Y., Landers, J. E., Bergren, S. K., Sapp, P. C., Grant, A. E., Jones, J. M., Everett, L., Lenk, G. M., McKenna-Yasek, D. M., Weisman, L. S., Figlewicz, D., Brown, R. H., & Meisler, M. H. (2009). Deleterious Variants of FIG4, a Phosphoinositide Phosphatase, in Patients with ALS. *American Journal of Human Genetics*, *84*(1), 85–88. https://doi.org/10.1016/j.ajhg.2008.12.010

Chu, J.-F., Majumder, P., Chatterjee, B., Huang, S.-L., & Shen, C.-K. J. (2019). TDP-43 Regulates Coupled Dendritic mRNA Transport-Translation Processes in Co-operation with FMRP and Staufen1. *Cell Reports*, *29*(10), 3118-3133.e6. https://doi.org/10.1016/j.celrep.2019.10.061

Cioni, J.-M., Lin, J. Q., Holtermann, A. V., Koppers, M., Jakobs, M. A. H., Azizi, A., Turner-Bridger, B., Shigeoka, T., Franze, K., Harris, W. A., & Holt, C. E. (2019). Late Endosomes Act as mRNA Translation Platforms and Sustain Mitochondria in Axons. *Cell*, *176*(1), 56-72.e15. https://doi.org/10.1016/j.cell.2018.11.030

Cirulli, E. T., Lasseigne, B. N., Petrovski, S., Sapp, P. C., Dion, P. A., Leblond, C. S., Couthouis, J., Lu, Y.-F., Wang, Q., Krueger, B. J., Ren, Z., Keebler, J., Han, Y., Levy, S. E., Boone, B. E., Wimbish, J. R., Waite, L. L., Jones, A. L., Carulli, J. P., … Goldstein, D. B. (2015). Exome sequencing in amyotrophic lateral sclerosis identifies risk genes and pathways. *Science*, *347*(6229), 1436–1441. https://doi.org/10.1126/science.aaa3650

Ciura, S., Lattante, S., Le Ber, I., Latouche, M., Tostivint, H., Brice, A., & Kabashi, E. (2013). Loss of function of C9orf72 causes motor deficits in a zebrafish model of amyotrophic lateral sclerosis. *Annals of Neurology*, *74*(2), 180–187. https://doi.org/10.1002/ana.23946

Clark, J. A., Yeaman, E. J., Blizzard, C. A., Chuckowree, J. A., & Dickson, T. C. (2016). A Case for Microtubule Vulnerability in Amyotrophic Lateral Sclerosis: Altered Dynamics During Disease. *Frontiers in Cellular Neuroscience*, *10*, 204. https://doi.org/10.3389/fncel.2016.00204

Clarke, B. E., Taha, D. M., Ziff, O. J., Alam, A., Thelin, E. P., García, N. M., Helmy, A., & Patani, R. (2020). Human stem cell-derived astrocytes exhibit region-specific heterogeneity in their secretory profiles. *Brain*, *143*(10), e85–e85. https://doi.org/10.1093/brain/awaa258

Clement, A. M., Nguyen, M. D., Roberts, E. A., Garcia, M. L., Boillée, S., Rule, M., McMahon, A. P., Doucette, W., Siwek, D., Ferrante, R. J., Brown, R. H., Julien, J.-P., Goldstein, L. S. B., & Cleveland, D. W. (2003). Wild-Type Nonneuronal Cells Extend Survival of SOD1 Mutant Motor Neurons in ALS Mice. *Science*, *302*(5642), 113–117. https://doi.org/10.1126/science.1086071

Cleveland, D. W., & Rothstein, J. D. (2001). From charcot to lou gehrig: Deciphering selective motor neuron death in als. *Nature Reviews Neuroscience*, *2*(11), 806–819. https://doi.org/10.1038/35097565

Cohen, E., Ivenshitz, M., Amor-Baroukh, V., Greenberger, V., & Segal, M. (2008). Determinants of spontaneous activity in networks of cultured hippocampus. *Brain Research*, *1235*, 21–30. https://doi.org/10.1016/j.brainres.2008.06.022

Colombrita, C., Zennaro, E., Fallini, C., Weber, M., Sommacal, A., Buratti, E., Silani, V., & Ratti, A. (2009). TDP-43 is recruited to stress granules in conditions of oxidative insult. *Journal of Neurochemistry*, *111*(4), 1051–1061. https://doi.org/10.1111/j.1471-4159.2009.06383.x

Conicella, A. E., Zerze, G. H., Mittal, J., & Fawzi, N. L. (2016). ALS mutations disrupt phase separation mediated by -helical structure in the TDP-43 low complexity C-terminal domain. *Structure*, *24*(9), 1537–1549. https://doi.org/10.1016/j.str.2016.07.007

Cooper-Knock, J., Bury, J. J., Heath, P. R., Wyles, M., Higginbottom, A., Gelsthorpe, C., Highley, J. R., Hautbergue, G., Rattray, M., Kirby, J., & Shaw, P. J. (2015). C9ORF72 GGGGCC Expanded Repeats Produce Splicing Dysregulation which Correlates with Disease Severity in Amyotrophic Lateral Sclerosis. *PLOS ONE*, *10*(5), e0127376. https://doi.org/10.1371/journal.pone.0127376

Cooper-Knock, J., Higginbottom, A., Stopford, M. J., Highley, J. R., Ince, P. G., Wharton, S. B., Pickering-Brown, S., Kirby, J., Hautbergue, G. M., & Shaw, P. J. (2015). Antisense RNA foci in the motor neurons of C9ORF72-ALS patients are associated with TDP-43 proteinopathy. *Acta Neuropathologica*, *130*(1), 63–75. https://doi.org/10.1007/s00401-015-1429-9

Corcia, P., Pradat, P.-F., Salachas, F., Bruneteau, G., Forestier, N. le, Seilhean, D., Hauw, J.-J., & Meininger, V. (2008). Causes of death in a post-mortem series of ALS patients. *Amyotrophic Lateral Sclerosis*, *9*(1), 59–62. https://doi.org/10.1080/17482960701656940

Cornelissen, F., Verstraelen, P., Verbeke, T., Pintelon, I., Timmermans, J.-P., Nuydens, R., & Meert, T. (2013). Quantitation of chronic and acute treatment effects on neuronal network activity using image and signal analysis: Toward a high-content assay. *Journal of Biomolecular Screening*, *18*(7), 807–819. https://doi.org/10.1177/1087057113486518

Corrado, L., Carlomagno, Y., Falasco, L., Mellone, S., Godi, M., Cova, E., Cereda, C., Testa, L., Mazzini, L., & D'Alfonso, S. (2011). A novel peripherin gene (PRPH) mutation identified in one sporadic amyotrophic lateral sclerosis patient. *Neurobiology of Aging*, *32*(3), 552.e1-6. https://doi.org/10.1016/j.neurobiolaging.2010.02.011

Coyne, A. N., Baskerville, V., Zaepfel, B. L., Dickson, D. W., Rigo, F., Bennett, F., Lusk, C. P., & Rothstein, J. D. (2021). Nuclear accumulation of CHMP7 initiates nuclear pore complex injury and subsequent TDP-43 dysfunction in sporadic and familial ALS. *Science Translational Medicine*, *13*(604). https://doi.org/10.1126/scitranslmed.abe1923

Coyne, A. N., Yamada, S. B., Siddegowda, B. B., Estes, P. S., Zaepfel, B. L., Johannesmeyer, J. S., Lockwood, D. B., Pham, L. T., Hart, M. P., Cassel, J. A., Freibaum, B., Boehringer, A. V., Taylor, J. P., Reitz, A. B., Gitler, A. D., & Zarnescu, D. C. (2015). Fragile X protein mitigates TDP-43 toxicity by remodeling RNA granules and restoring translation. *Human Molecular Genetics*, *24*(24), 6886–6898. https://doi.org/10.1093/hmg/ddv389

Cunningham, K. M., Maulding, K., Ruan, K., Senturk, M., Grima, J. C., Sung, H., Zuo, Z., Song, H., Gao, J., Dubey, S., Rothstein, J. D., Zhang, K., Bellen, H. J., & Lloyd, T. E. (2020). TFEB/Mitf links impaired nuclear import to autophagolysosomal dysfunction in C9-ALS. *ELife*, *9*, e59419. https://doi.org/10.7554/eLife.59419

Cuomo, A. S. E., Seaton, D. D., McCarthy, D. J., Martinez, I., Bonder, M. J., Garcia-Bernardo, J., Amatya, S., Madrigal, P., Isaacson, A., Buettner, F., Knights, A., Natarajan, K. N., HipSci Consortium, Vallier, L., Marioni, J. C., Chhatriwala, M., & Stegle, O. (2020). Single-cell RNA-sequencing of differentiating iPS cells reveals dynamic genetic effects on gene expression. *Nature Communications*, *11*(1), 810. https://doi.org/10.1038/s41467-020-14457-z

Dafinca, R., Barbagallo, P., Farrimond, L., Candalija, A., Scaber, J., Ababneh, N. A., Sathyaprakash, C., Vowles, J., Cowley, S. A., & Talbot, K. (2020). Impairment of Mitochondrial Calcium Buffering Links Mutations in C9ORF72 and TARDBP in iPS-Derived Motor Neurons from Patients with ALS/FTD. *Stem Cell Reports*, *14*(5), 892–908. https://doi.org/10.1016/j.stemcr.2020.03.023

D'Alton, S., Altshuler, M., Cannon, A., Dickson, D. W., Petrucelli, L., & Lewis, J. (2014). Divergent Phenotypes in Mutant TDP-43 Transgenic Mice Highlight Potential Confounds in TDP-43 Transgenic Modeling. *PLOS ONE*, *9*(1), e86513. https://doi.org/10.1371/journal.pone.0086513

D'Angelo, M. A., Raices, M., Panowski, S. H., & Hetzer, M. W. (2009). Age-dependent deterioration of nuclear pore complexes causes a loss of nuclear integrity in post-mitotic cells. *Cell*, *136*(2), 284–295. https://doi.org/10.1016/j.cell.2008.11.037

Daoud, H., Belzil, V., Martins, S., Sabbagh, M., Provencher, P., Lacomblez, L., Meininger, V., Camu, W., Dupré, N., Dion, P. A., & Rouleau, G. A. (2011). Association of Long ATXN2 CAG Repeat Sizes With Increased Risk of Amyotrophic Lateral Sclerosis. *Archives of Neurology*, *68*(6), 739–742. https://doi.org/10.1001/archneurol.2011.111

Daoud, H., Suhail, H., Szuto, A., Camu, W., Salachas, F., Meininger, V., Bouchard, J.-P., Dupré, N., Dion, P. A., & Rouleau, G. A. (2012). UBQLN2 mutations are rare in French and French–Canadian amyotrophic lateral sclerosis. *Neurobiology of Aging*, *33*(9), 2230.e1-2230.e5. https://doi.org/10.1016/j.neurobiolaging.2012.03.015

Daoud, H., Zhou, S., Noreau, A., Sabbagh, M., Belzil, V., Dionne-Laporte, A., Tranchant, C., Dion, P., & Rouleau, G. A. (2012). Exome sequencing reveals SPG11 mutations causing juvenile ALS. *Neurobiology of Aging*, *33*(4), 839.e5-9. https://doi.org/10.1016/j.neurobiolaging.2011.11.012

David, A., Bennink, J. R., & Yewdell, J. W. (2013). Emetine optimally facilitates nascent chain puromycylation and potentiates the RiboPuromycylation Method (RPM) applied to inert cells. *Histochemistry and Cell Biology*, *139*(3), 501–504. https://doi.org/10.1007/s00418-012-1063-8

Davis, S. A., Itaman, S., Khalid-Janney, C. M., Sherard, J. A., Dowell, J. A., Cairns, N. J., & Gitcho, M. A. (2018). TDP-43 interacts with mitochondrial proteins critical for mitophagy and mitochondrial dynamics. *Neuroscience Letters*, *678*, 8–15. https://doi.org/10.1016/j.neulet.2018.04.053

De Marco, G., Lomartire, A., Manera, U., Canosa, A., Grassano, M., Casale, F., Fuda, G., Salamone, P., Rinaudo, M. T., Colombatto, S., Moglia, C., Chiò, A., & Calvo, A. (2022). Effects of intracellular calcium accumulation on proteins encoded by the major genes underlying amyotrophic lateral sclerosis. *Scientific Reports*, *12*(1), 395. https://doi.org/10.1038/s41598-021-04267-8

Deflorio, C., Palma, E., Conti, L., Roseti, C., Manteca, A., Giacomelli, E., Catalano, M., Limatola, C., Inghilleri, M., & Grassi, F. (2012). Riluzole blocks human muscle acetylcholine receptors. *The Journal of Physiology*, *590*(10), 2519–2528. https://doi.org/10.1113/jphysiol.2012.230201

DeJesus-Hernandez, M., Mackenzie, I. R., Boeve, B. F., Boxer, A. L., Baker, M., Rutherford, N. J., Nicholson, A. M., Finch, N. A., Flynn, H., Adamson, J., Kouri, N., Wojtas, A., Sengdy, P., Hsiung, G.-Y. R., Karydas, A., Seeley, W. W., Josephs, K. A., Coppola, G., Geschwind, D. H., … Rademakers, R. (2011). Expanded GGGGCC Hexanucleotide Repeat in Noncoding Region of C9ORF72 Causes Chromosome 9p-Linked FTD and ALS. *Neuron*, *72*(2), 245–256. https://doi.org/10.1016/j.neuron.2011.09.011

Demy, D. L., Campanari, M. L., Munoz-Ruiz, R., Durham, H. D., Gentil, B. J., & Kabashi, E. (2020). Functional Characterization of Neurofilament Light Splicing and Misbalance in Zebrafish. *Cells*, *9*(5), 1238. https://doi.org/10.3390/cells9051238

Deng, H.-X., Chen, W., Hong, S.-T., Boycott, K. M., Gorrie, G. H., Siddique, N., Yang, Y., Fecto, F., Shi, Y., Zhai, H., Jiang, H., Hirano, M., Rampersaud, E., Jansen, G. H., Donkervoort, S., Bigio, E. H., Brooks, B. R., Ajroud, K., Sufit, R. L., … Siddique, T. (2011). Mutations in *UBQLN2* cause dominant X-linked juvenile and adult-onset ALS and ALS/dementia. *Nature*, *477*(7363), 211. https://doi.org/10.1038/nature10353

Deng, Z., Lim, J., Wang, Q., Purtell, K., Wu, S., Palomo, G. M., Tan, H., Manfredi, G., Zhao, Y., Peng, J., Hu, B., Chen, S., & Yue, Z. (2020). ALS-FTLD-linked mutations of SQSTM1/p62 disrupt selective autophagy and NFE2L2/NRF2 anti-oxidative stress pathway. *Autophagy*, *16*(5), 917–931. https://doi.org/10.1080/15548627.2019.1644076

Diaz-Garcia, S., Ko, V. I., Vazquez-Sanchez, S., Chia, R., Arogundade, O. A., Rodriguez, M. J., Traynor, B. J., Cleveland, D., & Ravits, J. (2021). Nuclear depletion of RNA-binding protein ELAVL3 (HuC) in sporadic and familial amyotrophic lateral sclerosis. *Acta Neuropathologica*. *142*, 985-1001 https://doi.org/10.1007/s00401-021-02374-4

Ding, X., Gu, S., Xue, S., & Luo, S.-Z. (2021). Disease-associated mutations affect TIA1 phase separation and aggregation in a proline-dependent manner. *Brain Research*, *1768*, 147589. https://doi.org/10.1016/j.brainres.2021.147589

Donato, R., Sorci, G., & Giambanco, I. (2017). S100A6 protein: Functional roles. *Cellular and Molecular Life Sciences*, *74*(15), 2749–2760. https://doi.org/10.1007/s00018-017-2526-9

Donnelly, C. J., Zhang, P.-W., Pham, J. T., Haeusler, A. R., Mistry, N. A., Vidensky, S., Daley, E. L., Poth, E. M., Hoover, B., Fines, D. M., Maragakis, N., Tienari, P. J., Petrucelli, L., Traynor, B. J., Wang, J., Rigo, F., Bennett, C. F., Blackshaw, S., Sattler, R., & Rothstein, J. D. (2013). RNA Toxicity from the ALS/FTD C9ORF72 Expansion Is Mitigated by Antisense Intervention. *Neuron*, *80*(2), 415–428. https://doi.org/10.1016/j.neuron.2013.10.015

Dormann, D., Rodde, R., Edbauer, D., Bentmann, E., Fischer, I., Hruscha, A., Than, M. E., Mackenzie, I. R. A., Capell, A., Schmid, B., Neumann, M., & Haass, C. (2010). ALS-associated fused in sarcoma (FUS) mutations disrupt Transportin-mediated nuclear import. *The EMBO Journal*, *29*(16), 2841–2857. https://doi.org/10.1038/emboj.2010.143

Douville, R. N., & Nath, A. (2017). Human Endogenous Retrovirus-K and TDP-43 Expression Bridges ALS and HIV Neuropathology. *Frontiers in Microbiology*, *8*. https://doi.org/10.3389/fmicb.2017.01986

Drexler, H. G., & Uphoff, C. C. (2002). Mycoplasma contamination of cell cultures: Incidence, sources, effects, detection, elimination, prevention. *Cytotechnology*, *39*(2), 75–90. https://doi.org/10.1023/A:1022913015916

Dyer, M. S., Woodhouse, A., & Blizzard, C. A. (2021). Cytoplasmic Human TDP-43 Mislocalization Induces Widespread Dendritic Spine Loss in Mouse Upper Motor Neurons. *Brain Sciences*, *11*(7), 883. https://doi.org/10.3390/brainsci11070883

Eaton, B. A., Fetter, R. D., & Davis, G. W. (2002). Dynactin Is Necessary for Synapse Stabilization. *Neuron*, *34*(5), 729–741. https://doi.org/10.1016/S0896-6273(02)00721-3

Eck, R. J., Kraemer, B. C., & Liachko, N. F. (2021). Regulation of TDP-43 phosphorylation in aging and disease. *GeroScience*, *43*(4), 1605–1614. https://doi.org/10.1007/s11357-021-00383-5

Ederle, H., & Dormann, D. (2017). TDP-43 and FUS en route from the nucleus to the cytoplasm. *FEBS Letters*, *591*(11), 1489–1507. https://doi.org/10.1002/1873-3468.12646

Ederle, H., Funk, C., Abou-Ajram, C., Hutten, S., Funk, E. B. E., Kehlenbach, R. H., Bailer, S. M., & Dormann, D. (2018). Nuclear egress of TDP-43 and FUS occurs independently of Exportin-1/CRM1. *Scientific Reports*, *8*. https://doi.org/10.1038/s41598-018-25007-5

Efrat, S. (2021). Epigenetic Memory: Lessons From iPS Cells Derived From Human β Cells. *Frontiers in Endocrinology*, *11*. https://www.frontiersin.org/article/10.3389/fendo.2020.614234

Egawa, N., Kitaoka, S., Tsukita, K., Naitoh, M., Takahashi, K., Yamamoto, T., Adachi, F., Kondo, T., Okita, K., Asaka, I., Aoi, T., Watanabe, A., Yamada, Y., Morizane, A., Takahashi, J., Ayaki, T., Ito, H., Yoshikawa, K., Yamawaki, S., … Inoue, H. (2012). Drug screening for ALS using patient-

specific induced pluripotent stem cells. *Science Translational Medicine*, *4*(145), 145ra104. https://doi.org/10.1126/scitranslmed.3004052

Eitan, C., Siany, A., Barkan, E., Olender, T., van Eijk, K. R., Moisse, M., Farhan, S. M. K., Danino, Y. M., Yanowski, E., Marmor-Kollet, H., Rivkin, N., Yacovzada, N. S., Hung, S.-T., Cooper-Knock, J., Yu, C.-H., Louis, C., Masters, S. L., Kenna, K. P., van der Spek, R. A. A., … Hornstein, E. (2022). Whole-genome sequencing reveals that variants in the Interleukin 18 Receptor Accessory Protein 3'UTR protect against ALS. *Nature Neuroscience*, *25*(4), 433–445. https://doi.org/10.1038/s41593-022-01040-6

El Oussini, H., Bayer, H., Scekic-Zahirovic, J., Vercruysse, P., Sinniger, J., Dirrig-Grosch, S., Dieterlé, S., Echaniz-Laguna, A., Larmet, Y., Müller, K., Weishaupt, J. H., Thal, D. R., van Rheenen, W., van Eijk, K., Lawson, R., Monassier, L., Maroteaux, L., Roumier, A., Wong, P. C., … Dupuis, L. (2016). Serotonin 2B receptor slows disease progression and prevents degeneration of spinal cord mononuclear phagocytes in amyotrophic lateral sclerosis. *Acta Neuropathologica*, *131*(3), 465–480. https://doi.org/10.1007/s00401-016-1534-4

Elden, A. C., Kim, H.-J., Hart, M. P., Chen-Plotkin, A. S., Johnson, B. S., Fang, X., Armakola, M., Geser, F., Greene, R., Lu, M. M., Padmanabhan, A., Clay-Falcone, D., McCluskey, L., Elman, L., Juhr, D., Gruber, P. J., Rüb, U., Auburger, G., Trojanowski, J. Q., … Gitler, A. D. (2010). Ataxin-2 intermediate-length polyglutamine expansions are associated with increased risk for ALS. *Nature*, *466*(7310), 1069–1075. https://doi.org/10.1038/nature09320

Enam, S. U., Zinshteyn, B., Goldman, D. H., Cassani, M., Livingston, N. M., Seydoux, G., & Green, R. (2020). Puromycin reactivity does not accurately localize translation at the subcellular level. *ELife*, *9*, e60303. https://doi.org/10.7554/eLife.60303

Fang, M. Y., Markmiller, S., Vu, A. Q., Javaherian, A., Dowdle, W. E., Jolivet, P., Bushway, P. J., Castello, N. A., Baral, A., Chan, M. Y., Linsley, J. W., Linsley, D., Mercola, M., Finkbeiner, S., Lecuyer, E., Lewcock, J. W., & Yeo, G. W. (2019). Small-Molecule Modulation of TDP-43 Recruitment to Stress Granules Prevents Persistent TDP-43 Accumulation in ALS/FTD. *Neuron*, *103*(5), 802-819.e11. https://doi.org/10.1016/j.neuron.2019.05.048

Fang, T., Khleifat, A. A., Meurgey, J.-H., Jones, A., Leigh, P. N., Bensimon, G., & Al-Chalabi, A. (2018). Stage at which riluzole treatment prolongs survival in patients with amyotrophic lateral sclerosis: A retrospective analysis of data from a dose-ranging study. *The Lancet Neurology*, *17*(5), 416–422. https://doi.org/10.1016/S1474-4422(18)30054-1

Farnaes, L., & Ditzel, H. J. (2003). Dissecting the Cellular Functions of Annexin XI Using Recombinant Human Annexin XI-specific Autoantibodies Cloned by Phage Display. *Journal of Biological Chemistry*, *278*(35), 33120–33126. https://doi.org/10.1074/jbc.M210852200

Farrawell, N. E., Lambert-Smith, I. A., Warraich, S. T., Blair, I. P., Saunders, D. N., Hatters, D. M., & Yerbury, J. J. (2015). Distinct partitioning of ALS associated TDP-43, FUS and SOD1 mutants into cellular inclusions. *Scientific Reports*, *5*(1), 13416. https://doi.org/10.1038/srep13416

Farrawell, N. E., McAlary, L., Lum, J. S., Chisholm, C. G., Warraich, S. T., Blair, I. P., Vine, K. L., Saunders, D. N., & Yerbury, J. J. (2020). Ubiquitin Homeostasis Is Disrupted in TDP-43 and FUS Cell Models of ALS. *IScience*, *23*(11). https://doi.org/10.1016/j.isci.2020.101700

Faruq, M., Kumar, D., Wadhwa, S., Shamim, U., Mathur, A., Parveen, S., Garg, A., & Srivastava, A. K. (2019). Intrafamilial variable spastic paraplegia/ataxia/ALS phenotype linked to a novel KIF5A mutation. *Clinical Genetics*. *96*, 271-273. https://doi.org/10.1111/cge.13585

Fathi, A., Mathivanan, S., Kong, L., Petersen, A. J., Harder, C. R. K., Block, J., Miller, J. M., Bhattacharyya, A., Wang, D., & Zhang, S.-C. (2022). Chemically induced senescence in human stem cell-derived neurons promotes phenotypic presentation of neurodegeneration. *Aging Cell*, *21*(1), e13541. https://doi.org/10.1111/acel.13541

Fazal, R., Boeynaems, S., Swijsen, A., De Decker, M., Fumagalli, L., Moisse, M., Vanneste, J., Guo, W., Boon, R., Vercruysse, T., Eggermont, K., Swinnen, B., Beckers, J., Pakravan, D., Vandoorne, T., Vanden Berghe, P., Verfaillie, C., Van Den Bosch, L., & Van Damme, P. (2021). HDAC6 inhibition restores TDP-43 pathology and axonal transport defects in human motor neurons with TARDBP mutations. *The EMBO Journal*, *40*(7), e106177. https://doi.org/10.15252/embj.2020106177

Fecto, F., Yan, J., Vemula, S. P., Liu, E., Yang, Y., Chen, W., Zheng, J. G., Shi, Y., Siddique, N., Arrat, H., Donkervoort, S., Ajroud-Driss, S., Sufit, R. L., Heller, S. L., Deng, H.-X., & Siddique, T. (2011). SQSTM1 Mutations in Familial and Sporadic Amyotrophic Lateral Sclerosis. *Archives of Neurology*, *68*(11), 1440–1446. https://doi.org/10.1001/archneurol.2011.250

Feigin, V. L., Abajobir, A. A., Abate, K. H., Abd-Allah, F., Abdulle, A. M., Abera, S. F., Abyu, G. Y., Ahmed, M. B., Aichour, A. N., Aichour, I., Aichour, M. T. E., Akinyemi, R. O., Alabed, S., Al-Raddadi, R., Alvis-Guzman, N., Amare, A. T., Ansari, H., Anwari, P., Ärnlöv, J., … Vos, T. (2017). Global, regional, and national burden of neurological disorders during 1990–2015: A systematic analysis for the Global Burden of Disease Study 2015. *The Lancet Neurology*, *16*(11), 877–897. https://doi.org/10.1016/S1474-4422(17)30299-5

Feneberg, E., Charles, P. D., Finelli, M. J., Scott, C., Kessler, B. M., Fischer, R., Ansorge, O., Gray, E., Talbot, K., & Turner, M. R. (2020). Detection and Quantification of Novel C-terminal TDP-43 Fragments in ALS-TDP. *Brain Pathology*, *31*(4), e12923. https://doi.org/10.1111/bpa.12923

Feneberg, E., Turner, M. R., Ansorge, O., & Talbot, K. (2020). Amyotrophic lateral sclerosis with a heterozygous D91A SOD1 variant and classical ALS-TDP neuropathology. *Neurology*, *95*(13), 595–596. https://doi.org/10.1212/WNL.0000000000010587

Fernandopulle, M., Wang, G., Nixon-Abell, J., Qamar, S., Balaji, V., Morihara, R., & St George-Hyslop, P. H. (2019). Inherited and Sporadic Amyotrophic Lateral Sclerosis and Fronto-Temporal Lobar Degenerations arising from Pathological Condensates of Phase Separating Proteins. *Human Molecular Genetics*, *28*(R2), R187–R196. https://doi.org/10.1093/hmg/ddz162

Ferraiuolo, L., Meyer, K., Sherwood, T. W., Vick, J., Likhite, S., Frakes, A., Miranda, C. J., Braun, L., Heath, P. R., Pineda, R., Beattie, C. E., Shaw, P. J., Askwith, C. C., McTigue, D., & Kaspar, B. K. (2016). Oligodendrocytes contribute to motor neuron death in ALS via SOD1-dependent mechanism. *Proceedings of the National Academy of Sciences*, *113*(42), E6496–E6505. https://doi.org/10.1073/pnas.1607496113

Fiesel, F. C., Schurr, C., Weber, S. S., & Kahle, P. J. (2011). TDP-43 knockdown impairs neurite outgrowth dependent on its target histone deacetylase 6. *Molecular Neurodegeneration*, *6*, 64. https://doi.org/10.1186/1750-1326-6-64

Figlewicz, D. A., Krizus, A., Martinoli, M. G., Meininger, V., Dib, M., Rouleau, G. A., & Julien, J. P. (1994). Variants of the heavy neurofilament subunit are associated with the development of amyotrophic lateral sclerosis. *Human Molecular Genetics*, *3*(10), 1757–1761. https://doi.org/10.1093/hmg/3.10.1757

Figley, M. D., Gu, W., Nanson, J. D., Shi, Y., Sasaki, Y., Cunnea, K., Malde, A. K., Jia, X., Luo, Z., Saikot, F. K., Mosaiab, T., Masic, V., Holt, S., Hartley-Tassell, L., McGuinness, H. Y., Manik, M. K., Bosanac, T., Landsberg, M. J., Kerry, P. S., … Ve, T. (2021). SARM1 is a metabolic sensor activated by an increased NMN/NAD+ ratio to trigger axon degeneration. *Neuron*, *109*(7), 1118-1136.e11. https://doi.org/10.1016/j.neuron.2021.02.009

Filiano, A. J., Martens, L. H., Young, A. H., Warmus, B. A., Zhou, P., Diaz-Ramirez, G., Jiao, J., Zhang, Z., Huang, E. J., Gao, F.-B., Farese, R. V., & Roberson, E. D. (2013). Dissociation of frontotemporal dementia-related deficits and neuroinflammation in progranulin haploinsufficient mice. *The Journal of Neuroscience: The Official Journal of the Society for Neuroscience*, *33*(12), 5352–5361. https://doi.org/10.1523/JNEUROSCI.6103-11.2013

Fiore, M., Parisio, R., Filippini, T., Mantione, V., Platania, A., Odone, A., Signorelli, C., Pietrini, V., Mandrioli, J., Teggi, S., Costanzini, S., Antonio, C., Zuccarello, P., Oliveri Conti, G., Nicoletti, A., Zappia, M., Vinceti, M., & Ferrante, M. (2020). Living near waterbodies as a proxy of cyanobacteria exposure and risk of amyotrophic lateral sclerosis: A population based case-control study. *Environmental Research*, *186*, 109530. https://doi.org/10.1016/j.envres.2020.109530

Fischer, J. W., Busa, V. F., Shao, Y., & Leung, A. K. L. (2020). Structure-Mediated RNA Decay by UPF1 and G3BP1. *Molecular Cell*, *78*(1), 70-84.e6. https://doi.org/10.1016/j.molcel.2020.01.021

Fischer, L. R., Culver, D. G., Tennant, P., Davis, A. A., Wang, M., Castellano-Sanchez, A., Khan, J., Polak, M. A., & Glass, J. D. (2004). Amyotrophic lateral sclerosis is a distal axonopathy: Evidence in

mice and man. *Experimental Neurology*, *185*(2), 232–240. https://doi.org/10.1016/j.expneurol.2003.10.004

Forostyak, S., Forostyak, O., Kwok, J. C. F., Romanyuk, N., Rehorova, M., Kriska, J., Dayanithi, G., Raha-Chowdhury, R., Jendelova, P., Anderova, M., Fawcett, J. W., & Sykova, E. (2020). Transplantation of Neural Precursors Derived from Induced Pluripotent Cells Preserve Perineuronal Nets and Stimulate Neural Plasticity in ALS Rats. *International Journal of Molecular Sciences*, *21*(24), 9593. https://doi.org/10.3390/ijms21249593

Fortuna, T. R., Kour, S., Anderson, E. N., Ward, C., Rajasundaram, D., Donnelly, C. J., Hermann, A., Wyne, H., Shewmaker, F., & Pandey, U. B. (2021). DDX17 is involved in DNA damage repair and modifies FUS toxicity in an RGG-domain dependent manner. *Acta Neuropathologica*, *142*, 515-536. https://doi.org/10.1007/s00401-021-02333-z

Fournier, C. N., Bedlack, R., Quinn, C., Russell, J., Beckwith, D., Kaminski, K. H., Tyor, W., Hertzberg, V., James, V., Polak, M., & Glass, J. D. (2020). Development and Validation of the Rasch-Built Overall Amyotrophic Lateral Sclerosis Disability Scale (ROADS). *JAMA Neurology*, *77*(4), 480–488. https://doi.org/10.1001/jamaneurol.2019.4490

Franchini, D.-M., Lanvin, O., Tosolini, M., Patras de Campaigno, E., Cammas, A., Péricart, S., Scarlata, C.-M., Lebras, M., Rossi, C., Ligat, L., Pont, F., Arimondo, P. B., Laurent, C., Ayyoub, M., Despas, F., Lapeyre-Mestre, M., Millevoi, S., & Fournié, J.-J. (2019). Microtubule-Driven Stress Granule Dynamics Regulate Inhibitory Immune Checkpoint Expression in T Cells. *Cell Reports*, *26*(1), 94-107.e7. https://doi.org/10.1016/j.celrep.2018.12.014

François-Moutal, L., Scott, D. D., Ambrose, A. J., Zerio, C. J., Rodriguez-Sanchez, M., Dissanayake, K., May, D. G., Carlson, J. M., Barbieri, E., Moutal, A., Roux, K. J., Shorter, J., Khanna, R., Barmada, S. J., McGurk, L., & Khanna, M. (2022). Heat shock protein Grp78/BiP/HspA5 binds directly to TDP-43 and mitigates toxicity associated with disease pathology. *Scientific Reports*, *12*(1), 8140. https://doi.org/10.1038/s41598-022-12191-8

Freibaum, B. D., Chitta, R., High, A. A., & Taylor, J. P. (2010). Global analysis of TDP-43 interacting proteins reveals strong association with RNA splicing and translation machinery. *Journal of Proteome Research*, *9*(2), 1104–1120. https://doi.org/10.1021/pr901076y

Freibaum, B. D., Lu, Y., Lopez-Gonzalez, R., Kim, N. C., Almeida, S., Lee, K.-H., Badders, N., Valentine, M., Miller, B. L., Wong, P. C., Petrucelli, L., Kim, H. J., Gao, F.-B., & Taylor, J. P. (2015). GGGGCC repeat expansion in C9orf72 compromises nucleocytoplasmic transport. *Nature*, *525*(7567), 129–133. https://doi.org/10.1038/nature14974

Freischmidt, A., Goswami, A., Limm, K., Zimyanin, V. L., Demestre, M., Glaß, H., Holzmann, K., Helferich, A. M., Brockmann, S. J., Tripathi, P., Yamoah, A., Poser, I., Oefner, P. J., Böckers, T. M., Aronica, E., Ludolph, A. C., Andersen, P. M., Hermann, A., Weis, J., … Weishaupt, J. H. (2021). A serum microRNA sequence reveals fragile X protein pathology in amyotrophic lateral sclerosis. *Brain*, *144*(4), 1214–1229. https://doi.org/10.1093/brain/awab018

Freischmidt, A., Wieland, T., Richter, B., Ruf, W., Schaeffer, V., Müller, K., Marroquin, N., Nordin, F., Hübers, A., Weydt, P., Pinto, S., Press, R., Millecamps, S., Molko, N., Bernard, E., Desnuelle, C., Soriani, M.-H., Dorst, J., Graf, E., … Weishaupt, J. H. (2015). Haploinsufficiency of TBK1 causes familial ALS and fronto-temporal dementia. *Nature Neuroscience*, *18*(5), 631–636. https://doi.org/10.1038/nn.4000

Fridovich, I. (1981). Superoxide Radical and Superoxide Dismutases. In D. L. Gilbert (Ed.), *Oxygen and Living Processes* (pp. 250–272). Springer. https://doi.org/10.1007/978-1-4612-5890-2_13

Frydrýšková, K., Mašek, T., & Pospíšek, M. (2020). Changing faces of stress: Impact of heat and arsenite treatment on the composition of stress granules. *Wiley Interdisciplinary Reviews. RNA*, e1596. https://doi.org/10.1002/wrna.1596

Fujimori, K., Ishikawa, M., Otomo, A., Atsuta, N., Nakamura, R., Akiyama, T., Hadano, S., Aoki, M., Saya, H., Sobue, G., & Okano, H. (2018). Modeling sporadic ALS in iPSC-derived motor neurons identifies a potential therapeutic agent. *Nature Medicine*, *24*(10), 1579–1589. https://doi.org/10.1038/s41591-018-0140-5

Fujimura, K., Katahira, J., Kano, F., Yoneda, Y., & Murata, M. (2009). Microscopic dissection of the process of stress granule assembly. *Biochimica et Biophysica Acta (BBA) - Molecular Cell Research*, *1793*(11), 1728–1737. https://doi.org/10.1016/j.bbamcr.2009.08.010

Fukuda, Y., Pazyra-Murphy, M. F., Silagi, E. S., Tasdemir-Yilmaz, O. E., Li, Y., Rose, L., Yeoh, Z. C., Vangos, N. E., Geffken, E. A., Seo, H.-S., Adelmant, G., Bird, G. H., Walensky, L. D., Marto, J. A., Dhe-Paganon, S., & Segal, R. A. (2021). Binding and transport of SFPQ-RNA granules by KIF5A/KLC1 motors promotes axon survival. *The Journal of Cell Biology*, *220*(1), e202005051. https://doi.org/10.1083/jcb.202005051

Fumagalli, L., Young, F. L., Boeynaems, S., Decker, M. D., Mehta, A. R., Swijsen, A., Fazal, R., Guo, W., Moisse, M., Beckers, J., Dedeene, L., Selvaraj, B. T., Vandoorne, T., Madan, V., Blitterswijk, M. van, Raitcheva, D., McCampbell, A., Poesen, K., Gitler, A. D., … Damme, P. V. (2021). C9orf72-derived arginine-containing dipeptide repeats associate with axonal transport machinery and impede microtubule-based motility. *Science Advances*, *7*(15), eabg3013. https://doi.org/10.1126/sciadv.abg3013

Furge, L. L., Chen, K., & Cohen, S. (1999). Annexin VII and Annexin XI Are Tyrosine Phosphorylated in Peroxovanadate-treated Dogs and in Platelet-derived Growth Factor-treated Rat Vascular Smooth Muscle Cells. *Journal of Biological Chemistry*, *274*(47), 33504–33509. https://doi.org/10.1074/jbc.274.47.33504

Gadgil, A., Walczak, A., Stępień, A., Mechtersheimer, J., Nishimura, A. L., Shaw, C. E., Ruepp, M.-D., & Raczyńska, K. D. (2021). ALS-linked FUS mutants affect the localization of U7 snRNP and replication-dependent histone gene expression in human cells. *Scientific Reports*, *11*(1), 11868. https://doi.org/10.1038/s41598-021-91453-3

Gal, J., Zhang, J., Kwinter, D. M., Zhai, J., Jia, H., Jia, J., & Zhu, H. (2011). Nuclear localization sequence of FUS and induction of stress granules by ALS mutants. *Neurobiology of Aging*, *32*(12), 2323.e27-2323.e40. https://doi.org/10.1016/j.neurobiolaging.2010.06.010

Gall, L. L., Duddy, W. J., Martinat, C., Mariot, V., Connolly, O., Milla, V., Anakor, E., Ouandaogo, Z. G., Millecamps, S., Lainé, J., Vijayakumar, U. G., Knoblach, S., Raoul, C., Lucas, O., Loeffler, J. P., Bede, P., Behin, A., Blasco, H., Bruneteau, G., … Pradat, P. F. (2021). Muscle cells of sporadic ALS patients secrete neurotoxic vesicles. *MedRxiv*, https://doi.org/10.1101/2021.03.11.21252078

Gao, J., Wang, L., Ren, X., Dunn, J. R., Peters, A., Miyagi, M., Fujioka, H., Zhao, F., Askwith, C., Liang, J., & Wang, X. (2021). Translational regulation in the brain by TDP-43 phase separation. *Journal of Cell Biology*, *220*(10), e202101019. https://doi.org/10.1083/jcb.202101019

Garofalo, S., Cocozza, G., Porzia, A., Inghilleri, M., Raspa, M., Scavizzi, F., Aronica, E., Bernardini, G., Peng, L., Ransohoff, R. M., Santoni, A., & Limatola, C. (2020). Natural killer cells modulate motor neuron-immune cell cross talk in models of Amyotrophic Lateral Sclerosis. *Nature Communications*, *11*(1), 1773. https://doi.org/10.1038/s41467-020-15644-8

Garone, M. G., Alfano, V., Salvatori, B., Braccia, C., Peruzzi, G., Colantoni, A., Bozzoni, I., Armirotti, A., & Rosa, A. (2020). Proteomics analysis of FUS mutant human motoneurons reveals altered regulation of cytoskeleton and other ALS-linked proteins via 3'UTR binding. *Scientific Reports*, *10*(1), 11827. https://doi.org/10.1038/s41598-020-68794-6

Garone, M. G., Birsa, N., Rosito, M., Salaris, F., Mochi, M., de Turris, V., Nair, R. R., Cunningham, T. J., Fisher, E. M. C., Morlando, M., Fratta, P., & Rosa, A. (2021). ALS-related FUS mutations alter axon growth in motoneurons and affect HuD/ELAVL4 and FMRP activity. *Communications Biology*, *4*(1), 1–17. https://doi.org/10.1038/s42003-021-02538-8

Gautam, M., Gunay, A., Chandel, N. S., & Ozdinler, P. H. (2022). Mitochondrial dysregulation occurs early in ALS motor cortex with TDP-43 pathology and suggests maintaining NAD+ balance as a therapeutic strategy. *Scientific Reports*, *12*(1), 4287. https://doi.org/10.1038/s41598-022-08068-5

Gautam, M., Jara, J. H., Kocak, N., Rylaarsdam, L. E., Kim, K. D., Bigio, E. H., & Hande Özdinler, P. (2019). Mitochondria, ER, and nuclear membrane defects reveal early mechanisms for upper motor neuron vulnerability with respect to TDP-43 pathology. *Acta Neuropathologica*, *137*(1), 47–69. https://doi.org/10.1007/s00401-018-1934-8

Gautam, M., Xie, E. F., Kocak, N., & Ozdinler, P. H. (2019). Mitoautophagy: A Unique Self-Destructive Path Mitochondria of Upper Motor Neurons With TDP-43 Pathology Take, Very Early in ALS. *Frontiers in Cellular Neuroscience*, *13*. https://www.frontiersin.org/articles/10.3389/fncel.2019.00489

Geisow, M. J., Walker, J. H., Boustead, C., & Taylor, W. (1987). Annexins—New family of Ca2+-regulated-phospholipid binding protein. *Bioscience Reports*, *7*(4), 289–298. https://doi.org/10.1007/BF01121450

Genç, B., Jara, J. H., Lagrimas, A. K. B., Pytel, P., Roos, R. P., Mesulam, M. M., Geula, C., Bigio, E. H., & Özdinler, P. H. (2017). Apical dendrite degeneration, a novel cellular pathology for Betz cells in ALS. *Scientific Reports*, *7*(1), 41765. https://doi.org/10.1038/srep41765

Genin, E. C., Madji Hounoum, B., Bannwarth, S., Fragaki, K., Lacas-Gervais, S., Mauri-Crouzet, A., Lespinasse, F., Neveu, J., Ropert, B., Augé, G., Cochaud, C., Lefebvre-Omar, C., Bigou, S., Chiot, A., Mochel, F., Boillée, S., Lobsiger, C. S., Bohl, D., Ricci, J.-E., & Paquis-Flucklinger, V. (2019). Mitochondrial defect in muscle precedes neuromuscular junction degeneration and motor neuron death in CHCHD10S59L/+ mouse. *Acta Neuropathologica*, *138*(1), 123–145. https://doi.org/10.1007/s00401-019-01988-z

Genin, E. C., Plutino, M., Bannwarth, S., Villa, E., Cisneros-Barroso, E., Roy, M., Ortega-Vila, B., Fragaki, K., Lespinasse, F., Pinero-Martos, E., Augé, G., Moore, D., Burté, F., Lacas-Gervais, S., Kageyama, Y., Itoh, K., Yu-Wai-Man, P., Sesaki, H., Ricci, J., … Paquis-Flucklinger, V. (2016). CHCHD10 mutations promote loss of mitochondrial cristae junctions with impaired mitochondrial genome maintenance and inhibition of apoptosis. *EMBO Molecular Medicine*, *8*(1), 58–72. https://doi.org/10.15252/emmm.201505496

Gerber, Y., Privat, A., & Perrin, F. (2013). Gacyclidine improves the survival and reduces motor deficits in a mouse model of amyotrophic lateral sclerosis. *Frontiers in Cellular Neuroscience*, *7*. https://www.frontiersin.org/article/10.3389/fncel.2013.00280

Gerke, V., & Moss, S. E. (2002). Annexins: From structure to function. *Physiol Rev*, *82*(2), 331-371. https://doi.org/10.1152/physrev.00030.2001

Giampetruzzi, A., Danielson, E. W., Gumina, V., Jeon, M., Boopathy, S., Brown, R. H., Ratti, A., Landers, J. E., & Fallini, C. (2019). Modulation of actin polymerization affects nucleocytoplasmic transport in multiple forms of amyotrophic lateral sclerosis. *Nature Communications*, *10*(1), 1–15. https://doi.org/10.1038/s41467-019-11837-y

Gibbs, K. L., Kalmar, B., Rhymes, E. R., Fellows, A. D., Ahmed, M., Whiting, P., Davies, C. H., Greensmith, L., & Schiavo, G. (2018). Inhibiting p38 MAPK alpha rescues axonal retrograde transport defects in a mouse model of ALS. *Cell Death & Disease*, *9*(6), 1–16. https://doi.org/10.1038/s41419-018-0624-8

Gijselinck, I., Van Mossevelde, S., van der Zee, J., Sieben, A., Philtjens, S., Heeman, B., Engelborghs, S., Vandenbulcke, M., De Baets, G., Bäumer, V., Cuijt, I., Van den Broeck, M., Peeters, K., Mattheijssens, M., Rousseau, F., Vandenberghe, R., De Jonghe, P., Cras, P., De Deyn, P. P., … BELNEU Consortium. (2015). Loss of TBK1 is a frequent cause of frontotemporal dementia in a Belgian cohort. *Neurology*, *85*(24), 2116–2125. https://doi.org/10.1212/WNL.0000000000002220

Gilley, J., Jackson, O., Pipis, M., Estiar, M. A., Al-Chalabi, A., Danzi, M. C., van Eijk, K. R., Goutman, S. A., Harms, M. B., Houlden, H., Iacoangeli, A., Kaye, J., Lima, L., Ravits, J., Rouleau, G. A., Schüle, R., Xu, J., Züchner, S., Cooper-Knock, J., … Coleman, M. P. (2021). Enrichment of SARM1 alleles encoding variants with constitutively hyperactive NADase in patients with ALS and other motor nerve disorders. *ELife*, *10*, e70905. https://doi.org/10.7554/eLife.70905

Giribaldi, F., Milanese, M., Bonifacino, T., Anna Rossi, P. I., Di Prisco, S., Pittaluga, A., Tacchetti, C., Puliti, A., Usai, C., & Bonanno, G. (2013). Group I metabotropic glutamate autoreceptors induce abnormal glutamate exocytosis in a mouse model of amyotrophic lateral sclerosis. *Neuropharmacology*, *66*, 253–263. https://doi.org/10.1016/j.neuropharm.2012.05.018

Gladman, M., & Zinman, L. (2015). The economic impact of amyotrophic lateral sclerosis: A systematic review. *Expert Review of Pharmacoeconomics & Outcomes Research*, *15*(3), 439–450. https://doi.org/10.1586/14737167.2015.1039941

Gomes, C., Sequeira, C., Barbosa, M., Cunha, C., Vaz, A. R., & Brites, D. (2020). Astrocyte regional diversity in ALS includes distinct aberrant phenotypes with common and causal pathological processes. *Experimental Cell Research*, *395*(2), 112209. https://doi.org/10.1016/j.yexcr.2020.112209

Gomes, C., Sequeira, C., Likhite, S., Dennys, C. N., Kolb, S. J., Shaw, P. J., Vaz, A. R., Kaspar, B. K., Meyer, K., & Brites, D. (2022). Neurotoxic Astrocytes Directly Converted from Sporadic and Familial ALS Patient Fibroblasts Reveal Signature Diversities and miR-146a Theragnostic Potential in Specific Subtypes. *Cells*, *11*(7), 1186. https://doi.org/10.3390/cells11071186

Gomez-Suaga, P., Mórotz, G. M., Markovinovic, A., Martín-Guerrero, S. M., Preza, E., Arias, N., Mayl, K., Aabdien, A., Gesheva, V., Nishimura, A., Annibali, A., Lee, Y., Mitchell, J. C., Wray, S., Shaw, C., Noble, W., & Miller, C. C. J. (2022). Disruption of ER-mitochondria tethering and signalling in C9orf72-associated amyotrophic lateral sclerosis and frontotemporal dementia. *Aging Cell*, e13549. https://doi.org/10.1111/acel.13549

Gómez-Tortosa, E., Gallego, J., Guerrero-López, R., Marcos, A., Gil-Neciga, E., Sainz, M. J., Díaz, A., Franco-Macías, E., Trujillo-Tiebas, M. J., Ayuso, C., & Pérez-Pérez, J. (2013). C9ORF72 hexanucleotide expansions of 20-22 repeats are associated with frontotemporal deterioration. *Neurology*, *80*(4), 366–370. https://doi.org/10.1212/WNL.0b013e31827f08ea

Gordon, P. M., Hamid, F., Makeyev, E. V., & Houart, C. (2021). A conserved role for the ALS-linked splicing factor SFPQ in repression of pathogenic cryptic last exons. *Nature Communications*, *12*(1), 1918. https://doi.org/10.1038/s41467-021-22098-z

Goutman, S. A., Hardiman, O., Al-Chalabi, A., Chió, A., Savelieff, M. G., Kiernan, M. C., & Feldman, E. L. (2022). Emerging insights into the complex genetics and pathophysiology of amyotrophic lateral sclerosis. *The Lancet Neurology*. *21*(5), 465-479. https://doi.org/10.1016/S1474-4422(21)00414-2

Graber, T. E., Hébert-Seropian, S., Khoutorsky, A., David, A., Yewdell, J. W., Lacaille, J.-C., & Sossin, W. S. (2013). Reactivation of stalled polyribosomes in synaptic plasticity. *Proceedings of the National Academy of Sciences*, *110*(40), 16205–16210. https://doi.org/10.1073/pnas.1307747110

Gruijs da Silva, L. A., Simonetti, F., Hutten, S., Riemenschneider, H., Sternburg, E. L., Pietrek, L. M., Gebel, J., Dötsch, V., Edbauer, D., Hummer, G., Stelzl, L. S., & Dormann, D. (2022). Disease-linked TDP-43 hyperphosphorylation suppresses TDP-43 condensation and aggregation. *The EMBO Journal*, e108443. https://doi.org/10.15252/embj.2021108443

Gundelfinger, E. D., Reissner, C., & Garner, C. C. (2016). Role of Bassoon and Piccolo in Assembly and Molecular Organization of the Active Zone. *Frontiers in Synaptic Neuroscience*, *7*. https://www.frontiersin.org/articles/10.3389/fnsyn.2015.00019

Guo, H., Lai, L., Butchbach, M. E. R., Stockinger, M. P., Shan, X., Bishop, G. A., & Lin, C. G. (2003). Increased expression of the glial glutamate transporter EAAT2 modulates excitotoxicity and delays the onset but not the outcome of ALS in mice. *Human Molecular Genetics*, *12*(19), 2519–2532. https://doi.org/10.1093/hmg/ddg267

Guo, Q., Lehmer, C., Martínez-Sánchez, A., Rudack, T., Beck, F., Hartmann, H., Pérez-Berlanga, M., Frottin, F., Hipp, M. S., Hartl, F. U., Edbauer, D., Baumeister, W., & Fernández-Busnadiego, R. (2018). In Situ Structure of Neuronal C9orf72 Poly-GA Aggregates Reveals Proteasome Recruitment. *Cell*, *172*(4), 696-705.e12. https://doi.org/10.1016/j.cell.2017.12.030

Guo, S.-M., Veneziano, R., Gordonov, S., Li, L., Danielson, E., Perez de Arce, K., Park, D., Kulesa, A. B., Wamhoff, E.-C., Blainey, P. C., Boyden, E. S., Cottrell, J. R., & Bathe, M. (2019). Multiplexed and high-throughput neuronal fluorescence imaging with diffusible probes. *Nature Communications*, *10*(1), 4377. https://doi.org/10.1038/s41467-019-12372-6

Guo, W., Naujock, M., Fumagalli, L., Vandoorne, T., Baatsen, P., Boon, R., Ordovás, L., Patel, A., Welters, M., Vanwelden, T., Geens, N., Tricot, T., Benoy, V., Steyaert, J., Lefebvre-Omar, C., Boesmans, W., Jarpe, M., Sterneckert, J., Wegner, F., … Van Den Bosch, L. (2017). HDAC6 inhibition reverses axonal transport defects in motor neurons derived from FUS-ALS patients. *Nature Communications*, *8*(1), 861. https://doi.org/10.1038/s41467-017-00911-y

Guttenplan, K. A., Weigel, M. K., Prakash, P., Wijewardhane, P. R., Hasel, P., Rufen-Blanchette, U., Münch, A. E., Blum, J. A., Fine, J., Neal, M. C., Bruce, K. D., Gitler, A. D., Chopra, G., Liddelow, S. A., & Barres, B. A. (2021). Neurotoxic reactive astrocytes induce cell death via saturated lipids. *Nature*, *599*(7883), 102–107. https://doi.org/10.1038/s41586-021-03960-y

Gwon, Y., Maxwell, B. A., Kolaitis, R.-M., Zhang, P., Kim, H. J., & Taylor, J. P. (2021). Ubiquitination of G3BP1 mediates stress granule disassembly in a context-specific manner. *Science*, *372*(6549). https://doi.org/10.1126/science.abf6548

Hadano, S., Hand, C. K., Osuga, H., Yanagisawa, Y., Otomo, A., Devon, R. S., Miyamoto, N., Showguchi-Miyata, J., Okada, Y., Singaraja, R., Figlewicz, D. A., Kwiatkowski, T., Hosler, B. A., Sagie, T., Skaug, J., Nasir, J., Brown, R. H., Scherer, S. W., Rouleau, G. A., … Ikeda, J.-E. (2001). A gene encoding a putative GTPase regulator is mutated in familial amyotrophic lateral sclerosis 2. *Nature Genetics*, *29*(2), 166–173. https://doi.org/10.1038/ng1001-166

Hagemann, C., Moreno Gonzalez, C., Guetta, L., Tyzack, G., Chiappini, C., Legati, A., Patani, R., & Serio, A. (2022). Axonal Length Determines Distinct Homeostatic Phenotypes in Human iPSC Derived Motor Neurons on a Bioengineered Platform. *Advanced Healthcare Materials*, e2101817. https://doi.org/10.1002/adhm.202101817

Haidet-Phillips, A. M., Hester, M. E., Miranda, C. J., Meyer, K., Braun, L., Frakes, A., Song, S., Likhite, S., Murtha, M. J., Foust, K. D., Rao, M., Eagle, A., Kammesheidt, A., Christensen, A., Mendell, J. R., Burghes, A. H. M., & Kaspar, B. K. (2011). Astrocytes from familial and sporadic ALS patients are toxic to motor neurons. *Nature Biotechnology*, *29*(9), 824. https://doi.org/10.1038/nbt.1957

Harjuhaahto, S., Rasila, T. S., Molchanova, S. M., Woldegebriel, R., Kvist, J., Konovalova, S., Sainio, M. T., Pennonen, J., Torregrosa-Muñumer, R., Ibrahim, H., Otonkoski, T., Taira, T., Ylikallio, E., & Tyynismaa, H. (2020). ALS and Parkinson's disease genes CHCHD10 and CHCHD2 modify synaptic transcriptomes in human iPSC-derived motor neurons. *Neurobiology of Disease*, *141*, 104940. https://doi.org/10.1016/j.nbd.2020.104940

Harlan, B. A., Killoy, K. M., Pehar, M., Liu, L., Auwerx, J., & Vargas, M. R. (2020). Evaluation of the NAD+ biosynthetic pathway in ALS patients and effect of modulating NAD+ levels in hSOD1-linked ALS mouse models. *Experimental Neurology*, *327*, 113219. https://doi.org/10.1016/j.expneurol.2020.113219

Harlan, B. A., Pehar, M., Sharma, D. R., Beeson, G., Beeson, C. C., & Vargas, M. R. (2016). Enhancing NAD+ Salvage Pathway Reverts the Toxicity of Primary Astrocytes Expressing Amyotrophic Lateral Sclerosis-linked Mutant Superoxide Dismutase 1 (SOD1). *Journal of Biological Chemistry*, *291*(20), 10836–10846. https://doi.org/10.1074/jbc.M115.698779

Harley, J., & Patani, R. (2020). Stress-Specific Spatiotemporal Responses of RNA-Binding Proteins in Human Stem-Cell-Derived Motor Neurons. *International Journal of Molecular Sciences*, *21*(21), 8346. https://doi.org/10.3390/ijms21218346

Harley, P., Neves, G., Riccio, F., Machado, C. B., Cheesbrough, A., R'Bibo, L., Burrone, J., & Lieberam, I. (2022). Pathogenic TDP-43 Disrupts Axon Initial Segment Structure and Neuronal Excitability in a Human iPSC Model of ALS. *bioRxiv*. https://doi.org/10.1101/2022.05.16.492186

Hartung, T., Rhein, M., Kalmbach, N., Thau-Habermann, N., Naujock, M., Müschen, L., Frieling, H., Sterneckert, J., Hermann, A., Wegner, F., & Petri, S. (2021). Methylation and Expression of Mutant FUS in Motor Neurons Differentiated From Induced Pluripotent Stem Cells From ALS Patients. *Frontiers in Cell and Developmental Biology*, *9*, 3162. https://doi.org/10.3389/fcell.2021.774751

Hasel, P., Dando, O., Jiwaji, Z., Baxter, P., Todd, A. C., Heron, S., Márkus, N. M., McQueen, J., Hampton, D. W., Torvell, M., Tiwari, S. S., McKay, S., Eraso-Pichot, A., Zorzano, A., Masgrau, R., Galea, E., Chandran, S., Wyllie, D. J. A., Simpson, T. I., & Hardingham, G. E. (2017). Neurons and neuronal activity control gene expression in astrocytes to regulate their development and metabolism. *Nature Communications*, *8*, 15132. https://doi.org/10.1038/ncomms15132

He, L., Zhu, C., Yu, X., Liu, X., Shu, M., & Jia, J. (2022). Circular RNA_0061587 is associated with the tumorigenesis of neurofibromatosis type 1. *Neurochemistry International*, *155*, 105299. https://doi.org/10.1016/j.neuint.2022.105299

Hedges, E. C., Topp, S., Shaw, C. E., & Nishimura, A. L. (2021). Generation of six induced pluripotent stem cell lines from patients with amyotrophic lateral sclerosis with associated genetic mutations in either FUS or ANXA11. *Stem Cell Research*, *52*, 102246. https://doi.org/10.1016/j.scr.2021.102246

Herta, T., Kersten, R., Chang, J.-C., Hubers, L., Go, S., Tolenaars, D., Paulusma, C. C., Nathanson, M. H., Elferink, R. O., Graaf, S. F. J. van de, & Beuers, U. (2021). Role of the IgG4-related cholangitis autoantigen annexin A11 in cholangiocyte protection. *Journal of Hepatology*, *76*(2), 319-331. https://doi.org/10.1016/j.jhep.2021.10.009

Herzog, E., Landry, M., Buhler, E., Bouali-Benazzouz, R., Legay, C., Henderson, C. E., Nagy, F., Dreyfus, P., Giros, B., & El Mestikawy, S. (2004). Expression of vesicular glutamate transporters, VGLUT1 and VGLUT2, in cholinergic spinal motoneurons. *The European Journal of Neuroscience*, *20*(7), 1752–1760. https://doi.org/10.1111/j.1460-9568.2004.03628.x

Hideyama, T., Yamashita, T., Aizawa, H., Tsuji, S., Kakita, A., Takahashi, H., & Kwak, S. (2012). Profound downregulation of the RNA editing enzyme ADAR2 in ALS spinal motor neurons. *Neurobiology of Disease*, *45*(3), 1121–1128. https://doi.org/10.1016/j.nbd.2011.12.033

Higashihara, M., Pavey, N., Bos, M. van den, Menon, P., Kiernan, M. C., & Vucic, S. (2021). Association of Cortical Hyperexcitability and Cognitive Impairment in Patients With Amyotrophic Lateral Sclerosis. *Neurology*, *96*(16), e2090–e2097. https://doi.org/10.1212/WNL.0000000000011798

Ho, T. S.-Y., & Rasband, M. N. (2011). Maintenance of Neuronal Polarity. *Developmental Neurobiology*, *71*(6), 474–482. https://doi.org/10.1002/dneu.20843

Ho, W. Y., Agrawal, I., Tyan, S.-H., Sanford, E., Chang, W.-T., Lim, K., Ong, J., Tan, B. S. Y., Moe, A. A. K., Yu, R., Wong, P., Tucker-Kellogg, G., Koo, E., Chuang, K.-H., & Ling, S.-C. (2021). Dysfunction in nonsense-mediated decay, protein homeostasis, mitochondrial function, and brain connectivity in ALS-FUS mice with cognitive deficits. *Acta Neuropathologica Communications*, *9*, 9. https://doi.org/10.1186/s40478-020-01111-4

Ho, W. Y., Chang, J.-C., Lim, K., Cazenave-Gassiot, A., Nguyen, A. T., Foo, J. C., Muralidharan, S., Viera-Ortiz, A., Ong, S. J. M., Hor, J. H., Agrawal, I., Hoon, S., Arogundade, O. A., Rodriguez, M. J., Lim, S. M., Kim, S. H., Ravits, J., Ng, S.-Y., Wenk, M. R., … Ling, S.-C. (2021). TDP-43 mediates SREBF2-regulated gene expression required for oligodendrocyte myelination. *Journal of Cell Biology*, *220*(9), e201910213. https://doi.org/10.1083/jcb.201910213

Hobson, B. D., Kong, L., Hartwick, E. W., Gonzalez, R. L., & Sims, P. A. (2020). Elongation inhibitors do not prevent the release of puromycylated nascent polypeptide chains from ribosomes. *ELife*, *9*, e60048. https://doi.org/10.7554/eLife.60048

Houen, G., & Trier, N. H. (2021). Epstein-Barr Virus and Systemic Autoimmune Diseases. *Frontiers in Immunology*, *11*, 3334. https://doi.org/10.3389/fimmu.2020.587380

Hoyaux, D., Alao, J., Fuchs, J., Kiss, R., Keller, B., Heizmann, C. W., Pochet, R., & Frermann, D. (2000). S100A6, a calcium- and zinc-binding protein, is overexpressed in SOD1 mutant mice, a model for amyotrophic lateral sclerosis. *Biochimica et Biophysica Acta (BBA) - Molecular Cell Research*, *1498*(2), 264–272. https://doi.org/10.1016/S0167-4889(00)00101-4

Hoyaux, D., Boom, A., Van Den Bosch, L., Belot, N., Martin, J.-J., Heizmann, C. W., Kiss, R., & Pochet, R. (2002). S100A6 Overexpression within Astrocytes Associated with Impaired Axons from Both ALS Mouse Model and Human Patients. *Journal of Neuropathology & Experimental Neurology*, *61*(8), 736–744. https://doi.org/10.1093/jnen/61.8.736

Hua, K., Li, Y., Zhao, Q., Fan, L., Tan, B., & Gu, J. (2018). Downregulation of Annexin A11 (ANXA11) Inhibits Cell Proliferation, Invasion, and Migration via the AKT/GSK-3β Pathway in Gastric Cancer. *Medical Science Monitor : International Medical Journal of Experimental and Clinical Research*, *24*, 149–160. https://doi.org/10.12659/MSM.905372

Huang, C. Y., Nicholson, M. W., Wang, J. Y., Ting, C. Y., Tsai, M. H., Cheng, Y. C., Liu, C. L., Chan, D. Z. H., Lee, Y. C., Hsu, C. C., Hsu, Y. H., Yang, C. F., Chang, C. M. C., Ruan, S. C., Lin, P. J., Lin, J. H.,

Chen, L. L., Hsieh, M. L., Cheng, Y. Y., … Hsieh, P. C. H. (2022). Population-based high-throughput toxicity screen of human iPSC-derived cardiomyocytes and neurons. *Cell Reports*, *39*(1). https://doi.org/10.1016/j.celrep.2022.110643

Huang, S., Xu, B., & Liu, Y. (2022). Calcium promotes α-synuclein liquid-liquid phase separation to accelerate amyloid aggregation. *Biochemical and Biophysical Research Communications*, *603*, 13–20. https://doi.org/10.1016/j.bbrc.2022.02.097

Huang, X., Roet, K. C. D., Zhang, L., Brault, A., Berg, A. P., Jefferson, A. B., Klug-McLeod, J., Leach, K. L., Vincent, F., Yang, H., Coyle, A. J., Jones, L. H., Frost, D., Wiskow, O., Chen, K., Maeda, R., Grantham, A., Dornon, M. K., Klim, J. R., … Woolf, C. J. (2021). Human amyotrophic lateral sclerosis excitability phenotype screen: Target discovery and validation. *Cell Reports*, *35*(10), 109224. https://doi.org/10.1016/j.celrep.2021.109224

Hubers, L. M., Vos, H., Schuurman, A. R., Erken, R., Oude Elferink, R. P., Burgering, B., van de Graaf, S. F. J., & Beuers, U. (2018). Annexin A11 is targeted by IgG4 and IgG1 autoantibodies in IgG4-related disease. *Gut*, *67*(4), 728–735. https://doi.org/10.1136/gutjnl-2017-314548

Hui-Yuen, J., McAllister, S., Koganti, S., Hill, E., & Bhaduri-McIntosh, S. (2011). Establishment of Epstein-Barr Virus Growth-transformed Lymphoblastoid Cell Lines. *Journal of Visualized Experiments : JoVE*, *57*, e3321. https://doi.org/10.3791/3321

Hulme, A. J., Maksour, S., Glover, M. S.-C., Miellet, S., & Dottori, M. (2021). Making neurons, made easy: The use of Neurogenin-2 in neuronal differentiation. *Stem Cell Reports*, *17*(1), 14-34. https://doi.org/10.1016/j.stemcr.2021.11.015

Iacoangeli, A., Al Khleifat, A., Jones, A. R., Sproviero, W., Shatunov, A., Opie-Martin, S., Morrison, K. E., Shaw, P. J., Shaw, C. E., Fogh, I., Dobson, R. J., Newhouse, S. J., Al-Chalabi, A., & Alzheimer's Disease Neuroimaging Initiative. (2019). C9orf72 intermediate expansions of 24–30 repeats are associated with ALS. *Acta Neuropathologica Communications*, *7*(1), 115. https://doi.org/10.1186/s40478-019-0724-4

Iguchi, Y., Katsuno, M., Niwa, J., Takagi, S., Ishigaki, S., Ikenaka, K., Kawai, K., Watanabe, H., Yamanaka, K., Takahashi, R., Misawa, H., Sasaki, S., Tanaka, F., & Sobue, G. (2013). Loss of TDP-43 causes age-dependent progressive motor neuron degeneration. *Brain: A Journal of Neurology*, *136*(5), 1371–1382. https://doi.org/10.1093/brain/awt029

Iino, S., Sudo, T., Niwa, T., Fukasawa, T., Hidaka, H., & Niki, I. (2000). Annexin XI may be involved in Ca2+- or GTP-γS-induced insulin secretion in the pancreatic β-cell. *FEBS Letters*, *479*(1), 46–50. https://doi.org/10.1016/S0014-5793(00)01877-9

Ikenaka, K., Ishigaki, S., Iguchi, Y., Kawai, K., Fujioka, Y., Yokoi, S., Abdelhamid, R. F., Nagano, S., Mochizuki, H., Katsuno, M., & Sobue, G. (2020). Characteristic Features of FUS Inclusions in Spinal Motor Neurons of Sporadic Amyotrophic Lateral Sclerosis. *Journal of Neuropathology & Experimental Neurology*, *79*(4), 370–377. https://doi.org/10.1093/jnen/nlaa003

Ikenaka, K., Kawai, K., Katsuno, M., Huang, Z., Jiang, Y.-M., Iguchi, Y., Kobayashi, K., Kimata, T., Waza, M., Tanaka, F., Mori, I., & Sobue, G. (2013). Dnc-1/dynactin 1 Knockdown Disrupts Transport of Autophagosomes and Induces Motor Neuron Degeneration. *PLOS ONE*, *8*(2), e54511. https://doi.org/10.1371/journal.pone.0054511

Iko, Y., Kodama, T. S., Kasai, N., Oyama, T., Morita, E. H., Muto, T., Okumura, M., Fujii, R., Takumi, T., Tate, S., & Morikawa, K. (2004). Domain Architectures and Characterization of an RNA-binding Protein, TLS. *Journal of Biological Chemistry*, *279*(43), 44834–44840. https://doi.org/10.1074/jbc.M408552200

Imamura, K., Izumi, Y., Watanabe, A., Tsukita, K., Woltjen, K., Yamamoto, T., Hotta, A., Kondo, T., Kitaoka, S., Ohta, A., Tanaka, A., Watanabe, D., Morita, M., Takuma, H., Tamaoka, A., Kunath, T., Wray, S., Furuya, H., Era, T., … Inoue, H. (2017). The Src/c-Abl pathway is a potential therapeutic target in amyotrophic lateral sclerosis. *Science Translational Medicine*, *9*(391). https://doi.org/10.1126/scitranslmed.aaf3962

Imamura, K., Yada, Y., Izumi, Y., Morita, M., Kawata, A., Arisato, T., Nagahashi, A., Enami, T., Tsukita, K., Kawakami, H., Nakagawa, M., Takahashi, R., & Inoue, H. (2021). Prediction model of ALS by deep learning with patient iPSCs. *Annals of Neurology*, *8*(6), 1227-1233. https://doi.org/10.1002/ana.26047

Imperatore, J. A., McAninch, D. S., Valdez-Sinon, A. N., Bassell, G. J., & Mihailescu, M. R. (2020). FUS Recognizes G Quadruplex Structures Within Neuronal mRNAs. *Frontiers in Molecular Biosciences*, *7*. https://www.frontiersin.org/article/10.3389/fmolb.2020.00006

Iradi, M. C. G., Triplett, J. C., Thomas, J. D., Davila, R., Crown, A. M., Brown, H., Lewis, J., Swanson, M. S., Xu, G., Rodriguez-Lebron, E., & Borchelt, D. R. (2018). Characterization of gene regulation and protein interaction networks for Matrin 3 encoding mutations linked to amyotrophic lateral sclerosis and myopathy. *Scientific Reports*, *8*, 4049. https://doi.org/10.1038/s41598-018-21371-4

Ishigaki, S., Masuda, A., Fujioka, Y., Iguchi, Y., Katsuno, M., Shibata, A., Urano, F., Sobue, G., & Ohno, K. (2012). Position-dependent FUS-RNA interactions regulate alternative splicing events and transcriptions. *Scientific Reports*, *2*, 529. https://doi.org/10.1038/srep00529

Ishigaki, S., Riku, Y., Fujioka, Y., Endo, K., Iwade, N., Kawai, K., Ishibashi, M., Yokoi, S., Katsuno, M., Watanabe, H., Mori, K., Akagi, A., Yokota, O., Terada, S., Kawakami, I., Suzuki, N., Warita, H., Aoki, M., Yoshida, M., & Sobue, G. (2020). Aberrant interaction between FUS and SFPQ in neurons in a wide range of FTLD spectrum diseases. *Brain*, *143*(8), 2398–2405. https://doi.org/10.1093/brain/awaa196

Ishiguro, A., Kimura, N., Noma, T., Shimo-Kon, R., Ishihama, A., & Kon, T. (2020). Molecular dissection of ALS-linked TDP-43—Involvement of the Gly-rich domain in interaction with G-quadruplex mRNA. *FEBS Letters*. https://doi.org/10.1002/1873-3468.13800

Ishiguro, A., Kimura, N., Watanabe, Y., Watanabe, S., & Ishihama, A. (2016). TDP-43 binds and transports G-quadruplex-containing mRNAs into neurites for local translation. *Genes to Cells*, *21*(5), 466–481. https://doi.org/10.1111/gtc.12352

Ivanov, P. A., Chudinova, E. M., & Nadezhdina, E. S. (2003). Disruption of microtubules inhibits cytoplasmic ribonucleoprotein stress granule formation. *Experimental Cell Research*, *290*(2), 227–233. https://doi.org/10.1016/S0014-4827(03)00290-8

Izumikawa, K., Nobe, Y., Yoshikawa, H., Ishikawa, H., Miura, Y., Nakayama, H., Nonaka, T., Hasegawa, M., Egawa, N., Inoue, H., Nishikawa, K., Yamano, K., Simpson, R. J., Taoka, M., Yamauchi, Y., Isobe, T., & Takahashi, N. (2017). TDP-43 stabilises the processing intermediates of mitochondrial transcripts. *Scientific Reports*, *7*(1), 7709. https://doi.org/10.1038/s41598-017-06953-y

Jaiswal, M. K. (2014). Selective vulnerability of motoneuron and perturbed mitochondrial calcium homeostasis in amyotrophic lateral sclerosis: Implications for motoneurons specific calcium dysregulation. *Molecular and Cellular Therapies*, *2*, 26. https://doi.org/10.1186/2052-8426-2-26

Jankovic, M., Novakovic, I., Gamil Anwar Dawod, P., Gamil Anwar Dawod, A., Drinic, A., Abdel Motaleb, F. I., Ducic, S., & Nikolic, D. (2021). Current Concepts on Genetic Aspects of Mitochondrial Dysfunction in Amyotrophic Lateral Sclerosis. *International Journal of Molecular Sciences*, *22*(18), 9832. https://doi.org/10.3390/ijms22189832

Jensen, B. K., Schuldi, M. H., McAvoy, K., Russell, K. A., Boehringer, A., Curran, B. M., Krishnamurthy, K., Wen, X., Westergard, T., Ma, L., Haeusler, A. R., Edbauer, D., Pasinelli, P., & Trotti, D. (2020). Synaptic dysfunction induced by glycine-alanine dipeptides in C9orf72-ALS/FTD is rescued by SV2 replenishment. *EMBO Molecular Medicine*, *12*(5), e10722. https://doi.org/10.15252/emmm.201910722

Jeon, G. S., Shim, Y.-M., Lee, D.-Y., Kim, J.-S., Kang, M., Ahn, S. H., Shin, J.-Y., Geum, D., Hong, Y. H., & Sung, J.-J. (2019). Pathological Modification of TDP-43 in Amyotrophic Lateral Sclerosis with SOD1 Mutations. *Molecular Neurobiology*, *56*(3), 2007–2021. https://doi.org/10.1007/s12035-018-1218-2

Jia, W., Kim, S. H., Scalf, M. A., Tonzi, P., Millikin, R. J., Guns, W. M., Liu, L., Mastrocola, A. S., Smith, L. M., Huang, T. T., & Tibbetts, R. S. (2021). Fused in sarcoma regulates DNA replication timing and kinetics. *Journal of Biological Chemistry*, *297*(3), 101049. https://doi.org/10.1016/j.jbc.2021.101049

Jiang, L.-L., Zhu, B., Zhao, Y., Li, X., Liu, T., Pina-Crespo, J., Zhou, L., Xu, W., Rodriguez, M. J., Yu, H., Cleveland, D. W., Ravits, J., Cruz, S. D., Long, T., Huang, T. Y., & Xu, H. (2019). Membralin

deficiency dysregulates astrocytic glutamate homeostasis, leading to ALS-like impairment. *Journal of Clinical Investigation*. *129*(8), 3103-3120. https://doi.org/10.1172/JCI127695

Jiang, Y.-M., Yamamoto, M., Kobayashi, Y., Yoshihara, T., Liang, Y., Terao, S., Takeuchi, H., Ishigaki, S., Katsuno, M., Adachi, H., Niwa, J., Tanaka, F., Doyu, M., Yoshida, M., Hashizume, Y., & Sobue, G. (2005). Gene expression profile of spinal motor neurons in sporadic amyotrophic lateral sclerosis. *Annals of Neurology*, *57*(2), 236–251. https://doi.org/10.1002/ana.20379

Jiang, Y.-M., Yamamoto, M., Tanaka, F., Ishigaki, S., Katsuno, M., Adachi, H., Niwa, J., Doyu, M., Yoshida, M., Hashizume, Y., & Sobue, G. (2007). Gene Expressions Specifically Detected in Motor Neurons (Dynactin 1, Early Growth Response 3, Acetyl-CoA Transporter, Death Receptor 5, and Cyclin C) Differentially Correlate to Pathologic Markers in Sporadic Amyotrophic Lateral Sclerosis. *Journal of Neuropathology & Experimental Neurology*, *66*(7), 617–627. https://doi.org/10.1097/nen.0b013e318093ece3

Jo, M., Lee, S., Jeon, Y.-M., Kim, S., Kwon, Y., & Kim, H.-J. (2020). The role of TDP-43 propagation in neurodegenerative diseases: Integrating insights from clinical and experimental studies. *Experimental & Molecular Medicine*, *52*(10), 1652–1662. https://doi.org/10.1038/s12276-020-00513-7

Johari, M., Papadimas, G., Papadopoulos, C., Xirou, S., Kanavaki, A., Chrysanthou-Piterou, M., Rusanen, S., Savarese, M., Hackman, P., & Udd, B. (2022). Adult-onset dominant muscular dystrophy in Greek families caused by Annexin A11. *Annals of Clinical and Translational Neurology*, 2328–9503. https://doi.org/10.1002/acn3.51665

Johnson, J. O., Glynn, S. M., Gibbs, J. R., Nalls, M. A., Sabatelli, M., Restagno, G., Drory, V. E., Chiò, A., Rogaeva, E., & Traynor, B. J. (2014). Mutations in the CHCHD10 gene are a common cause of familial amyotrophic lateral sclerosis. *Brain*, *137*(12), e311. https://doi.org/10.1093/brain/awu265

Johnson, J. O., Mandrioli, J., Benatar, M., Abramzon, Y., Deerlin, V. M. V., Trojanowski, J. Q., Gibbs, J. R., Brunetti, M., Gronka, S., Wuu, J., Ding, J., McCluskey, L., Martinez-Lage, M., Falcone, D., Hernandez, D. G., Arepalli, S., Chong, S., Schymick, J. C., Rothstein, J., … Traynor, B. J. (2010). Exome Sequencing Reveals VCP Mutations as a Cause of Familial ALS. *Neuron*, *68*(5), 857–864. https://doi.org/10.1016/j.neuron.2010.11.036

Johnson, J. O., Pioro, E. P., Boehringer, A., Chia, R., Feit, H., Renton, A. E., Pliner, H. A., Abramzon, Y., Marangi, G., Winborn, B. J., Gibbs, J. R., Nalls, M. A., Morgan, S., Shoai, M., Hardy, J., Pittman, A., Orrell, R. W., Malaspina, A., Sidle, K. C., … Traynor, B. J. (2014). Mutations in the Matrin 3 gene cause familial amyotrophic lateral sclerosis. *Nature Neuroscience*, *17*(5), 664–666. https://doi.org/10.1038/nn.3688

Joilin, G., Leigh, P. N., Newbury, S. F., & Hafezparast, M. (2019). An Overview of MicroRNAs as Biomarkers of ALS. *Frontiers in Neurology*, *10*. https://doi.org/10.3389/fneur.2019.00186

Jones, A. R., Iacoangeli, A., Adey, B. N., Bowles, H., Shatunov, A., Troakes, C., Garson, J. A., McCormick, A. L., & Al-Chalabi, A. (2021). A HML6 endogenous retrovirus on chromosome 3 is upregulated in amyotrophic lateral sclerosis motor cortex. *Scientific Reports*, *11*(1), 14283. https://doi.org/10.1038/s41598-021-93742-3

Ju, J.-S., Fuentealba, R. A., Miller, S. E., Jackson, E., Piwnica-Worms, D., Baloh, R. H., & Weihl, C. C. (2009). Valosin-containing protein (VCP) is required for autophagy and is disrupted in VCP disease. *The Journal of Cell Biology*, *187*(6), 875–888. https://doi.org/10.1083/jcb.200908115

Juan, I. G. S., Nash, L. A., Smith, K. S., Leyton-Jaimes, M. F., Qian, M., Klim, J. R., Limone, F., Dorr, A. B., Couto, A., Pintacuda, G., Joseph, B. J., Whisenant, D. E., Noble, C., Melnik, V., Potter, D., Holmes, A., Burberry, A., Verhage, M., & Eggan, K. (2022). Loss of mouse Stmn2 function causes motor neuropathy. *Neuron*, *110*(10), 1674-1688.e6. https://doi.org/10.1016/j.neuron.2022.02.011

Jumper, J., Evans, R., Pritzel, A., Green, T., Figurnov, M., Ronneberger, O., Tunyasuvunakool, K., Bates, R., Žídek, A., Potapenko, A., Bridgland, A., Meyer, C., Kohl, S. A. A., Ballard, A. J., Cowie, A., Romera-Paredes, B., Nikolov, S., Jain, R., Adler, J., … Hassabis, D. (2021). Highly accurate

protein structure prediction with AlphaFold. *Nature*, *596*(7873), 583–589. https://doi.org/10.1038/s41586-021-03819-2

Jurcau, A. (2021). Insights into the Pathogenesis of Neurodegenerative Diseases: Focus on Mitochondrial Dysfunction and Oxidative Stress. *International Journal of Molecular Sciences*, *22*(21), 11847. https://doi.org/10.3390/ijms222111847

Jutzi, D., Campagne, S., Schmidt, R., Reber, S., Mechtersheimer, J., Gypas, F., Schweingruber, C., Colombo, M., von Schroetter, C., Loughlin, F. E., Devoy, A., Hedlund, E., Zavolan, M., Allain, F. H.-T., & Ruepp, M.-D. (2020). Aberrant interaction of FUS with the U1 snRNA provides a molecular mechanism of FUS induced amyotrophic lateral sclerosis. *Nature Communications*, *11*(1), 6341. https://doi.org/10.1038/s41467-020-20191-3

Kabashi, E., Valdmanis, P. N., Dion, P., Spiegelman, D., McConkey, B. J., Vande Velde, C., Bouchard, J.-P., Lacomblez, L., Pochigaeva, K., Salachas, F., Pradat, P.-F., Camu, W., Meininger, V., Dupre, N., & Rouleau, G. A. (2008). TARDBP mutations in individuals with sporadic and familial amyotrophic lateral sclerosis. *Nature Genetics*, *40*(5), 572–574. https://doi.org/10.1038/ng.132

Kamelgarn, M., Chen, J., Kuang, L., Jin, H., Kasarskis, E. J., & Zhu, H. (2018). ALS mutations of FUS suppress protein translation and disrupt the regulation of nonsense-mediated decay. *Proceedings of the National Academy of Sciences*, *115*(51), E11904–E11913. https://doi.org/10.1073/pnas.1810413115

Kandemir, B., Gulfidan, G., Arga, K. Y., Yilmaz, B., & Kurnaz, I. A. (2020). Transcriptomic profile of Pea3 family members reveal regulatory codes for axon outgrowth and neuronal connection specificity. *Scientific Reports*, *10*(1), 18162. https://doi.org/10.1038/s41598-020-75089-3

Karakaya, B., van der Vis, J. J., Veltkamp, M., Biesma, D. H., Grutters, J. C., & van Moorsel, C. H. M. (2022). ANXA11 rs1049550 Associates with Löfgren's Syndrome and Chronic Sarcoidosis Patients. *Cells*, *11*(9), 1557. https://doi.org/10.3390/cells11091557

Katz, J. S., Dimachkie, M. M., & Barohn, R. J. (2015). Amyotrophic Lateral Sclerosis: A Historical Perspective. *Neurologic Clinics*, *33*(4), 727–734. https://doi.org/10.1016/j.ncl.2015.07.013

Kavanaugh, M. S., Cho, C. C., Howard, M., Fee, D., & Barkhaus, P. E. (2020). US data on children and youth caregivers in amyotrophic lateral sclerosis. *Neurology*, *94*(14), e1452–e1459. https://doi.org/10.1212/WNL.0000000000009217

Kavanaugh, M. S., Howard, M., & Banker-Horner, L. (2018). Feasibility of a multidisciplinary caregiving training protocol for young caregivers in families with ALS. *Social Work in Health Care*, *57*(1), 1–12. https://doi.org/10.1080/00981389.2017.1378284

Kawahara, Y., Ito, K., Sun, H., Aizawa, H., Kanazawa, I., & Kwak, S. (2004). RNA editing and death of motor neurons. *Nature*, *427*(6977), 801–801. https://doi.org/10.1038/427801a

Kaye, E. D., Petrovic-Poljak, A., Verhoeff, N. P. L. G., & Freedman, M. (2010). Frontotemporal Dementia and Pharmacologic Interventions. *The Journal of Neuropsychiatry and Clinical Neurosciences*, *22*(1), 19–29. https://doi.org/10.1176/jnp.2010.22.1.19

Keating, S. S., San Gil, R., Swanson, M. E. V., Scotter, E. L., & Walker, A. K. (2022). TDP-43 pathology: From noxious assembly to therapeutic removal. *Progress in Neurobiology*, 102229. https://doi.org/10.1016/j.pneurobio.2022.102229

Kedersha, N., Cho, M. R., Li, W., Yacono, P. W., Chen, S., Gilks, N., Golan, D. E., & Anderson, P. (2000). Dynamic shuttling of TIA-1 accompanies the recruitment of mRNA to mammalian stress granules. *The Journal of Cell Biology*, *151*(6), 1257–1268. https://doi.org/10.1083/jcb.151.6.1257

Keiten-Schmitz, J., Wagner, K., Piller, T., Kaulich, M., Alberti, S., & Müller, S. (2020). The Nuclear SUMO-Targeted Ubiquitin Quality Control Network Regulates the Dynamics of Cytoplasmic Stress Granules. *Molecular Cell*. *79*(1), 54-67.e7. https://doi.org/10.1016/j.molcel.2020.05.017

Kenna, K. P., van Doormaal, P. T. C., Dekker, A. M., Ticozzi, N., Kenna, B. J., Diekstra, F. P., van Rheenen, W., van Eijk, K. R., Jones, A. R., Keagle, P., Shatunov, A., Sproviero, W., Smith, B. N., van Es, M. A., Topp, S. D., Kenna, A., Miller, J. W., Fallini, C., Tiloca, C., … Landers, J. E. (2016).

NEK1 variants confer susceptibility to amyotrophic lateral sclerosis. *Nature Genetics*, *48*(9), 1037-1042. https://doi.org/10.1038/ng.3626

Kerk, S. Y., Bai, Y., Smith, J., Lalgudi, P., Hunt, C., Kuno, J., Nuara, J., Yang, T., Lanza, K., Chan, N., Coppola, A., Tang, Q., Espert, J., Jones, H., Fannell, C., Zambrowicz, B., & Chiao, E. (2022). Homozygous ALS-linked FUS P525L mutations cell- autonomously perturb transcriptome profile and chemoreceptor signaling in human iPSC microglia. *Stem Cell Reports*, *17*(3), 678-692. https://doi.org/10.1016/j.stemcr.2022.01.004

Khalfallah, Y., Kuta, R., Grasmuck, C., Prat, A., Durham, H. D., & Velde, C. V. (2018). TDP-43 regulation of stress granule dynamics in neurodegenerative disease-relevant cell types. *Scientific Reports*, *8*(1), 1–13. https://doi.org/10.1038/s41598-018-25767-0

Kharbikar, B. N., Mohindra, P., & Desai, T. A. (2022). Biomaterials to enhance stem cell transplantation. *Cell Stem Cell*, *29*(6), 692-721. https://doi.org/10.1016/j.stem.2022.04.002

Khare, S. D., Caplow, M., & Dokholyan, N. V. (2006). FALS mutations in Cu, Zn superoxide dismutase destabilize the dimer and increase dimer dissociation propensity: A large-scale thermodynamic analysis. *Amyloid: The International Journal of Experimental and Clinical Investigation: The Official Journal of the International Society of Amyloidosis*, *13*(4), 226–235. https://doi.org/10.1080/13506120600960486

Kia, A., McAvoy, K., Krishnamurthy, K., Trotti, D., & Pasinelli, P. (2018). Astrocytes expressing ALS-linked mutant FUS induce motor neuron death through release of tumor necrosis factor-alpha. *Glia*, *66*(5), 1016–1033. https://doi.org/10.1002/glia.23298

Kiernan, M. C., Vucic, S., Cheah, B. C., Turner, M. R., Eisen, A., Hardiman, O., Burrell, J. R., & Zoing, M. C. (2011). Amyotrophic lateral sclerosis. *The Lancet*, *377*(9769), 942–955. https://doi.org/10.1016/S0140-6736(10)61156-7

Kim, H. J., Kim, N. C., Wang, Y.-D., Scarborough, E. A., Moore, J., Diaz, Z., MacLea, K. S., Freibaum, B., Li, S., Molliex, A., Kanagaraj, A. P., Carter, R., Boylan, K. B., Wojtas, A. M., Rademakers, R., Pinkus, J. L., Greenberg, S. A., Trojanowski, J. Q., Traynor, B. J., … Taylor, J. P. (2013). Mutations in prion-like domains in hnRNPA2B1 and hnRNPA1 cause multisystem proteinopathy and ALS. *Nature*, *495*(7442), 467–473. https://doi.org/10.1038/nature11922

Kim, H., Kim, H. Y., Choi, M. R., Hwang, S., Nam, K.-H., Kim, H.-C., Han, J. S., Kim, K. S., Yoon, H. S., & Kim, S. H. (2010). Dose-dependent efficacy of ALS-human mesenchymal stem cells transplantation into cisterna magna in SOD1-G93A ALS mice. *Neuroscience Letters*, *468*(3), 190–194. https://doi.org/10.1016/j.neulet.2009.10.074

Kim, H.-Y. (2017). Statistical notes for clinical researchers: Chi-squared test and Fisher's exact test. *Restorative Dentistry & Endodontics*, *42*(2), 152–155. https://doi.org/10.5395/rde.2017.42.2.152

Kim, S., Ghil, S.-H., Kim, S.-S., Myeong, H.-H., Lee, Y.-D., & Suh-Kim, H. (2002). Overexpression of neurogenin1 induces neurite outgrowth in F11 neuroblastoma cells. *Experimental & Molecular Medicine*, *34*(6), 469–475. https://doi.org/10.1038/emm.2002.65

Kirwan, P., Turner-Bridger, B., Peter, M., Momoh, A., Arambepola, D., Robinson, H. P. C., & Livesey, F. J. (2015). Development and function of human cerebral cortex neural networks from pluripotent stem cells in vitro. *Development*, *142*(18), 3178–3187. https://doi.org/10.1242/dev.123851

Kiskinis, E., Sandoe, J., Williams, L. A., Boulting, G. L., Moccia, R., Wainger, B. J., Han, S., Peng, T., Thams, S., Mikkilineni, S., Mellin, C., Merkle, F. T., Davis-Dusenbery, B. N., Ziller, M., Oakley, D., Ichida, J., Dicostanza, S., Atwater, N., Maeder, M. L., … Eggan, K. (2014). Pathways Disrupted in Human ALS Motor Neurons Identified Through Genetic Correction of Mutant SOD1. *Cell Stem Cell*, *14*(6), 781–795. https://doi.org/10.1016/j.stem.2014.03.004

Kitamura, A., Nakayama, Y., Shibasaki, A., Taki, A., Yuno, S., Takeda, K., Yahara, M., Tanabe, N., & Kinjo, M. (2016). Interaction of RNA with a C-terminal fragment of the amyotrophic lateral sclerosis-associated TDP43 reduces cytotoxicity. *Scientific Reports*, *6*(1), 19230. https://doi.org/10.1038/srep19230

Klavžar, P., Koritnik, B., Leonardis, L., Grošelj, L. D., Kirbiš, M., Kovačič, S. R., Klinar, P., Perme, M. P., & Zidar, J. (2020). Improvements in the multidisciplinary care are beneficial for survival in

amyotrophic lateral sclerosis (ALS): Experience from a tertiary ALS center. *Amyotrophic Lateral Sclerosis and Frontotemporal Degeneration*, *21*(3-4), 203-208. https://doi.org/10.1080/21678421.2020.1746809

Koehler, L. C., Grese, Z. R., Bastos, A. C. S., Mamede, L. D., Heyduk, T., & Ayala, Y. M. (2022). TDP-43 Oligomerization and Phase Separation Properties Are Necessary for Autoregulation. *Frontiers in Neuroscience*, *16*. https://doi.org/10.3389/fnins.2022.818655

Koike, Y., Sugai, A., Hara, N., Ito, J., Yokoseki, A., Ishihara, T., Yamagishi, T., Tsuboguchi, S., Tada, M., Ikeuchi, T., Kakita, A., & Onodera, O. (2021). Age-related demethylation of the TDP-43 autoregulatory region in the human motor cortex. *Communications Biology*, *4*(1), 1–11. https://doi.org/10.1038/s42003-021-02621-0

Komiya, H., Takeuchi, H., Ogawa, Y., Hatooka, Y., Takahashi, K., Katsumoto, A., Kubota, S., Nakamura, H., Kunii, M., Tada, M., Doi, H., & Tanaka, F. (2020). CCR2 is localized in microglia and neurons, as well as infiltrating monocytes, in the lumbar spinal cord of ALS mice. *Molecular Brain*, *13*(1), 64. https://doi.org/10.1186/s13041-020-00607-3

Konopka, A., & Atkin, J. D. (2022). DNA Damage, Defective DNA Repair, and Neurodegeneration in Amyotrophic Lateral Sclerosis. *Frontiers in Aging Neuroscience*, *14*. https://doi.org/10.3389/fnagi.2022.786420

Koppers, M., van Blitterswijk, M. M., Vlam, L., Rowicka, P. A., van Vught, P. W. J., Groen, E. J. N., Spliet, W. G. M., Engelen-Lee, J., Schelhaas, H. J., de Visser, M., van der Kooi, A. J., van der Pol, W.-L., Pasterkamp, R. J., Veldink, J. H., & van den Berg, L. H. (2012). VCP mutations in familial and sporadic amyotrophic lateral sclerosis. *Neurobiology of Aging*, *33*(4), 837.e7-13. https://doi.org/10.1016/j.neurobiolaging.2011.10.006

Korobeynikov, V. A., Lyashchenko, A. K., Blanco-Redondo, B., Jafar-Nejad, P., & Shneider, N. A. (2022). Antisense oligonucleotide silencing of FUS expression as a therapeutic approach in amyotrophic lateral sclerosis. *Nature Medicine*, *28*, 104-116. https://doi.org/10.1038/s41591-021-01615-z

Kraemer, B. C., Schuck, T., Wheeler, J. M., Robinson, L. C., Trojanowski, J. Q., Lee, V. M. Y., & Schellenberg, G. D. (2010). Loss of murine TDP-43 disrupts motor function and plays an essential role in embryogenesis. *Acta Neuropathologica*, *119*(4), 409–419. https://doi.org/10.1007/s00401-010-0659-0

Krainer, G., Welsh, T. J., Joseph, J. A., Espinosa, J. R., Wittmann, S., de Csilléry, E., Sridhar, A., Toprakcioglu, Z., Gudiškytė, G., Czekalska, M. A., Arter, W. E., Guillén-Boixet, J., Franzmann, T. M., Qamar, S., George-Hyslop, P. S., Hyman, A. A., Collepardo-Guevara, R., Alberti, S., & Knowles, T. P. J. (2021). Reentrant liquid condensate phase of proteins is stabilized by hydrophobic and non-ionic interactions. *Nature Communications*, *12*(1), 1085. https://doi.org/10.1038/s41467-021-21181-9

Kuijk, E., Jager, M., van der Roest, B., Locati, M. D., Van Hoeck, A., Korzelius, J., Janssen, R., Besselink, N., Boymans, S., van Boxtel, R., & Cuppen, E. (2020). The mutational impact of culturing human pluripotent and adult stem cells. *Nature Communications*, *11*, 2493. https://doi.org/10.1038/s41467-020-16323-4

Kuijlaars, J., Oyelami, T., Diels, A., Rohrbacher, J., Versweyveld, S., Meneghello, G., Tuefferd, M., Verstraelen, P., Detrez, J. R., Verschuuren, M., De Vos, W. H., Meert, T., Peeters, P. J., Cik, M., Nuydens, R., Brône, B., & Verheyen, A. (2016). Sustained synchronized neuronal network activity in a human astrocyte co-culture system. *Scientific Reports*, *6*(1), 36529. https://doi.org/10.1038/srep36529

Kuijpers, M., Kochlamazashvili, G., Stumpf, A., Puchkov, D., Swaminathan, A., Lucht, M. T., Krause, E., Maritzen, T., Schmitz, D., & Haucke, V. (2020). Neuronal Autophagy Regulates Presynaptic Neurotransmission by Controlling the Axonal Endoplasmic Reticulum. *Neuron*, *109*(2), 299-313.e9. https://doi.org/10.1016/j.neuron.2020.10.005

Kumar, S., Curran, J. E., Glahn, D. C., & Blangero, J. (2016). Utility of Lymphoblastoid Cell Lines for Induced Pluripotent Stem Cell Generation. *Stem Cells International*, *2016*. https://doi.org/10.1155/2016/2349261

Kumar, S., Phaneuf, D., Cordeau, P., Boutej, H., Kriz, J., & Julien, J.-P. (2021). Induction of autophagy mitigates TDP-43 pathology and translational repression of neurofilament mRNAs in mouse models of ALS/FTD. *Molecular Neurodegeneration*, *16*, 1. https://doi.org/10.1186/s13024-020-00420-5

Kuo, P.-H., Chiang, C.-H., Wang, Y.-T., Doudeva, L. G., & Yuan, H. S. (2014). The crystal structure of TDP-43 RRM1-DNA complex reveals the specific recognition for UG- and TG-rich nucleic acids. *Nucleic Acids Research*, *42*(7), 4712–4722. https://doi.org/10.1093/nar/gkt1407

Kwak, S., & Kawahara, Y. (2005). Deficient RNA editing of GluR2 and neuronal death in amyotropic lateral sclerosis. *Journal of Molecular Medicine*, *83*(2), 110–120. https://doi.org/10.1007/s00109-004-0599-z

Kwiatkowski, T. J., Bosco, D. A., LeClerc, A. L., Tamrazian, E., Vanderburg, C. R., Russ, C., Davis, A., Gilchrist, J., Kasarskis, E. J., Munsat, T., Valdmanis, P., Rouleau, G. A., Hosler, B. A., Cortelli, P., Jong, P. J. de, Yoshinaga, Y., Haines, J. L., Pericak-Vance, M. A., Yan, J., … Brown, R. H. (2009). Mutations in the FUS/TLS Gene on Chromosome 16 Cause Familial Amyotrophic Lateral Sclerosis. *Science*, *323*(5918), 1205–1208. https://doi.org/10.1126/science.1166066

La Cognata, V., Gentile, G., Aronica, E., & Cavallaro, S. (2020). Splicing Players Are Differently Expressed in Sporadic Amyotrophic Lateral Sclerosis Molecular Clusters and Brain Regions. *Cells*, *9*(1), 159. https://doi.org/10.3390/cells9010159

Lacomblez, L., Bensimon, G., Leigh, P. N., Guillet, P., & Meininger, V. (1996). Dose-ranging study of riluzole in amyotrophic lateral sclerosis. Amyotrophic Lateral Sclerosis/Riluzole Study Group II. *Lancet*, *347*(9013), 1425–1431. https://doi.org/10.1016/s0140-6736(96)91680-3

Lagier-Tourenne, C., Polymenidou, M., Hutt, K. R., Vu, A. Q., Baughn, M., Huelga, S. C., Clutario, K. M., Ling, S.-C., Liang, T. Y., Mazur, C., Wancewicz, E., Kim, A. S., Watt, A., Freier, S., Hicks, G. G., Donohue, J. P., Shiue, L., Bennett, C. F., Ravits, J., … Yeo, G. W. (2012). Divergent roles of ALS-linked proteins FUS/TLS and TDP-43 intersect in processing long pre-mRNAs. *Nature Neuroscience*, *15*(11), 1488–1497. https://doi.org/10.1038/nn.3230

Laird, F. M., Farah, M. H., Ackerley, S., Hoke, A., Maragakis, N., Rothstein, J. D., Griffin, J., Price, D. L., Martin, L. J., & Wong, P. C. (2008). Motor Neuron Disease Occurring in a Mutant Dynactin Mouse Model Is Characterized by Defects in Vesicular Trafficking. *The Journal of Neuroscience*, *28*(9), 1997–2005. https://doi.org/10.1523/JNEUROSCI.4231-07.2008

Lall, D., Lorenzini, I., Mota, T. A., Bell, S., Mahan, T. E., Ulrich, J. D., Davtyan, H., Rexach, J. E., Muhammad, A. K. M. G., Shelest, O., Landeros, J., Vazquez, M., Kim, J., Ghaffari, L., O'Rourke, J. G., Geschwind, D. H., Blurton-Jones, M., Holtzman, D. M., Sattler, R., & Baloh, R. H. (2021). C9orf72 deficiency promotes microglial-mediated synaptic loss in aging and amyloid accumulation. *Neuron*, *109*(14), 2275-2291.e8. https://doi.org/10.1016/j.neuron.2021.05.020

Laneve, P., Tollis, P., & Caffarelli, E. (2021). RNA Deregulation in Amyotrophic Lateral Sclerosis: The Noncoding Perspective. *International Journal of Molecular Sciences*, *22*(19), 10285. https://doi.org/10.3390/ijms221910285

Larroquette, F., Seto, L., Gaub, P. L., Kamal, B., Wallis, D., Larivière, R., Vallée, J., Robitaille, R., & Tsuda, H. (2015). Vapb/Amyotrophic lateral sclerosis 8 knock-in mice display slowly progressive motor behavior defects accompanying ER stress and autophagic response. *Human Molecular Genetics*, *24*(22), 6515–6529. https://doi.org/10.1093/hmg/ddv360

Leal, S. S., & Gomes, C. M. (2015). Calcium dysregulation links ALS defective proteins and motor neuron selective vulnerability. *Frontiers in Cellular Neuroscience*, *9*. https://doi.org/10.3389/fncel.2015.00225

Leary, R. J., Cummins, J., Wang, T.-L., & Velculescu, V. E. (2007). Digital karyotyping. *Nature Protocols*, *2*(8), 1973–1986. https://doi.org/10.1038/nprot.2007.276

Lecona, E., Turnay, J., Olmo, N., Guzmán-Aránguez, A., Morgan, R. O., Fernandez, M.-P., & Lizarbe, M. A. (2003). Structural and functional characterization of recombinant mouse annexin A11: Influence of calcium binding. *Biochemical Journal*, *373*(2), 437–449. https://doi.org/10.1042/BJ20021721

Lee, B. J., Cansizoglu, A. E., Süel, K. E., Louis, T. H., Zhang, Z., & Chook, Y. M. (2006). Rules for Nuclear Localization Sequence Recognition by Karyopherinβ2. *Cell*, *126*(3), 543–558. https://doi.org/10.1016/j.cell.2006.05.049

Lee, D.-Y., Jeon, G. S., & Sung, J.-J. (2020). ALS-Linked Mutant SOD1 Associates with TIA-1 and Alters Stress Granule Dynamics. *Neurochemical Research*, *45*(12), 2884–2893. https://doi.org/10.1007/s11064-020-03137-5

Lee, J., Bignone, P. A., Coles, L. S., Liu, Y., Snyder, E., & Larocca, D. (2020). Induced pluripotency and spontaneous reversal of cellular aging in supercentenarian donor cells. *Biochemical and Biophysical Research Communications*. *525*(3), 563-569. https://doi.org/10.1016/j.bbrc.2020.02.092

Lee, J., Nguyen, P. T., Shim, H. S., Hyeon, S. J., Im, H., Choi, M.-H., Chung, S., Kowall, N. W., Lee, S. B., & Ryu, H. (2019). EWSR1, a multifunctional protein, regulates cellular function and aging via genetic and epigenetic pathways. *Biochimica et Biophysica Acta (BBA) - Molecular Basis of Disease*, *1865*(7), 1938–1945. https://doi.org/10.1016/j.bbadis.2018.10.042

Lee, T., Cho, I.-S., Bashyal, N., Naya, F. J., Tsai, M.-J., Yoon, J. S., Choi, J.-M., Park, C.-H., Kim, S.-S., & Suh-Kim, H. (2020). ERK Regulates NeuroD1-mediated Neurite Outgrowth via Proteasomal Degradation. *Experimental Neurobiology*, *29*(3), 189–206. https://doi.org/10.5607/en20021

Lee, Y.-B., Chen, H.-J., Peres, J. N., Gomez-Deza, J., Attig, J., Štalekar, M., Troakes, C., Nishimura, A. L., Scotter, E. L., Vance, C., Adachi, Y., Sardone, V., Miller, J. W., Smith, B. N., Gallo, J.-M., Ule, J., Hirth, F., Rogelj, B., Houart, C., & Shaw, C. E. (2013). Hexanucleotide Repeats in ALS/FTD Form Length-Dependent RNA Foci, Sequester RNA Binding Proteins, and Are Neurotoxic. *Cell Reports*, *5*(5), 1178–1186. https://doi.org/10.1016/j.celrep.2013.10.049

Lehmkuhl, E. M., Loganathan, S., Alsop, E., Blythe, A. D., Kovalik, T., Mortimore, N. P., Barrameda, D., Kueth, C., Eck, R. J., Siddegowda, B. B., Joardar, A., Ball, H., Macias, M. E., Bowser, R., Van Keuren-Jensen, K., & Zarnescu, D. C. (2021). TDP-43 proteinopathy alters the ribosome association of multiple mRNAs including the glypican Dally-like protein (Dlp)/GPC6. *Acta Neuropathologica Communications*, *9*(1), 52. https://doi.org/10.1186/s40478-021-01148-z

Leigh, P. N., Whitwell, H., Garofalo, O., Buller, J., Swash, M., Martin, J. E., Gallo, J.-M., Weller, R. O., & Anderton, B. H. (1991). Ubiquitin-immunoreactive intraneuronal inclusions in amyotrophic lateral sclerosis, morphology, distribution, and specificity. *Brain*, *114*(2), 775–788. https://doi.org/10.1093/brain/114.2.775

Leoni, T. B., González-Salazar, C., Rezende, T. J. R., Hernández, A. L. C., Mattos, A. H. B., Neto, A. R. C., da Graça, F. F., Gonçalves, J. P. N., Martinez, A. R. M., Taniguti, L., Kitajima, J. P., Kok, F., Rogério, F., da Silva, A. M. S., de Oliveira, A. L. R., Zanoteli, E., Nucci, A., & França Jr, M. C. (2021). A novel multisystem proteinopathy caused by a missense ANXA11 variant. *Annals of Neurology*, *90*(2), 239-252. https://doi.org/10.1002/ana.26136

Leroy, F., Lamotte d'Incamps, B., Imhoff-Manuel, R. D., & Zytnicki, D. (2014). Early intrinsic hyperexcitability does not contribute to motoneuron degeneration in amyotrophic lateral sclerosis. *ELife*, *3*, e04046. https://doi.org/10.7554/eLife.04046

Leśniak, W., Szczepańska, A., & Kuźnicki, J. (2005). Calcyclin (S100A6) expression is stimulated by agents evoking oxidative stress via the antioxidant response element. *Biochimica et Biophysica Acta (BBA) - Molecular Cell Research*, *1744*(1), 29–37. https://doi.org/10.1016/j.bbamcr.2004.11.003

Levone, B. R., Lenzken, S. C., Antonaci, M., Maiser, A., Rapp, A., Conte, F., Reber, S., Mechtersheimer, J., Ronchi, A. E., Mühlemann, O., Leonhardt, H., Cardoso, M. C., Ruepp, M.-D., & Barabino, S. M. L. (2021). FUS-dependent liquid-liquid phase separation is important for DNA repair initiation. *The Journal of Cell Biology*, *220*(5), e202008030. https://doi.org/10.1083/jcb.202008030

Levy, J. R., Sumner, C. J., Caviston, J. P., Tokito, M. K., Ranganathan, S., Ligon, L. A., Wallace, K. E., LaMonte, B. H., Harmison, G. G., Puls, I., Fischbeck, K. H., & Holzbaur, E. L. F. (2006). A motor neuron disease–associated mutation in p150Glued perturbs dynactin function and induces protein aggregation. *Journal of Cell Biology*, *172*(5), 733–745. https://doi.org/10.1083/jcb.200511068

Li, K., Hala, T. J., Seetharam, S., Poulsen, D. J., Wright, M. C., & Lepore, A. C. (2015). GLT1 overexpression in SOD1G93A mouse cervical spinal cord does not preserve diaphragm function or extend disease. *Neurobiology of Disease*, *78*, 12–23. https://doi.org/10.1016/j.nbd.2015.03.010

Li, W., Lee, M.-H., Henderson, L., Tyagi, R., Bachani, M., Steiner, J., Campanac, E., Hoffman, D. A., von Geldern, G., Johnson, K., Maric, D., Morris, H. D., Lentz, M., Pak, K., Mammen, A., Ostrow, L., Rothstein, J., & Nath, A. (2015). Human endogenous retrovirus-K contributes to motor neuron disease. *Science Translational Medicine*, *7*(307), 307ra153. https://doi.org/10.1126/scitranslmed.aac8201

Li, X., Lu, L., Bush, D. J., Zhang, X., Zheng, L., Suswam, E. A., & King, P. H. (2009). Mutant copper-zinc superoxide dismutase associated with amyotrophic lateral sclerosis binds to adenine/uridine-rich stability elements in the vascular endothelial growth factor 3'-untranslated region. *Journal of Neurochemistry*, *108*(4), 1032–1044. https://doi.org/10.1111/j.1471-4159.2008.05856.x

Li, X., Yu, B., Sun, Q., Zhang, Y., Ren, M., Zhang, X., Li, A., Yuan, J., Madisen, L., Luo, Q., Zeng, H., Gong, H., & Qiu, Z. (2018). Generation of a whole-brain atlas for the cholinergic system and mesoscopic projectome analysis of basal forebrain cholinergic neurons. *Proceedings of the National Academy of Sciences*, *115*(2), 415–420. https://doi.org/10.1073/pnas.1703601115

Liachko, N. F., Guthrie, C. R., & Kraemer, B. C. (2010). Phosphorylation Promotes Neurotoxicity in a Caenorhabditis elegans Model of TDP-43 Proteinopathy. *Journal of Neuroscience*, *30*(48), 16208–16219. https://doi.org/10.1523/JNEUROSCI.2911-10.2010

Liang, B., Thapa, R., Zhang, G., Moffitt, C., Zhang, Y., Zhang, L., Johnston, A., Ruby, H. P., Barbera, G., Wong, P. C., Zhang, Z., Chen, R., Lin, D.-T., & Li, Y. (2022). Aberrant neural activity in prefrontal pyramidal neurons lacking TDP-43 precedes neuron loss. *Progress in Neurobiology*, *215*, 102297. https://doi.org/10.1016/j.pneurobio.2022.102297

Liao, D., Liao, Q., Huang, C., & Bi, F. (2018). Mutations of G38R and D40G cause amyotrophic lateral sclerosis by reducing Annexin A11 protein stability. *Zhong nan da xue xue bao Yi xue ban = Journal of Central South University. Medical sciences*, *43*(6), 577–582. https://doi.org/10.11817/j.issn.1672-7347.2018.06.001

Liao, Y.-C., Fernandopulle, M. S., Wang, G., Choi, H., Hao, L., Drerup, C. M., Patel, R., Qamar, S., Nixon-Abell, J., Shen, Y., Meadows, W., Vendruscolo, M., Knowles, T. P. J., Nelson, M., Czekalska, M. A., Musteikyte, G., Gachechiladze, M. A., Stephens, C. A., Pasolli, H. A., … Ward, M. E. (2019). RNA Granules Hitchhike on Lysosomes for Long-Distance Transport, Using Annexin A11 as a Molecular Tether. *Cell*, *179*(1), 147-164.e20. https://doi.org/10.1016/j.cell.2019.08.050

Lillebostad, P. A. G., Raasakka, A., Hjellbrekke, S. J., Patil, S., Røstbø, T., Hollås, H., Sakya, S. A., Szigetvari, P. D., Vedeler, A., & Kursula, P. (2020). Structure of the ALS Mutation Target Annexin A11 Reveals a Stabilising N-Terminal Segment. *Biomolecules*, *10*(4), 660. https://doi.org/10.3390/biom10040660

Lin, Y.-C., Kumar, M. S., Ramesh, N., Anderson, E. N., Nguyen, A. T., Kim, B., Cheung, S., McDonough, J. A., Skarnes, W. C., Lopez-Gonzalez, R., Landers, J. E., Fawzi, N. L., Mackenzie, I. R. A., Lee, E. B., Nickerson, J. A., Grunwald, D., Pandey, U. B., & Bosco, D. A. (2021). Interactions between ALS-linked FUS and nucleoporins are associated with defects in the nucleocytoplasmic transport pathway. *Nature Neuroscience*, *24*, 1077-1088. https://doi.org/10.1038/s41593-021-00859-9

Lin, Z., Kim, E., Ahmed, M., Han, G., Simmons, C., Redhead, Y., Bartlett, J., Pena Altamira, L. E., Callaghan, I., White, M. A., Singh, N., Sawiak, S., Spires-Jones, T., Vernon, A. C., Coleman, M. P., Green, J., Henstridge, C., Davies, J. S., Cash, D., & Sreedharan, J. (2021). MRI-guided histology of TDP-43 knock-in mice implicates parvalbumin interneuron loss, impaired neurogenesis and aberrant neurodevelopment in amyotrophic lateral sclerosis-frontotemporal dementia. *Brain Communications*, *3*(2), fcab114. https://doi.org/10.1093/braincomms/fcab114

Ling, J. P., Pletnikova, O., Troncoso, J. C., & Wong, P. C. (2015). TDP-43 repression of nonconserved cryptic exons is compromised in ALS-FTD. *Science*, *349*(6248), 650–655. https://doi.org/10.1126/science.aab0983

Ling, S.-C. (2018). Synaptic Paths to Neurodegeneration: The Emerging Role of TDP-43 and FUS in Synaptic Functions. *Neural Plasticity*, *2018*. https://doi.org/10.1155/2018/8413496

Ling, S.-C., Dastidar, S. G., Tokunaga, S., Ho, W. Y., Lim, K., Ilieva, H., Parone, P. A., Tyan, S.-H., Tse, T. M., Chang, J.-C., Platoshyn, O., Bui, N. B., Bui, A., Vetto, A., Sun, S., McAlonis-Downes, M., Han, J. S., Swing, D., Kapeli, K., … Cleveland, D. W. (2019). Overriding FUS autoregulation in mice triggers gain-of-toxic dysfunctions in RNA metabolism and autophagy-lysosome axis. *ELife*, *8*. https://doi.org/10.7554/eLife.40811

Ling, S.-C., Polymenidou, M., & Cleveland, D. W. (2013). Converging Mechanisms in ALS and FTD: Disrupted RNA and Protein Homeostasis. *Neuron*, *79*(3), 416–438. https://doi.org/10.1016/j.neuron.2013.07.033

Liu, M.-L., Zang, T., Zou, Y., Chang, J. C., Gibson, J. R., Huber, K. M., & Zhang, C.-L. (2013). Small molecules enable neurogenin 2 to efficiently convert human fibroblasts into cholinergic neurons. *Nature Communications*, *4*(1), 2183. https://doi.org/10.1038/ncomms3183

Liu, Q., Shu, S., Wang, R. R., Liu, F., Cui, B., Guo, X. N., Lu, C. X., Li, X. G., Liu, M. S., Peng, B., Cui, L., & Zhang, X. (2016). Whole-exome sequencing identifies a missense mutation in hnRNPA1 in a family with flail arm ALS. *Neurology*, *87*(17), 1763–1769. https://doi.org/10.1212/WNL.0000000000003256

Liu, S., Guo, C., Wang, J., Wang, B., Qi, H., & Sun, M.-Z. (2016). ANXA11 regulates the tumorigenesis, lymph node metastasis and 5-fluorouracil sensitivity of murine hepatocarcinoma Hca-P cells by targeting c-Jun. *Oncotarget*, *7*(13), 16297–16310. https://doi.org/10.18632/oncotarget.7484

Liu, S., Wang, J., Guo, C., Qi, H., & Sun, M.-Z. (2015). Annexin A11 knockdown inhibits in vitro proliferation and enhances survival of Hca-F cell via Akt2/FoxO1 pathway and MMP-9 expression. *Biomedicine & Pharmacotherapy*, *70*, 58–63. https://doi.org/10.1016/j.biopha.2015.01.011

Liu, X., Wu, C., He, J., Zhang, N., & Fan, D. (2019). Two rare variants of the ANXA11 gene identified in Chinese patients with amyotrophic lateral sclerosis. *Neurobiology of Aging*, *74*, 235.e9-235.e12. https://doi.org/10.1016/j.neurobiolaging.2018.09.020

Liu, Y.-J., Kuo, H.-C., & Chern, Y. (2021). A system-wide mislocalization of RNA-binding proteins in motor neurons is a new feature of ALS. *Neurobiology of Disease*, *160*, 105531. https://doi.org/10.1016/j.nbd.2021.105531

Liu, Y.-J., Lee, L.-M., Lai, H.-L., & Chern, Y. (2015). Aberrant activation of AMP-activated protein kinase contributes to the abnormal distribution of HuR in amyotrophic lateral sclerosis. *FEBS Letters*, *589*(4), 432–439. https://doi.org/10.1016/j.febslet.2014.12.029

Liu-Yesucevitz, L., Bilgutay, A., Zhang, Y.-J., Vanderwyde, T., Citro, A., Mehta, T., Zaarur, N., McKee, A., Bowser, R., Sherman, M., Petrucelli, L., & Wolozin, B. (2010). Tar DNA Binding Protein-43 (TDP-43) Associates with Stress Granules: Analysis of Cultured Cells and Pathological Brain Tissue. *PLOS ONE*, *5*(10), e13250. https://doi.org/10.1371/journal.pone.0013250

Loffreda, A., Nizzardo, M., Arosio, A., Ruepp, M.-D., Calogero, R. A., Volinia, S., Galasso, M., Bendotti, C., Ferrarese, C., Lunetta, C., Rizzuti, M., Ronchi, A. E., Mühlemann, O., Tremolizzo, L., Corti, S., & Barabino, S. M. L. (2020). miR-129-5p: A key factor and therapeutic target in amyotrophic lateral sclerosis. *Progress in Neurobiology*, *190*, 101803. https://doi.org/10.1016/j.pneurobio.2020.101803

Logroscino, G., & Piccininni, M. (2019). Amyotrophic Lateral Sclerosis Descriptive Epidemiology: The Origin of Geographic Difference. *Neuroepidemiology*, *52*(1–2), 93–103. https://doi.org/10.1159/000493386

Logroscino, G., Traynor, B. J., Hardiman, O., Chio', A., Couratier, P., Mitchell, J. D., Swingler, R. J., Beghi, E., & Eurals, F. (2008). Descriptive epidemiology of amyotrophic lateral sclerosis: New evidence and unsolved issues. *Journal of Neurology, Neurosurgery & Psychiatry*, *79*(1), 6–11. https://doi.org/10.1136/jnnp.2006.104828

Lomen-Hoerth, C., Anderson, T., & Miller, B. (2002). The overlap of amyotrophic lateral sclerosis and frontotemporal dementia. *Neurology*, *59*(7), 1077–1079. https://doi.org/10.1212/wnl.59.7.1077

Loncke, J., Kaasik, A., Bezprozvanny, I., Parys, J. B., Kerkhofs, M., & Bultynck, G. (2021). Balancing ER-Mitochondrial Ca2+ Fluxes in Health and Disease. *Trends in Cell Biology*, *31*(7), 598-612. https://doi.org/10.1016/j.tcb.2021.02.003

López-Bastida, J., Perestelo-Pérez, L., Montón-Alvarez, F., Serrano-Aguilar, P., & Alfonso-Sanchez, J. L. (2009). Social economic costs and health-related quality of life in patients with amyotrophic lateral sclerosis in Spain. *Amyotrophic Lateral Sclerosis: Official Publication of the World Federation of Neurology Research Group on Motor Neuron Diseases*, *10*(4), 237–243. https://doi.org/10.1080/17482960802430781

López-Erauskin, J., Tadokoro, T., Baughn, M. W., Myers, B., McAlonis-Downes, M., Chillon-Marinas, C., Asiaban, J. N., Artates, J., Bui, A. T., Vetto, A. P., Lee, S. K., Le, A. V., Sun, Y., Jambeau, M., Boubaker, J., Swing, D., Qiu, J., Hicks, G. G., Ouyang, Z., … Cruz, S. D. (2018). ALS/FTD-Linked Mutation in FUS Suppresses Intra-axonal Protein Synthesis and Drives Disease Without Nuclear Loss-of-Function of FUS. *Neuron*, *100*(4), 816-830.e7. https://doi.org/10.1016/j.neuron.2018.09.044

Lorenzini, I., Alsop, E., Levy, J., Gittings, L. M., Rabichow, B. E., Lall, D., Moore, S., Bustos, L., Pevey, R., Burciu, C., Saul, J., McQuade, A., Tzioras, M., Mota, T. A., Logemann, A., Rose, J., Almeida, S., Gao, F.-B., Bowser, R., … Sattler, R. (2020). Activated iPSC-microglia from C9orf72 ALS/FTD patients exhibit endosomal-lysosomal dysfunction. *BioRxiv*. https://doi.org/10.1101/2020.09.03.277459

Loschi, M., Leishman, C. C., Berardone, N., & Boccaccio, G. L. (2009). Dynein and kinesin regulate stress-granule and P-body dynamics. *Journal of Cell Science*, *122*(21), 3973–3982. https://doi.org/10.1242/jcs.051383

Lourenco, G. F., Janitz, M., Huang, Y., & Halliday, G. M. (2015). Long noncoding RNAs in TDP-43 and FUS/TLS-related frontotemporal lobar degeneration (FTLD). *Neurobiology of Disease*, *82*, 445–454. https://doi.org/10.1016/j.nbd.2015.07.011

Lovejoy, C., Alatza, A., Arber, C., Galasso, G., Bradshaw, T. Y., Verheyen, A., Lashley, T., Revesz, T., Hardy, J., Karch, C. M., & Wray, S. (2022). Engineered Cerebral Organoids Recapitulate Adult Tau Expression and Disease-relevant Changes in Tau Splicing. *Research Square*. https://doi.org/10.21203/rs.3.rs-37620/v1

Lu, Y.-Q., Chen, J.-M., Lin, H., Feng, S.-Y., Che, C.-H., Liu, C.-Y., Huang, H.-P., & Zou, Z.-Y. (2022). Novel Intronic Mutations of TBK1 Promote Aberrant Splicing Modes in Amyotrophic Lateral Sclerosis. *Frontiers in Molecular Neuroscience*, *15*. https://www.frontiersin.org/article/10.3389/fnmol.2022.691534

Luisier, R., Tyzack, G. E., Hall, C. E., Mitchell, J. S., Devine, H., Taha, D. M., Malik, B., Meyer, I., Greensmith, L., Newcombe, J., Ule, J., Luscombe, N. M., & Patani, R. (2018). Intron retention and nuclear loss of SFPQ are molecular hallmarks of ALS. *Nature Communications*, *9*, 2010. https://doi.org/10.1038/s41467-018-04373-8

Lynch, E. M., Robertson, S., FitzGibbons, C., Reilly, M., Switalski, C., Eckardt, A., Tey, S., Hayakawa, K., & Suzuki, M. (2021). Transcriptome analysis using patient iPSC-derived skeletal myocytes: Bet1L as a new molecule possibly linked to neuromuscular degeneration in ALS. *Experimental Neurology*, *345*, 113815. https://doi.org/10.1016/j.expneurol.2021.113815

Ma, L., Shi, Y., Chen, Z., Li, S., & Zhang, J. (2018). A novel SETX gene mutation associated with Juvenile amyotrophic lateral sclerosis. *Brain and Behavior*, *8*(9), e01066. https://doi.org/10.1002/brb3.1066

Ma, X. R., Prudencio, M., Koike, Y., Vatsavayai, S. C., Kim, G., Harbinski, F., Briner, A., Rodriguez, C. M., Guo, C., Akiyama, T., Schmidt, H. B., Cummings, B. B., Wyatt, D. W., Kurylo, K., Miller, G., Mekhoubad, S., Sallee, N., Mekonnen, G., Ganser, L., … Gitler, A. D. (2022). TDP-43 represses cryptic exon inclusion in the FTD–ALS gene UNC13A. *Nature*, *603*(7899), 124–130. https://doi.org/10.1038/s41586-022-04424-7

Mackenzie, I. R. A., Bigio, E. H., Ince, P. G., Geser, F., Neumann, M., Cairns, N. J., Kwong, L. K., Forman, M. S., Ravits, J., Stewart, H., Eisen, A., McClusky, L., Kretzschmar, H. A., Monoranu, C. M., Highley, J. R., Kirby, J., Siddique, T., Shaw, P. J., Lee, V. M.-Y., & Trojanowski, J. Q. (2007). Pathological TDP-43 distinguishes sporadic amyotrophic lateral sclerosis from amyotrophic lateral sclerosis with SOD1 mutations. *Annals of Neurology*, *61*(5), 427–434. https://doi.org/10.1002/ana.21147

Mackenzie, I. R., Nicholson, A. M., Sarkar, M., Messing, J., Purice, M. D., Pottier, C., Annu, K., Baker, M., Perkerson, R. B., Kurti, A., Matchett, B. J., Mittag, T., Temirov, J., Hsiung, G.-Y. R., Krieger, C., Murray, M. E., Kato, M., Fryer, J. D., Petrucelli, L., … Rademakers, R. (2017). TIA1 mutations in amyotrophic lateral sclerosis and frontotemporal dementia promote phase separation and alter stress granule dynamics. *Neuron*, *95*(4), 808-816.e9. https://doi.org/10.1016/j.neuron.2017.07.025

MacNair, L., Xiao, S., Miletic, D., Ghani, M., Julien, J.-P., Keith, J., Zinman, L., Rogaeva, E., & Robertson, J. (2016). MTHFSD and DDX58 are novel RNA-binding proteins abnormally regulated in amyotrophic lateral sclerosis. *Brain*, *139*(1), 86–100. https://doi.org/10.1093/brain/awv308

Madruga, E., Maestro, I., & Martínez, A. (2021). Mitophagy Modulation, a New Player in the Race against ALS. *International Journal of Molecular Sciences*, *22*(2), 740. https://doi.org/10.3390/ijms22020740

Maessen, M., Veldink, J. H., Onwuteaka-Philipsen, B. D., Hendricks, H. T., Schelhaas, H. J., Grupstra, H. F., van der Wal, G., & van den Berg, L. H. (2014). Euthanasia and physician-assisted suicide in amyotrophic lateral sclerosis: A prospective study. *Journal of Neurology*, *261*(10), 1894–1901. https://doi.org/10.1007/s00415-014-7424-6

Majounie, E., Renton, A. E., Mok, K., Dopper, E. G., Waite, A., Rollinson, S., Chiò, A., Restagno, G., Nicolaou, N., Simon-Sanchez, J., van Swieten, J. C., Abramzon, Y., Johnson, J. O., Sendtner, M., Pamphlett, R., Orrell, R. W., Mead, S., Sidle, K. C., Houlden, H., … Traynor, B. J. (2012). Frequency of the C9orf72 hexanucleotide repeat expansion in patients with amyotrophic lateral sclerosis and frontotemporal dementia: A cross-sectional study. *The Lancet Neurology*, *11*(4), 323–330. https://doi.org/10.1016/S1474-4422(12)70043-1

Majumder, P., Chu, J.-F., Chatterjee, B., Swamy, K. B. S., & Shen, C.-K. J. (2016). Co-regulation of mRNA translation by TDP-43 and Fragile X Syndrome protein FMRP. *Acta Neuropathologica*, *132*(5), 721–738. https://doi.org/10.1007/s00401-016-1603-8

Mangeol, P., Prevo, B., & Peterman, E. J. G. (2016). KymographClear and KymographDirect: Two tools for the automated quantitative analysis of molecular and cellular dynamics using kymographs. *Molecular Biology of the Cell*, *27*(12), 1948–1957. https://doi.org/10.1091/mbc.E15-06-0404

Manjaly, Z. R., Scott, K. M., Abhinav, K., Wijesekera, L., Ganesalingam, J., Goldstein, L. H., Janssen, A., Dougherty, A., Willey, E., Stanton, B. R., Turner, M. R., Ampong, M.-A., Sakel, M., Orrell, R. W., Howard, R., Shaw, C. E., Leigh, P. N., & Al-Chalabi, A. (2010). The sex ratio in amyotrophic lateral sclerosis: A population based study. *Amyotrophic Lateral Sclerosis*, *11*(5), 439–442. https://doi.org/10.3109/17482961003610853

Mann, J. R., & Donnelly, C. J. (2021). RNA modulates physiological and neuropathological protein phase transitions. *Neuron*, *109*(17), 2663-2681. https://doi.org/10.1016/j.neuron.2021.06.023

Manzano, R., Toivonen, J. M., Calvo, A. C., Oliván, S., Zaragoza, P., Rodellar, C., Montarras, D., & Osta, R. (2013). Altered in vitro Proliferation of Mouse SOD1-G93A Skeletal Muscle Satellite Cells. *Neurodegenerative Diseases*, *11*(3), 153–164. https://doi.org/10.1159/000338061

Mao, F., Robinson, J. L., Unger, T., Posavi, M., Amado, D. A., Elman, L., Grossman, M., Wolk, D. A., Lee, E. B., Van Deerlin, V. M., Porta, S., Lee, V. M. Y., Trojanowski, J. Q., & Chen-Plotkin, A. S. (2021). TMEM106B modifies TDP-43 pathology in human ALS brain and cell-based models of TDP-43 proteinopathy. *Acta Neuropathologica*. *142*, 629-642 https://doi.org/10.1007/s00401-021-02330-2

March, Z. M., King, O. D., & Shorter, J. (2016). Prion-like domains as epigenetic regulators, scaffolds for subcellular organization, and drivers of neurodegenerative disease. *Brain Research*, *1647*, 9–18. https://doi.org/10.1016/j.brainres.2016.02.037

Marciano, R., Leprivier, G., & Rotblat, B. (2018). Puromycin labeling does not allow protein synthesis to be measured in energy-starved cells. *Cell Death & Disease*, *9*(2), 39. https://doi.org/10.1038/s41419-017-0056-x

Marin, B., Boumédiene, F., Logroscino, G., Couratier, P., Babron, M.-C., Leutenegger, A. L., Copetti, M., Preux, P.-M., & Beghi, E. (2017). Variation in worldwide incidence of amyotrophic lateral sclerosis: A meta-analysis. *International Journal of Epidemiology*, *46*(1), 57. https://doi.org/10.1093/ije/dyw061

Marin, B., Fontana, A., Arcuti, S., Copetti, M., Boumédiene, F., Couratier, P., Beghi, E., Preux, P. M., & Logroscino, G. (2018). Age-specific ALS incidence: A dose–response meta-analysis. *European Journal of Epidemiology*, *33*(7), 621–634. https://doi.org/10.1007/s10654-018-0392-x

Markert, S. M., Skoruppa, M., Yu, B., Mulcahy, B., Zhen, M., Gao, S., Sendtner, M., & Stigloher, C. (2020). Overexpression of an ALS-associated FUS mutation in C. elegans disrupts NMJ morphology and leads to defective neuromuscular transmission. *Biology Open*, *9*(12). https://doi.org/10.1242/bio.055129

Markmiller, S., Soltanieh, S., Server, K. L., Mak, R., Jin, W., Fang, M. Y., Luo, E.-C., Krach, F., Yang, D., Sen, A., Fulzele, A., Wozniak, J. M., Gonzalez, D. J., Kankel, M. W., Gao, F.-B., Bennett, E. J., Lécuyer, E., & Yeo, G. W. (2018). Context-Dependent and Disease-Specific Diversity in Protein Interactions within Stress Granules. *Cell*, *172*(3), 590-604.e13. https://doi.org/10.1016/j.cell.2017.12.032

Marmor-Kollet, H., Siany, A., Kedersha, N., Knafo, N., Rivkin, N., Danino, Y. M., Moens, T. G., Olender, T., Sheban, D., Cohen, N., Dadosh, T., Addadi, Y., Ravid, R., Eitan, C., Toth Cohen, B., Hofmann, S., Riggs, C. L., Advani, V. M., Higginbottom, A., … Hornstein, E. (2020). Spatiotemporal Proteomic Analysis of Stress Granule Disassembly Using APEX Reveals Regulation by SUMOylation and Links to ALS Pathogenesis. *Molecular Cell*. *80*(5), 876-891. https://doi.org/10.1016/j.molcel.2020.10.032

Marques, R. F., Engler, J. B., Küchler, K., Jones, R. A., Lingner, T., Salinas, G., Gillingwater, T. H., Friese, M. A., & Duncan, K. E. (2020). Motor neuron translatome reveals deregulation of SYNGR4 and PLEKHB1 in mutant TDP-43 amyotrophic lateral sclerosis models. *Human Molecular Genetics*, *29*(16), 2647–2661. https://doi.org/10.1093/hmg/ddaa140

Marrone, L., Poser, I., Casci, I., Japtok, J., Reinhardt, P., Janosch, A., Andree, C., Lee, H. O., Moebius, C., Koerner, E., Reinhardt, L., Cicardi, M. E., Hackmann, K., Klink, B., Poletti, A., Alberti, S., Bickle, M., Hermann, A., Pandey, U. B., … Sterneckert, J. L. (2018). Isogenic FUS-eGFP iPSC Reporter Lines Enable Quantification of FUS Stress Granule Pathology that Is Rescued by Drugs Inducing Autophagy. *Stem Cell Reports*, *10*(2), 375–389. https://doi.org/10.1016/j.stemcr.2017.12.018

Martin, E. W., Thomasen, F. E., Milkovic, N. M., Cuneo, M. J., Grace, C. R., Nourse, A., Lindorff-Larsen, K., & Mittag, T. (2021). Interplay of folded domains and the disordered low-complexity domain in mediating hnRNPA1 phase separation. *Nucleic Acids Research*, *49*(5), 2931–2945. https://doi.org/10.1093/nar/gkab063

Martin, L. J., Liu, Z., Chen, K., Price, A. C., Pan, Y., Swaby, J. A., & Golden, W. C. (2007). Motor neuron degeneration in amyotrophic lateral sclerosis mutant superoxide dismutase-1 transgenic mice: Mechanisms of mitochondriopathy and cell death. *Journal of Comparative Neurology*, *500*(1), 20–46. https://doi.org/10.1002/cne.21160

Martin, S., Zekri, L., Metz, A., Maurice, T., Chebli, K., Vignes, M., & Tazi, J. (2013). Deficiency of G3BP1, the stress granules assembly factor, results in abnormal synaptic plasticity and calcium homeostasis in neurons. *Journal of Neurochemistry*, *125*(2), 175–184. https://doi.org/10.1111/jnc.12189

Martinez, F. J., Pratt, G. A., Van Nostrand, E. L., Batra, R., Huelga, S. C., Kapeli, K., Freese, P., Chun, S. J., Ling, K., Gelboin-Burkhart, C., Fijany, L., Wang, H. C., Nussbacher, J. K., Broski, S. M., Kim,

H. J., Lardelli, R., Sundararaman, B., Donohue, J. P., Javaherian, A., … Yeo, G. W. (2016). Protein-RNA Networks Regulated by Normal and ALS-Associated Mutant HNRNPA2B1 in the Nervous System. *Neuron*, *92*(4), 780–795. https://doi.org/10.1016/j.neuron.2016.09.050

Martinez-Macias, M. I., Moore, D. A., Green, R. L., Gomez-Herreros, F., Naumann, M., Hermann, A., Van Damme, P., Hafezparast, M., & Caldecott, K. W. (2019). FUS (fused in sarcoma) is a component of the cellular response to topoisomerase I-induced DNA breakage and transcriptional stress. *Life Science Alliance*, *2*(2), e201800222. https://doi.org/10.26508/lsa.201800222

Maruyama, H., Morino, H., Ito, H., Izumi, Y., Kato, H., Watanabe, Y., Kinoshita, Y., Kamada, M., Nodera, H., Suzuki, H., Komure, O., Matsuura, S., Kobatake, K., Morimoto, N., Abe, K., Suzuki, N., Aoki, M., Kawata, A., Hirai, T., … Kawakami, H. (2010). Mutations of optineurin in amyotrophic lateral sclerosis. *Nature*, *465*(7295), 223–226. https://doi.org/10.1038/nature08971

Matus, S., Valenzuela, V., Medinas, D. B., & Hetz, C. (2013). ER Dysfunction and Protein Folding Stress in ALS. *International Journal of Cell Biology*, *2013*, e674751. https://doi.org/10.1155/2013/674751

Maury, Y., Come, J., Piskorowski, R. A., Salah-Mohellibi, N., Chevaleyre, V., Peschanski, M., Martinat, C., & Nedelec, S. (2015). Combinatorial analysis of developmental cues efficiently converts human pluripotent stem cells into multiple neuronal subtypes. *Nat Biotech*, *33*(1), 89–96. https://doi.org/10.1038/nbt.3049

May, S., Hornburg, D., Schludi, M. H., Arzberger, T., Rentzsch, K., Schwenk, B. M., Grässer, F. A., Mori, K., Kremmer, E., Banzhaf-Strathmann, J., Mann, M., Meissner, F., & Edbauer, D. (2014). C9orf72 FTLD/ALS-associated Gly-Ala dipeptide repeat proteins cause neuronal toxicity and Unc119 sequestration. *Acta Neuropathologica*, *128*(4), 485–503. https://doi.org/10.1007/s00401-014-1329-4

Mayfield, J. E., Pollak, A. J., Worby, C. A., Xu, J. C., Tandon, V., Newton, A. C., & Dixon, J. E. (2021). Ca2+-dependent liquid-liquid phase separation underlies intracellular Ca2+ stores. *bioRxiv*. https://doi.org/10.1101/2021.07.06.451223

Mazzini, L., Ferrero, I., Luparello, V., Rustichelli, D., Gunetti, M., Mareschi, K., Testa, L., Stecco, A., Tarletti, R., Miglioretti, M., Fava, E., Nasuelli, N., Cisari, C., Massara, M., Vercelli, R., Oggioni, G. D., Carriero, A., Cantello, R., Monaco, F., & Fagioli, F. (2010). Mesenchymal stem cell transplantation in amyotrophic lateral sclerosis: A Phase I clinical trial. *Experimental Neurology*, *223*(1), 229–237. https://doi.org/10.1016/j.expneurol.2009.08.007

Mazzini, L., Mareschi, K., Ferrero, I., Miglioretti, M., Stecco, A., Servo, S., Carriero, A., Monaco, F., & Fagioli, F. (2012). Mesenchymal stromal cell transplantation in amyotrophic lateral sclerosis: A long-term safety study. *Cytotherapy*, *14*(1), 56–60. https://doi.org/10.3109/14653249.2011.613929

McAlary, L., Plotkin, S. S., Yerbury, J. J., & Cashman, N. R. (2019). Prion-Like Propagation of Protein Misfolding and Aggregation in Amyotrophic Lateral Sclerosis. *Frontiers in Molecular Neuroscience*, *12*. https://doi.org/10.3389/fnmol.2019.00262

McCann, E. P., Henden, L., Fifita, J. A., Zhang, K. Y., Grima, N., Bauer, D. C., Fat, S. C. M., Twine, N. A., Pamphlett, R., Kiernan, M. C., Rowe, D. B., Williams, K. L., & Blair, I. P. (2021). Evidence for polygenic and oligogenic basis of Australian sporadic amyotrophic lateral sclerosis. *Journal of Medical Genetics*, *58*(2), 87–95. https://doi.org/10.1136/jmedgenet-2020-106866

McCombe, P. A., Lee, J. D., Woodruff, T. M., & Henderson, R. D. (2020). The Peripheral Immune System and Amyotrophic Lateral Sclerosis. *Frontiers in Neurology*, *11*. https://doi.org/10.3389/fneur.2020.00279

McCord, J. M., & Fridovich, I. (1969). Superoxide Dismutase an enzymatic function for erythrocuprein. *Journal of Biological Chemistry*, *244*(22), 6049–6055.

McDonald, K. K., Aulas, A., Destroismaisons, L., Pickles, S., Beleac, E., Camu, W., Rouleau, G. A., & Vande Velde, C. (2011). TAR DNA-binding protein 43 (TDP-43) regulates stress granule dynamics via differential regulation of G3BP and TIA-1. *Human Molecular Genetics*, *20*(7), 1400–1410. https://doi.org/10.1093/hmg/ddr021

McGown, A., McDearmid, J. R., Panagiotaki, N., Tong, H., Al Mashhadi, S., Redhead, N., Lyon, A. N., Beattie, C. E., Shaw, P. J., & Ramesh, T. M. (2013). Early interneuron dysfunction in ALS: Insights from a mutant sod1 zebrafish model. *Annals of Neurology*, *73*(2), 246–258. https://doi.org/10.1002/ana.23780

McGurk, L., Lee, V. M., Trojanowksi, J. Q., Van Deerlin, V. M., Lee, E. B., & Bonini, N. M. (2014). Poly-A binding protein-1 localization to a subset of TDP-43 inclusions in amyotrophic lateral sclerosis occurs more frequently in patients harboring an expansion in C9orf72. *Journal of Neuropathology and Experimental Neurology*, *73*(9), 837–845. https://doi.org/10.1097/NEN.0000000000000102

McIntire, E., Taapken, S., Leonhard, K., & Larson, A. L. (2020). Genomic Stability Testing of Pluripotent Stem Cells. *Current Protocols in Stem Cell Biology*, *52*(1), e107. https://doi.org/10.1002/cpsc.107

McMillan, M., Gomez, N., Bekier, M., Li, X., Miguez, R., Tank, E. M., & Barmada, S. J. (2022). RNA methylation influences TDP43 binding and disease pathogenesis in models of amyotrophic lateral sclerosis and frontotemporal dementia. *bioRxiv*. https://doi.org/10.1101/2022.04.03.486880

Mehta, A. R., Gregory, J. M., Dando, O., Carter, R. N., Burr, K., Nanda, J., Story, D., McDade, K., Smith, C., Morton, N. M., Mahad, D. J., Hardingham, G. E., Chandran, S., & Selvaraj, B. T. (2021). Mitochondrial bioenergetic deficits in C9orf72 amyotrophic lateral sclerosis motor neurons cause dysfunctional axonal homeostasis. *Acta Neuropathologica*. 141, 257-279. https://doi.org/10.1007/s00401-020-02252-5

Mejia Maza, A., Jarvis, S., Lee, W. C., Cunningham, T. J., Schiavo, G., Secrier, M., Fratta, P., Sleigh, J. N., Fisher, E. M. C., & Sudre, C. H. (2021). NMJ-Analyser identifies subtle early changes in mouse models of neuromuscular disease. *Scientific Reports*, *11*(1), 12251. https://doi.org/10.1038/s41598-021-91094-6

Meng, L., Bian, A., Jordan, S., Wolff, A., Shefner, J. M., & Andrews, J. (2018). Profile of medical care costs in patients with amyotrophic lateral sclerosis in the Medicare programme and under commercial insurance. *Amyotrophic Lateral Sclerosis and Frontotemporal Degeneration*, *19*(1–2), 134–142. https://doi.org/10.1080/21678421.2017.1363242

Merkle, F. T., Ghosh, S., Genovese, G., Handsaker, R. E., Kashin, S., Meyer, D., Karczewski, K. J., O'Dushlaine, C., Pato, C., Pato, M., MacArthur, D. G., McCarroll, S. A., & Eggan, K. (2022). Whole-genome analysis of human embryonic stem cells enables rational line selection based on genetic variation. *Cell Stem Cell*, *29*(3), 472-486.e7. https://doi.org/10.1016/j.stem.2022.01.011

Merkle, F. T., Ghosh, S., Kamitaki, N., Mitchell, J., Avior, Y., Mello, C., Kashin, S., Mekhoubad, S., Ilic, D., Charlton, M., Saphier, G., Handsaker, R. E., Genovese, G., Bar, S., Benvenisty, N., McCarroll, S. A., & Eggan, K. (2017). Human pluripotent stem cells recurrently acquire and expand dominant negative P53 mutations. *Nature*, *545*(7653), 229–233. https://doi.org/10.1038/nature22312

Mertens, J., Herdy, J. R., Traxler, L., Schafer, S. T., Schlachetzki, J. C. M., Böhnke, L., Reid, D. A., Lee, H., Zangwill, D., Fernandes, D. P., Agarwal, R. K., Lucciola, R., Zhou-Yang, L., Karbacher, L., Edenhofer, F., Stern, S., Horvath, S., Paquola, A. C. M., Glass, C. K., … Gage, F. H. (2021). Age-dependent instability of mature neuronal fate in induced neurons from Alzheimer's patients. *Cell Stem Cell*. *28*(9), 1533-1548.e6. https://doi.org/10.1016/j.stem.2021.04.004

Mertens, J., Paquola, A. C. M., Ku, M., Hatch, E., Böhnke, L., Ladjevardi, S., McGrath, S., Campbell, B., Lee, H., Herdy, J. R., Gonçalves, J. T., Toda, T., Kim, Y., Winkler, J., Yao, J., Hetzer, M. W., & Gage, F. H. (2015). Directly Reprogrammed Human Neurons Retain Aging-Associated Transcriptomic Signatures and Reveal Age-Related Nucleocytoplasmic Defects. *Cell Stem Cell*, *17*(6), 705–718. https://doi.org/10.1016/j.stem.2015.09.001

Meyer, C., Garzia, A., Morozov, P., Molina, H., & Tuschl, T. (2020). The G3BP1-Family-USP10 Deubiquitinase Complex Rescues Ubiquitinated 40S Subunits of Ribosomes Stalled in Translation from Lysosomal Degradation. *Molecular Cell*, *77*(6), 1193-1205.e5. https://doi.org/10.1016/j.molcel.2019.12.024

Meyer, K., Ferraiuolo, L., Miranda, C. J., Likhite, S., McElroy, S., Renusch, S., Ditsworth, D., Lagier-Tourenne, C., Smith, R. A., Ravits, J., Burghes, A. H., Shaw, P. J., Cleveland, D. W., Kolb, S. J., & Kaspar, B. K. (2014). Direct conversion of patient fibroblasts demonstrates non-cell autonomous toxicity of astrocytes to motor neurons in familial and sporadic ALS. *Proceedings of the National Academy of Sciences*, *111*(2), 829–832. https://doi.org/10.1073/pnas.1314085111

Miller, K. E., & Suter, D. M. (2018). An Integrated Cytoskeletal Model of Neurite Outgrowth. *Frontiers in Cellular Neuroscience*, *12*. https://www.frontiersin.org/articles/10.3389/fncel.2018.00447

Minciacchi, D., Kassa, R. M., Del Tongo, C., Mariotti, R., & Bentivoglio, M. (2009). Voronoi-based spatial analysis reveals selective interneuron changes in the cortex of FALS mice. *Experimental Neurology*, *215*(1), 77–86. https://doi.org/10.1016/j.expneurol.2008.09.005

Mirsaeidi, M., Gidfar, S., Vu, A., & Schraufnagel, D. (2016). Annexins family: Insights into their functions and potential role in pathogenesis of sarcoidosis. *Journal of Translational Medicine*, *14*(1), 89. https://doi.org/10.1186/s12967-016-0843-7

Mitchell, C. S., Lee, R. H., & Coulter, W. H. (2012). Cargo distributions differentiate pathological axonal transport impairments. *Journal of Theoretical Biology*, *300*, 277–291. https://doi.org/10.1016/j.jtbi.2012.01.019

Mitchell, J., Paul, P., Chen, H.-J., Morris, A., Payling, M., Falchi, M., Habgood, J., Panoutsou, S., Winkler, S., Tisato, V., Hajitou, A., Smith, B., Vance, C., Shaw, C., Mazarakis, N. D., & Belleroche, J. de. (2010). Familial amyotrophic lateral sclerosis is associated with a mutation in D-amino acid oxidase. *Proceedings of the National Academy of Sciences*, *107*(16), 7556–7561. https://doi.org/10.1073/pnas.0914128107

Mitsuzawa, S., Suzuki, N., Akiyama, T., Ishikawa, M., Sone, T., Kawada, J., Funayama, R., Shirota, M., Mitsuhashi, H., Morimoto, S., Ikeda, K., Shijo, T., Ohno, A., Nakamura, N., Ono, H., Ono, R., Osana, S., Nakagawa, T., Nishiyama, A., … Aoki, M. (2021). Reduced PHOX2B stability causes axonal growth impairment in motor neurons with TARDBP mutations. *Stem Cell Reports*, *16*(6), 1527-1541. https://doi.org/10.1016/j.stemcr.2021.04.021

Miyashiro, K. Y., Beckel-Mitchener, A., Purk, T. P., Becker, K. G., Barret, T., Liu, L., Carbonetto, S., Weiler, I. J., Greenough, W. T., & Eberwine, J. (2003). RNA Cargoes Associating with FMRP Reveal Deficits in Cellular Functioning in Fmr1 Null Mice. *Neuron*, *37*(3), 417–431. https://doi.org/10.1016/S0896-6273(03)00034-5

Mizielinska, S., Lashley, T., Norona, F. E., Clayton, E. L., Ridler, C. E., Fratta, P., & Isaacs, A. M. (2013). C9orf72 frontotemporal lobar degeneration is characterised by frequent neuronal sense and antisense RNA foci. *Acta Neuropathologica*, *126*(6), 845–857. https://doi.org/10.1007/s00401-013-1200-z

Mizuno, Y., Amari, M., Takatama, M., Aizawa, H., Mihara, B., & Okamoto, K. (2006). Immunoreactivities of p62, an ubiqutin-binding protein, in the spinal anterior horn cells of patients with amyotrophic lateral sclerosis. *Journal of the Neurological Sciences*, *249*(1), 13–18. https://doi.org/10.1016/j.jns.2006.05.060

Mizutani, A., Tokumitsu, H., Kobayashi, R., & Hidaka, H. (1993). Phosphorylation of annexin XI (CAP-50) in SR-3Y1 cells. *Journal of Biological Chemistry*, *268*(21), 15517–15522.

Mizutani, A., Watanabe, N., Kitao, T., Tokumitsu, H., & Hidaka, H. (1995). The Long Amino-Terminal Tail Domain of Annexin XI Is Necessary for Its Nuclear Localization. *Archives of Biochemistry and Biophysics*, *318*(1), 157–165. https://doi.org/10.1006/abbi.1995.1216

Mofatteh, M. (2020). MRNA localization and local translation in neurons. *AIMS Neuroscience*, *7*(3), 299–310. https://doi.org/10.3934/Neuroscience.2020016

Monday, H. R., Kharod, S. C., Yoon, Y. J., Singer, R. H., & Castillo, P. E. (2022). Presynaptic FMRP and local protein synthesis support structural and functional plasticity of glutamatergic axon terminals. *Neuron*, *110*(16), 2588-2606.e6. https://doi.org/10.1016/j.neuron.2022.05.024

Morgan, R. O., Bell, D. W., Testa, J. R., & Fernandez, M. P. (1998). Genomic Locations ofANX11andANX13and the Evolutionary Genetics of Human Annexins. *Genomics*, *48*(1), 100–110. https://doi.org/10.1006/geno.1997.5148

Mori, K., Lammich, S., Mackenzie, I. R. A., Forné, I., Zilow, S., Kretzschmar, H., Edbauer, D., Janssens, J., Kleinberger, G., Cruts, M., Herms, J., Neumann, M., Van Broeckhoven, C., Arzberger, T., & Haass, C. (2013). HnRNP A3 binds to GGGGCC repeats and is a constituent of p62-positive/TDP43-negative inclusions in the hippocampus of patients with C9orf72 mutations. *Acta Neuropathologica*, *125*(3), 413–423. https://doi.org/10.1007/s00401-013-1088-7

Mori, K., Weng, S.-M., Arzberger, T., May, S., Rentzsch, K., Kremmer, E., Schmid, B., Kretzschmar, H. A., Cruts, M., Broeckhoven, C. V., Haass, C., & Edbauer, D. (2013). The C9orf72 GGGGCC Repeat Is Translated into Aggregating Dipeptide-Repeat Proteins in FTLD/ALS. *Science*, *339*(6125), 1335–1338. https://doi.org/10.1126/science.1232927

Moss, S. E., & Morgan, R. O. (2004). The annexins. *Genome Biology*, *5*(4), 219. https://doi.org/10.1186/gb-2004-5-4-219

Moustaqim-Barrette, A., Lin, Y. Q., Pradhan, S., Neely, G. G., Bellen, H. J., & Tsuda, H. (2014). The amyotrophic lateral sclerosis 8 protein, VAP, is required for ER protein quality control. *Human Molecular Genetics*, *23*(8), 1975–1989. https://doi.org/10.1093/hmg/ddt594

Moya, M. V., Kim, R. D., Rao, M. N., Cotto, B. A., Pickett, S. B., Sferrazza, C. E., Heintz, N., & Schmidt, E. F. (2022). Unique molecular features and cellular responses differentiate two populations of motor cortical layer 5b neurons in a preclinical model of ALS. *Cell Reports*, *38*(12), 110556. https://doi.org/10.1016/j.celrep.2022.110556

Müller, F.-J., Schuldt, B. M., Williams, R., Mason, D., Altun, G., Papapetrou, E. P., Danner, S., Goldmann, J. E., Herbst, A., Schmidt, N. O., Aldenhoff, J. B., Laurent, L. C., & Loring, J. F. (2011). A bioinformatic assay for pluripotency in human cells. *Nature Methods*, *8*(4), 315–317. https://doi.org/10.1038/nmeth.1580

Müller, K., Brenner, D., Weydt, P., Meyer, T., Grehl, T., Petri, S., Grosskreutz, J., Schuster, J., Volk, A. E., Borck, G., Kubisch, C., Klopstock, T., Zeller, D., Jablonka, S., Sendtner, M., Klebe, S., Knehr, A., Günther, K., Weis, J., … German ALS network MND-NET. (2018). Comprehensive analysis of the mutation spectrum in 301 German ALS families. *Journal of Neurology, Neurosurgery, and Psychiatry*, *89*(8), 817–827. https://doi.org/10.1136/jnnp-2017-317611

Münch, C., O'Brien, J., & Bertolotti, A. (2011). Prion-like propagation of mutant superoxide dismutase-1 misfolding in neuronal cells. *Proceedings of the National Academy of Sciences*, *108*(9), 3548–3553. https://doi.org/10.1073/pnas.1017275108

Münch, C., Rolfs, A., & Meyer, T. (2008). Heterozygous S44L missense change of the spastin gene in amyotrophic lateral sclerosis. *Amyotrophic Lateral Sclerosis*, *9*(4), 251–253. https://doi.org/10.1080/17482960801900172

Murakami, T., Qamar, S., Lin, J. Q., Schierle, G. S. K., Rees, E., Miyashita, A., Costa, A. R., Dodd, R. B., Chan, F. T. S., Michel, C. H., Kronenberg-Versteeg, D., Li, Y., Yang, S.-P., Wakutani, Y., Meadows, W., Ferry, R. R., Dong, L., Tartaglia, G. G., Favrin, G., … St George-Hyslop, P. (2015). ALS/FTD Mutation-Induced Phase Transition of FUS Liquid Droplets and Reversible Hydrogels into Irreversible Hydrogels Impairs RNP Granule Function. *Neuron*, *88*(4), 678–690. https://doi.org/10.1016/j.neuron.2015.10.030

Murch, S. J., Cox, P. A., & Banack, S. A. (2004). A mechanism for slow release of biomagnified cyanobacterial neurotoxins and neurodegenerative disease in Guam. *Proceedings of the National Academy of Sciences*, *101*(33), 12228–12231. https://doi.org/10.1073/pnas.0404926101

Nagano, S., Jinno, J., Abdelhamid, R. F., Jin, Y., Shibata, M., Watanabe, S., Hirokawa, S., Nishizawa, M., Sakimura, K., Onodera, O., Okada, H., Okada, T., Saito, Y., Takahashi-Fujigasaki, J., Murayama, S., Wakatsuki, S., Mochizuki, H., & Araki, T. (2020). TDP-43 transports ribosomal protein mRNA to regulate axonal local translation in neuronal axons. *Acta Neuropathologica*, *140*(5), 695–713. https://doi.org/10.1007/s00401-020-02205-y

Nagy, Z. F., Pál, M., Salamon, A., Kafui Esi Zodanu, G., Füstös, D., Klivényi, P., & Széll, M. (2022). Re-analysis of the Hungarian amyotrophic lateral sclerosis population and evaluation of novel ALS genetic risk variants. *Neurobiology of Aging*, *116*, 1–11. https://doi.org/10.1016/j.neurobiolaging.2022.04.002

Nahm, M., Lim, S. M., Kim, Y.-E., Park, J., Noh, M.-Y., Lee, S., Roh, J. E., Hwang, S.-M., Park, C.-K., Kim, Y. H., Lim, G., Lee, J., Oh, K.-W., Ki, C.-S., & Kim, S. H. (2020). ANXA11 mutations in ALS cause dysregulation of calcium homeostasis and stress granule dynamics. *Science Translational Medicine*, *12*(566). https://doi.org/10.1126/scitranslmed.aax3993

Nakaya, T. (2020). Dissection of FUS domains involved in regulation of SnRNP70 gene expression. *FEBS Letters*, *594*(21), 3518–3529. https://doi.org/10.1002/1873-3468.13924

Nakaya, T. (2022). A specific gene-splicing alteration in the SNRNP70 gene as a hallmark of an ALS subtype. *Gene*, *818*, 146203. https://doi.org/10.1016/j.gene.2022.146203

Namboori, S. C., Thomas, P., Ames, R., Hawkins, S., Garrett, L. O., Willis, C. R. G., Rosa, A., Stanton, L. W., & Bhinge, A. (2021). Single-cell transcriptomics identifies master regulators of neurodegeneration in SOD1 ALS iPSC-derived motor neurons. *Stem Cell Reports*, *16*(12), 3020-3035. https://doi.org/10.1016/j.stemcr.2021.10.010

Narai, H., Manabe, Y., Nagai, M., Nagano, I., Ohta, Y., Murakami, T., Takehisa, Y., Kamiya, T., & Abe, K. (2009). Early detachment of neuromuscular junction proteins in ALS mice with SODG93A mutation. *Neurology International*, *1*(1), e16–e16. https://doi.org/10.4081/ni.2009.e16

Nassif, M., Woehlbier, U., & Manque, P. A. (2017). The Enigmatic Role of C9ORF72 in Autophagy. *Frontiers in Neuroscience*, *11*. https://www.frontiersin.org/article/10.3389/fnins.2017.00442

Naujock, M., Stanslowsky, N., Bufler, S., Naumann, M., Reinhardt, P., Sterneckert, J., Kefalakes, E., Kassebaum, C., Bursch, F., Lojewski, X., Storch, A., Frickenhaus, M., Boeckers, T. M., Putz, S., Demestre, M., Liebau, S., Klingenstein, M., Ludolph, A. C., Dengler, R., … Petri, S. (2016). 4-Aminopyridine Induced Activity Rescues Hypoexcitable Motor Neurons from Amyotrophic Lateral Sclerosis Patient-Derived Induced Pluripotent Stem Cells. *Stem Cells*, *34*(6), 1563–1575. https://doi.org/10.1002/stem.2354

Naumann, M., Pal, A., Goswami, A., Lojewski, X., Japtok, J., Vehlow, A., Naujock, M., Günther, R., Jin, M., Stanslowsky, N., Reinhardt, P., Sterneckert, J., Frickenhaus, M., Pan-Montojo, F., Storkebaum, E., Poser, I., Freischmidt, A., Weishaupt, J. H., Holzmann, K., … Hermann, A. (2018). Impaired DNA damage response signaling by FUS-NLS mutations leads to neurodegeneration and FUS aggregate formation. *Nature Communications*, *9*(1), 335. https://doi.org/10.1038/s41467-017-02299-1

Neelagandan, N., Gonnella, G., Dang, S., Janiesch, P. C., Miller, K. K., Küchler, K., Marques, R. F., Indenbirken, D., Alawi, M., Grundhoff, A., Kurtz, S., & Duncan, K. E. (2019). TDP-43 enhances translation of specific mRNAs linked to neurodegenerative disease. *Nucleic Acids Research*, *47*(1), 341–361. https://doi.org/10.1093/nar/gky972

Nehme, R., Zuccaro, E., Ghosh, S. D., Li, C., Sherwood, J. L., Pietilainen, O., Barrett, L. E., Limone, F., Worringer, K. A., Kommineni, S., Zang, Y., Cacchiarelli, D., Meissner, A., Adolfsson, R., Haggarty, S., Madison, J., Muller, M., Arlotta, P., Fu, Z., … Eggan, K. (2018). Combining NGN2 Programming with Developmental Patterning Generates Human Excitatory Neurons with NMDAR-Mediated Synaptic Transmission. *Cell Reports*, *23*(8), 2509–2523. https://doi.org/10.1016/j.celrep.2018.04.066

Nel, M., Mahungu, A. C., Monnakgotla, N., Botha, G. R., Mulder, N. J., Wu, G., Rampersaud, E., Blitterswijk, M. van, Wuu, J., Cooley, A., Myers, J., Rademakers, R., Taylor, J. P., Benatar, M., & Heckmann, J. M. (2022). Revealing the Mutational Spectrum in Southern Africans With Amyotrophic Lateral Sclerosis. *Neurology Genetics*, *8*(1). https://doi.org/10.1212/NXG.0000000000000654

Neumann, M., Kwong, L. K., Lee, E. B., Kremmer, E., Flatley, A., Xu, Y., Forman, M. S., Troost, D., Kretzschmar, H. A., Trojanowski, J. Q., & Lee, V. M.-Y. (2009). Phosphorylation of S409/410 of TDP-43 is a consistent feature in all sporadic and familial forms of TDP-43 proteinopathies. *Acta Neuropathologica*, *117*(2), 137–149. https://doi.org/10.1007/s00401-008-0477-9

Neumann, M., Rademakers, R., Roeber, S., Baker, M., Kretzschmar, H. A., & Mackenzie, I. R. A. (2009). A new subtype of frontotemporal lobar degeneration with FUS pathology. *Brain*, *132*(11), 2922–2931. https://doi.org/10.1093/brain/awp214

Neumann, M., Sampathu, D. M., Kwong, L. K., Truax, A. C., Micsenyi, M. C., Chou, T. T., Bruce, J., Schuck, T., Grossman, M., Clark, C. M., McCluskey, L. F., Miller, B. L., Masliah, E., Mackenzie, I. R., Feldman, H., Feiden, W., Kretzschmar, H. A., Trojanowski, J. Q., & Lee, V. M.-Y. (2006). Ubiquitinated TDP-43 in frontotemporal lobar degeneration and amyotrophic lateral sclerosis. *Science*, *314*(5796), 130–133. https://doi.org/10.1126/science.1134108

Nguyen, A. D., Nguyen, T. A., Zhang, J., Devireddy, S., Zhou, P., Karydas, A. M., Xu, X., Miller, B. L., Rigo, F., Ferguson, S. M., Huang, E. J., Walther, T. C., & Farese, R. V. (2018). Murine knockin model for progranulin-deficient frontotemporal dementia with nonsense-mediated mRNA decay. *Proceedings of the National Academy of Sciences*, *115*(12), E2849–E2858. https://doi.org/10.1073/pnas.1722344115

Ni, J., Liu, Z., Li, W., Yuan, Y., Huang, L., Hu, Y., Liu, P., Hou, X., Jiao, B., Li, J., Shen, L., Jiang, H., Tang, B., & Wang, J. (2021). Rare, pathogenic variants in LRP10 are associated with amyotrophic lateral sclerosis in patients from mainland China. *Neurobiology of Aging*, *97*, 145.e17-145.e22. https://doi.org/10.1016/j.neurobiolaging.2020.06.013

Nicolas, A., Kenna, K. P., Renton, A. E., Ticozzi, N., Faghri, F., Chia, R., Dominov, J. A., Kenna, B. J., Nalls, M. A., Keagle, P., Rivera, A. M., van Rheenen, W., Murphy, N. A., van Vugt, J. J. F. A., Geiger, J. T., Van der Spek, R. A., Pliner, H. A., Shankaracharya, null, Smith, B. N., … Landers, J. E. (2018). Genome-wide Analyses Identify KIF5A as a Novel ALS Gene. *Neuron*, *97*(6), 1268-1283.e6. https://doi.org/10.1016/j.neuron.2018.02.027

Nijssen, J., Aguila, J., & Hedlund, E. (2019). Axon-seq for in Depth Analysis of the RNA Content of Neuronal Processes. *Bio-Protocol*, *9*(14), e3312. https://doi.org/10.21769/BioProtoc.3312

Nikitina, T. V., Kashevarova, A. A., & Lebedev, I. N. (2019). Chromosomal Instability and Karyotype Correction in Human Induced Pluripotent Stem Cells. *Russian Journal of Genetics*, *55*(10), 1183–1195. https://doi.org/10.1134/S1022795419100090

Nikolaou, N., Gordon, P. M., Hamid, F., Taylor, R., Makeyev, E. V., & Houart, C. (2020). Cytoplasmic pool of spliceosome protein SNRNP70 regulates the axonal transcriptome and development of motor connectivity. *bioRxiv*. https://doi.org/10.1101/2020.05.25.097444

Nishimura, A. L., & Arias, N. (2021). Synaptopathy Mechanisms in ALS Caused by C9orf72 Repeat Expansion. *Frontiers in Cellular Neuroscience*, *15*. https://doi.org/10.3389/fncel.2021.660693

Nishimura, A. L., Mitne-Neto, M., Silva, H. C. A., Richieri-Costa, A., Middleton, S., Cascio, D., Kok, F., Oliveira, J. R. M., Gillingwater, T., Webb, J., Skehel, P., & Zatz, M. (2004). A mutation in the vesicle-trafficking protein VAPB causes late-onset spinal muscular atrophy and amyotrophic lateral sclerosis. *American Journal of Human Genetics*, *75*(5), 822–831. https://doi.org/10.1086/425287

Nociti, V., Frisullo, G., Marti, A., Luigetti, M., Iorio, R., Patanella, A. K., Bianco, A., Tonali, P. A., Grillo, R. L., Sabatelli, M., & Batocchi, A. P. (2010). Epstein-Barr virus antibodies in serum and cerebrospinal fluid from multiple sclerosis, chronic inflammatory demyelinating polyradiculoneuropathy and amyotrophic lateral sclerosis. *Journal of Neuroimmunology*, *225*(1–2), 149–152. https://doi.org/10.1016/j.jneuroim.2010.04.007

Noh, M.-Y., Kwon, M.-S., Oh, K.-W., Nahm, M., Park, J., Young-Eun Kim, Chang-Seok Ki, Hee Kyung Jin, Jae-sung Bae, & Kim, S. H. (2020). Defective phagocytic function of induced microglia-like cells is correlated with rapid progression of sporadic ALS. *Research Square*. https://doi.org/10.21203/rs.3.rs-29976/v1

Nolan, M., Scott, C., Gamarallage, M. P., Lunn, D., Carpenter, K., McDonough, E., Meyer, D., Kaanumalle, S., Santamaria-Pang, A., Turner, M. R., Talbot, K., & Ansorge, O. (2020). Quantitative patterns of motor cortex proteinopathy across ALS genotypes. *Acta Neuropathologica Communications*, *8*(1), 98. https://doi.org/10.1186/s40478-020-00961-2

Nonaka, T., Arai, T., Buratti, E., Baralle, F. E., Akiyama, H., & Hasegawa, M. (2009). Phosphorylated and ubiquitinated TDP-43 pathological inclusions in ALS and FTLD-U are recapitulated in SH-SY5Y cells. *FEBS Letters*, *583*(2), 394–400. https://doi.org/10.1016/j.febslet.2008.12.031

Nonaka, T., Suzuki, G., Tanaka, Y., Kametani, F., Hirai, S., Okado, H., Miyashita, T., Saitoe, M., Akiyama, H., Masai, H., & Hasegawa, M. (2016). Phosphorylation of TAR DNA-binding Protein

of 43 kDa (TDP-43) by Truncated Casein Kinase 1δ Triggers Mislocalization and Accumulation of TDP-43. *Journal of Biological Chemistry*, *291*(11), 5473–5483. https://doi.org/10.1074/jbc.M115.695379

Noyes, M. D., Harvey, W. T., Porubsky, D., Sulovari, A., Li, R., Rose, N. R., Audano, P. A., Munson, K. M., Lewis, A. P., Hoekzema, K., Mantere, T., Graves-Lindsay, T. A., Sanders, A. D., Goodwin, S., Kramer, M., Mokrab, Y., Zody, M. C., Hoischen, A., Korbel, J. O., … Eichler, E. E. (2022). Familial long-read sequencing increases yield of de novo mutations. *The American Journal of Human Genetics*, *109*(4), 631-646. https://doi.org/10.1016/j.ajhg.2022.02.014

Nunes Gonçalves, J. P., Leoni, T. B., Martins, M. P., Peluzzo, T. M., Dourado, M. E. T., Saute, J. A. M., Paranhos Miranda Covaleski, A. P., Bulle de Oliveira, A. S., Claudino, R., Marques, W., Nucci, A., & França, M. C. (2021). Genetic epidemiology of familial ALS in Brazil. *Neurobiology of Aging*. *102*, 227.e1-227.e4. https://doi.org/10.1016/j.neurobiolaging.2021.01.007

Obrador, E., Salvador-Palmer, R., López-Blanch, R., Dellinger, R. W., & Estrela, J. M. (2021). NAD+ Precursors and Antioxidants for the Treatment of Amyotrophic Lateral Sclerosis. *Biomedicines*, *9*(8), 1000. https://doi.org/10.3390/biomedicines9081000

Ohlemacher, S. K., White, N. R., Gillespie, K., O'Neil, O., Kovarik, M. M., Sullen, K., Nudelman, K. N. H., Schwantes-An, T.-H., Abreu, M., Marshall, J. D., Faber, K. M., Mitchell, C. M., Edler, M. C., Meyer, J. S., & Foroud, T. M. (2021). Establishing a centralized repository of human pluripotent stem cells for neurodegeneration research. *Alzheimer's & Dementia*, *17*(S3), e053911. https://doi.org/10.1002/alz.053911

Ohta, Y., Yamashita, T., Nomura, E., Hishikawa, N., Ikegami, K., Osakada, Y., Matsumoto, N., Kawahara, Y., Yunoki, T., Takahashi, Y., Takamiya, M., Tadokoro, K., Sasaki, R., Nakano, Y., Tsunoda, K., Sato, K., Omote, Y., Takemoto, M., & Abe, K. (2020). Improvement of a decreased anti-oxidative activity by edaravone in amyotrophic lateral sclerosis patients. *Journal of the Neurological Sciences*, *415*, 116906. https://doi.org/10.1016/j.jns.2020.116906

Okamoto, K., Hirai, S., Shoji, M., Senoh, Y., & Yamazaki, T. (1990). Axonal swellings in the corticospinal tracts in amyotrophic lateral sclerosis. *Acta Neuropathologica*, *80*(2), 222–226. https://doi.org/10.1007/BF00308929

Okamoto, Y., Ihara, M., Urushitani, M., Yamashita, H., Kondo, T., Tanigaki, A., Oono, M., Kawamata, J., Ikemoto, A., Kawamoto, Y., Takahashi, R., & Ito, H. (2011). An autopsy case of SOD1-related ALS with TDP-43 positive inclusions. *Neurology*, *77*(22), 1993–1995. https://doi.org/10.1212/WNL.0b013e31823a0cfc

Oliveira, D., Morales-Vicente, D. A., Amaral, M. S., Luz, L., Sertié, A. L., Leite, F. S., Navarro, C., Kaid, C., Esposito, J., Goulart, E., Caires, L., Alves, L. M., Melo, U. S., Figueiredo, T., Mitne-Neto, M., Okamoto, O. K., Verjovski-Almeida, S., & Zatz, M. (2020). Different gene expression profiles in iPSC-derived motor neurons from ALS8 patients with variable clinical courses suggest mitigating pathways for neurodegeneration. *Human Molecular Genetics*, *29*(9), 1465–1475. https://doi.org/10.1093/hmg/ddaa069

Oliveira, P. H., da Silva, C. L., & Cabral, J. M. S. (2014). Concise Review: Genomic Instability in Human Stem Cells: Current Status and Future Challenges. *Stem Cells*, *32*(11), 2824–2832. https://doi.org/10.1002/stem.1796

O'Rourke, J. G., Bogdanik, L., Yáñez, A., Lall, D., Wolf, A. J., Muhammad, A. K. M. G., Ho, R., Carmona, S., Vit, J. P., Zarrow, J., Kim, K. J., Bell, S., Harms, M. B., Miller, T. M., Dangler, C. A., Underhill, D. M., Goodridge, H. S., Lutz, C. M., & Baloh, R. H. (2016). C9orf72 is required for proper macrophage and microglial function in mice. *Science*, *351*(6279), 1324–1329. https://doi.org/10.1126/science.aaf1064

Orozco, D., Tahirovic, S., Rentzsch, K., Schwenk, B. M., Haass, C., & Edbauer, D. (2012). Loss of fused in sarcoma (FUS) promotes pathological Tau splicing. *EMBO Reports*, *13*(8), 759–764. https://doi.org/10.1038/embor.2012.90

Orrù, S., Coni, P., Floris, A., Littera, R., Carcassi, C., Sogos, V., & Brancia, C. (2016). Reduced stress granule formation and cell death in fibroblasts with the A382T mutation of TARDBP gene:

Evidence for loss of TDP-43 nuclear function. *Human Molecular Genetics*, *25*(20), 4473–4483. https://doi.org/10.1093/hmg/ddw276

Oyston, L. J., Ubiparipovic, S., Fitzpatrick, L., Hallupp, M., Boccanfuso, L. M., Kwok, J. B., & Dobson-Stone, C. (2021). Rapid in vitro quantification of TDP-43 and FUS mislocalisation for screening of gene variants implicated in frontotemporal dementia and amyotrophic lateral sclerosis. *Scientific Reports*, *11*(1), 14881. https://doi.org/10.1038/s41598-021-94225-1

Ozdinler, P. H., Benn, S., Yamamoto, T. H., Güzel, M., Brown, R. H., & Macklis, J. D. (2011). Corticospinal motor neurons and related subcerebral projection neurons undergo early and specific neurodegeneration in hSOD1G$^{93}$A transgenic ALS mice. *The Journal of Neuroscience: The Official Journal of the Society for Neuroscience*, *31*(11), 4166–4177. https://doi.org/10.1523/JNEUROSCI.4184-10.2011

Öztürk, Z., O'Kane, C. J., & Pérez-Moreno, J. J. (2020). Axonal Endoplasmic Reticulum Dynamics and Its Roles in Neurodegeneration. *Frontiers in Neuroscience*, *14*. https://doi.org/10.3389/fnins.2020.00048

Palombo, F., Peron, C., Caporali, L., Iannielli, A., Maresca, A., Meo, I. D., Fiorini, C., Segnali, A., Sciacca, F. L., Rizzo, A., Levi, S., Suomalainen, A., Prigione, A., Broccoli, V., Carelli, V., & Tiranti, V. (2021). The relevance of mitochondrial DNA variants fluctuation during reprogramming and neuronal differentiation of human iPSCs. *Stem Cell Reports*, *16*(8), 1953-1967. https://doi.org/10.1016/j.stemcr.2021.06.016

Paonessa, F., Evans, L. D., Solanki, R., Larrieu, D., Wray, S., Hardy, J., Jackson, S. P., & Livesey, F. J. (2019). Microtubules Deform the Nuclear Membrane and Disrupt Nucleocytoplasmic Transport in Tau-Mediated Frontotemporal Dementia. *Cell Reports*, *26*(3), 582-593.e5. https://doi.org/10.1016/j.celrep.2018.12.085

Park, S. B., Kiernan, M. C., & Vucic, S. (2017). Axonal Excitability in Amyotrophic Lateral Sclerosis. *Neurotherapeutics*, *14*(1), 78–90. https://doi.org/10.1007/s13311-016-0492-9

Parkinson, N., Ince, P. G., Smith, M. O., Highley, R., Skibinski, G., Andersen, P. M., Morrison, K. E., Pall, H. S., Hardiman, O., Collinge, J., Shaw, P. J., & Fisher, E. C. (2006). ALS phenotypes with mutations in CHMP2B (charged multivesicular body protein 2B). *Neurology*, *67*(6), 1074. https://doi.org/10.1212/01.wnl.0000231510.89311.8b

Pasinelli, P., Belford, M. E., Lennon, N., Bacskai, B. J., Hyman, B. T., Trotti, D., & Brown, R. H. (2004). Amyotrophic lateral sclerosis-associated SOD1 mutant proteins bind and aggregate with Bcl-2 in spinal cord mitochondria. *Neuron*, *43*(1), 19–30. https://doi.org/10.1016/j.neuron.2004.06.021

Patel, A. N., & Mathew, D. (2020). A Study of Gene Expression Changes in Human Spinal and Oculomotor Neurons; Identifying Potential Links to Sporadic ALS. *Genes*, *11*(4), 448. https://doi.org/10.3390/genes11040448

Paul, P., & de Belleroche, J. (2014). The role of D-serine and glycine as co-agonists of NMDA receptors in motor neuron degeneration and amyotrophic lateral sclerosis (ALS). *Frontiers in Synaptic Neuroscience*, *6*. https://www.frontiersin.org/article/10.3389/fnsyn.2014.00010

Peggion, C., Massimino, M. L., Bonadio, R. S., Lia, F., Lopreiato, R., Cagnin, S., Calì, T., & Bertoli, A. (2021). Regulation of Endoplasmic Reticulum–Mitochondria Tethering and Ca2+ Fluxes by TDP-43 via GSK3β. *International Journal of Molecular Sciences*, *22*(21), 11853. https://doi.org/10.3390/ijms222111853

Pensato, V., Tiloca, C., Corrado, L., Bertolin, C., Sardone, V., Del Bo, R., Calini, D., Mandrioli, J., Lauria, G., Mazzini, L., Querin, G., Ceroni, M., Cantello, R., Corti, S., Castellotti, B., Soldà, G., Duga, S., Comi, G. P., Cereda, C., … Silani, V. (2015). TUBA4A gene analysis in sporadic amyotrophic lateral sclerosis: Identification of novel mutations. *Journal of Neurology*, *262*(5), 1376–1378. https://doi.org/10.1007/s00415-015-7739-y

Pereda, A. E. (2014). Electrical synapses and their functional interactions with chemical synapses. *Nature Reviews Neuroscience*, *15*(4), 250–263. https://doi.org/10.1038/nrn3708

Perkins, E. M., Burr, K., Banerjee, P., Mehta, A. R., Dando, O., Selvaraj, B. T., Suminaite, D., Nanda, J., Henstridge, C. M., Gillingwater, T. H., Hardingham, G. E., Wyllie, D. J. A., Chandran, S., & Livesey, M. R. (2021). Altered network properties in C9ORF72 repeat expansion cortical

neurons are due to synaptic dysfunction. *Molecular Neurodegeneration*, *16*(1), 13. https://doi.org/10.1186/s13024-021-00433-8

Personius, K. E., Chang, Q., Mentis, G. Z., O'Donovan, M. J., & Balice-Gordon, R. J. (2007). Reduced gap junctional coupling leads to uncorrelated motor neuron firing and precocious neuromuscular synapse elimination. *Proceedings of the National Academy of Sciences*, *104*(28), 11808–11813. https://doi.org/10.1073/pnas.0703357104

Petrou, P., Gothelf, Y., Argov, Z., Gotkine, M., Levy, Y. S., Kassis, I., Vaknin-Dembinsky, A., Ben-Hur, T., Offen, D., Abramsky, O., Melamed, E., & Karussis, D. (2016). Safety and Clinical Effects of Mesenchymal Stem Cells Secreting Neurotrophic Factor Transplantation in Patients With Amyotrophic Lateral Sclerosis: Results of Phase 1/2 and 2a Clinical Trials. *JAMA Neurology*, *73*(3), 337–344. https://doi.org/10.1001/jamaneurol.2015.4321

Petrov, D., Mansfield, C., Moussy, A., & Hermine, O. (2017). ALS Clinical Trials Review: 20 Years of Failure. Are We Any Closer to Registering a New Treatment? *Frontiers in Aging Neuroscience*, *9*. https://doi.org/10.3389/fnagi.2017.00068

Picchiarelli, G., Demestre, M., Zuko, A., Been, M., Higelin, J., Dieterlé, S., Goy, M.-A., Mallik, M., Sellier, C., Scekic-Zahirovic, J., Zhang, L., Rosenbohm, A., Sijlmans, C., Aly, A., Mersmann, S., Sanjuan-Ruiz, I., Hübers, A., Messaddeq, N., Wagner, M., … Storkebaum, E. (2019). FUS-mediated regulation of acetylcholine receptor transcription at neuromuscular junctions is compromised in amyotrophic lateral sclerosis. *Nature Neuroscience*, *22*(11), 1793–1805. https://doi.org/10.1038/s41593-019-0498-9

Polymenidou, M., Lagier-Tourenne, C., Hutt, K. R., Huelga, S. C., Moran, J., Liang, T. Y., Ling, S.-C., Sun, E., Wancewicz, E., Mazur, C., Kordasiewicz, H., Sedaghat, Y., Donohue, J. P., Shiue, L., Bennett, C. F., Yeo, G. W., & Cleveland, D. W. (2011). Long pre-mRNA depletion and RNA missplicing contribute to neuronal vulnerability from loss of TDP-43. *Nature Neuroscience*, *14*(4), 459. https://doi.org/10.1038/nn.2779

Portet, F., Cadilhac, C., Touchon, J., & Camu, W. (2001). Cognitive impairment in motor neuron disease with bulbar onset. *Amyotrophic Lateral Sclerosis and Other Motor Neuron Disorders: Official Publication of the World Federation of Neurology, Research Group on Motor Neuron Diseases*, *2*(1), 23–29. https://doi.org/10.1080/146608201300079382

Pottier, C., Bieniek, K. F., Finch, N., van de Vorst, M., Baker, M., Perkersen, R., Brown, P., Ravenscroft, T., van Blitterswijk, M., Nicholson, A. M., DeTure, M., Knopman, D. S., Josephs, K. A., Parisi, J. E., Petersen, R. C., Boylan, K. B., Boeve, B. F., Graff-Radford, N. R., Veltman, J. A., … Rademakers, R. (2015). Whole-genome sequencing reveals important role for TBK1 and OPTN mutations in frontotemporal lobar degeneration without motor neuron disease. *Acta Neuropathologica*, *130*(1), 77–92. https://doi.org/10.1007/s00401-015-1436-x

Pourtoy-Brasselet, S., Sciauvaud, A., Boza-Moran, M.-G., Cailleret, M., Jarrige, M., Polvèche, H., Polentes, J., Chevet, E., Martinat, C., Peschanski, M., & Aubry, L. (2021). Human iPSC-derived neurons reveal early developmental alteration of neurite outgrowth in the late-occurring neurodegenerative Wolfram syndrome. *The American Journal of Human Genetics*, *108*(11), 2171-2185. https://doi.org/10.1016/j.ajhg.2021.10.001

Prasad, A., Bharathi, V., Sivalingam, V., Girdhar, A., & Patel, B. K. (2019). Molecular Mechanisms of TDP-43 Misfolding and Pathology in Amyotrophic Lateral Sclerosis. *Frontiers in Molecular Neuroscience*, *12*. https://doi.org/10.3389/fnmol.2019.00025

Protter, D. S. W., & Parker, R. (2016). Principles and Properties of Stress Granules. *Trends in Cell Biology*, *26*(9), 668–679. https://doi.org/10.1016/j.tcb.2016.05.004

Puls, I., Jonnakuty, C., LaMonte, B. H., Holzbaur, E. L. F., Tokito, M., Mann, E., Floeter, M. K., Bidus, K., Drayna, D., Oh, S. J., Brown, R. H., Ludlow, C. L., & Fischbeck, K. H. (2003). Mutant dynactin in motor neuron disease. *Nature Genetics*, *33*(4), 455–456. https://doi.org/10.1038/ng1123

Quek, H., Cuní-López, C., Stewart, R., Colletti, T., Notaro, A., Nguyen, T. H., Sun, Y., Guo, C. C., Lupton, M. K., Roberts, T. L., Lim, Y. C., Oikari, L. E., La Bella, V., & White, A. R. (2022). ALS monocyte-derived microglia-like cells reveal cytoplasmic TDP-43 accumulation, DNA damage, and cell-specific impairment of phagocytosis associated with disease progression. *Journal of Neuroinflammation*, *19*(1), 58. https://doi.org/10.1186/s12974-022-02421-1

Quintana-Bustamante, O., & Segovia, J. C. (2014). Generation of Patient-Specific induced Pluripotent Stem Cell from Peripheral Blood Mononuclear Cells by Sendai Reprogramming Vectors. In *Patient-Specific Induced Pluripotent Stem Cell Models* (pp. 1–11). Humana Press, New York, NY. https://doi.org/10.1007/7651_2014_170

Quist, E., Trovato, F., Avaliani, N., Zetterdahl, O. G., Gonzalez-Ramos, A., Hansen, M. G., Kokaia, M., Canals, I., & Ahlenius, H. (2022). Transcription factor-based direct conversion of human fibroblasts to functional astrocytes. *Stem Cell Reports*, *17*(7), 1620-1635. https://doi.org/10.1016/j.stemcr.2022.05.015

Raitano, S., Ordovàs, L., De Muynck, L., Guo, W., Espuny-Camacho, I., Geraerts, M., Khurana, S., Vanuytsel, K., Tóth, B. I., Voets, T., Vandenberghe, R., Cathomen, T., Van Den Bosch, L., Vanderhaeghen, P., Van Damme, P., & Verfaillie, C. M. (2014). Restoration of Progranulin Expression Rescues Cortical Neuron Generation in an Induced Pluripotent Stem Cell Model of Frontotemporal Dementia. *Stem Cell Reports*, *4*(1), 16–24. https://doi.org/10.1016/j.stemcr.2014.12.001

Rajesh, D., Dickerson, S. J., Yu, J., Brown, M. E., Thomson, J. A., & Seay, N. J. (2011). Human lymphoblastoid B-cell lines reprogrammed to EBV-free induced pluripotent stem cells. *Blood*, *118*(7), 1797–1800. https://doi.org/10.1182/blood-2011-01-332064

Rakhit, R., Cunningham, P., Furtos-Matei, A., Dahan, S., Qi, X.-F., Crow, J. P., Cashman, N. R., Kondejewski, L. H., & Chakrabartty, A. (2002). Oxidation-induced misfolding and aggregation of superoxide dismutase and its implications for amyotrophic lateral sclerosis. *The Journal of Biological Chemistry*, *277*(49), 47551–47556. https://doi.org/10.1074/jbc.M207356200

Ramesh, N., & Pandey, U. B. (2017). Autophagy Dysregulation in ALS: When Protein Aggregates Get Out of Hand. *Frontiers in Molecular Neuroscience*, *10*. https://doi.org/10.3389/fnmol.2017.00263

Ramos, D. M., Skarnes, W. C., Singleton, A. B., Cookson, M. R., & Ward, M. E. (2021). Tackling neurodegenerative diseases with genomic engineering: A new stem cell initiative from the NIH. *Neuron*, *109*(7), 1080–1083. https://doi.org/10.1016/j.neuron.2021.03.022

Ratti, A., Gumina, V., Lenzi, P., Bossolasco, P., Fulceri, F., Volpe, C., Bardelli, D., Pregnolato, F., Maraschi, A., Fornai, F., Silani, V., & Colombrita, C. (2020). Chronic stress induces formation of stress granules and pathological TDP-43 aggregates in human ALS fibroblasts and iPSC-motoneurons. *Neurobiology of Disease*, *145*, 105051. https://doi.org/10.1016/j.nbd.2020.105051

Reber, S., Stettler, J., Filosa, G., Colombo, M., Jutzi, D., Lenzken, S. C., Schweingruber, C., Bruggmann, R., Bachi, A., Barabino, S. M., Mühlemann, O., & Ruepp, M.-D. (2016). Minor intron splicing is regulated by FUS and affected by ALS-associated FUS mutants. *The EMBO Journal*, *35*(14), 1504–1521. https://doi.org/10.15252/embj.201593791

Rebuzzini, P., Zuccotti, M., Redi, C. A., & Garagna, S. (2015). Chromosomal Abnormalities in Embryonic and Somatic Stem Cells. *Cytogenetic and Genome Research*, *147*(1), 1–9. https://doi.org/10.1159/000441645

Renton, A. E., Majounie, E., Waite, A., Simón-Sánchez, J., Rollinson, S., Gibbs, J. R., Schymick, J. C., Laaksovirta, H., van Swieten, J. C., Myllykangas, L., Kalimo, H., Paetau, A., Abramzon, Y., Remes, A. M., Kaganovich, A., Scholz, S. W., Duckworth, J., Ding, J., Harmer, D. W., … Traynor, B. J. (2011). A Hexanucleotide Repeat Expansion in C9ORF72 Is the Cause of Chromosome 9p21-Linked ALS-FTD. *Neuron*, *72*(2), 257–268. https://doi.org/10.1016/j.neuron.2011.09.010

Ringholz, G. M., Appel, S. H., Bradshaw, M., Cooke, N. A., Mosnik, D. M., & Schulz, P. E. (2005). Prevalence and patterns of cognitive impairment in sporadic ALS. *Neurology*, *65*(4), 586. https://doi.org/10.1212/01.wnl.0000172911.39167.b6

Rizzuti, M., Filosa, G., Melzi, V., Calandriello, L., Dioni, L., Bollati, V., Bresolin, N., Comi, G. P., Barabino, S., Nizzardo, M., & Corti, S. (2018). MicroRNA expression analysis identifies a subset of downregulated miRNAs in ALS motor neuron progenitors. *Scientific Reports*, *8*(1), 10105. https://doi.org/10.1038/s41598-018-28366-1

Rizzuti, M., Melzi, V., Gagliardi, D., Resnati, D., Meneri, M., Dioni, L., Masrori, P., Hersmus, N., Poesen, K., Locatelli, M., Biella, F., Silipigni, R., Bollati, V., Bresolin, N., Comi, G. P., Van Damme, P., Nizzardo, M., & Corti, S. (2022). Insights into the identification of a molecular signature for amyotrophic lateral sclerosis exploiting integrated microRNA profiling of iPSC-derived motor neurons and exosomes. *Cellular and Molecular Life Sciences*, *79*(3), 189. https://doi.org/10.1007/s00018-022-04217-1

Rogelj, B., Easton, L. E., Bogu, G. K., Stanton, L. W., Rot, G., Curk, T., Zupan, B., Sugimoto, Y., Modic, M., Haberman, N., Tollervey, J., Fujii, R., Takumi, T., Shaw, C. E., & Ule, J. (2012). Widespread binding of FUS along nascent RNA regulates alternative splicing in the brain. *Scientific Reports*, *2*(1), 603. https://doi.org/10.1038/srep00603

Rosen, D. R., Siddique, T., Patterson, D., Figlewicz, D. A., Sapp, P., Hentati, A., Donaldson, D., Goto, J., O'Regan, J. P., Deng, H.-X., Rahmani, Z., Krizus, A., McKenna-Yasek, D., Cayabyab, A., Gaston, S. M., Berger, R., Tanzi, R. E., Halperin, J. J., Herzfeldt, B., … Jr, R. H. B. (1993). Mutations in Cu/Zn superoxide dismutase gene are associated with familial amyotrophic lateral sclerosis. *Nature*, *362*(6415), 59. https://doi.org/10.1038/362059a0

Rossi, A., Lickfett, S., Martins, S., & Prigione, A. (2022). A call for consensus guidelines on monitoring the integrity of nuclear and mitochondrial genomes in human pluripotent stem cells. *Stem Cell Reports*, *17*(4), 707-710. https://doi.org/10.1016/j.stemcr.2022.01.019

Rossi, D., Brambilla, L., Valori, C. F., Roncoroni, C., Crugnola, A., Yokota, T., Bredesen, D. E., & Volterra, A. (2008). Focal degeneration of astrocytes in amyotrophic lateral sclerosis. *Cell Death & Differentiation*, *15*(11), 1691–1700. https://doi.org/10.1038/cdd.2008.99

Rothstein, J. D., Martin, L. J., & Kuncl, R. W. (1992). Decreased Glutamate Transport by the Brain and Spinal Cord in Amyotrophic Lateral Sclerosis. *New England Journal of Medicine*, *326*(22), 1464–1468. https://doi.org/10.1056/NEJM199205283262204

Rothstein, J. D., Van Kammen, M., Levey, A. I., Martin, L. J., & Kuncl, R. W. (1995). Selective loss of glial glutamate transporter GLT-1 in amyotrophic lateral sclerosis. *Annals of Neurology*, *38*(1), 73–84. https://doi.org/10.1002/ana.410380114

Russo, A., Scardigli, R., La Regina, F., Murray, M. E., Romano, N., Dickson, D. W., Wolozin, B., Cattaneo, A., & Ceci, M. (2017). Increased cytoplasmic TDP-43 reduces global protein synthesis by interacting with RACK1 on polyribosomes. *Human Molecular Genetics*, *26*(8), 1407–1418. https://doi.org/10.1093/hmg/ddx035

Ryu, A. H., Eckalbar, W. L., Kreimer, A., Yosef, N., & Ahituv, N. (2017). Use antibiotics in cell culture with caution: Genome-wide identification of antibiotic-induced changes in gene expression and regulation. *Scientific Reports*, *7*(1), 7533. https://doi.org/10.1038/s41598-017-07757-w

Saberi, S., Stauffer, J. E., Schulte, D. J., & Ravits, J. (2015). Neuropathology of Amyotrophic Lateral Sclerosis and Its Variants. *Neurologic Clinics*, *33*(4), 855–876. https://doi.org/10.1016/j.ncl.2015.07.012

Sackmann, C., Sackmann, V., & Hallbeck, M. (2020). TDP-43 Is Efficiently Transferred Between Neuron-Like Cells in a Manner Enhanced by Preservation of Its N-Terminus but Independent of Extracellular Vesicles. *Frontiers in Neuroscience*, *14*. https://doi.org/10.3389/fnins.2020.00540

Sahadevan, S., Hembach, K. M., Tantardini, E., Pérez-Berlanga, M., Hruska-Plochan, M., Megat, S., Weber, J., Schwarz, P., Dupuis, L., Robinson, M. D., Rossi, P. D., & Polymenidou, M. (2021). Synaptic FUS accumulation triggers early misregulation of synaptic RNAs in a mouse model of ALS. *Nature Communications*, *12*(1), 1–17. https://doi.org/10.1038/s41467-021-23188-8

Sahoo, P. K., Lee, S. J., Jaiswal, P. B., Alber, S., Kar, A. N., Miller-Randolph, S., Taylor, E. E., Smith, T., Singh, B., Ho, T. S.-Y., Urisman, A., Chand, S., Pena, E. A., Burlingame, A. L., Woolf, C. J., Fainzilber, M., English, A. W., & Twiss, J. L. (2018). Axonal G3BP1 stress granule protein limits axonal mRNA translation and nerve regeneration. *Nature Communications*, *9*, 3358. https://doi.org/10.1038/s41467-018-05647-x

Sainouchi, M., Hatano, Y., Tada, M., Ishihara, T., Ando, S., Kato, T., Tokunaga, J., Ito, G., Miyahara, H., Toyoshima, Y., Yokoseki, A., Ozawa, T., Akazawa, K., Onodera, O., & Kakita, A. (2021). A novel splicing variant of ANXA11 in a patient with amyotrophic lateral sclerosis: Histologic and

biochemical features. *Acta Neuropathologica Communications*, *9*, 106. https://doi.org/10.1186/s40478-021-01202-w

Salam, S., Tacconelli, S., Smith, B. N., Mitchell, J. C., Glennon, E., Nikolaou, N., Houart, C., & Vance, C. (2021). Identification of a novel interaction of FUS and syntaphilin may explain synaptic and mitochondrial abnormalities caused by ALS mutations. *Scientific Reports*, *11*, 13613. https://doi.org/10.1038/s41598-021-93189-6

Salamatina, A., Yang, J. H., Brenner-Morton, S., Bikoff, J. B., Fang, L., Kintner, C. R., Jessell, T. M., & Sweeney, L. B. (2020). Differential Loss of Spinal Interneurons in a Mouse Model of ALS. *Neuroscience*, *450*, 81–95. https://doi.org/10.1016/j.neuroscience.2020.08.011

Salvatori, I., Ferri, A., Scaricamazza, S., Giovannelli, I., Serrano, A., Rossi, S., D'Ambrosi, N., Cozzolino, M., Giulio, A. D., Moreno, S., Valle, C., & Carrì, M. T. (2018). Differential toxicity of TAR DNA-binding protein 43 isoforms depends on their submitochondrial localization in neuronal cells. *Journal of Neurochemistry*, *146*(5), 585–597. https://doi.org/10.1111/jnc.14465

Sampson, T. R., Debelius, J. W., Thron, T., Janssen, S., Shastri, G. G., Ilhan, Z. E., Challis, C., Schretter, C. E., Rocha, S., Gradinaru, V., Chesselet, M.-F., Keshavarzian, A., Shannon, K. M., Krajmalnik-Brown, R., Wittung-Stafshede, P., Knight, R., & Mazmanian, S. K. (2016). Gut Microbiota Regulate Motor Deficits and Neuroinflammation in a Model of Parkinson's Disease. *Cell*, *167*(6), 1469-1480.e12. https://doi.org/10.1016/j.cell.2016.11.018

Sanchez-Freire, V., Lee, A. S., Hu, S., Abilez, O. J., Liang, P., Lan, F., Huber, B. C., Ong, S.-G., Hong, W. X., Huang, M., & Wu, J. C. (2014). Effect of Human Donor Cell Source on Differentiation and Function of Cardiac Induced Pluripotent Stem Cells. *Journal of the American College of Cardiology*, *64*(5), 436–448. https://doi.org/10.1016/j.jacc.2014.04.056

Sareen, D., O'Rourke, J. G., Meera, P., Muhammad, A. K. M. G., Grant, S., Simpkinson, M., Bell, S., Carmona, S., Ornelas, L., Sahabian, A., Gendron, T., Petrucelli, L., Baughn, M., Ravits, J., Harms, M. B., Rigo, F., Bennett, C. F., Otis, T. S., Svendsen, C. N., & Baloh, R. H. (2013). Targeting RNA foci in iPSC-derived motor neurons from ALS patients with a C9ORF72 repeat expansion. *Science Translational Medicine*, *5*(208), 208ra149. https://doi.org/10.1126/scitranslmed.3007529

Sasabe, J., Chiba, T., Yamada, M., Okamoto, K., Nishimoto, I., Matsuoka, M., & Aiso, S. (2007). D-serine is a key determinant of glutamate toxicity in amyotrophic lateral sclerosis. *The EMBO Journal*, *26*(18), 4149–4159. https://doi.org/10.1038/sj.emboj.7601840

Sasaki, S. (2010). Endoplasmic Reticulum Stress in Motor Neurons of the Spinal Cord in Sporadic Amyotrophic Lateral Sclerosis. *Journal of Neuropathology & Experimental Neurology*, *69*(4), 346–355. https://doi.org/10.1097/NEN.0b013e3181d44992

Sasaki, S., & Iwata, M. (1999). Ultrastructural change of synapses of Betz cells in patients with amyotrophic lateral sclerosis. *Neuroscience Letters*, *268*(1), 29–32. https://doi.org/10.1016/s0304-3940(99)00374-2

Sasaki, S., & Iwata, M. (2007). Mitochondrial Alterations in the Spinal Cord of Patients With Sporadic Amyotrophic Lateral Sclerosis. *Journal of Neuropathology & Experimental Neurology*, *66*(1), 10–16. https://doi.org/10.1097/nen.0b013e31802c396b

Sasaki, S., Komori, T., & Iwata, M. (2000). Excitatory amino acid transporter 1 and 2 immunoreactivity in the spinal cord in amyotrophic lateral sclerosis. *Acta Neuropathologica*, *100*(2), 138–144. https://doi.org/10.1007/s004019900159

Sasaki, S., & Maruyama, S. (1992). Increase in diameter of the axonal initial segment is an early change in amyotrophic lateral sclerosis. *Journal of the Neurological Sciences*, *110*(1–2), 114–120. https://doi.org/10.1016/0022-510x(92)90017-f

Saxena, S., Roselli, F., Singh, K., Leptien, K., Julien, J.-P., Gros-Louis, F., & Caroni, P. (2013). Neuroprotection through excitability and mTOR required in ALS motoneurons to delay disease and extend survival. *Neuron*, *80*(1), 80–96. https://doi.org/10.1016/j.neuron.2013.07.027

Scaramozza, A., Marchese, V., Papa, V., Salaroli, R., Sorarù, G., Angelini, C., & Cenacchi, G. (2014). Skeletal Muscle Satellite Cells in Amyotrophic Lateral Sclerosis. *Ultrastructural Pathology*, *38*(5), 295–302. https://doi.org/10.3109/01913123.2014.937842

Schaniel, C., Dhanan, P., Hu, B., Xiong, Y., Raghunandan, T., Gonzalez, D. M., Dariolli, R., D'Souza, S. L., Yadaw, A. S., Hansen, J., Jayaraman, G., Mathew, B., Machado, M., Berger, S. I., Tripodig, J., Najfeld, V., Garg, J., Miller, M., Surlyn, C. S., … Iyengar, R. (2021). A library of induced pluripotent stem cells from clinically well-characterized, diverse healthy human individuals. *Stem Cell Reports*, *16*(12), 3036-3049. https://doi.org/10.1016/j.stemcr.2021.10.005

Schiff, L., Migliori, B., Chen, Y., Carter, D., Bonilla, C., Hall, J., Fan, M., Tam, E., Ahadi, S., Fischbacher, B., Geraschenko, A., Hunter, C. J., Venugopalan, S., DesMarteau, S., Narayanaswamy, A., Jacob, S., Armstrong, Z., Ferrarotto, P., Williams, B., … Johannesson, B. (2022). Integrating deep learning and unbiased automated high-content screening to identify complex disease signatures in human fibroblasts. *Nature Communications*, *13*, 1590. https://doi.org/10.1038/s41467-022-28423-4

Schmidt, E. K., Clavarino, G., Ceppi, M., & Pierre, P. (2009). SUnSET, a nonradioactive method to monitor protein synthesis. *Nature Methods*, *6*(4), 275–277. https://doi.org/10.1038/nmeth.1314

Scotter, E. L., Vance, C., Nishimura, A. L., Lee, Y.-B., Chen, H.-J., Urwin, H., Sardone, V., Mitchell, J. C., Rogelj, B., Rubinsztein, D. C., & Shaw, C. E. (2014). Differential roles of the ubiquitin proteasome system and autophagy in the clearance of soluble and aggregated TDP-43 species. *Journal of Cell Science*, *127*(6), 1263–1278. https://doi.org/10.1242/jcs.140087

Seelaar, H., Rohrer, J. D., Pijnenburg, Y. A. L., Fox, N. C., & Swieten, J. C. van. (2011). Clinical, genetic and pathological heterogeneity of frontotemporal dementia: A review. *Journal of Neurology, Neurosurgery & Psychiatry*, *82*(5), 476–486. https://doi.org/10.1136/jnnp.2010.212225

Selvaraj, B. T., Livesey, M. R., Zhao, C., Gregory, J. M., James, O. T., Cleary, E. M., Chouhan, A. K., Gane, A. B., Perkins, E. M., Dando, O., Lillico, S. G., Lee, Y.-B., Nishimura, A. L., Poreci, U., Thankamony, S., Pray, M., Vasistha, N. A., Magnani, D., Borooah, S., … Chandran, S. (2018). C9ORF72 repeat expansion causes vulnerability of motor neurons to Ca 2+ -permeable AMPA receptor-mediated excitotoxicity. *Nature Communications*, *9*, 347. https://doi.org/10.1038/s41467-017-02729-0

Sephton, C. F., Cenik, C., Kucukural, A., Dammer, E. B., Cenik, B., Han, Y., Dewey, C. M., Roth, F. P., Herz, J., Peng, J., Moore, M. J., & Yu, G. (2011). Identification of Neuronal RNA Targets of TDP-43-containing Ribonucleoprotein Complexes. *Journal of Biological Chemistry*, *286*(2), 1204–1215. https://doi.org/10.1074/jbc.M110.190884

Sephton, C. F., Good, S. K., Atkin, S., Dewey, C. M., Mayer, P., Herz, J., & Yu, G. (2010). TDP-43 Is a Developmentally Regulated Protein Essential for Early Embryonic Development. *The Journal of Biological Chemistry*, *285*(9), 6826–6834. https://doi.org/10.1074/jbc.M109.061846

Sephton, C. F., Tang, A. A., Kulkarni, A., West, J., Brooks, M., Stubblefield, J. J., Liu, Y., Zhang, M. Q., Green, C. B., Huber, K. M., Huang, E. J., Herz, J., & Yu, G. (2014). Activity-dependent FUS dysregulation disrupts synaptic homeostasis. *Proceedings of the National Academy of Sciences of the United States of America*, *111*(44), E4769–E4778. https://doi.org/10.1073/pnas.1406162111

Sévigny, M., Julien, I. B., Venkatasubramani, J. P., Hui, J. B., Dutchak, P. A., & Sephton, C. F. (2020). FUS contributes to mTOR-dependent inhibition of translation. *Journal of Biological Chemistry*, *295*(52), 18459–18473. https://doi.org/10.1074/jbc.RA120.013801

Shahidullah, M., Le Marchand, S. J., Fei, H., Zhang, J., Pandey, U. B., Dalva, M. B., Pasinelli, P., & Levitan, I. B. (2013). Defects in Synapse Structure and Function Precede Motor Neuron Degeneration in Drosophila Models of FUS-Related ALS. *The Journal of Neuroscience*, *33*(50), 19590–19598. https://doi.org/10.1523/JNEUROSCI.3396-13.2013

Shao, Q., Liang, C., Chang, Q., Zhang, W., Yang, M., & Chen, J.-F. (2019). C9orf72 deficiency promotes motor deficits of a C9ALS/FTD mouse model in a dose-dependent manner. *Acta Neuropathologica Communications*, *7*(1), 32. https://doi.org/10.1186/s40478-019-0685-7

Sharma, Y., Saha, S., Joseph, A., Krishnan, H., & Raghu, P. (2020). In vitro human stem cell derived cultures to monitor calcium signaling in neuronal development and function. *Wellcome Open Research*, *5*, 16. https://doi.org/10.12688/wellcomeopenres.15626.1

Shatunov, A., Mok, K., Newhouse, S., Weale, M. E., Smith, B., Vance, C., Johnson, L., Veldink, J. H., van Es, M. A., van den Berg, L. H., Robberecht, W., Van Damme, P., Hardiman, O., Farmer, A. E., Lewis, C. M., Butler, A. W., Abel, O., Andersen, P. M., Fogh, I., … Al-Chalabi, A. (2010). Chromosome 9p21 in sporadic amyotrophic lateral sclerosis in the UK and seven other countries: A genome-wide association study. *The Lancet Neurology*, *9*(10), 986–994. https://doi.org/10.1016/S1474-4422(10)70197-6

Shenouda, M., Xiao, S., MacNair, L., Lau, A., & Robertson, J. (2022). A C-Terminally Truncated TDP-43 Splice Isoform Exhibits Neuronal Specific Cytoplasmic Aggregation and Contributes to TDP-43 Pathology in ALS. *Frontiers in Neuroscience*, *16*. https://www.frontiersin.org/article/10.3389/fnins.2022.868556

Shi, Y., Lin, S., Staats, K. A., Li, Y., Chang, W.-H., Hung, S.-T., Hendricks, E., Linares, G. R., Wang, Y., Son, E. Y., Wen, X., Kisler, K., Wilkinson, B., Menendez, L., Sugawara, T., Woolwine, P., Huang, M., Cowan, M. J., Ge, B., … Ichida, J. K. (2018). Haploinsufficiency leads to neurodegeneration in C9ORF72 ALS/FTD human induced motor neurons. *Nature Medicine*, *24*(3), 313–325. https://doi.org/10.1038/nm.4490

Shibata, H., Kanadome, T., Sugiura, H., Yokoyama, T., Yamamuro, M., Moss, S. E., & Maki, M. (2015). A New Role for Annexin A11 in the Early Secretory Pathway via Stabilizing Sec31A Protein at the Endoplasmic Reticulum Exit Sites (ERES). *Journal of Biological Chemistry*, *290*(8), 4981–4993. https://doi.org/10.1074/jbc.M114.592089

Shin, Y., & Brangwynne, C. P. (2017). Liquid phase condensation in cell physiology and disease. *Science*, *357*(6357), eaaf4382. https://doi.org/10.1126/science.aaf4382

Si, Y., Kazamel, M., Benatar, M., Wuu, J., Kwon, Y., Kwan, T., Jiang, N., Kentrup, D., Faul, C., Alesce, L., & King, P. H. (2021). FGF23, a novel muscle biomarker detected in the early stages of ALS. *Scientific Reports*, *11*, 12062. https://doi.org/10.1038/s41598-021-91496-6

Siddique, T., Figlewicz, D. A., Pericak-Vance, M. A., Haines, J. L., Rouleau, G., Jeffers, A. J., Sapp, P., Hung, W. Y., Bebout, J., & McKenna-Yasek, D. (1991). Linkage of a gene causing familial amyotrophic lateral sclerosis to chromosome 21 and evidence of genetic-locus heterogeneity. *The New England Journal of Medicine*, *324*(20), 1381–1384. https://doi.org/10.1056/NEJM199105163242001

Simkin, D., Papakis, V., Bustos, B. I., Ambrosi, C. M., Ryan, S. J., Baru, V., Williams, L. A., Dempsey, G. T., McManus, O. B., Landers, J. E., Lubbe, S. J., George, A. L., & Kiskinis, E. (2022). Homozygous might be hemizygous: CRISPR/Cas9 editing in iPSCs results in detrimental on-target defects that escape standard quality controls. *Stem Cell Reports*, *17*(4), 993-1008. https://doi.org/10.1016/j.stemcr.2022.02.008

Simpson, C. L., Lemmens, R., Miskiewicz, K., Broom, W. J., Hansen, V. K., van Vught, P. W. J., Landers, J. E., Sapp, P., Van Den Bosch, L., Knight, J., Neale, B. M., Turner, M. R., Veldink, J. H., Ophoff, R. A., Tripathi, V. B., Beleza, A., Shah, M. N., Proitsi, P., Van Hoecke, A., … Al-Chalabi, A. (2009). Variants of the elongator protein 3 ELP3 gene are associated with motor neuron degeneration. *Human Molecular Genetics*, *18*(3), 472–481. https://doi.org/10.1093/hmg/ddn375

Singh, T., Jiao, Y., Ferrando, L. M., Yablonska, S., Li, F., Horoszko, E. C., Lacomis, D., Friedlander, R. M., & Carlisle, D. L. (2021). Neuronal mitochondrial dysfunction in sporadic amyotrophic lateral sclerosis is developmentally regulated. *Scientific Reports*, *11*, 18916. https://doi.org/10.1038/s41598-021-97928-7

Sivadasan, R., Hornburg, D., Drepper, C., Frank, N., Jablonka, S., Hansel, A., Lojewski, X., Sterneckert, J., Hermann, A., Shaw, P. J., Ince, P. G., Mann, M., Meissner, F., & Sendtner, M. (2016). C9ORF72 interaction with cofilin modulates actin dynamics in motor neurons. *Nature Neuroscience*, *19*(12), 1610–1618. https://doi.org/10.1038/nn.4407

Skibinski, G., Parkinson, N. J., Brown, J. M., Chakrabarti, L., Lloyd, S. L., Hummerich, H., Nielsen, J. E., Hodges, J. R., Spillantini, M. G., Thusgaard, T., Brandner, S., Brun, A., Rossor, M. N., Gade, A., Johannsen, P., Sørensen, S. A., Gydesen, S., Fisher, E. M. C., & Collinge, J. (2005). Mutations in the endosomal ESCRTIII-complex subunit CHMP2B in frontotemporal dementia. *Nature Genetics*, *37*(8), 806–808. https://doi.org/10.1038/ng1609

Sleigh, J. N., Tosolini, A. P., Gordon, D., Devoy, A., Fratta, P., Fisher, E. M. C., Talbot, K., & Schiavo, G. (2020). Mice Carrying ALS Mutant TDP-43, but Not Mutant FUS, Display In Vivo Defects in Axonal Transport of Signaling Endosomes. *Cell Reports*, *30*(11), 3655-3662.e2. https://doi.org/10.1016/j.celrep.2020.02.078

Smethurst, P., Risse, E., Tyzack, G. E., Mitchell, J. S., Taha, D. M., Chen, Y.-R., Newcombe, J., Collinge, J., Sidle, K., & Patani, R. (2020). Distinct responses of neurons and astrocytes to TDP-43 proteinopathy in amyotrophic lateral sclerosis. *Brain*, *143*(2), 430–440. https://doi.org/10.1093/brain/awz419

Smith, A. S. T., Chun, C., Hesson, J., Mathieu, J., Valdmanis, P. N., Mack, D. L., Choi, B.-O., Kim, D.-H., & Bothwell, M. (2021). Human Induced Pluripotent Stem Cell-Derived TDP-43 Mutant Neurons Exhibit Consistent Functional Phenotypes Across Multiple Gene Edited Lines Despite Transcriptomic and Splicing Discrepancies. *Frontiers in Cell and Developmental Biology*, *9*, 2696. https://doi.org/10.3389/fcell.2021.728707

Smith, B. N., Ticozzi, N., Fallini, C., Gkazi, A. S., Topp, S., Kenna, K. P., Scotter, E. L., Kost, J., Keagle, P., Miller, J. W., Calini, D., Vance, C., Danielson, E. W., Troakes, C., Tiloca, C., Al-Sarraj, S., Lewis, E. A., King, A., Colombrita, C., … Landers, J. E. (2014). Exome-wide Rare Variant Analysis Identifies TUBA4A Mutations Associated with Familial ALS. *Neuron*, *84*(2), 324–331. https://doi.org/10.1016/j.neuron.2014.09.027

Smith, B. N., Topp, S. D., Fallini, C., Shibata, H., Chen, H.-J., Troakes, C., King, A., Ticozzi, N., Kenna, K. P., Soragia-Gkazi, A., Miller, J. W., Sato, A., Dias, D. M., Jeon, M., Vance, C., Wong, C. H., Majo, M. de, Kattuah, W., Mitchell, J. C., … Shaw, C. E. (2017). Mutations in the vesicular trafficking protein annexin A11 are associated with amyotrophic lateral sclerosis. *Science Translational Medicine*, *9*(388), eaad9157. https://doi.org/10.1126/scitranslmed.aad9157

So, E., Mitchell, J. C., Memmi, C., Chennell, G., Vizcay-Barrena, G., Allison, L., Shaw, C. E., & Vance, C. (2018). Mitochondrial abnormalities and disruption of the neuromuscular junction precede the clinical phenotype and motor neuron loss in hFUSWT transgenic mice. *Human Molecular Genetics*, *27*(3), 463–474. https://doi.org/10.1093/hmg/ddx415

Sommer, D., Rajkumar, S., Seidel, M., Aly, A., Ludolph, A., Ho, R., Boeckers, T. M., & Catanese, A. (2022). Aging-Dependent Altered Transcriptional Programs Underlie Activity Impairments in Human C9orf72-Mutant Motor Neurons. *Frontiers in Molecular Neuroscience*, *15*. https://www.frontiersin.org/article/10.3389/fnmol.2022.894230

Song, J., Shih Ie, M., Chan, D. W., & Zhang, Z. (2009). Suppression of annexin A11 in ovarian cancer: Implications in chemoresistance. *Neoplasia*, *11*. https://doi.org/10.1593/neo.09286

Song, Y. (2020). Synaptic Actions of Amyotrophic Lateral Sclerosis-Associated G85R-SOD1 in the Squid Giant Synapse. *ENeuro*, *7*(2). https://doi.org/10.1523/ENEURO.0369-19.2020

Spalloni, A., Nutini, M., & Longone, P. (2013). Role of the N-methyl-d-aspartate receptors complex in amyotrophic lateral sclerosis. *Biochimica et Biophysica Acta (BBA) - Molecular Basis of Disease*, *1832*(2), 312–322. https://doi.org/10.1016/j.bbadis.2012.11.013

Spijkers, X. M., Pasteuning-Vuhman, S., Dorleijn, J. C., Vulto, P., Wevers, N. R., & Pasterkamp, R. J. (2021). A directional 3D neurite outgrowth model for studying motor axon biology and disease. *Scientific Reports*, *11*, 2080. https://doi.org/10.1038/s41598-021-81335-z

Sposito, T., Preza, E., Mahoney, C. J., Setó-Salvia, N., Ryan, N. S., Morris, H. R., Arber, C., Devine, M. J., Houlden, H., Warner, T. T., Bushell, T. J., Zagnoni, M., Kunath, T., Livesey, F. J., Fox, N. C., Rossor, M. N., Hardy, J., & Wray, S. (2015). Developmental regulation of tau splicing is disrupted in stem cell-derived neurons from frontotemporal dementia patients with the 10 + 16 splice-site mutation in MAPT. *Human Molecular Genetics*, *24*(18), 5260–5269. https://doi.org/10.1093/hmg/ddv246

Sproviero, D., Gagliardi, S., Zucca, S., Arigoni, M., Giannini, M., Garofalo, M., Olivero, M., Dell'Orco, M., Pansarasa, O., Bernuzzi, S., Avenali, M., Cotta Ramusino, M., Diamanti, L., Minafra, B., Perini, G., Zangaglia, R., Costa, A., Ceroni, M., Perrone-Bizzozero, N. I., … Cereda, C. (2021). Different miRNA Profiles in Plasma Derived Small and Large Extracellular Vesicles from Patients with Neurodegenerative Diseases. *International Journal of Molecular Sciences*, *22*(5), 2737. https://doi.org/10.3390/ijms22052737

Sproviero, D., La Salvia, S., Giannini, M., Crippa, V., Gagliardi, S., Bernuzzi, S., Diamanti, L., Ceroni, M., Pansarasa, O., Poletti, A., & Cereda, C. (2018). Pathological Proteins Are Transported by Extracellular Vesicles of Sporadic Amyotrophic Lateral Sclerosis Patients. *Frontiers in Neuroscience*, *12*. https://doi.org/10.3389/fnins.2018.00487

Sreedharan, J., Blair, I. P., Tripathi, V. B., Hu, X., Vance, C., Rogelj, B., Ackerley, S., Durnall, J. C., Williams, K. L., Buratti, E., Baralle, F., Belleroche, J. de, Mitchell, J. D., Leigh, P. N., Al-Chalabi, A., Miller, C. C., Nicholson, G., & Shaw, C. E. (2008). TDP-43 Mutations in Familial and Sporadic Amyotrophic Lateral Sclerosis. *Science*, *319*(5870), 1668–1672. https://doi.org/10.1126/science.1154584

Stephens, B., Guiloff, R. J., Navarrete, R., Newman, P., Nikhar, N., & Lewis, P. (2006). Widespread loss of neuronal populations in the spinal ventral horn in sporadic motor neuron disease. A morphometric study. *Journal of the Neurological Sciences*, *244*(1), 41–58. https://doi.org/10.1016/j.jns.2005.12.003

Stifani, N. (2014). Motor neurons and the generation of spinal motor neurons diversity. *Frontiers in Cellular Neuroscience*, *8*. https://www.frontiersin.org/articles/10.3389/fncel.2014.00293

Stoklund Dittlau, K., Krasnow, E. N., Fumagalli, L., Vandoorne, T., Baatsen, P., Kerstens, A., Giacomazzi, G., Pavie, B., Rossaert, E., Beckers, J., Sampaolesi, M., Van Damme, P., & Van Den Bosch, L. (2021). Human motor units in microfluidic devices are impaired by FUS mutations and improved by HDAC6 inhibition. *Stem Cell Reports*, *16*(9), 2213–2227. https://doi.org/10.1016/j.stemcr.2021.03.029

Strässler, E. T., Aalto-Setälä, K., Kiamehr, M., Landmesser, U., & Kränkel, N. (2018). Age Is Relative—Impact of Donor Age on Induced Pluripotent Stem Cell-Derived Cell Functionality. *Frontiers in Cardiovascular Medicine*, *5*. https://doi.org/10.3389/fcvm.2018.00004

Strohm, L., Hu, Z., Suk, Y., Rühmkorf, A., Sternburg, E., Gattringer, V., Riemenschneider, H., Berutti, R., Graf, E., Weishaupt, J. H., Brill, M. S., Harbauer, A. B., Dormann, D., Dengjel, J., Edbauer, D., & Behrends, C. (2022). Multi-omics profiling identifies a deregulated FUS-MAP1B axis in ALS/FTD–associated UBQLN2 mutants. *Life Science Alliance*, *5*(11). https://doi.org/10.26508/lsa.202101327

Stronati, E., Biagioni, S., Fiore, M., Giorgi, M., Poiana, G., Toselli, C., & Cacci, E. (2021). Wild-Type and Mutant FUS Expression Reduce Proliferation and Neuronal Differentiation Properties of Neural Stem Progenitor Cells. *International Journal of Molecular Sciences*, *22*(14), 7566. https://doi.org/10.3390/ijms22147566

Strong, M. J., Volkening, K., Hammond, R., Yang, W., Strong, W., Leystra-Lantz, C., & Shoesmith, C. (2007). TDP43 is a human low molecular weight neurofilament (hNFL) mRNA-binding protein. *Molecular and Cellular Neuroscience*, *35*(2), 320–327. https://doi.org/10.1016/j.mcn.2007.03.007

Sudo, T., & Hidaka, H. (1998). Regulation of Calcyclin (S100A6) Binding by Alternative Splicing in the N-terminal Regulatory Domain of Annexin XI Isoforms. *Journal of Biological Chemistry*, *273*(11), 6351–6357. https://doi.org/10.1074/jbc.273.11.6351

Sugai, A., Kato, T., Koyama, A., Koike, Y., Konno, T., Ishihara, T., & Onodera, O. (2019). Non-genetically modified models exhibit TARDBP mRNA increase due to perturbed TDP-43 autoregulation. *Neurobiology of Disease*, *130*, 104534. https://doi.org/10.1016/j.nbd.2019.104534

Suk, T. R., & Rousseaux, M. W. C. (2020). The role of TDP-43 mislocalization in amyotrophic lateral sclerosis. *Molecular Neurodegeneration*, *15*(1), 45. https://doi.org/10.1186/s13024-020-00397-1

Sukumaran, P., Nascimento Da Conceicao, V., Sun, Y., Ahamad, N., Saraiva, L. R., Selvaraj, S., & Singh, B. B. (2021). Calcium Signaling Regulates Autophagy and Apoptosis. *Cells*, *10*(8), 2125. https://doi.org/10.3390/cells10082125

Sumi, H., Kato, S., Mochimaru, Y., Fujimura, H., Etoh, M., & Sakoda, S. (2009). Nuclear TAR DNA Binding Protein 43 Expression in Spinal Cord Neurons Correlates With the Clinical Course in Amyotrophic Lateral Sclerosis. *Journal of Neuropathology & Experimental Neurology*, *68*(1), 37–47. https://doi.org/10.1097/NEN.0b013e3181919cb5

Svetoni, F., Frisone, P., & Paronetto, M. P. (2016). Role of FET proteins in neurodegenerative disorders. *RNA Biology*, *13*(11), 1089–1102. https://doi.org/10.1080/15476286.2016.1211225

Synofzik, M., Maetzler, W., Grehl, T., Prudlo, J., vom Hagen, J. M., Haack, T., Rebassoo, P., Munz, M., Schöls, L., & Biskup, S. (2012). Screening in ALS and FTD patients reveals 3 novel UBQLN2 mutations outside the PXX domain and a pure FTD phenotype. *Neurobiology of Aging*, *33*(12), 2949.e13-2949.e17. https://doi.org/10.1016/j.neurobiolaging.2012.07.002

Szewczyk, B., Günther, R., Sterneckert, J., Petri, S., Wegner, F., & Hermann, A. (2021). FUS Is Not Mislocalized in Spinal Motor Neurons Derived From Human Induced Pluripotent Stem Cells of Main Non-FUS ALS Subtypes. *Journal of Neuropathology & Experimental Neurology*, *80*(7), 720–722. https://doi.org/10.1093/jnen/nlaa154

Taapken, S. M., Nisler, B. S., Newton, M. A., Sampsell-Barron, T. L., Leonhard, K. A., McIntire, E. M., & Montgomery, K. D. (2011). Karyotypic abnormalities in human induced pluripotent stem cells and embryonic stem cells. *Nature Biotechnology*, *29*(4), 313–314. https://doi.org/10.1038/nbt.1835

Taga, A., Dastgheyb, R., Habela, C., Joseph, J., Richard, J.-P., Gross, S. K., Lauria, G., Lee, G., Haughey, N., & Maragakis, N. J. (2019). Role of Human-Induced Pluripotent Stem Cell-Derived Spinal Cord Astrocytes in the Functional Maturation of Motor Neurons in a Multielectrode Array System. *STEM CELLS Translational Medicine*, *8*(12), 1272–1285. https://doi.org/10.1002/sctm.19-0147

Takahashi, K., Tanabe, K., Ohnuki, M., Narita, M., Ichisaka, T., Tomoda, K., & Yamanaka, S. (2007). Induction of pluripotent stem cells from adult human fibroblasts by defined factors. *Cell*, *131*(5), 861–872. https://doi.org/10.1016/j.cell.2007.11.019

Takahashi, K., & Yamanaka, S. (2006). Induction of Pluripotent Stem Cells from Mouse Embryonic and Adult Fibroblast Cultures by Defined Factors. *Cell*, *126*(4), 663–676. https://doi.org/10.1016/j.cell.2006.07.024

Takahashi, M., Kitaura, H., Kakita, A., Kakihana, T., Katsuragi, Y., Onodera, O., Iwakura, Y., Nawa, H., Komatsu, M., & Fujii, M. (2022). USP10 inhibits aberrant cytoplasmic aggregation of TDP-43 by promoting stress granule clearance. *Molecular and Cellular Biology*. *42*(3). https://doi.org/10.1128/MCB.00393-21

Takeuchi, H., Kobayashi, Y., Ishigaki, S., Doyu, M., & Sobue, G. (2002). Mitochondrial localization of mutant superoxide dismutase 1 triggers caspase-dependent cell death in a cellular model of familial amyotrophic lateral sclerosis. *The Journal of Biological Chemistry*, *277*(52), 50966–50972. https://doi.org/10.1074/jbc.M209356200

Takeuchi, H., Kobayashi, Y., Ishigaki, S., Doyu, M., & Sobue, G. (2016). Mitochondrial localization of mutant superoxide dismutase 1 triggers caspase-dependent cell death in a cellular model of familial amyotrophic lateral sclerosis. *The Journal of Biological Chemistry*, *291*(42), 22341–22343. https://doi.org/10.1074/jbc.A116.209356

Takuma, H., Kwak, S., Yoshizawa, T., & Kanazawa, I. (2001). Reduction of GluR2 RNA editing, a molecular change that increases calcium influx through AMPA receptors, selective in the spinal ventral gray of patients with amyotrophic lateral sclerosis. *Annals of Neurology*, *46*(6), 806–815. https://doi.org/10.1002/1531-8249(199912)46:6<806::AID-ANA2>3.0.CO;2-S

Talbot, K. (2009). Motor neuron disease: The Bare Essentials. *Practical Neurology*, *9*(5), 303–309. https://doi.org/10.1136/jnnp.2009.188151

Tam, O. H., Rozhkov, N. V., Shaw, R., Kim, D., Hubbard, I., Fennessey, S., Propp, N., Phatnani, H., Kwan, J., Sareen, D., Broach, J. R., Simmons, Z., Arcila-Londono, X., Lee, E. B., Van Deerlin, V. M., Shneider, N. A., Fraenkel, E., Ostrow, L. W., Baas, F., … Gale Hammell, M. (2019). Postmortem Cortex Samples Identify Distinct Molecular Subtypes of ALS: Retrotransposon Activation, Oxidative Stress, and Activated Glia. *Cell Reports*, *29*(5), 1164-1177.e5. https://doi.org/10.1016/j.celrep.2019.09.066

Tamaki, Y., Ross, J. P., Alipour, P., Catoire, H., Rochefort, D., Urushitani, M., Takahashi, R., Sonnen, J. A., Stifani, S., Dion, P. A., & Rouleau, G. A. (2022). Spinal cord extracts of amyotrophic lateral

sclerosis spread TDP-43 pathology in cerebral organoids. *bioRxiv*. https://www.biorxiv.org/content/10.1101/2022.05.05.490760v1

Tanaka, Y., Nonaka, T., Suzuki, G., Kametani, F., & Hasegawa, M. (2016). Gain-of-function profilin 1 mutations linked to familial amyotrophic lateral sclerosis cause seed-dependent intracellular TDP-43 aggregation. *Human Molecular Genetics*, *25*(7), 1420–1433. https://doi.org/10.1093/hmg/ddw024

Tao, Z., Wang, H., Xia, Q., Li, K., Li, K., Jiang, X., Xu, G., Wang, G., & Ying, Z. (2015). Nucleolar stress and impaired stress granule formation contribute to C9orf72 RAN translation-induced cytotoxicity. *Human Molecular Genetics*, *24*(9), 2426–2441. https://doi.org/10.1093/hmg/ddv005

Taylor, J. P., Brown, R. H., & Cleveland, D. W. (2016). Decoding ALS: From Genes to Mechanism. *Nature*, *539*(7628), 197–206. https://doi.org/10.1038/nature20413

Tcw, J., Wang, M., Pimenova, A. A., Bowles, K. R., Hartley, B. J., Lacin, E., Machlovi, S. I., Abdelaal, R., Karch, C. M., Phatnani, H., Slesinger, P. A., Zhang, B., Goate, A. M., & Brennand, K. J. (2017). An Efficient Platform for Astrocyte Differentiation from Human Induced Pluripotent Stem Cells. *Stem Cell Reports*, *9*(2), 600–614. https://doi.org/10.1016/j.stemcr.2017.06.018

Tedeschi, V., Petrozziello, T., & Secondo, A. (2019). Calcium Dyshomeostasis and Lysosomal Ca2+ Dysfunction in Amyotrophic Lateral Sclerosis. *Cells*, *8*(10), 1216. https://doi.org/10.3390/cells8101216

Tedeschi, V., Petrozziello, T., & Secondo, A. (2021). Ca2+ dysregulation in the pathogenesis of amyotrophic lateral sclerosis. In *International Review of Cell and Molecular Biology*. Academic Press. https://doi.org/10.1016/bs.ircmb.2021.02.014

Teyssou, E., Muratet, F., Amador, M.-D.-M., Ferrien, M., Lautrette, G., Machat, S., Boillée, S., Larmonier, T., Saker, S., Leguern, E., Cazeneuve, C., Marie, Y., Guegan, J., Gyorgy, B., Cintas, P., Meininger, V., Le Forestier, N., Salachas, F., Couratier, P., … Millecamps, S. (2020). Genetic screening of ANXA11 revealed novel mutations linked to Amyotrophic Lateral Sclerosis. *Neurobiology of Aging*. *99*, 102.e11-102.e20. https://doi.org/10.1016/j.neurobiolaging.2020.10.015

The UniProt Consortium. (2019). UniProt: A worldwide hub of protein knowledge. *Nucleic Acids Research*, *47*(D1), D506–D515. https://doi.org/10.1093/nar/gky1049

Thielsen, K. D., Moser, J. M., Schmitt-John, T., Jensen, M. S., Jensen, K., & Holm, M. M. (2013). The Wobbler Mouse Model of Amyotrophic Lateral Sclerosis (ALS) Displays Hippocampal Hyperexcitability, and Reduced Number of Interneurons, but No Presynaptic Vesicle Release Impairments. *PLOS ONE*, *8*(12), e82767. https://doi.org/10.1371/journal.pone.0082767

Thiry, L., Clément, J.-P., Haag, R., Kennedy, T. E., & Stifani, S. (2021). Optimization of long-term human iPSC-derived spinal motor neuron culture using a dendritic polyglycerol amine-based substrate. *bioRxiv*. https://doi.org/10.1101/2021.09.14.460098

Ticozzi, N., LeClerc, A. L., Keagle, P., Glass, J. D., Wills, A.-M., van Blitterswijk, M., Bosco, D. A., Rodriguez-Leyva, I., Gellera, C., Ratti, A., Taroni, F., McKenna-Yasek, D. M., Sapp, P. C., Silani, V., Furlong, C. E., Brown, R. H., & Landers, J. E. (2010). Paraoxonase Gene Mutations in Amyotrophic Lateral Sclerosis. *Annals of Neurology*, *68*(1), 102–107. https://doi.org/10.1002/ana.21993

Ticozzi, N., Vance, C., Leclerc, A. L., Keagle, P., Glass, J. D., McKenna-Yasek, D., Sapp, P. C., Silani, V., Bosco, D. A., Shaw, C. E., Brown, R. H., & Landers, J. E. (2011). Mutational analysis reveals the FUS homolog TAF15 as a candidate gene for familial amyotrophic lateral sclerosis. *American Journal of Medical Genetics. Part B, Neuropsychiatric Genetics: The Official Publication of the International Society of Psychiatric Genetics*, *156B*(3), 285–290. https://doi.org/10.1002/ajmg.b.31158

Tisdale, E. J., Azizi, F., & Artalejo, C. R. (2009). Rab2 utilizes glyceraldehyde-3-phosphate dehydrogenase and protein kinase C to associate with microtubules and to recruit dynein. *The Journal of Biological Chemistry*, *284*(9), 5876–5884. https://doi.org/10.1074/jbc.M807756200

Tisdale, S., Alstyne, M. V., Simon, C. M., Mentis, G. Z., & Pellizzoni, L. (2022). SMN controls neuromuscular junction integrity through U7 snRNP. *Cell Reports*, *40*(12), 111393. https://doi.org/10.1016/j.celrep.2022.111393

Tokutake, Y., Yamada, K., Ohata, M., Obayashi, Y., Tsuchiya, M., & Yonekura, S. (2015). ALS-Linked P56S-VAPB Mutation Impairs the Formation of Multinuclear Myotube in C2C12 Cells. *International Journal of Molecular Sciences*, *16*(8), 18628–18641. https://doi.org/10.3390/ijms160818628

Tollervey, J. R., Curk, T., Rogelj, B., Briese, M., Cereda, M., Kayikci, M., Hortobágyi, T., Nishimura, A. L., Župunski, V., Patani, R., Chandran, S., Rot, G., Zupan, B., Shaw, C. E., & Ule, J. (2011). Characterising the RNA targets and position-dependent splicing regulation by TDP-43; implications for neurodegenerative diseases. *Nature Neuroscience*, *14*(4), 452–458. https://doi.org/10.1038/nn.2778

Tomas, A., & Moss, S. E. (2003). Calcium- and Cell Cycle-dependent Association of Annexin 11 with the Nuclear Envelope. *Journal of Biological Chemistry*, *278*(22), 20210–20216. https://doi.org/10.1074/jbc.M212669200

Tomkins, J., Usher, P., Slade, J. Y., Ince, P. G., Curtis, A., Bushby, K., & Shaw, P. J. (1998). Novel insertion in the KSP region of the neurofilament heavy gene in amyotrophic lateral sclerosis (ALS). *Neuroreport*, *9*(17), 3967–3970. https://doi.org/10.1097/00001756-199812010-00036

Tomov, M. L., O'Neil, A., Abbasi, H. S., Cimini, B. A., Carpenter, A. E., Rubin, L. L., & Bathe, M. (2021). Resolving cell state in iPSC-derived human neural samples with multiplexed fluorescence imaging. *Communications Biology*, *4*(1), 1–9. https://doi.org/10.1038/s42003-021-02276-x

Tong, J., Huang, C., Bi, F., Wu, Q., Huang, B., Liu, X., Li, F., Zhou, H., & Xia, X.-G. (2013). Expression of ALS-linked TDP-43 mutant in astrocytes causes non-cell-autonomous motor neuron death in rats. *The EMBO Journal*, *32*(13), 1917–1926. https://doi.org/10.1038/emboj.2013.122

Traxinger, K., Kelly, C., Johnson, B. A., Lyles, R. H., & Glass, J. D. (2013). Prognosis and epidemiology of amyotrophic lateral sclerosis. *Neurology: Clinical Practice*, *3*(4), 313. https://doi.org/10.1212/CPJ.0b013e3182a1b8ab

Tremblay, E., Martineau, É., & Robitaille, R. (2017). Opposite Synaptic Alterations at the Neuromuscular Junction in an ALS Mouse Model: When Motor Units Matter. *The Journal of Neuroscience*, *37*(37), 8901–8918. https://doi.org/10.1523/JNEUROSCI.3090-16.2017

Tripathi, P., Rodriguez-Muela, N., Klim, J. R., Boer, A. S. de, Agrawal, S., Sandoe, J., Lopes, C. S., Ogliari, K. S., Williams, L. A., Shear, M., Rubin, L. L., Eggan, K., & Zhou, Q. (2017). Reactive Astrocytes Promote ALS-like Degeneration and Intracellular Protein Aggregation in Human Motor Neurons by Disrupting Autophagy through TGF-β1. *Stem Cell Reports*, *9*(2), 667–680. https://doi.org/10.1016/j.stemcr.2017.06.008

Tristan, C., Shahani, N., Sedlak, T. W., & Sawa, A. (2011). The diverse functions of GAPDH: Views from different subcellular compartments. *Cellular Signalling*, *23*(2), 317–323. https://doi.org/10.1016/j.cellsig.2010.08.003

Trnka, F., Hoffmann, C., Wang, H., Sansevrino, R., Rankovic, B., Rost, B. R., Schmitz, D., Schmidt, H. B., & Milovanovic, D. (2021). Aberrant Phase Separation of FUS Leads to Lysosome Sequestering and Acidification. *Frontiers in Cell and Developmental Biology*, *9*. https://doi.org/10.3389/fcell.2021.716919

Trokovic, R., Weltner, J., Noisa, P., Raivio, T., & Otonkoski, T. (2015). Combined negative effect of donor age and time in culture on the reprogramming efficiency into induced pluripotent stem cells. *Stem Cell Research*, *15*(1), 254–262. https://doi.org/10.1016/j.scr.2015.06.001

Tsai, R. M., & Boxer, A. L. (2014). Treatment of Frontotemporal Dementia. *Current Treatment Options in Neurology*, *16*(11), 319. https://doi.org/10.1007/s11940-014-0319-0

Tsuiji, H., Inoue, I., Takeuchi, M., Furuya, A., Yamakage, Y., Watanabe, S., Koike, M., Hattori, M., & Yamanaka, K. (2017). TDP-43 accelerates age-dependent degeneration of interneurons. *Scientific Reports*, *7*(1), 14972. https://doi.org/10.1038/s41598-017-14966-w

Tu, S., Huang, M., Caga, J., Mahoney, C. J., & Kiernan, M. C. (2021). Brainstem Correlates of Pathological Laughter and Crying Frequency in ALS. *Frontiers in Neurology*, *12*. https://doi.org/10.3389/fneur.2021.704059

Turner, M. R., Al-Chalabi, A., Chio, A., Hardiman, O., Kiernan, M. C., Rohrer, J. D., Rowe, J., Seeley, W., & Talbot, K. (2017). Genetic screening in sporadic ALS and FTD. *J Neurol Neurosurg Psychiatry*, *88*(12), 1042–1044. https://doi.org/10.1136/jnnp-2017-315995

Turner, M. R., Barnwell, J., Al-Chalabi, A., & Eisen, A. (2012). Young-onset amyotrophic lateral sclerosis: Historical and other observations. *Brain*, *135*(9), 2883–2891. https://doi.org/10.1093/brain/aws144

Tushev, G., Glock, C., Heumüller, M., Biever, A., Jovanovic, M., & Schuman, E. M. (2018). Alternative 3′ UTRs Modify the Localization, Regulatory Potential, Stability, and Plasticity of mRNAs in Neuronal Compartments. *Neuron*, *98*(3), 495-511.e6. https://doi.org/10.1016/j.neuron.2018.03.030

Tutukova, S., Tarabykin, V., & Hernandez-Miranda, L. R. (2021). The Role of Neurod Genes in Brain Development, Function, and Disease. *Frontiers in Molecular Neuroscience*, *14*. https://www.frontiersin.org/article/10.3389/fnmol.2021.662774

Tyzack, G. E., Luisier, R., Taha, D. M., Neeves, J., Modic, M., Mitchell, J. S., Meyer, I., Greensmith, L., Newcombe, J., Ule, J., Luscombe, N. M., & Patani, R. (2019). Widespread FUS mislocalization is a molecular hallmark of amyotrophic lateral sclerosis. *Brain: A Journal of Neurology*, *142*(9), 2572–2580. https://doi.org/10.1093/brain/awz217

Tyzack, G. E., Neeves, J., Crerar, H., Klein, P., Ziff, O., Taha, D. M., Luisier, R., Luscombe, N. M., & Patani, R. (2021). Aberrant cytoplasmic intron retention is a blueprint for RNA binding protein mislocalization in VCP-related amyotrophic lateral sclerosis. *Brain*, 144(7), 1985-1993. https://doi.org/10.1093/brain/awab078

Tziortzouda, P., Bosch, L. V. D., & Hirth, F. (2021). Triad of TDP43 control in neurodegeneration: Autoregulation, localization and aggregation. *Nature Reviews Neuroscience*, *22*, 197-208. https://doi.org/10.1038/s41583-021-00431-1

Uhlen., M, Oksvold, P., Fagerberg, L., Lundberg., E., Jonasson., Forsbery., M., Zwahlen., M., Kampf, C., Wester., K., Hober., S., Wernerus., Björling, L., Ponten., F. (2010). Towards a knowledge-based Human Protein Atlas. *Nature Biotechnology*, *28*, 1248-1250. https://doi.org/10.1038/nbt1210-1248

Upmanyu, N., Jin, J., Emde, H. von der, Ganzella, M., Bösche, L., Malviya, V. N., Zhuleku, E., Politi, A. Z., Ninov, M., Silbern, I., Leutenegger, M., Urlaub, H., Riedel, D., Preobraschenski, J., Milosevic, I., Hell, S. W., Jahn, R., & Sambandan, S. (2022). Colocalization of different neurotransmitter transporters on synaptic vesicles is sparse except for VGLUT1 and ZnT3. *Neuron*, *110*(9), 1483-1497.e7. https://doi.org/10.1016/j.neuron.2022.02.008

Van Damme, P., Bogaert, E., Dewil, M., Hersmus, N., Kiraly, D., Scheveneels, W., Bockx, I., Braeken, D., Verpoorten, N., Verhoeven, K., Timmerman, V., Herijgers, P., Callewaert, G., Carmeliet, P., Bosch, L. V. D., & Robberecht, W. (2007). Astrocytes regulate GluR2 expression in motor neurons and their vulnerability to excitotoxicity. *Proceedings of the National Academy of Sciences*, *104*(37), 14825–14830. https://doi.org/10.1073/pnas.0705046104

Van Damme, P., Braeken, D., Callewaert, G., Robberecht, W., & Van Den Bosch, L. (2005). GluR2 Deficiency Accelerates Motor Neuron Degeneration in a Mouse Model of Amyotrophic Lateral Sclerosis. *Journal of Neuropathology & Experimental Neurology*, *64*(7), 605–612. https://doi.org/10.1097/01.jnen.0000171647.09589.07

Van Damme, P., Hoecke, A. V., Lambrechts, D., Vanacker, P., Bogaert, E., Swieten, J. van, Carmeliet, P., Bosch, L. V. D., & Robberecht, W. (2008). Progranulin functions as a neurotrophic factor to regulate neurite outgrowth and enhance neuronal survival. *J Cell Biol*, *181*(1), 37–41. https://doi.org/10.1083/jcb.200712039

van Es, M. A., Veldink, J. H., Saris, C. G. J., Blauw, H. M., van Vught, P. W. J., Birve, A., Lemmens, R., Schelhaas, H. J., Groen, E. J. N., Huisman, M. H. B., van der Kooi, A. J., de Visser, M., Dahlberg, C., Estrada, K., Rivadeneira, F., Hofman, A., Zwarts, M. J., van Doormaal, P. T. C., Rujescu, D., … van den Berg, L. H. (2009). Genome-wide association study identifies 19p13.3 (UNC13A)

and 9p21.2 as susceptibility loci for sporadic amyotrophic lateral sclerosis. *Nature Genetics*, *41*(10), 1083–1087. https://doi.org/10.1038/ng.442

Van Mossevelde, S., van der Zee, J., Cruts, M., & Van Broeckhoven, C. (2017). Relationship between C9orf72 repeat size and clinical phenotype. *Current Opinion in Genetics & Development*, *44*, 117–124. https://doi.org/10.1016/j.gde.2017.02.008

van Rheenen, W., Shatunov, A., Dekker, A. M., McLaughlin, R. L., Diekstra, F. P., Pulit, S. L., van der Spek, R. A. A., Võsa, U., de Jong, S., Robinson, M. R., Yang, J., Fogh, I., van Doormaal, P. T., Tazelaar, G. H. P., Koppers, M., Blokhuis, A. M., Sproviero, W., Jones, A. R., Kenna, K. P., … Veldink, J. H. (2016). Genome-wide association analyses identify new risk variants and the genetic architecture of amyotrophic lateral sclerosis. *Nature Genetics*, *48*(9), 1043–1048. https://doi.org/10.1038/ng.3622

Vance, C., Rogelj, B., Hortobágyi, T., De Vos, K. J., Nishimura, A. L., Sreedharan, J., Hu, X., Smith, B., Ruddy, D., Wright, P., Ganesalingam, J., Williams, K. L., Tripathi, V., Al-Saraj, S., Al-Chalabi, A., Leigh, P. N., Blair, I. P., Nicholson, G., de Belleroche, J., … Shaw, C. E. (2009). Mutations in FUS, an RNA processing protein, cause familial amyotrophic lateral sclerosis type 6. *Science, 323*(5918), 1208–1211. https://doi.org/10.1126/science.1165942

Varadi, M., Anyango, S., Deshpande, M., Nair, S., Natassia, C., Yordanova, G., Yuan, D., Stroe, O., Wood, G., Laydon, A., Žídek, A., Green, T., Tunyasuvunakool, K., Petersen, S., Jumper, J., Clancy, E., Green, R., Vora, A., Lutfi, M., … Velankar, S. (2022). AlphaFold Protein Structure Database: Massively expanding the structural coverage of protein-sequence space with high-accuracy models. *Nucleic Acids Research*, *50*(D1), D439–D444. https://doi.org/10.1093/nar/gkab1061

Varghese, D. S., Parween, S., Ardah, M. T., Emerald, B. S., & Ansari, S. A. (2017). Effects of Aminoglycoside Antibiotics on Human Embryonic Stem Cell Viability during Differentiation In Vitro. *Stem Cells International*. *2017*, 2451927. https://doi.org/10.1155/2017/2451927

Veldink, J. H., Wokke, J. H. J., van der Wal, G., Vianney de Jong, J. M. B., & van den Berg, L. H. (2002). Euthanasia and Physician-Assisted Suicide among Patients with Amyotrophic Lateral Sclerosis in the Netherlands. *New England Journal of Medicine*, *346*(21), 1638–1644. https://doi.org/10.1056/NEJMsa012739

Vercelli, A., Mereuta, O. M., Garbossa, D., Muraca, G., Mareschi, K., Rustichelli, D., Ferrero, I., Mazzini, L., Madon, E., & Fagioli, F. (2008). Human mesenchymal stem cell transplantation extends survival, improves motor performance and decreases neuroinflammation in mouse model of amyotrophic lateral sclerosis. *Neurobiology of Disease*, *31*(3), 395–405. https://doi.org/10.1016/j.nbd.2008.05.016

Versluys, L., Ervilha Pereira, P., Schuermans, N., De Paepe, B., De Bleecker, J. L., Bogaert, E., & Dermaut, B. (2022). Expanding the TDP-43 Proteinopathy Pathway From Neurons to Muscle: Physiological and Pathophysiological Functions. *Frontiers in Neuroscience*, *16*. https://www.frontiersin.org/article/10.3389/fnins.2022.815765

Verzat, C., Harley, J., Patani, R., & Luisier, R. (2022). Image-based deep learning reveals the responses of human motor neurons to stress and VCP-related ALS. *Neuropathology and Applied Neurobiology*, *48*(2), e12770. https://doi.org/10.1111/nan.12770

Vierbuchen, T., Ostermeier, A., Pang, Z. P., Kokubu, Y., Südhof, T. C., & Wernig, M. (2010). Direct conversion of fibroblasts to functional neurons by defined factors. *Nature*, *463*(7284), 1035–1041. https://doi.org/10.1038/nature08797

Volk, A. E., Weishaupt, J. H., Andersen, P. M., Ludolph, A. C., & Kubisch, C. (2018). Current knowledge and recent insights into the genetic basis of amyotrophic lateral sclerosis. *Medizinische Genetik*, *30*(2), 252–258. https://doi.org/10.1007/s11825-018-0185-3

Vucic, S., & Kiernan, M. C. (2006). Axonal excitability properties in amyotrophic lateral sclerosis. *Clinical Neurophysiology*, *117*(7), 1458–1466. https://doi.org/10.1016/j.clinph.2006.04.016

Wainger, B. J., Kiskinis, E., Mellin, C., Wiskow, O., Han, S. S. W., Sandoe, J., Perez, N. P., Williams, L. A., Lee, S., Boulting, G., Berry, J. D., Brown, R. H., Cudkowicz, M. E., Bean, B. P., Eggan, K., & Woolf, C. J. (2014). Intrinsic membrane hyperexcitability of amyotrophic lateral sclerosis

patient-derived motor neurons. *Cell Reports*, *7*(1), 1–11. https://doi.org/10.1016/j.celrep.2014.03.019

Wainger, B. J., Macklin, E. A., Vucic, S., McIlduff, C. E., Paganoni, S., Maragakis, N. J., Bedlack, R., Goyal, N. A., Rutkove, S. B., Lange, D. J., Rivner, M. H., Goutman, S. A., Ladha, S. S., Mauricio, E. A., Baloh, R. H., Simmons, Z., Pothier, L., Kassis, S. B., La, T., … Cudkowicz, M. E. (2021). Effect of Ezogabine on Cortical and Spinal Motor Neuron Excitability in Amyotrophic Lateral Sclerosis: A Randomized Clinical Trial. *JAMA Neurology*, *78*(2), 186–196. https://doi.org/10.1001/jamaneurol.2020.4300

Wang, J., Guo, C., Liu, S., Qi, H., Yin, Y., Liang, R., Sun, M.-Z., & Greenaway, F. T. (2014). Annexin A11 in disease. *Clinica Chimica Acta*, *431*(Supplement C), 164–168. https://doi.org/10.1016/j.cca.2014.01.031

Wang, L., Chen, S.-R., Ma, H., Chen, H., Hittelman, W. N., & Pan, H.-L. (2018). Regulating nociceptive transmission by VGluT2-expressing spinal dorsal horn neurons. *Journal of Neurochemistry*, *147*(4), 526–540. https://doi.org/10.1111/jnc.14588

Wang, L., Yi, F., Fu, L., Yang, J., Wang, S., Wang, Z., Suzuki, K., Sun, L., Xu, X., Yu, Y., Qiao, J., Belmonte, J. C. I., Yang, Z., Yuan, Y., Qu, J., & Liu, G.-H. (2017). CRISPR/Cas9-mediated targeted gene correction in amyotrophic lateral sclerosis patient iPSCs. *Protein & Cell*, *8*(5), 365–378. https://doi.org/10.1007/s13238-017-0397-3

Wang, M.-D., Little, J., Gomes, J., Cashman, N. R., & Krewski, D. (2017). Identification of risk factors associated with onset and progression of amyotrophic lateral sclerosis using systematic review and meta-analysis. *NeuroToxicology*, *61*, 101–130. https://doi.org/10.1016/j.neuro.2016.06.015

Wang, P., Deng, J., Dong, J., Liu, J., Bigio, E. H., Mesulam, M., Wang, T., Sun, L., Wang, L., Lee, A. Y.-L., McGee, W. A., Chen, X., Fushimi, K., Zhu, L., & Wu, J. Y. (2019). TDP-43 induces mitochondrial damage and activates the mitochondrial unfolded protein response. *PLOS Genetics*, *15*(5), e1007947. https://doi.org/10.1371/journal.pgen.1007947

Wang, W., Wang, L., Lu, J., Siedlak, S. L., Fujioka, H., Liang, J., Jiang, S., Ma, X., Jiang, Z., da Rocha, E. L., Sheng, M., Choi, H., Lerou, P. H., Li, H., & Wang, X. (2016). The inhibition of TDP-43 mitochondrial localization blocks its neuronal toxicity. *Nature Medicine*, *22*(8), 869–878. https://doi.org/10.1038/nm.4130

Wang, Y.-T., Kuo, P.-H., Chiang, C.-H., Liang, J.-R., Chen, Y.-R., Wang, S., Shen, J. C. K., & Yuan, H. S. (2013). The Truncated C-terminal RNA Recognition Motif of TDP-43 Protein Plays a Key Role in Forming Proteinaceous Aggregates. *The Journal of Biological Chemistry*, *288*(13), 9049–9057. https://doi.org/10.1074/jbc.M112.438564

Watanabe, S., Inami, H., Oiwa, K., Murata, Y., Sakai, S., Komine, O., Sobue, A., Iguchi, Y., Katsuno, M., & Yamanaka, K. (2020). Aggresome formation and liquid–liquid phase separation independently induce cytoplasmic aggregation of TAR DNA-binding protein 43. *Cell Death & Disease*, *11*(10), 1–15. https://doi.org/10.1038/s41419-020-03116-2

Weskamp, K., Tank, E. M., Miguez, R., McBride, J. P., Gómez, N. B., White, M., Lin, Z., Gonzalez, C. M., Serio, A., Sreedharan, J., & Barmada, S. J. (2020). Shortened TDP43 isoforms upregulated by neuronal hyperactivity drive TDP43 pathology in ALS. *The Journal of Clinical Investigation*, *130*(3), 1139–1155. https://doi.org/10.1172/JCI130988

Wheeler, J. R., Matheny, T., Jain, S., Abrisch, R., & Parker, R. (2016). Distinct stages in stress granule assembly and disassembly. *ELife*, *5*, e18413. https://doi.org/10.7554/eLife.18413

White, M. A., Massenzio, F., Li, X., Coleman, M. P., Barmada, S. J., & Sreedharan, J. (2021). Inhibiting glycogen synthase kinase 3 suppresses TDP-43-mediated neurotoxicity in a caspase-dependant manner. *BioRxiv*. https://doi.org/10.1101/2021.02.03.429569

Wiedner, H. J., & Giudice, J. (2021). It's not just a phase: Function and characteristics of RNA-binding proteins in phase separation. *Nature Structural & Molecular Biology*, *28*(6), 465–473. https://doi.org/10.1038/s41594-021-00601-w

Williams, K. L., Topp, S., Yang, S., Smith, B., Fifita, J. A., Warraich, S. T., Zhang, K. Y., Farrawell, N., Vance, C., Hu, X., Chesi, A., Leblond, C. S., Lee, A., Rayner, S. L., Sundaramoorthy, V., Dobson-Stone, C., Molloy, M. P., van Blitterswijk, M., Dickson, D. W., … Blair, I. P. (2016). CCNF

mutations in amyotrophic lateral sclerosis and frontotemporal dementia. *Nature Communications*, *7*(1), 1–8. https://doi.org/10.1038/ncomms11253

Williams, K. L., Warraich, S. T., Yang, S., Solski, J. A., Fernando, R., Rouleau, G. A., Nicholson, G. A., & Blair, I. P. (2012). UBQLN2/ubiquilin 2 mutation and pathology in familial amyotrophic lateral sclerosis. *Neurobiology of Aging*, *33*(10), 2527.e3-2527.e10. https://doi.org/10.1016/j.neurobiolaging.2012.05.008

Wang, Duan, X., Zhou, X., Wang, R., Zhang, X., Cao, Z., Wang, X., Zhou, Z., Sun, Y., & Peng, D. (2022). ANXA11 mutations are associated with amyotrophic lateral sclerosis–frontotemporal dementia. Frontiers in Neurology, 13. https://www.frontiersin.org/articles/10.3389/fneur.2022.886887

Wolozin, B., & Ivanov, P. (2019). Stress granules and neurodegeneration. *Nature Reviews. Neuroscience*, *20*(11), 649–666. https://doi.org/10.1038/s41583-019-0222-5

Wong, C.-E., Jin, L.-W., Chu, Y.-P., Wei, W.-Y., Ho, P.-C., & Tsai, K.-J. (2021). TDP-43 proteinopathy impairs mRNP granule mediated postsynaptic translation and mRNA metabolism. *Theranostics*, *11*(1), 330–345. https://doi.org/10.7150/thno.51004

Wood, A., Gurfinkel, Y., Polain, N., Lamont, W., & Lyn Rea, S. (2021). Molecular Mechanisms Underlying TDP-43 Pathology in Cellular and Animal Models of ALS and FTLD. *International Journal of Molecular Sciences*, *22*(9), 4705. https://doi.org/10.3390/ijms22094705

Writing Group & Edaravone (MCI-186) ALS 19 Study Group. (2017). Safety and efficacy of edaravone in well defined patients with amyotrophic lateral sclerosis: A randomised, double-blind, placebo-controlled trial. *The Lancet. Neurology*, *16*(7), 505–512. https://doi.org/10.1016/S1474-4422(17)30115-1

Wu, C.-H., Fallini, C., Ticozzi, N., Keagle, P. J., Sapp, P. C., Piotrowska, K., Lowe, P., Koppers, M., McKenna-Yasek, D., Baron, D. M., Kost, J. E., Gonzalez-Perez, P., Fox, A. D., Adams, J., Taroni, F., Tiloca, C., Leclerc, A. L., Chafe, S. C., Mangroo, D., … Landers, J. E. (2012). Mutations in the Profilin 1 Gene Cause Familial Amyotrophic Lateral Sclerosis. *Nature*, *488*(7412), 499–503. https://doi.org/10.1038/nature11280

Wu, J. J., Cai, A., Greenslade, J. E., Higgins, N. R., Fan, C., Le, N. T. T., Tatman, M., Whiteley, A. M., Prado, M. A., Dieriks, B. V., Curtis, M. A., Shaw, C. E., Siddique, T., Faull, R. L. M., Scotter, E. L., Finley, D., & Monteiro, M. J. (2020). ALS/FTD mutations in UBQLN2 impede autophagy by reducing autophagosome acidification through loss of function. *Proceedings of the National Academy of Sciences*. *177*(26), 15230-15241. https://doi.org/10.1073/pnas.1917371117

Wu, L.-S., Cheng, W.-C., Hou, S.-C., Yan, Y.-T., Jiang, S.-T., & Shen, C.-K. J. (2010). TDP-43, a neuro-pathosignature factor, is essential for early mouse embryogenesis. *Genesis 48*(1), 56–62. https://doi.org/10.1002/dvg.20584

Wu, R., Zhou, D., Shen, X., Chen, F., Liu, F., & Gu, J. (2021). Phosphorylation of trans-active response DNA-binding protein-of 43 kDa promotes its cytoplasmic aggregation and modulates its function in tau mRNA stability and exon 10 alternative splicing. *Journal of Neurochemistry*, *158*(3), 766–778. https://doi.org/10.1111/jnc.15450

Xiao, S., McKeever, P. M., Lau, A., & Robertson, J. (2019). Synaptic localization of C9orf72 regulates post-synaptic glutamate receptor 1 levels. *Acta Neuropathologica Communications*, *7*(1), 161. https://doi.org/10.1186/s40478-019-0812-5

Xu, Y.-F., Gendron, T. F., Zhang, Y.-J., Lin, W.-L., D'Alton, S., Sheng, H., Casey, M. C., Tong, J., Knight, J., Yu, X., Rademakers, R., Boylan, K., Hutton, M., McGowan, E., Dickson, D. W., Lewis, J., & Petrucelli, L. (2010). Wild-Type Human TDP-43 Expression Causes TDP-43 Phosphorylation, Mitochondrial Aggregation, Motor Deficits, and Early Mortality in Transgenic Mice. *Journal of Neuroscience*, *30*(32), 10851–10859. https://doi.org/10.1523/JNEUROSCI.1630-10.2010

Yang, C., Qiao, T., Yu, J., Wang, H., Guo, Y., Salameh, J., Metterville, J., Parsi, S., Yusuf, I., Brown, R. H., Cai, H., & Xu, Z. (2022). Low-level overexpression of wild type TDP-43 causes late-onset, progressive neurodegeneration and paralysis in mice. *PloS One*, *17*(2), e0255710. https://doi.org/10.1371/journal.pone.0255710

Yang, Y., Hentati, A., Deng, H.-X., Dabbagh, O., Sasaki, T., Hirano, M., Hung, W.-Y., Ouahchi, K., Yan, J., Azim, A. C., Cole, N., Gascon, G., Yagmour, A., Ben-Hamida, M., Pericak-Vance, M., Hentati,

F., & Siddique, T. (2001). The gene encoding alsin, a protein with three guanine-nucleotide exchange factor domains, is mutated in a form of recessive amyotrophic lateral sclerosis. *Nature Genetics*, *29*(2), 160–165. https://doi.org/10.1038/ng1001-160

Yasuda, K., Clatterbuck-Soper, S. F., Jackrel, M. E., Shorter, J., & Mili, S. (2017). FUS inclusions disrupt RNA localization by sequestering kinesin-1 and inhibiting microtubule detyrosination. *Journal of Cell Biology*, *216*(4), 1015–1034. https://doi.org/10.1083/jcb.201608022

Yasuda, K., Zhang, H., Loiselle, D., Haystead, T., Macara, I. G., & Mili, S. (2013). The RNA-binding protein Fus directs translation of localized mRNAs in APC-RNP granules. *The Journal of Cell Biology*, *203*(5), 737–746. https://doi.org/10.1083/jcb.201306058

Yoon, H., Walters, G., Paulsen, A. R., & Scarisbrick, I. A. (2017). Astrocyte heterogeneity across the brain and spinal cord occurs developmentally, in adulthood and in response to demyelination. *PLoS ONE*, *12*(7), e0180697. https://doi.org/10.1371/journal.pone.0180697

Yu, C.-H., Davidson, S., Harapas, C. R., Hilton, J. B., Mlodzianoski, M. J., Laohamonthonkul, P., Louis, C., Low, R. R. J., Moecking, J., Nardo, D. D., Balka, K. R., Calleja, D. J., Moghaddas, F., Ni, E., McLean, C. A., Samson, A. L., Tyebji, S., Tonkin, C. J., Bye, C. R., … Masters, S. L. (2020). TDP-43 Triggers Mitochondrial DNA Release via mPTP to Activate cGAS/STING in ALS. *Cell*, *183*(3), 636-649. https://doi.org/10.1016/j.cell.2020.09.020

Yu, J., Lai, C., Shim, H., Xie, C., Sun, L., Long, C.-X., Ding, J., Li, Y., & Cai, H. (2018). Genetic ablation of dynactin p150Glued in postnatal neurons causes preferential degeneration of spinal motor neurons in aged mice. *Molecular Neurodegeneration*, *13*, 10. https://doi.org/10.1186/s13024-018-0242-z

Zaepfel, B. L., & Rothstein, J. D. (2021). RNA Is a Double-Edged Sword in ALS Pathogenesis. *Frontiers in Cellular Neuroscience*, *15*. https://doi.org/10.3389/fncel.2021.708181

Zarei, S., Carr, K., Reiley, L., Diaz, K., Guerra, O., Altamirano, P. F., Pagani, W., Lodin, D., Orozco, G., & Chinea, A. (2015). A comprehensive review of amyotrophic lateral sclerosis. *Surgical Neurology International*, *6*(171). https://doi.org/10.4103/2152-7806.169561

Zhang, J., Hirst, A. J., Duan, F., Qiu, H., Huang, R., Ji, Y., Bai, L., Zhang, F., Robinson, D., Jones, M., Li, L., Wang, P., Jiang, P., Andrews, P. W., Barbaric, I., & Na, J. (2019). Anti-apoptotic Mutations Desensitize Human Pluripotent Stem Cells to Mitotic Stress and Enable Aneuploid Cell Survival. *Stem Cell Reports*, *12*(3), 557–571. https://doi.org/10.1016/j.stemcr.2019.01.013

Zhang, K., Donnelly, C. J., Haeusler, A. R., Grima, J. C., Machamer, J. B., Steinwald, P., Daley, E. L., Miller, S. J., Cunningham, K. M., Vidensky, S., Gupta, S., Thomas, M. A., Hong, I., Chiu, S.-L., Huganir, R. L., Ostrow, L. W., Matunis, M. J., Wang, J., Sattler, R., … Rothstein, J. D. (2015). The C9orf72 repeat expansion disrupts nucleocytoplasmic transport. *Nature*, *525*(7567), 56–61. https://doi.org/10.1038/nature14973

Zhang, K., Liu, Q., Liu, K., Shen, D., Tai, H., Shu, S., Ding, Q., Fu, H., Liu, S., Wang, Z., Li, X., Liu, M., Zhang, X., & Cui, L. (2018). *ANXA11* mutations prevail in Chinese ALS patients with and without cognitive dementia. *Neurology Genetics*, *4*(3), e237. https://doi.org/10.1212/NXG.0000000000000237

Zhang, L. I., & Poo, M. M. (2001). Electrical activity and development of neural circuits. *Nature Neuroscience*, *4 Suppl*, 1207–1214. https://doi.org/10.1038/nn753

Zhang, S., Cooper-Knock, J., Weimer, A. K., Shi, M., Moll, T., Marshall, J. N. G., Harvey, C., Nezhad, H. G., Franklin, J., Souza, C. dos S., Ning, K., Wang, C., Li, J., Dilliott, A. A., Farhan, S., Elhaik, E., Pasniceanu, I., Livesey, M. R., Eitan, C., … Snyder, M. P. (2022). Genome-wide identification of the genetic basis of amyotrophic lateral sclerosis. *Neuron*, *110*(6), 992-1008.e11. https://doi.org/10.1016/j.neuron.2021.12.019

Zhang, Y., Chen, K., Sloan, S. A., Bennett, M. L., Scholze, A. R., O'Keeffe, S., Phatnani, H. P., Guarnieri, P., Caneda, C., Ruderisch, N., Deng, S., Liddelow, S. A., Zhang, C., Daneman, R., Maniatis, T., Barres, B. A., & Wu, J. Q. (2014). An RNA-Sequencing Transcriptome and Splicing Database of Glia, Neurons, and Vascular Cells of the Cerebral Cortex. *Journal of Neuroscience*, *34*(36), 11929–11947. https://doi.org/10.1523/JNEUROSCI.1860-14.2014

Zhang, Y., Sloan, S. A., Clarke, L. E., Caneda, C., Plaza, C. A., Blumenthal, P. D., Vogel, H., Steinberg, G. K., Edwards, M. S. B., Li, G., Duncan, J. A., Cheshier, S. H., Shuer, L. M., Chang, E. F., Grant, G.

A., Gephart, M. G. H., & Barres, B. A. (2016). Purification and Characterization of Progenitor and Mature Human Astrocytes Reveals Transcriptional and Functional Differences with Mouse. *Neuron*, *89*(1), 37–53. https://doi.org/10.1016/j.neuron.2015.11.013

Zhao, C., Devlin, A.-C., Chouhan, A. K., Selvaraj, B. T., Stavrou, M., Burr, K., Brivio, V., He, X., Mehta, A. R., Story, D., Shaw, C. E., Dando, O., Hardingham, G. E., Miles, G. B., & Chandran, S. (2020). Mutant C9orf72 human iPSC-derived astrocytes cause non-cell autonomous motor neuron pathophysiology. *Glia*, *68*(5), 1046–1064. https://doi.org/10.1002/glia.23761

Zhao, C.-P., Zhang, C., Zhou, S.-N., Xie, Y.-M., Wang, Y.-H., Huang, H., Shang, Y.-C., Li, W.-Y., Zhou, C., Yu, M.-J., & Feng, S.-W. (2007). Human mesenchymal stromal cells ameliorate the phenotype of SOD1-G93A ALS mice. *Cytotherapy*, *9*(5), 414–426. https://doi.org/10.1080/14653240701376413

Zhao, J., Wang, X., Huo, Z., Chen, Y., Liu, J., Zhao, Z., Meng, F., Su, Q., Bao, W., Zhang, L., Wen, S., Wang, X., Liu, H., & Zhou, S. (2022). The Impact of Mitochondrial Dysfunction in Amyotrophic Lateral Sclerosis. *Cells*, *11*(13), 2049. https://doi.org/10.3390/cells11132049

Zhao, M., Kao, C. S., Arndt, C., Tran, D. D., Cho, W. I., Maksimovic, K., Chen, X. X. L., Khan, M., Zhu, H., Qiao, J., Peng, K., Hong, J., Xu, J., Kim, D., Kim, J. R., Lee, J., van Bruggen, R., Yoon, W. H., & Park, J. (2020). Knockdown of genes involved in axonal transport enhances the toxicity of human neuromuscular disease-linked MATR3 mutations in Drosophila. *FEBS Letters*. https://doi.org/10.1002/1873-3468.13858

Zhou, L., & Too, H.-P. (2011). Mitochondrial localized STAT3 is involved in NGF induced neurite outgrowth. *PloS One*, *6*(6), e21680. https://doi.org/10.1371/journal.pone.0021680

Zhou, T., Benda, C., Duzinger, S., Huang, Y., Li, X., Li, Y., Guo, X., Cao, G., Chen, S., Hao, L., Chan, Y.-C., Ng, K.-M., Ho, J. C., Wieser, M., Wu, J., Redl, H., Tse, H.-F., Grillari, J., Grillari-Voglauer, R., … Esteban, M. A. (2011). Generation of Induced Pluripotent Stem Cells from Urine. *Journal of the American Society of Nephrology*, *22*(7), 1221–1228. https://doi.org/10.1681/ASN.2011010106

Zhou, W., Wang, K., Ruan, W., Bo, Z., Liu, L., Cao, Z., Chai, L., & Cao, G. (2013). Higher methylation in genomic DNA indicates incomplete reprogramming in induced pluripotent stem cells. *Cellular Reprogramming*, *15*(1), 92–99. https://doi.org/10.1089/cell.2012.0043

Zhou, Y., & Danbolt, N. C. (2014). Glutamate as a neurotransmitter in the healthy brain. *Journal of Neural Transmission*, *121*(8), 799–817. https://doi.org/10.1007/s00702-014-1180-8

Ziff, O. J., Clarke, B. E., Taha, D. M., Crerar, H., Luscombe, N. M., & Patani, R. (2021). Meta-analysis of human and mouse ALS astrocytes reveals multi-omic signatures of inflammatory reactive states. *Genome Research*. https://doi.org/10.1101/gr.275939.121

Ziff, O. J., Taha, D. M., Crerar, H., Clarke, B. E., Chakrabarti, A. M., Kelly, G., Neeves, J., Tyzack, G. E., Luscombe, N. M., & Patani, R. (2021). Reactive astrocytes in ALS display diminished intron retention. *Nucleic Acids Research*, *49*(6), 3168–3184. https://doi.org/10.1093/nar/gkab115

Ziff, O., Neeves, J., Mitchell, J., Tyzack, G., Ruiz, C., McGranahan, N., Luisier, R., Chakrabarti, A., Boulton, S., Kelly, G., Humphrey, J., & Patani, R. (2022). Genome instability underlies an augmented DNA damage response in familial and sporadic ALS human iPSC-derived motor neurons. *Research Square*. https://doi.org/10.21203/rs.3.rs-2049501/v1

Zu, T., Liu, Y., Bañez-Coronel, M., Reid, T., Pletnikova, O., Lewis, J., Miller, T. M., Harms, M. B., Falchook, A. E., Subramony, S. H., Ostrow, L. W., Rothstein, J. D., Troncoso, J. C., & Ranum, L. P. W. (2013). RAN proteins and RNA foci from antisense transcripts in C9ORF72 ALS and frontotemporal dementia. *Proceedings of the National Academy of Sciences*, *110*(51), E4968–E4977. https://doi.org/10.1073/pnas.1315438110

Zuo, X., Zhou, J., Li, Y., Wu, K., Chen, Z., Luo, Z., Zhang, X., Liang, Y., Esteban, M. A., Zhou, Y., & Fu, X.-D. (2021). TDP-43 aggregation induced by oxidative stress causes global mitochondrial imbalance in ALS. *Nature Structural & Molecular Biology*, *28*, 132-142. https://doi.org/10.1038/s41594-020-00537-7

# 9 Appendix

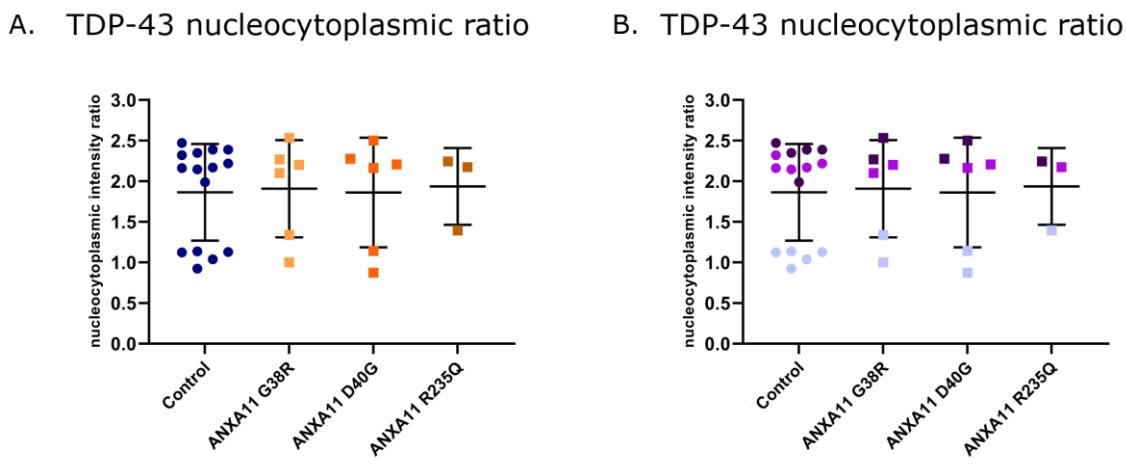


***Figure 9.1 Batch effects in high-throughput analysis***

High-throughput image analysis, as included throughout Chapter 4, often yielded large variability between biological replicates. (A) The nucleocytoplasmic ratio of TDP-43 in day-42 neurons shows large SEM due to spread of data within *ANXA11* mutation status groups. (B) When data is represented by biological replicate (each biological replicate is indicated with a different colour), it is evident that data spread is caused by fluctuations between biological replicates, and that the relationship between cell lines in one replicate remains relatively consistent.

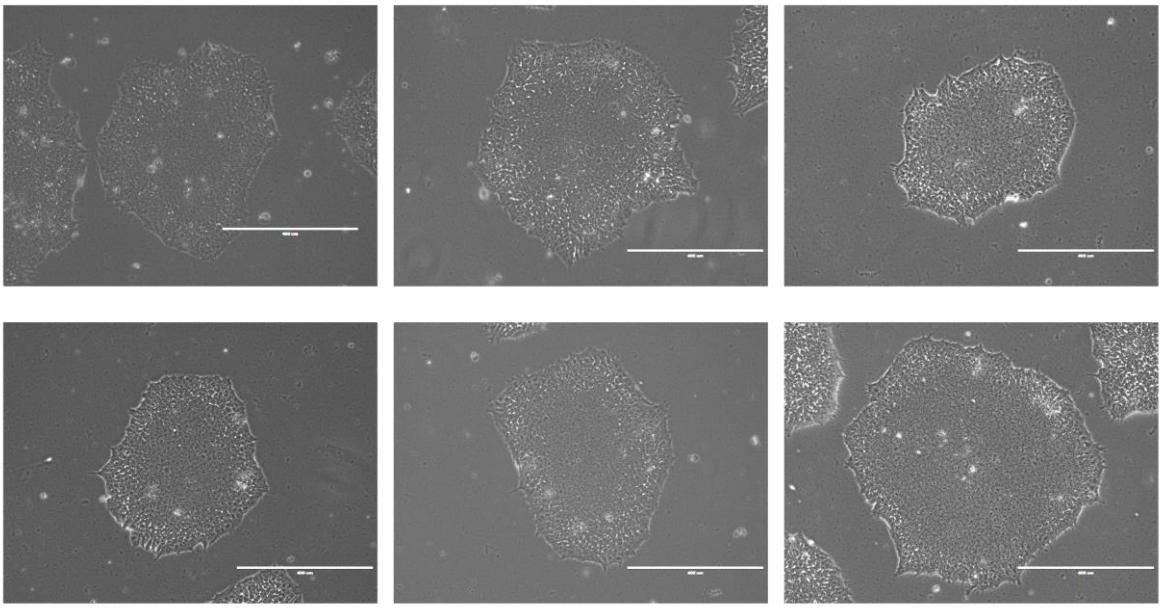

***Figure 9.2 Newly derived iPSCs show typical iPSC morphology***

iPSCs in culture were imaged with an in-hood EVOS light microscope. iPSCs show typical iPSC morphology with small round cells with large nuclei, growing in colonies with well-defined edges. Scale bars represent 400µm.

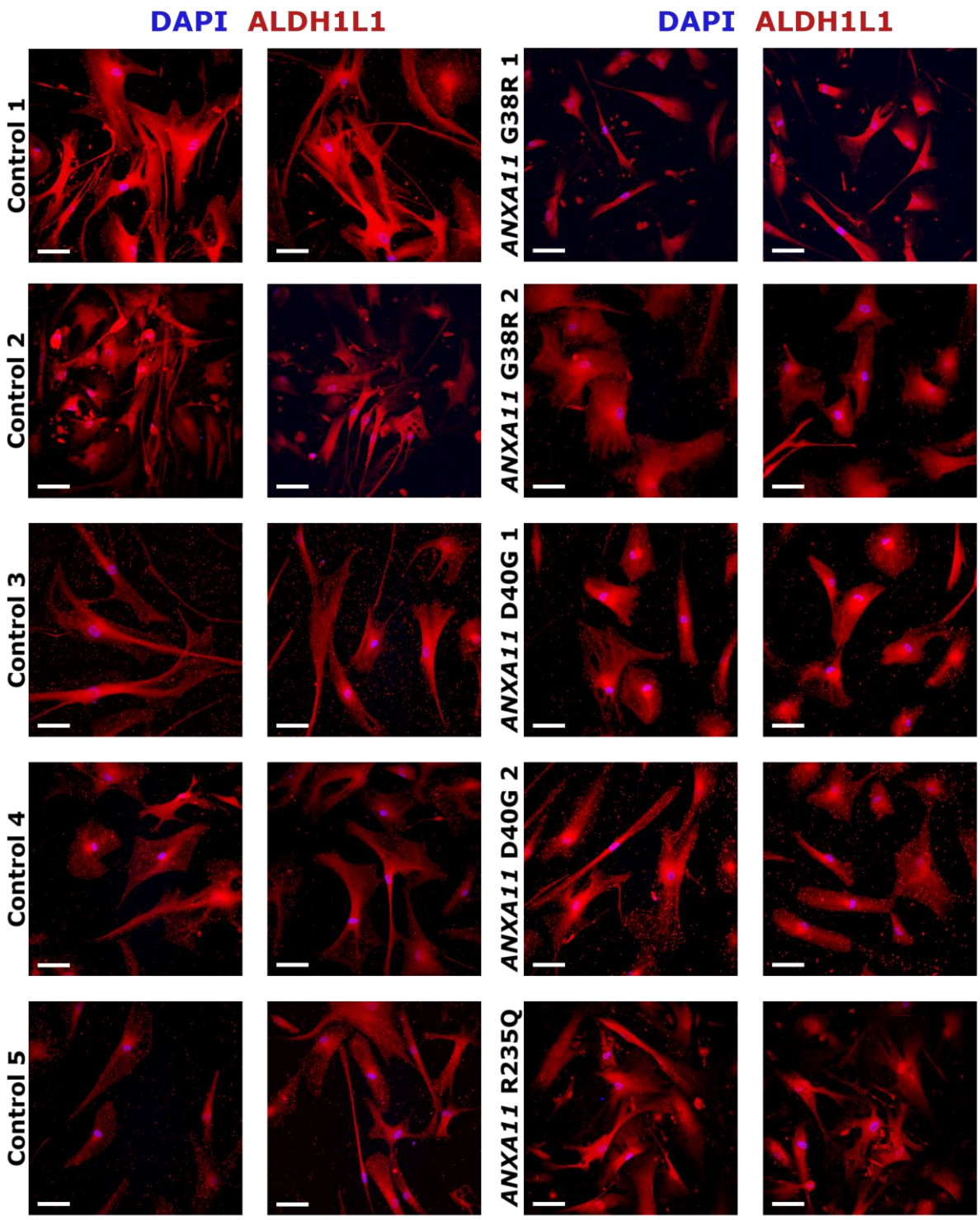


***Figure 9.3 Cell cultures following astrocyte derivation are positive for ALDH1L1***

iPSCs were differentiated into astrocytes until day ~50, immunolabelled for the astrocytic marker ALDH1L1 (red), and stained with DAPI (blue). Representative images are included to demonstrate the presence of ALDH1L1 positive cells with typical astrocyte morphology, indicating that astrocyte derivation was achieved. Scale bars represent 100µm.

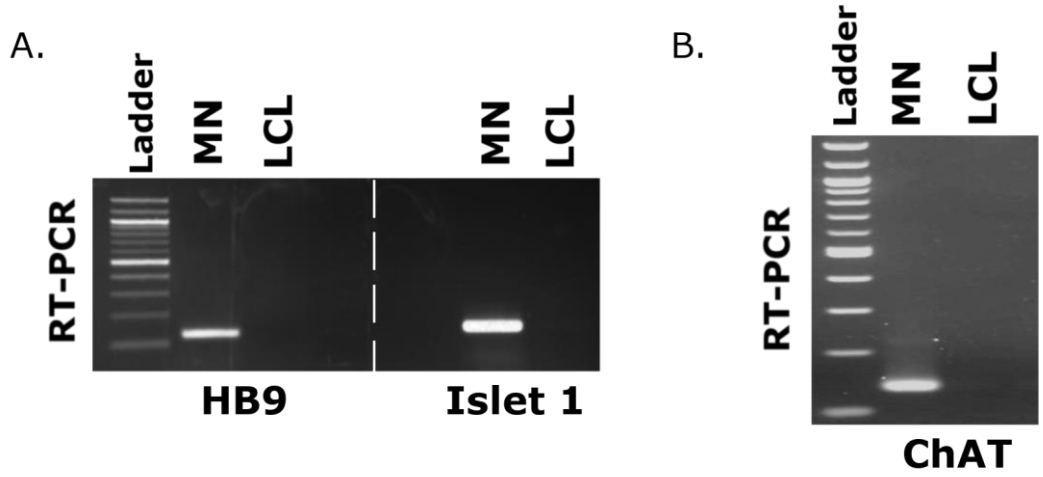


***Figure 9.4 Motor neurons express the motor neuron markers HB9 and ChAT***

(A) HB9 and Islet 1 were detected in day-17 motor neuron cDNA but not LCL cDNA, measured by RT-PCR. (B) cDNA from motor neurons at day 21 of differentiation was positive for ChAT by RT-PCR, which was absent in LCL cDNA. Samples used in experiments had been previously validated for presence of cDNA, however house-keeping genes are not included in the representative image.

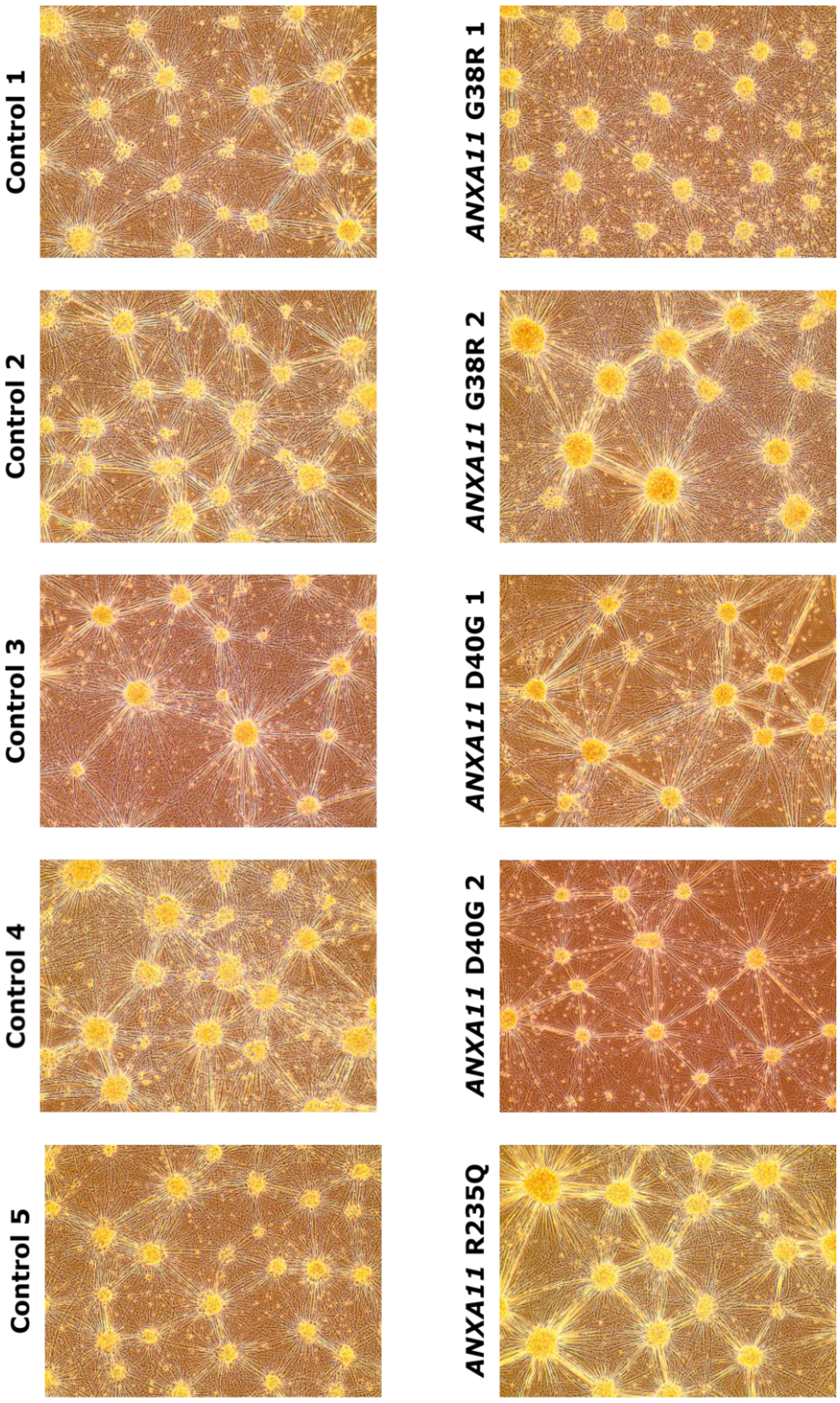


***Figure 9.5 Typical motor neuron cultures harvested for western blotting***

Representative images of live neuronal cultures before harvesting for western blot. To ensure that western blot data represented signal from neurons, visual inspection of cultures was implemented before protein harvesting, confirming absence of contamination with other cell types. Images taken with an in-hood EVOS light microscope with 4x magnification.

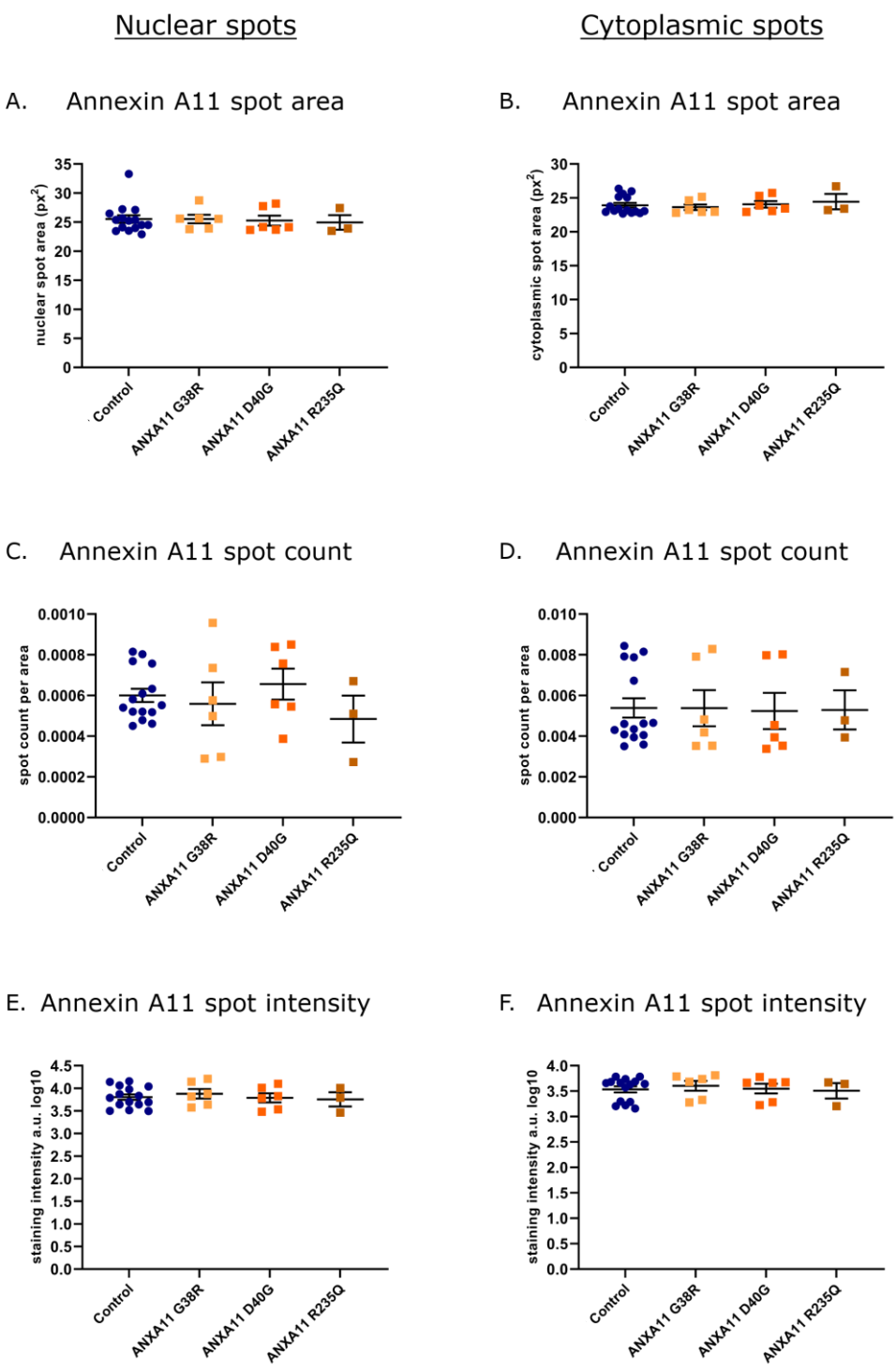


***Figure 9.6 Annexin A11 spot characteristics in young motor neurons***

Quantification of data represented in Figure 4.1 and Figure 4.2. Spot characteristics measured with Harmony® in control and *ANXA11mut* pure motor neuron populations, fixed on day 17 of motor neuron differentiation. (A) Annexin A11 spot size was unchanged between cell lines in the nucleus and (B) cytoplasm. (C) Spot count is represented as the number of Annexin A11 spots per nuclear and (D) cytoplasmic area. (E) Fluorescent intensity of Annexin A11 spots was consistent in the

nucleus and (F) cytoplasm. Data are presented as mean ± SEM, *n* = 3. Each data point represents one cell line in one motor neuron induction, with each induction comprised of three technical replicates. Control lines are grouped and *ANXA11mut* patient lines are grouped by mutation. Statistical analysis: Ordinary one-way ANOVA with Dunnett's multiple comparisons test ($p > 0.5$).

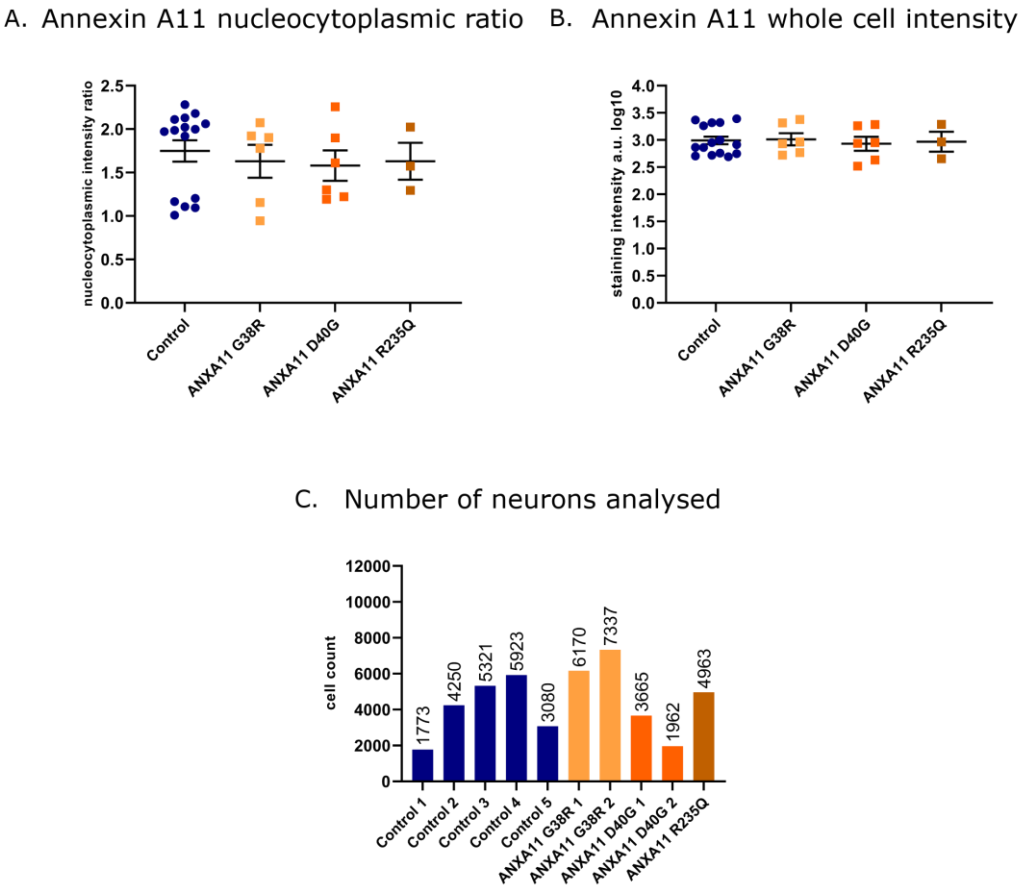


***Figure 9.7 Annexin A11 characteristics in young motor neurons***

Quantification of data represented in Figures 4.1 and 4.2. (A) The nucleocytoplasmic ratio of Annexin A11 showed large variability and was not statistically different between cell lines. (B) Annexin A11 intensity was consistent across control and *ANXA11mut* motor neurons. Data are presented as mean ± SEM, number of motor neuron inductions = 3. Each data point represents one cell line in one induction, with each biological replicate comprised of three technical replicates. Control lines are grouped and *ANXA11* ALS patient lines are grouped by mutation. Statistical analysis: Ordinary one-way ANOVA with Dunnett's multiple comparisons test ($p > 0.05$). (C) Graphical representation of the total number of motor neurons included in analysis across all biological and technical replicates.

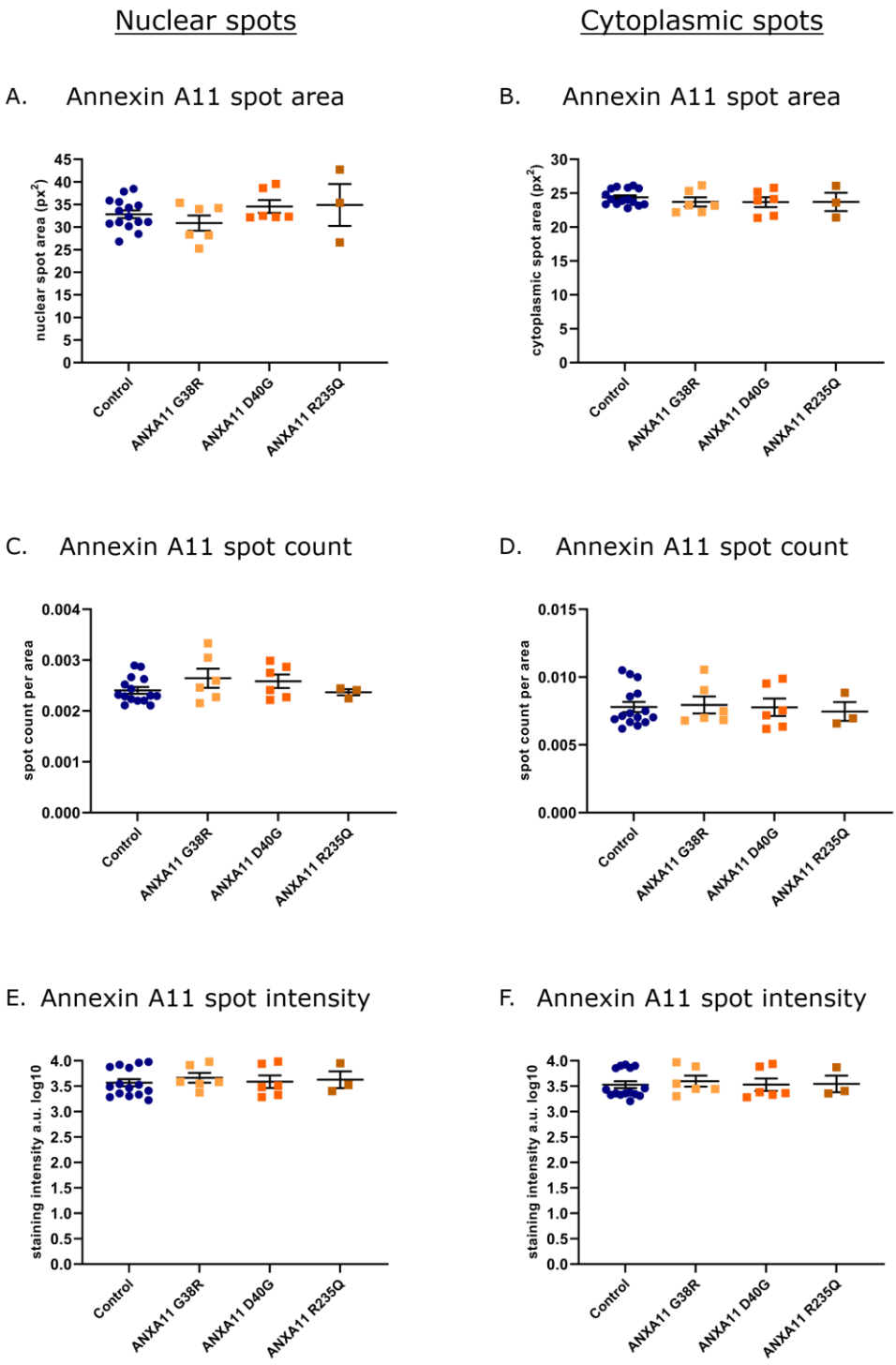


***Figure 9.8 Annexin A11 spot characteristics in young motor neurons maintained in co-culture with astrocytes***

Quantification of data represented in Figure 4.3 and Figure 4.4. Spot characteristics measured with Harmony® in control and *ANXA11mut* motor neurons maintained in co-culture with astrocytes, fixed on day 17 of motor neuron differentiation. (A) Annexin A11 spot size the nucleus and (B) cytoplasm. (C) Spot count is represented as the number of Annexin A11 spots per nuclear and (D) cytoplasmic

area. (E) Fluorescent intensity of Annexin A11 spots was consistent in the nucleus and (F) cytoplasm. Data are presented as mean ± SEM, number of motor neuron inductions = 3. Each data point represents one cell line in one induction, with each biological replicate comprised of three technical replicates. Control lines are grouped and *ANXA11mut* patient lines are grouped by mutation. Statistical analysis: Ordinary one-way ANOVA with Dunnett's multiple comparisons test ($p > 0.5$).

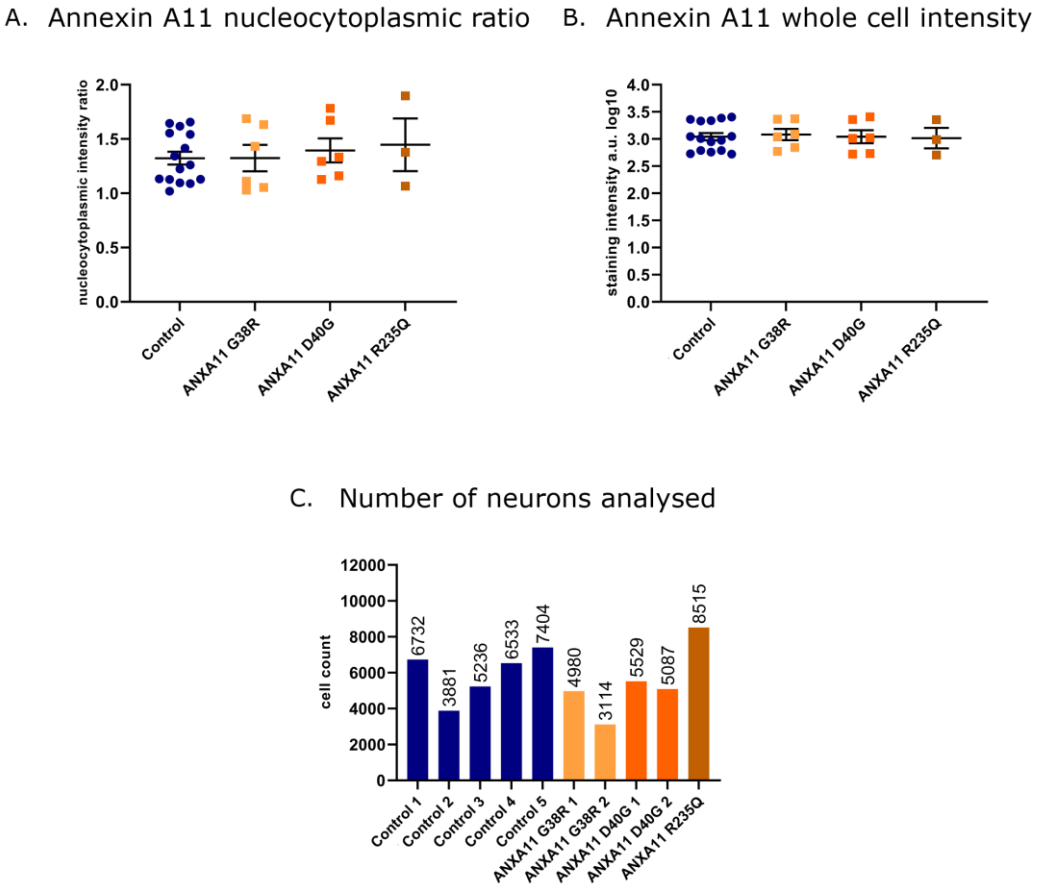


***Figure 9.9 Annexin A11 in young motor neurons maintained in co-culture with astrocytes***

Quantification of data represented in Figures 4.3 and 4.4. (A) The nucleocytoplasmic ratio of Annexin A11 was not statistically different between cell lines. (B) Annexin A11 intensity was consistent across control and *ANXA11mut* motor neurons. Data are presented as mean ± SEM, number of motor neuron inductions = 3. Each data point represents one cell line in one induction, with each biological replicate comprised of three technical replicates. Control lines are grouped and *ANXA11mut* lines are grouped by mutation. Statistical analysis: Ordinary one-way ANOVA with Dunnett's multiple comparisons test ($p > 0.05$). (C) Graphical representation of the total number of motor neurons included in analysis across all biological and technical replicates.

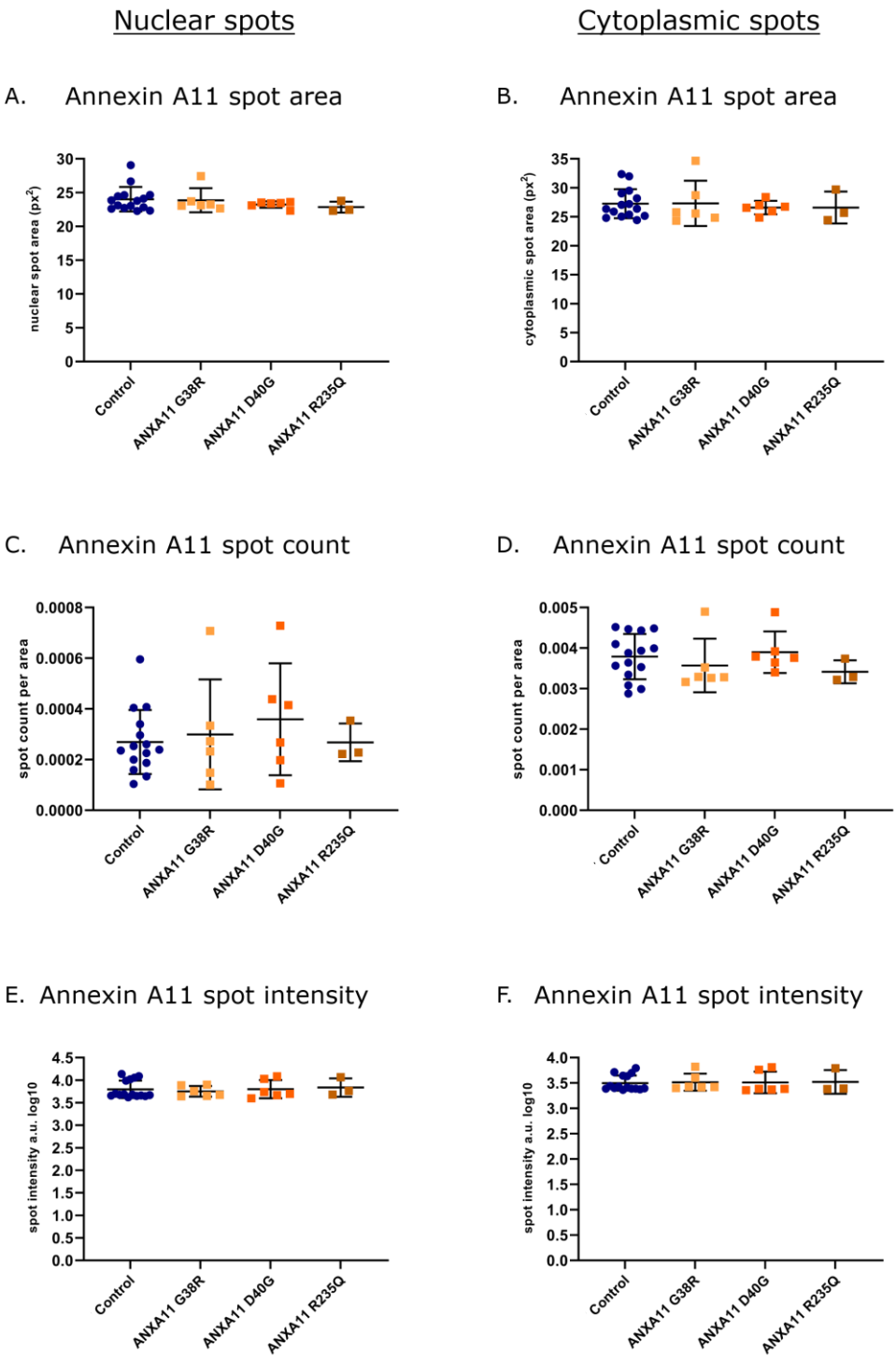


***Figure 9.10 Annexin A11 spots in aged motor neurons maintained in co-culture with astrocytes***

Quantification of data represented in Figure 4.5 and Figure 4.6. Spot characteristics measured with Harmony® in control and *ANXA11mut* motor neurons maintained in co-culture with astrocytes, fixed on day 42 of motor neuron differentiation. (A) Annexin A11 spot size in motor neuron nuclei. (B) Annexin A11 spot size in motor neuron cytoplasm. (C) Annexin A11 spot count in the nucleus was variable across experimental repeats with no statistically significant differences detected between

groups. (D) Annexin A11 spot count normalised to cytoplasmic area. (E) Fluorescent intensity of Annexin A11 spots was consistent in the nucleus and (F) cytoplasm. Data are presented as mean ± SEM, number of motor neuron inductions = 3. Each data point represents one cell line in one induction, with each biological replicate comprised of three technical replicates. Control lines are grouped and *ANXA11mut* patient lines are grouped by mutation. Statistical analysis: Ordinary one-way ANOVA with Dunnett's multiple comparisons test ($p > 0.5$).

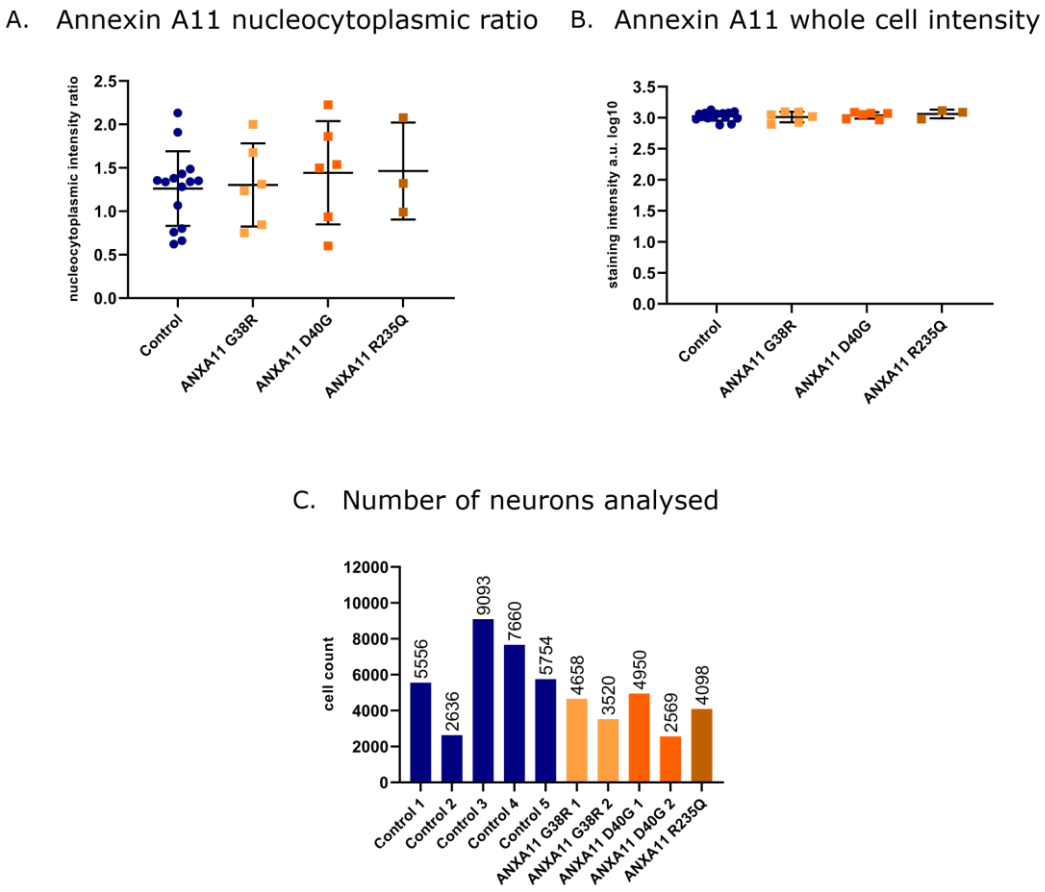


***Figure 9.11 Annexin A11 in aged motor neurons maintained in co-culture with astrocytes***

Quantification of data represented in Figures 4.5 and 4.6. (A) The nucleocytoplasmic ratio of Annexin A11 fluctuated largely across experimental repeats and was not statistically different between cell lines. (B) Annexin A11 intensity was consistent across control and *ANXA11mut* motor neurons. Data are presented as mean ± SEM, number of motor neuron inductions = 3. Each data point represents one cell line in one induction, with each biological replicate comprised of three technical replicates. Control lines are grouped and *ANXA11mut* lines are grouped by mutation. Statistical analysis: Ordinary one-way ANOVA with Dunnett's multiple comparisons test ($p > 0.05$). (C) Graphical

representation of the total number of motor neurons included in analysis across all biological and technical replicates.

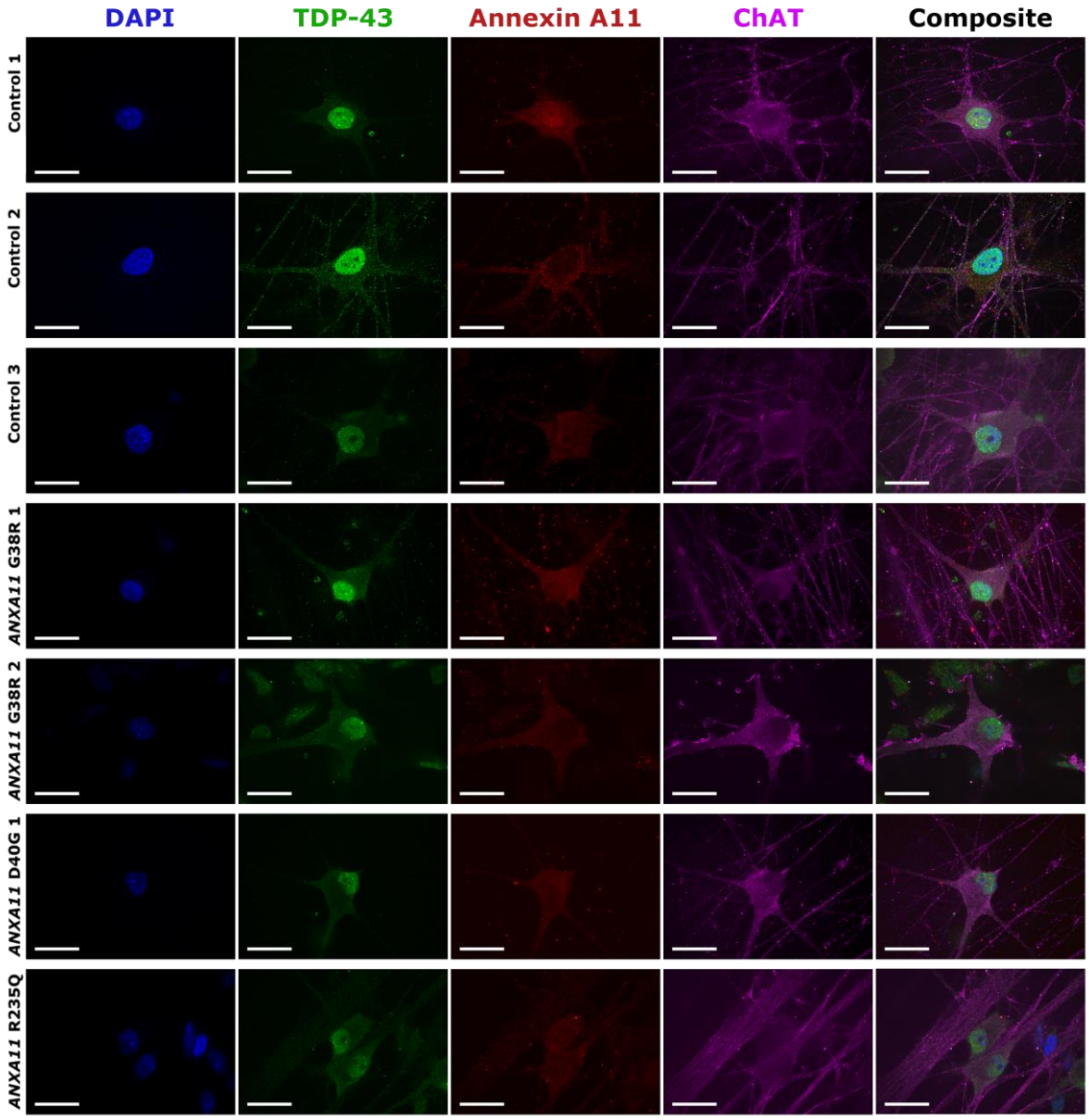


***Figure 9.12 High-resolution imaging of Annexin A11 and TDP-43 in day-42 co-culture with control astrocytes***

Motor neurons maintained in co-cultured were fixed on day 42 of differentiation, subject to immunocytochemistry with antibodies targeting TDP-43 (green), Annexin A11 (red), and ChAT (magenta), and co-stained with DAPI (blue). Cells were imaged with super resolution microscopy (iSIM). Scale bars represent 20µm.

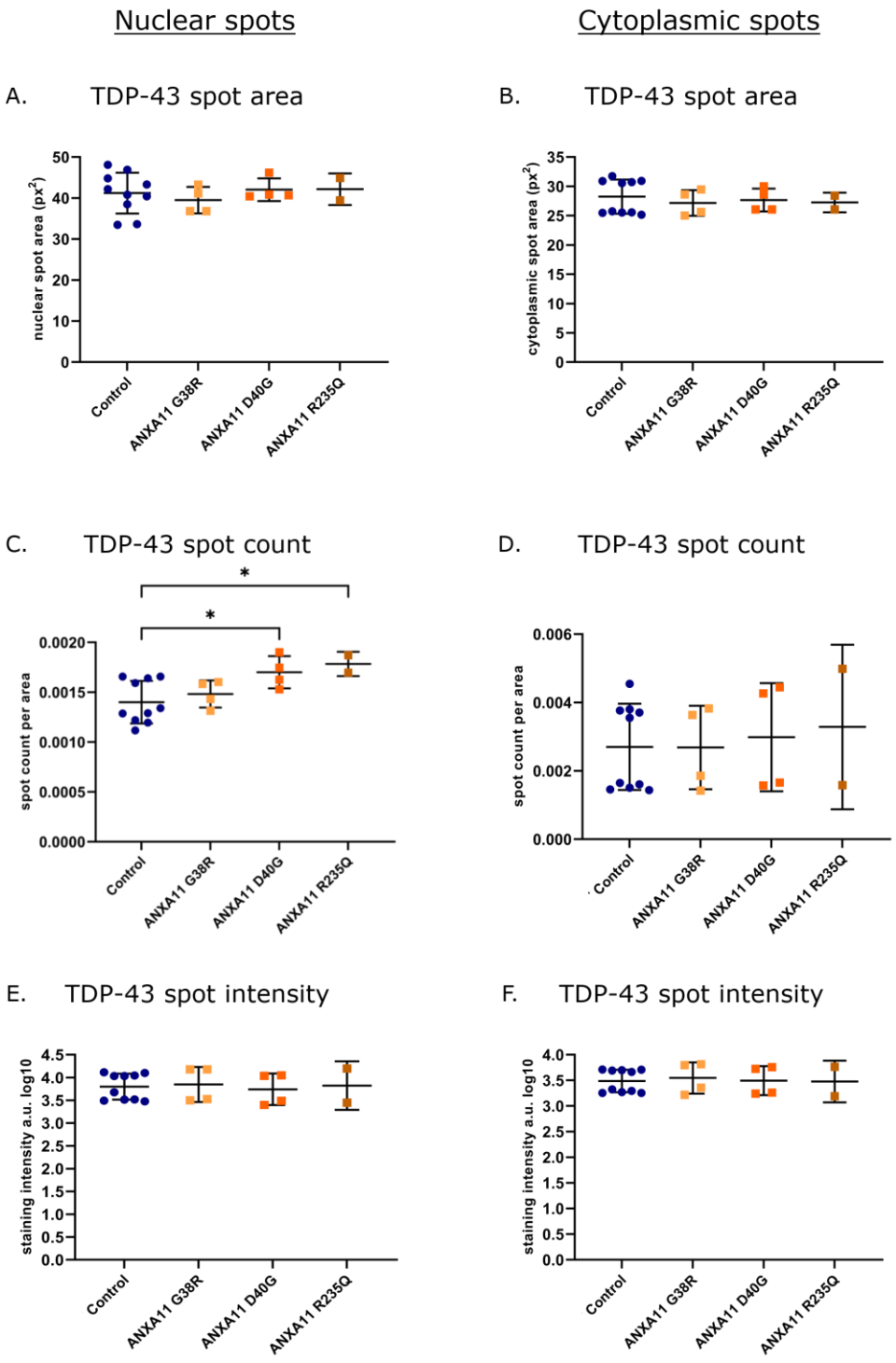


***Figure 9.13 TDP-43 spot characteristics in young motor neurons maintained in co-culture***

Quantification of data represented in Figures 4.13 and 4.14. Spot characteristics measured with Harmony® across control and *ANXA11mut* motor neurons maintained in co-culture with astrocytes, fixed at day 17 of motor neuron differentiation. (A) TDP-43 spot size in the nucleus was consistent across groups. (B) TDP-43 spot size in the cytoplasm. (C) An increase in the number of nuclear TDP-43 spots is seen in *ANXA11* D40G ($p$ = 0.0419) and *ANXA11* R235Q ($p$ = 0.0486) groups compared to

control. (D) TDP-43 spot count in the cytoplasm was variable between biological replicates but not statistically different between groups. (E) TDP-43 spot intensity in the nucleus. (F) TDP-43 spot intensity in the cytoplasm. Data are presented as mean ± SEM, number of motor neuron inductions = 2. Each data point represents one cell line in one induction, with each biological replicate comprised of three technical replicates. Control lines are grouped and *ANXA11* ALS patient lines are grouped by mutation. Statistical analyses: (A, C, F) Ordinary one-way ANOVA, (B, D, E) Brown-Forsythe one-way ANOVA, both with Dunnett's multiple comparisons test (* = $p \leq 0.05$; indicates statistical significance vs. the control group).

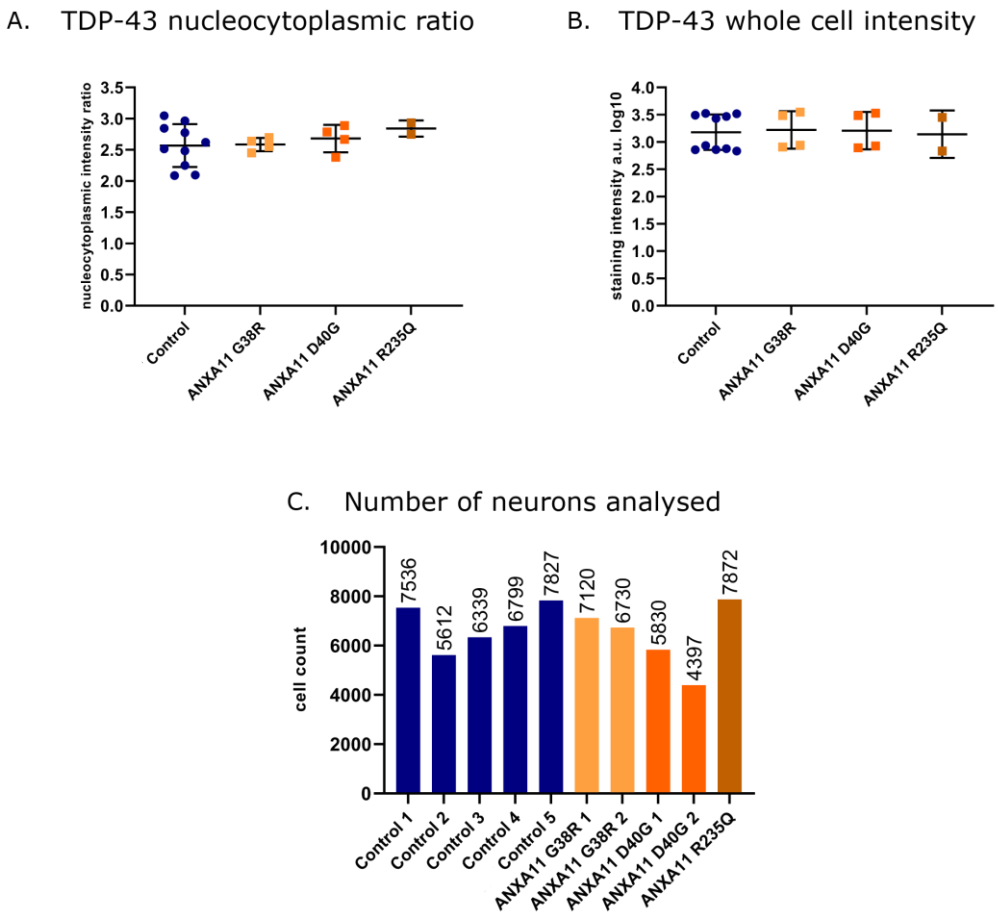


***Figure 9.14 TDP-43 characteristics in young motor neurons maintained in co-culture with astrocytes***

Quantification of data represented in Figures 4.13 and 4.14. (A) The nucleocytoplasmic ratio of TDP-43. (B) TDP-43 intensity was consistent across control and *ANXA11mut* motor neurons. Data are presented as mean ± SEM, number of motor neuron inductions = 2. Each data point represents one cell line in one biological replicate, with each biological replicate comprised of three technical replicates. Control lines are grouped and *ANXA11mut* lines are grouped by mutation. Statistical

analysis: Ordinary one-way ANOVA with Dunnett's multiple comparisons test ($p > 0.05$). (C) Graphical representation of the total number of motor neurons included in analysis across all biological and technical replicates.

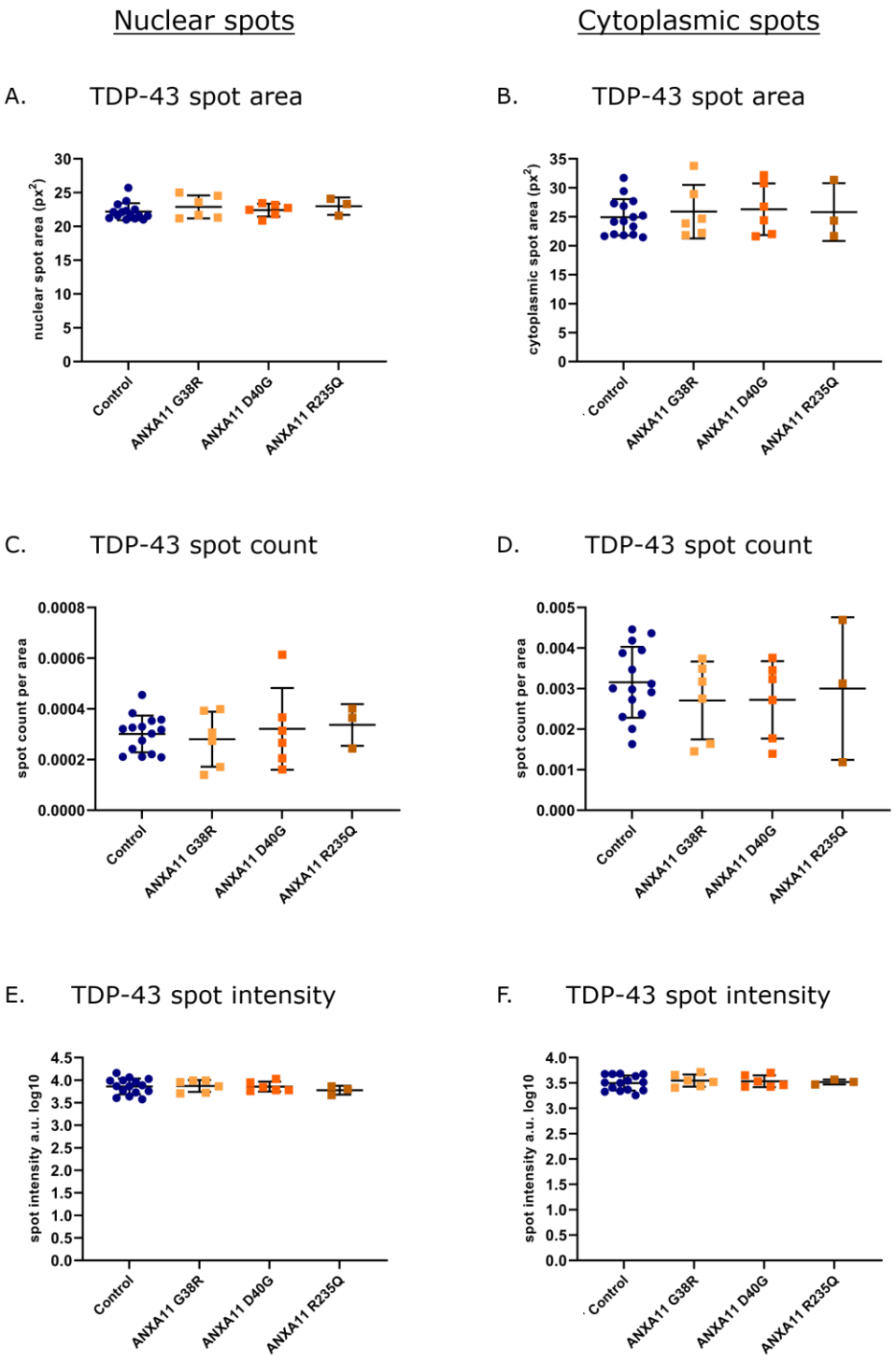


***Figure 9.15 TDP-43 spot analysis in aged motor neurons maintained in co-culture with astrocytes***

Quantification of data represented in Figure 4.15 and Figure 4.16. Spot characteristics measured with Harmony® across control and *ANXA11mut* motor neurons maintained in co-culture with astrocytes, fixed on day 42 of motor neuron differentiation. (A) TDP-43 spot size in motor neuron nuclei. (B) TDP-43 spot size in motor neuron cytoplasm. (C) TDP-43 spot count in the nucleus. (D) TDP-43 spot count normalised to cytoplasmic area. (E) Fluorescent intensity of TDP-43 spots was consistent in the

nucleus and (F) cytoplasm. Data are presented as mean ± SEM, number of motor neuron inductions = 3. Each data point represents one cell line in one induction, with each biological replicate comprised of three technical replicates. Control lines are grouped and *ANXA11mut* patient lines are grouped by mutation. Statistical analysis: Ordinary one-way ANOVA with Dunnett's multiple comparisons test ($p > 0.5$).

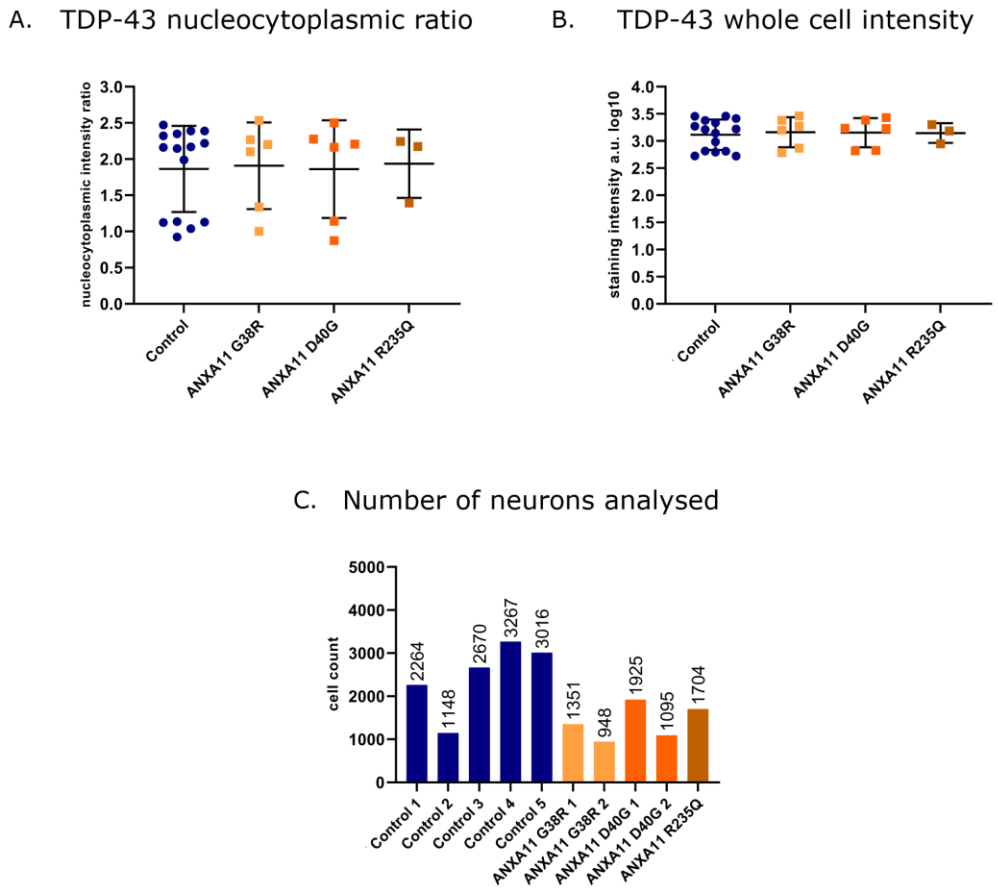


***Figure 9.16 TDP-43 characteristics in aged motor neurons maintained in co-culture with astrocytes***

Quantification of data represented in Figures 4.15 and 4.16. (A) The nucleocytoplasmic ratio of TDP-43 showed large variability across experimental repeats, with no statistically significant differences between groups. (B) TDP-43 intensity was consistent across control and *ANXA11mut* motor neurons. Data are presented as mean ± SEM, number of motor neuron inductions = 2. Each data point represents one cell line in one induction, with each biological replicate comprised of three technical replicates. Control lines are grouped and *ANXA11mut* lines are grouped by mutation. Statistical analysis: Ordinary one-way ANOVA with Dunnett's multiple comparisons test ($p > 0.05$). (C) Graphical representation of the total number of motor neurons included in analysis across all biological and technical replicates.

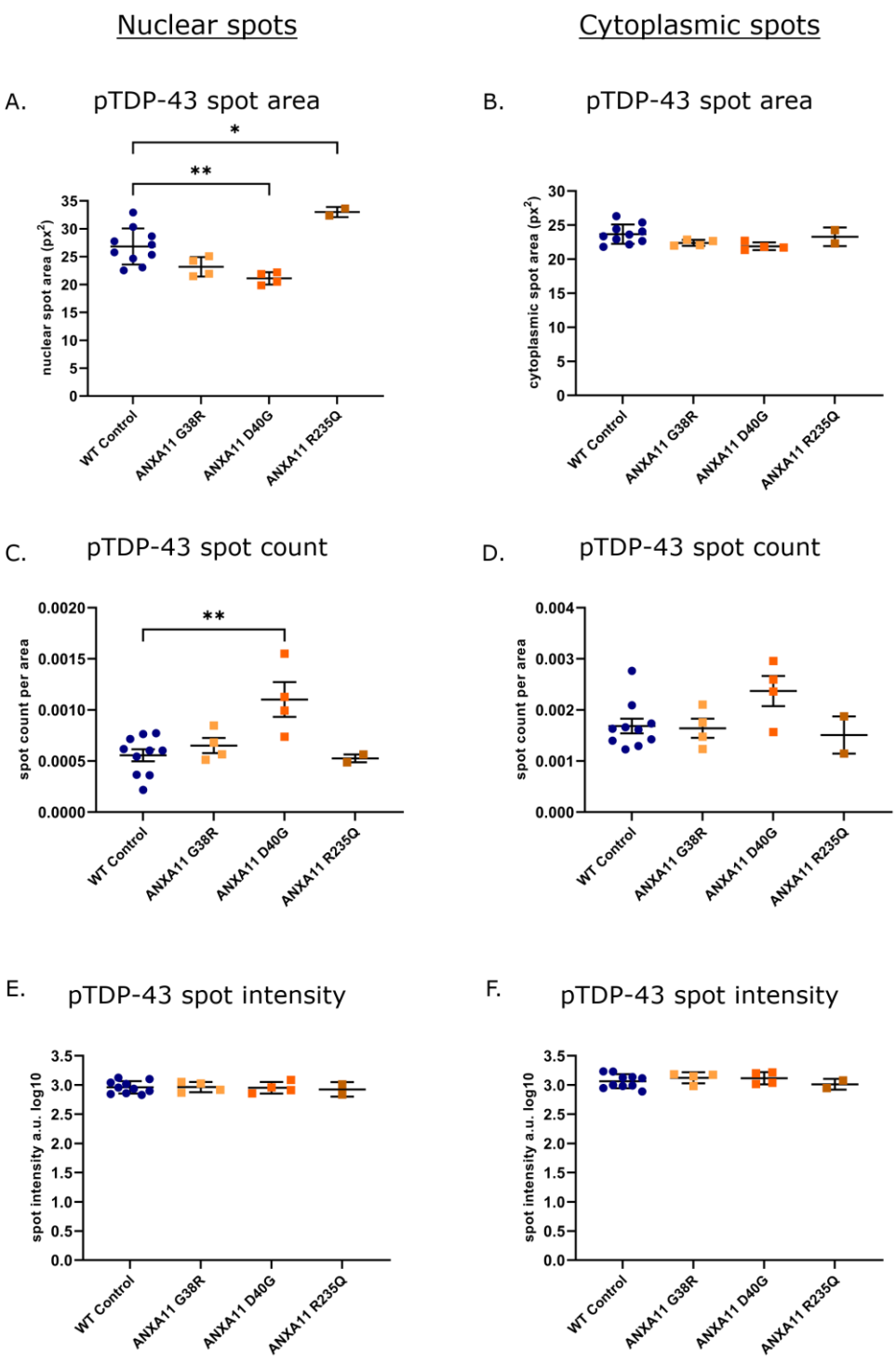


***Figure 9.17 pTDP-43 spot characteristics in young motor neurons***

Quantification of data represented in Figure 4.22 and Figure 4.23. Spot characteristics measured with Harmony® across control and *ANXA11mut* motor neurons fixed at day 17 of motor neuron differentiation. (A) pTDP-43 spot size was reduced in *ANXA11* D40G ($p$ = 0.0053), and increased in *ANXA11* R235Q ($p$ = 0.0205) compared to control. (B) Cytoplasmic pTDP-43 spot size was unchanged across groups. (C) An increase in the number of nuclear pTDP-43 spots was observed in *ANXA11*

D40G compared to control ($p$ = 0.0080). (D) Cytoplasmic pTDP-43 spot Data are presented as mean ± SEM, $n$ = 2. Each data point represents one cell line in one biological replicate, with each biological replicate comprised of three technical replicates. control lines are grouped and *ANXA11* ALS patient lines are grouped by mutation. Statistical analysis: Ordinary one-way ANOVA with Dunnett's multiple comparisons test. (* = $p \leq 0.05$, ** = $p \leq 0.01$; indicates statistical significance vs. the control group).

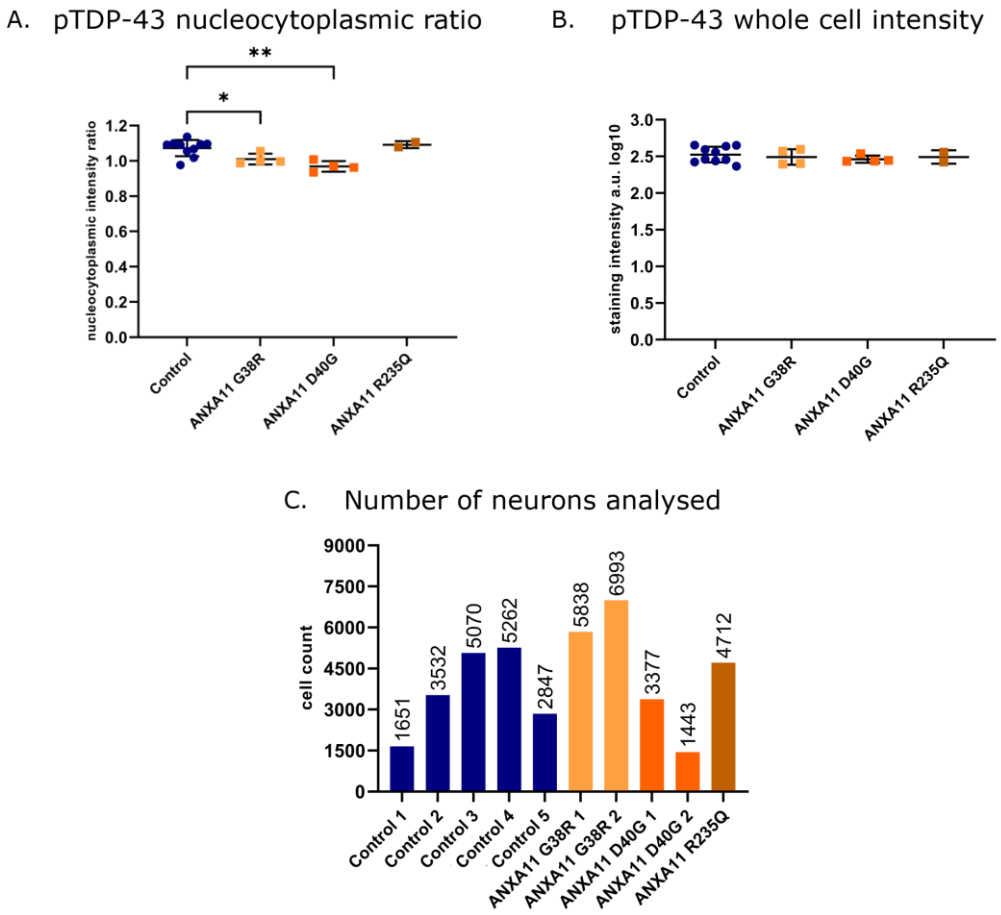


***Figure 9.18 pTDP-43 characteristics in young motor neurons***

Quantification of data represented in Figures 4.22 and 4.23. (A) The nucleocytoplasmic ratio of pTDP-43 was decreased in *ANXA11* G38R ($p$ = 0.0475) and *ANXA11* D40G ($p$ = 0.0013) compared to control. (B) TDP-43 intensity was consistent across control and *ANXA11mut* motor neurons. Data are presented as mean ± SEM, number of motor neuron inductions = 2. Each data point represents one cell line in one induction, with each biological replicate comprised of three technical replicates. Control lines are grouped and *ANXA11mut* lines are grouped by mutation. Statistical analysis: Ordinary one-way ANOVA with Dunnett's multiple comparisons test (* = $p \leq 0.05$; ** = $p \leq 0.01$; indicates significance vs. the control group). (C) Graphical representation of the total number of motor neurons included in analysis across all biological and technical replicates.

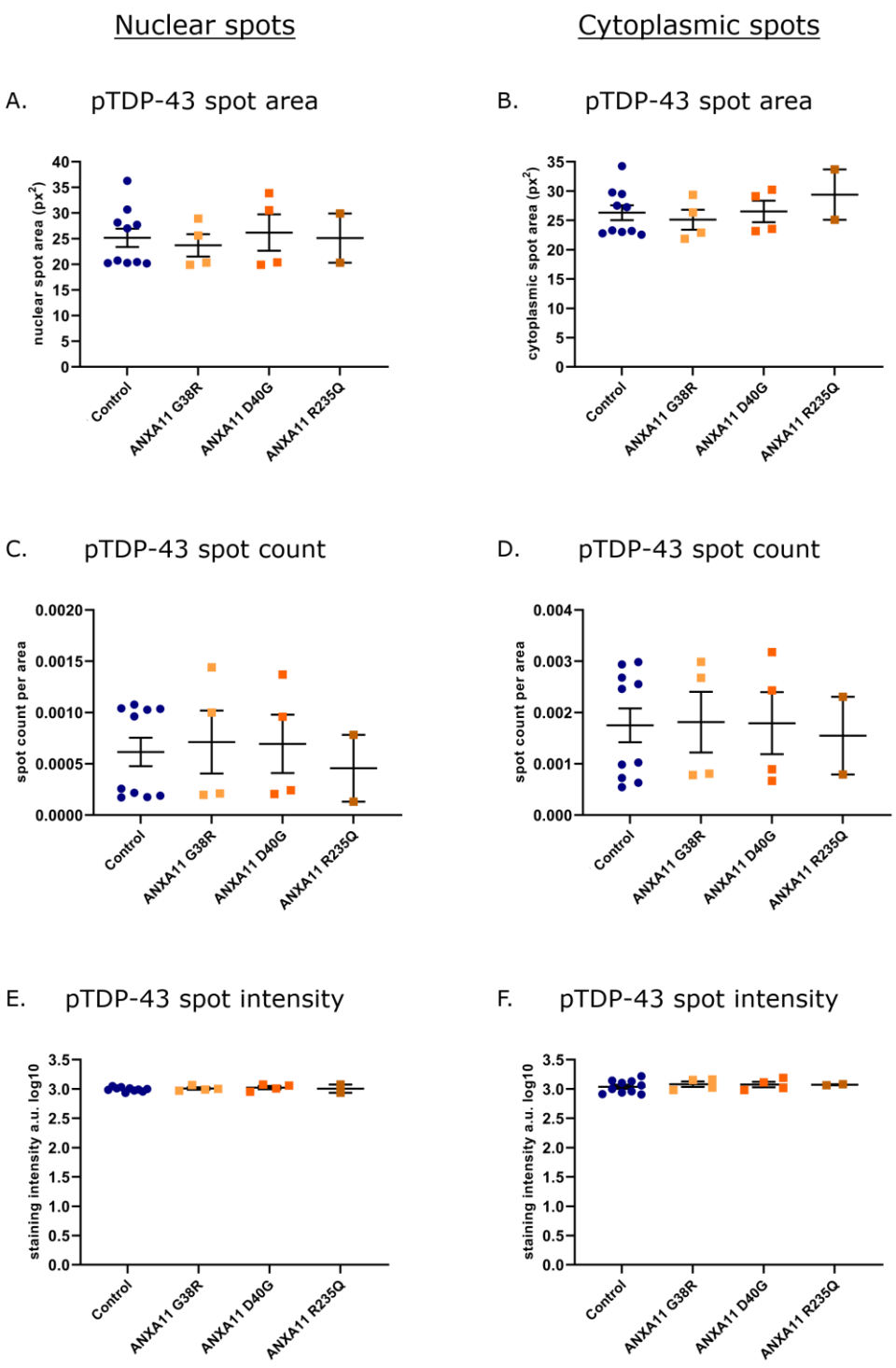


***Figure 9.19 pTDP-43 spot characteristics in young motor neurons maintained in co-culture***

Quantification of data represented in Figures 4.24 and 4.25. Spot characteristics measured with Harmony® across control and *ANXA11mut* motor neurons maintained in co-culture with astrocytes, fixed at day 17 of motor neuron differentiation. (A) pTDP-43 spot size in motor neuron nuclei. (B) pTDP-43 spot size in motor neuron cytoplasm. (C) pTDP-43 spot count in the nucleus was variable and not statistically different between groups. (D) pTDP-43 spot count in the cytoplasm fluctuated

across experimental repeats but was not statistically different across groups. (E) Fluorescent intensity of TDP-43 spots was consistent in the nucleus and (F) cytoplasm. Data are presented as mean ± SEM, number of motor neuron inductions = 2. Each data point represents one cell line in one induction, with each biological replicate comprised of three technical replicates. Control lines are grouped and *ANXA11mut* patient lines are grouped by mutation. Statistical analysis: Ordinary one-way ANOVA with Dunnett's multiple comparisons test ($p > 0.5$).

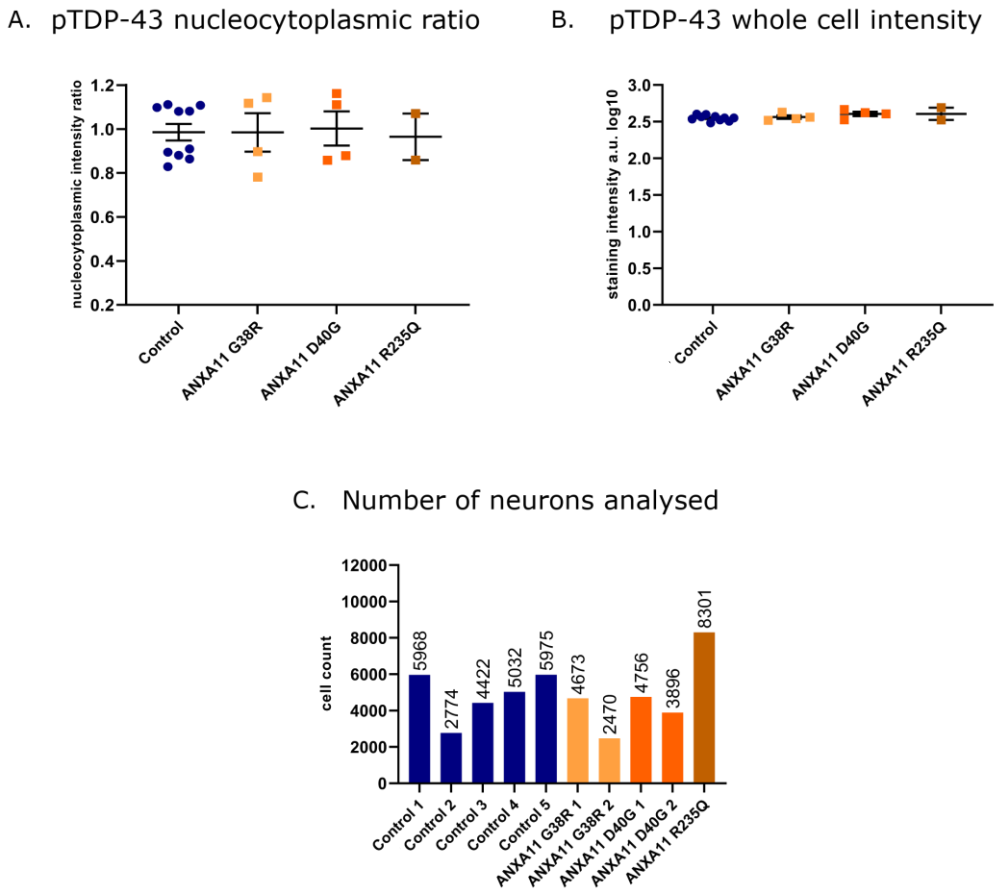


***Figure 9.20 pTDP-43 in young motor neurons maintained in co-culture with astrocytes***

Quantification of data represented in Figures 4.24 and 4.25. (A) The nucleocytoplasmic ratio of pTDP-43. (B) pTDP-43 intensity was consistent across control and *ANXA11mut* motor neurons. Data are presented as mean ± SEM, number of motor neuron inductions = 2. Each data point represents one cell line in one induction, with each biological replicate comprised of three technical replicates. Control lines are grouped and *ANXA11mut* lines are grouped by mutation. Statistical analysis: (A) Ordinary one-way ANOVA, (B) Brown-Forsythe one-way ANOVA, both with Dunnett's multiple comparisons test ($p > 0.05$). (C) Graphical representation of the total number of motor neurons included in analysis across all biological and technical replicates.

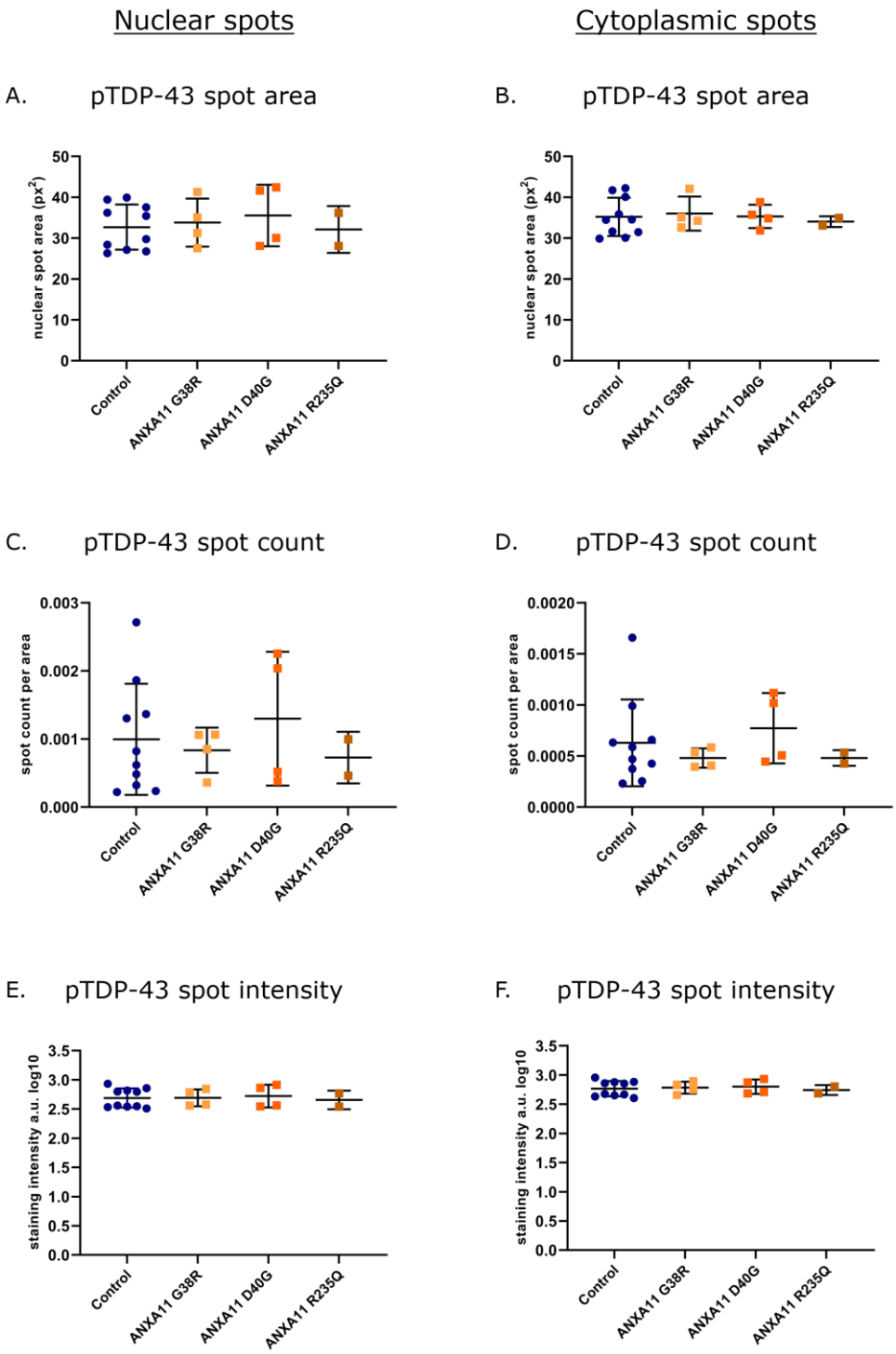


***Figure 9.21 pTDP-43 spot characteristics in aged motor neurons maintained in co-culture***

Quantification of data represented in Figures 4.26 and 4.27. Spot characteristics measured with Harmony® across control and *ANXA11mut* motor neurons maintained in co-culture with astrocytes, fixed at day 42 of motor neuron differentiation. (A) pTDP-43 spot size in motor neuron nuclei. (B) pTDP-43 spot size in motor neuron cytoplasm. (C) pTDP-43 spot count in the nucleus was variable and not statistically different between groups. (D) pTDP-43 spot count in the cytoplasm. (E)

Fluorescent intensity of TDP-43 spots was consistent in the nucleus and (F) cytoplasm. Data are presented as mean ± SEM, number of motor neuron inductions = 2. Each data point represents one cell line in one induction, with each biological replicate comprised of three technical replicates. Control lines are grouped and *ANXA11mut* patient lines are grouped by mutation. Statistical analysis: Ordinary one-way ANOVA with Dunnett's multiple comparisons test ($p > 0.5$).

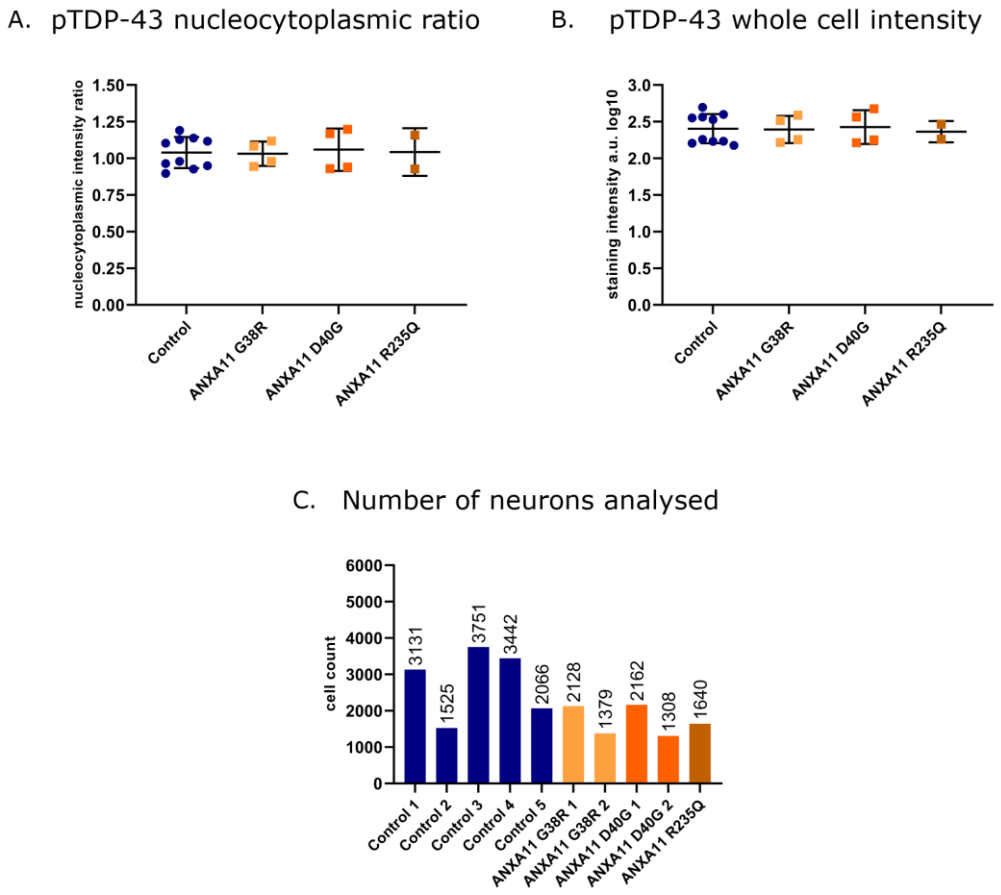


***Figure 9.22 pTDP-43 characteristics in aged motor neurons maintained in co-culture***

Quantification of data represented in Figures 4.26 and 4.27. (A) The nucleocytoplasmic ratio of pTDP-43. (B) pTDP-43 intensity was consistent across control and *ANXA11mut* motor neurons. Data are presented as mean ± SEM, number of motor neuron inductions = 2. Each data point represents one cell line in one induction, with each biological replicate comprised of three technical replicates. Control lines are grouped and *ANXA11mut* lines are grouped by mutation. Statistical analysis: (A) Ordinary one-way ANOVA, (B) Brown-Forysthe one-way ANOVA, both with Dunnett's multiple comparisons test ($p > 0.05$). (C) Graphical representation of the total number of motor neurons included in analysis across all biological and technical replicates.

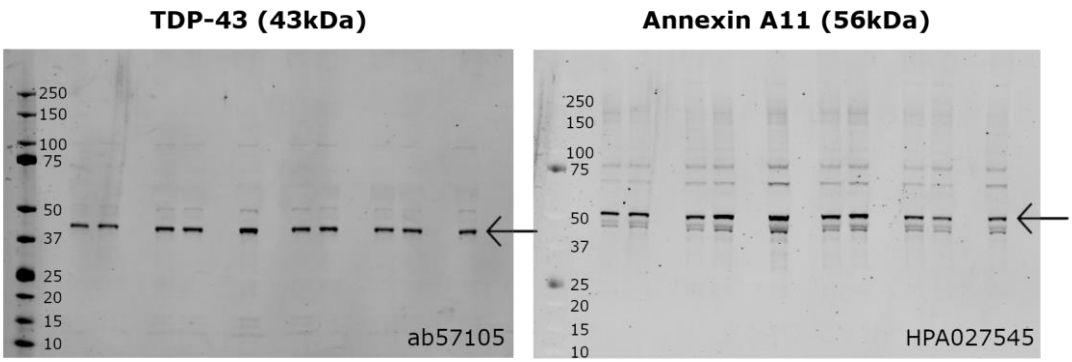


***Figure 9.23 TDP-43 and Annexin A11 full western blot***

Representative western blots with all detected protein bands, the predicted bands which were quantified in western blot analysis are indicated with black arrows.

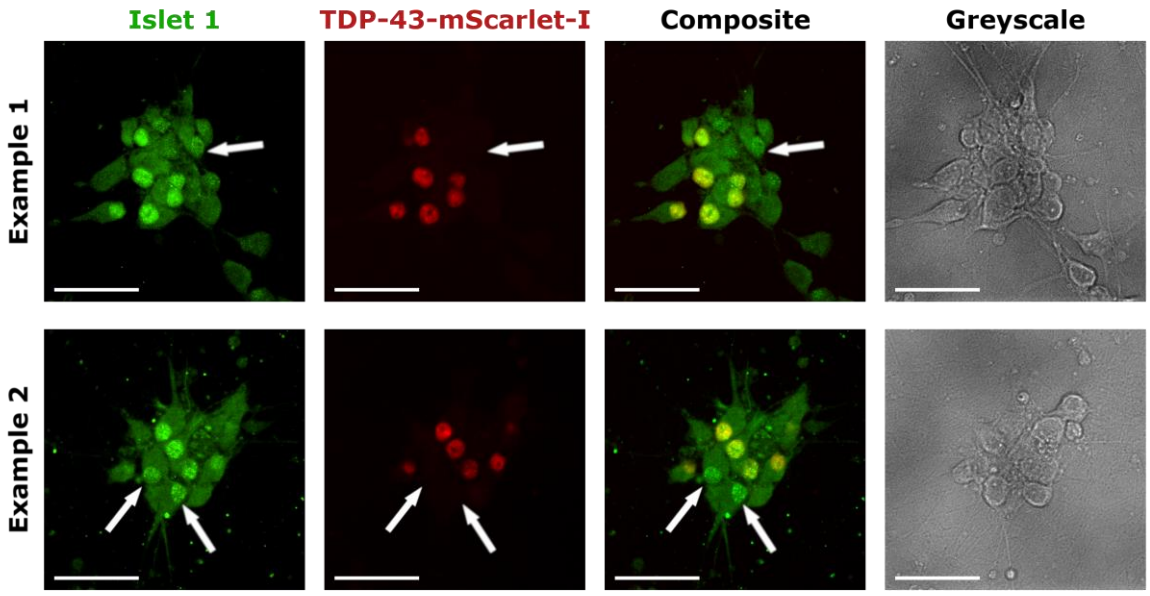


***Figure 9.24 TDP-43 signal partially co-localises with Islet 1 positive neurons***

To assess whether the intensity of nuclear TDP-43 was associated with neuronal subtypes in culture, a control iPSC line with TDP-43 endogenously tagged with the fluorescent protein mScarlet-I (red) was fixed on day 17 of differentiation and immunolabelled with the motor neuron marker Islet 1 (green). Some neurons with comparatively reduced TDP-43 and Islet 1 signal in the nucleus can be seen. Islet 1 positive neurons with no TDP-43 signal are highlighted with white arrows to indicate that reduced TDP-43 signal is not specifically associated with non-motor neuronal cells. Scale bars represent 50µm.

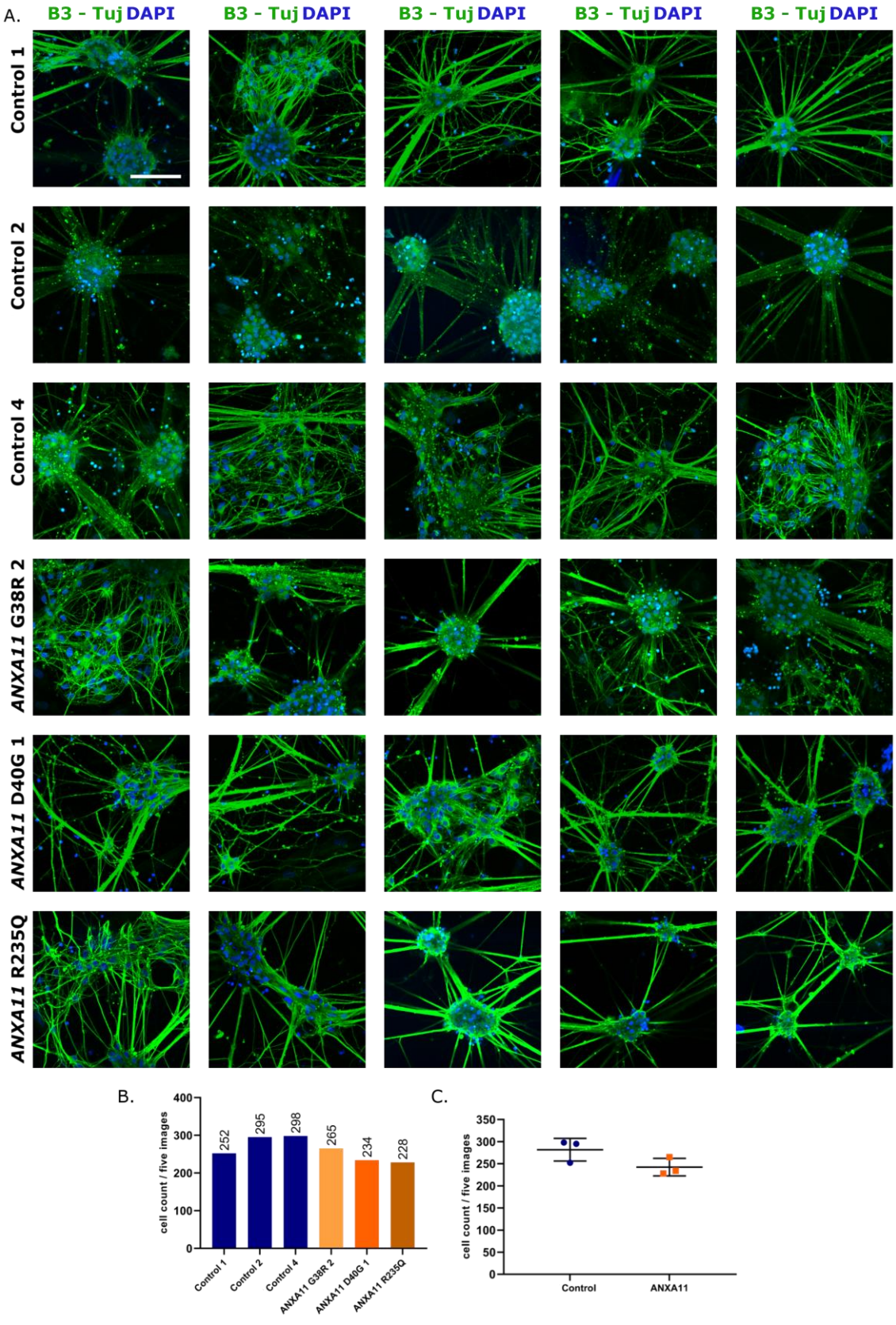


***Figure 9.25 Cell density in microfluidic devices***

Cell plating compartments in Experiment 1 in Figure 5.8. Nuclei count was completed to compare the number of neurons in microfluidic devices. (A) Representative images of cell bodies in the cell

plating compartment of microfluidic devices immunolabelled for $\beta$3-Tubulin (green) and stained with DAPI (blue). (B) Cell count across representative images. (C) Comparison of the number of nuclei in control and *ANXA11mut* neurons in microfluidic devices showed no statistical difference. Statistical test: Unpaired T-test ($p > 0.05$). Scale bar represents 100µm.

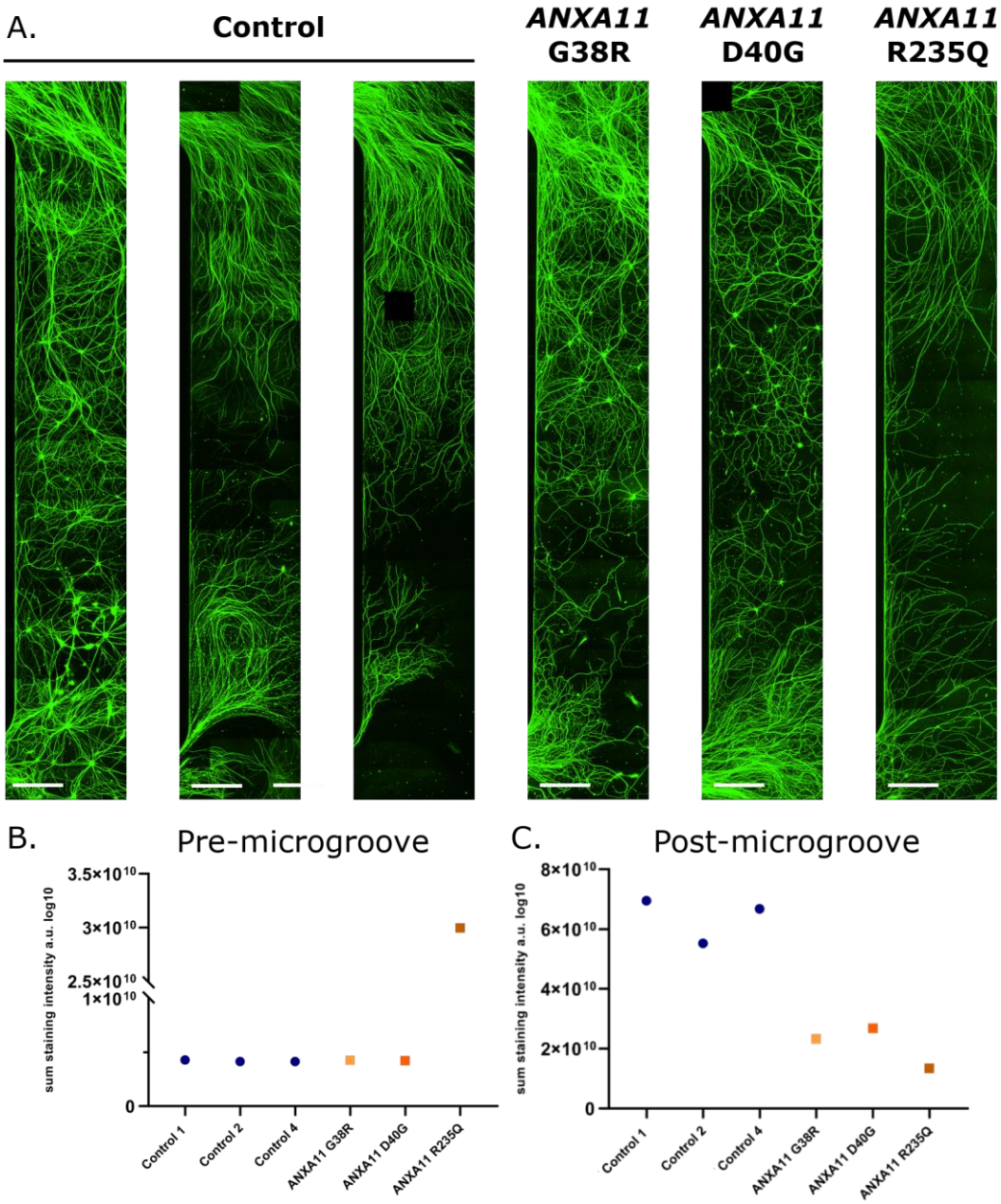


***Figure 9.26 Proximal neurites in microfluidic devices***

Pre-microgroove compartments in Experiment 1 in Figure 5.8. (A) Representative images of $\beta$3-Tubulin (green) positive neurons in the microfluidic compartment prior to microgrooves. (B) Total fluorescent intensity from whole images was measured, indicating comparable neuronal signal across lines (excluding *ANXA11* R235Q which showed increased intensity compared to other cell lines). (C) Total fluorescent intensity from post-microgroove compartments in the same experiment (Experiment 1, Figure 5.8), indicating reduced neuronal signal from *ANXA11mut* lines compared to control. Scale bars represent 500µm.

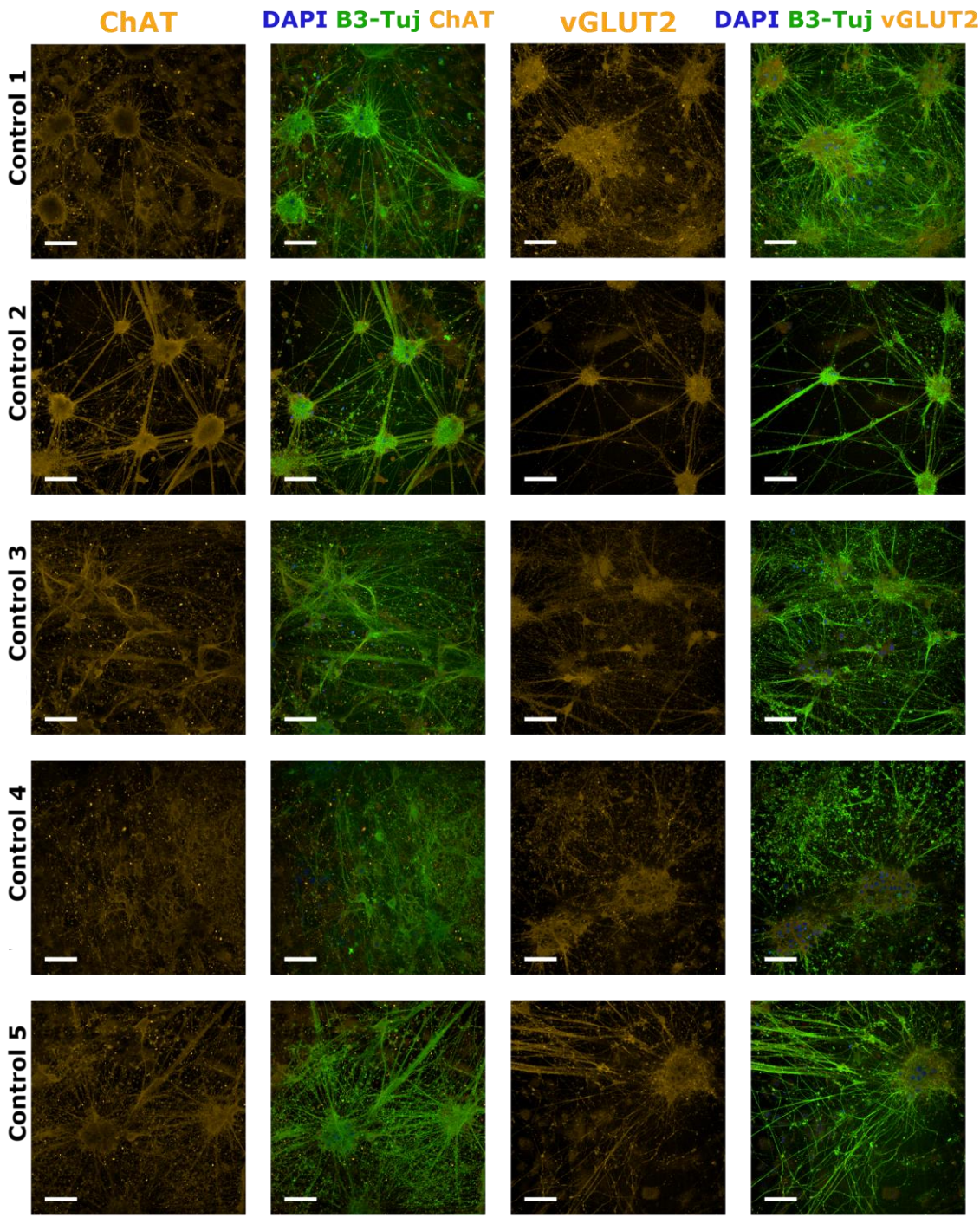


***Figure 9.27 Interrogation of control cultures for ChAT and vGLUT2 positive neurons***

Motor neurons derived from control motor neurons were probed for spontaneous calcium fluctuations (5.3.2), then fixed and immunolabelled for the neuronal marker $\beta$3-Tubulin (B3-Tuj, green), DAPI (blue), and probed for ChAT (orange - left hand panel), and vGLUT2 (orange – right hand panel). Scale bar represents 100µm.

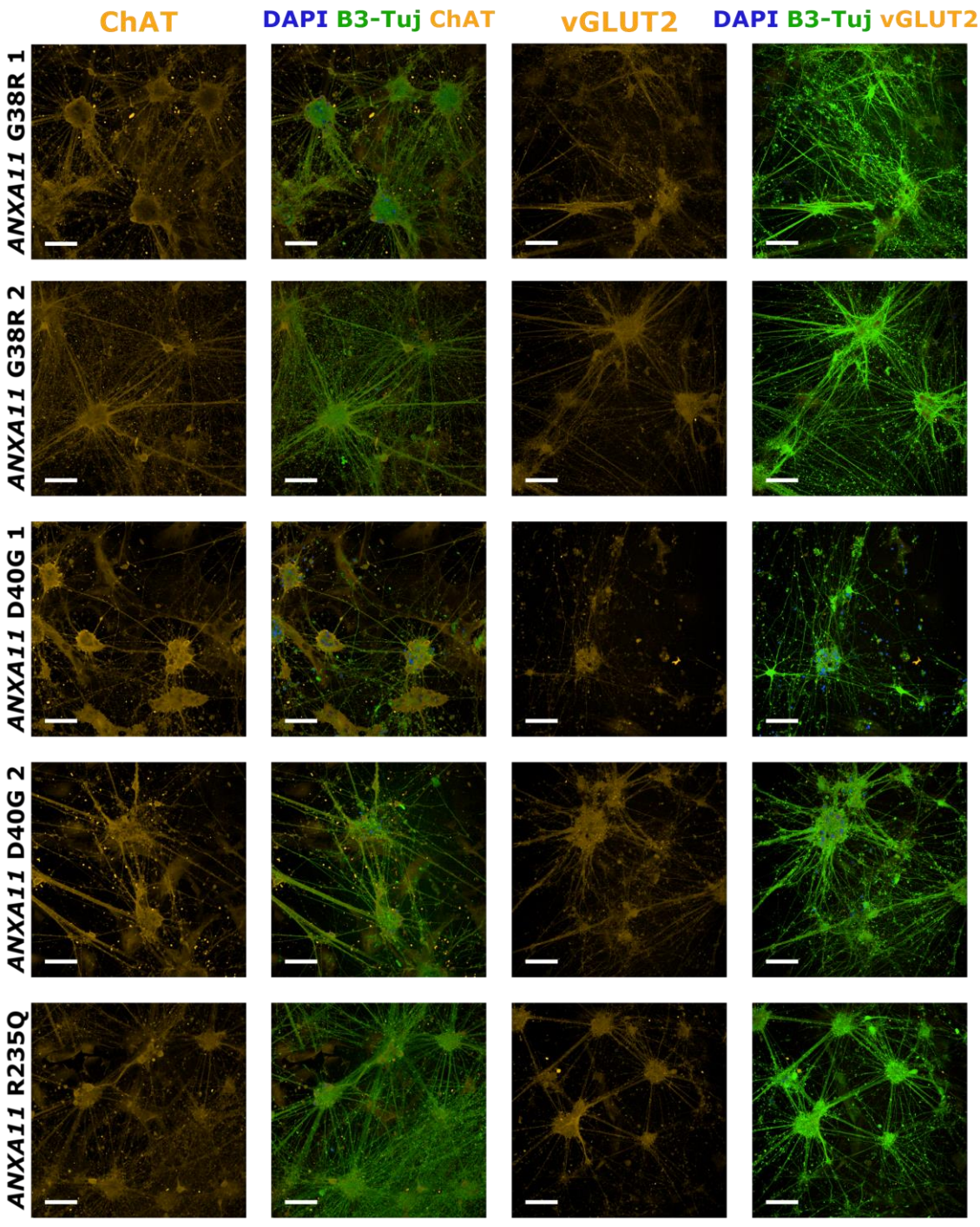


***Figure 9.28 Interrogation of ANXA11mut cultures for ChAT and vGLUT2 positive neurons***

Motor neurons derived from *ANXA11mut* motor neurons were probed for spontaneous calcium fluctuations (5.3.2), then fixed and imunolabelled for the neuronal marker $\beta$3-Tubulin (B3-Tuj, green), DAPI (blue and probed for ChAT (orange - left hand panel), and vGLUT2 (orange – right hand panel). Scale bar represents 100µm.

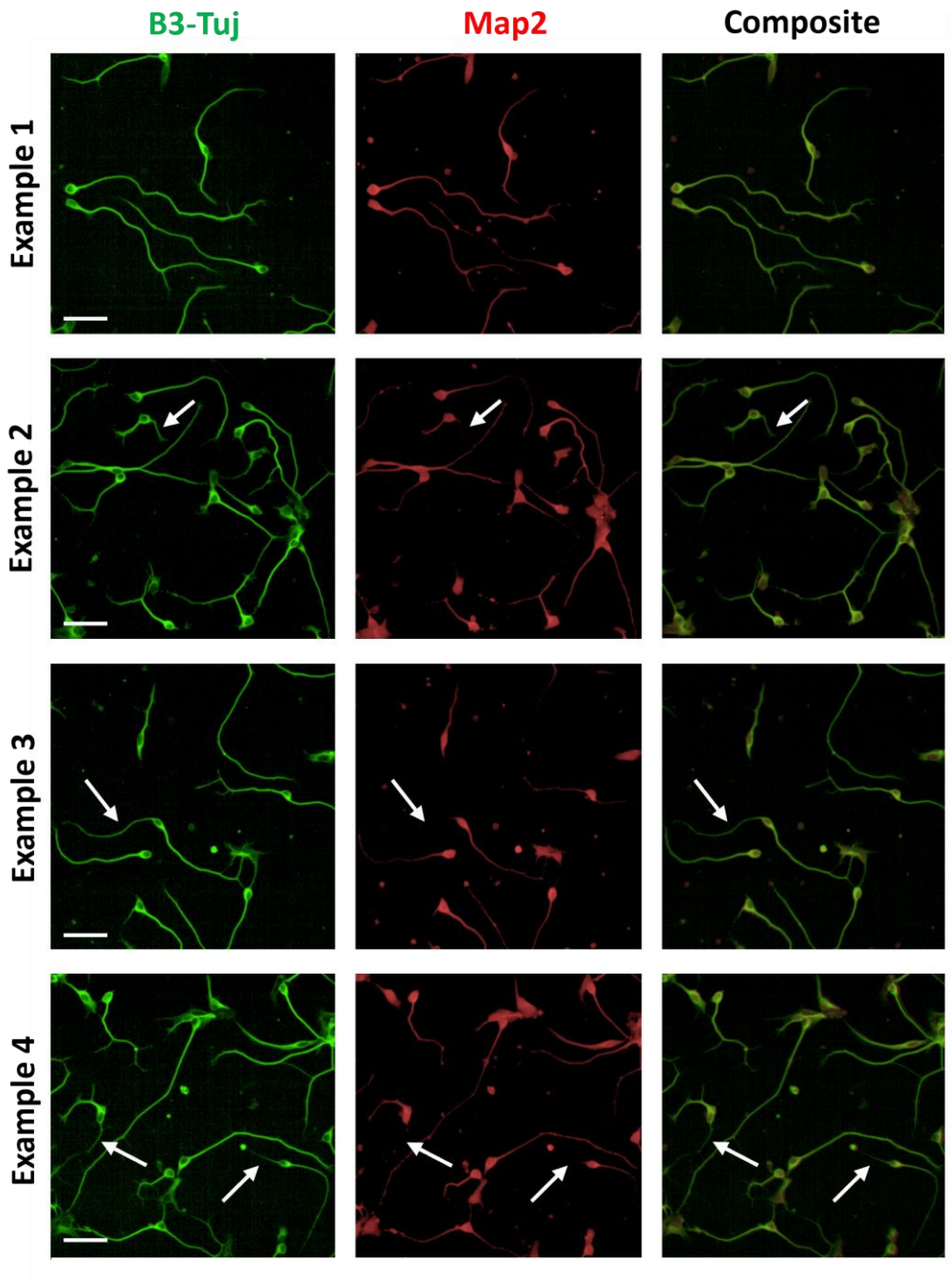


***Figure 9.29 Day-12 motor neuron neurites are mostly positive for Map2***

Motor neurons fixed on day 12 of differentiation, 20 hours after dissociation, were probed for the pan-neuronal marker $\beta$3-Tubulin (green) and the dendritic marker Map2 (red). White arrows indicate neurites positive for $\beta$3-Tubulin in the absence of Map2 signal. Scale bar represents 200µm.

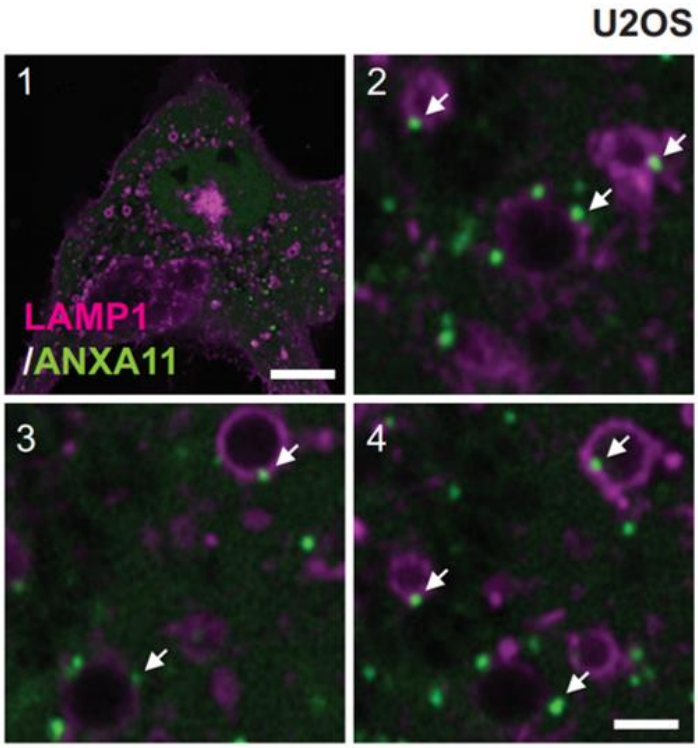


***Figure 9.30 Lamp1 vesicles associated with Annexin A11 in U2OS cells***

Taken from (Liao et al., 2019). Fluorescently tagged Lamp1-HaloTag positive vesicles (magenta) were shown to harbour small Annexin A11-mEmerald (green) puncta at the edge of vesicles in heat-shocked U2OS cells, mirroring the staining pattern seen in Figure 6.16. (1) A U2OS cell. (2-4) Zoomed in regions of (1). Scale bar in (4) represents 1µm.

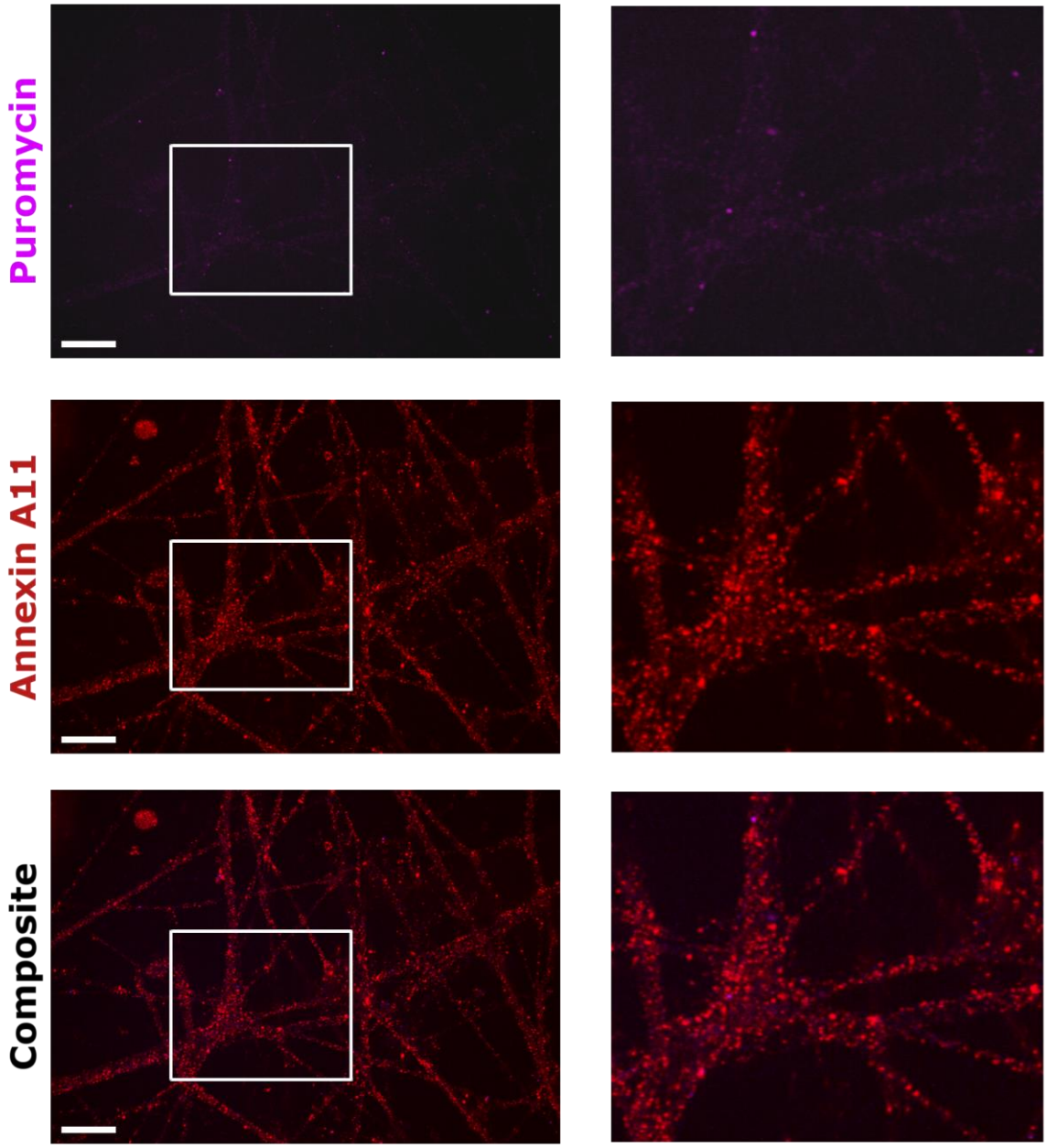


***Figure 9.31 Ribopuromycylation untreated control***

Untreated control motor neurons were fixed and incubated with antibodies detecting puromycin (magenta) and Annexin A11 (red). Some unspecific binding from the puromycin antibody is detected, however the signal is reduced in comparison to motor neurons subject to ribopuromycylation (6.3.3). Scale bar represents 10µm.

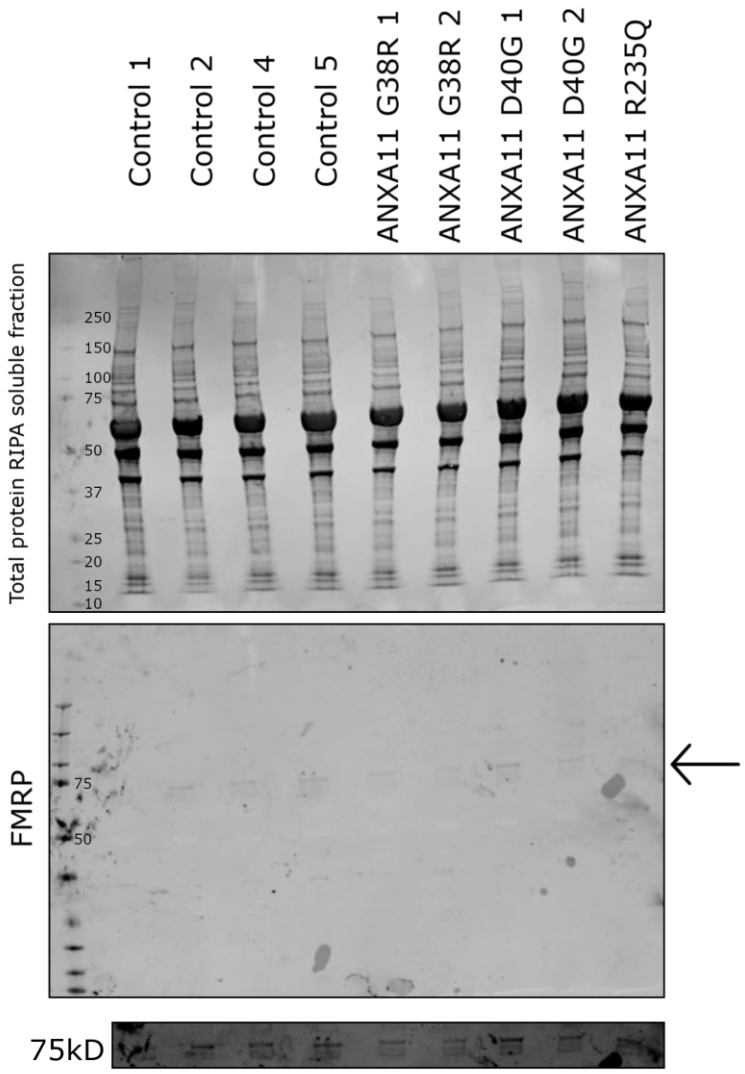


***Figure 9.32 Poor FMRP protein detection in western blotting***

Motor neurons were harvested in RIPA buffer on day 17 of differentiation and separated via western blot. Total protein stain indicates sufficient protein loading. Incubation with an FMRP antibody resulted in extremely feint protein band detection, the expected band indicated by a black arrow, which was not quantifiable in contrast adjusted images due to co-enhancement of background staining (bottom panel).

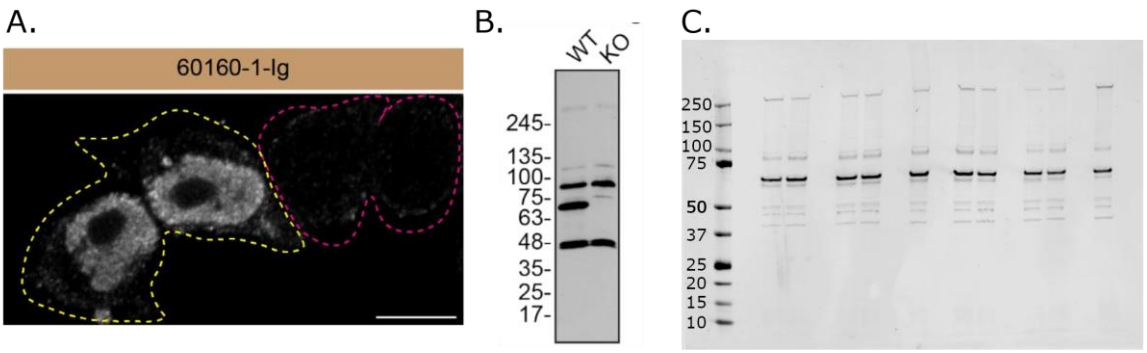


***Figure 9.33 FUS antibody specificity***

Characterisation of the FUS antibody 60160-1-1g was included in (Alshafie et al., 2021), including (A) staining in WT HeLa (highlighted with yellow) and *FUS* knockout HeLa (highlighted with red) which showed specific staining, and (B) western blotting of WT and FUS knockout HeLa which highlighted some unspecific protein detection. (C) Western blot detecting FUS protein in 17-day old motor neurons, as shown in Figure 6.32, with the entire blot shown to highlight detection of some unspecific bands, which were not included in quantification.